University of Glasgow

Synthesis and Characterisation of Cerium Based Nanocomposites

Bradley Wilson

Submitted in fulfilment of the requirements for degree of Doctor of Philosophy

School of Chemistry
College of Science and Engineering
University of Glasgow

September 2022

Abstract

This thesis presents the novel, solution based, single step methodology of reactive infiltration (RI) as a way of synthesising cerium based nanoparticles (CeNP) inside metal organic framework (MOF) structures. Through the complementary precursor-host pairing, the highly basic CeN''_3 precursor reacts spontaneous within the protic MOF808 host structure, yielding the composite: CeNP@MOF808. The CeNP@MOF808 was fully characterised using a number of spectroscopic techniques, demonstrating that the structural integrity of the MOF808 host remains unchanged following the RI process, specifically the crystalline arrange and high surface area of MOF808 are retained. A combination of XAS, XPS and EELS spectroscopies demonstrated that the CeNP@MOF808 composite consists of both Ce^{3+} and Ce^{4+} oxidation states, in a 3:1 respectively, with a surface Ce ions all existing in the 3+ state.

Post-synthetic modifications, thermal and oxidative, of CeNP@MOF808 are presented, along with spectroscopic characterisation of the physio-electronic properties of the modified composites. A notable link between the microstructure of the composite and electronic Ce^{3+}:Ce^{4+} structure is observed whereby thermal and oxidative post-synthetic modifications that resulted in the loss of MOF808 crystalline arrangement exhibited a concurrent reduction in the Ce^{3+} proportions.

Given the redox active nature of the Ce^{3+}:Ce^{4+} couple, the CeNP@MOF808 composite was screened as a possible catalyst for the decomposition of the nerve agent simulant dimethyl p-nitrophenylphosphate (DMNP). Through an standard optimised methodology it was demonstrated that the CeNP@MOF808 composite exhibited improve catalytic activity towards the hydrolysis of DMNP, relative to the control MOF808 host structure.

The synthesis and characterisation of lanthanide β-ketoiminate complexes $Y\{OC(Me)CHC(Me)N^iPr\}_3$ (**1**) and $Ce_2\{OC(Me)CHC(Me)N^iPr\}_6$ (**2**) was reported. Compound 2 is investigated as a possible broad spectrum precursor in the synthesis of CeO_2 based nanomaterials through thermal decomposition and RI with MOF808.

Declaration

The work described in this thesis was carried out at the University of Glasgow between 2018 and 2022 under the supervision of Dr Joy H. Farnaby. All the work submitted is my own, unless stated to the contrary and has not been previously submitted for any degree at this or any other university.

Bradley Wilson

September 2022

Acknowledgements

I would like to thank Dr Joy Farnaby for her dedication over the last four years, especially the time, supervision and guidance that she has provided. One does not simply learn facts, theories and figures to become a scientist, rather a true scientist adopts a certain state of thinking, a way of viewing the world that involves multilevel critical reasoning and analysis – coupled with a quiet, yet solid scepticism. It is through Dr Farnaby's example and mentorship – and a significant number of group meeting discussions – that I have developed this way of thinking, and I will carry it with me for the rest of my life.

It is often in casual discussion with others that true scientific advances are made, and in this respect I would like to thank Dr Samuel Horsewill for his advice and insights over the last 3 years of my PhD studies.

A special acknowledgment to Tajrian Chowdhury who started as a BSc student, working on many of the initial studies featured in this thesis – and whom I now consider a good friend.

A special homage also to University of Glasgow, College of Science and Engineering for funding my PhD *via* the college scholarship programme.

Finally a special thanks to my Grandmother, and particularly my Mother who has sacrificed endlessly to ensure that I had the opportunities that come rarely to a boy growing up on a council scheme in Lanarkshire.

Thesis Contributions

The best science is achieved through collaboration. Some of the work detailed in this thesis was performed in collaboration with others. Listed below are the details of collaboration.

- MOF808 synthesis and surface area characterisation *via* N_2 adsorption isotherms was performed by Ignas Pakamore, Forgan Group, University of Glasgow.
- SEM measurements acquired by Peter Chung, School of Geographical & Earth Sciences ,University of Glasgow.
- ICP-OES measurements performed by Stephen Goodall, MEDAC Ltd.
- Elemental microanalysis measurements performed by Gangi Reddy Ubbara, University of Glasgow.
- Single crystal and powder X-ray diffraction measurements performed by Dr Claire Wilson, University of Glasgow.
- EDX spectroscopy measurements performed by James Gallagher, University of Glasgow.
- Raman spectroscopy measurements performed by Dr Angela Daisley, University of Glasgow.
- XAS measurements were performed at the Diamond Lightsource Synchrotron, Research Complex Harwell, by beamline scientists Dr Nitya Ramanan and Dr June Callison; time provided by the Catalysis Hub. XANES and EXAFS analyses performed by Dr Emma Gibson and Lucy Costley-Wood using Athena software package.
- XPS measurements, precursor TGA profiles and PXRD acquired by Dr Caroline Knapp, University College London.
- STEM and EELS measurements performed by Dr Donald Maclaren, University of Glasgow.
- Statistical analysis of DMNP hydrolysis rates performed in collaboration with Dr William Peveler.

Abbreviations

NP – Nanoparticle

MOF – Metal organic framework

BTC – benzene tricarboxylate

BDC – benzene dicarboxylate

RI – Reactive infiltration

N'' – $N(SiMe_3)_2$

OTf – O_3SCF_3

TTMS – $Si(SiMe_3)_4$

THF – Tetrahydrofuran

DMSO – Dimethyl sulfoxide

NMR – Nuclear magnetic resonance

SEM – Scanning electron microscopy

EDX – Energy dispersive X-ray

ICP-OES – Inductively coupled plasma optical emission spectroscopy

PXRD – Powder X-ray Diffraction

TGA – Thermal gravimetric analysis

IR – Infra red

FT – Fourier transform

ATR – Attenuated total reflectance

wt% – Weight percentage

BET – Brunauer, Emmett and Teller

eqv – Equivalents

std. dev. – Standard deviation

λ – Wavelength

eV – Electron volt

XAS – X-ray absorption spectroscopy

XANES – X-ray absorption near edge structure

EXAFS – Extended X-ray absorption fine structure

TEM – Transmission electron microscopy

STEM – Scanning transmission electron microscopy

HAADF – High angle annular dark field

EELS – Electron energy loss spectroscopy

UV – Ultraviolet

Cp – Cyclopentadienyl (C_5H_5)

Bu – Butyl (C_4H_9)

^{i}Pr – Isopropyl ($CHMe_2$)

DMNP – Dimethyl *p*-nitrophenylphosphate

$t_{1/2}$ – Time taken for half of DMNP to be hydrolysed

μ_{eff} – Effective magnetic moment

Table of Contents

1 Introduction

1.1 Rare Earth Elements

The lanthanides, denoted by the generalised chemical symbol 'Ln', are the 15 elements from lanthanum to lutetium and are ubiquitous in the modern world with various applications, particularly in the field of electronics.[1] Often the group 3 metals scandium and yttrium are considered alongside the lanthanides due to their physical and chemical similarities, and the term 'Rare Earth Elements' (REE) is typically applied to describe the lanthanide series and group 3 (see Figure 1.1).

Periodic Table of the Elements

1 H Hydrogen 1.0079																	2 He Helium 4.0026
3 Li Lithium 6.941	4 Be Beryllium 9.0122											5 B Boron 10.81	6 C Carbon 12.011	7 N Nitrogen 14.007	8 O Oxygen 15.999	9 F Fluorine 18.998	10 Ne Neon 20.179
11 Na Sodium 22.99	12 Mg Magnesium 24.305											13 Al Aluminium 26.982	14 Si Silicon 28.086	15 P Phosphorus 30.974	16 S Sulfur 32.06	17 Cl Chlorine 35.453	18 Ar Argon 39.948
19 K Potassium 39.098	20 Ca Calcium 40.08	21 Sc Scandium 44.956	22 Ti Titanium 47.9	23 V Vanadium 50.941	24 Cr Chromium 51.996	25 Mn Manganese 54.938	26 Fe Iron 55.847	27 Co Cobalt 58.933	28 Ni Nickel 58.71	29 Cu Copper 63.546	30 Zn Zinc 65.38	31 Ga Gallium 69.72	32 Ge Germanium 72.59	33 As Arsenic 74.922	34 Se Selenium 78.96	35 Br Bromine 79.904	36 Kr Krypton 83.8
37 Rb Rubidium 85.468	38 Sr Strontium 87.62	39 Y Yttrium 88.906	40 Zr Zirconium 91.22	41 Nb Niobium 92.906	42 Mo Molybdenum 95.94	43 Tc Technetium (98)	44 Ru Ruthenium 101.07	45 Rh Rhodium 102.91	46 Pd Palladium 106.4	47 Ag Silver 107.87	48 Cd Cadmium 112.41	49 In Indium 114.82	50 Sn Tin 118.69	51 Sb Antimony 121.75	52 Te Tellurium 127.6	53 I Iodine 126.9	54 Xe Xenon 131.3
55 Cs Caesium 132.91	56 Ba Barium 137.33	57 *La Lanthanum 138.91	72 Hf Hafnium 178.49	73 Ta Tantalum 180.95	74 W Tungsten 183.85	75 Re Rhenium 186.21	76 Os Osmium 190.2	77 Ir Iridium 192.22	78 Pt Platinum 195.09	79 Au Gold 196.97	80 Hg Mercury 200.59	81 Tl Thallium 204.37	82 Pb Lead 207.2	83 Bi Bismuth 208.98	84 Po Polonium (209)	85 At Astatine (210)	86 Rn Radon (222)
87 Fr Francium (223)	88 Ra Radium (226)	89 †Ac Actinium (227)	104 Rf Rutherfordium (267)	105 Db Dubnium (268)	106 Sg Seaborgium (271)	107 Bh Bohrium (272)	108 Hs Hassium (270)	109 Mt Meitnerium (276)	110 Ds Darmstadtium (281)	111 Rg Roentgenium (280)	112 Cn Copernicium (285)	113 Nh Nihonium (284)	114 Fl Flerovium (289)	115 Mc Moscovium (288)	116 Lv Livermorium (293)	117 Ts Tennessine (294)	118 Og Oganesson (294)

58 Ce Cerium 140.12	59 Pr Praseodymium 140.91	60 Nd Neodymium 144.24	61 Pm Promethium (145)	62 Sm Samarium 150.4	63 Eu Europium 151.96	64 Gd Gadolinium 157.25	65 Tb Terbium 158.93	66 Dy Dysprosium 162.5	67 Ho Holmium 164.93	68 Er Erbium 167.26	69 Tm Thulium 168.93	70 Yb Ytterbium 173.04	71 Lu Lutetium 174.97
90 Th Thorium 232.04	91 Pa Protactinium 231.04	92 U Uranium 238.03	93 Np Neptunium (237)	94 Pu Plutonium (244)	95 Am Americium (243)	96 Cm Curium (247)	97 Bk Berkelium (247)	98 Cf Californium (251)	99 Es Einsteinium (252)	100 Fm Fermium (257)	101 Md Mendelevium (258)	102 No Nobelium (259)	103 Lr Lawrencium (262)

Figure 1.1: Periodic Table of Elements with Rare Earth Elements (REE) highlighted yellow.

The lanthanide elements exhibit distinctly unique chemical and physical properties – particularly magnetic and optical properties that originate from their specific f-electronic configuration.[2] As such, it is vital to understand the f-orbitals to in order to explain, manipulate and expand the chemistry and physics of the lanthanides. The lanthanides are the lightest elements which occupy the 4f orbitals. However, the f-orbitals do not extend beyond the 5p and 5s orbitals, giving them a 'core-like' character and minimising their interactions ligands. This results in the lanthanide elements mainly exhibiting ionic bonding, where the sterics of the ligand and ionic radius of the lanthanide dominate chemical properties. The general (shortened) electronic structure of the lanthanides is written as $[Xe]6s^2 5d^1 4f^n$, where n = 0 for Ln = La and n = 14 for Ln = Lu. The 4f orbitals are largely inaccessible to oxidation due

to their aforementioned core-like nature, therefore upon oxidation of lanthanides it is electrons residing in the higher-energy 6s and 5d orbitals that are removed first. Thus, in the majority of cases, the lanthanides preferentially form the 3+ (trivalent) oxidation state with the electronic structure of $[Xe]4f^n$.

As electrons are added to the core-like f-orbitals across the series, the lanthanides exhibit a significant and uniform decrease in the ionic radii of the trivalent ions across the series, this is known as the lanthanide contraction (see Figure 1.2). This is primarily due to the poor shielding effect of additional f-electrons not being able to compensate for the increasing nuclear charge across the lanthanide series.

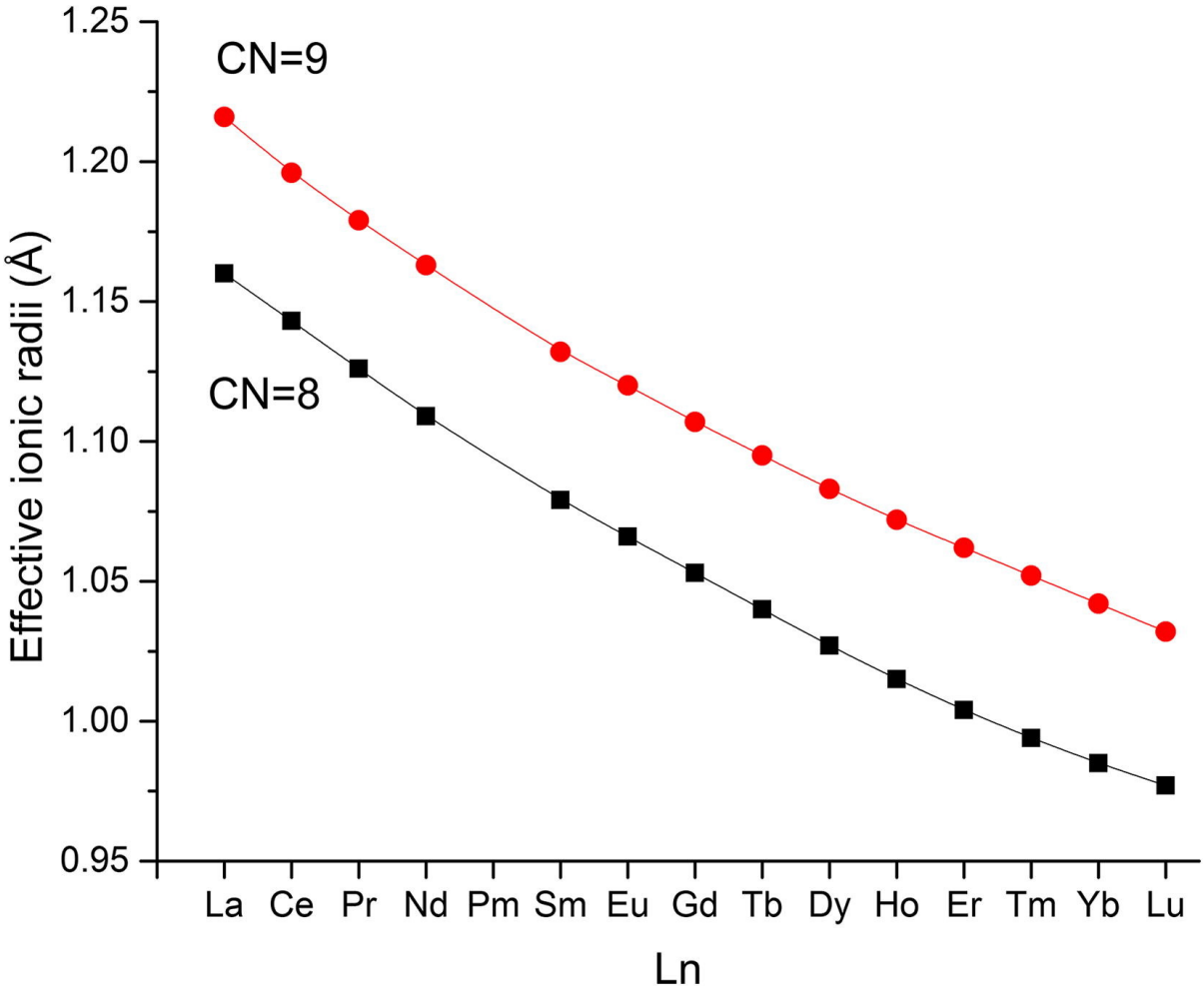

Figure 1.2: Lanthanide contraction: from La to Lu the ionic radius of the atom decreases with increasing atomic number.[3]

This smooth decrease in ionic radius of the lanthanides has non-trivial outcomes in terms of chemical properties of the lanthanides. For example, the thermodynamic stability (quantified

through stability constants) of lanthanide complexes with ethylenediaminetetraacetate (EDTA) ligands, $[Ln(EDTA)]^-$, are positively correlated with the lanthanide ionic radius.[4] Therefore, given that the chemistry of lanthanide materials is largely a function of the ionic radius of the specific lanthanide, it is essential that attention is paid to influence that ionic radius can have on the chemistry of the material and potential applications.

Oxidation states other than Ln^{3+} are accessible. When either oxidation or reduction would result in an empty ($4f^0$), half-filled ($4f^7$) or full ($4f^{14}$) set of 4f orbitals, this can stabilise the 2+ or 4+ oxidation states significantly due to the symmetry of the orbital configurations. For example, Ce^{4+} ($4f^0$) is stabilised by this mechanism, meaning that cerium based materials are often termed to as being 'redox active', being able to shift between the Ce^{3+} and Ce^{4+} oxidation states. This thesis will set out the development of a novel methodology that allows for the synthesis of cerium based nanomaterials, particularly the redox active compound CeO_2, in Chapter 2, 3, 4 and 5. Therefore, the subsequent introduction will set out the general chemistry of bulk CeO_2, how the chemistry of CeO_2 is influenced by reductions to the nanoscale and where this finds applications in the modern world. This should serve to set the context in which a large amount of interest is being focused on the development of nanoscale cerium materials, including in this thesis.

1.2 Chemistry of Ceria and Nanoceria

The structure and chemistry of ceria is well understood, with solid state CeO_2 adopting a fluorite type lattice structure (see Figure 1.3). In stoichiometric CeO_2, every cerium ion is in the 4+ oxidation state. Like other ionic solids, CeO_2 is susceptible to intrinsic defects, in sub-stoichiometric CeO_{2-x} oxide anions are released in the form of molecular oxygen, leaving behind electrons that reduce the Ce ions to the 3+ oxidation state. This results in the generation of oxide vacancies, V_o which are essential to the applications of CeO_2 – particularly catalysis.[5] This is summarised below in Scheme 1.1, using the Kröger-Vink notation, where lower case indicated the position of the species in the CeO_2 lattice structure and dashes/circles show charge states.

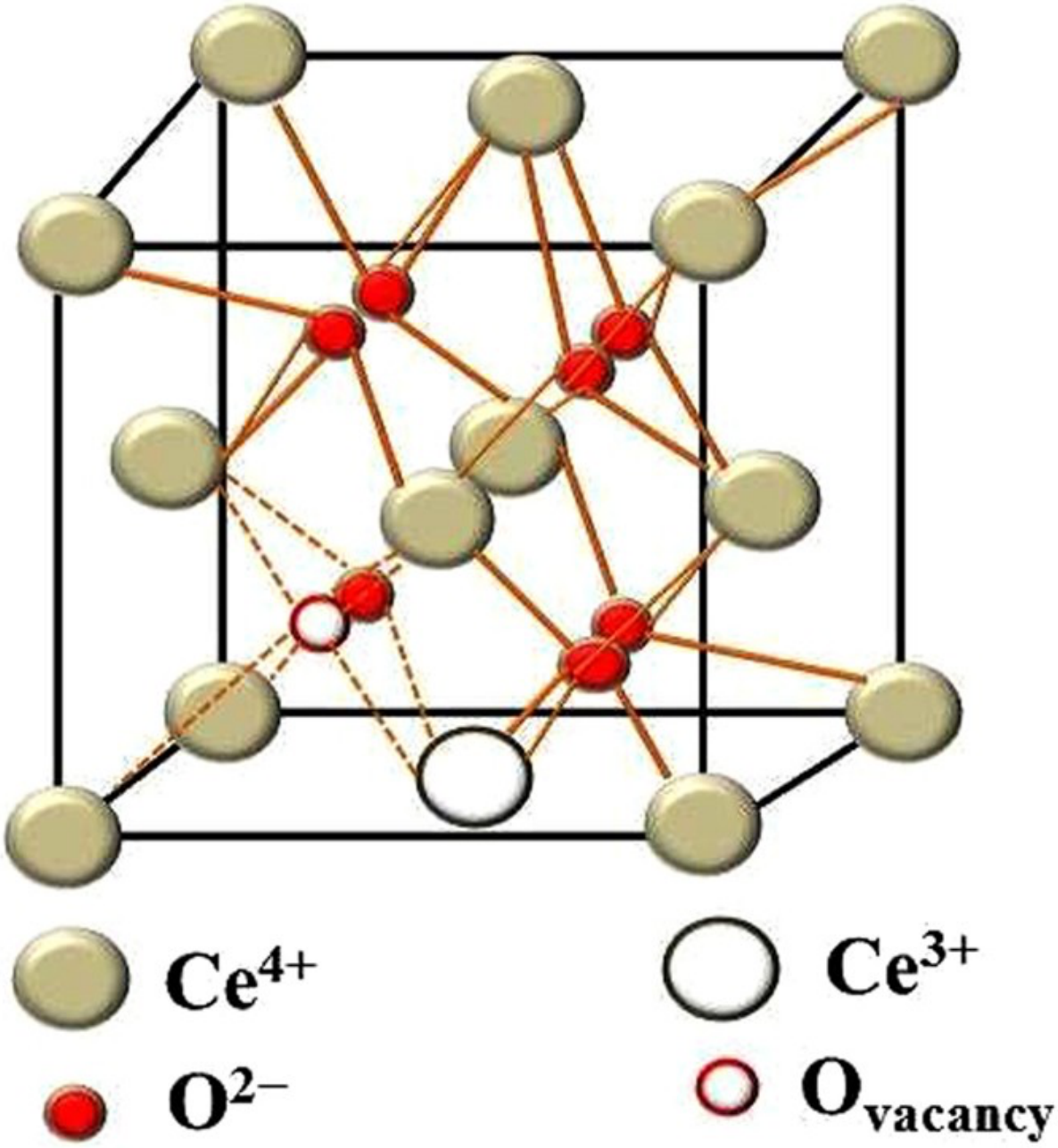

Figure 1.3: Fluorite lattice structure of solid state sub-stoichiometric CeO_{2-x}, showing a lattice vacancy.[6]

$$2Ce_{Ce} + O_o \rightleftharpoons 2Ce'_{Ce} + V_o^{\bullet\bullet} + \frac{1}{2}O_2$$

Scheme 1.1: Kröger-Vink notation for the generation of an oxygen vacancy within CeO_2. Where Ce' is a reduced (negative) valence state of Ce (*i.e.* 3+) and $V^{\bullet\bullet}$ is the oxidised (positive) residual vacancy.

The introduction of oxygen vacancies to the ceria crystal structure causes changes in the electronic band structure. Normally CeO_2 exists with a valence band composed of full 2p states (based on oxygen), a conduction based composed of empty 5d states (cerium based) and a narrow band within the bandgap made up of empty 4f states (cerium based). Oxygen vacancies formed within ceria cause the 4f band to become split into an occupied 4f band and an unoccupied 4f band (see Figure 1.4).[7]

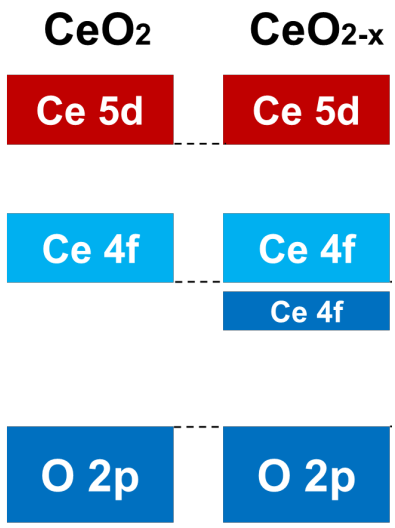

Figure 1.4: Electronic structure of CeO_2 and sub-stoichiometric CeO_{2-x}.[7]

Oxygen vacancies allow charge migration through the solid lattice making it a functional solid-state electrolyte for various applications. CeO_2 has found use in various applications: three way catalysts (TWC) for the oxidation of NO_x and CO in exhaust fumes,[8] ionic conductors in solid fuel cells,[9] and UV absorber in cosmetic formulation.[10]

The word nano represents a fraction that indicates one billionth of a unit quantity (*i.e.* 10^{-9}), where nanoparticles are usually defined as particles with dimensions less than 100 nm.[11] It is a general property of materials than when they are taken from the bulk to the nanoscale dimension, a change in chemical and physical properties can often be observed. These novel properties of the nanoparticles often find new applications,

particularly in the field of science and technology, see Table 1.1 for a non-exhaustive list of examples of applications using nanoparticles.

Table 1.1: Examples of nanoparticles, associated properties and applications.

Nanoparticle	Property	Application	Ref
Quantum Dots (*e.g.* ZnSeTe)	Light Emission	Light emitting diode (LED) displays	[12]
Fe_3O_4	Superparamagnetism	MRI contrast agents	[13]
TiO_2	Photocatalytically active	Photocatalytic degradation of small organic molecules	[14]

On the nanoscale, nanoparticles of ceria exhibit more oxygen vacancies, large surface-to-volume ratios, high surface areas, expanded lattice dimensions and porous morphologies. This improves the catalytic activity of ceria significantly. For example, ceria NPs synthesised *via* precipitation of Ce^{3+} salts in NH_3 solution and templated to a biopolymer exhibited catalytic activity towards CO conversion at temperatures 30 – 60 °C lower than commercial bulk ceria.[15] The expansion of the lattice volume for ceria NPs was postulated to be a major driving force in this reduction in conversion temperature, by aiding the formation of oxygen vacancies on the surface of the ceria.[15]

Many of these applications arise due to the ability of cerium in cerium dioxide to alternate between the Ce^{3+} and Ce^{4+} oxidation states. The ease at which cerium can shuttle between these two oxidation states, and the relative proportions is a key factor in determining the performance of cerium oxide nanoparticles in a particular application. For example, López *et al* published a study into the relationship between the proportion of Ce^{3+} states in ceria nanoparticles and the catalytic activity of the nanoparticles towards toluene oxidation.[16] It was discovered that with a higher

proportion of Ce^{3+} states (as determined *via* X-ray photoelectron spectroscopy), the nanoparticles exhibited higher catalytic activity, see Figure 1.5 below. This is not unexpected given that the higher proportion of Ce^{3+} will concurrently result in a higher proportion of oxygen vacancies in the ceria lattice structure, which are assumed to be the catalyst's active site.[16]

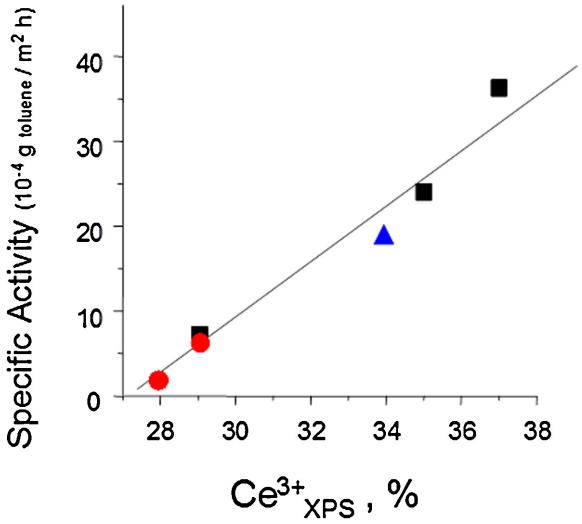

Figure 1.5: Catalytic activity of ceria nanoparticles, rods (■), cubes (●) commercial (▲), towards the oxidation of toluene vs. Ce^{3+} proportions determined via XPS.[16]

The ability to defect engineer ceria based nanomaterials has therefore become of increasing importance. The number of Ce^{3+} states, and therefore the number of oxygen vacancies in ceria nanomaterials is dependent on a number of variables. One significant factor is the shape of the nanoparticles, as seen in Figure 1.5 ceria nanoparticles in the form of rods tend to have higher proportions of Ce^{3+} states and consequently have higher catalytic activities. This is a reflection of the rods having a higher surface area, and therefore: (a) greater exchange with atmospheric oxygen can take place and (b) a larger number of active sites are exposed. A second important factor in controlling the number of Ce^{3+} states is the dimensions of the ceria nanoparticles (controlling for shape). Wu *et al* synthesised a series of ceria based nanoparticles, of varying sizes, through vapour phase condensation.[17] Using electron energy loss spectroscopy (EELS), it was possible to quantify the Ce^{3+} states, which were

expressed in terms of an outer layer of Ce_2O_3 surrounding the core layer of CeO_2. As the nanoparticle dimensions were reduced, the thickness of the Ce_2O_3 layer, and therefore the number of Ce^{3+} states, increased exponentially (see Figure 1.6), being fully reduced below 3 nm.[17]

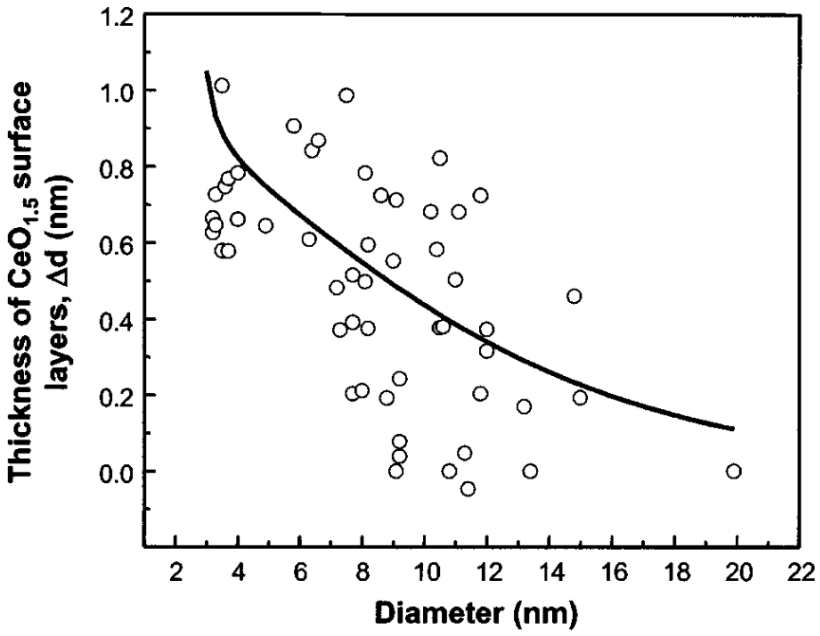

Figure 1.6: The Ce_2O_3 layer thickness as a function of particle size.[17]

Tsunekawa *et al* published a study which involved synthesising ceria nanoparticles *via* low temperature microemulsion.[18] The same trend was observed in that reducing the dimensions of the ceria nanoparticles resulted in an increase in the proportion of Ce^{3+} states. However, comparing the trends quantitatively, it was shown that the ceria nanoparticles synthesised by Tsunekawa *et al* showed a steeper rise in the number Ce^{3+} states, with decreasing particle dimension, compared with those synthesised by Wu *et al*.[17,18] This highlights the importance of the synthetic methodology to the redox activity of the ceria nanoparticles formed. Different synthetic methodologies will result in the formation of nanoparticles of different shapes, and will have specific surface face exposed. Ceria particles that have the (100) crystal plane exposed are more susceptible to oxygen vacancy formation than those with the more stable (110) and (111) planes exposed.[17-19]

It is possible to introduce oxygen vacancies to the ceria lattice structure by addition of other rare earth elements.[20] This extrinsic doping mechanism can be represented by the Kröger-Vink notation shown in Scheme 1.2. Here the rare earth element (REE) substitutes into the CeO_2 lattice structure at substitutional sites.[20] The however, for every two Ce^{4+} ions substituted for two REE^{3+} ions, only three oxide anions are available. This yields a single oxygen vacancy.

$$REE_2O_3 \longleftrightarrow 2REE'_{Ce} + V_o^{\bullet\bullet} + 3O_o^x$$

Scheme 1.2: Kröger-Vink notation for the substitution of REE ions into the CeO_2 lattice structure, yielding an oxygen vacancy.

The importance of the lanthanide contraction is brought into sharp focus with this example in that as the size of the ionic radius decreases, the migration energy of the lattice oxygen vacancies also decreases, yielding higher ionic conductivities. In a separate study, Pr^{3+} and Gd^{3+} ions were substituted into CeO_2 structures to investigate what effect the doping of rare earth elements would have on the catalytic activity of the doped ceria towards the steam reforming of methane.[21] As expected based on previous computation studies showing decreasing energy of oxygen vacancy migration with decreasing rare earth ionic radius,[20] the smaller Gd^{3+} ion yielded a superior catalyst ($Ce_{0.9}Gd_{0.1}O_{2-x}$) compared to the larger Pr^{3+} ion ($Ce_{0.9}Pr_{0.1}O_{2-x}$). XPS studies of the substituted catalysts also revealed the $Ce_{0.9}Gd_{0.1}O_{2-x}$ to have a higher proportion of Ce^{3+} oxidation states, compared with $Ce_{0.9}Pr_{0.1}O_{2-x}$, which is shown to be conducive to superior catalytic abilities (see Table 1.2).

Table 1.2: Selected Ce^{3+} % (determined via XPS) and methane conversion rates for CeO_2, $Ce_{0.9}Gd_{0.1}O_{2-x}$ and $Ce_{0.9}Pr_{0.1}O_{2-x}$.[21]

Catalyst	Ce^{3+} %	Methane Conversion ($\mu mol\ s^{-1}\ m^{-2}$)

CeO_2	33	0.16
$Ce_{0.9}Gd_{0.1}O_{2-x}$	31	0.20
$Ce_{0.9}Pr_{0.1}O_{2-x}$	17	0.12

Therefore being able to monitor and modulate the Ce^{3+}/Ce^{4+} proportions is of significant importance when designing ceria based materials. As described in previous examples, Ce^{3+} oxidation state proportions, and inferred oxygen vacancy concentration, are often determined through spectroscopic techniques such as XPS and EELS.[16-18,21] However, it has been observed in literature that these spectroscopic methods when employed alone are not sufficient to gauge confident estimates of the Ce^{3+} proportions.[22] When analysing a serious of ceria nanoparticle samples of varying dimensions, it was found that there is variation in Ce^{3+} proportions estimated from EELS and XPS, see Figure 1.7.

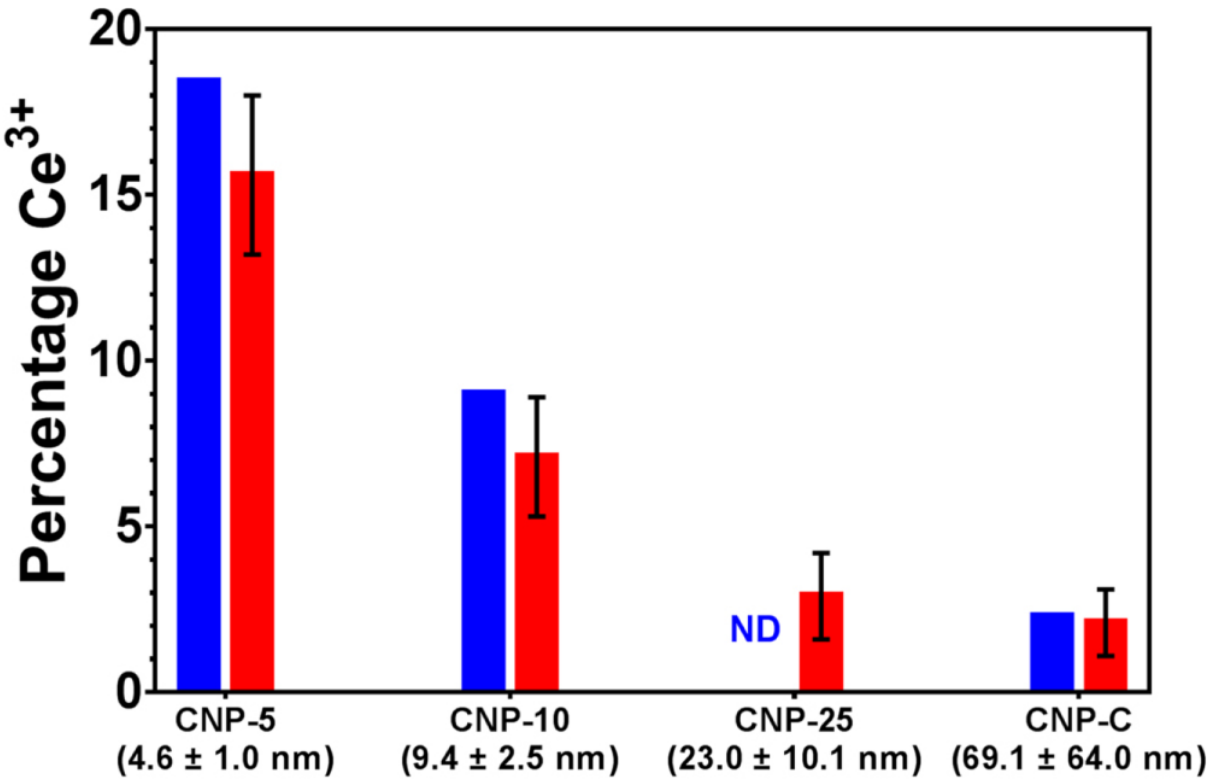

Figure 1.7: Percentage Ce^{3+} states of commercial ceria nanoparticle samples determined by XPS (blue) and EELS (red) with respect to TEM-determined average particle size.[22]

The authors concluded that using a combination of spectroscopic techniques, so called 'orthogonal analysis' was more appropriate when characterising ceria oxidation states. This shall be explored in greater detail in Chapter 3.

The ability to control the assembly of ceria nanoparticles is key, it has been shown in a limited number of studies that ceria type nanoparticles and clusters can be formed inside host frameworks, namely metal organic frameworks. The second half of this thesis introduction will focus on these host materials and cerium based nanocomposites formed with metal organic frameworks, before introducing the novel methodology of reactive infiltration in Chapter 2 which allows for the synthesise of cerium based nanoparticles inside MOF structures.

1.3 Metal Organic Frameworks

Porous materials have been a topic of research within the chemical sciences for hundreds of years. In 1756 the Swedish mineralogist Alex Cronstedt discovered the first zeolite structure, stellerite, $(Ca_{4.03}Mg_{0.01}Na_{0.03}K_{0.11})$ $[Si_{27.81}Al_{8.19}O_{72}]\cdot 28.6H_2O$.[23] Zeolites are aluminosilicate structures whereby silicon atoms in orthosilicate networks are substituted for aluminium atoms, yielding a structure which is overall negatively charged. To balance the negative charge of the network, metal cations are incorporated into the structure. It is the variation of the positive metal ions, along with alterations in the silicate chain linkage topology, that give different zeolites. Zeolites can by synthesised synthetically, and have found applications as molecular sieves, whereby the pores sequestrate water molecules from various liquids, and as catalysts for various industrial reactions.[24] Zeolites are limited however in that their versatility, with surface areas restricted to several hundred m^2/g. This has led chemical scientists to explore the development of porous materials that are more modular in nature, allowing for greater versatility and ultimately larger surface areas. This was achieved in the discovery of highly porous materials knowns as metal-organic frameworks.[25]

The term "Metal-Organic framework" (MOF) was put forward by Omar Yaghi in 1995 upon the discovery of an organic-inorganic hybrid porous material consisting of Co^{2+} metal centres coordinated to benzene-1,3,5-tricarboxylate (BTC) ligands.[26] MOFs are defined as 1-, 2-, or 3-

dimensional crystalline coordination networks consisting of repeating units of metal or metal-containing secondary building unites (SBU), also termed metal cluster nodes, linked together *via* organic struts, termed linkers. These novel organic-inorganic hybrid materials exhibit permanent porosity allowing for high internal surface area. The ability to select nodes and linkers has allowed for unprecedented control of the porous dimensions of the material and topological morphology. Omar Yaghi *et al* in 1999 went on to synthesise MOF-5 which consisted of Zn_4O cluster nodes, linked to three benzene-1,4-dicarboxylate (BDC) linkers, forming a regular well-ordered crystalline network, see Figure 1.8 below, with a surface area of 2,900 m^2/g.[27]

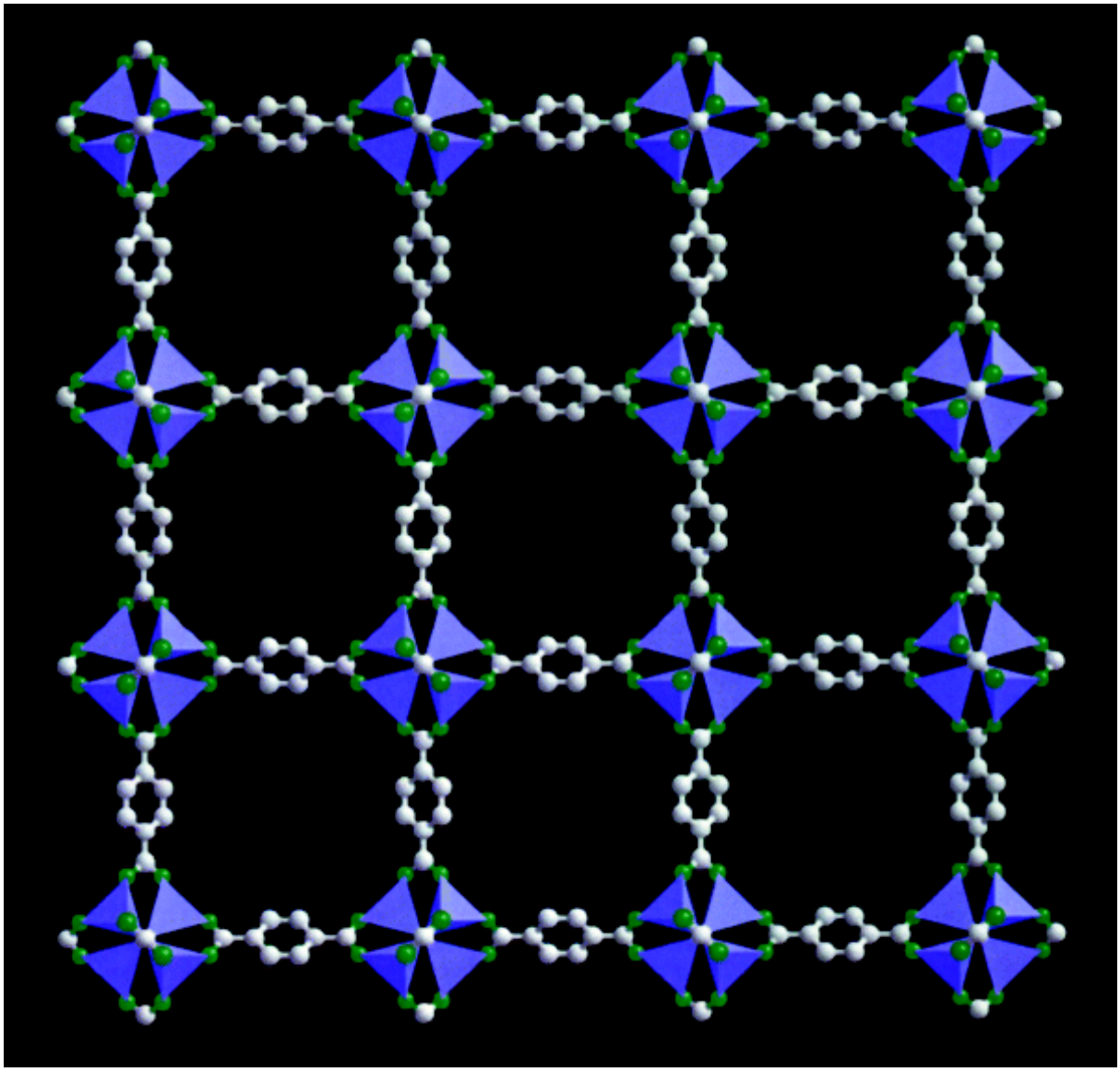

Figure 1.8: Representation of a {100} layer of the MOF-5 framework shown along the a-axis (C, grey; O, green). The ZnO4 tetrahedra are indicated in purple.[27]

At the time of writing, the highest surface area MOF reported in literature was NU-110, with a surface area of 7140 m^2/g.[28] This is approaching what is thought to be the theoretical ceiling on MOF surface areas, at 10500 m^2/g,[29] but leaves space for further development. The high surface area of MOFs is largely derived from their pore based network structures. The dimensions of the pores, like the surface area of the MOF, can be tuned by selecting the appropriate cluster node and linker. MOFs can exhibit more than one type of pore consisting of typically a primary pore/channel and a secondary smaller pore/channel. These pores can be explicitly one size or a combination of micro (<2 nm), meso (2-50 nm), or even macro porous (>50 nm).[30]

Many researchers have exploited MOF pores for applications including gas storage,[31,32] gas separation,[33,34] solid-phase microextraction,[35,36] water purification,[37] toxic chemical and heavy metal remediation chemical sensing,[38,39] drug delivery,[40] water splitting,[41] and energy storage.[42]

1.4 Chemistry of MOF808

Interest in Zr based MOFs began with the discovery of the MOF UiO-66 ($Zr_6O_4(OH)_4(BDC)_6$; BDC = benzene-1,4-dicarboxylate) published by Cavka *et al.* in 2008,[43] which displayed a remarkable robustness in its thermal stability (decomposed above 500 °C) and resistance to most chemicals. This stability is derived from their fcu structure, consisting of each $[Zr_6(\mu_3\text{-}O)_4(\mu_3\text{-}OH)_4]^{12+}$ cluster node fully connected by 12 BDC linkers. This provides a saturated, 12-coordinated cluster node where any deviation from this 12-coordination can be referred to as an unsaturated cluster node with one or more structural vacancies present – commonly referred to as 'missing linker'. MOF structures based on the Zr_6 cluster nodes have remained a benchmark standard for the development of new MOFs owing to their high surface area, well defined pore dimensions and ground breaking stability. However, although a fully 12-coordinated Zr_6 cluster nodes does impart great stability to the MOF structure, an unsaturated cluster node can often be desired since a lesser connected cluster will have more accessible metal sites. Hence, several MOFs have recently shown interesting catalytic properties due to structural vacancies.[44,45]

Such vacancies are achieved by structural defectivity or by the MOF's inherent topology. Examples of Zr-MOFs with inherent topological vacancies are DUT69 (10-coordinated),[46] NU-1000 (8-coordinated),[47] MOF808 (6 coordinated),[48] and NU-1400 (4-coordinated).[49] Specifically, MOF808 was first described by the Omar Yaghi *et al* in 2014, formed by solvothermal reaction of H_3BTC with $ZrOCl_2.8H_2O$ at 100 °C for 7 days in a sealed reaction container.[48] Although sharing the same Zr_6 cluster node as UiO-66, the crystal structure of MOF808 differs greatly, as it consists of only six tritopic linkers (BTC) coordinating each cluster node. This topology (spn) requires an additional six monotopic ligands (L) to be located in an equatorial belt around the cluster node to provide charge compensation: $Zr_6O_4(OH)_4(L)_6(BTC)_2$. These six non-structural ligands which have been described in the literature to be a mixture of formate, acetate, benzoate, H_2O and OH^- (see Figure 1.9 below), are relatively labile and therefore easily exchanged.[50-52] Therefore it is often common to think of MOF808 not as a single material, but rather as a family of materials with varying degrees of non-structural ligand substitution. Throughout the rest of this thesis MOF808, unless otherwise stated, will refer to the formulation whereby the non-structural ligands are formate.

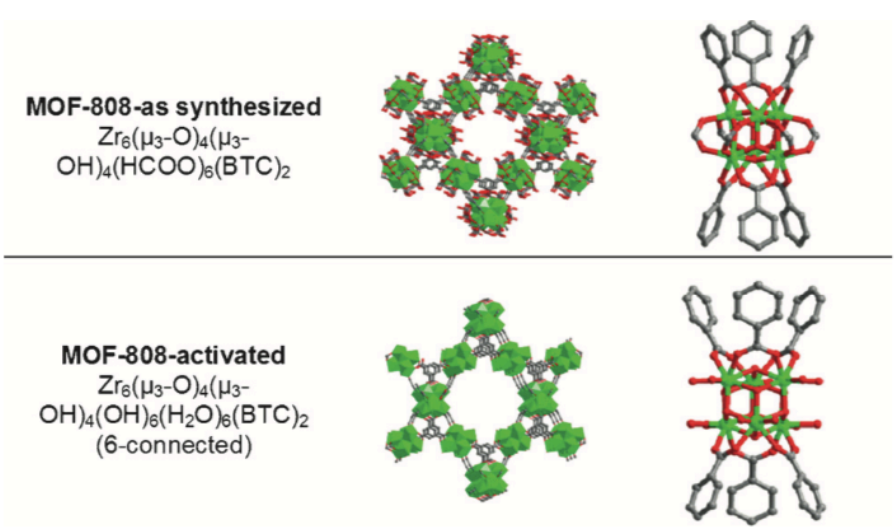

Figure 1.9: Formulae and cluster nodes of MOF808 and MOF808 where formate ligands have been substituted for hydroxo and aqua ligands.[53]

The topology of MOF808 is best described as corner-sharing tetrahedral subunits consisting of Zr_6 clusters on the vertices and linkers on the faces (Figure 1.10a). These form a network described with the spn topology with two pore shapes: a cage within each tetrahedral subunit

(Figure 1.10b) and one large adamantane-shaped pore with a pseudohexagonal pore window (Figure 1.10c).[54,55] MOF808 is therefore a microporous substance, with a smaller micropore at *ca.* 10Å and a larger micropore at 18Å.[56,57]

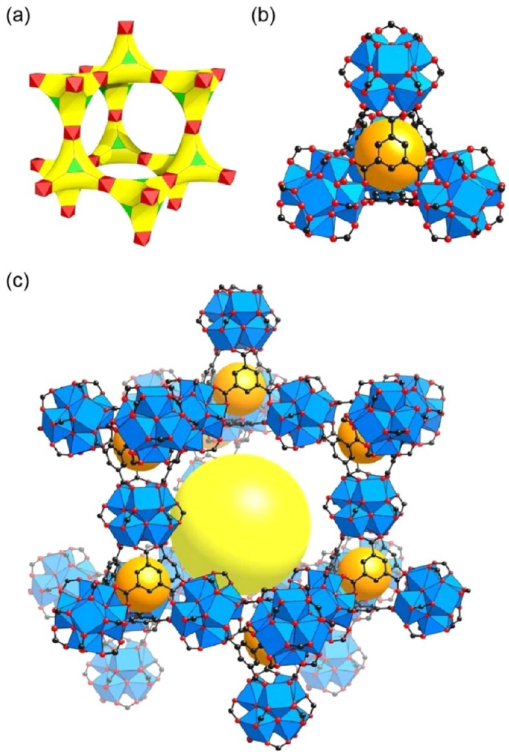

Figure 1.10: (a) condensed view of MOF808 tetrahedral subunits, (b) MOF808 tetrahedral subunit cage (highlighted orange), (c) Adamantane-shaped pore (highlighted yellow) surrounded by tetrahedral subunits.[48]

As a consequence of the geometry of MOF808, each non-structural ligand (*i.e.* formate) is pointing directly into a large pore. The ligand position ensures availability to guest molecules and, combined with the aforementioned lability of ligands, provides a reliable and effective way of introducing new functionality into the MOF. Several procedures have previously been developed to incorporate functionality such as metal-coordinating ligands,[58] proton conductivity,[46] and superacidity into MOF808.[59] It also presents a potential reaction site within the MOF808 pore, something which will be further explored in Chapter 2.

Indeed the permanently high surface areas and large, well defined pores of MOF808 make it an ideal candidate for the assembly of host-guest composites whereby guest molecules of

varying sizes and structures are introduced to the MOF808 host to form completely new novel materials with new exciting properties and applications.

1.5 Composites and Guest@MOF808 composites

A composite material can be broadly defined as combination of two or more different materials to form a new substance with properties that differ from the original combining materials.

MOFs have shown great potential in the formation of composite materials, where the pore sites can act as abundant adsorption sites for individual molecules, polymers and nanoparticles (NP), often denoted as guest@MOF systems.[60-63] Nanoparticles can be incorporated into the MOF structure through several mechanisms which fall into the binary categories of 'bottle-around-the-ship' or 'ship-in-a-bottle'.[64]

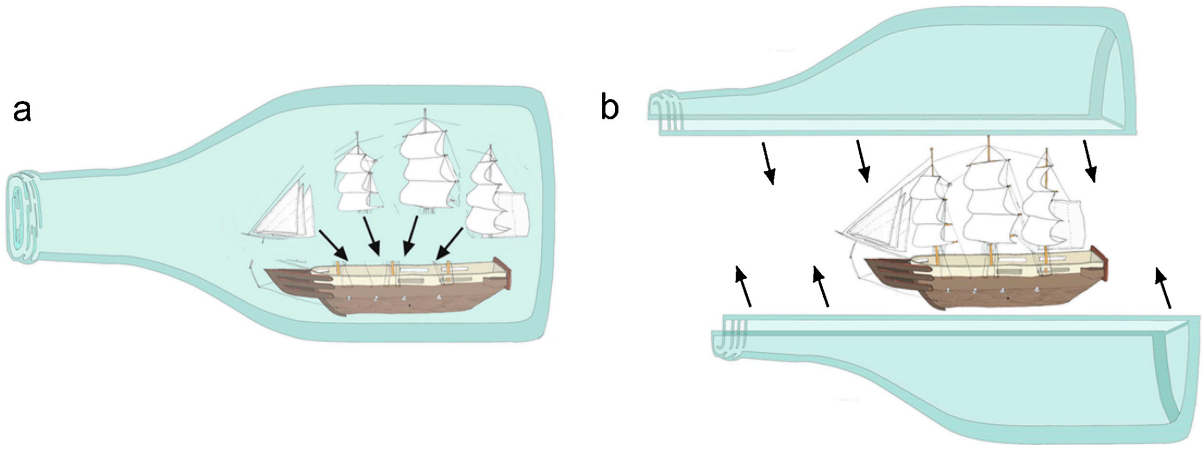

Figure 1.11: Schematic representation of the two broad methodologies for synthesising NP@MOF composites: (a) 'ship-in-a-bottle' and (b) 'bottle-around-a-ship'.[64]

The 'bottle-around-the-ship' methodology involves the templated synthesis of the MOF host structure around pre-formed nanoparticles. Incorporation of the nanoparticles using the 'ship-in-a-bottle' methodology often involves a two-stage process whereby precursor molecules are first allowed to percolate into the MOF structure and then subsequently 'activated' by an external input (e.g. heating, exposure to high energy light, microwave irradiation, application of a vacuum, addition

of a reducing agent, *etc*.) to self-assemble into nanoparticles of the metal within the precursor.[65] The 'ship-in-a-bottle' methods include solid grinding, solution infiltration, incipient wetness, vapour phase infiltration and plasma arc deposition.[64,65] Nanoparticles composited within the MOF structure can nucleate within the pores of the MOF and/or on the surface. The exact deposition of the particles within the matrix depends on the relative resistances to diffusion on the surface and the interior of the MOF, with diffusion limited internally due to narrow pores often resulting in nanoparticles being preferentially loaded onto the surface of the MOF.[65] Several catalytic systems have been developed whereby the activity of the nanoparticles is enhanced upon incorporation within the MOF structure.[65] Furthermore, the ordered network structure of the MOF offers a stable platform upon which further chemical modifications of the nanoparticles can be performed (*e.g.* oxidation, reduction, etc.).[66] This is of particular importance to redox active ceria nanoparticles which can exhibit a range of Ce^{3+}/Ce^{4+} proportions. Only one example has been reported in the literature that demonstrates the assembly of metal oxide nanoparticles (Fe_2O_3) onto the MOF structure in a one-step, low energy process.[67] The process works by the reaction Fe^{3+} salts with MOF structures featuring phenolic moieties that interact and allow Fe^{3+} to accumulate at the MOF surface and subsequently become hydrolysed forming Fe_2O_3.

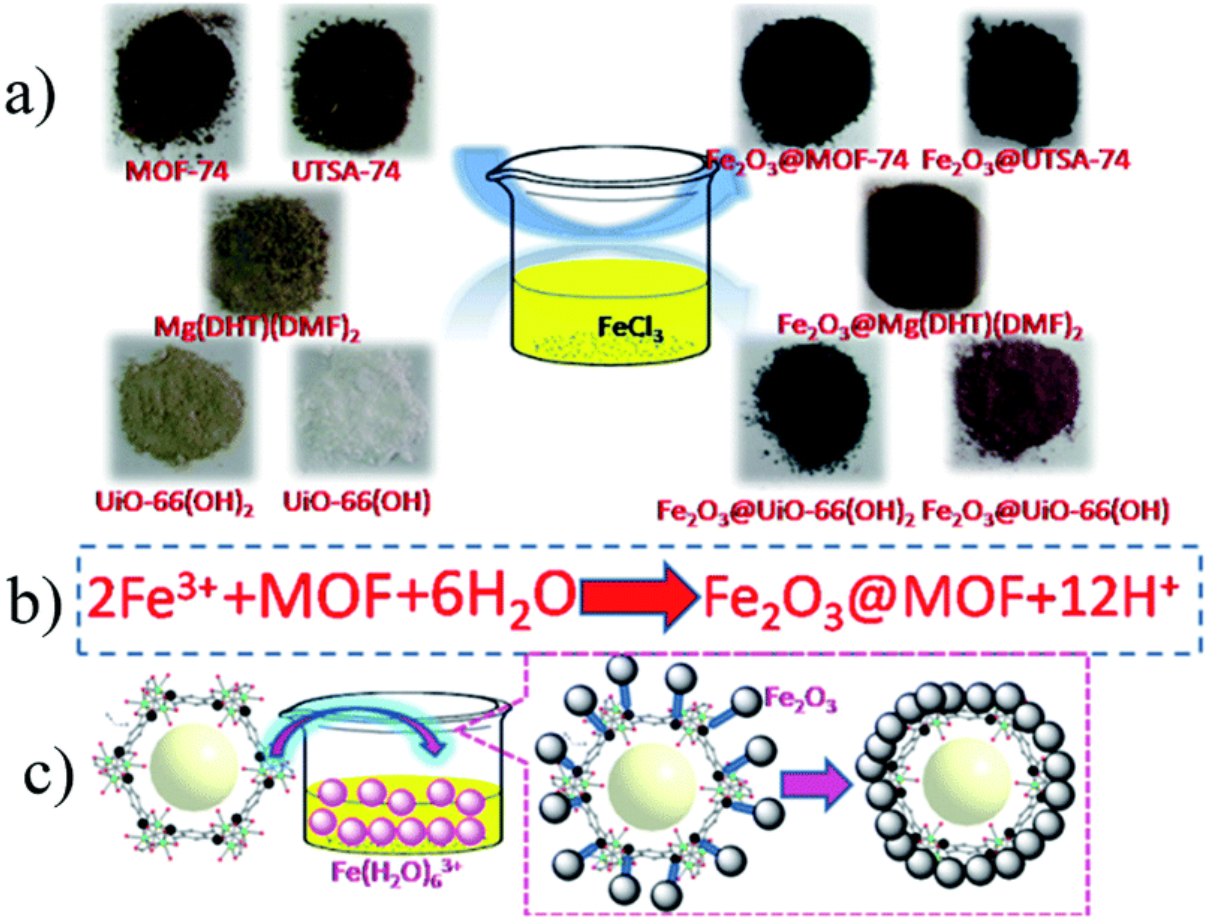

Figure 1.12: contact and enrichment when the MOF samples contact with the Fe^{3+} solution, where the inherent driving power derived from typical 'phenol-Fe^{3+}' coordination interactions largely accelerates the enrichment of Fe^{3+} on the MOF surface; deep hydrolysis and nucleation, where such enrichment of Fe^{3+} on the MOF surface causes the hydrolysis of Fe^{3+} for the nucleation of Fe_2O_3; and the final growth of Fe_2O_3 on the MOF surface to generate Fe_2O_3@MOF composites.[67]

No examples of one step methodologies have been reported for NP@MOF808 composite materials where the nanoparticles contain cerium (CeNP). However, several examples exist in the literature of CeNP@MOF composites whereby the composites are formed either through a 'bottle-around-a-ship' methodology or *via* a two-step 'ship-in-a-bottle' strategy, these are summarised in Table 1.3.

Kumaraguru *et al* published the synthesis of a CeNP@Cu-BTC composite formed *via* a 'bottle-around-a-ship' synthetic methodology.[68] CeNPs, in the form of CeO_2, were synthesised by the reaction of $CeCl_3$ with *Gloriosa superba* leaf extract at 80 °C for 4 – 6 hours, yielding a

precipitate of CeO_2 which was calcined at 400 °C for 2 hours. The CeNP were then subsequently dispersed in a solution of $CuCl_2$ and H_3BTC, precursors for the cluster nodes and linker of the MOF host, where upon the addition of triethylamine precipitation of the Cu-BTC is induced. The Cu-BTC assembles around the preformed CeNPs, forming the CeNP@Cu-BTC composite as a light blue precipitate. The precipitate was washed several times with DMF and CH_2Cl_2 and dried at 70 °C. This is summarised below in Figure 1.13.

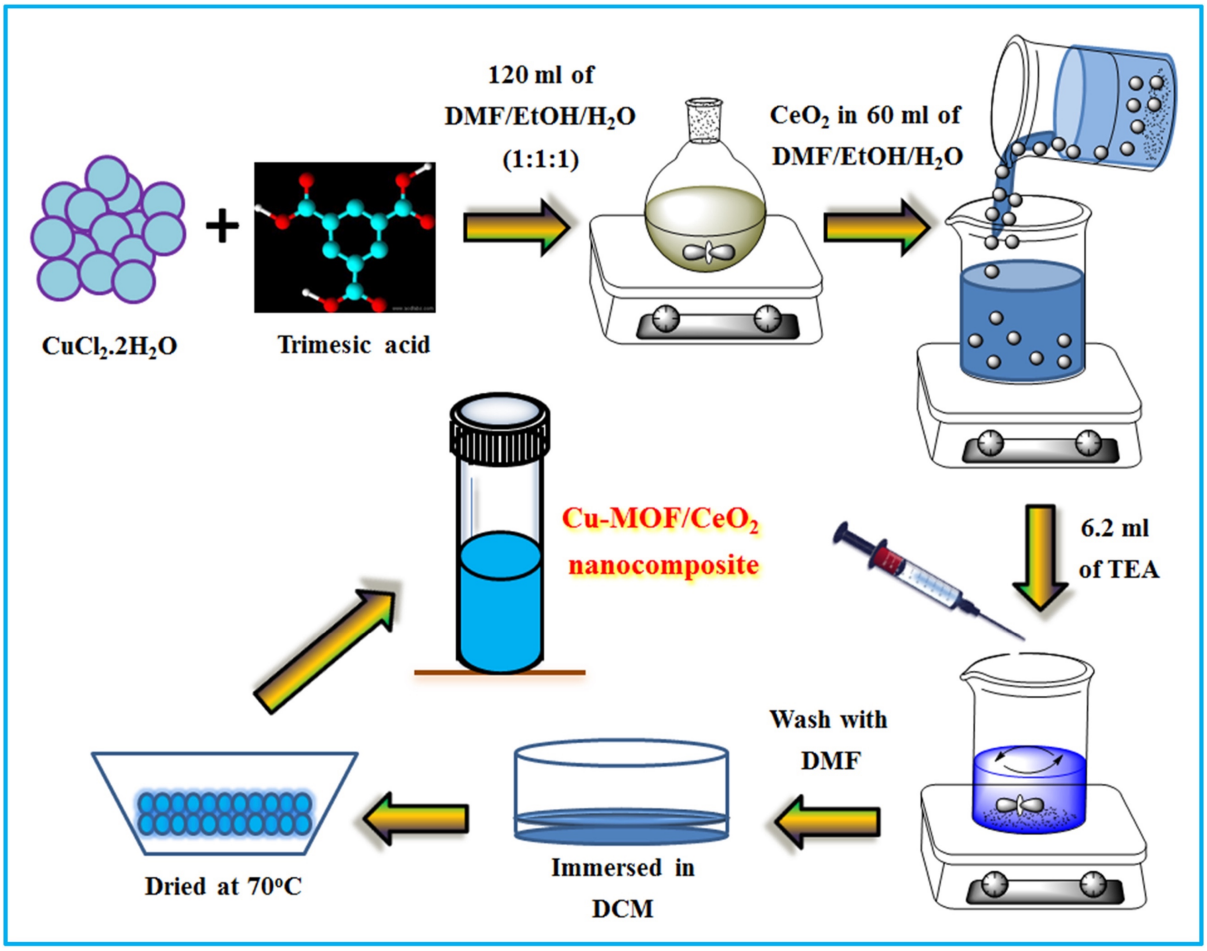

Figure 1.13: Preparation process for the synthesis of CeNP@Cu-BTC.[68]

Successful incorporation of the CeNP within the Cu-BTC host was confirmed by characteristic X-ray peaks (33.7 wt%) in the EDX spectrum, Ce–O stretches at 460 cm^{-1} in the Raman spectrum and reflections at 28.67°, 33.22°, 47.36°, and 56.34° in the PXRD diffractogram of CeNP@Cu-BTC. The CeNP were found to be homogeneously distributed throughout the Cu-BTC host with dot like patterns present in the SEM images of individual CeNP@Cu-BTC particles (see Figure 1.14).[68]

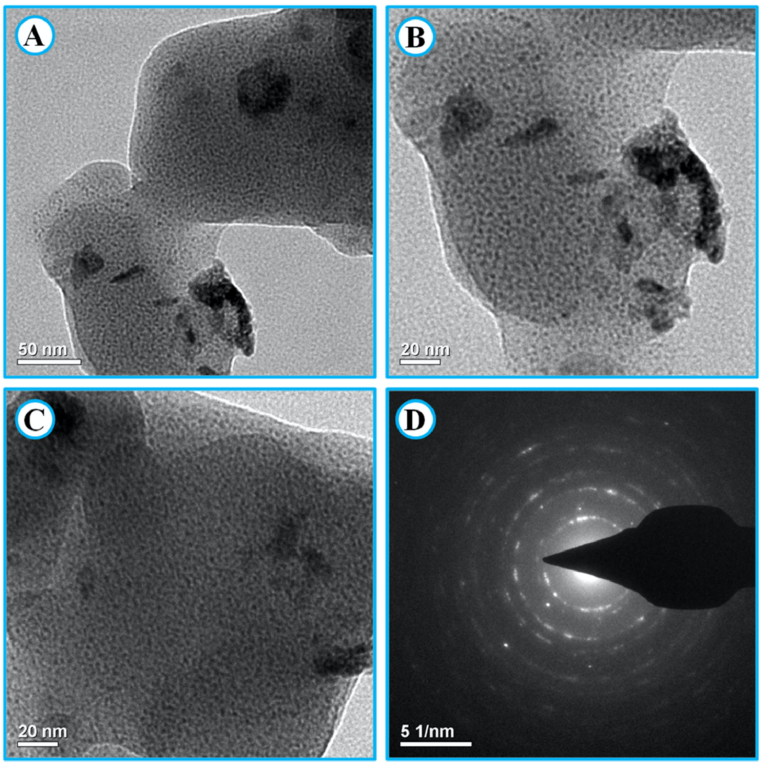

Figure 1.14: A-C TEM images of CeNP@Cu-BTC, D SAED pattern of CeNP@Cu-BTC.[68]

The CeNP@Cu-BTC composite showed great promise in the fields of renewable energy with an overpotential of 145.9 mV (at 10 mA cm^{-2}) and Tafel slope of 54.6 mV dec^{-1}, which are both significantly lower than that of the sole Cu-BTC host framework at 270 mV (at 10 mA cm^{-2}) and 155 mV dec^{-1}, indicating that CeNP@Cu-BTC would make a superior electrocatalyst in the hydrogen evolution reaction.[69] This highlights the fundamental attribute of composite materials in that the composite will often exhibit properties that are superior to those of the lone component materials.

Hassan *et al* published a study into the synthesis, using a 'bottle-around-a-ship' synthetic methodology, of a composite with CeNPs, in the form of CeO_2, stabilised in a matrix of Ce-BDC.[70] The CeO_2 NPs were synthesised *via* precipitation methods by reacting $Ce(NO_3)_3$ with ammonium hydroxide, at 100 °C. The CeNPs were then subsequently dispersed in DMF and mixed with H_2BDC and $(NH_4)_2Ce(NO_3)_6$, at 100 °C, causing the Ce-BDC MOF structure to assemble around the pre-formed CeNPs. The precipitate was filtered, washed with DMF,

ethanol and dried at 80 °C for 2 hours and at 100 °C for a further 16 hours. This is summarised below in Figure *1.15*.[70]

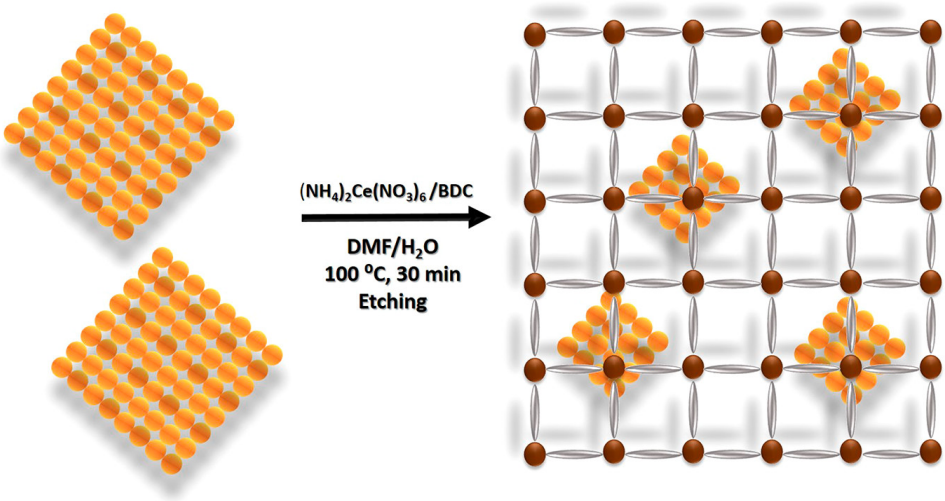

Figure 1.15: Schematic representation of the 'bottle-around-a-ship' synthesis of CeNP@Ce-BDC.[70]

Successful synthesis of the CeNP@Ce-BDC composite was confirmed by a range of spectroscopic techniques: 'dot like' patterns visible in high resolution TEM images; a broad reflection at 28.7° in the PXRD diffractogram characteristic of CeO_2; IR vibration at 1060 cm^{-1} caused by the Ce–O stretch and a red-shifted F_{2g} Raman active stretch at 426 cm^{-1}.[70] The CeNP@Ce-BDC composite was tested as a potential catalyst in the hydrolysis of nerve agent simulant DMNP, a point that is further discussed in Chapter 4, and showed superior catalytic ability towards the hydrolysis reaction than the parent materials.

Liu *et al* published the only study to date of a 'ship-in-a-bottle' methodology,[66] whereby under an inert atmosphere a molecular precursor bearing Ce enters the pores of MOF NU-1000 (dispersed in a toluene solution of the precursor) over a period of 12 hours at 80 °C. The 'loaded' NU-1000 was isolated, dried *in vacuo* at at 100 °C and then placed into an ALD chamber where the MOF was subjected to pulsed steam waves at 120 °C overnight and dried again *in vacuo* at 120 °C. This process is summarised in Figure 1.16. Liu *et al* termed this synthetic methodology solvothermal installation in MOFs (SIM) and it is the closest 'ship-in-a-bottle' methodology in the literature – published to date – to that which is presented in Chapter 2 for synthesis CeNP@MOF composites. Two precursor molecules were employed,

forming two different composite materials. The solvothermal insertion of $Ce(Cp^{i}Pr)_3$ ($Cp^{i}Pr$ = $C_5[CH\{CH_3\}_2]_5$) or $Ce(tmhd)_4$ (tmhd = 2,2,6,6-tetramethyl-3,5-heptanedionate) into NU-1000 resulted in the formation of composites $CeNP^{n}$@NU-1000 and $CeNP^{l}$@NU-1000^{l}, respectively, where $CeNP^{n}$ and $CeNP^{l}$ are cluster species of the form $Ce_xO_yH_z$.

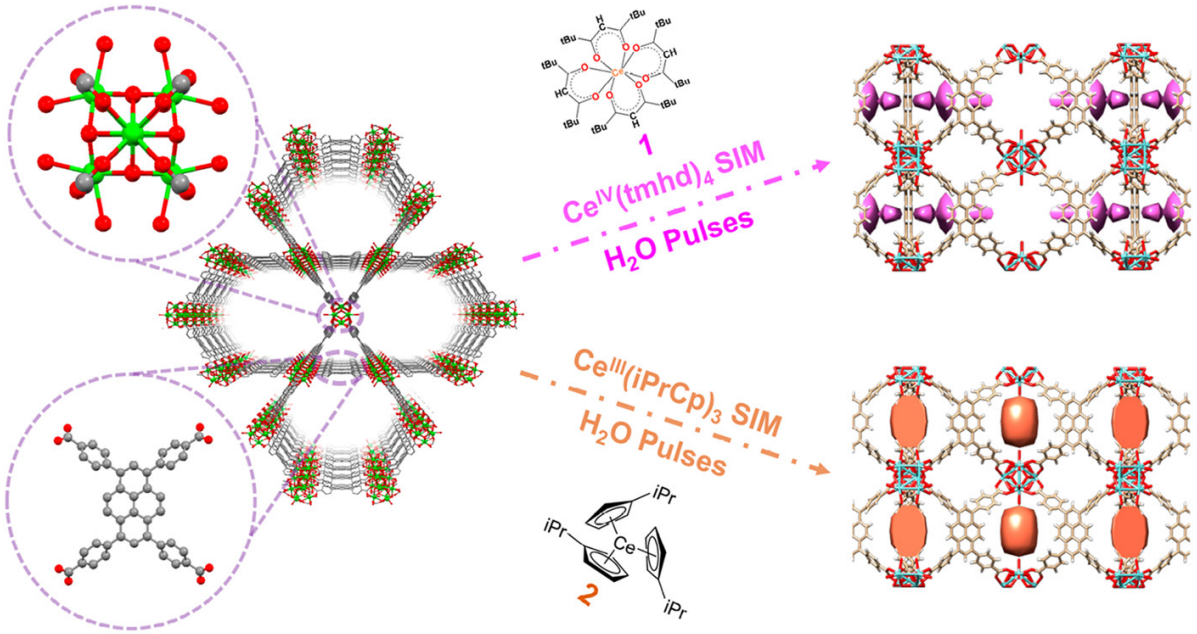

Figure 1.16: Schematic Representation of the Preparation of the Ce-l/n-SIM-NU-1000 Samples.[66]

The success of the solvothermal installation methodology was confirmed by difference envelope density analyses of X-ray scattering from the CeNP@NU-1000 samples, with the $Ce(Cp^{i}Pr)_3$ precursor forming clusters sited between Zr_6 cluster nodes of NU-1000 (see Figure 1.16), while $Ce(tmhd)_4$ formed clusters sited between tetra-phenyl-pyrene linkers (see Figure 1.16). No evidence of direct grafting to the Zr_6 cluster nodes was observed.

Table 1.3: Summary of literature CeNP@MOF composites formed by either 'bottle-around-a-ship' or 'ship-in-a-bottle'synthetic methodologies.

Ce Precursor	MOF Host	Composite	Synthesis	Applications
CeO_2 (preformed NPs)	Cu-BTC	CeNP@Cu-BTC	At room temperature, triethylamine added to a solution mixture of CeO_2 NPs, H_3BTC and $CoCl_2$, inducing precipitation over 24 hours. Precipitate washed with DMF/CH_2Cl_2 and dried at 70 °C.[68]	Electrocatalysis for hydrogen evolution. Targeted drug delivery.
CeO_2 (preformed NPs)	Ce-BDC	CeNP@Ce-BDC	At 100 °C ,CeNPs were dispersed in a solution of H_2BDC and $(NH_4)_2Ce(NO_3)_6$. Precipitate washed with acetone and dried *in vacuo*.[70]	Catalytic degradation of nerve agent simulant DMNP.[b]
$Ce(Cp^{iPr})_3$	NU-1000	$CeNP^n$@NU-1000[a]	Under an inert atmosphere, NU-1000 was stirred in a solution of the precursor molecule, at 80 °C, for 12 hours. Solids were washed with acetone, dried *in vacuo* at 100 °C, treated with pulsed steam at 120 °C overnight and dried again *in vacuo* at 120 °C.[66]	
$Ce(tmhd)_4$	NU-1000	$CeNP^l$@NU-1000[a]		

[a] $CeNP^{n/l}$: $Ce_xO_yH_z$

[b] Discussed further in Chapter 4.

1.6 Thesis Scope and Aims

There are only a few examples in the literature of cerium based nanoparticle (CeNP) composites with MOF structures. Given the highly catalytic nature of cerium based materials, particularly ceria, this remains a surprisingly unexplored area of materials development. Of the methodologies that do exist for synthesising nanocomposites with MOFs, they are largely energy intensive, requiring many steps and interventions. This thesis presents a new, simple, low energy methodology for assembling cerium based nanoparticles in MOF structures. The methodology is termed reactive infiltration (RI) and works at room temperature, occurring spontaneously when a small molecule, highly basic, precursor in solution comes into contact with the protic MOF structure – yielding the composite CeNP@MOF808. The process of optimising the methodology, and the subsequent optimised procedure is be presented in detail in Chapter 2, along with detailed structural and spectroscopic characterisation of the CeNP@MOF808 composite. The aim is to determine what effect, if any, the introduction of CeNP into MOF808 has on the host structure, as well as determining possible sites of reaction for reactive infiltration.

Post-synthetic modification is an essential part of materials science. In the first section of Chapter 3 thermal and oxidative post-synthetic treatments of the CeNP@MOF808 composite are explored in detail to determine if chemical changes in the composite can be induced. The second part of Chapter 3 focuses on the electronic structure of the CeNP@MOF808 composite, namely the Ce^{3+} and Ce^{4+} oxidation state proportions which are essential to the function of many cerium based materials. Through a process of combined, independent spectroscopic analyses (XANES, EXAFS, XPS and EELS) it will be established what the exact proportions of Ce^{3+} and Ce^{4+} are and how they are distributed in the composite material. Examination of possible speciations of the CeNP will also be investigated.

The redox active nature of cerium based materials and the presence of Lewis acidic metal sites in MOF structures has often lead to both materials finding application in the field of catalysis, specifically the decomposition of organophosphate nerve agents. In Chapter 4 the ability of the CeNP@MOF808 composite to catalyse the degradation of the nerve agent

simulant dimethyl 4-nitrophenylphosphate (DMNP) is investigated through a series of optimised ^{31}P NMR experiments.

Finally, in Chapter 5, a simple synthetic methodology is presented for the synthesis of lanthanide based β – ketoiminate precursor molecules. Studies are presented into forming new cerium based materials with the Ce β – ketoiminate precursor molecule, $Ce_2[OC(Me)CHC(Me)N^iPr]_6$, using both thermal degradation and reactive infiltration with MOF808.

1.7 References for Chapter 1

1. G. Charalampides, K. I. Vatalis, B. Apostoplos and B. Ploutarch-Nikolas, *Procedia Economics and Finance*, 2015, **24**, 126-135.
2. R. A. Layfield and M. Murugesu, *Lanthanides and actinides in molecular magnetism*, John Wiley & Sons, 2015.
3. J. A. Peters, K. Djanashvili, C. F. Geraldes and C. Platas-Iglesias, *Coordination Chemistry Reviews*, 2020, **406**, 213146.
4. G. Anderegg, *Critical Survey of Stability Constants of EDTA Complexes: Critical Evaluation of Equilibrium Constants in Solution: Stability Constants of Metal Complexes*, Elsevier, 2013.
5. X. Vendrell, Y. Kubyshin, L. Mestres and J. Llorca, *ChemCatChem*, 2020, **12**, 5926-5931.
6. M. E. Khan, M. M. Khan and M. H. Cho, *Scientific reports*, 2017, **7**, 1-17.
7. J. Kullgren, C. W. Castleton, C. Müller, D. M. Ramo and K. Hermansson, *The Journal of chemical physics*, 2010, **132**, 054110.
8. J. Kašpar, P. Fornasiero and M. Graziani, *Catalysis Today*, 1999, **50**, 285-298.
9. S. Omar, E. D. Wachsman and J. C. Nino, *Applied Physics Letters*, 2007, **91**, 144106.
10. S. Yabe and T. Sato, *Journal of Solid State Chemistry*, 2003, **171**, 7-11.
11. S. K. Murthy, *International journal of nanomedicine*, 2007, **2**, 129.
12. J. Yang, M. K. Choi, U. J. Yang, S. Y. Kim, Y. S. Kim, J. H. Kim, D.-H. Kim and T. Hyeon, *Nano Letters*, 2020, **21**, 26-33.
13. L. Li, W. Jiang, K. Luo, H. Song, F. Lan, Y. Wu and Z. Gu, *Theranostics*, 2013, **3**, 595.
14. A. Gautam, A. Kshirsagar, R. Biswas, S. Banerjee and P. K. Khanna, *RSC advances*, 2016, **6**, 2746-2759.
15. D. Valechha, S. Lokhande, M. Klementova, J. Subrt, S. Rayalu and N. Labhsetwar, *Journal of Materials Chemistry*, 2011, **21**, 3718-3725.
16. J. M. López, A. L. Gilbank, T. García, B. Solsona, S. Agouram and L. Torrente-Murciano, *Applied Catalysis B: Environmental*, 2015, **174**, 403-412.
17. L. Wu, H. Wiesmann, A. Moodenbaugh, R. Klie, Y. Zhu, D. Welch and M. Suenaga, *Physical Review B*, 2004, **69**, 125415.
18. S. Tsunekawa, T. Fukuda and A. Kasuya, *Surface Science*, 2000, **457**, L437-L440.

19. F. Zhang, S.-W. Chan, J. E. Spanier, E. Apak, Q. Jin, R. D. Robinson and I. P. Herman, *Applied physics letters*, 2002, **80**, 127-129.
20. M. Nakayama and M. Martin, *Physical Chemistry Chemical Physics*, 2009, **11**, 3241-3249.
21. M. Florea, G. Postole, F. Matei-Rutkovska, A. Urda, F. Neaţu, L. Massin and P. Gelin, *Catalysis Science & Technology*, 2018, **8**, 1333-1348.
22. C. M. Sims, R. A. Maier, A. C. Johnston-Peck, J. M. Gorham, V. A. Hackley and B. C. Nelson, *Nanotechnology*, 2018, **30**, 085703.
23. C. Colella and A. F. Gualtieri, *Microporous and Mesoporous Materials*, 2007, **105**, 213-221.
24. J. D. Sherman, *Proceedings of the National Academy of Sciences*, 1999, **96**, 3471-3478.
25. T. T. H. Ta, N. T. Pham and S. Do Ngoc, *VNU Journal of Science: Mathematics-Physics*, 2016, **32**.
26. O. M. Yaghi, G. Li and H. Li, *Nature*, 1995, **378**, 703-706.
27. H. Li, M. Eddaoudi, M. O'Keeffe and O. M. Yaghi, *nature*, 1999, **402**, 276-279.
28. O. K. Farha, I. Eryazici, N. C. Jeong, B. G. Hauser, C. E. Wilmer, A. A. Sarjeant, R. Q. Snurr, S. T. Nguyen, A. O. z. r. Yazaydın and J. T. Hupp, *Journal of the American Chemical Society*, 2012, **134**, 15016-15021.
29. J. K. Schnobrich, K. Koh, K. N. Sura and A. J. Matzger, *Langmuir*, 2010, **26**, 5808-5814.
30. H. V. Doan, H. Amer Hamzah, P. Karikkethu Prabhakaran, C. Petrillo and V. P. Ting, *Nano-Micro Letters*, 2019, **11**, 1-33.
31. A. A. Olajire, *Renewable and Sustainable Energy Reviews*, 2018, **92**, 570-607.
32. Y. Lin, C. Kong, Q. Zhang and L. Chen, *Advanced Energy Materials*, 2017, **7**, 1601296.
33. H. Li, K. Wang, Y. Sun, C. T. Lollar, J. Li and H.-C. Zhou, *Materials Today*, 2018, **21**, 108-121.
34. H. Li, L. Li, R.-B. Lin, W. Zhou, Z. Zhang, S. Xiang and B. Chen, *EnergyChem*, 2019, **1**, 100006.
35. M. Lashgari and Y. Yamini, *Talanta*, 2019, **191**, 283-306.
36. J. Zhang and Z. Chen, *Journal of Chromatography A*, 2017, **1530**, 1-18.
37. M. S. Samuel, V. Kirankumar and E. Selvarajan, *Journal of Environmental Chemical Engineering*, 2021, **9**, 104966.

38. N. Singh, I. Srivastava, J. Dwivedi and N. Sankararamakrishnan, *Chemosphere*, 2021, **270**, 129490.
39. D. Chen, Y. Cao, N. Chen and P. Feng, *Journal of Inorganic and Organometallic Polymers and Materials*, 2021, **31**, 1231-1240.
40. Y. Wang, J. Yan, N. Wen, H. Xiong, S. Cai, Q. He, Y. Hu, D. Peng, Z. Liu and Y. Liu, *Biomaterials*, 2020, **230**, 119619.
41. D. A. Reddy, Y. Kim, M. Gopannagari, D. P. Kumar and T. K. Kim, *Sustainable Energy & Fuels*, 2021, **5**, 1597-1618.
42. A. E. Baumann, D. A. Burns, B. Liu and V. S. Thoi, *Communications Chemistry*, 2019, **2**, 1-14.
43. J. H. Cavka, S. Jakobsen, U. Olsbye, N. Guillou, C. Lamberti, S. Bordiga and K. P. Lillerud, *Journal of the American Chemical Society*, 2008, **130**, 13850-13851.
44. Y. Liu, R. C. Klet, J. T. Hupp and O. Farha, *Chemical Communications*, 2016, **52**, 7806-7809.
45. D. Yang and B. C. Gates, *Acs Catalysis*, 2019, **9**, 1779-1798.
46. V. Bon, I. Senkovska, I. A. Baburin and S. Kaskel, *Crystal growth & design*, 2013, **13**, 1231-1237.
47. J. E. Mondloch, W. Bury, D. Fairen-Jimenez, S. Kwon, E. J. DeMarco, M. H. Weston, A. A. Sarjeant, S. T. Nguyen, P. C. Stair and R. Q. Snurr, *Journal of the American Chemical Society*, 2013, **135**, 10294-10297.
48. H. Furukawa, F. Gandara, Y.-B. Zhang, J. Jiang, W. L. Queen, M. R. Hudson and O. M. Yaghi, *Journal of the American Chemical Society*, 2014, **136**, 4369-4381.
49. Y. Zhang, X. Zhang, J. Lyu, K.-i. Otake, X. Wang, L. R. Redfern, C. D. Malliakas, Z. Li, T. Islamoglu and B. Wang, *Journal of the American Chemical Society*, 2018, **140**, 11179-11183.
50. H.-Q. Zheng, Y.-N. Zeng, J. Chen, R.-G. Lin, W.-E. Zhuang, R. Cao and Z.-J. Lin, *Inorganic Chemistry*, 2019, **58**, 6983-6992.
51. C. A. Trickett, T. M. Osborn Popp, J. Su, C. Yan, J. Weisberg, A. Huq, P. Urban, J. Jiang, M. J. Kalmutzki and Q. Liu, *Nature chemistry*, 2019, **11**, 170-176.
52. E. Aunan, C. W. Affolter, U. Olsbye and K. P. Lillerud, *Chemistry of Materials*, 2021, **33**, 1471-1476.

53. S. Y. Moon, Y. Liu, J. T. Hupp and O. K. Farha, *Angewandte Chemie*, 2015, **127**, 6899-6903.
54. N. L. Rosi, J. Kim, M. Eddaoudi, B. Chen, M. O'Keeffe and O. M. Yaghi, *Journal of the American Chemical Society*, 2005, **127**, 1504-1518.
55. B. F. Hoskins and R. Robson, *Journal of the American Chemical Society*, 1990, **112**, 1546-1554.
56. C. Castillo-Blas, I. Romero-Muñiz, A. Mavrandonakis, L. Simonelli and A. E. Platero-Prats, *Chemical Communications*, 2020, **56**, 15615-15618.
57. H.-Q. Zheng, C.-Y. Liu, X.-Y. Zeng, J. Chen, J. Lü, R.-G. Lin, R. Cao, Z.-J. Lin and J.-W. Su, *Inorganic chemistry*, 2018, **57**, 9096-9104.
58. Y. L. Zhao, L. Liu, W. Zhang, C. H. Sue, Q. Li, O. Š. Miljanić, O. M. Yaghi and J. F. Stoddart, *Chemistry–A European Journal*, 2009, **15**, 13356-13380.
59. J. Jiang, F. Gándara, Y.-B. Zhang, K. Na, O. M. Yaghi and W. G. Klemperer, *Journal of the American Chemical Society*, 2014, **136**, 12844-12847.
60. M. Bláha, V. c. Valeš, Z. k. Bastl, M. Kalbáč and H. Shiozawa, *The Journal of Physical Chemistry C*, 2020, **124**, 24245-24250.
61. K. A. McDonald, J. C. Bennion, A. K. Leone and A. J. Matzger, *Chemical Communications*, 2016, **52**, 10862-10865.
62. S. Begum, Z. Hassan, S. Bräse and M. Tsotsalas, *Langmuir*, 2020, **36**, 10657-10673.
63. W. Xiang, Y. Zhang, H. Lin and C.-j. Liu, *Molecules*, 2017, **22**, 2103.
64. P. Railey, Y. Song, T. Liu and Y. Li, *Materials Research Bulletin*, 2017, **96**, 385-394.
65. C. Rösler and R. A. Fischer, *CrystEngComm*, 2015, **17**, 199-217.
66. J. Liu, L. R. Redfern, Y. Liao, T. Islamoglu, A. Atilgan, O. K. Farha and J. T. Hupp, *ACS applied materials & interfaces*, 2019, **11**, 47822-47829.
67. C. S. Yan, H. Y. Gao, L. F. Ma, L. L. Dang, L. Zhang, P. P. Meng and F. Luo, *Journal of Materials Chemistry A*, 2016, **4**, 13603-13610.
68. S. Kumaraguru, R. Nivetha, K. Gopinath, E. Sundaravadivel, B. O. Almutairi, M. H. Almutairi, S. Mahboob, M. Kavipriya, M. Nicoletti and M. Govindarajan, *Journal of Materials Research and Technology*, 2022, **18**, 1732-1745.
69. M. Zhang, D. Hu, Z. Xu, B. Liu, M. Boubeche, Z. Chen, Y. Wang, H. Luo and K. Yan, *Journal of Materials Science & Technology*, 2021, **72**, 172-179.

70. M. H. Hassan, D. Andreescu and S. Andreescu, *ACS Applied Nano Materials*, 2020, **3**, 3288-3294.

2 Development of Novel, Solution Based Reactive Infiltration (RI)

2.1 Abstract

Previous synthesises of nanoparticle-metal organic framework (NP@MOF) composites have often relied on intense, multi-stage reaction conditions with high temperatures, reducing atmospheres and high energy light irradiation. Chapter 2 shall report the development of a novel, solution based, optimised methodology known as *reactive infiltration* (RI) for synthesising the cerium based nanoparticle-metal organic framework composite: CeNP@MOF808 (MOF808 = $Zr_6O_4(OH)_4(OOCH)_6(BTC)_2$; BTC = benzene-1,3,5-tricarboxylate), at room temperature in a single reaction step, with no supplementary energy intensive stages required. RI works by reaction of the moisture sensitive, highly basic Ce precursor, CeN''_3 (N'' = $N(SiMe_3)_2$), with the complementary protic, porous MOF808 structure to form Ce based nanoparticles (CeNP) within the MOF pores. Initial ^1H NMR studies resulted in the optimisation of RI, based on the experimental variables: precursor weight %, solvent polarity, pre-reaction MOF808 thermal treatment and reaction time. The scaled up, optimised RI yielded the CeNP@MOF808 composite, which was fully characterised by SEM, EDX, digestion NMR, ICP-OES, elemental microanalysis, PXRD, TGA, potentiometric titration, IR spectroscopy and N_2 adsorption isotherm studies. Replicated syntheses of CeNP@MOF808, coupled with a control RI protocol, were employed to demonstrate the reproducibility of the RI methodology. The CeNP@MOF808 composite showed retention of the MOF808 porous structure, with PXRD reflections and IR absorptions characteristic of MOF808, and a microporous specific surface area of 1248 ± 34 m^2/g, similar to that of the parent MOF808. The Zr_6 cluster hydroxides remained unchanged following RI, with measured pK_a values indistinguishable from MOF808. Cluster formate ligands (OOCH) were unchanged after RI with, with formate:BTC ratios of CeNP@MOF808 indistinguishable from those of MOF808. A Ce loading of *ca.* 3 wt% was confirmed by EDX and ICP-OE spectroscopy. With the synergistic relationship between the high surface area of MOF808 and the redox activity of CeNPs, this novel CeNP@MOF808 composite is an exciting platform from which to investigate a wide range of catalytic reactions.

2.2 Reactive Infiltration: The Theory

Reactive infiltration was hypothesised to combine the two stages that make up the traditional methodology for synthesising NP@MOF composites into one single, simple step *via* use of a highly basic precursor that is complementary in reactivity to the protic interior of the MOF. By using an air- and moisture-sensitive metal precursor in combination with a highly protic MOF structure, the materials complement and react with one another. The precursor infiltrates the porous MOF structure where it comes into contact with multiple different protic environments (*e.g.* free linker, open metal sites, cluster hydroxides ligands, cluster aqua ligands, formate modulator ligands and residual solvent) and reacts, eliminating the basic ligand group and assembling into NPs within the MOF pores and/or on the MOF surface. It should be noted that the complementary precursor-host hypothesis could be expanded beyond protic-basic systems, such as one adopted in this study, to those such as precipitation based, polarity differences, *etc*.

There were several variables associated with the reactive infiltration methodology identified from the outset that had to be tuned: metal precursor choice and design; MOF choice, design and pre-insertion treatments; reaction conditions such as temperature, solvent and loading weights. Therefore, significant optimisation of reactive infiltration was required to ensure that a CeNP@MOF composite was successfully synthesised in significant quantities and with reproducible properties.

2.3 Precursor Choice and Synthesis

When selecting a precursor the choice was made on (a) ease of synthesis and (b) being sufficiently basic to react readily with the various protic sites within the MOF host. Cerium tris(bis(trimethylsilyl)amide), CeN''_3 ($N'' = N(SiMe_3)_2$), is a highly air- and moisture-sensitive precursor. CeN''_3 has also found limited applications in solid-state materials synthesis through bottom-up processes such as atomic-layer deposition (ALD) for depositing thin-films of CeO_2[1] However, use of CeN''_3 towards the synthesis of cerium based nanoparticles remained largely unexplored. The precursor has the advantage of being easy to synthesise and of simple

structure, with highly basic N'' ligands that when protonated act as a thermodynamic driving force for the reactive infiltration, ensuring feasibility and favouring fast reaction kinetics.

Metal precursor choice is particularly important in f-element chemistry. To avoid problems associated with Ce halides, mainly the formation of oxychlorides and non-integer stoichiometries, the decision was made that CeN''_3 should be synthesised from the parent triflate, $Ce(OTf)_3$ (OTf = O_3SCF_3). $Ce(OTf)_3$ was synthesised *via* the reaction of a $Ce_2(CO_3)_3$ suspension with an excess of triflic acid under reflux at 101 °C for 18 hours. This yielded a colourless solution that was pumped down to remove water, yielding a white paste. The paste was dried on a Gooch crucible and washed several times with diethyl ether and hexane to remove the remaining acid and yield a white powder. The white powder was dried at 220 °C, over 36 hours, to produce a dehydrated, free flowing white powder; $Ce(OTf)_3$, in a yield of 49% (see Scheme 2.1).

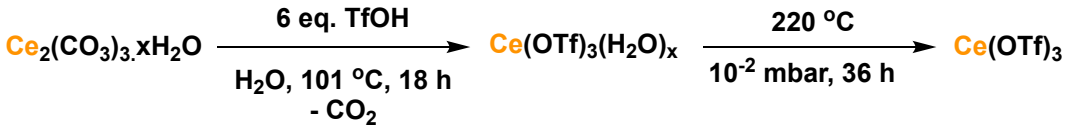

Scheme 2.1: Reaction of $Ce_2(CO_3)_3$ with triflic acid to form $Ce(OTf)_3$.

Purity of the $Ce(OTf)_3$ was confirmed *via* ^{19}F NMR with a resonance at δ = -76.40 ppm, corresponding to CF_3 groups of the triflate ions (see Supplementary Figure 2.1). The lack of a resonance at δ = 2.13 ppm in the ^1H NMR spectrum (see Supplementary Figure 2.2), and the absence of a broad stretching frequency at 3300 cm^{-1} in the IR spectrum are indicative of anhydrous triflate (see Supplementary Figure 2.3). It should be noted that $Ce_2(CO_3)_3$ was used rather than CeO_2 because of improved solubility and that Ce(III) was targeted, rather than Ce(IV) or a mixed-oxidation state precursor.

KN'' was synthesised, in modest yields (49%), *via* the direct deprotonation of HN'' with KH. ^1H NMR confirmed the purity of the KN'' with only one resonance being visible at δ = 0.13 ppm (see Figure 2.1).

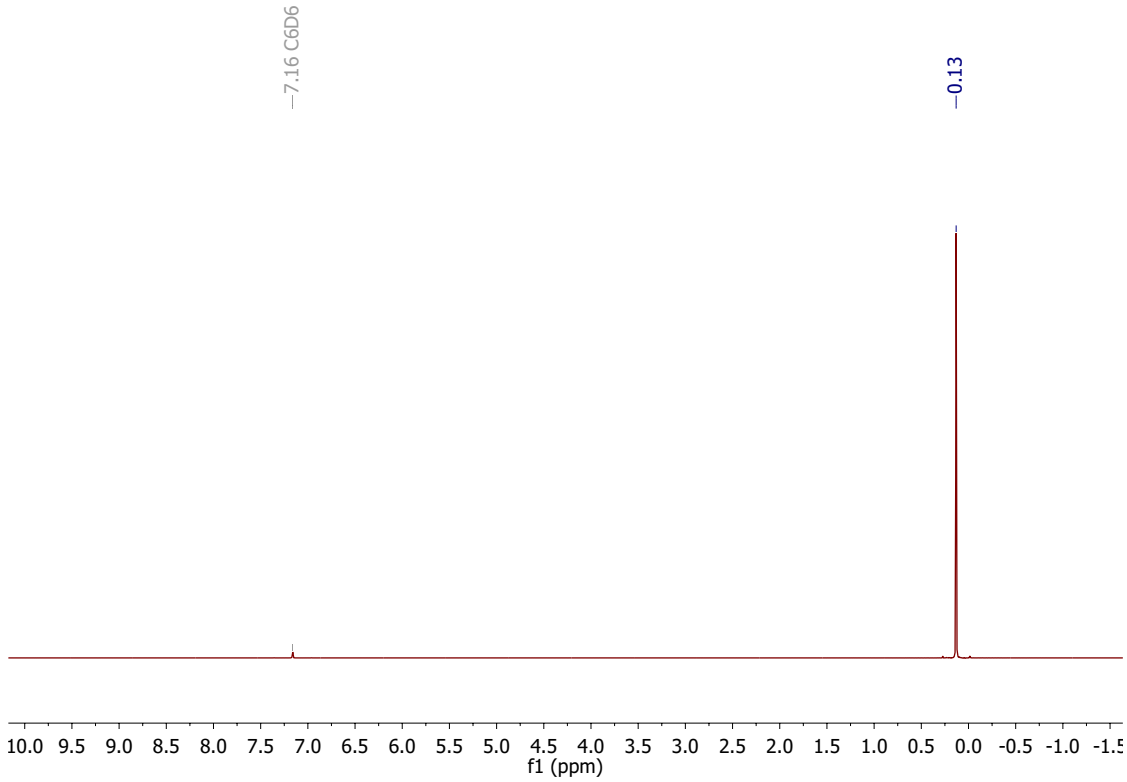

Figure 2.1: ^{1}H NMR (d_6 – benzene) of KN''

CeN''$_3$ was synthesised *via* a single, one-pot salt metathesis reaction between Ce(OTf)$_3$ and KN'' in THF at room temperature for 1 hour, with a distinct colour change occurring from colourless to yellow. The reaction mixture was pumped down to remove the THF and then extracted into toluene. Subsequent recrystallisation from toluene, and several washings with hexanes, produced a bright yellow powder in a yield of 57% (Scheme 2.2). Purity of the CeN''$_3$ was confirmed *via* ^{1}H NMR spectroscopy, with a characteristic resonance at δ = -3.40 ppm, corresponding the methyl groups of the N'' ligand (see Supplementary Figure 2.4).

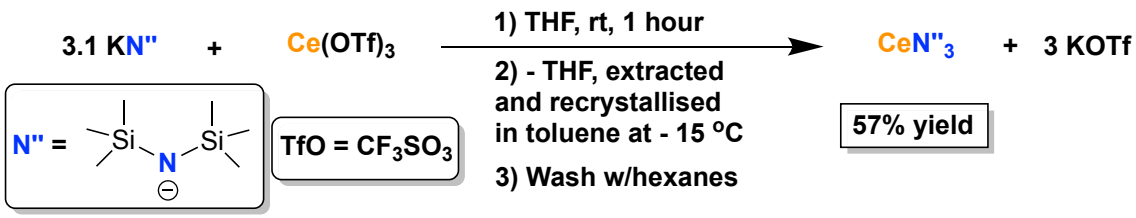

Scheme 2.2 Synthesis of CeN''$_3$ *via* the salt metathesis reaction between KN'' and Ce(OTf)$_3$.

2.4 MOF Host Choice and Synthesis

MOF structures are incredibly versatile due to the large choice of secondary building units. Two important structural features of MOFs are their pore dimensions and defects (which often act as reaction sites), both of which can be tuned and altered with secondary building units. Zirconium based MOFs are ubiquitous and find particular applications in catalytic and biological applications owing to their stability towards high temperatures and hydrolysis, ease of synthesis and versatility. Two Zr based MOF candidates were initially investigated as possible MOF host structures: MOF808 ($Zr_6O_4(OH)_4(OOCH)_6BTC_2$, BTC = 1,3,5-benzene tricarboxylate) and UiO-66 ($Zr_6O_4(OH)_4BDC_2$, BDC = 1,4-benzene dicarboxylate). However, due to the small pore diameter and access channels of UiO-66, at 7 Å, this MOF host would have been largely inaccessible to the CeN''_3 precursor molecule with a diameter of *ca.* 12 Å and therefore was eliminated early on from further investigation. MOF808 however, exhibited large, accessible pores at 18.4 Å and a relatively high 'proticity' owing to the presence of defects in the form of missing liker. Furthermore, MOF808 has shown strong stability in aqueous media, over a variety of pH.[2,3] Therefore, MOF808 was chosen as the porous matrix in which to further investigate reactive infiltration using CeN''_3.

The synthesis of MOF808 was adapted from literature procedures.[4] $ZrCl_4$, 1,3,5-benzenetricarboxylic acid (H_3BTC), DMF and formic acid were mixed and sonicated for 20 minutes. The reaction mixture was subsequently heated at 120 °C, over 24 hours, in a sealed hydrothermal reactor. The reaction precipitated a white powder which was isolated and washed with DMF and THF. The precipitate was then dried *in vacuo* at room temperature for 48 hours to give a white, free flowing powder, MOF808, in a good yield of 75%. In order to perform air-sensitive manipulation with MOF808, the solid had to be dried for several hours, *in vacuo*, heated at 120 °C – this process is referred to as *activation*. Note that alternative thermal treatment temperatures were investigated during the optimisation of the reactive infiltration process.

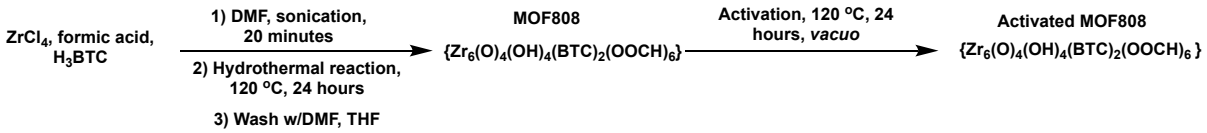

Scheme 2.3: Synthesis and activation of MOF808.

The MOF808 host was characterised by a collection of spectroscopic techniques which are discussed in detail in Section 2.7.

2.5 Optimisation of Reactive Infiltration: ^{1}H NMR Experiments

After having selected CeN''_3 and MOF808 as the complementary guest – host paring a series of ^{1}H NMR experiments were designed to investigate the feasibility of reactive infiltration between these two materials. Optimisation of reactive infiltration through various experimental parameters such as loading weight of CeN''_3, polarity of solvent and thermal pre-treatments of the MOF808 host structure were investigate, with the aim of achieving a standardised, streamlined synthetic methodology that allowed for the easy, simple synthesis of the CeNP@MOF808 composite.

2.5.1 Optimisation of Reactive Infiltration: ^{1}H NMR Experiments: Solvent Choice

Reactive infiltration is a solution based methodology, and as such the solvent choice was an essential component of the reaction system. Of primary interest was what effect the solvent polarity and coordinating ability had on the reactive infiltration reaction (*i.e.* the rate, products formed, *etc.*). This was investigated through a series of NMR scale experiments whereby a solution was made up of 1 mg of CeN''_3 and 3 mg of internal standard TTMS [$Si(TMS)_4$] (TMS = $SiMe_3$), in either d_6-benzene of d_8-THF, forming a clear yellow solution (*ca.* 3 mL). This CeN''_3 solution was subsequently mixed with 4 mg of MOF808 in an NMR tube. This corresponded to a 20 wt% loading of the CeN''_3 precursor, with the CeN''_3 making up 20% of the *total* reaction mixture mass. This method for defining loading weights is not one typically used in literature was therefore corrected for after optimisation, where CeN''_3 is 20% of the total mass of the host (MOF808). The time at which the solution was transferred to the

NMR tube and sealed, t, was recorded as 0 hours. ^{1}H NMR spectra were then taken periodically of the sample for 24 hours.

Based on the hypothesis that reactive infiltration involves the CeN''$_3$ precursor reacting on/within the MOF808 host structure to form cerium based nanoparticles, it was expected that the elimination of the protonated ligand, HN'', would be observed should reactive infiltration be taking place. HN'' had a single resonance at *ca.* δ = 0.09 ppm (solvent dependent), which could be integrated relative to the 36 protons on TTMS internal standard and therefore allowed for the tracking of reaction progress. Note that because the mass of the internal standard was known, 3 mg of TTMS, it was possible to convert the relative proton integrals into μmolar quantities. The experiment was conducted using d_6-benzene and d_8-THF, with d_6-benzene (0 debye) and d_8-THF (1.75 debye) being non-polar and polar, respectively.[5] Shown below in Figure 2.2 is a plot of HN'' concentration (μmols) against time (hours) for the NMR scale reaction of CeN''$_3$ with MOF808 in d_6-benzene and d_8-THF.

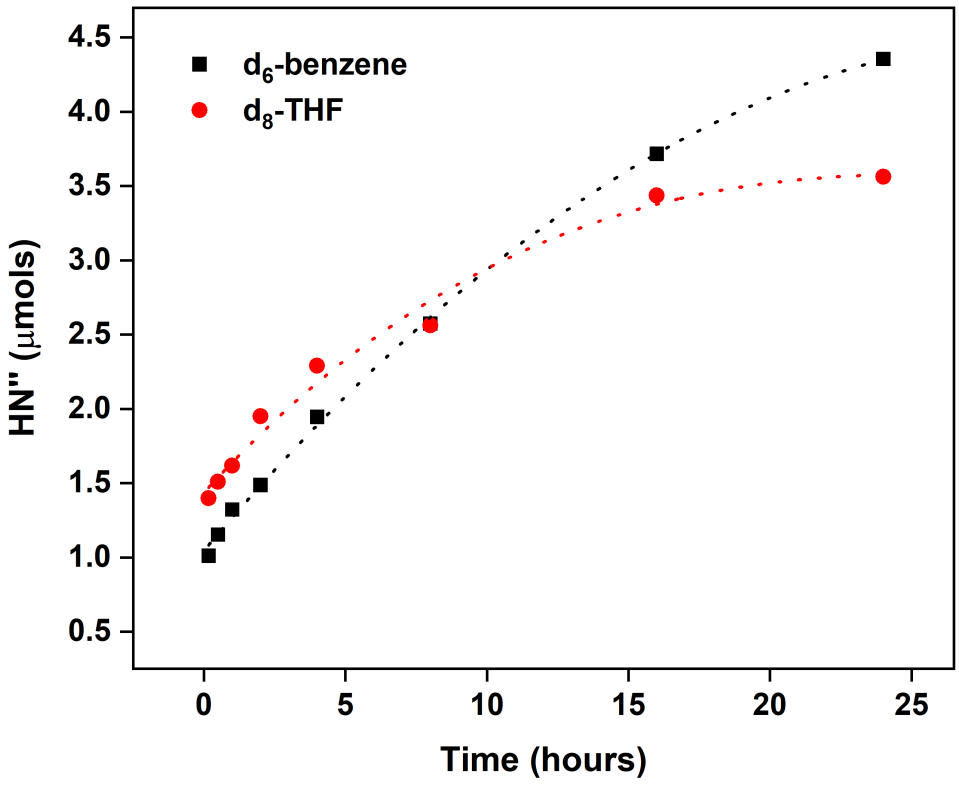

Figure 2.2 Plot of HN'' concentration (µmols) *vs.* time (hours) for the reactive infiltration reaction between CeN''_3 and MOF808 with solvents d_6-benzene and d_8-THF of varying polarity over 24 hours. General trend line: third order polynomial of the form $ax^3 + bx^2 + cx + d$.

The observation of HN'' and its continued evolution, although declining rate of evolution over time, was consistent with the hypothesis of the CeN''_3 precursor reacting within the pores and on the surface of MOF808, eliminating the protonated ligand HN'' in the process. Therefore, this was confirmation that reactive infiltration was occurring. Secondly, reactive infiltration occurred in both polar and non-polar solvent with the similar yields of HN''. In both solvent systems the reaction rate levels off at around 22 hours indicating that the reaction was complete after 22 hours. The similar rates of reactive infiltration using both benzene and THF as solvents confirmed that there is no influence on the rate of reaction from possible solvent coordination, that is THF is a Lewis base and is known to strongly coordinate to lanthanides and produce solvates with distinct chemistry.[6] Because there is limited

differences between the two solvent systems, and too avoid coordination of THF to the composite product,

It was decided to continue with d_6-benzene for all further optimisation experiments using ^{1}H NMR. It is noteworthy to mention that repeat measurements were not made and therefore only limited conclusions can be drawn from this data – that is, we cannot conclusively state that using d_6-benzene gives higher overall amounts of HN'' and therefore a greater extent of reactive infiltration.

2.5.2 Optimisation of Reactive Infiltration: ^{1}H NMR Experiments: Thermal Pre-treatment of MOF808

The second experimental parameter that had to be optimised was the thermal pre-treatment temperature used for the MOF808 host. Three activation thermal treatments of MOF808, 120, 180 and 230 °C, were investigated using a methodology similar to that used in Section 2.5.1. It was hypothesised that treating the MOF808 host to higher temperatures, prior to reactive infiltration, would introduce more 'reactive sites' (*e.g.* dehydroxylation of the cluster or breakdown of formate modulator ligands, yielding open metal sites) and therefore could result in a higher rate for reactive infiltration. Thermal treatment of MOF808 has been shown previously to cause vaporisation of adsorbed water (dehydration) at *ca.* 100 °C, followed by the removal of carboxylate modulator ligands and dehydroxylation of the cluster in the broad region of 100 – 400 °C.[7] However, as seen in Figure 2.3, thermal pre-treatment of MOF808 at 120 °C yields the most efficient reaction conditions with the fastest rate of reaction and highest yield of HN''. Thermal pre-treatments, conversely, at 180 °C and 230 °C showed slower reaction rates and overall half the yield of HN''. Post-synthetic thermal treatments of the resulting composite were further investigated in Chapter 3. This could be due to the fact that higher temperature treatments remove reactive sites, as opposed to the initial theory that it would introduce them. Reaction sites could include residual solvent from the MOF808 synthesis (*e.g.* THF and DMF) within the MOF pores that is removed by the thermal treatment, as well as coordinated cluster water, hydroxide and formate ligands. The rate of reaction can also once again be seen to level off at around 22 hours.

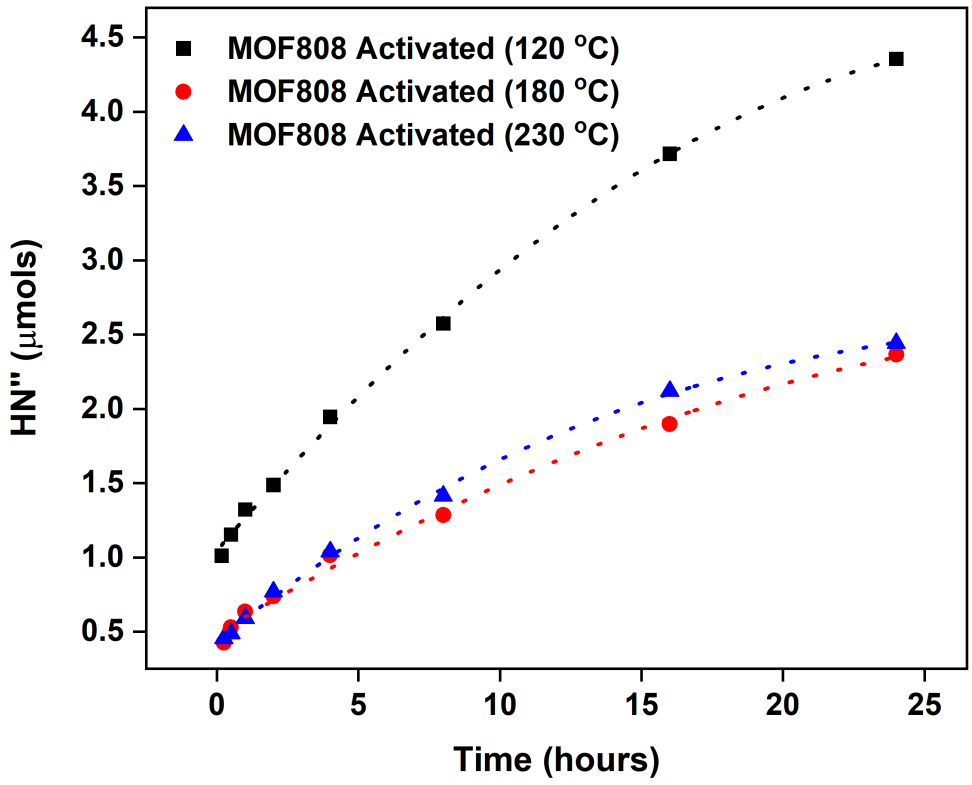

Figure 2.3 Plot of HN'' concentration (µmols) *vs.* time (hours) for the reactive infiltration reaction between CeN''$_3$ and MOF808 (thermally pre-treated at 120, 180 and 230 °C), in d_6-bezene over 24 hours. General trend line: third order polynomial of the form $ax^3 + bx^2 + cx + d$.

2.5.3 Optimisation of Reactive Infiltration: ^{1}H NMR Experiments: Reaction Time

In both previous optimisation experiments of the reactive infiltration methodology between CeN''$_3$ and MOF808 (see Sections 2.5.1 and 2.5.2), it was observed that the rate of reactive infiltration levelled off after *ca.* 22 hours. However, it was of interest what, if any, behaviour of the reactive infiltration system would be observed with longer exposure times. The ^{1}H NMR experiment were repeated, using 20 wt% loading of CeN''$_3$, d_6-benzene and MOF808 thermally pre-treated to 120 °C, with periodic ^{1}H NMR spectra taken of the sample mixture over 168 hours. As seen in Figure 2.4, there is the formation of HN'' after 30 minutes of reactive infiltration, and the amount of HN'' produced increases with time, peaking at 45 hours, after which there is a steady decline in the amount of HN''. Initially it was hypothesised

that this decrease in HN'' after 45 hours was due to absorption by the porous MOF808 structure. However, further investigation of the ^{1}H NMR spectra revealed the existence of a subtle resonance at δ = 0.125 ppm which forms after 8 hours and grows significantly after 48 hours. The resonance was compared with THF, DMF and water resonances as these solvents may have been displaced from the pores by the HN'', however no values were close to δ = 0.125 ppm. The presence in the largely shielded region of the 1H NMR spectrum suggests that it is an aliphatic environment, possibly associated with the breakdown of HN''.

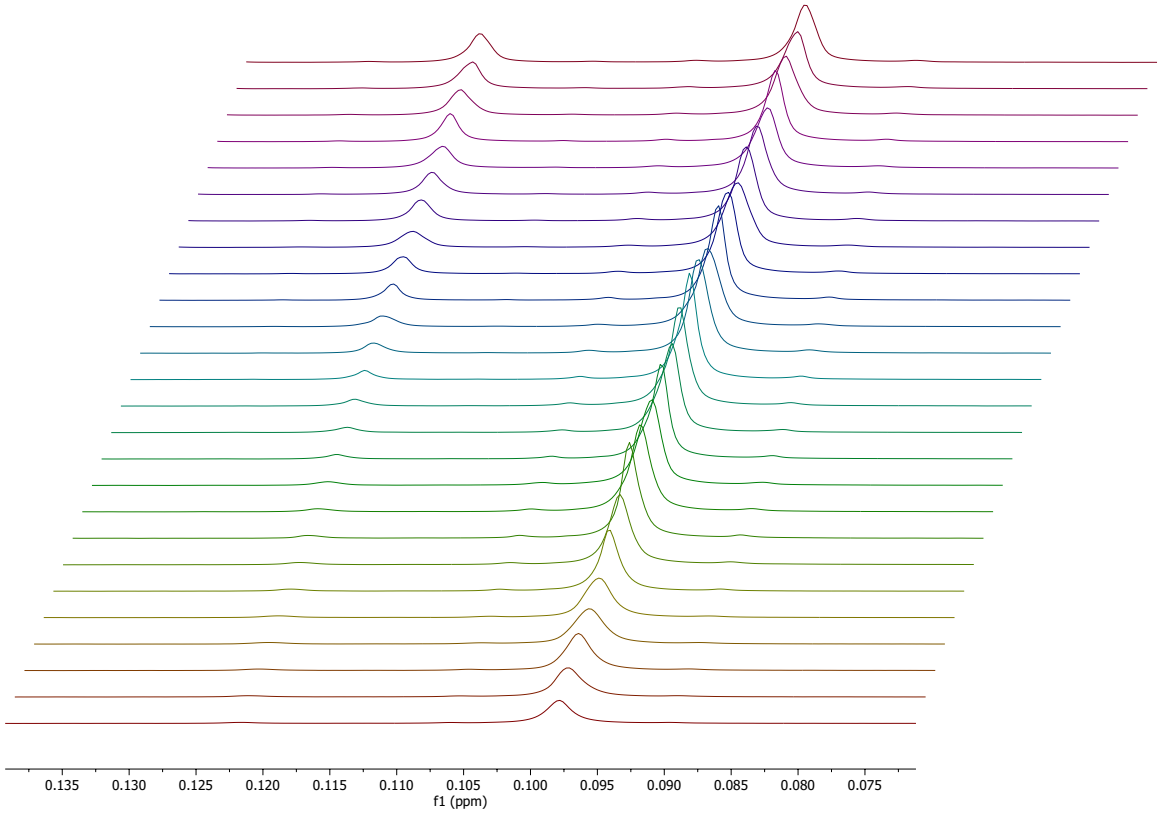

Figure 2.4 Stacked ^{1}H NMR spectra for the reactive infiltration reaction between CeN''$_3$ and MOF808 (thermally pre-treated at 120 °C), in d_6-bezene over 168 hours. Resonance at δ = 0.095 ppm corresponds to HN'' and grows up to 48 hours and resonance δ = 0.125 ppm begins to form after 8 hours, significantly growing after 48 hours.

Scaled up optimisation experiments were performed in an analogous manner to those of Sections 2.5.1, 2.5.2 and 2.5.3, whereby a 20 wt% loading of CeN''_3 with MOF808 was performed using toluene, THF and acetonitrile in a syringe reaction vessel over a period of 24 hours. The resulting composites were analysed using powder X-ray diffractions (PXRD), low resolution scanning electron microscopy (SEM), N_2 adsorption isotherms and energy dispersive X-ray (EDX) spectroscopy. The experiments showed that in optimising the scaled up reactive infiltration synthesis, a dynamic stirring mechanism was preferred to the static solution to ensure high surface area powders and that toluene was the ideal solvent system to avoid evaporation. Ce loading of the composite was confirmed to be ca. 3 wt%, consistent with literature loadings of similar NP@MOF systems, with the larger micropore of MOF808 being occupied and a significant reduction in surface area from ca. 1300 m^2/g (literature value for MOF808) to 784 m^2/g, when toluene was used as the reaction solvent. Details of the experimental procedure and corresponding data can be found in Section 2.10.5

After establishing that the scaled up optimised reactive infiltration methodology using 20 wt% loading of CeN''_3 resulted in a Ce loading in the composite of *ca.* 3 wt%, a series of experiments using higher loading concentrations of CeN''_3 was performed to establish if higher Ce loadings in the composite could be achieved, and how this would affect the properties of the composite. The experiments showed that the CeNP@MOF808 composite retained the MOF808 crystallinity, although reflections were broadened indicating reduced crystallinity, and there was a significant amorphous background in the diffractograms. The larger micropore was not occupied, contrasting with lower loading weights of 20 wt% which showed loading of the larger micropore. Therefore, in order to achieve successful loading of CeNP within MOF808 we determined that the optimised conditions for reactive infiltration were for the reactive infiltration to place within MOF808 that had been thermally pre-treated at 120 °C, at a 20 wt% loading of CeN''_3 in toluene. Details of the experimental procedure and corresponding data (including powder X-ray diffractograms, low resolution SEM images and pore size distribution plots) can be found in Section 2.10.6.

2.5.4 Optimisation of Reactive Infiltration: Control Reactions

The fundamental driving force of reactive infiltration between CeN''_3 and MOF808 is the complementary basicity-acidity. In order to confirm this driving force, small scale control reactions were performed using MOF808 with $Ce(OTf)_3$ as the precursor, rather than CeN''_3. The $Ce(OTf)_3$ precursor is, in comparison to CeN''_3, a poor base and therefore should not undergo reactive infiltration with MOF808 if the driving force is the complementary basicity-acidity of the precursor-host mixture. The experimental set up was analogous to that adopted in Sections 2.5.1, 2.5.2 and 2.5.3. Under an atmosphere of air the $Ce(OTf)_3$ precursor was dissolved, separately, in d_3-MeCN and D_2O (*ca.* 3 mL) to form a colourless solutions. The $Ce(OTf)_3$ solutions were transferred to NMR tubes containing 4 mg of MOF808. The reaction mixtures were capped and monitored *via* $^{19}F\{^1H\}$ NMR over a 16 hour period. If reactive infiltration was occurring between $Ce(OTf)_3$ and MOF808, in a similar fashion to that which occurred between CeN''_3 and MOF808, then the protonated form of the precursor ligand, HOTf (triflic acid), would be a by-product of the reaction and observed at δ = -79 ppm and δ = -79.5 ppm, in d_3-MeCN and D_2O, respectively. In both reaction systems, d_3-MeCN and D_2O, only one resonance was visible at δ = -78.3 ppm and δ = -78.9 ppm, respectively, corresponding to unreacted $Ce(OTf)_3$, see Supplementary Figure 2.10 and Supplementary Figure 2.11. No additional resonances are observed that would correspond to the formation of the protonated HOTf ligand. This implies that reactive infiltration does not occur between the non-basic $Ce(OTf)_3$ precursor and MOF808, confirming that the reactive infiltration reaction is driven by the complementary basicity-acidity of the precursor-host mixture.

2.6 Optimisation: Conclusions

In conclusion, it was determined that at a 20 wt% loading of CeN''_3, the solvent best suited for reactive infiltration was toluene. ^1H NMR studies showed successful reactive infiltration with toluene, with by-product HN'' being observed to evolve over time, giving a reaction time of *ca.* 22 hours. A significant reduction in the BET derived specific microporous surface area, from *ca.* 1300 m^2/g to 784 m^2/g, was determined for the CeNP@MOF808 composite synthesised by reactive infiltration in toluene and a complete occupation of the lager micropore was observed in the PSD plots. The CeNP@MOF808 composite showed retention of the MOF808 crystallinity following reactive infiltration and a loading weight of 3.2 wt% Ce.

2.7 Optimised Reactive Infiltration

Based on the ^{1}H NMR optimisation experiments in Section 2.5 it was possible to devise a simple one-pot, optimised reactive infiltration methodology for synthesising CeNP@MOF808 composites. The optimised procedure involved dissolving 125 mg of CeN''_3 in 10 mL of toluene, in an inert atmosphere of N_2, to form a bright yellow solution. The CeN''_3 solution was subsequently transferred to a glass vial charged with 625 mg of MOF808 (activated for several hours at 120 °C, *in vacuo*), see Figure 2.5. The reaction mixture was immediately stirred, over 30 minutes the suspension changed colour from cloudy yellow to cloudy cream. The reaction mixture was stirred for 17 hours at room temperature, after which the mixture was removed from the inert atmosphere, centrifuged and washed by sonicating in toluene, this process was repeated two more times. The isolated beige solids were then dried *in vacuo*, at room temperature, over 48 hours to yield off-white solids: CeNP@MOF808. The reactive infiltrations were repeated 3 times to ensure reproducibility of the reactive infiltration process. A control reactive infiltration protocol was performed in parallel, involving only MOF808, with stirring in the same overall volume of toluene and with no CeN''_3 present. The purpose of the control reactive infiltration protocol was to demonstrate that any changes in structural and electronic properties of the MOF host arise from the loading of CeNP. Solids were isolated and characterised using a number of spectroscopic techniques.

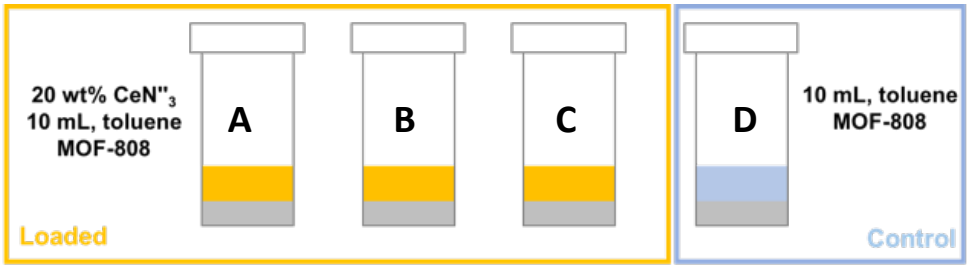

Figure 2.5 Schematic representation of the optimised reactive infiltration process, showing parallel, triplicate reactions (A, B and C), as well as control reaction with only MOF808, labelled D. Overall, the volumes of the CeN''_3 solution and neat toluene were the same at 10 mL.

2.7.1 Scanning Electron Microscopy Studies of Control MOF808 and CeNP@MOF808

Previous attempts to characterise the MOF808 and CeNP@MOF808 composite surface using SEM were limited due to the low resolution of the resulting images. This occurred due to a combination of poor instrumentation (Carl Zeiss Sigma VP Analytical SEM) and charging effects on the MOF surface. In order to obtain better contrast, samples were sputter coated with conductive 15 nm Au/Pd coatings and analysed using the Carl Zeiss Sigma VP (5 kV) SEM.

High resolution SEM images were obtained of activated and control MOF808 (*i.e.* MOF808 that went through the control reactive infiltration procedure) to determine what impact the reactive infiltration methodology had on the MOF808 surface crystallite morphology, see Figure 2.6 and Figure 2.7. The combination of a high accelerating voltage and conductive coatings allowed for good sample-background contrast, with individual MOF nanoparticles being easily discernible. This is in contrast to the lower resolution SEM images obtained during the optimisation process which showed the formation of large aggregates, with no individual MOF particles being observable (see Sections 2.10.5 and 2.10.6). Both activated and control MOF808 show regular octahedral crystallites, which have been noted in previous literature synthesises, and are characteristic of MOF808 nanoparticles.[8-10] The octahedral crystallites are *ca.* 100 – 200 nm in diameter for both activated and control MOF808. Therefore the methodology of reactive infiltration does not change the MOF808 crystallite morphology.

SEM surface images were acquired of the composite CeNP@MOF808, see Figure 2.8. By comparing the particle surface morphology of CeNP@MOF808 with that of control MOF808 one can ascertain to what extent the reactive infiltration process changes the macroscopic crystallite structure. The composite crystallites are octahedral in shape, with *ca.* 100 – 200 nm diameters. Therefore, the macroscopic surface morphology of the MOF808 host remains unchanged following reactive infiltration with CeN''_3. Common to composite and reference samples (activated and control MOF808) are aggregated monolithic structures which are not a result of the reactive infiltration process with CeN''_3 but rather a result of the hydrothermal synthesis of MOF808 itself (see Scheme 2.3). No individual nanoparticles of CeNP were observed for any of the CeNP@MOF808 composites. This would suggest that the CeNP either

adopt small cluster type structures that are not discernible to the electron beam contrast or that the cerium material forms a nanocoating.

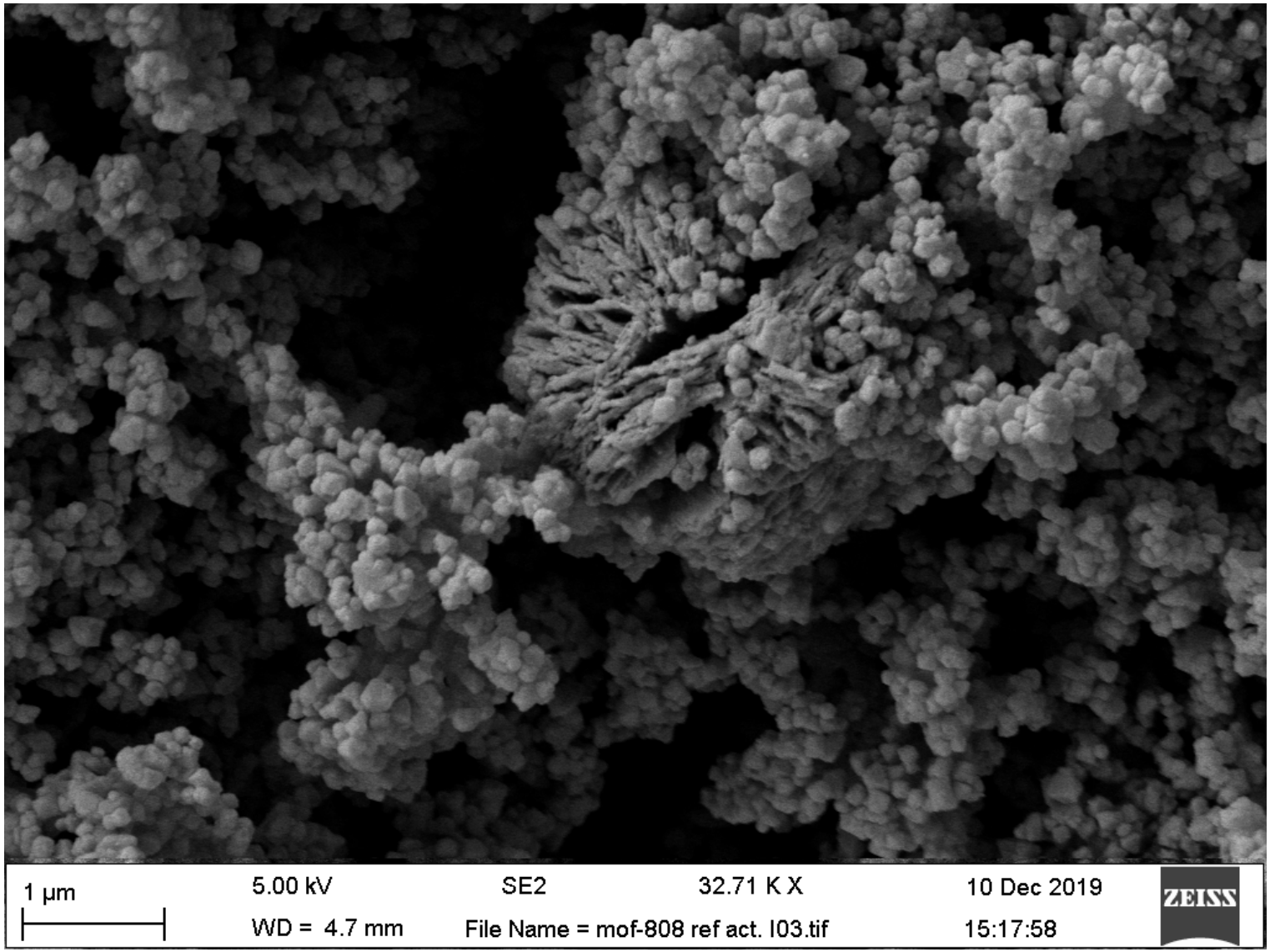

Figure 2.6: High resolution SEM image of activated MOF808 sputter coated with 15 nm Au/Pd.

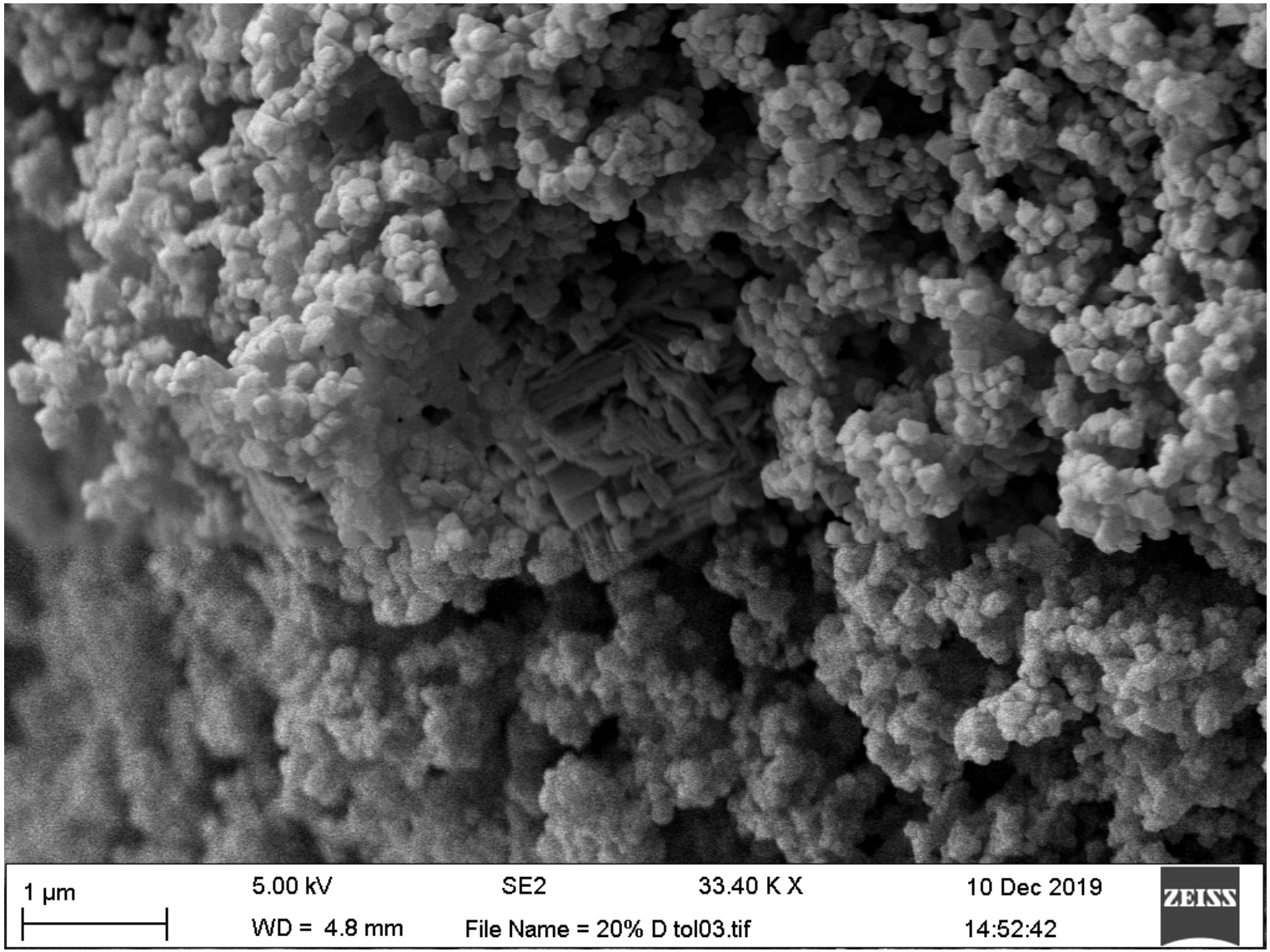

Figure 2.7: High resolution SEM image of control MOF808 sputter coated with 15 nm Au/Pd.

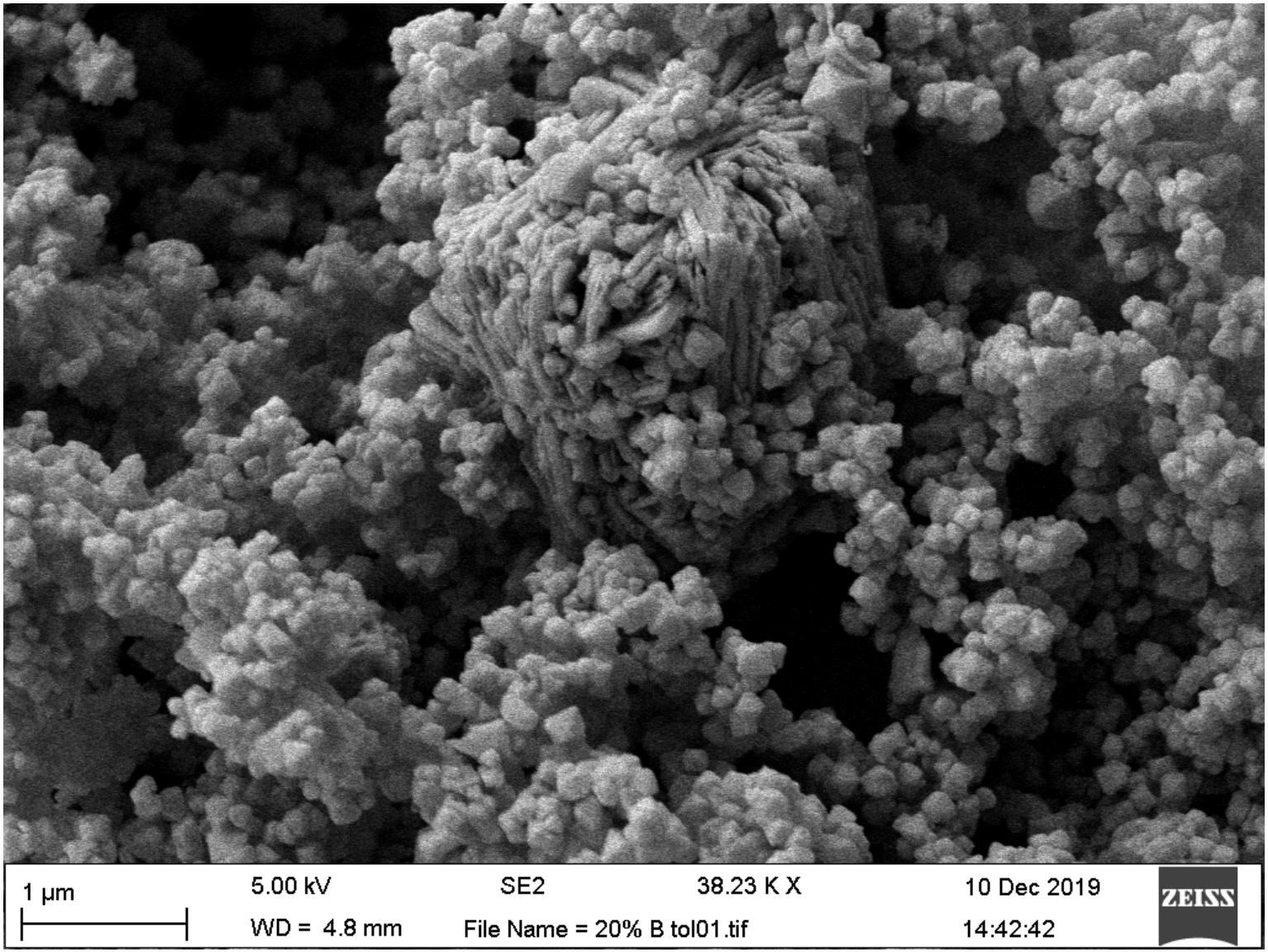

Figure 2.8: High resolution SEM image of CeNP@MOF808 sputter coated with 15 nm Au/Pd.

2.7.2 Energy Dispersive X-ray Spectroscopy Studies of Control MOF808 and CeNP@MOF808

In order to obtain EDX spectra of CeNP@MOF808, the samples were sputter coated in 15 nm of carbon and measured using Oxford Instrument Aztec EDX analyser (20 kV). EDX spectra show the X-rays given off by a sample following irradiation with a high energy electron beam. Incoming electrons collide with core electrons, within the atom, and transfer energy to them *via* inelastic collisions, causing the core electrons to be ejected from the atom (termed secondary electrons).[11,12] The vacancy generated is occupied by an electron in a higher energy shell falling down into the vacancy, releasing energy in the process as a photon of X-ray radiation. The X-rays are characteristic of the elements from which they originate due to the quantised nature of atomic energy levels and are labelled based on the shell that the electron vacancy was generated within (*e.g.* K lines are generated by vacancies being occupied in the K-shell), see Figure 2.9.

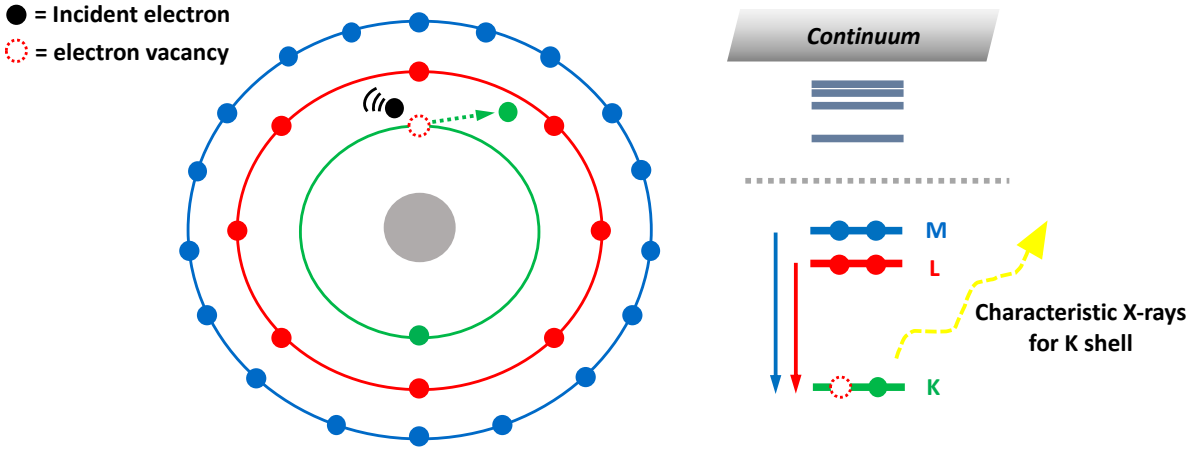

Figure 2.9 Schematic representation of the generation of characteristic X-rays. Left hand side shows core electron on the K-shell being ejected via an inelastic collision with incident electrons. Right hand side shows possible energy transitions for occupying the vacancy. Note that the red transition would be denoted the K_α while the blue transition would be denoted K_β, based on the shell of the occupying electron.

Selecting peaks corresponding to characteristic X-rays of a particular element and integrating the area under each peak allows for the determination of the atomic (at%) and weight (wt%)

percentages of those elements. It is noteworthy to mention that atomic and weight percentages can be highly inaccurate if not all elements are accounted for and included in calculations. Given that MOF808 has the formula $Zr_6O_4(OH)_4(OOCH)_6(BTC)_2$ and that the CeNP were postulated to be of a cerium oxide-hydroxide nature, the elements that were always accounted for in calculations were Ce ($M_{\alpha 1}$, $L_{\alpha 1,2}$, $L_{\beta 1}$), Zr (L_1, $L_{\alpha 1,2}$, $L_{\beta 1,2}$, $L_{\gamma 1}$), O ($K_{\alpha 1,2}$) and C ($K_{\alpha 1,2}$). Several samples had characteristic X-ray peaks corresponding to Si, it was determined that these arose from a combination of: silicate glass contamination of the samples and residual HN'' by-product, and thus were not included in the EDX measurements. To ensure representative sample sizes were taken, multiple EDX profiles were recorded over different areas of the sample surface (see Figure 2.10), these values were then tabulated and collated to yield average values and errors expressed as standard deviations.

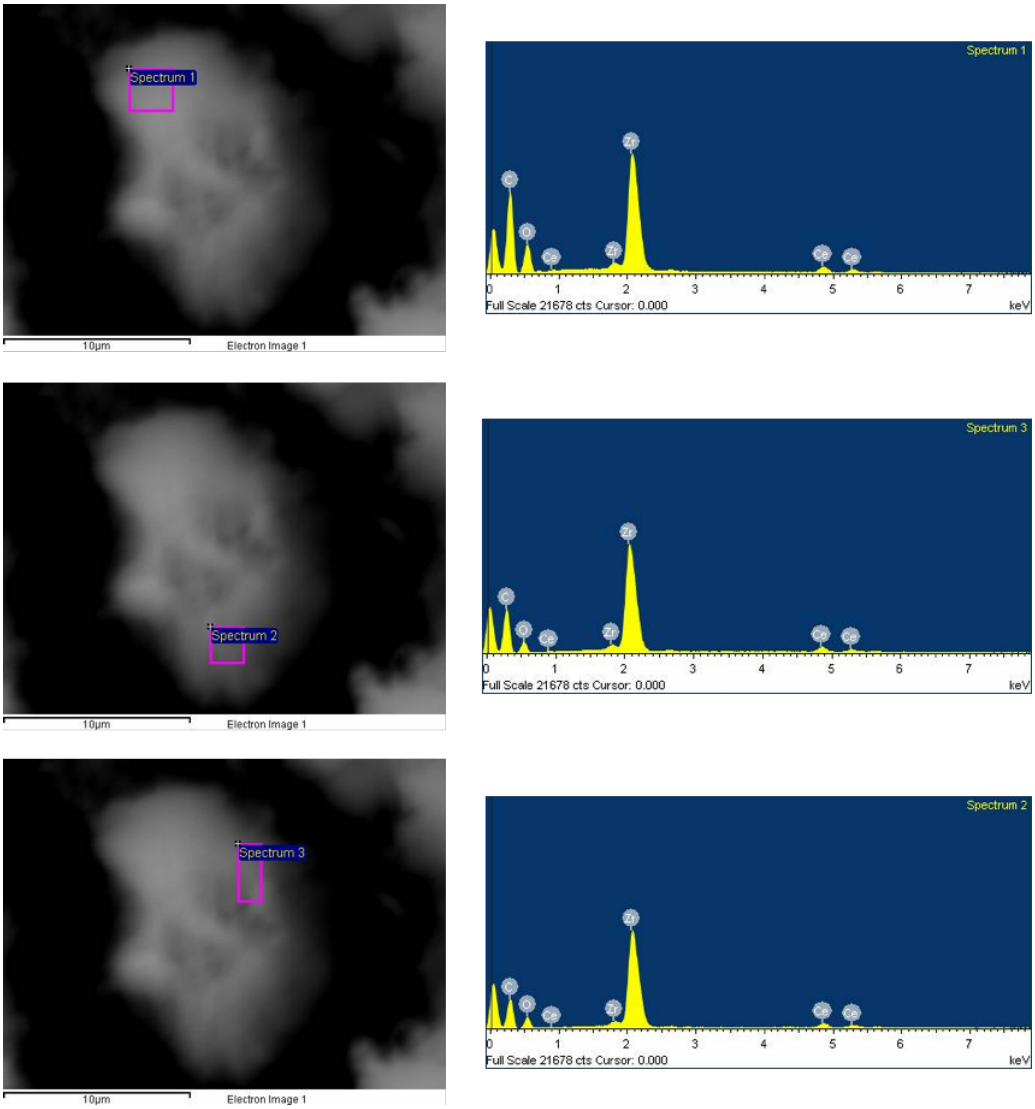

Figure 2.10: Example low resolution SEM image of CeNP@MOF808, showing scan area and corresponding EDX spectra, showing characteristic X-rays for carbon, oxygen, cerium and zirconium.

This process of acquiring multiple EDX spectra was performed on repeated reactive infiltration experiments to improve the reliability of the Ce wt% determined. Shown below in Figure 2.11, are the average Ce, Zr, O and C wt% for control MOF808 and CeNP@MOF808 composites of repeated reactive infiltration experiments, with error bars based on standard deviations.

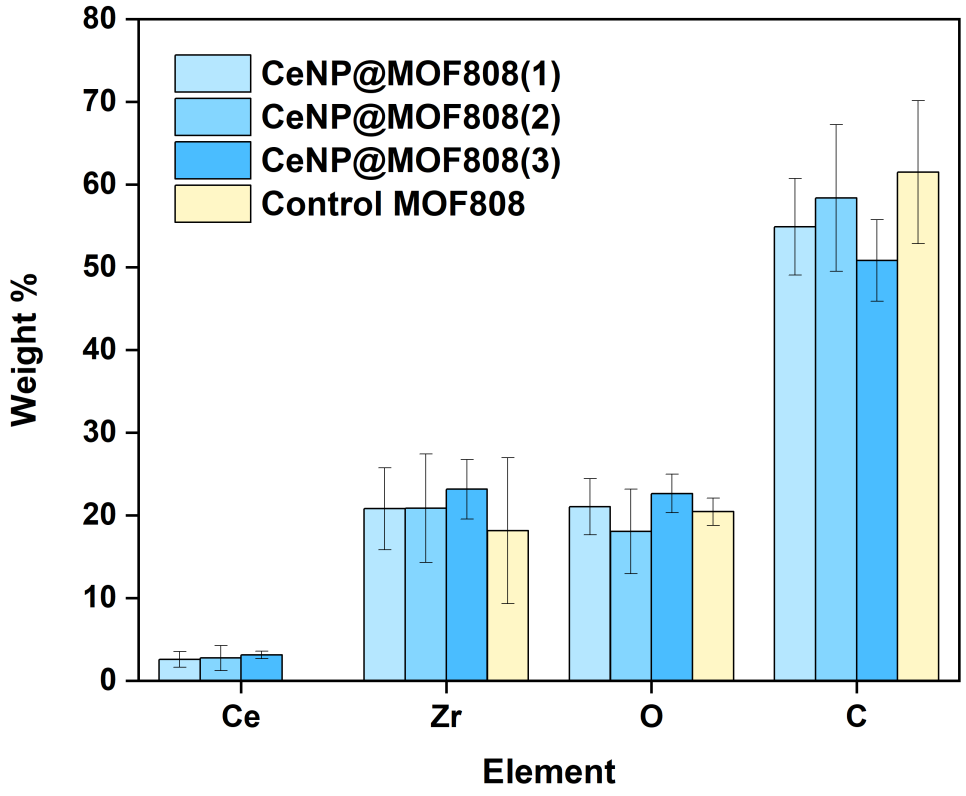

Figure 2.11: Weight percentages (wt%) of Ce, Zr, O and C determined *via* EDX for control MOF808 and repeated CeNP@MOF808 samples.

The presence of Ce was confirmed when comparing Ce wt% of CeNP@MOF808 to control MOF808, showing that reactive infiltration resulted in Ce incorporation. With small variations in Ce wt% across the particle surface it was concluded that the distribution of Ce across CeNP@MOF808 was statistically homogenous. Zr, O and C wt% remain similar between all samples. EDX profiles of replicated reactive infiltration samples showed statistically similar weight percentages of Ce dispersal across the sample, this demonstrates the reproducible nature of the Ce loading *via* reactive infiltration with CeN''_3 in MOF808, with an average loading of 2.8 ± 1.0 wt% (*ca.* 0.32 at%) of Ce. This loading of Ce remained statistically unchanged at 3.1 ± 0.9 wt%, after drying CeNP@MOF808 at 120 °C for 1 hour to remove excess toluene. This was consistent with values determined from the optimisation experiments at 3.2 wt% (see Supplementary Table 2.5). This corresponds to a loading efficiency ranging from 39% to 82% based on the theoretical maximum loading of 4.6 wt% Ce

(CeN''_3). The possibility of post-synthetic exchange (PSE) whereby Ce ions exchange with the Zr ions in the cluster nodes of MOF808 was considered but deemed unlikely when comparing at% of Ce and Zr, see Table 2.1 below. Had PSE occurred during reactive infiltration there would have been a decrease in the Zr at% with the concurrent increase in Ce at%, instead an increase in the Zr at% is observed following reactive infiltration.

Table 2.1: Atomic weight percentages of Ce and Zr in control MOF808 and CeNP@MOF808, determined via EDX.

Sample	Ce at%	Zr at%
Control MOF808	0	3.0
CeNP@MOF808	0.32	3.9

The EDX measurements should be considered to be representative of bulk elemental distribution and instead of isolated to the surface, this is due to penetration depths being in the order of 10^2–10^3 nm meaning a large portion, if not all of the MOF particles (*ca.* 100 nm in diameter) are exposed to the incident electron beam.[13,14]

The synthesis of CeNP@MOF808 composites involved a rigorous washing stage where the material is washed three times *via* sonication in toluene to remove unreacted precursor, by-products and debris. The presence of Ce after this washing stage highlights that there is a chemical/mechanical nature of the Ce binding to the MOF aggregates. Further evidence of this was obtained from 'pseudo-loading' of CeN''_3 on ZrO_2. After being stirred in toluene for 17 hours and washed in the same rigorous manner as samples A, B and C, it displayed 0 wt% Ce in multiple EDX profiles, despite presence of polar Zr–OH groups which could react with the CeN''_3 precursor.[15] This gives extra weight to the conclusions that that it is the combination of the pre-organised structure of the MOF, coupled with protic environments that make Ce loading *via* reactive infiltration possible.

2.7.3 Inductively Coupled Plasma – Optical Emission Spectroscopy (ICP-OES) Studies of Control MOF808 and CeNP@MOF808

After establishing that the loading of Ce within the composite CeNP@MOF808 was *ca.* 3 wt% a separate investigation was performed using inductively coupled plasma – optical emission spectroscopy (ICP-OES) to independently verify the Ce wt% of the composite. Samples of both control MOF808 and CeNP@MOF808 were separately digested using a mixture of HNO_3/HCl/H_2O_2 and analysed using the optical emission spectrometer, whereby the intensity of light emitted is proportional to the centration of the metal dissolved in solution. The Ce wt% of CeNP@MOF808 was determined by ICP-OES to be 3.015 ± 0.007 wt%. As expected, the control MOF808 sample showed no Ce loading at 0 wt%. Both ICP-OES and EDX are in agreement with a Ce loading weight of *ca.* 3 wt% for the CeNP@MOF808 composite (see Table 2.2). The Zr wt% was also determined for both control MOF808 and CeNP@MOF808 *via* ICP-OES. There is good agreement again between the Zr wt% determined by ICP-OES and EDX for both control MOF808 and CeNP@MOF808. The wt% of Zr is, as expected, higher for control MOF808 given that there is no heavy Ce metal present in the sample.

Table 2.2: Ce and Zr elemental weight percentages (wt%) for control MOF808 and CeNP@MOF808, determined via ICP-OES and EDX. Values reported as an average (± std.dev.).

Sample	ICP-OES	EDX
Control MOF808	[Zr]: 34.24 (±0.10)	[Zr]: 31.93 (±8.54)
CeNP @MOF808	[Ce]: 3.015 (±0.007) [Zr]: 27.67	[Ce]: 3.10 (±0.90) [Zr]: 25.39 (±5.76)

2.7.4 Digestion ^{1}H NMR Studies of Control MOF808 and CeNP@MOF808

In order to establish what possible mechanism may be involved in the reactive infiltration process occurring between CeN''_3 and MOF808, digestion NMR was performed on MOF808 samples are various stages of the reactive infiltration methodology. The process of digestion NRM involved complete digesting the samples using D_2SO_4 in d_6-DMSO with heating (up to 189 °C) and agitation. After complete dissolution of the sample, a ^{1}H NMR spectrum was collected sample, revealing linker (BTC, δ = 8.5 ppm) and modulator (formate, δ = 8.0 ppm), as well as any residual solvents (DMF, δ = 7.9 ppm; toluene, δ = 7.05-7.15 ppm). In a stoichiometrically precise MOF808 sample, $Zr_6(\mu\text{–}O)_4(OH)_4(OOCH)_6(BTC)_2$, the number of formate H environments is equal to the number of BTC H environments. Therefore, the relative integrals of the formate and BTC should be 1:1 and give a decimal value of 1.0. This is called the 'formate:BTC ratio' and will be expressed henceforth in decimal form. The formate:BTC ratios are determined by integrating the area under the formate resonance in the digestion ^{1}H NMR, setting the formate area to 1, and then dividing by the relative integrated area under the BTC resonance. The digestion ^{1}H NMR of activated MOF808 is shown below in Figure 2.12.

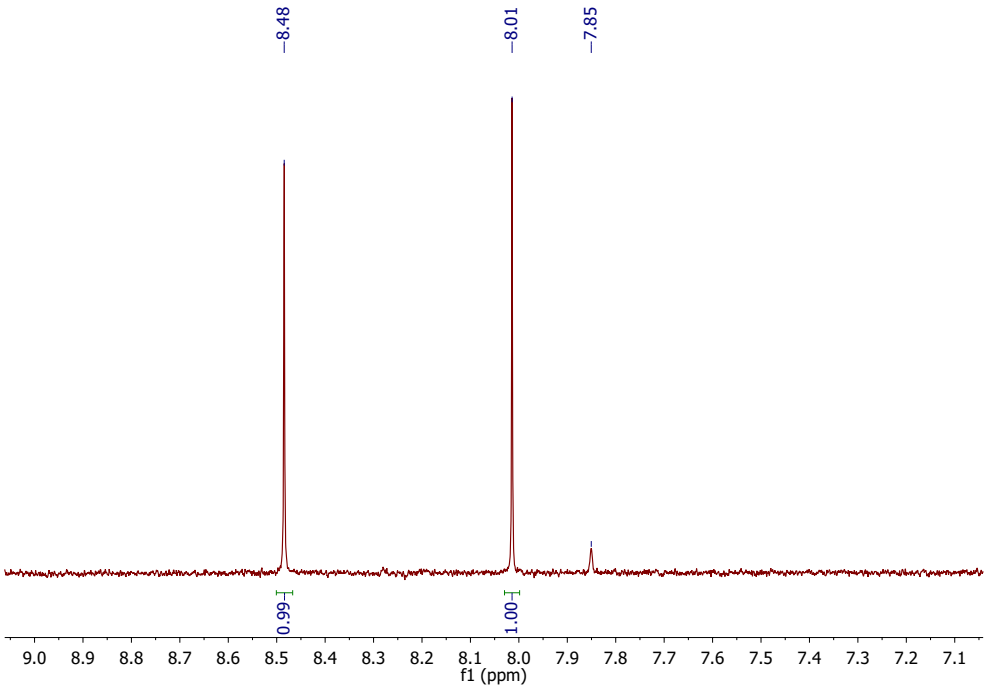

Figure 2.12: Digestion ^{1}H NMR (d_6-DMSO) of activated MOF808.

Three singlet resonances are observed in the digestion ^{1}H NMR of activated MOF808, with resonances at δ = 8.48 ppm and δ = 8.01 ppm corresponding to BTC linker and formate modulator, respectively. The resonance at δ = 7.85 ppm is caused by the presence of residual DMF from the MOF808 synthesis. The activated MOF808 sample therefore has a formate:BTC ratio of 1.01 (1.00 ÷ 0.99). Two more digestion ^{1}H NMR spectra of activated MOF808 were collected to give an average formate:BTC ratio of 1.01 ± 0.02, where the error is the standard deviation. This indicates the activated MOF808 sample is largely stoichiometric with a slight deficiency in BTC linker, indicating the existence of open metal sites at the Zr_6 cluster noted. The value is consistent with literature reference values.[16]

The digestion ^{1}H NMR of control MOF808 was acquired and compared to that of activated MOF808 (see Figure 2.12) to determine the effect of the reactive infiltration process on the MOF808 host without the CeN''_3 precursor present, this is shown below in Figure 2.13.

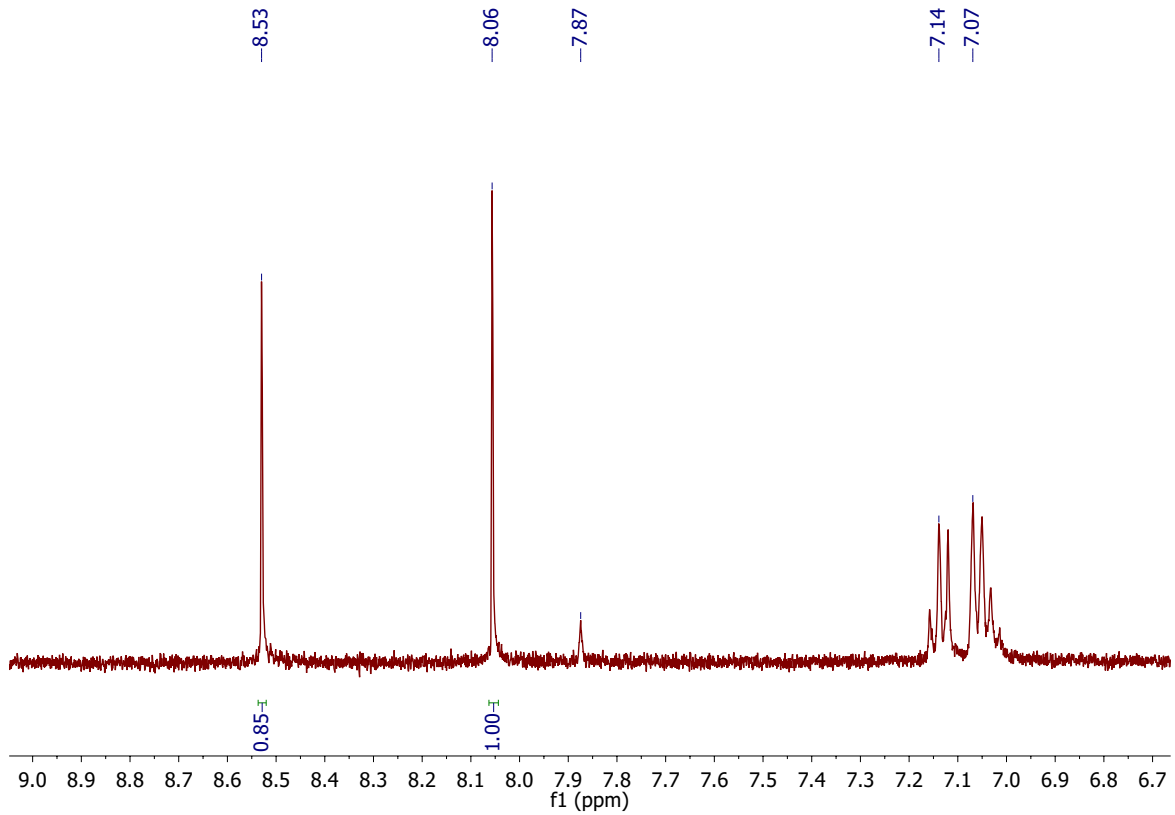

Figure 2.13: Digestion ^{1}H NMR (d_6-DMSO) of control MOF808.

Three singlet resonances are observed at δ = 8.53 ppm, δ = 8.06 ppm and δ = 7.87 ppm corresponding to BTC, formate and DMF – respectively. An additional two triplet resonances at δ = 7.14 ppm and δ = 7.07 ppm are observed which correspond to toluene. The presence of toluene is expected given that large quantities are used in the reactive infiltration process. Two additional digestion ^{1}H NMR spectra of control MOF808 were acquired to give an average formate:BTC ratio of 1.17 ± 0.03. There is an increase the formate:BTC ratio when comparing activated MOF808 to control MOF808, which would suggest an increase in the number of open metal sites, through loss of BTC, during the reactive infiltration methodology without CeN''_3 being present. The digestion ^{1}H NMR spectrum of CeNP@MOF808 is shown below in Figure 2.14. Three singlet resonances are observed at δ = 8.52 ppm, δ = 8.04 ppm and δ = 7.87 ppm corresponding to BTC, formate and DMF – respectively. Two additional digestion ^{1}H NMR spectra of CeNP@MOF808 were acquired to give an average formate:BTC ratio of 1.01 ± 0.30, statistically identical to the control, suggesting that the CeN''_3 precursor does not react to any significant extent with formate modulators or BTC linkers.

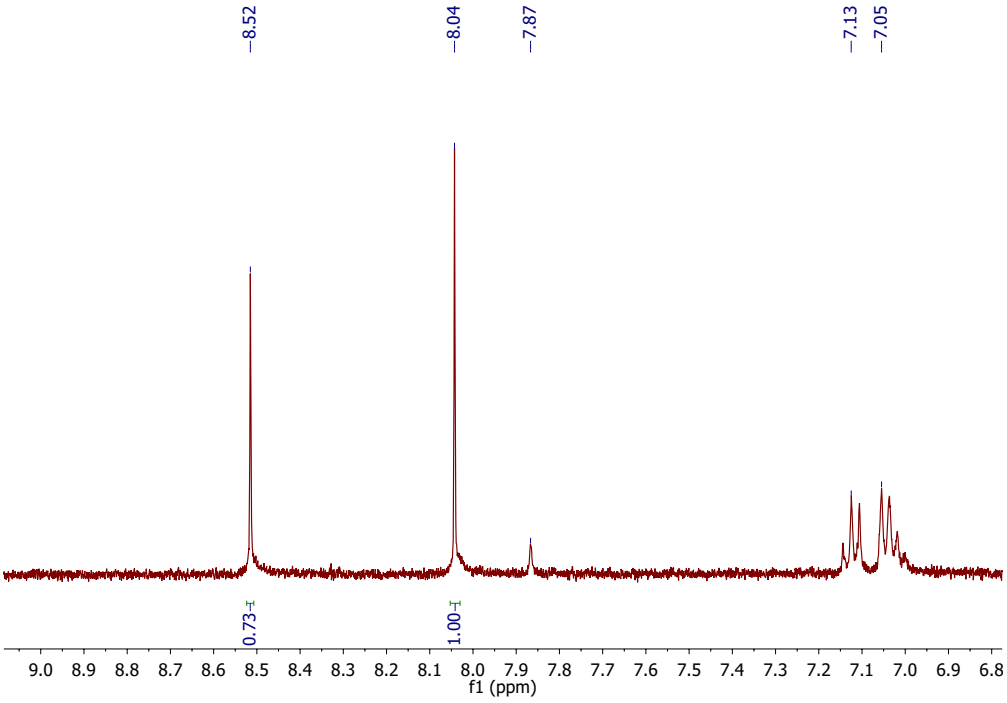

Figure 2.14: Digestion ^{1}H NMR (d_6-DMSO) of CeNP@MOF808.

It is worth considering that the formate:BTC ratios are based on relative integrals, as opposed to absolute integrals measured against an internal standard. In the case where both BTC and formate are lost and/or degraded – and to similar extents stoichiometrically – this would not be observed *via* the relative integrals.

It was also observed that the digestion samples of CeNP@MOF808 all contained DMF (δ = 7.87 ppm), indicating that DMF is not consumed following reactive infiltration and therefore is unlikely to act as a reaction site.

2.7.5 Elemental Microanalysis Studies of Control MOF808 and CeNP@MOF808

Significant structural changes in MOF materials can be characterised by microanalysis of the C, H and N elemental percentages. Samples of both control MOF808 and CeNP@MOF808 were combusted in excess oxygen to yield CO_2, H_2O and NO_x gases and subsequently detected and quantified. From the mass of each gaseous oxide, the relative weight percentage of each element can be determined. The C%, H% and N% of control MOF808 and CeNP@MOF808 are shown below in Table 2.3, along with reference literature values from separate studies. Note that both control MOF808 and CeNP@MOF808 were thermally treated at 120 °C for 1 hour to remove residual toluene solvent from the sample.

Table 2.3: C%, H% and N% of control MOF808 and CeNP@MOF808, determined via elemental microanalysis – with reference literature values for MOF808.

Sample	C%	H%	N%	Ref.
MOF808	20.36	2.81	0	[17]
MOF808	21.02	1.37	0	[16]
Control MOF808	17.28	2.19	0.62	This Work
CeNP@MOF808	17.14	2.02	0.70	This Work

As shown in Table 2.3, control MOF808 has a lower C% relative to literature reference values, while the H% is within the range of literature values. This may reflect differences in synthetic methodology. Control MOF808 has a N% of 0.62%, while both literature reference MOF808 structures showed no N content. This is not unexpected in that digestion NMR of control MOF808 showed the presence of residual DMF from the MOF synthesis (see Figure 2.13).

CeNP@MOF808 shows similar C%, H% and N% to that of control MOF808, indicating no significant change in the structural composition of the MOF808 host following reactive infiltration with the CeN''_3 precursor.

2.7.6 Powder X-ray Diffraction Studies of Control MOF808 and CeNP@MOF808

The working theory of reactive infiltration was that CeN''_3 is a highly reactive and basic precursor which would react with the various protic sites found inside MOF808. However, it would also be possible for CeN''_3 to react with the organic linkers of MOF808, causing the internal porous structure to collapse and drastically reducing the desirable high surface area. Previous optimisation studies have shown that 20 wt% loading of CeN''_3 within MOF808 does not result in a loss of crystallinity (see Section 2.10.5), however due to the larger scale of the reactive infiltration set-up for the optimised procedure, as well as a change from the static syringe infiltration to the constant stirring method, further investigation was required to confirm this retention of crystallinity following reactive infiltration of CeN''_3 within MOF808.

Powder X-ray diffractograms of activated and control MOF808 were recorded in order to confirm that the reactive infiltration methodology itself (*i.e.* without the CeN''_3 precursor present) does not cause any changes to the MOF808 host crystallinity, see Figure 2.15 below.

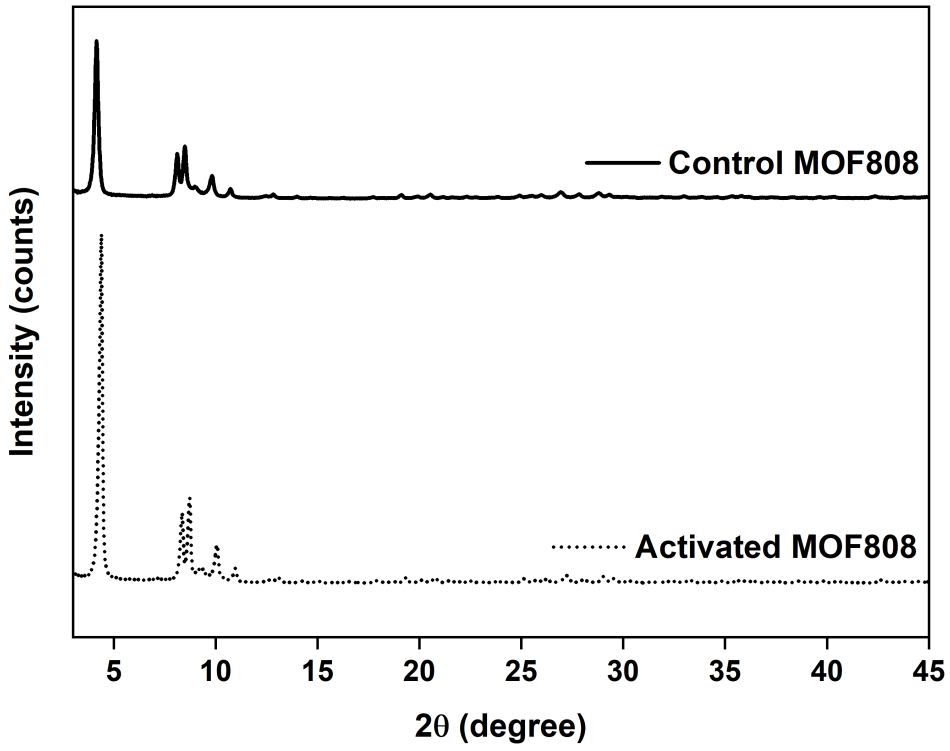

Figure 2.15: Powder X-ray diffractograms of activated and control MOF808.

As seen in Figure 2.15, the diffractograms of both activated and control MOF808 are identical, with both diffractograms showing reflections at low angles; 2θ = 4° (111) 8° (311) 9° (222) 10° (400) 11° (331). Therefore, the reactive infiltration methodology itself does not cause any changes to the crystallinity of the MOF808 host structure.

In order to establish what effect the reactive infiltration of CeN''_3 within the host framework had on the hosts crystallinity, powder X-ray diffractograms were acquired for the composite CeNP@MOF808 and referenced to control MOF808. For the reactive infiltration of CeN''_3 into MOF808 the crystallinity is conserved with the afore mentioned characteristic peaks for MOF808 observed at low angles, see Figure 2.16.

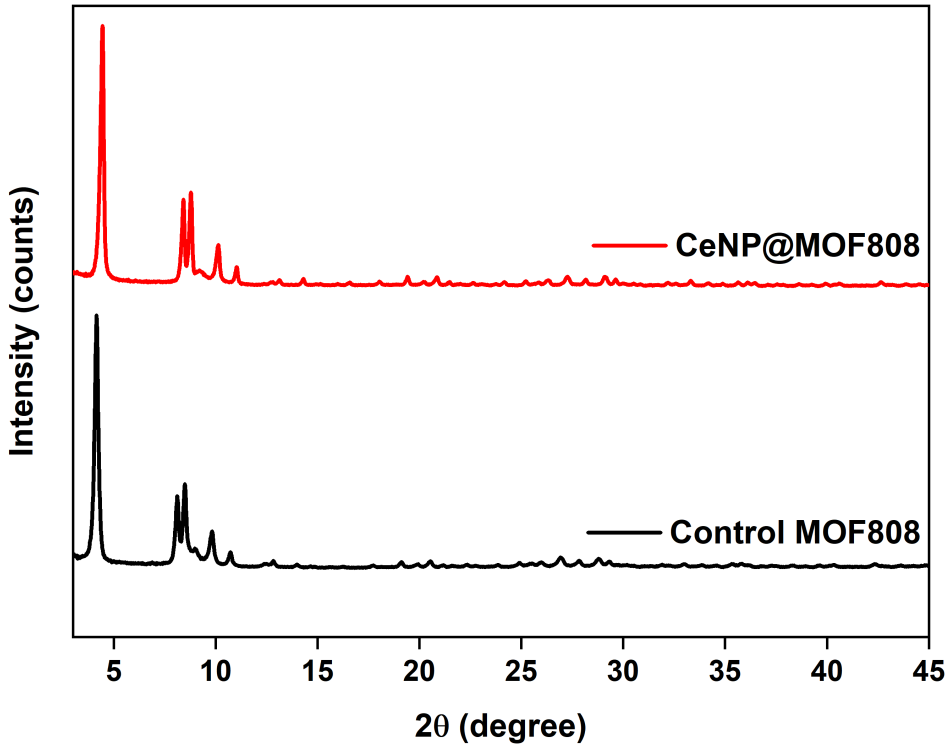

Figure 2.16: Powder X-ray diffractograms of control MOF808 and CeNP@MOF808.

In order to demonstrate the reliability of this retention in the MOF808 crystallinity following reactive infiltration, separate PXRD diffractograms were taken of the composites from the repeated reactive infiltrations. Reflections characteristic of MOF808 at low angles were

observed in all three samples (see Supplementary Figure 2.26), demonstrating the reproducibility of reactive infiltration with consistent properties. The difference in relative peak intensity between control MOF808 and CeNP@MOF808 is evidence of changes in the local electronic structure of the MOF808 host structure following reactive infiltration (*i.e.*, the inclusion of the CeNP guest species). The lack of peak broadening indicates that the reactive infiltration process does not change the crystallite size or introduce mechanical defects, consistent with the observations made during the scaled up optimisation investigation (see Supplementary Figure 2.13) and the high resolution SEM images of control MOF808 and CeNP@MOF808 (see Figure 2.7 and Figure 2.8) which show no significant change in crystallite size. There are no additional peaks seen in the PXRD diffractograms of CeNP@MOF808, this includes at higher angles between 25° and 35° where two peaks are expected due to nanoceria corresponding to the 111 and 200 reflections, respectively, see Figure 2.17. This is expected given that the CeNPs will adopt dimensions on the nanoscale which would yield peaks significantly broadened into the baseline of the diffractogram.

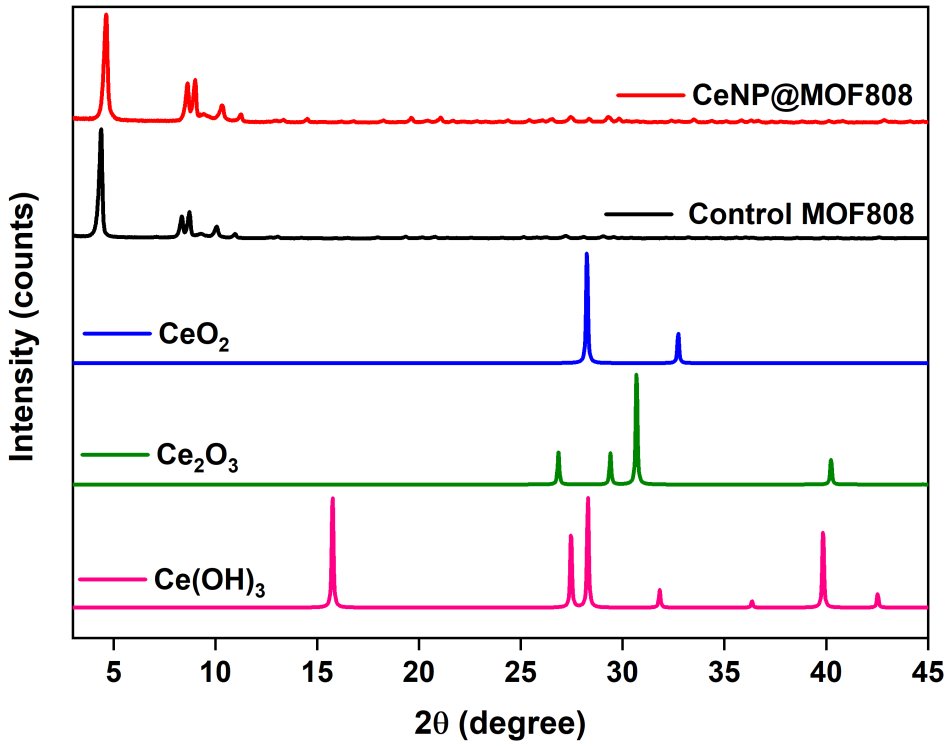

Figure 2.17 Powder X-ray diffractograms of CeNP@MOF808, MOF808 (activated) and speciation references Ce_2O_3 (27° ($1\bar{1}1$) 29° (002) 31° ($1\bar{1}1$) 40° ($10\bar{2}$)), CeO_2 (28° (111) 33°

(200)) and $Ce(OH)_3$ (16° (100) 27° ($2\bar{1}0$) 28° (101) 32° (200) 35° ($2\bar{1}1$) 40° (201) 43° ($3\bar{2}0$)).[18-22]

2.7.7 Potentiometric Titration Studies of Control MOF808 and CeNP@MOF808

MOF808 features incredibly protic pores which are essential to the reactive infiltration methodology, with the protic sites being complementary to the highly basic CeN''_3 precursor. During the reactive infiltration process the CeN''_3 precursor could react with one or more of these sites to generate HN'' and assemble CeNPs within the host MOF808 structure. The protic sites in MOF808 include free linker carboxylic acid groups (COOH), bridging hydroxide ligands and terminal aqua ligands of the cluster nodes. By reacting the MOF host with a strong base such as NaOH it is possible to monitor the pH and obtain pK_a values that reflect the acidity of some of these protic environments (*i.e.* those associated with the cluster nodes, but not free linker carboxylic acid groups).

In order to perform the titrations a procedure was adapted from literature,[23] whereby MOF808 samples were suspended in $NaNO_3$ solution, sonicated for 20 minutes and subsequently allowed to equilibrate for 18 hours. Aqueous 0.1 M HCl was added to the sample to reduce the pH to approximately 3.0. The sample suspension was titrated with 0.1 M aqueous NaOH, with constant stirring at room temperature, until a pH of approximately 11.0 was obtained. Potentiometric titrations were performed on activated and control MOF808 to determine what effect the reactive infiltration methodology, without reactive infiltration taking place, had on the structural integrity of the cluster nodes. Equivalence points were obtained from the first derivative of the resulting titration curve of pH as a function of volume of titrant (NaOH) added, where the maximum peaks in the derivative curve correspond to inflection points and indicate equivalence points. The pK_a is subsequently determined by taking the pH at the point half-way between equivalence points, or in the case of the initial equivalence point taken half-way between the point and 0 µL of base. The pH = pK_a relationship arises from the Henderson-Hasselbalch equation (see eqn. 1),[24] with have the acid being neutralised to generate a conjugate salt of equal concentration.

$$pH = pK_a + \log\left(\frac{[HA]}{[A^-]}\right) \quad (eqn. 1)$$

Shown below in Figure 2.18 are the titration plots of activated and control MOF808. From the method described above, three inflection points and thus three pK_a values were determined for both activated and control MOF808 at 3.8, 6.2, 8.9 and 3.8, 5.8, 8.7, respectively.

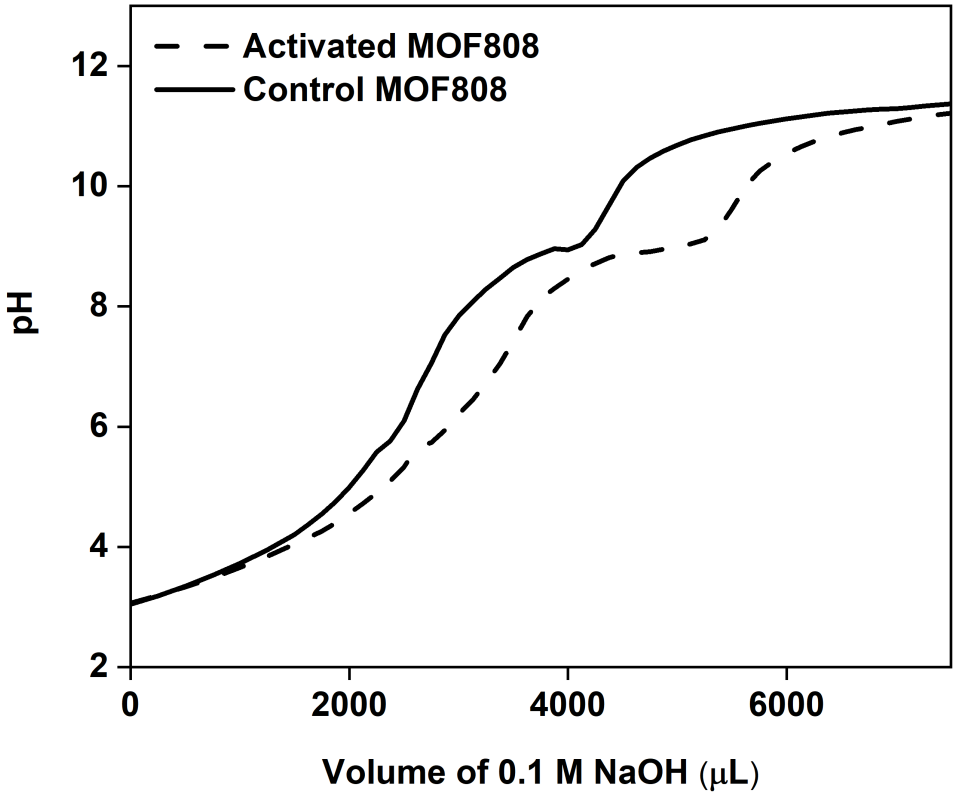

Figure 2.18: Titration plots, pH vs. volume of NaOH added, for activated and control MOF808.

The most acidic pK_a value, pK_{a1}, at 3.8 for both control and activated MOF808, corresponds to the bridging hydroxide ligand of the cluster nodes: $Zr_6(\mu\text{–}O)_4(\boldsymbol{\mu\text{–}OH})_4(OOCH)_{6\text{-}x}(OH)_x(OH_2)_x$ and remains unchanged going through the reactive infiltration methodology without the CeN''_3 precursor. The value of pK_{a1} for both activated and control MOF808 is consistent with literature observations for titrations of MOF808 using NaOH which showed a value of 3.6.[23] The second pK_{a2} values, at 6.2 and 5.8 for activated and control MOF808, respectively, are essentially the same and consistent with literature observations at 6.2. pK_{a2} corresponds to the terminally coordinated aqua ligand, which is introduced during the solvent washing stages of the MOF treatment: $Zr_6(\mu\text{–}O)_4(\mu\text{–}OH)_4(OOCH)_{6\text{-}x}(OH)_x(\boldsymbol{OH_2})_x$. The third pK_{a3} value

corresponds to the terminally coordinated hydroxide ligands of the cluster nodes: $Zr_6(\mu–O)_4(\mu–OH)_4(OOCH)_{6-x}(\boldsymbol{OH})_x(OH_2)_x$. The final pK_{a3} value of 8.9 and 8.7, for activated and control MOF808, respectively, are again the same and similar to literature values of 8.2.[23] The pK_{a3} value of both activated and control MOF808 deviates slightly from the literature value 8.2. One hypothesis for this observed discrepancy is that the activation process in the literature is a solvent-thermal based method,[23] while samples CeNP@MOF808, control MOF808 and activated MOF808 were activated in a dry-thermal based method. The activation of MOF808 would result in a loss of both coordinated aqua and hydroxide ligands, however these are present in the activated samples as a result of re-coordination in aqueous media (*i.e.*, the nitrate solution).

The similarity of the pK_a values of control MOF808 to both activated MOF808 and literature values confirms the structural integrity of MOF808 and is consistent with PXRD patterns, which show reflections characteristic of MOF808. Potentiometric titrations were then performed on the CeNP@MOF808 composite to probe possible changes in the acidities of protic sites associated with the cluster to determine if they are altered by the reactive infiltration process with CeN''_3.

Potentiometric titration plots for control MOF808 and CeNP@MOF808 are shown below in Figure 2.19.

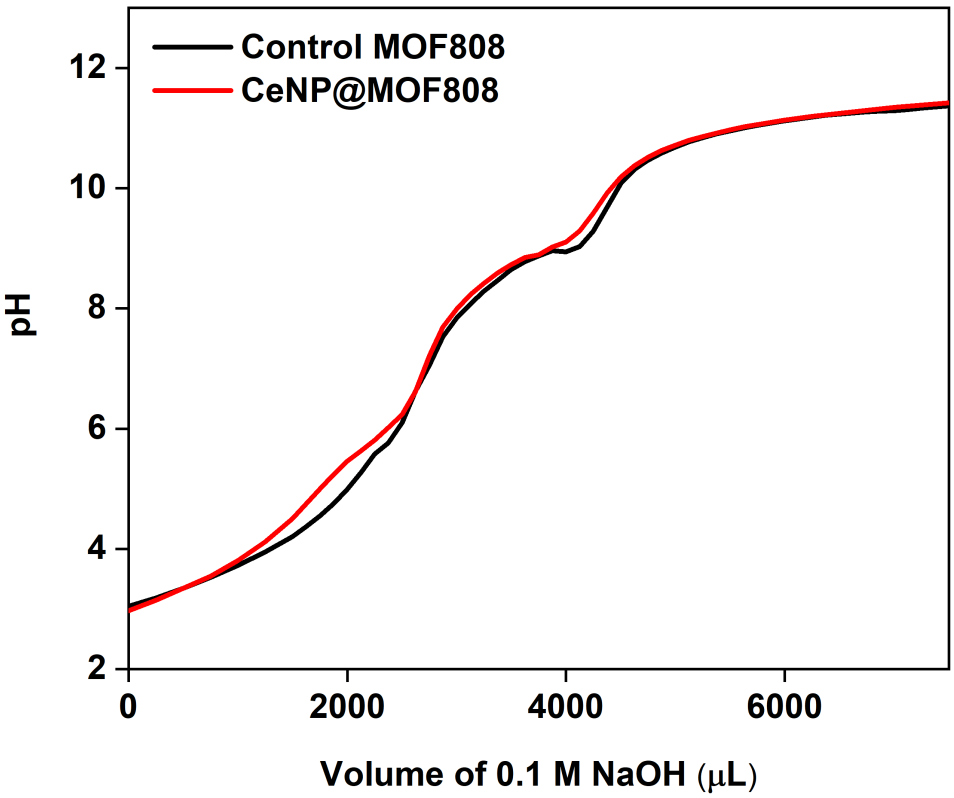

Figure 2.19: Titration plots, pH vs. volume of NaOH added, for control MOF808 and CeNP@MOF808.

The calculated pK_a values for CeNP@MOF808 are consistent with literature values for pK_{a1} and pK_{a2} at 3.6 and 6.2, respectively, and are identical to those of control MOF808. The third pK_{a3} values, corresponding to terminally coordinated hydroxide ions of the Zr_6 node, is identical to that of control MOF808 at 8.7. This suggests that the process of reactive infiltration does not significantly affect the Zr_6 nodes of the MOF808 framework, consistent with PXRD diffractograms which show retention of the MOF808 crystallinity.

Had the reactive infiltration process involved the reaction of CeN''_3 with the Zr_6 cluster node hydroxide ligands or aqua ligands this would have resulted in a loss of those protic hydrogen environments, and in turn removed the associated pK_a value. Therefore given that there are three distinct pK_a values for CeNP@MOF808 that match well with literature values for MOF808 and control MOF808 it can be concluded that the reactive infiltration process does not involve any significant acid-base type reactions occurring between the CeN''_3 precursor molecule and protic cluster hydroxide and aqua ligand environments.

2.7.8 Infrared Spectroscopy Studies of Control MOF808 and CeNP@MOF808

MOF808 has a number of structural motifs that can be observed in the infrared (IR) spectrum. IR absorption bands are caused when bonds and collections of bonds within the structure absorb IR light of a certain energy and begin to vibrate, if the vibration yields a change in the dipole moment of the bond, or group, then the vibration shall be IR active, and observed in the IR spectrum. The IR spectrum of the samples (activated, control MOF808 and CeNP@MOF808) were recorded using an attenuated total reflectance spectrometer, whereby the IR light beam is passed into a crystal above a certain angle (the critical angle). The beam of light within the crystal exhibits total internal reflection whereby the light bounces back and forth within the crystal before exiting at the opposing ends of the crystal to the detector. When the light is reflected at the surface of the crystal-sample interface it generates an evanescent wave that acts as a standing IR wave and interacts with the sample.[25] These evanescent waves interfere with the IR light propagating through the crystal and carry chemical information through to the detector which can then be constructed into an IR spectrum through a Fourier transform function. This allows for neat solid and liquid samples to be analysed without the need for dispersing within a KBr disc or Nujol mull.

There are two significant structural motifs associated with the MOF808 structure; the cluster nodes and BTC organic linker. Both of these motifs have been observed in literature, with cluster nodes exhibiting characteristic Zr–O stretches at ca. 650 cm^{-1},[26] while BTC linker showing coordinated carboxylate asymmetric and symmetric stretches at ca. 1600 cm^{-1} and 1400 cm^{-1} and aromatic stretches at ca. 1440 cm^{-1}.[26,27] Therefore, IR spectroscopy serves as a useful technique in probing the structural connectivity of the MOF808 host structure before and after reactive infiltration. ATR-IR spectra of activated and control MOF808 were first collected to establish what effect the reactive infiltration methodology has on the structural connectivity of the MOF808 host, without the CeN''_3 precursor being involved. These spectra, along with assignments of major absorption bands, are shown in Figure 2.20.

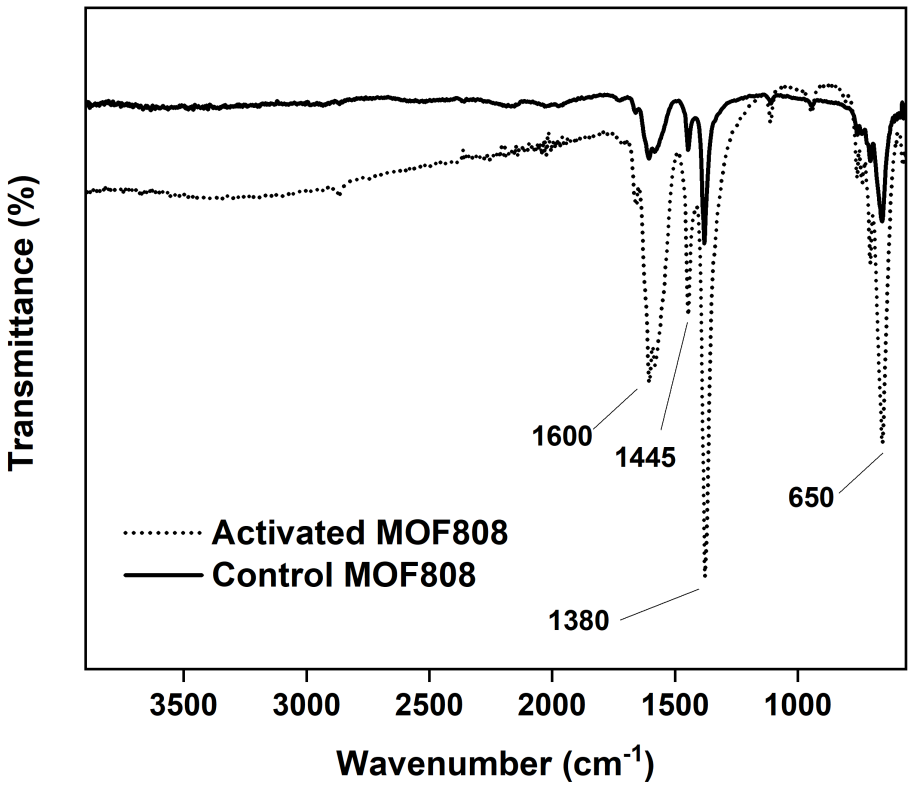

Figure 2.20: ATR-IR spectra of activated and control MOF808.

Lack of an broad absorption band at 3300 cm^{-1}, in both activated and control MOF808, is indicative of an anhydrous solid with no water present. This is not unexpected given that both samples are thermally treated at 120 °C, which is sufficient to evaporate water from the structure. Absorption bands at 1600, 1445 and 1380 cm^{-1} correspond to carboxylate and aromatic ring vibrations of the BTC linker within the MOF808 structure, these bands are present in both activated and control MOF808, indicating no significant change to the BTC linker molecules within the structure. The absorption band at 650 cm^{-1} is present for both activated and control MOF808, and was assigned to Zr–O stretches – again indicating no change to the cluster nodes of the MOF808 structure. Therefore, the reactive infiltration methodology did not cause any changes to the structural connectivity of the MOF808 structure.

An ATR-IR spectrum was acquired for the CeNP@MOF808 composite, see Figure 2.21, to determine what effect the reactive infiltration of the CeN''_3 precursor within the MOF808 host had on its structural connectivity.

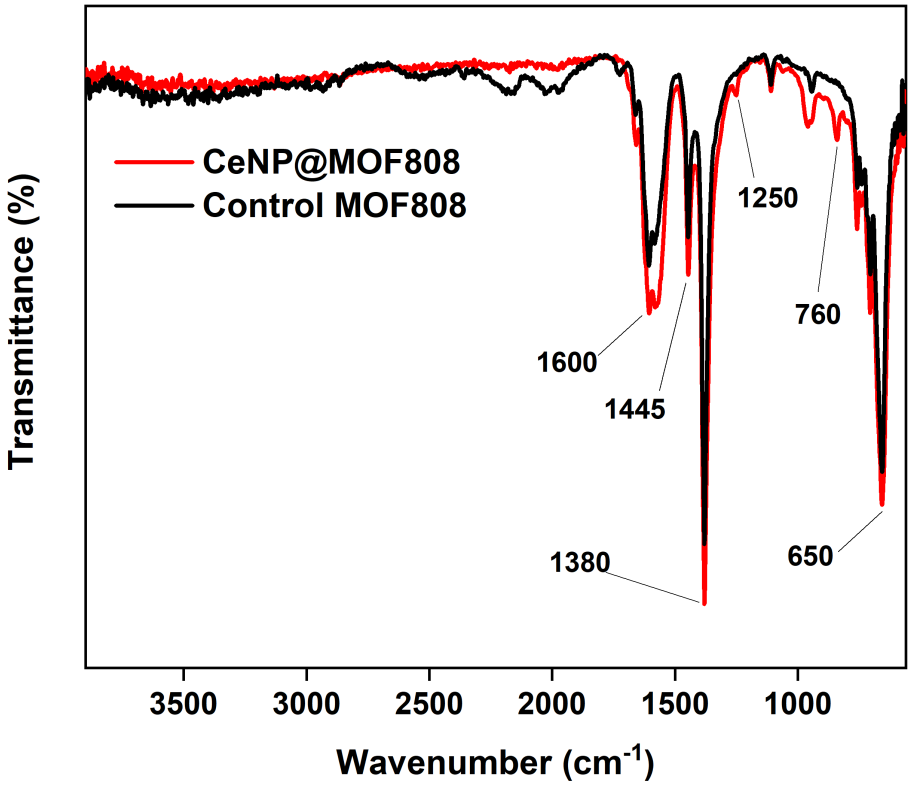

Figure 2.21: ATR-IR spectra of control MOF808 and CeNP@MOF808.

There is no significant shift in absorption bands when comparing CeNP@MOF808 to control MOF808, with absorptions at 1600, 1445 and 1380 cm^{-1} corresponding to carboxylate and aromatic ring vibrations of the BTC linker. This demonstrates that the reactive infiltration process does not result in the degradation of the MOF808 structure, consistent with digestion NMR of CeNP@MOF808 that shows intact BTC linker (see Figure 2.14) and PXRD diffractograms of CeNP@MOF808 (see Figure 2.16) which show retention of the MOF808 crystallinity. The absorption band at 650 cm^{-1} is present for both MOF808 and CeNP@MOF808, assigned to Zr–O stretches of the cluster nodes. This is consistent with potentiometric titrations which show no change to the acidities of the coordinated hydroxide

and aqua ligands (see Figure 2.19), implying no cluster degradation following reactive infiltration.

The penetration depth of the evanescent waves is dependent upon a number of factors which are important when investigating a composite such as CeNP@MOF808. Firstly, the penetration depth is inversely proportional to the wavenumber, with higher penetration depths occurring at smaller wavenumbers.[25] CeO_2 has two IR active Ce–O vibrations at 1500 cm^{-1} and 650-500 cm^{-1},[28] and thus the vibration at 1500 cm^{-1} may be dampened in intensity due to reduced penetration depths. CeNPs generated within the MOF particles may also be unevenly distributed and thus the resulting low penetration depths and subsequent detection of the 1500 cm^{-1} could be impeded further still. The absorption band at 650 cm^{-1} is present for both MOF808 and CeNP@MOF808, was assigned to Zr–O stretches. Ce–O bond stretches can also occur at 650 cm^{-1}, however these would not be observable in the CeNP@MOF808 IR spectrum due to significant overlap with the strong Zr-O absorption band. No absorption band at 1500 cm^{-1}, corresponding to Ce–O bond stretching, is observed for CeNP@MOF808. Two weak absorption bands are observed for CeNP@MOF808, but not control MOF808, at 1250 cm^{-1} and 760 cm^{-1}, possibly arising from complex multi-vibrational modes of Ce oxy-hydroxide based clusters (e.g., CeNPs).

2.7.9 N_2 Adsorption Isotherms Studies of Control MOF808 and CeNP@MOF808

Porous materials such as metal organic frameworks have incredibly high surface areas. These surface areas can be quantified by applying the theory of Brunauer, Emmett and Teller (BET) to nitrogen adsorption isotherms of the porous material measured at 77 K.[29] Despite BET theory relying on several assumptions that do not hold entirely for microporous substances such as MOF808, namely multilayer adsorbate adsorption and absence of pore filling mechanisms, computational studies of MOF crystal structure surface areas have shown good agreement with BET measurements.[30] Furthermore, while absolute BET surface areas values for novel MOF structures may be limited, relative comparisons such as those of control MOF808 and CeNP@MOF808 are significantly meaningful. It was first necessary to establish the surface area of the control MOF808 sample and compare with literature values. The BET surface areas of MOF808 have been shown previously to be dependent upon the starting material, with $ZrCl_4$ the specific surface area quoted in literature of MOF808 is approximately 1300 m^2/g.[4] The N_2 adsorption isotherm for control MOF808 is shown below in Figure 2.22.

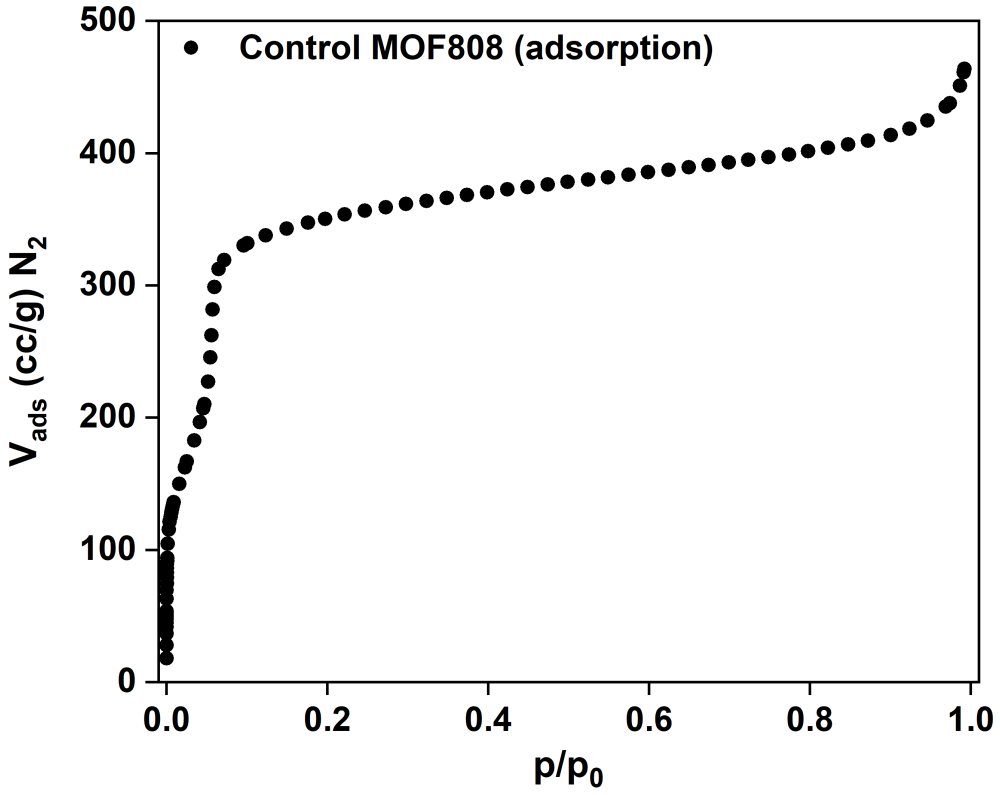

Figure 2.22: N_2 adsorption isotherm of control MOF808 at 77 K.

The adsorption of N_2 involves the initial formation of a monolayer of the gas on the apertures. Nitrogen is adsorbed onto the surface of the solid via formation of weak quadrupole-quadrupole intermolecular forces. Multilayers develop over time, causing pressure to increase and yield a sharp rise in N_2 adsorption. The gas is subsequently forced through the aperture to begin occupying the larger micropore. Pressure increases further resulting in the gas condensing and yielding a sharp upturn in adsorption of N_2 in the isotherm plot. The application of BET theory to the above isotherm in Figure 2.22, within the relative pressure (p/p_0) range of 0.05 – 0.3, yielded a specific surface area of 1349 m^2/g, similar to that reported in literature. The N_2 adsorption isotherm of MOF808 was a mixture of type I and IV isotherms, reflective of the microporous nature of MOF808.[31] A pore size distribution was calculated for MOF808 based on the N_2 adsorption isotherm profile in Figure 2.22 and is shown below in Figure 2.23. Two micropores were observed at *ca.* 13 Å and *ca.* 22 Å, consistent with literature observations.[32] Note that the larger micropore measured at *ca.* 22 Å would technically meet the definition of a mesopore – however, the measured pore diameters derived from the pore size distribution plots are based on a model which is standardised against materials such as

active charcoal. Therefore, the values determined are somewhat divergent from the true value (*e.g.*, 18 Å for the larger micropore).

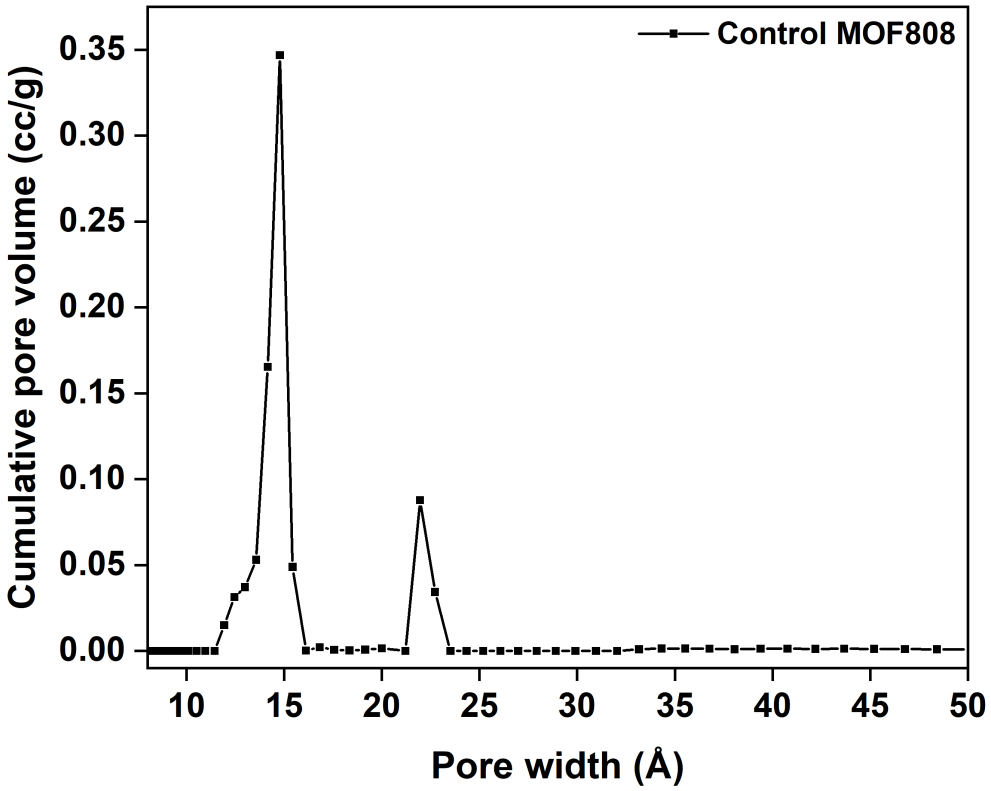

Figure 2.23: Pore size distribution for control MOF808.

The similarity of the specific surface area and pore size distribution of MOF808 to quoted literature values confirms the structural integrity of MOF808. Having confirmed the surface of the host MOF808 structure, N_2 adsorption isotherms were then subsequently collected for CeNP@MOF808 to determine if the process of reactive infiltration with CeN''_3 affected the microporous surface area of MOF808. The larger micropore of MOF808 is an adamantane-shaped pore, 18.4 Å in diameter, surrounded by inaccessible tetrahedral pores, 4.8 Å in diameter.[9,10] The aperture leading into the large micropore has a diameter of 14 Å and is considered microporous. The diameter of the precursor CeN''_3, is approximately 12 Å and is capable of passing through the aperture into the large micropore to undergo reactive infiltration.[1]

Shown below in Figure 2.24 are the N_2 adsorption isotherms of control MOF808 and CeNP@MOF808 at 77 K.

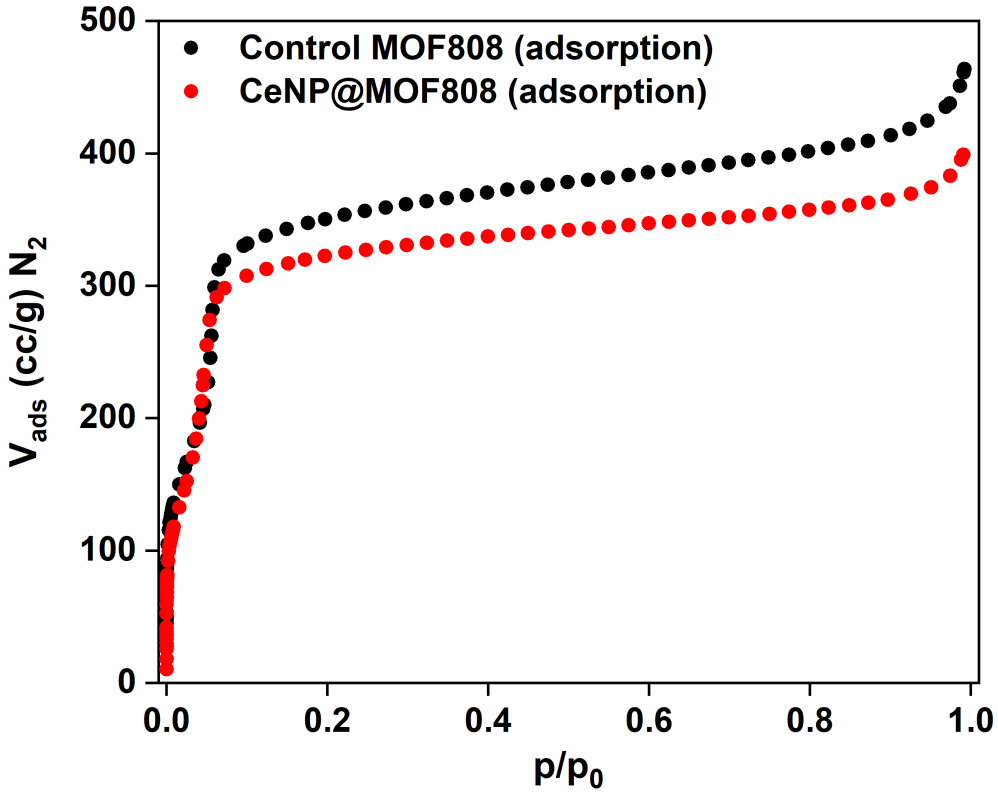

Figure 2.24: N_2 adsorption isotherms for control MOF808 and CeNP@MOF808 at 77 K.

CeNP@MOF808 exhibited a N_2 adsorption isotherm that, similarly to control MOF808, was a mix of type I and IV isotherms. The volume of N_2 adsorbed is similar, at low relative pressures below 0.1, for CeNP@MOF808 and control MOF808, as seen by an overlap of the isotherms in Figure 2.24. It is evident that the volume of N_2 adsorbed by control MOF808 is different to that of CeNP@MOF808, particularly in the higher-pressure region (>0.3 p/p_0) of the adsorption isotherms which corresponds to the large micropore of MOF808 and therefore not accounted for in the BET calculation which is performed at lower relative pressures associated with the smaller microporous surface area. N_2 adsorption isotherms were collected twice more for two separate samples from repeated reactive infiltration reactions, with BET specific surface area calculated and tabulated before in Table 2.4.

Table 2.4: BET specific surface areas for CeNP@MOF808 samples.

Sample	Specific Surface Area (m^2/g)
CeNP@MOF808 (1)	1226
CeNP@MOF808 (2)	1288
CeNP@MOF808 (3)	1232
Average (± std. dev.)	1249 (± 34)

The average BET calculated microporous specific surface area for CeNP@MOF808 was calculated to be 1249 ± 34 m^2/g, which is marginally lower than specific surface area of control MOF808 at 1349 m^2/g. This small reduction in specific surface area was similar to that observed in a separate study which involved loading of metallic Pd nanoparticles into MOF808.[33] It can be concluded from comparisons of the microporous surface areas that the process of reactive infiltration does not change the surface area of MOF808 to any significant extent. This is in contrast to initial results observed in the optimisation studies which showed significant decreases in the microporous surface area following reactive infiltration, with 20 wt% loading of CeN''_3 in both toluene and THF resulting in a decrease in the specific surface from *ca.* 1300 m^2/g to 784 m^2/g and 875 m^2/g, respectively. One possible cause of this discrepancy could be the difference in the infiltration experimental methodology, where with the optimisation reactive infiltration was performed in a syringe, using *ca.* 50 mg of MOF808 and a stagnant 20 wt% CeN''_3 solution, while in the optimised procedure 625 mg of MOF808 was stirred constantly with a 20 wt% CeN''_3 solution. This difference in specific surface area reductions with different loading methodologies serves as an example of the importance of the experimental procedure to the properties of the resulting composite, hence why it is essential to have a standardised methodology.

Pore size distribution plots were calculated for CeNP@MOF808 and are shown below in Figure 2.25. The larger micropore is no longer accessible, while the smaller micropore at 13 Å remains open following reactive infiltration. This is consistent with a CeNP structure occupying the larger micropore, while the small micropore entrance channel remains un-obstructed.

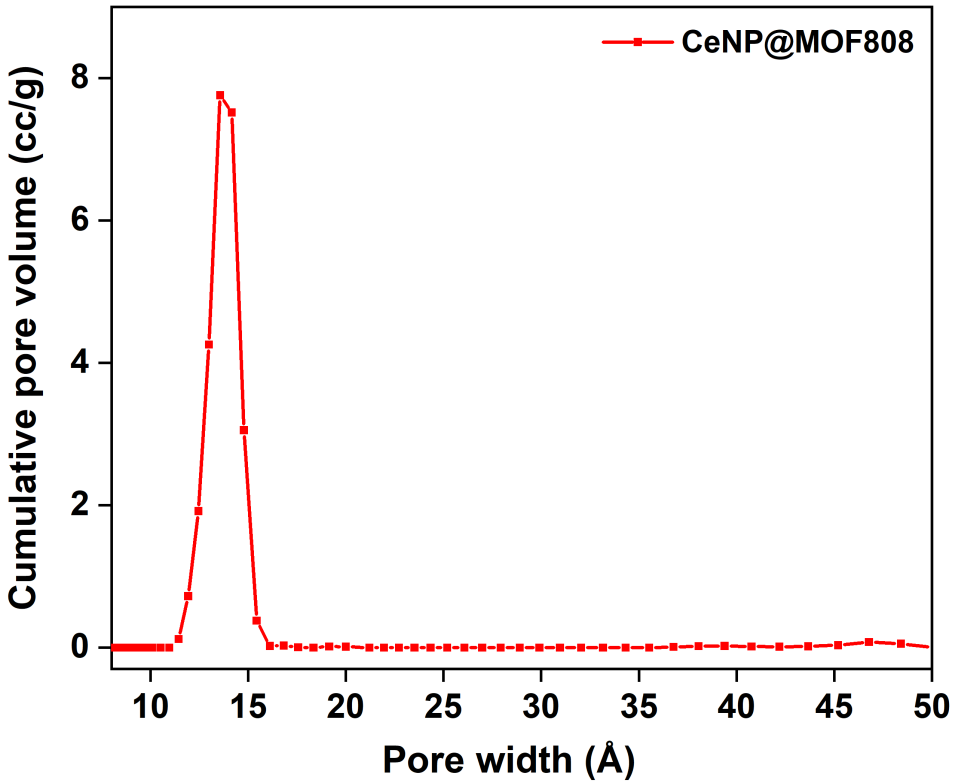

Figure 2.25: Pore size distribution for CeNP@MOF808.

In conclusion, calculated specific surfaces using BET methods showed that the processs of reactive infiltration does not change the surface area of the host MOF808 structure. Pore size distribution calculations revealed loading of CeNP into the large micropore of MOF808.

2.8 Conclusions

In conclusion, it has been demonstrated that reactive infiltration occurs with the complementary pairing of CeN''_3 – MOF808, whereby the reaction takes place in a single one-step process, without any additional external energetic inputs. Through the process of optimisation, an optimised methodology of reactive infiltration was devised and subsequently applied, with replication, to synthesise the CeNP@MOF808 composite.

Extensive characterisation of the CeNP@MOF808 composite was performed, referenced to control MOF808, and is summarised in Table 2.5 shown on the next page. Following reactive infiltration of CeN''_3 within MOF808, it can be shown conclusively through a combination of SEM, digestion NMR, elemental microanalysis, powder X-ray diffraction, titration, infrared spectroscopy and N_2 adsorption isotherm studies that the macroscopic structure (crystallite size, morphology and surface area) and microscopic structure (linker – node connectivity, crystallinity) of the MOF808 host is retained. Characterisation of the Ce wt% loading, *via* independent methods of EDX and ICP-OES, show a loading of *ca.* 3 wt%.

The exact speciation (*i.e.* chemical composition, structure, size) of the CeNP composited within MOF808 remains elusive following characterisation. No reflections are observed in the PXRD diffractograms that would be characteristic of the crystalline CeO_2, no individual CeO_2 nanoparticles are visibly imbedded on the surface of the MOF crystallites in the high resolution SEM images of CeNP@MOF808 and no IR vibrations are present that would indicated CeO_2 being present. This is most likely due to either: (a) CeO_2 are in fact formed but are of such small dimensions, and low loading weights, that they are not observed in the various characterisations outlined in Table 2.5 or (b) that the CeNP take on a more complicated speciation. This latter point will be explored later in Chapter 3, whereby the possibility of forming a cerium oxy-hydroxide species, of the form $CeO_x(OH)_y$, will be further investigated.

Table 2.5: Summary of characterisation of control MOF808 and CeNP@MOF808.

Characterisation	Control MOF808	CeNP@MOF808
Particle Size (SEM)	100 – 200 nm	100 – 200 nm
Ce wt% (EDX)	0	2.8 ± 1.0
Ce wt% (ICP-OES)	0	3.015 ± 0.007
Formate: BTC (^{1}H NMR)	1.17 ± 0.03	1.01 ± 0.30
CHN % (microanalysis)	17.28, 2.19, 0.62	17.14, 2.02, 0.70
Crystallinity (PXRD)	Crystalline (MO808) 4° (111) 8° (311) 9° (222) 10° (400) 11° (331)	Crystalline (MOF808) 4° (111) 8° (311) 9° (222) 10° (400) 11° (331)
pK_a	3.8 (μ–OH) 5.8 (OH_2) 8.7 (OH)	3.8 (μ–OH) 5.8 (OH_2) 8.7 (OH)
IR Stretches	1600 cm^{-1} (carboxylate) 1445 cm^{-1} (aromatic ring) 1380 cm^{-1} (carboxylate) 650 cm^{-1} (Zr – O)	1600 cm^{-1} (carboxylate) 1445 cm^{-1} (aromatic ring) 1380 cm^{-1} (carboxylate) 1250 cm^{-1} (?) 760 cm^{-1} (?) 650 cm^{-1} (Zr – O)
Specific Surface Area (BET)	1349 m^2/g	1249 ± 34 m^2/g

2.9 Experimental Details for Chapter 2

2.9.1 Synthesis of $Ce(OTf)_3$

A Teflon-sealed ampoule was charged with $Ce_2(CO_3)_3.xH_2O$ (4.64 g, 10.1 mmol, 1 eqv) and suspended in 20 mL of deionised water. HOTf (10.00 g, 66.7 mmol, 6.6 eqv) was added to the suspension, with stirring, resulting in an immediate vigorous fuming of the solution. The reaction mixture was sealed under partial vacuum and refluxed at 101 °C for 18 hours. After 18 hours all solids had dissolved, leaving a colourless solution. Water was removed *via* rotary evaporation in a pear-shaped evaporation flask. White solids were isolated on a Gooch crucible and washed with Et_2O (4 × 10 mL) and hexanes (2 × 10 mL), and dried at 220 °C for 36 hours; yielding a white free flowing powder $Ce(OTf)_3$ (5.76 g, 9.8 mmol, 49%). $^{19}F\{^1H\}$ NMR (d_3-MeCN): δ -76.40 (s, C***F***$_3SO_4$) ppm.

2.9.2 Synthesis of KN''

Synthesis of KN'' was adapted from an established literature procedure.[34] A Teflon-sealed ampoule was charged with KH (2.0 g, 50 mmol, 1 eqv) and suspended in 20 mL of toluene. The colourless liquid of HN'' (8.05 g, 50 mmol, 1 eqv) was degassed by three freeze–thaw cycles and added to the KH suspension *via* cannula at -78 °C, with stirring. The mixture equilibrated to room temperature for 20 minutes. The reaction mixture was refluxed at 120 °C for 12 hours under partial vacuum, giving a colour change from light grey to orange after 1 hour; and to dark brown after 12 hours. The reaction mixture was filtered on a frit through dry Celite®, leaving a dark brown residue. The residue was washed with hexanes (2 × 10 mL). The washings and filtrate were combined in a Schlenk flask and cooled at -15 °C for 12 hours after which white crystals crystallised out of solution. The mother liquor was removed from the crystals *via* cannula. Crystals were washed with cold hexanes (2 × 20 mL) at -78 °C. The white crystals were dried under vacuum for 30 minutes yielding a white free flowing powder KN'' (4.90 g, 24.62 mmol, 49%). ^1H NMR (d_6-benzene): δ 0.13 (s, Si***Me***$_3$) ppm.

2.9.3 Synthesis of CeN''_3

Synthesis was adapted from an established literature procedure.[35] A Schlenk flask was charged with $Ce(OTf)_3$ (3.16 g, 5.38 mmol, 1 eqv) and suspended in 30 mL of THF. A separate Schlenk flask was charged with KN'' (3.32 g, 16.68 mmol, 3.1 eqv) and dissolved in 20 mL of THF forming a pale-yellow solution. The KN'' was added to the $Ce(OTf)_3$ suspension *via* cannula, with stirring, forming a yellow solution which turned into a yellow cloudy suspension after *ca.* 15 minutes. The reaction mixture was stirred for 1 hour at room temperature, before the THF was removed *in vacuo* yielding cream-yellow solids which were dried for 1 hour *in vacuo*. The cream-yellow solids were extracted into dry toluene (3 × 10 mL). The toluene washings were combined, reduced to saturation *in vacuo* and recrystallised over 18 hours by slow-cooling to -15 °C using an isopropyl alcohol jacket. Yellow needle-like crystals were isolated from the mother liquor *via* cannula and washed with dry hexanes (2 × 10 mL) at -78 °C. The yellow solids were dried *in vacuo* for 30 minutes yielding a bright yellow free-flowing powder CeN''_3 (1.91 g, 3.08 mmol, 57%). ^{1}H NMR (d_6-benzene): δ -3.40 (s, Si***Me***$_3$) ppm.

2.9.4 Optimisation of Reactive Infiltration

Small NMR scale reactions were conducted to investigate the optimum conditions to facilitate the reactive infiltration of CeN''_3 inside activated MOF808. The progress of the reactions was monitored *via* ^{1}H-NMR, with formation of by-product HN'' measured over a 24 hour period. Use of an internal standard tetrakis(trimethylsilyl)silane (TTMS) allowed for the quantification of HN'' (µmols). Note that there is a significant error associated with the measuring of 1 mg of CeN''_3 and 3 mg of TTMS.

2.9.4.1 NMR Studies of CeN''_3 Reactive Infiltration into MOF808 (d_6 – benzene)

Yellow solid, CeN''_3 (1 mg, 0.002 mmol), was dissolved in d_6 – benzene to form a bright yellow solution in a Teflon sealed NMR tube. Colourless solid, TTMS (3 mg, 0.0098 mmol), was dissolved in the CeN''_3 solution as an internal standard, solution remains bright yellow upon complete dissolution of solids. MOF808 (4 mg) added to the CeN''_3 and recorded as t = 0

hours. NMR tube sealed under a nitrogen atmosphere with ^{1}H-NMR spectra recorded over a 24-hour period.

2.9.4.2 NMR Studies of CeN''$_3$ Reactive Infiltration into MOF808 (d_8 – THF)

Procedure analogous to that for Section 2.9.4.1, using CeN''$_3$ (1 mg, 0.002 mmol), TTMS (3 mg, 0.0098 mmol), MOF808 (4 mg) and d_8 – THF.

2.9.4.3 NMR Studies of CeN''$_3$ Reactive Infiltration into MOF808 (d_3 – MeCN)

Procedure analogous to that for Section 2.9.4.1 using CeN''$_3$ (1 mg, 0.002 mmol) and MOF808 (4 mg) and d_3 – MeCN. Note that TTMS did not dissolve in d_3 – MeCN.

2.9.5 Optimised Reactive Infiltration

Under an inert N_2 atmosphere, CeN''$_3$ (125 mg, 0.2 mmol, 20 wt%, 4.6 wt% Ce) was dissolved in toluene (10 mL) yielding a bright yellow solution, the solution was added dropwise to a glass vial charged with MOF808 (625 mg) at room temperature. Upon mixing the solution forms a bright yellow suspension which fades over 30 minutes to a pale-yellow suspension. The reaction mixture was stirred at room temperature for 17 hours, after which an off-white suspension was visible. The reaction vial was removed from the inert nitrogen atmosphere into ambient conditions. The beige solids from the suspension were isolated *via* centrifugation (4000 rpm, 10 minutes) and washed by sonicating in toluene (3 × 20 mL, 30 seconds per sonication step), with centrifugation in between washings. The isolated beige solids were dried *in vacuo* over 48 hours yielding off-white solids. Reactive infiltration of CeN''$_3$ (125 mg, 0.2 mmol, 20 wt%, 4.6 wt% Ce) into MOF808 (625 mg) was repeated twice for reproducibility. Ce_xO_y@MOF808. IR (ATR): 2960 (w, ν_{CH}) 2860 (w, ν_{CH}) 1620 (m, ν_{CO}) 1560 (m, ν_{CC}) 1380 (s, ν_{CH}) 1250 (w, ν_{CH}) 960 (w) 840 (w) 630 (s) cm^{-1}. PXRD (λ CuK: 1.54 Å): 2θ 4 (111) 8 (311) 9 (222) 10 (400) 11 (331) °. ^{1}H Digestion NMR (d_6-DMSO/d_2-sulfuric acid): δ 12.44 (s, H_2SO_4), 8.54 (s, BTC), 8.07 (s, HCOO), 7.88 (s, DMF), 7.15 (m, toluene), 7.08 (m, toluene), 2.82 (s, DMF), 2.56 (s, DMF), 2.19 (s, toluene), 0.05 (grease/HN'') ppm. pKa: 3.8, 5.8 and 8.7.

EDX (as synthesised): 2.8 (± 1.0) wt% Ce, 21.5 (± 5.1) wt% Zr. EDX (heated at 120 °C): 3.13 (± 0.90) wt% Ce, 25.39 (± 5.76) wt% Zr. ICP (heated at 120 °C): 3.015 (± 0.007) wt% Ce, 27.67 wt% Zr. Specific Surface Area (BET); 1248 ± 34 m^2 / g. PSD = 13 – 14 Å.

2.9.6 Control Optimised Reactive Infiltration

Under an inert N_2 atmosphere, a glass vial was charged with MOF808 (625 mg) and stirred with toluene (10 mL) over 17 hours, after which a white suspension was visible. The reaction vial was removed from the inert nitrogen atmosphere into ambient conditions. The white solids from the suspension were isolated *via* centrifugation (4000 rpm, 10 minutes) and washed by sonication in toluene (3 × 20 mL, 30 seconds per sonication step), with centrifugation in between washings. The isolated white solids were dried *in vacuo* over 48 hours yielding off-white solids. IR (ATR): 2860 (w, ν_{CH}) 1600 (m, ν_{CO}) 1440 (m, ν_{CC}) 1380 (s, ν_{CH}) 1110 (w) 940 (w) 890 (w) 650 (s) cm^{-1}. PXRD (λ CuK: 1.54 Å): 2θ 4 (111) 8 (311) 9 (222) 10 (400) 11 (331) °. ^{1}H Digestion NMR (d_6-DMSO/d_2-sulfuric acid): δ 12.38 (s, H_2SO_4), 8.55 (s, BTC), 8.07 (s, HCOO), 7.88 (s, DMF), 7.16 (m, toluene), 7.09 (m, toluene), 2.82 (s, DMF), 2.66 (s, DMF), 2.20 (s, toluene) ppm. pKa: 3.8, 5.8 and 8.7. EDX (as synthesised): 18.1 (± 8.8) wt% Zr. EDX (heated at 120 °C): 31.9 (± 8.5) wt% Zr. ICP (heated at 120 °C): 34.24 (± 0.10) wt% Zr. Surface Area; 1349 m^2 / g. PSD = 15, 22 Å.

2.9.7 Scanning Electron Microscopy Measurements

The samples of activated MOF808, control MOF808 and CeNP@MOF808 were coated with either 15 nm of Au/Pd by a Quorum Q150T Plus – Turbomolecular pumped coater for SEM and imaged using a Carl Zeiss Sigma VP (at 5 kV, 30 µm aperture, at 5 mm working distance).

2.9.8 Energy Dispersive X-ray Spectroscopy Measurements

Samples of control MOF808 and CeNP@MOF808 were scattered on pure carbon tabs and mounted on aluminium stubs. Samples were coated using a Polaron SC7640 sputter coater with Au/Pd target to make them electrically conductive. The EDX detector used was an Oxford

Instruments X-act system with INCA 500 software and calibrated relative to a Cu reference. All EDX scans were taken at 5000 magnification. EDX measurements were obtained by taking three surface profiles on 3 separate particles to ensure representative elemental weight percentage, elemental weight percentages are determined as average values ± the standard deviation.

2.9.9 Inductively Coupled Plasma – Optical Emission Spectroscopy Measurements

ICP-OES analysis was performed by dissolving samples of control MOF808 and CeNP@MOF808 into mixture of HNO_3/HCl/H_2O_2 and using a Varian Vista MPX ICP-OES system measuring Zr and Ce weight percentages. Samples measured in duplicate with values reported as averages ± the standard deviation.

2.9.10 Nuclear Magnetic Resonance Measurements

Digestion ^{1}H NMR spectra of activated MOF808, control MOF808 and CeNP@MOF808 were obtained by suspending ca. 0.5 mg of sample in d_6-DMSO (2-3 mL) and mixing with 2-3 drops of D_2SO_4. Samples were sonicated for *ca.* 15 minutes to form a cloudy colloidal mixture that was transferred to a NMR tube and heated gently with agitation, up to 189 °C, until a colourless clear solution formed.

2.9.11 Elemental Microanalysis Measurements

Elemental microanalysis was performed using an Exeter CE-440 elemental analyser. Samples measured in duplicate.

2.9.12 Powder X-ray Diffraction Measurements

Powder X-Ray Diffraction measurements were carried out at 25 °C, in the Bragg-Brentano geometry, using a Rigaku Miniflex600 benchtop diffractometer CuKα (λ = 1.4505 Å). Powdered samples were centred on a bracket and diffraction patterns were measured from

3° to 45° with a step size of 0.01° and speed of 10.0° min^{-1}. For all samples, the spinning speed of 10 rpm was used.

2.9.13 Potentiometric Titration Measurements

Separate samples (50.0 mg) of activated MOF808, control MOF808 and CeNP@MOF808 were suspended in a $NaNO_3$ solution (60 mL, 0.01 M). The suspension was sonicated for 20 minutes and subsequently allowed to equilibrate for 18 hours. The pH of the suspension was recorded using a Thermo scientific ORION STAR A214 pH/ISE meter equipped with an ORION Ross Ultra Combination pH probe. The pH probe was equilibrated at known pH values with buffers at pH values 4.01, 7.00 and 10.01. A solution of HCl (0.10 M) was added to the suspension dropwise, with stirring, in order to bring the pH to *ca.* 3.0. The suspension was then titrated first with 250 µL aliquots of NaOH (0.1 M) up to 1.5 mL, and then with aliquots of 125 µL up to 8.25 mL to improve the resolution of the data at the equivalence points. The titrations were performed at 25 °C. For determining the pK_a values, the equivalence points of the titration were calculated from the plots by taking the first derivative. The pK_a values were determined by calculating half the volume of base required to reach the equivalence point (either from the beginning of the titration or from the previous equivalence point), and reading off the pH after that quantity of base had been added.

2.9.14 Infrared Spectroscopy Measurements

Solid state ATR – IR spectra were collected for activated MOF808, control MOF808 and CeNP@MOF808 using a Shimadzu FTIR 8400S spectrometer.

2.9.15 N_2 Adsorption Isotherm Measurements

N_2 adsorption and desorption isotherms of control MOF808 and CeNP@MOF808 were recorded at –196 °C on a Quantachrome Autosorb iQ gas sorption analyser. Samples were degassed under vacuum at 150 °C for 20 hours using the internal turbo pump. Brunauer-Emmett-Teller (BET) surface areas were calculated from the isotherms using the Micropore

BET Assistant in the Quantachrome ASiQwin operating software. Pore size distributions were calculated by using the N_2 at –196 °C on carbon (slit pore, QSDFT, equilibrium model) calculation model within the Quantachrome ASiQwin operating software.

2.10 Supplementary Information for Chapter 2

2.10.1 Precursor Synthesis

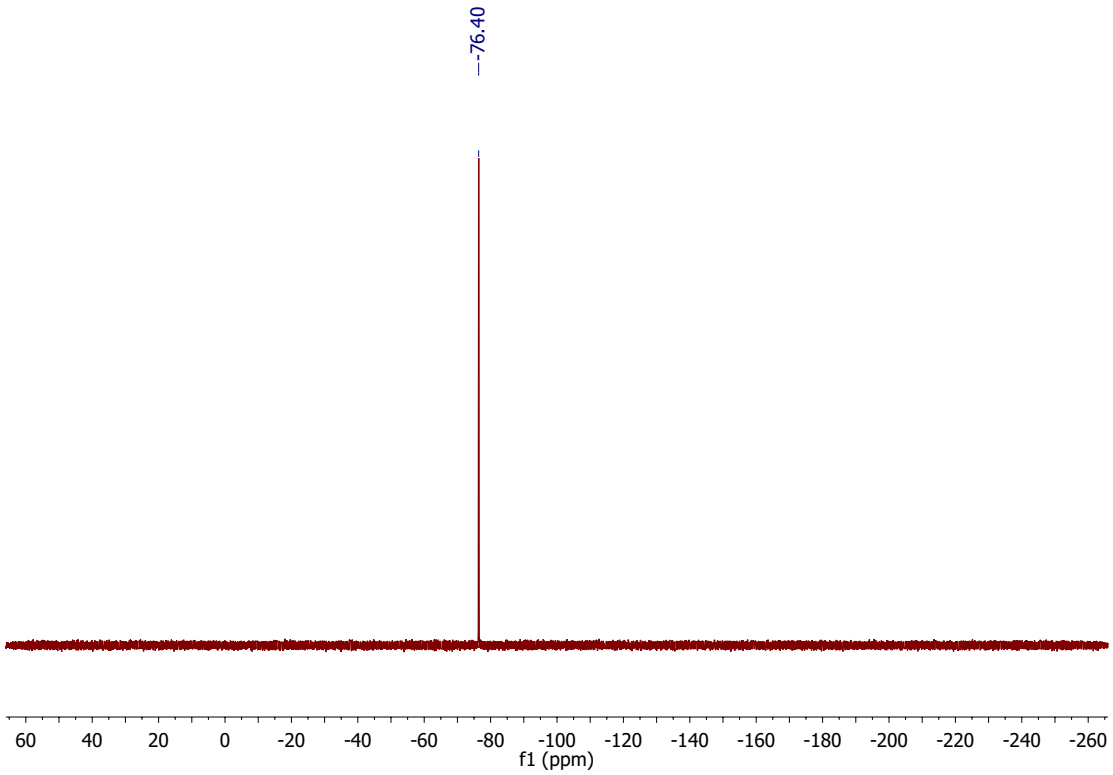

Supplementary Figure 2.1: ^{19}F NMR (d_3 – MeCN) of $Ce(OTf)_3$.

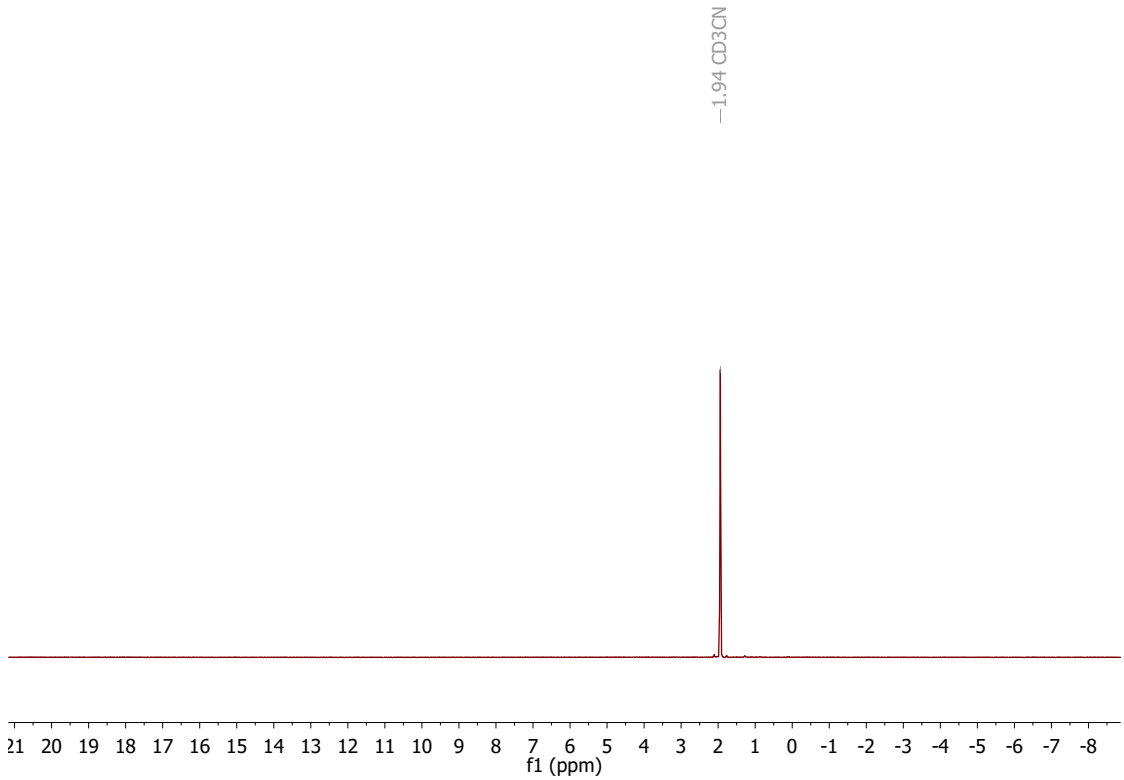

Supplementary Figure 2.2: ^{1}H NMR (d_3 – MeCN) of $Ce(OTf)_3$.

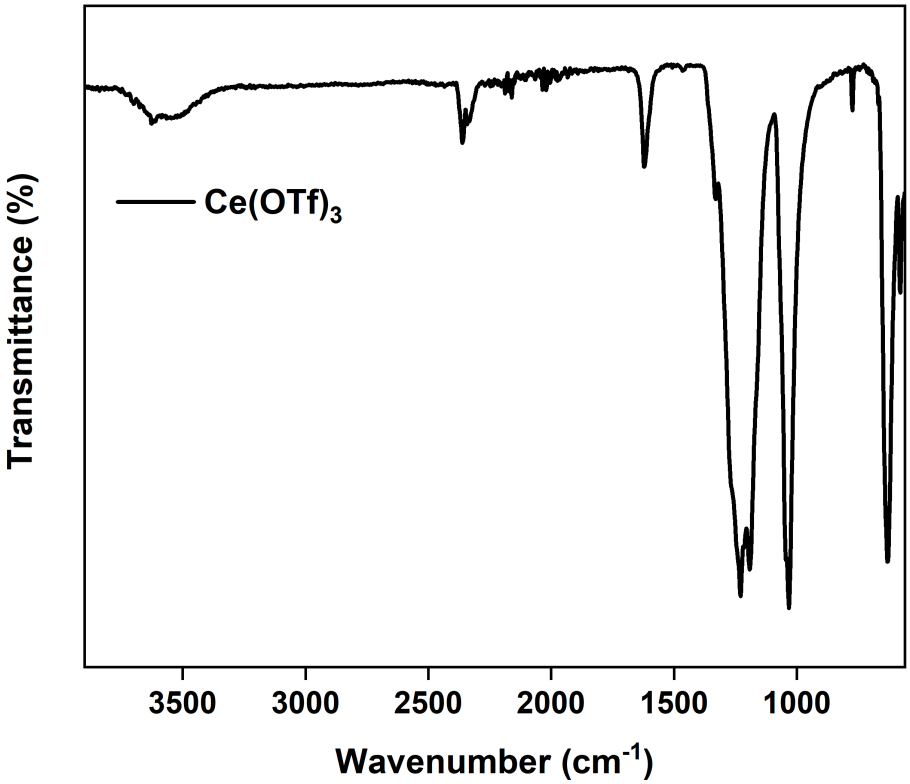

Supplementary Figure 2.3: ATR-IR spectrum of $Ce(OTf)_3$.

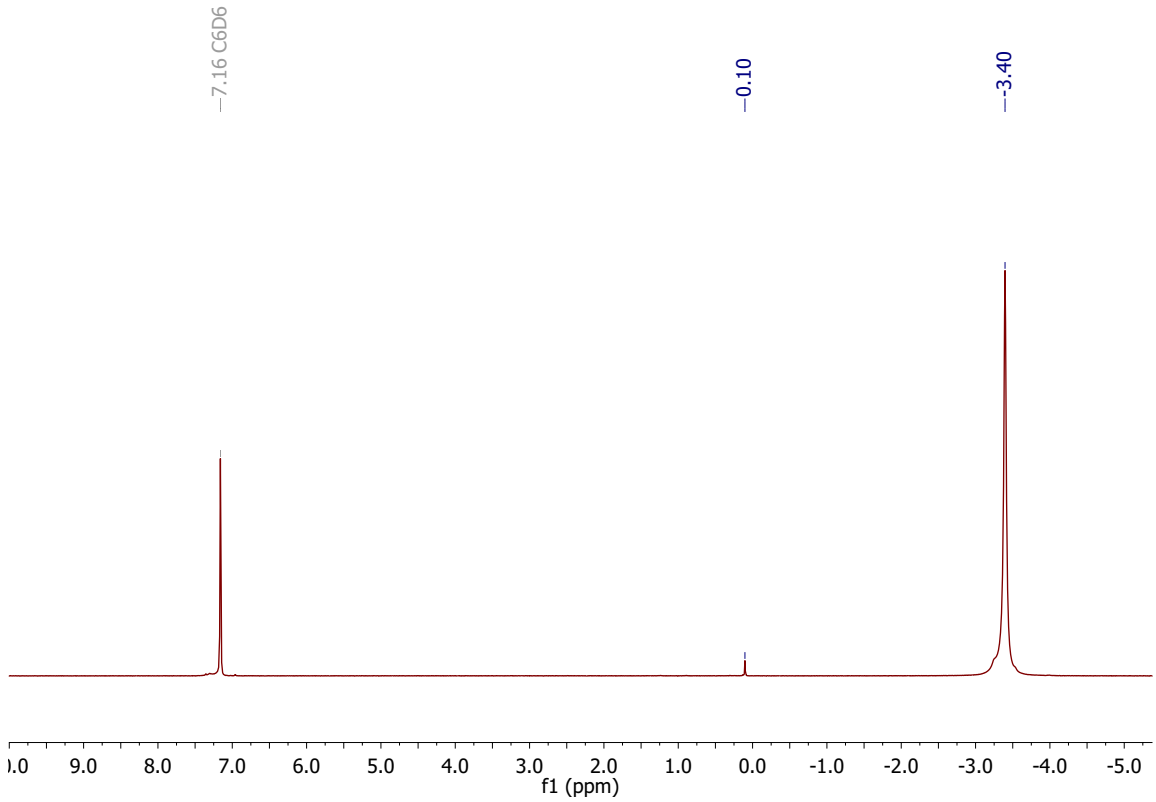

Supplementary Figure 2.4: ^{1}H-NMR (d_6 – benzene) of CeN''$_3$

2.10.2 ^{1}H NMR Optimisation: Solvent Choice

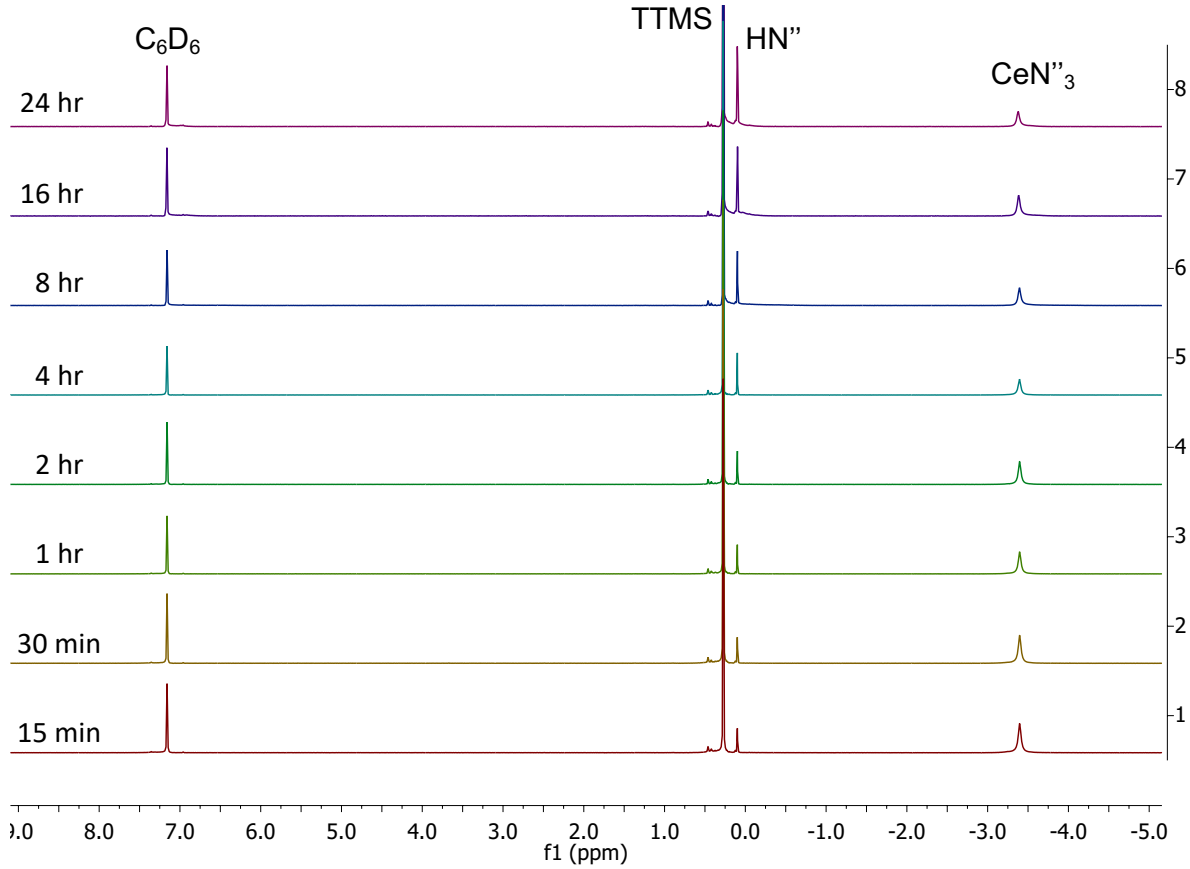

Supplementary Figure 2.5: Stacked ^{1}H-NMR (d_6-benzene) of the reactive infiltration of CeN''$_3$ in MOF808, over 24 hours.

Supplementary Table 2.1: Change in HN'' quantity over time for the reactive infiltration of CeN''$_3$ in MOF808, over 24 hours (based on ^{1}H-NMR (d_6-benzene)).

Time	HN'' (µmols)
15 minutes	1.01093
30 minutes	1.15301
1 hour	1.3224
2 hours	1.48634
4 hours	1.94536
8 hours	2.57377
16 hours	3.71585
24 hours	4.35519

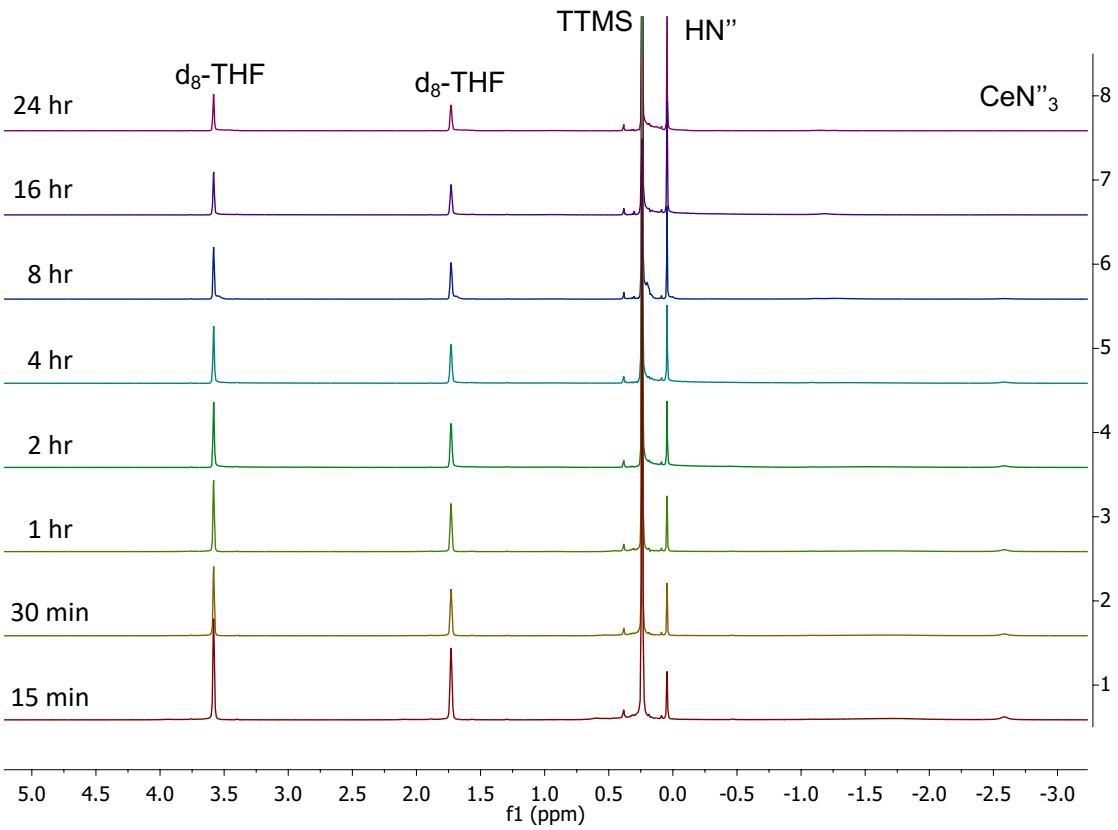

Supplementary Figure 2.6: ^{1}H-NMR (d_8-THF) of the reactive infiltration of CeN''$_3$ in MOF808, over 24 hours

Supplementary Table 2.2: Change in HN'' quantity over time for the reactive infiltration of CeN''$_3$ in MOF808, over 24 hours (based on ^{1}H-NMR (d_8-THF)).

Time	HN'' (µmols)
15 minutes	1.39891
30 minutes	1.5082
1 hour	1.61749
2 hours	1.95082
4 hours	2.28962
8 hours	2.56284
16 hours	3.43716
24 hours	3.56284

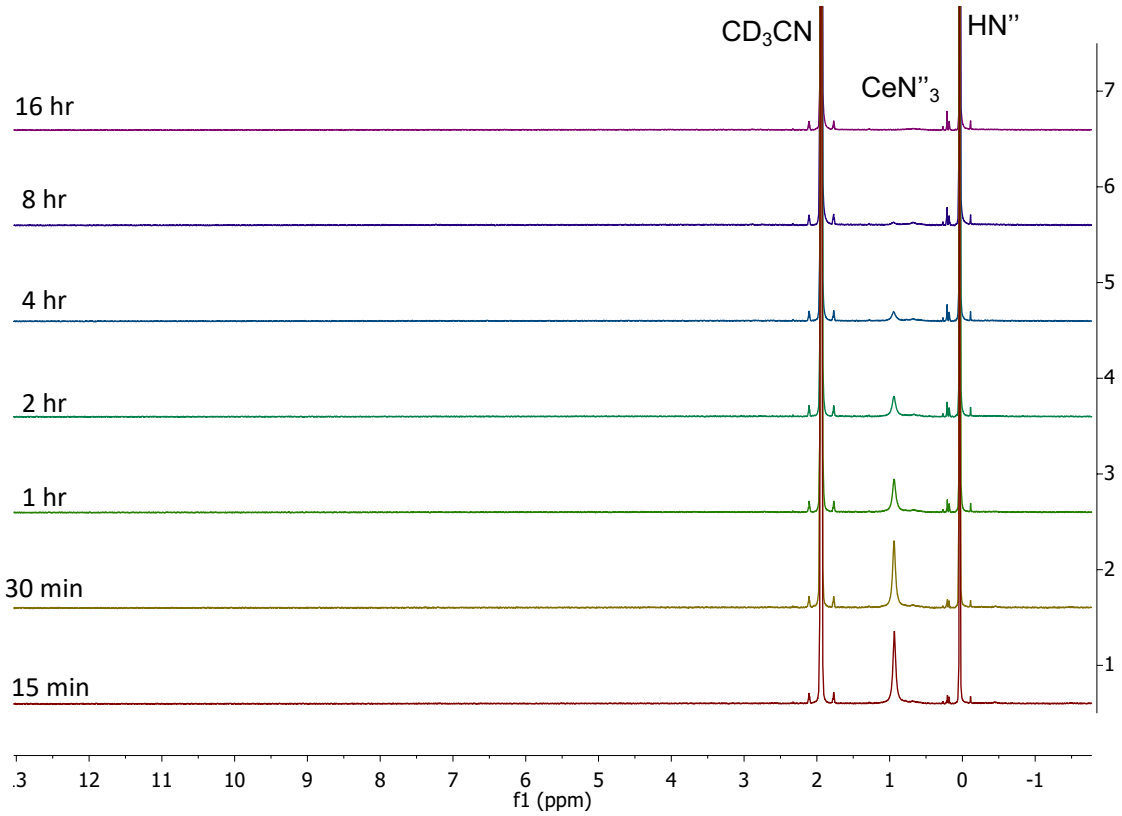

Supplementary Figure 2.7: Stacked ^{1}H-NMR (d_3-MeCN) of the reactive infiltration of CeN''$_3$ in MOF808, over 16 hours. Note: TTMS is insoluble in acetonitrile, therefore no quantification of the HN'' was possible.

2.10.3 ^{1}H NMR Optimisation: Thermal Pre-treatment

The reactive infiltration of CeN''$_3$ into activated MOF808 (heated to 120 °C *in vacuo* for *ca.* 24 hours) was compared with MOF808 thermally treated at elevated temperatures (180 °C and 230 °C) by measuring the quantity (µmols) of by-product HN'' produced over time. Both thermal treatments were performed for 1 hour, under an atmosphere of air.

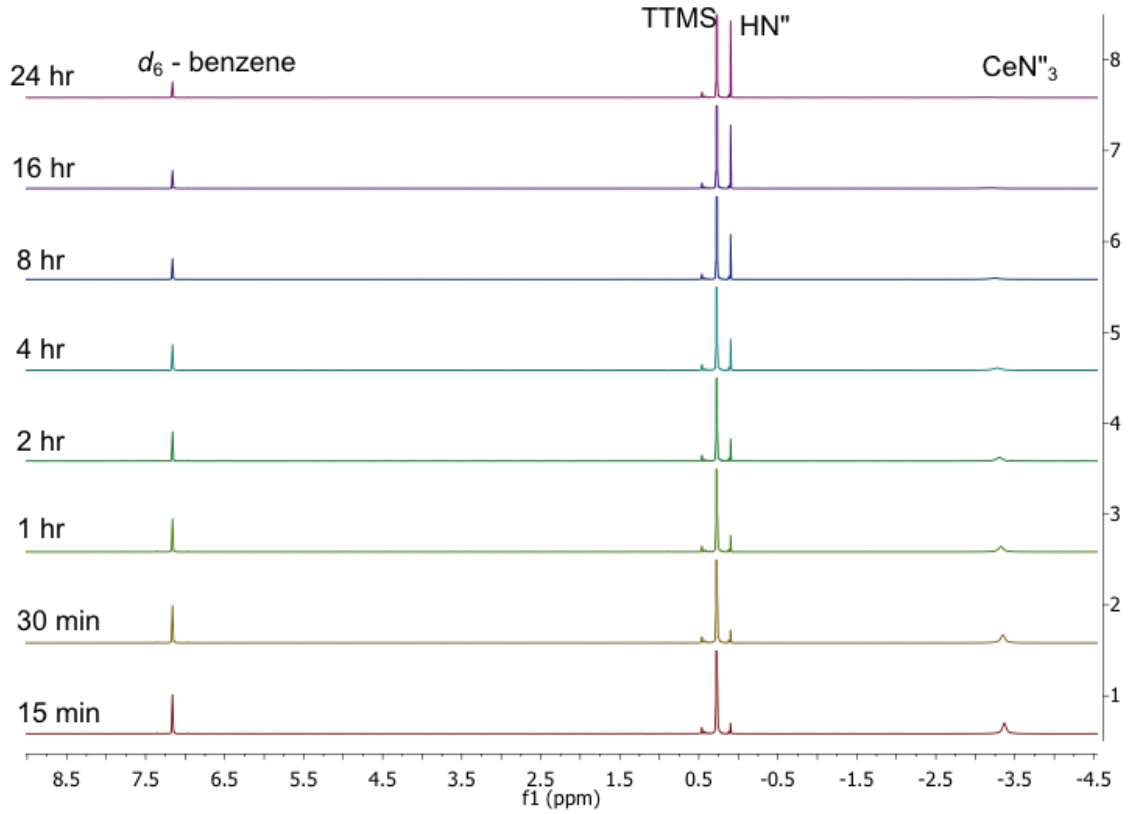

Supplementary Figure 2.8: Stacked ^{1}H NMR (d_6-benzene) of the reactive infiltration of CeN''$_3$ in MOF808 (calcined at 180 °C), over 24 hours.

Supplementary Table 2.3: Change in HN'' quantity over time for the reactive infiltration of CeN''$_3$ in MOF808 (calcined at 180 °C), over 24 hours (based on ^{1}H-NMR (d_6-benzene)).

Time	HN'' (µmols)
15 minutes	0.42623
30 minutes	0.53005
1 hour	0.63388
2 hours	0.7377
4 hours	1.01639
8 hours	1.28415
16 hours	1.89617
24 hours	2.36612

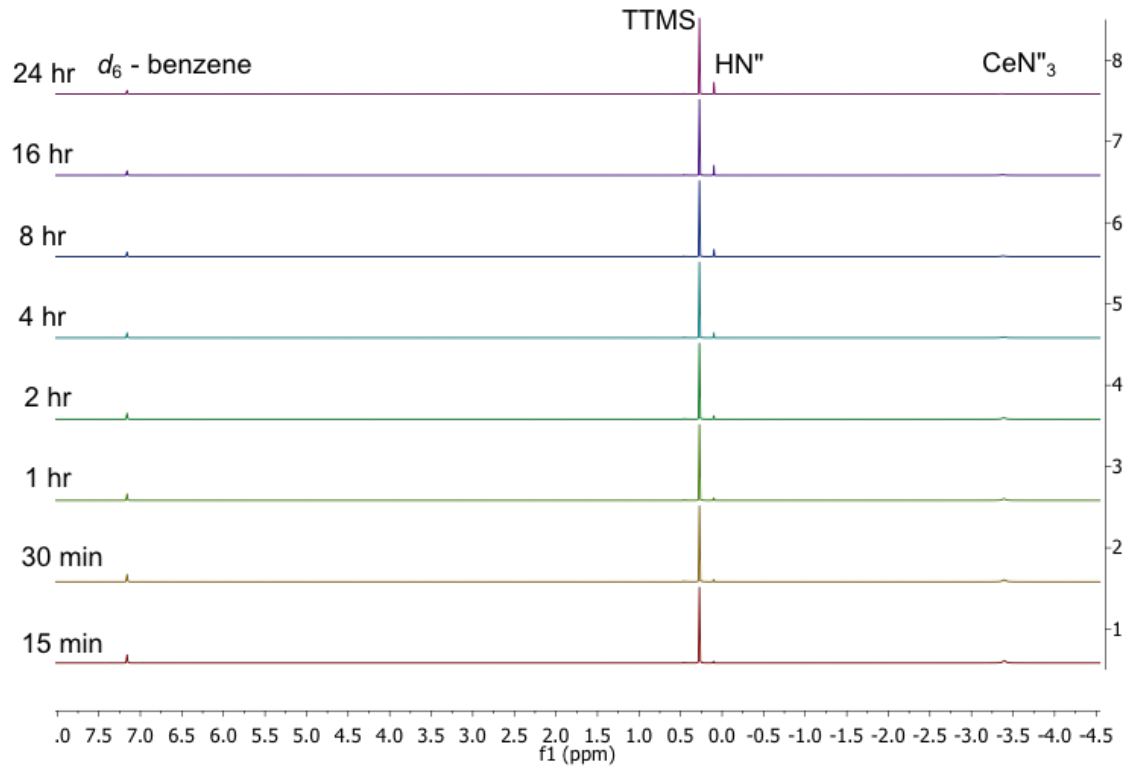

Supplementary Figure 2.9: Stacked ^{1}H NMR (d_6-benzene) of the reactive infiltration of CeN''$_3$ in MOF808 (calcined at 230 °C), over 24 hours.

Supplementary Table 2.4: Change in HN'' quantity over time for the reactive infiltration of CeN''$_3$ in MOF808 (calcined at 230 °C), over 24 hours (based on ^{1}H-NMR d_6-benzene)).

Time	HN'' (µmols)
15 minutes	0.45355
30 minutes	0.48634
1 hour	0.59016
2 hours	0.77049
4 hours	1.03825
8 hours	1.4153
16 hours	2.12022
24 hours	2.44262

2.10.4 ^{1}H NMR Optimisation: Control Reactions

Control reactive infiltration reactions were performed in both d_3 – MeCN and D_2O on the NMR scale using 4 mg of activated MOF808 and 1 mg of $Ce(OTf)_3$. Procedure analogous to that for 'NMR Studies of CeN''_3 Reactive Infiltration into MOF808 (d_6 – benzene)'. Reactive infiltration progress (if any) was monitored via $^{19}F\{^1H\}$-NMR. Reference spectra were taken of the starting material $Ce(OTf)_3$, as well as of possible by-product triflic acid (HOTf), in both solvents.

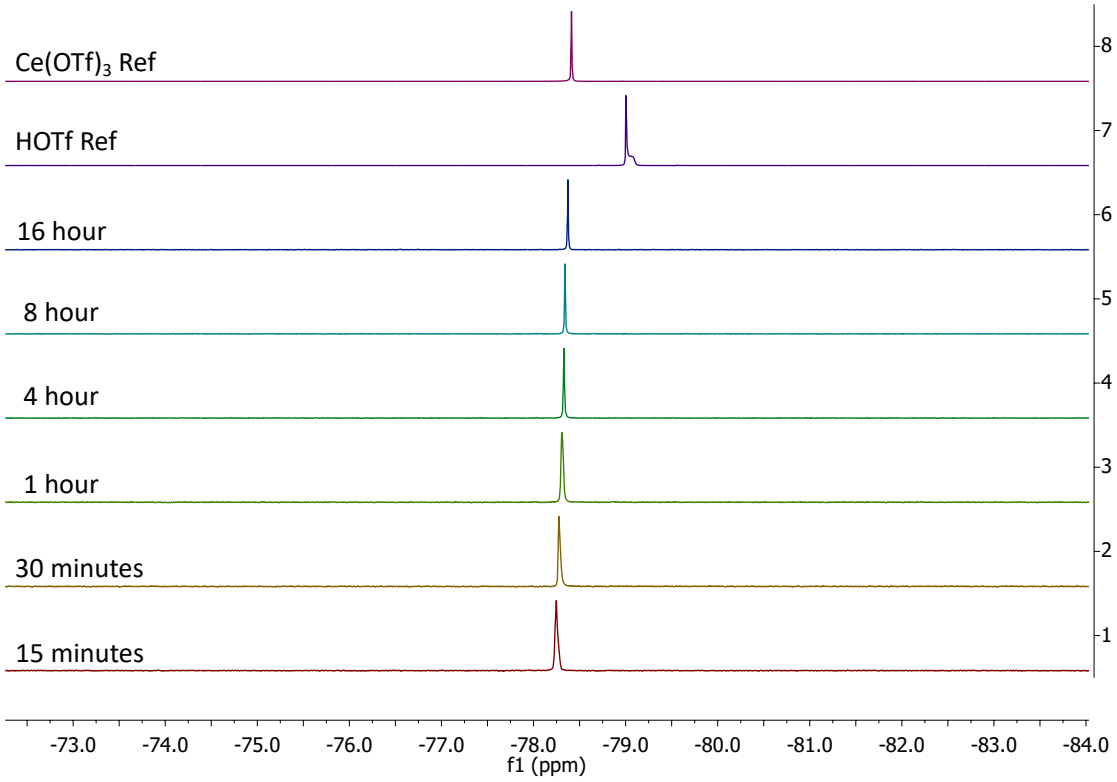

Supplementary Figure 2.10: $^{19}F\{^1H\}$ NMR (d_3 – MeCN) of control reactive infiltration with $Ce(OTf)_3$ in MOF808.

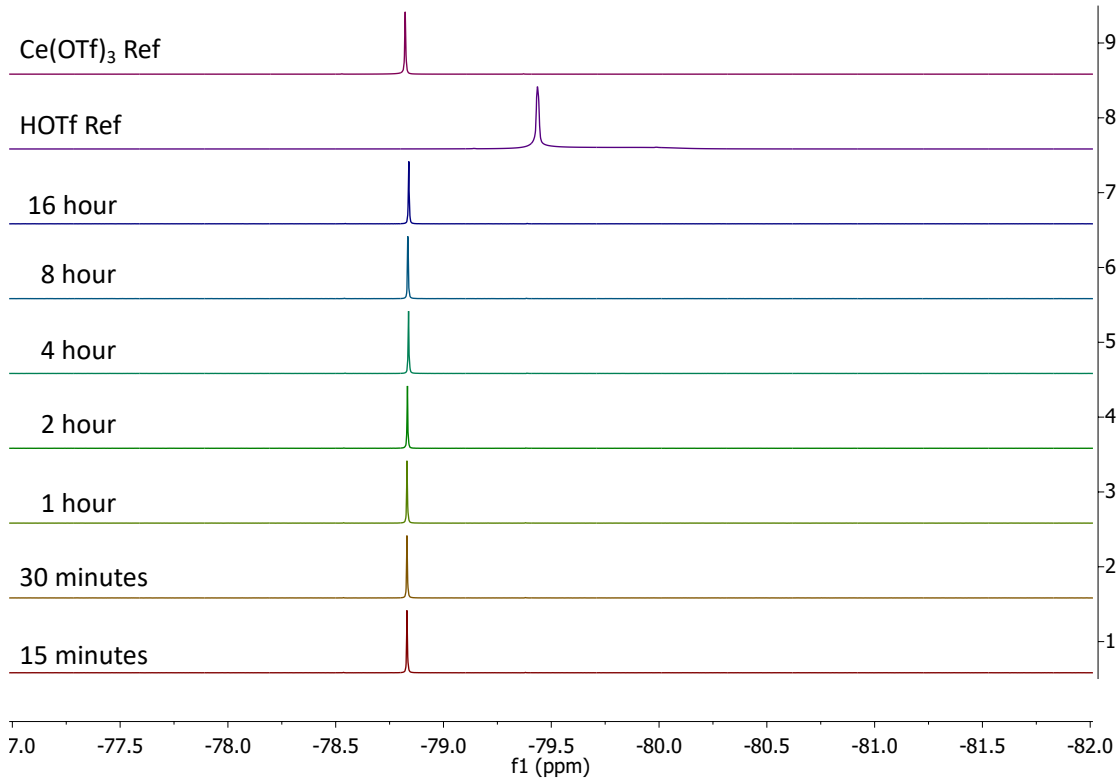

Supplementary Figure 2.11: $^{19}F\{^{1}H\}$ NMR (D_2O) of control reactive infiltration with $Ce(OTf)_3$ in MOF808.

2.10.5 Optimisation of Reactive Infiltration: Scaled Up Synthesis of CeNP@MOF808

Previous ^{1}H NMR experiments investigating the optimisation of reactive infiltration of CeN''_3 with MOF808 involved using a CeN''_3 precursor loading of 20 wt%, which corresponds to a theoretical maximum loading weight of cerium metal of 4.6%. From these initial results it was possible to scale up the reactive infiltration to the 50 mg scale, allowing *preliminary* SEM, EDX, BET and PXRD analysis to be performed on the resulting CeNP@MOF808 composite material. The aim was to determine which experimental parameters in the scaled up methodology were best suited to yielding a CeNP@MOF808 composite with successful and high loading of Ce, retention of MOF crystallinity and porosity and occupation of MOF pores.

As demonstrated previously in Optimisation of Reactive Infiltration: ^{1H} NMR Experiments: Solvent Choice, reactive infiltration of CeN''_3 could occur in both polar and non-polar solvents,

with no significant differences in reaction rate or yield. A scaled up experiment was performed in a manner similar to those performed in Sections 2.5.1, 2.5.2 and 2.5.3, with the NMR tube being substituted for a syringe. Under an inert atmosphere of N_2, 10 mg of CeN''_3 which was dissolved, separately, in 20 mL of toluene, THF and acetonitrile (MeCN). These CeN''_3 solutions were then subsequently transferred to the capped filter-syringe charged with 40 mg of MOF808. Thus the CeN''_3 loading was 20 wt%. The experimental set up is shown below in Supplementary Figure 2.12.

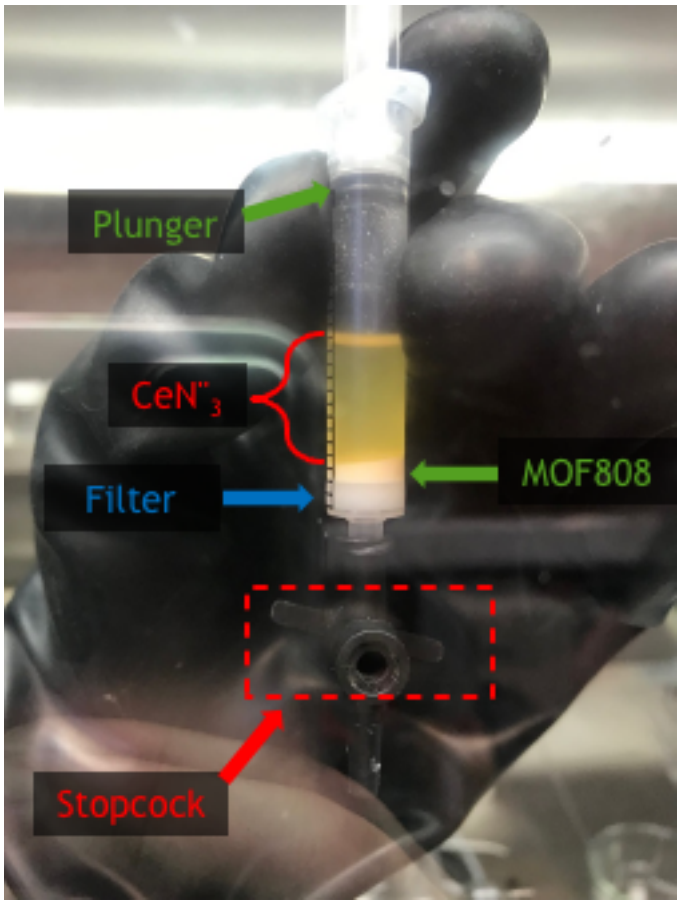

Supplementary Figure 2.12: Experimental set up for the scaled up reactive infiltration of CeN''_3 and MOF808, at 20 wt% loading of CeN''_3. Photo taken at the start of reactive infiltration with the cloudy yellow solution CeN''_3 solution clearly visible.

The syringe was upturned and shaken several times and left to settle over 48 hours. The mixed suspensions were all initially a cloudy yellow colour, after several hours the solution slowly turned colourless and clear – solids had at this point settled to the bottom of the syringe. The solid composite was separated from the solvent by pushing down on the syringe plunger,

then washed three times with the appropriate solvent and dried *in-vacuo* at room temperature. Removing the washed solid from the filter-syringe was difficult due to the static nature of the MOF, with significant loss of material that became imbedded within the filter plug. Despite the syringe being capped, the plunger offered a poor seal in the experimental design, leading to significant loss of solvent over time due to evaporation, particularly for volatile solvents THF and MeCN. This is noteworthy as it demonstrates a limitation of this experimental design and could have had the effect of changing the concentration of the CeN''_3 solutions and in turn influencing the reactive infiltration. Therefore, toluene was concluded to be the ideal solvent for the optimised reactive infiltration methodology as the solvent is less volatile compared to THF and MeCN and therefore less likely to evaporate during the reaction.

PXRD diffractograms of the 20 wt% loaded CeNP@MOF808 up scaled samples, synthesised using toluene, THF and MeCN as reactive infiltration solvents, are shown below in Supplementary Figure 2.13, with the reference MOF808 diffractogram.

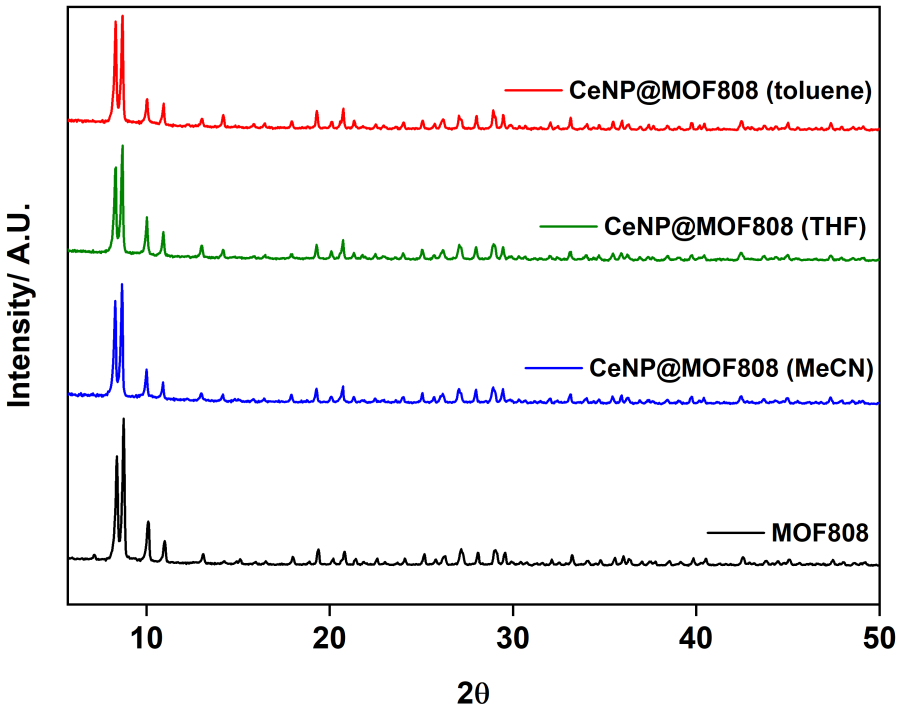

Supplementary Figure 2.13: Powder X-ray diffractograms for reference and 20 wt% loaded CeNP@MOF808 (powders prepared using capped syringe experimental set up).

The reference MOF808 diffractogram shows reflections that are characteristic of MOF808, particularly at low angles, 2θ = 4° (111) 8° (311) 9° (222) 10° (400) 11° (331). These low angle reflections are observed in the diffractograms for 20 wt% loaded CeNP@MOF808, indicating that the MOF host retains its crystallinity after reactive infiltration – regardless of solvent polarity. This is consistent with the observations made in Section 2.5.1, which showed no significant divergence in reactive infiltration rate or yield with solvent polarity. Reflections are also not significantly broadened following reactive infiltration, indicating that crystalline domain sizes for the MOF crystals remain unchanged. There are slight changes in the relative intensities of the diffractograms of CeNP@MOF808 compared with those in reference MOF808, evidence of guest loading of CeNP into the host MOF808 structure yielding changes in the local electronic environment. There were no strong reflections or broad peaks characteristic of CeO_2 nanoparticles observed. At the time it was suspected that this could be due to: a) the small loading weights of Ce (theoretical maximum 4.6 wt%) and/or b) because the CeN''_3 had reacted mostly on the surface of the MOF and formed nanoparticles that were not chemically or mechanically bound to the MOF structure and so removed during the washing stage and/or c) that the cerium based nanoparticles formed were too small or amorphous.

MOF808 has small and large microporous channels, with a large specific surface area of approximately 1300 m^2/g, associated with the microporous surface. N_2 adsorption-desorption isotherms of CeNP@MOF808 (synthesised using toluene and THF) were acquired to determine if the reactive infiltration process would show a significant reduction in the microporous surface area of the solid and occupation of either micropores, see Supplementary Figure 2.14. Both CeNP@MOF808 samples, formed using toluene and THF, showed a reduction in the specific microporous surface area, of similar magnitudes, at 784 m^2/g and 875 m^2/g, respectively. From the N_2 adsorption-desorption isotherms pore size distributions (PSD) were calculated that showed the number and size of channels and pores that are accessible to the nitrogen gas molecules. The PSD calculated for the CeNP@MOF808 composites showed complete occupation/blocking of the larger micropore at 22 Å for the CeNP@MOF808 sample prepared using toluene, while the sample prepared using THF showed only partial occupation of the larger micropore (see Supplementary Figure 2.14 below).

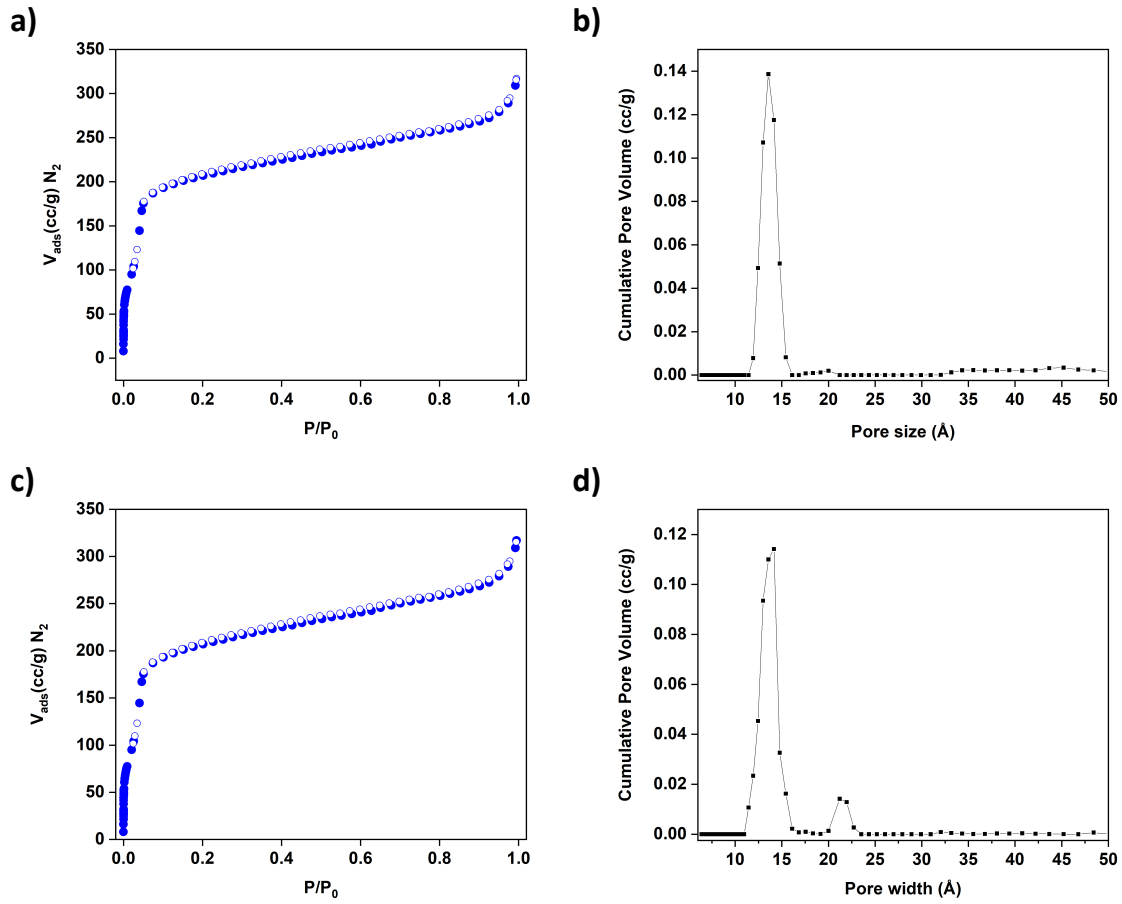

Supplementary Figure 2.14: a) and c): N_2 adsorption-desorption isotherms for 20wt% loaded CeNP@MOF808 using toluene and THF respectively. b) and d): PSD plots for 20 wt% loaded CeNP@MOF808 using toluene and THF respectively, showing complete occupation of the larger micropore for loading in toluene and partial occupation of the larger micropore for loading in THF, at 22 Å. In both solvents the micropore access channel remain open.

The smaller microporous access channels at 14 Å remain unchanged and fully accessible following reactive infiltration at 20 wt% loading using both toluene and THF as a solvent. Only the sample loaded using toluene shows a concurrent occupation of the larger micropore. While both solvent systems would be appropriate for reactive infiltration, toluene offered a more efficient reaction with a greater reduction in the specific microporous surface area and a complete occupation of the larger micropore. However, it should be noted that experiments were not repeated and that the calculated surface areas and PSDs are based on one single sample. It is also worth considering that the BET methodology was designed for the

characterisation of porous activated carbon and zeolite materials – not metal organic frameworks – and therefore should be considered with caution.

Low resolution scanning electron microscopy (SEM) images of MOF808 were obtained using a Carl Zeiss Sigma Variable Pressure Analytical SEM. MOF808 particles naturally form static charged surfaces, this is a significant challenge when trying to obtain SEM images with high resolution with good surface-background contrast. The charging of sample surfaces reduces the number of secondary electrons emitted from the surface that reach the SEM detector, in turn limiting the SEM image resolution and contrast. To suppress charge effects on the surface the sample powders were bound to adhesive tabs and sputter coated with conductive Au/Pd metal coatings for 150 seconds to form a conductive surface on the particles. SEM images of 20 wt% loaded CeNP@MOF808 samples prepared using toluene, THF and MeCN showed grainy, low resolution images due to the static charge of the MOF particles. Large aggregates were observed for all three samples (see Supplementary Figure 2.15, Supplementary Figure 2.16 and Supplementary Figure 2.17). These aggregates are distinctly different from those seen of the reference MOF808 in Supplementary Figure 2.18, which show well defined cubic aggregate particles 4 µm in size. Instead, the CeNP@MOF808 samples all show large, cracked flake-like aggregates, regardless of the solvent used during reactive infiltration. Therefore, the flake-like aggregates most likely arise as a result of the samples being compacted inside the syringe during reactive infiltration for several hours – rather than chemical-structural changes to the MOF which would have shown concurrent changes in the reflections of the PXRD diffractograms in Supplementary Figure 2.13. The presence of flake-like aggregates is not desirable given that the aggregation of the CeNP@MOF808 would limit the exposed surface area of the material. It was therefore concluded that the optimised methodology should employ a dynamic stirring mechanism, rather than a stagnant mechanism during the reactive infiltration reaction.

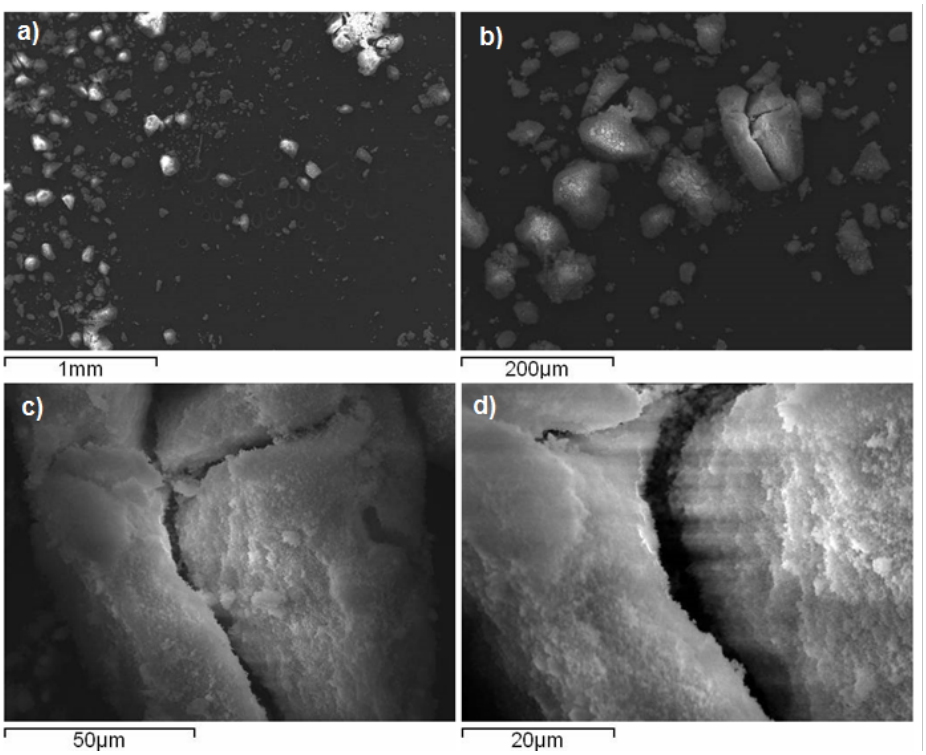

Supplementary Figure 2.15: Low resolution SEM images of 20 wt% loaded CeNP@MOF808, using toluene, sputter coated with Au/Pd at various magnifications (a) – (d).

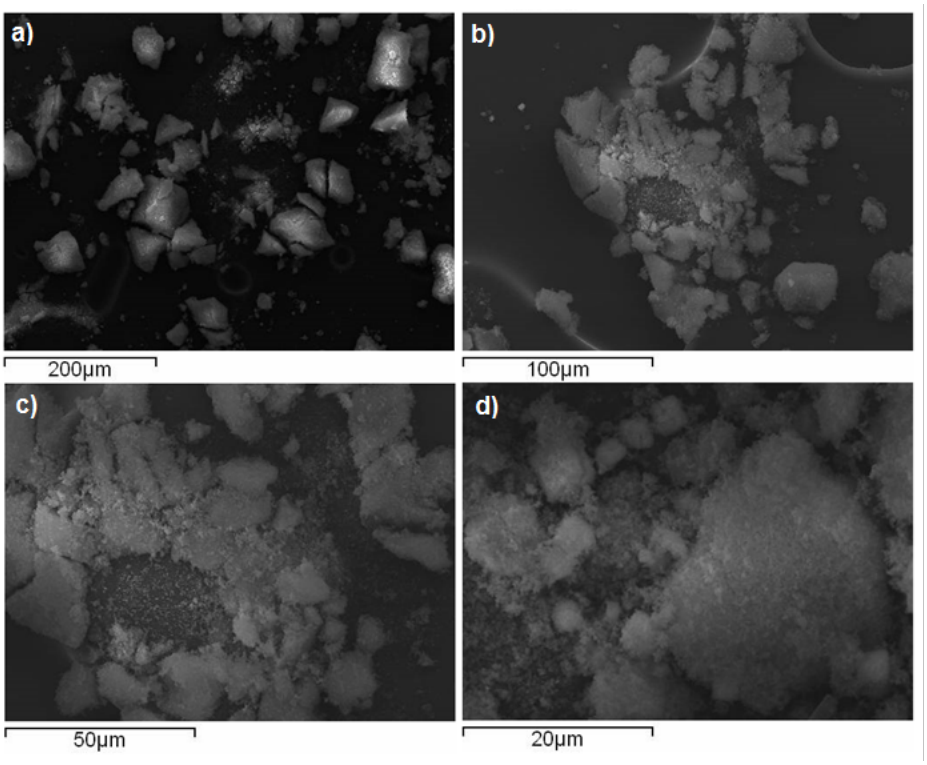

Supplementary Figure 2.16: Low resolution SEM images of 20 wt% loaded CeNP@MOF808, using THF, sputter coated with Au/Pd at various magnifications (a) – (d).

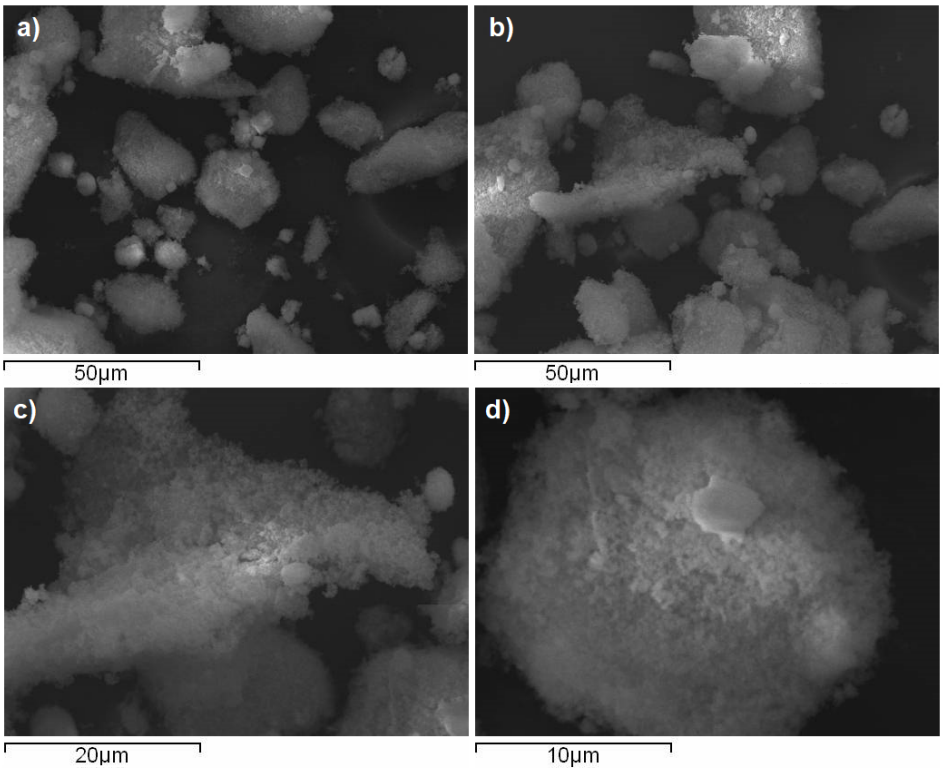

Supplementary Figure 2.17: Low resolution SEM images of 20 wt% loaded CeNP@MOF808, using MeCN, sputter coated with Au/Pd at various magnifications (a) – (d).

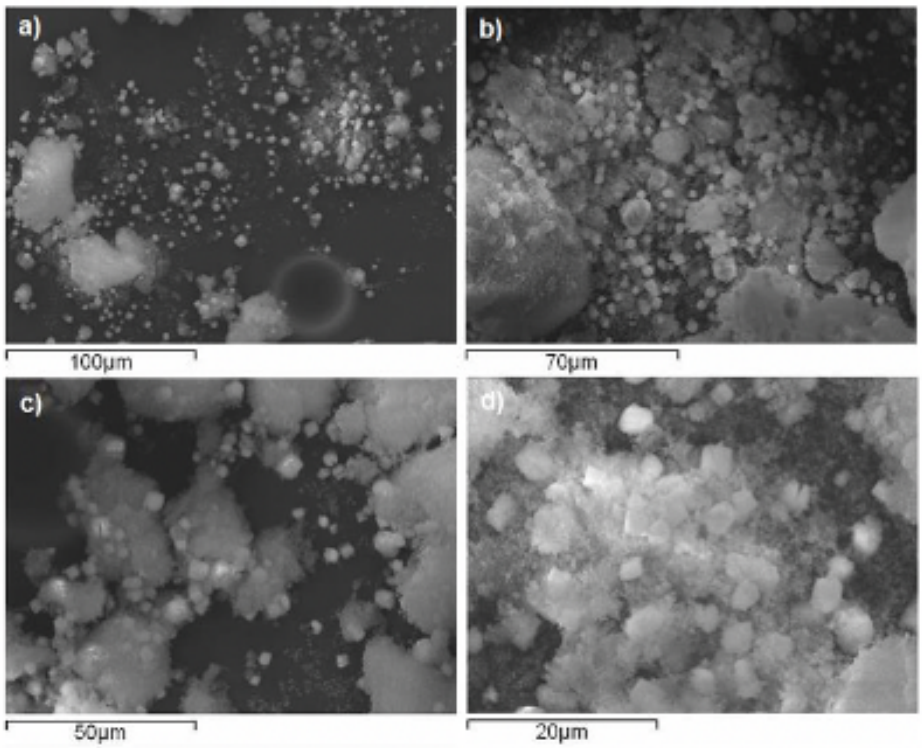

Supplementary Figure 2.18: Low resolution SEM images of reference MOF808 sputter coated with Au/Pd, showing well defined cubic aggregate particles 4 µm in size.

Energy dispersive X-ray (EDX) spectra were taken of the CeNP@MOF808 samples, to measure the loading weights of Ce present, results are summarised in Supplementary Table 2.5.

Supplementary Table 2.5: EDX determined loading weights of Ce, as wt%, for CeNP@MOF808 composites formed by a 20 wt% loading of CeN''_3, synthesised via reactive infiltration using toluene, THF and MeCN as solvents.

Solvent	Ce wt%	Number of Scans
Toluene	3.2	2
THF	1.8	4
MeCN	11.3	1

As seen in Supplementary Table 2.5, the highest loading weight of Ce in the CeNP@MOF808 composites occurs when using MeCN as the solvent during the reactive infiltration, with Ce loading at 11.3 wt%. However, due to a limited amount of sample and a small number of scans there is a significantly lower confidence in this determination. It was also the case that when the EDX spectrum of the CeNP@MOF808 composite formed using MeCN, that only X-rays characteristic of Ce and Zr were accounted for – ignoring values and composition accounted for by elements such as C and O which exist in significant quantities in the CeNP@MOF808 composite. Reactive infiltration with toluene and THF showed lower loading weights of Ce at 3.2 and 1.8 wt% respectively, however with the increased number of scans and accounting for C and O as well as Zr and Ce, more weight can be given to this determination. These values are also more consistent with loading weights typically seen for transition metal based NP@MOF composites synthesised using traditional bottom-up methodologies.

2.10.6 Optimisation of Reactive Infiltration: Higher Loading Weights

The use of higher loading weights of CeN''_3 was investigated in the synthesis of CeNP@MOF808 composites *via* reactive infiltration, and what effect this would have on the Ce loading weight of the CeNP@MOF808 composite and the structural properties of the MOF host (*e.g.* crystallinity, particle morphology). CeN''_3 loadings of 40, 60 and 75 wt% were investigated, however due to the larger amounts of material required for these higher

loadings and the undesirable particle aggregate morphology observed when performing the reactive infiltration in a syringe vessel, an alternative experimental methodology had to be devised. Previous scaled up loadings of CeN''$_3$ with MOF808 were performed, under inert N_2 atmospheres, using a capped syringes with the samples upturned several times and then left static for several hours (as was used for the 20 wt% loadings, see Supplementary Figure 2.12). The syringe was substituted for a larger reaction vial (20 mL), 10 mL of the selected solvent (toluene, THF, MeCN) and constant stirring for 24 hours. The experimental set up is shown below in Supplementary Figure 2.19. The solids were then transferred to a syringe and filtered, washed several times with the appropriate solvent (toluene, THF, MeCN) and subsequently air-dried.

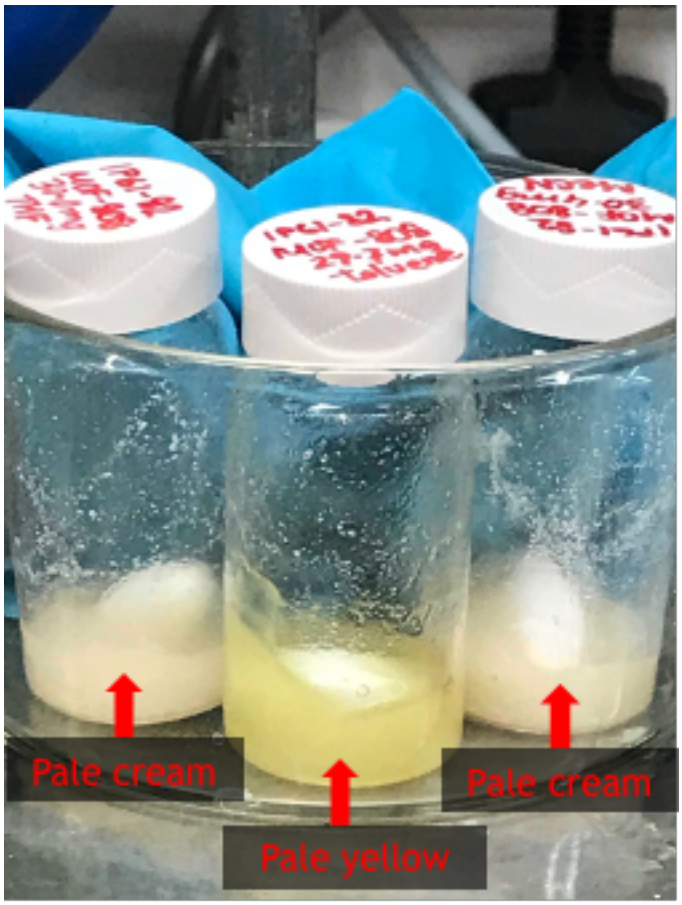

Supplementary Figure 2.19: Experimental set up for the scaled up reactive infiltration of CeN''3 and MOF808, at 40, 60 and 75 wt% loading of CeN''3. Photo taken at the start of reactive infiltration, with the reaction in toluene showing a cloudy yellow suspension, while the reactions in THF and MeCN show more cloudy suspensions.

Supplementary Table 2.6 below summarises relative amounts of material (MOF808 and CeN''_3) in mg, solvents and colour changes for each reactive infiltration experiment. Higher loading weights of CeN''_3 appeared to result in the formation of CeNP@MOF808 composites with darker orange/brown surfaces, compared to the CeNP@MOF808 composites synthesised at the lower 20 wt% loading of CeN''_3, this was suggestive of a higher cerium content. It was striking that higher polarity solvents (THF and MeCN) results in what appears to be a faster consumption of the CeN''_3 compared to non-polar toluene - despite ^1H NMR investigations suggesting that in both solvent polarities reactive infiltration takes place at similar rates and with comparable yields of HN''. This can be observed in Supplementary Figure 2.19 which shows that the CeN''_3 solution used in reactive infiltration with THF and MeCN loses its characteristic bright yellow colour more quickly compared to an identical CeN''_3 solution used with toluene.

Supplementary Table 2.6: Experimental parameters used for the reactive infiltration of CeN''_3 in MOF808, with solvent, mass of MOF808, mass of CeN''_3, colour change and CeNP@MOF808 surface colour noted.

Solvent	Mass of MOF808 (g)	Mass of CeN''_3 (g)	Colour Change (of suspension)	CeNP@MOF808 colour
40 wt% CeN''_3 Loading				
toluene	29.7	20.1	gradual change from yellow to pale cream	pale brown
MeCN	30.4	19.7	instant change from yellow to pale cream	pale brown
THF	30.0	19.9	instant change from yellow to pale cream	pale brown
60 wt% CeN''_3 Loading				
toluene	42.8	60.0	yellow to pale yellow	dark brown
MeCN	40.5	59.0	pale brown to pale cream	pale cream
THF	37.4	62.3	pale brown to white	pale cream

75 wt% CeN''_3 Loading				
toluene	48.0	151.5	dark yellow to yellow	dark brown

PXRD diffractogram of CeNP@MOF808 formed *via* reactive infiltration of CeN''_3, in toluene, THF and MeCN, at loading weights of 40, 60 and 75 wt% are shown below in Supplementary Figure 2.20, Supplementary Figure 2.21 and Supplementary Figure 2.22.

It was shown that for all higher loading weights (40, 60 and 75 wt%) of CeN''_3, regardless of solvent polarity, the crystallinity of the MOF808 host was retained with characteristic reflections still observed in the PXRD diffractogram, particularly at lower angles. Albeit these low angle reflections are slightly broadened following reactive infiltration indicating reduced crystallite domains and changes in particle size. However, it can be observed that higher angle reflections are significantly reduced in intensity, with the intensity reducing further higher loading weights. Loading of CeN''_3 at 75 wt% showed a significant increase in the amorphous background in the region of $25° < 2\theta < 30°$ of the diffractogram. This is suspected to be caused by the coating of the MOF808 crystallites with amorphous cerium oxy-hydroxide species, leading to the growth of an amorphous background in the PXRD diffractogram of CeNP@MOF808.

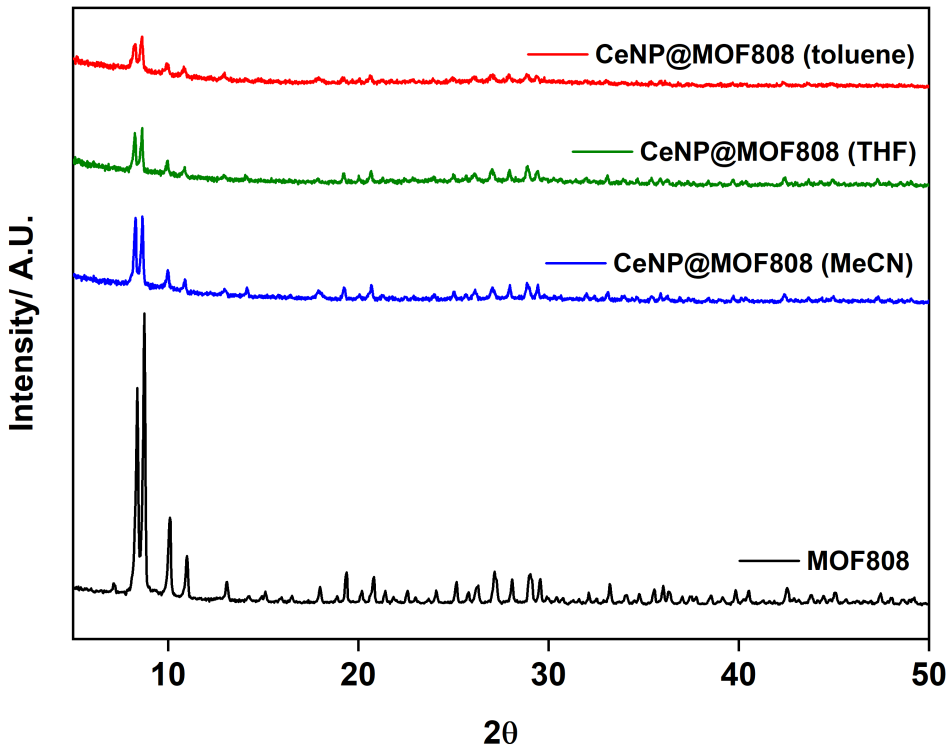

Supplementary Figure 2.20: Powder X-ray diffractograms of MOF808 and CeNP@MOF808 (40 wt% CeN''_3 wt% loading), using toluene, THF and MeCN as the reactive infiltration solvents.

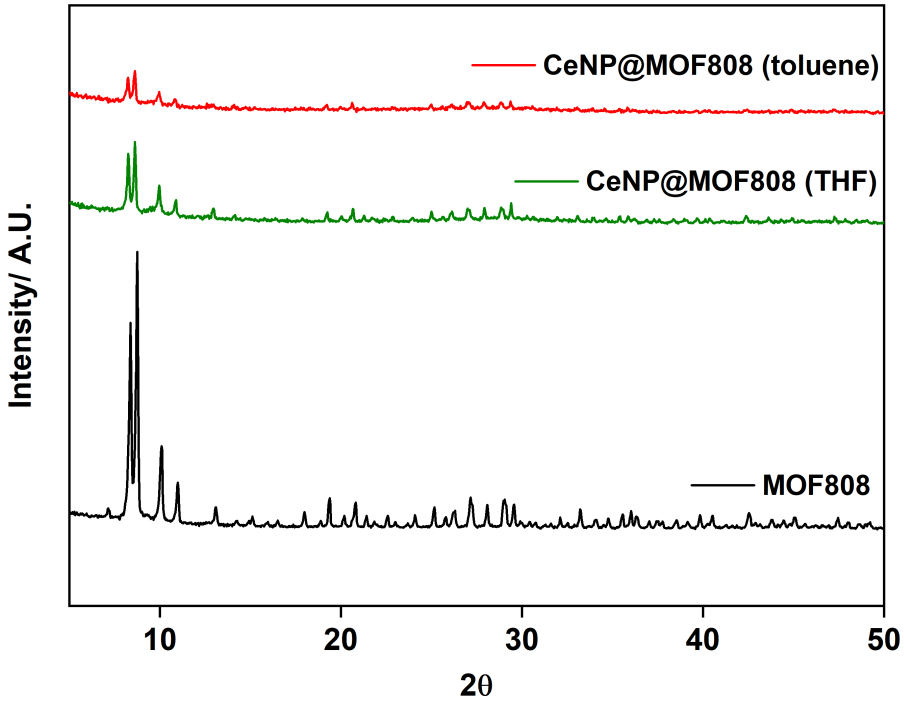

Supplementary Figure 2.21: Powder X-ray diffractograms of MOF808 and CeNP@MOF808 (60 wt% CeN''3 wt% loading), using toluene and THF as the reactive infiltration solvents.

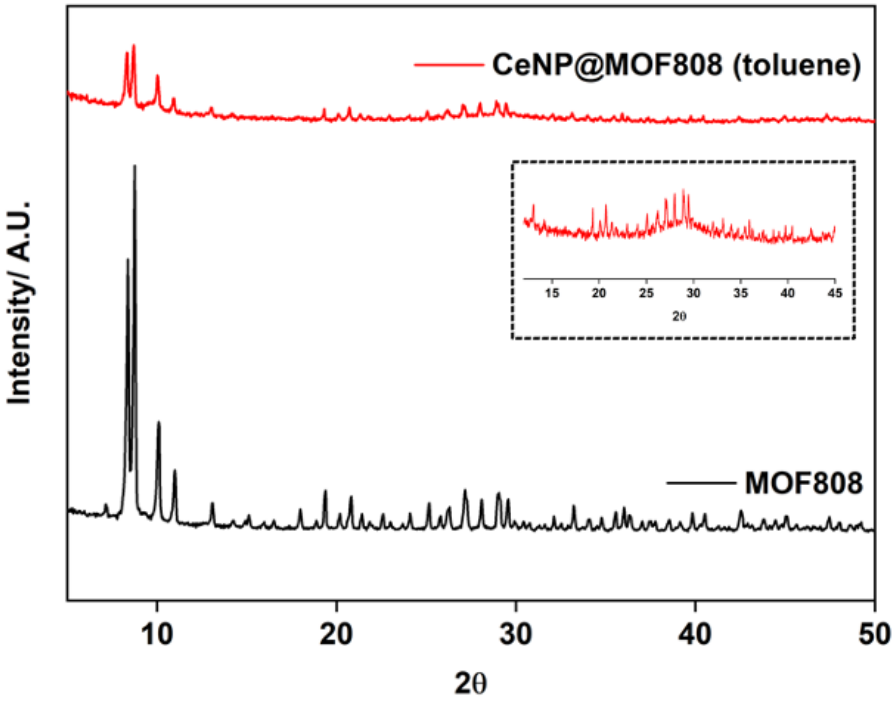

Supplementary Figure 2.22: Powder X-ray diffractograms of MOF808 and CeNP@MOF808 (75 CeN''_3 wt% loading), using toluene as the reactive infiltration solvent. Insert shows a scaled section of the diffractogram between 12° and 45° to show the amorphous background formed between 25° and 30°.

BET microporous surface area values were determined for CeNP@MOF808 at a 60 wt% loading of CeN''_3, showing a reduction in surface area for loading with toluene at 882 m^2/g, however, no significant reduction using either THF or MeCN at 1346 and 1245 m^2/g, respectively. Surface areas for CeNP@MOF808 loaded at 75 wt% CeN''_3 showed a reduction at 860 m^2/g. Despite the reduction in microporous surface area at 60 and 75 wt% loadings, when using toluene, PSD calculations reveal that the larger micropore remains open – despite the higher loading weights of 60 and 75 wt% CeN''_3. This occupation of the larger micropore at lower loading weights may be due to concentration effects, with similar volumes of solvent used in 20, 60 and 75 wt% loadings, with the more concentrated 60 and 75 wt% solutions yielding a faster reaction that results in the majority of reactive infiltration occurring on the surface of MOF808. Alternatively, it may be due to the change in reactive infiltration experimental methodology, in the 20 wt% loading a largely 'static' set up is used whereby the CeN''_3 solution sits stagnant upon the MOF808 solid slowly percolating into the solid, while in

the 60 and 75 wt% loading, a dynamic mixing set up is used with the MOF808 powder constantly being dispersed throughout the CeN''_3 solution. Both THF and MeCN also, as expected, show no loading of the larger micropore at 60 wt% loading. This was consistent with the lower loading of 20 wt% of CeN''_3 (see Supplementary Figure 2.14).

SEM images and EDX spectra were taken for CeNP@MOF808 composites loaded at 75 wt% CeN''_3 in toluene. SEM images show surfaces that are largely aggregated and of low quality, owing once again to the static surface of MOF808. The aggregates exist largely as irregular shaped solids, however can be clearly seen to be composed of smaller MOF808 particles even at low resolutions. Thus, the experimental methodology used for reactive infiltration is important in that it can dramatically influence the morphology and aggregation of the MOF808 particles, which can in effect influence the properties of the material, particularly catalytic behaviour.

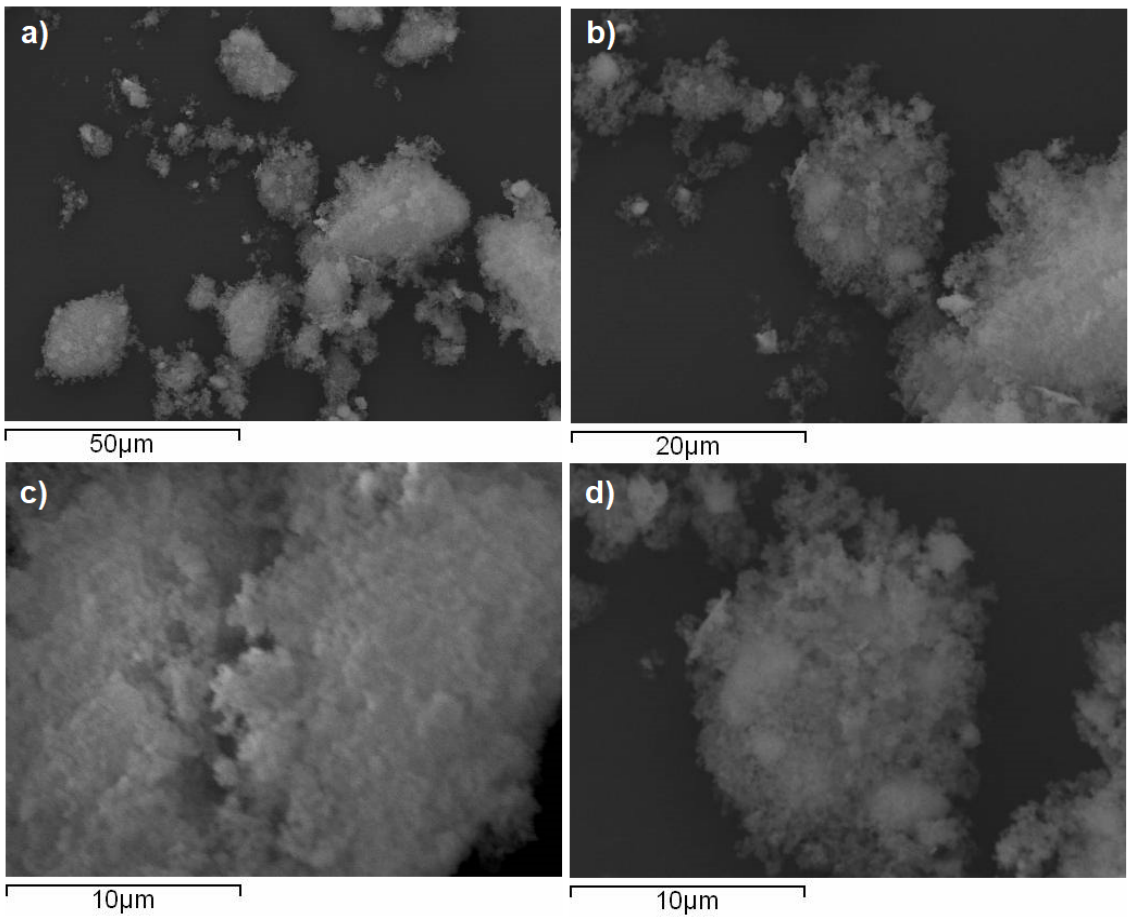

Supplementary Figure 2.23: Low resolution SEM images of 75 wt% loaded CeNP@MOF808, using MeCN, sputter coated with Au/Pd at various magnifications (a) – (d).

EDX spectra show Ce wt% loadings of 30.67 and 17.12 wt% for 60 and 75 wt% loading of CeN''_3.

In conclusion, it was shown that the synthesis of CeNP@MOF808 using higher loading weights of CeN''_3 (inc. 40, 60 and 75 wt%) yielded a composite with a retention of the MOF808 specific microporous surface area and crystallinity and successful loading of Ce metal. However, loading at higher wt% failed to show occupation of the larger micropore of MOF808 and, particularly at higher loading weights, there is the growth of an amorphous background between 25 and 30°.

Therefore in order to achieve successful loading of CeNP within MOF808 we determined that the optimised conditions for reactive infiltration were for the reactive infiltration to place within MOF808 that had been thermally pre-treated at 120 °C, at a 20 wt% loading of CeN''_3 in toluene and with stirring for at least 8 hours.

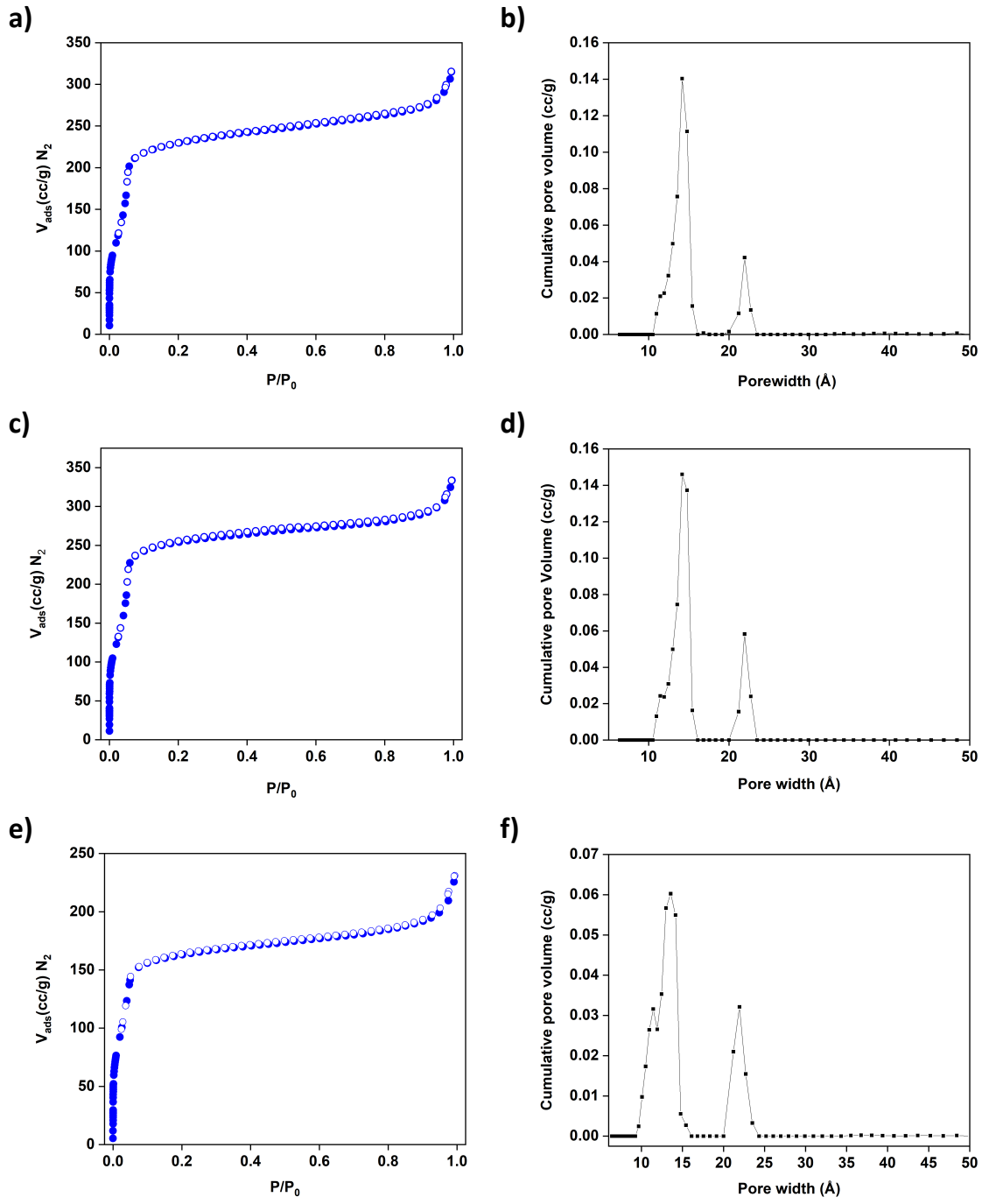

Supplementary Figure 2.24: a, c, e): N_2 adsorption-desorption isotherms for 60 wt% loaded CeNP@MOF808 using toluene, THF and MeCN respectively. b, d, f): PSD plots for 60 wt% loaded CeNP@MOF808 using toluene, THF and MeCN respectively, showing no occupation of the larger micropore for any of the reactive infiltrations, at 60 wt% loading.

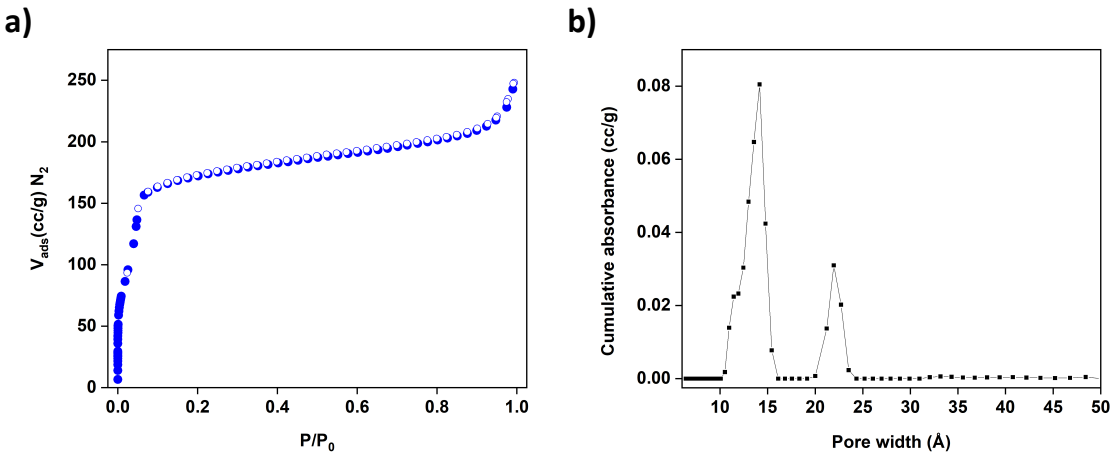

Supplementary Figure 2.25: a): N2 adsorption-desorption isotherms for 75 wt% loaded CeNP@MOF808 using toluene. b): PSD plots for 75 wt% loaded CeNP@MOF808 using toluene, showing no occupation of the larger micropore.

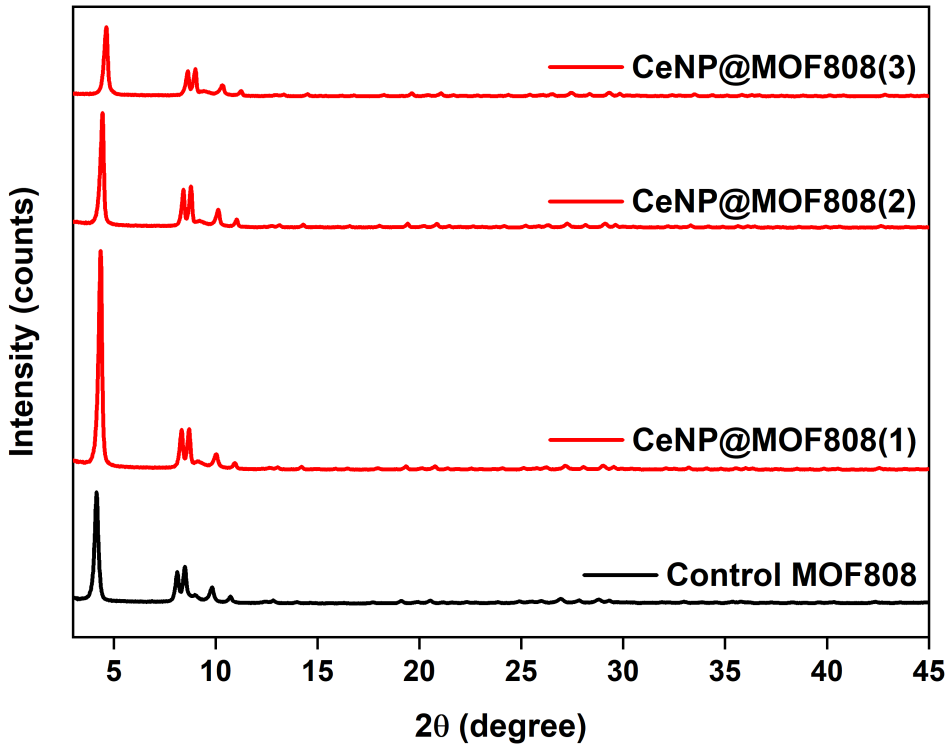

Supplementary Figure 2.26: Powder X-ray diffractograms of control MOF808 and replicated CeNP@MOF808 samples.

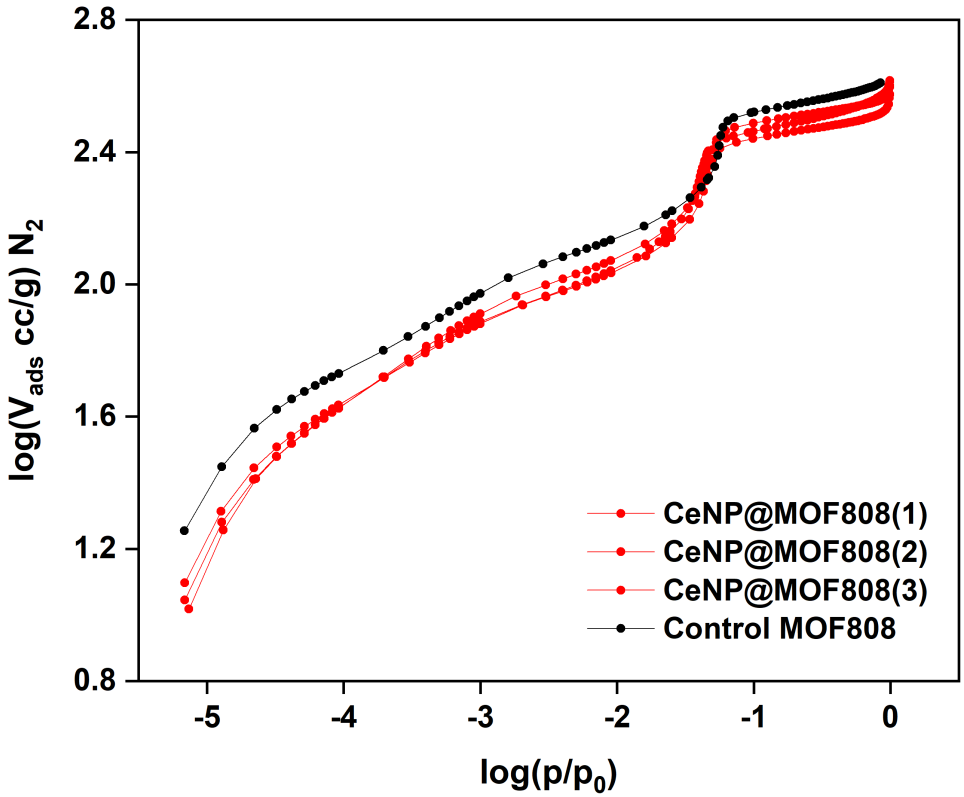

Supplementary Figure 2.27: N_2 adsorption isotherms of control MOF808 and replicated CeNP@MOF808, at -196 °C.

2.11 References for Chapter 2

1. W. S. Rees Jr, O. Just and D. S. Van Derveer, *Journal of Materials Chemistry*, 1999, **9**, 249-252.
2. P.-H. Chang, C.-Y. Chen, R. Mukhopadhyay, W. Chen, Y.-M. Tzou and B. Sarkar, *Journal of Colloid and Interface Science*, 2022.
3. R. Hardian, S. Dissegna, A. Ullrich, P. L. Llewellyn, M. V. Coulet and R. A. Fischer, *Chemistry–A European Journal*, 2021, **27**, 6804-6814.
4. C. Ardila-Suárez, J. Rodríguez-Pereira, V. G. Baldovino-Medrano and G. E. Ramírez-Caballero, *CrystEngComm*, 2019, **21**, 1407-1415.
5. C.-P. Li and M. Du, *Chemical Communications*, 2011, **47**, 5958-5972.
6. K. Izod, S. T. Liddle and W. Clegg, *Inorganic chemistry*, 2004, **43**, 214-218.
7. C. Ardila-Suárez, A. M. Díaz-Lasprilla, L. A. Díaz-Vaca, P. B. Balbuena, V. G. Baldovino-Medrano and G. E. Ramírez-Caballero, *CrystEngComm*, 2019, **21**, 3014-3030.
8. H.-H. Mautschke, F. Drache, I. Senkovska, S. Kaskel and F. L. i Xamena, *Catalysis Science & Technology*, 2018, **8**, 3610-3616.
9. H.-Q. Zheng, C.-Y. Liu, X.-Y. Zeng, J. Chen, J. Lü, R.-G. Lin, R. Cao, Z.-J. Lin and J.-W. Su, *Inorganic chemistry*, 2018, **57**, 9096-9104.
10. H.-Q. Zheng, Y.-N. Zeng, J. Chen, R.-G. Lin, W.-E. Zhuang, R. Cao and Z.-J. Lin, *Inorganic Chemistry*, 2019, **58**, 6983-6992.
11. M. Scimeca, S. Bischetti, H. K. Lamsira, R. Bonfiglio and E. Bonanno, *European journal of histochemistry: EJH*, 2018, **62**.
12. C. M. Hussain, D. Rawtani, G. Pandey and M. Tharmavaram, *Handbook of Analytical Techniques for Forensic Samples: Current and Emerging Developments*, Elsevier, 2020.
13. K. Kanaya and S. Okayama, *Journal of Physics D: Applied Physics*, 1972, **5**, 43.
14. J. I. Goldstein, D. E. Newbury, J. R. Michael, N. W. Ritchie, J. H. J. Scott and D. C. Joy, *Scanning electron microscopy and X-ray microanalysis*, Springer, 2017.
15. S. Kouva, K. Honkala, L. Lefferts and J. Kanervo, *Catalysis science & technology*, 2015, **5**, 3473-3490.
16. J. Jiang, F. Gándara, Y.-B. Zhang, K. Na, O. M. Yaghi and W. G. Klemperer, *Journal of the American Chemical Society*, 2014, **136**, 12844-12847.

17. H.-B. Luo, Q. Ren, P. Wang, J. Zhang, L. Wang and X.-M. Ren, *ACS applied materials & interfaces*, 2019, **11**, 9164-9171.
18. A. Nilchi, M. Yaftian, G. Aboulhasanlo and S. Rasouli Garmarodi, *Journal of Radioanalytical and Nuclear Chemistry*, 2009, **279**, 65-74.
19. A. Ansari and A. Kaushik, *Journal of Semiconductors*, 2010, **31**, 033001.
20. C. Artini, G. A. Costa, M. Pani, A. Lausi and J. Plaisier, *Journal of Solid State Chemistry*, 2012, **190**, 24-28.
21. D. F. Mullica, J. D. Oliver and W. Milllgan, *Acta Crystallographica Section B: Structural Crystallography and Crystal Chemistry*, 1979, **35**, 2668-2670.
22. W. Zachariasen, *Zeitschrift für Physikalische Chemie*, 1926, **123**, 134-150.
23. R. C. Klet, Y. Liu, T. C. Wang, J. T. Hupp and O. K. Farha, *Journal of Materials Chemistry A*, 2016, **4**, 1479-1485.
24. L. J. Henderson, *American Journal of Physiology-Legacy Content*, 1908, **21**, 173-179.
25. P. Larkin, *Infrared and Raman spectroscopy: principles and spectral interpretation*, Elsevier, 2017.
26. J. Xu, J. Liu, Z. Li, X. Wang, Y. Xu, S. Chen and Z. Wang, *New Journal of Chemistry*, 2019, **43**, 4092-4099.
27. J. Feng, Y. Zhong, M. Xie, M. Li and S. Jiang, *Catalysis Letters*, 2021, **151**, 86-94.
28. D. Arumugam, M. Thangapandian, A. Jayaram, G. S. Okram, N. P. Lalla and M. F. B. Amirtham, *The Journal of Physical Chemistry C*, 2016, **120**, 26544-26555.
29. S. Brunauer, P. H. Emmett and E. Teller, *Journal of the American chemical society*, 1938, **60**, 309-319.
30. K. S. Walton and R. Q. Snurr, *Journal of the American Chemical Society*, 2007, **129**, 8552-8556.
31. M. Thommes, K. Kaneko, A. V. Neimark, J. P. Olivier, F. Rodriguez-Reinoso, J. Rouquerol and K. S. Sing, *Pure and applied chemistry*, 2015, **87**, 1051-1069.
32. C. Castillo-Blas, I. Romero-Muñiz, A. Mavrandonakis, L. Simonelli and A. E. Platero-Prats, *Chemical Communications*, 2020, **56**, 15615-15618.
33. J. Xu, J. Liu, Z. Li, X. Wang and Z. Wang, *Journal of Materials Science*, 2019, **54**, 12911-12924.
34. J. Åhman and P. Somfai, *Synthetic communications*, 1995, **25**, 2301-2303.

35. D. C. Bradley, J. S. Ghotra and F. A. Hart, *Journal of the Chemical Society, Dalton Transactions*, 1973, 1021-1023.

3 Post-synthetic Modification and Oxidation State Studies of The CeNP@MOF808 Composite

3.1 Abstract

Thermal and oxidative post-synthetic modifications of the CeNP@MOF808 composite are shown to produce materials with new and distinctly different physio-electronic properties from that of the parent composite material. The goal was to tailor the physio-electronic properties of the composite CeNP@MOF808 nanomaterial, with a view to targeting specific catalytic applications. Here we show that by modifying the CeNP@MOF808 composite through thermal treatments or oxidation with H_2O_2, the physical properties and electronic properties of the composite can be better understood. The CeNP@MOF808 composite lost its structural integrity between 230 °C and 320 °C, with Infra-red (IR) spectroscopy, powder X-ray diffraction (PXRD) and thermal gravimetric analysis (TGA) studies being consistent with the breakdown of the $Zr_6O_4(OH)_4(OOCH)_6$ cluster within this temperature range. IR spectroscopy and PXRD studies showed that thermal treatments of the CeNP@MOF808 composite at 550 °C, and above, yielded ZrO_2, however, no evidence of mixed $Ce_xZr_{1-x}O_2$ was observed. Through a combination of X-ray absorption near edge structures (XANES) spectroscopy, X-ray photoelectron spectroscopy (XPS) and electron energy loss spectroscopy (EELS) studies were it was possible to characterise the electronic structure of CeNP@MOF808, and its post-synthetically modified counterpart structures. The composite is shown to exist largely, 75%, in the Ce^{3+} oxidation state, with the surface of the composite particles being composed entirely, 100%, of Ce^{3+} states. Thus CeNP@MOF808 is a rare example of cerium nanoparticle-composite material where the Ce ions are predominantly in the 3+ oxidation state – without the need for high temperature treatments or use of strong reducing agents. Thermal treatments up to 230 °C had no effect on the mixed Ce^{3+}:Ce^{4+} state proportions, however at 230 °C, and above, the Ce^{3+} reduce significantly. Oxidative treatments showed significant reductions in the Ce^{3+} proportions. It is often difficult to determine oxidation state and local speciation (*e.g.* $Ce(OH)_3$, Ce_2O_3, CeO_2) of the CeNP structures. Fitting the extended X-ray absorption fine structure (EXAFS), based on theoretical scatter pathways of possible CeNP speciation showed that the Ce–O bond distances in CeNP@MOF808 were 2.54 Å and fit best with $Ce(OH)_3$, with a residual bond error of 1% and R_{fac} value of 0.07. These studies demonstrated that the CeNP@MOF808 composite is structurally stable up to at least 230 °C, with a Ce^{3+} proportion of 75% and the most likely speciation of the CeNP being $Ce(OH)_3$.

3.2 Post-synthetic Modification of CeNP@MOF808: Thermal Treatment

The catalytic activity and behaviour of cerium based materials is largely a function of temperature and degree of oxidation (*i.e.* relative Ce^{3+} and Ce^{4+} state proportions). To this end we wished to investigate the effect of thermal and oxidative treatments on the structural properties and electronic properties of the composite.

3.2.1 Thermal Gravimetric Analysis of MOF808

Thermal gravimetric analysis (TGA) is an analytical technique which allows for the identification of specific decomposition events within a material. Note that the term 'decomposition event' does not necessarily refer to chemical breakdown of the composite, and can include events such as desolvation and minor chemical changes of the material. The material (*i.e.* composite CeNP@MOF808) is heated at a constant rate from room temperature to beyond 600 °C. While being exposed to a steady rising temperature, the sample is continuously weighed relative to a standard platinum pan. Any decomposition events are recorded as % mass changes relative to the starting mass. This yields a TGA profile, also termed a 'thermogram', with % mass plotted against the temperature. TGA profiles for MOF808 under air generally show three main decomposition regions: the first region (I), from 40 °C and 100 °C corresponding to the vaporisation of low boiling point solvents (*e.g.* THF and water).[1] The second region (II), from 120 °C to 350 °C, assigned to the vaporisation of higher boiling point solvents (*e.g.* toluene, formic acid and DMF) and the dehydroxylation of the $Zr_6(O)_4(\boldsymbol{OH})_4(OOCH)_6$ cluster.[1] The third region (III), from 450 °C to 700 °C, results from the cleavage of cluster node – linker coordinate bonds, giving a plateau from 700 °C onwards corresponding to the formation of ZrO_2. The plateau should fall in the range of 54% of the samples original mass based on the relative formula mass of both MOF808 (1364 g mol^{-1}) and ZrO_2 (123 g mol^{-1}).[1,2] TGA plots, and corresponding derivative plots, are shown in Figure 3.1 for control, activated and pristine MOF808 under an atmosphere of air.

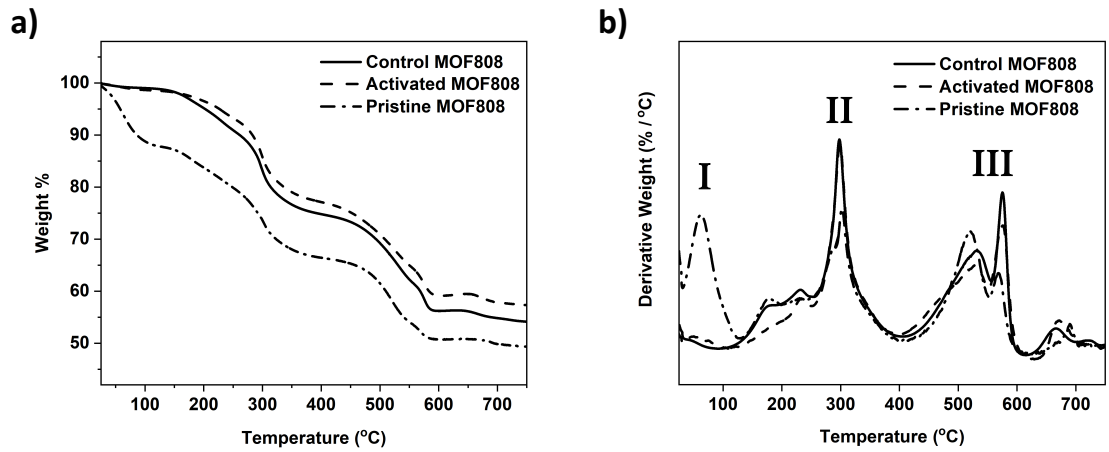

Figure 3.1: (a) TGA plot for control, activated and pristine MOF808, under air. (b) Corresponding derivative plot for control, activated and pristine MOF808, under air, with regions I, II and III marked.

As demonstrated in Figure 3.1 (a), both control and activated MOF808 have similar decomposition profiles, owing to the similar nature of their processing. The only difference is that control MOF808 has additional residual quantities of toluene from the control protocol for reactive infiltration. This results in Control MOF808 having a slightly lower final decomposition weight percentage of 54%, compared with activated MOF808 which has a final decomposition weight percentage of 57%, as a greater percentage of its original mass was made up of volatile toluene (*ca.* 3%). A final decomposition weight percentage of 54% is consistent with literature observations for the thermal decomposition of MOF808 under air.[1,2] Pristine MOF808, which refers to as-synthesised MOF808 (*i.e.* MOF808 formed after the hydrothermal synthesis of $ZrCl_4$ and BTC, with subsequent solvent exchange, see the experimental section of Chapter 2), has a significantly lower final decomposition weight percentage of 50%, this is a result of pristine MOF808 containing significant amounts of pore solvents, namely THF and acetone from the solvent exchange process.

The specific decomposition regions are more easily observed in Figure 3.1 (b). Control and activated MOF808 have almost identical decomposition events: region II (high boiling point solvent vaporisation and dehydroxylation of the cluster) and region III (cluster – linker cleavage) occurring at *ca.* 300 °C and 600°C, respectively. Pristine MOF808 displays regions II and III, but also region I, *ca.* 80 °C, owing to the presence of significant amounts of low boiling

point solvents acetone and THF. Therefore, the similarity in decomposition events in the TGA profiles of MOF808 before (pristine and activated) and after (control MOF808) the control protocol for reactive infiltration indicates that the process of stirring MOF808 for several hours in toluene does not induce changes in the MOF structure or change its structural stability, consistent with PXRD and FT-IR observations which show retention of MOF crystallinity and BTC linkers in control MOF808, as demonstrated in Chapter 2.

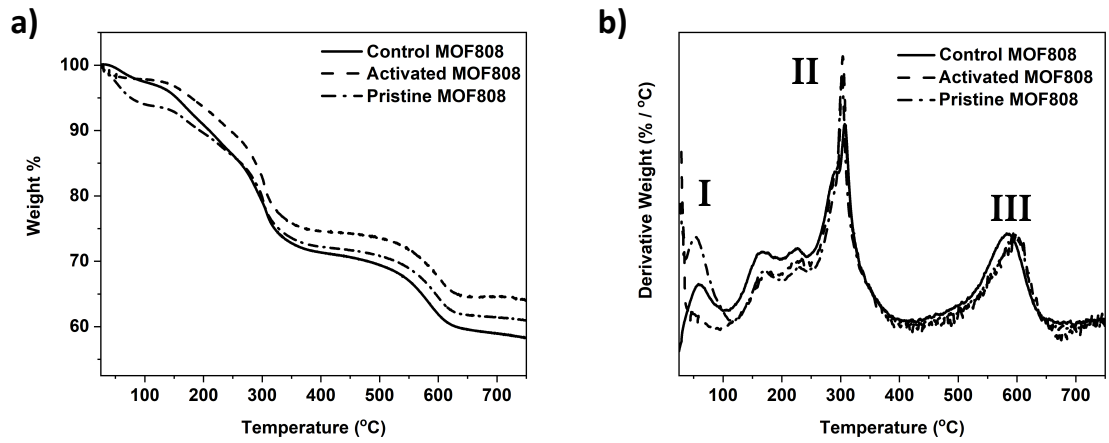

Figure 3.2: (a) TGA plot for control, activated and pristine MOF808, under nitrogen. (b) Corresponding derivative plot for control, activated and pristine MOF808, under nitrogen, with regions I, II and III marked.

Decomposition events I, II and III observed for pristine, activated and control MOF808 are present also under a nitrogen atmosphere (anaerobic), occurring over similar temperature ranges (see Figure 3.2). Decomposition region III is a single, 'broad peak' event at 600 °C under an atmosphere of nitrogen, while under air the decomposition occurs as two, 'sharp peak' events at 500 °C and 580 °C. The decomposition event III most likely occurs through a pyrolysis mechanism of the BTC linker rather than combustion. However, the literature is scarce in identifying the exact mechanism behind these events under an atmosphere of nitrogen and may deviate from that under an atmosphere of air. Evidence for the pyrolysis mechanism can be found in the higher final decomposition weight percentages of pristine, active and control MOF808 at 61%, 64% and 58%, respectively – relative to those under air. Pyrolysis decomposition mechanisms tends to yield charred carbonaceous masses, with a higher resulting mass. Similar to its behaviour under an atmosphere of air, activated MOF808

decomposes under an atmosphere of nitrogen with the highest final decomposition weight, compared with control and pristine MOF808. This is expected given that activated MOF808 would have the lowest solvent content of any of the MOF808 samples. What is surprising is that control MOF808 has a lower final decomposition weight percentage compared with pristine MOF808 (58% vs. 61%), this is contradicts the observations made under air where control MOF808 had a higher final decomposition weight. However this most likely arises due to slight variation in solvent loadings between samples.

It can be concluded that the experimental procedure adopted to perform reactive infiltration, whereby the MOF structure is heated for several hours under vacuum (*i.e.* activation) and subsequently stirred for several hours in toluene (*i.e.* the control reactive infiltration protocol), does not induce structural or stability changes. This is evident from the TGA decomposition plots which show similar decomposition events occurring over similar temperature ranges for pristine, activated and control MOF808 – under both aerobic and anaerobic atmospheres. Once it had been established that the control reactive infiltration procedure was not inducing changes in the MOF808 thermal stability, TGA studies could be expanded to investigate the impact that loading CeNP into the MOF808 structure has on the MOF808 thermal stability.

3.2.2 Thermal Gravimetric Analysis of CeNP@MOF808

TGA profiles were recorded before and after the reactive insertion of precursor CeN''_3 to determine what effect, if any, the process of reactive infiltration has on the structural integrity and thermal stability of the MOF host structure. If the precursor reacted with major structural components of the MOF (*e.g.* organic linker or cluster nodes) then this would be evident by distinct changes in the decomposition pathways recorded during TGA.[3-5] As demonstrated in Chapter 2, the composite CeNP@MOF808 shows retention of the MOF crystalline structure following reactive infiltration in PXRD diffractograms. What impact the incorporation of CeNP into the MOF808 host has on the MOF structure and stability would be revealed through TGA study of CeNP@MOF808.

The TGA profiles of CeNP@MOF and control MOF under anaerobic conditions are shown in Figure 3.3. The TGA profiles were consistent between repeat samples demonstrating sample reproducibility in the reactive infiltration process (see Section 3.7). The similar overlap of derivative TGA plots shown in Figure 3.3 (b) indicates no significant changes in temperature ranges for the decomposition regions II and III, occurring at *ca.* 300 °C and 600°C, respectively. As expected, CeNP@MOF808 displays little decomposition activity in region I due to lack of exposure to low boiling point solvents, similar to that observed with control MOF808. Final weight percentages of MOF808 and CeNP@MOF808 were 59% and 62%, respectively. This difference in final decomposition weight percentage is the Ce loading. At 3 wt% this is in agreement with EDX spectroscopy and ICP-OES measurements which showed Ce loadings of 3.13 wt% and 3.015 wt%, respectively. The lack of a temperature shifts in the onsets of regions II and III under anaerobic atmospheres highlights that no change the structural stability of the MOF808 host after incorporating CeNP into the structure.

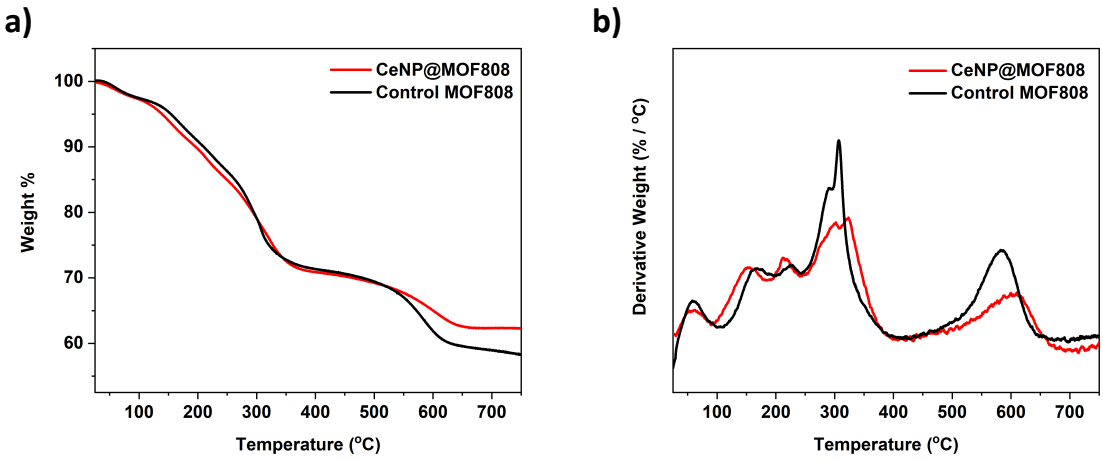

Figure 3.3: (a) TGA plot for CeNP@MOF808 and Control MOF808, under nitrogen. (b) Corresponding derivative plot for CeNP@MOF808 and Control MOF808, under nitrogen.

The TGA profiles for CeNP@MOF and control MOF808 are shown, with corresponding derivatives, in Figure 3.4. The TGA profiles of CeNP@MOF and control MOF808, under aerobic conditions, are consistent within region II, however there is a distinctive shift to a lower temperature range for region III of CeNP@MOF808, from 550 °C to 400 °C.

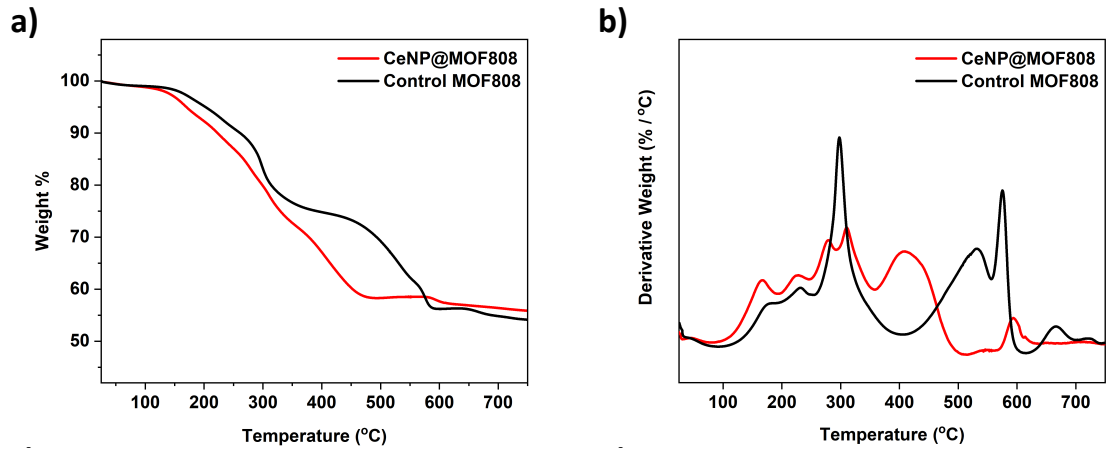

Figure 3.4: (a) TGA plot for CeNP@MOF808 and Control MOF808, under air. (b) Corresponding derivative plot for CeNP@MOF808 and Control MOF808, under air.

The loading of nanoparticles into MOF structures has shown a variety of effects on the structural stability of the MOF host in the literature, these are summarised below in Table 3.1. There is no clear trend in the stabilising effect that the incorporation of NPs into MOF framework has on the framework thermal stability, indeed the exact location of the NP (*i.e.*, within pores, bonded to cluster nodes, on the external surface, *etc.*) will have a strong influence over whether the incorporated NPs stabilise or destabilise the host structure. Therefore, Table 3.1 is only included as brief summary of the effects that incorporation of metal NPs can have on the thermal stability of the MOF host.

It is proposed that the CeNP composited within MOF808 framework offers a lower energy, oxidative pathway for region III, which remains inaccessible under anaerobic conditions. The redox activity of CeNPs has found applications, particularly in the field of oxidative degradation of small organic molecules,[6-9] and will be further explored in Chapter 4 where the degradation of small organophosphate molecules is investigated using the CeNP@MOF808 composite.

Table 3.1: Summarised examples from literature of temperature shifts in MOF decomposition with NP incorporation.

MOF	NP	Temperature Shift in Organic Linker (°C)	Stabilising / Destabilising	Reference
Ce-MOF	Pd	+ 150	Stabilising	[3]
MOF-199	Au/SWNT [a]	0	No Effect	[10]
CuBTC	Au	0	No Effect	[11]
UiO-67	Pt	- 105	Destabilising	[12]
MOF808	Ce	- 150	Destabilising	This Work
[a] SWNT: Single walled nanotubes				

The final weight percentages of control MOF808 and CeNP@MOF808 were 54% and 56%, respectively. The 2% increase in final weight percent of CeNP@MOF808 is in good agreement with the increase in final decomposition weight under anaerobic conditions, EDX spectroscopy and ICP-OES determined loadings which indicated Ce loading of *ca.* 3 wt%. Therefore, it can be concluded that Ce loading for the CeNP@MOF808 synthesised *via* reactive infiltration was *ca.* 3 wt%, and that the introduction of CeNP into the MOF structure did not change the thermal stability under anaerobic conditions, but did exhibit a destabilising effect, under aerobic conditions, with a *ca.* 150 °C shift in region III corresponding to the decomposition of the organic BTC linker.

3.2.3 Powder X-ray Diffraction Studies of Thermally Treated CeNP@MOF808

The derivative TGA profile of CeNP@MOF808, see Figure 3.4 (b), revealed several troughs (or plateaus) following decomposition events at 180, 230, 320, 550 and 650 °C. It was noted that these selected points in the TGA profiles would be appropriate temperatures for thermal treatments. The troughs in the derivative TGAs represent products following the immediately preceding decomposition event which could be characterised in a manner similar to that of the parent CeNP@MOF808 in Chapter 2 *via* a combination of TGA, FT-IR, EDX spectroscopy, digestion NMR and elemental microanalysis. Through this series of characterisation techniques, coupled with literature knowledge of decomposition events typical of MOF808, it was possible to infer possible speciations for each material following on from a decomposition event at the noted temperatures above. Samples of CeNP@MOF808 were collected in either glass vials (thermal treatments less than 500 °C) or ceramic weighing boats (thermal treatments greater than 500 °C) and subjected to the selected thermal treatment temperature (180, 230, 320, 550 or 650 °C) for 1 hours. The characterisation of these thermally treated CeNP@MOF808 samples is summarised Table 3.6.

PXRD diffractograms of CeNP@MOF808 and control MOF808 revealed in Chapter 2 that the crystallinity of MOF808 was retained after formation of the composite nanomaterial using the novel methodology of reactive infiltration. The question arises however in when will the composite lose its crystalline arrangement and does the temperature at which the composite loses it crystalline arrangement deviate to any significant extent from that of the MOF808 host structure without incorporated CeNP? This was further investigated through a series of PXRD diffractograms taken of the CeNP@MOF808 composite after thermal treatment at 180, 230, 320, 550 and 650 °C for 1 hour under aerobic atmospheres, see Figure 3.5.

As displayed in Figure 3.5 crystallinity of CeNP@MOF808 is retained after thermal treatments at 180 °C and 230 °C, for 1 hour under aerobic atmospheres. However, between 230 °C and 320 °C the composite loses crystallinity and becomes amorphous, with the PXRD diffractogram of CeNP@MOF808 heated at 320 °C showing no reflections characteristic of MOF808. This is consistent with literature observations with MOF808 losing crystallinity

between 230 °C and 250 °C.[2,13,14] Therefore, the thermal crystalline stability of the MOF808 host was retained after the formation of the composite nanomaterial using the novel methodology of reactive infiltration.

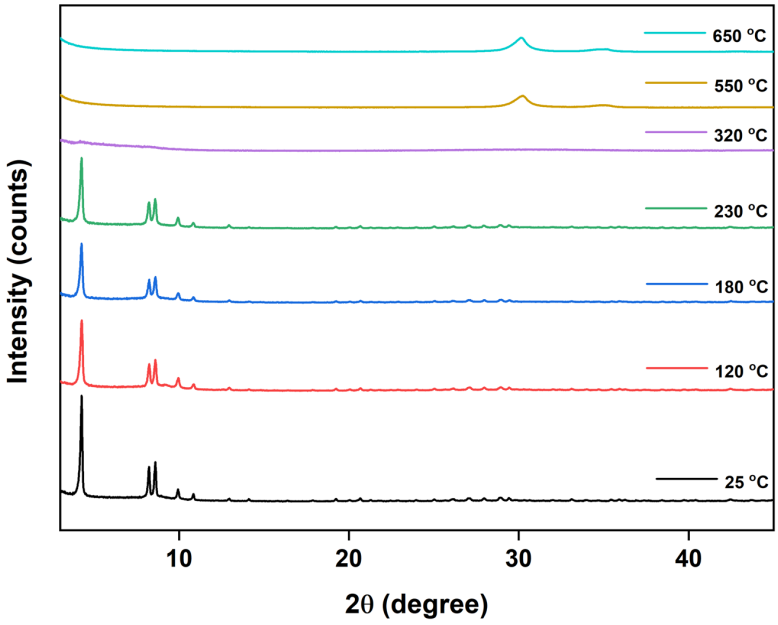

Figure 3.5: Powder X-ray diffractograms of CeNP@MOF808 and CeNP@MOF808 thermally treated at 120, 180, 230, 320, 550 and 650 °C, for 1 hour.

High temperature thermal treatments of CeNP@MOF808 at 550 °C and 650 °C resulted in the formation of ZrO_2, with characteristic reflections at 2θ = 30° (111), 35° (200) and 50° (220) (cubic and/or tetragonal polymorphs), see Figure 3.6.[15-17] This is characteristic of MOF808, with several reports citing the formation of ZrO_2 after the region III decomposition at *ca.* 600 °C.[18] MOF808 thermally treated at 650 °C has a small, broad peak at 30° associated with the $(\bar{1}11)$ reflection of the minor monoclinic phase. This is not present in the CeNP@MO808 sample thermally treated at 650 °C, suggesting that the incorporation of CeNP into the MOF host favours the cubic and/or tetragonal polymorphs. Reflections are not observed for CeO_2, which would be present at 2θ = 28° (111), 33° (200) and 47° (220) in the PXRD diffractogram.[19-21] This is despite exposures to significantly high temperatures of 650 °C, which has been shown in literature to cause an enhancement of peak reflection intensity corresponding to improved crystallinity of the CeO_2 and would therefore cause CeO_2 to become visible in the PXRD diffractograms of Figure 3.6.[22,23]

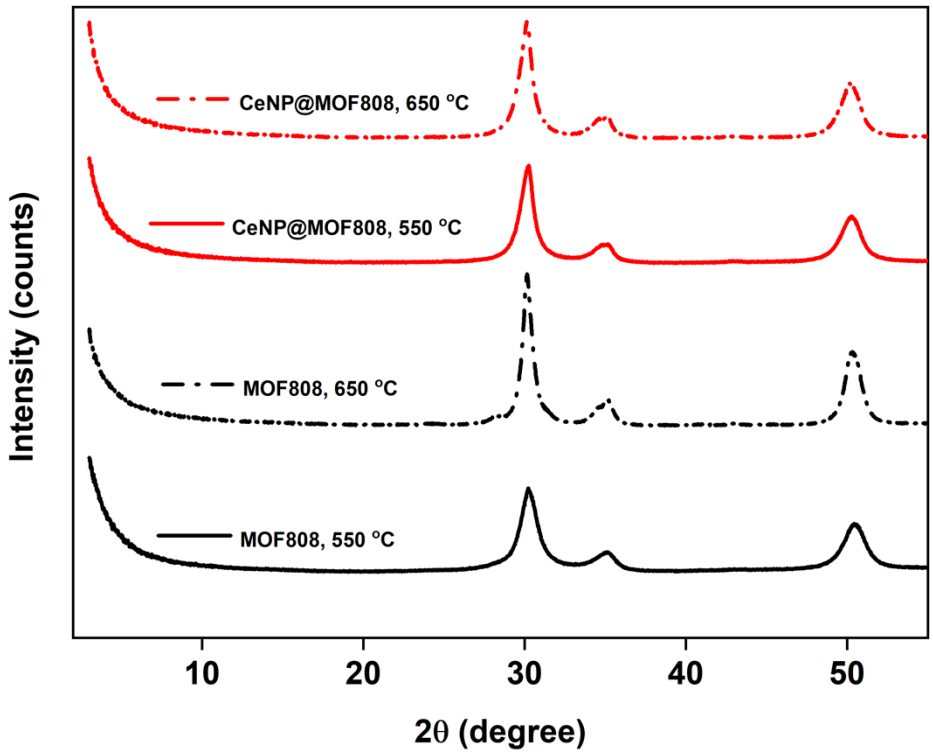

Figure 3.6: Powder X-ray diffractograms of control MOF808 and CeNP@MOF808 thermally treated at 550 °C and 650 °C, for 1 hour.

It is possible that the reflections observed in Figure 3.6 result from a solid solution of $Ce_xZr_{1-x}O_2$, with the loading weights of Ce at 4.4 wt% and 6.1 wt% for CeNP@MOF808 heated to 550 °C and 650 °C respectively (see Section 3.2.6), corresponding to $Ce_{0.2}Zr_{0.8}O_2$. It was not possible to conclude whether this was a true solid solution or a phase separated mixture of ZrO_2 and CeO_2 where the CeO_2 is present in such minute quantities that it is simply not detected. It is possible that the CeO_2 remained in an amorphous form and would therefore not show any reflections in the diffractogram.

Thermal treatment of CeNP@MOF808 at 230 °C for 1 hour in air showed retention of the MOF808 crystallinity (see Figure 3.5). However, thermal treatment of CeNP@MOF808 at 230 °C over a longer time period, 24 hours, resulted in the composite becoming amorphous, with no reflections characteristic of MOF808 visible, see Figure 3.7.

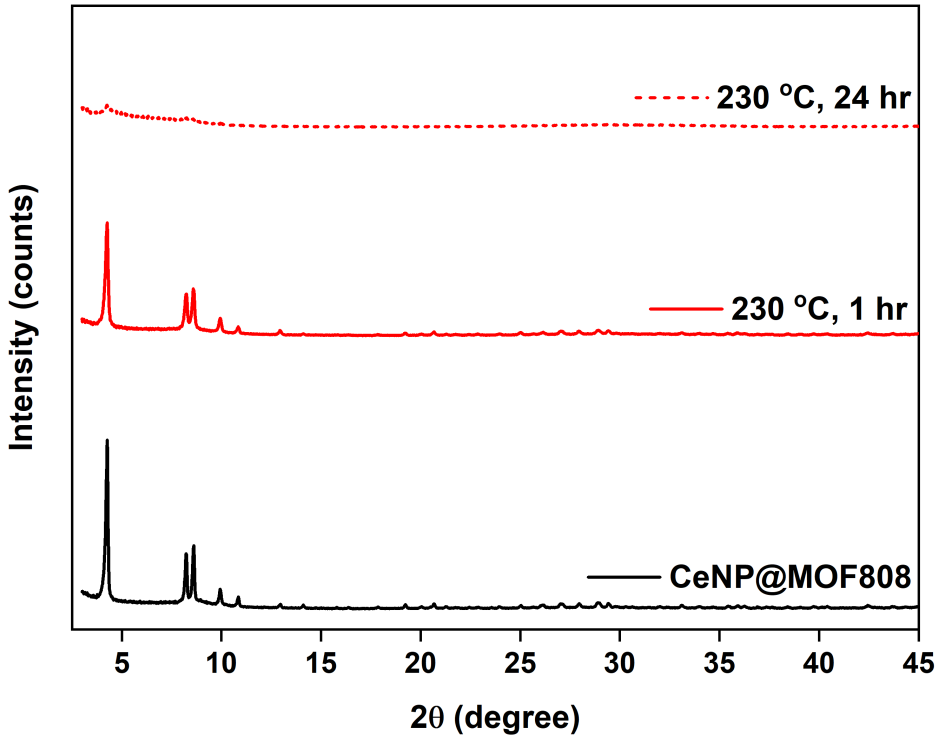

Figure 3.7: Powder X-ray diffractograms of CeNP@MOF808 and CeNP@MOF808 thermally treated at 230 °C, for 1 hour and 24 hours.

This leads to a more nuanced understanding of the thermal stability of the composite. It is not the case there this a particular degradation temperature of the composite, beyond which the host framework shall decompose, regardless of exposure time. Instead, the composite appears to have a degradation temperature that is dependent upon the length of exposure to the thermal treatment; longer exposure, lower degradation temperature. This is again consistent with literature observations where the exact temperature, or rather temperature range, that loss of the MOF808 host loses its crystalline structure is dependent upon the thermal treatment conditions (*e.g.* heating time, atmosphere). This shifting of the temperature window over which MOF808 loses its crystallinity is summarised in Table 3.2 using examples from literature and comparing with the CeNP@MOF808 composite. It is evident from the thermal crystalline stability studies of MOF808 collected from literature, as well as the thermal crystalline stability studies of CeNP@MOF808, that the greater the energy intensity of the thermal treatment (*e.g.* longer thermal treatments, under high vacuums) the lower the temperature window over which MOF808 loses its crystalline structure.

Table 3.2: Summary of temperature windows over which MOF808 loses its crystallinity, comparison made with CeNP@MOF808.

Material	Highest Temperature Where Crystalline (°C)	Lowest Temperature Where Amorphous (°C)	Heating Time (hours)	Atmosphere	Reference
MOF808	140	180	Overnight (*ca.* 12 hours)	*Vacuo*	[13]
	200	250	16	Air	[14]
	150	200	16	*Vacuo*	[2]
CeNP@MOF808	230	320	1	Air	This Work
	/	230	24	Air	This Work

Powder diffractograms of CeNP@MOF808 thermally treated at several temperatures for 1 hour under aerobic conditions therefore reveal no changes in the crystalline stability of the MOF host framework upon incorporation of CeNPs when compared to equivalent literature examples.[14] Thermal treatments up to 650 °C failed to crystallise CeO_2 nanoparticles, with no characteristic reflections being observed, however it may be that the Ce ions become incorporated into a solid solution, of the form $Ce_xZr_{1-x}O_2$, at higher temperatures; 550 °C and 650 °C, or that the CeO_2 remains amorphous. Thermal treatments for longer periods of time were found to lower the temperature at which MOF808 lost its crystallinity, again in keeping with literature observations.

3.2.4 Thermal Gravimetric Analysis of Thermally Treated CeNP@MOF808

Given that previous PXRD studies had shown that the crystallinity of CeNP@MOF808 was lost at, or before, 320 °C samples of CeNP@MOF808 were treated at 180, 230 and 320 °C for 1 hour, under an aerobic atmosphere to investigate what effect, if any, thermal treatments had

on the thermal stability of the CeNP@MOF808 composite and how this would compare to the thermal crystalline stability.

As expected, the traces for all of the thermally treated samples show an absence of decomposition events up to the temperature of treatment, after which the normal decomposition pathway is resumed, see Figure 3.8. Note that CeNP@MOF808, un-treated, is included in Figure 3.8 for comparison. CeNP@MOF808 treated at 180 °C showed a similar decomposition pathway to that of CeNP@MOF808, with decomposition regions II and III largely unaffected (some loss of peak resolution was observed in region II) at *ca.* 300 °C and 600 °C. Thermal treatment of CeNP@MOF808 at 230 °C resulted in a decomposition pathway that lacked the lower peaks of region II, most likely the evaporation of higher boiling point solvents which would have been removed from the material during the 230 °C treatment. Thermal treatment of CeNP@MOF808 at 320 °C produced a material which undergoes one main decomposition event, region III, at *ca.* 300 °C. This suggests that thermal treatment of CeNP@MOF808 at 320 °C results in successful desolvation and dehydroxylation of the cluster nodes (*i.e.* speciation $Zr_6O_4(BTC)_2$). All thermally treated samples (180, 230 and 320 °C) samples still showed the destabilised shift in region III to *ca.* 300 °C, relative to control MOF808. Final weight percentages were consistent with thermal treatment temperatures, with higher temperatures resulting in higher final weight percentages. This is expected given that higher temperatures will result in solvent evaporation and decomposition occurring before the TGA measurement, therefore there is less overall mass to lose.

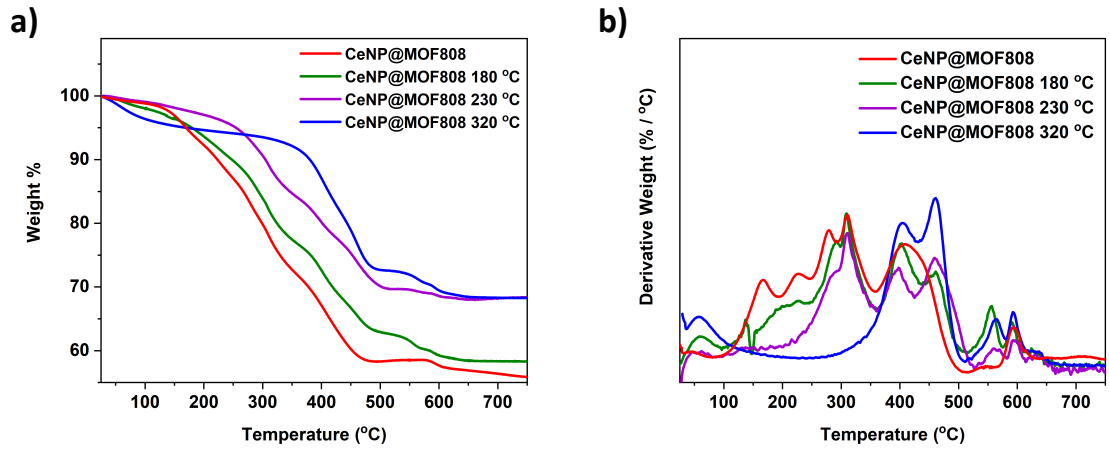

Figure 3.8: (a) TGA plot for CeNP@MOF808 thermally treated at 120, 180, 230 and 320 °C, under air. (b) Corresponding derivative plot for CeNP@MOF808 thermally treated at 120, 180, 230 and 320 °C, under air.

Comparing the derivative TGA plots in Figure 3.8 (b) with the diffractograms of Figure 3.5, it is possible that the loss of crystallinity of the CeNP@MOF808 composite that occurs between 230 °C and 320 °C is concurrent with the loss of the decomposition event in region II between 230 °C and 320 °C. This would indicate that the dehydroxylation of the cluster nodes of MOF808 is responsible for the loss of the MOF808 crystallinity.

3.2.5 Fourier Transform Infra-red Spectroscopy Studies of Thermally Treated CeNP@MOF808

Previously it was established in Chapter 2 that MOF808 had a collection of strong IR absorption bands at *ca.* 1600 (br), 1445 (s) and 1380 (s) cm^{-1}, assigned to aromatic ring and coordinated carboxylate stretches of the organic BTC linker.[24,25] A sharp absorption band at 650 cm^{-1} was assigned to Zr–O stretches of the MOF808 cluster nodes.[25] FT-IR spectra of thermally treated control MOF808 samples showed retention of these absorption bands up to 230 °C, see Figure 3.9 (a). At thermal treatments of 550 °C, and beyond, the absorption bands assigned to the organic BTC linker and the metal cluster nodes of MOF808 are lost, replaced by weaker absorption bands at 2360 cm^{-1} assigned to surface Zr–OH groups of ZrO_2 (the decomposition product of MOF808),[26,27] and at 500 cm^{-1}, assigned to Zr–O stretches of ZrO_2,[26] see Figure 3.9 (a). This is indicative of ZrO_2 forming, consistent with TGA measurements of control MOF808 which show a residual weight percentage, under both aerobic and anaerobic conditions, that would expected for MOF808 being the final decomposition product (see Section 3.2.1).

It was previously established in Chapter 2 that the loading of CeNPs into the MOF808 host structure did not change the structural connectivity of the MOF host to any significant extent, that is that stretching frequencies assigned to the organic BTC linker, coordinated carboxylate groups and cluster nodes were all present in the FT-IR spectrum of CeNP@MOF808.[24,25] FT-IR spectra of thermally treated CeNP@MOF808 were similar to those of thermally treated control MOF808, see Figure 3.9 (a) and (b). The CeNP@MOF808 composite showed strong absorption bands characteristic of MOF808 (i.e. BTC linker and metal cluster nodes) up to 230 °C. At a thermal treatments of 550 °C, and beyond, these characteristic absorption bands

were lost and replaced with stretching frequencies at 2360 cm^{-1} and 500 cm^{-1}, assigned to Zr–OH and Zr–O moieties of ZrO_2 – identical to those seen with thermally treated control MOF808 at 550 °C and 650 °C. This was consistent with diffractograms taken of CeNP@MOF808 (see Section 3.2.3) which showed loss of crystallinity between 230 °C and 320 °C – as would be expected with the loss of structural integrity indicated by the IR spectra of thermally treated CeNP@MOF808. At higher temperatures of 550 °C and 650 °C, no vibrations associated with BTC linker at *ca.* 1600 – 1400 cm^{-1} can be observed, consistent with TGA studies of CeNP@MOF808 (see Section 3.2.2) which showed the decomposition of BTC occurring in region III at *ca.* 600 °C.

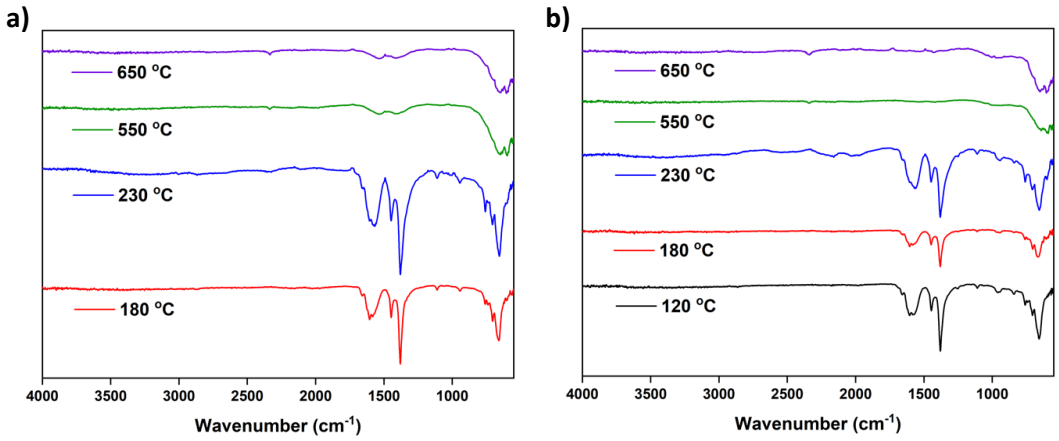

Figure 3.9: a) FT-IR Spectra of control MOF808 thermally treated at treated at 180, 230, 550 and 650 °C, b) FT-IR Spectra of CeNP@MOF808 thermally treated at 120, 180, 230, 550 and 650 °C.

3.2.6 Energy Dispersive X-ray Spectroscopy, Digestion NMR and Elemental Microanalysis Studies of Thermally Treated CeNP@MOF808

It was previously established in Chapter 2 that the CeNP@MOF808 composite had a Ce wt% of . Energy Dispersive X-ray Spectroscopy was subsequently performed on thermally treated CeNP@MOF808 samples to investigate Ce wt% loading as a function of the thermal treatment temperature. Ce wt%, and associated errors expressed in terms of standard deviations, of thermally treated CeNP@MOF808 samples are reported below in Table 3.3.

Table 3.3: Ce wt% of CeNP@MOF808, determined *via* EDX spectroscopy, as a function of thermal treatment temperature.

Temperature (°C)	Ce wt% (± std. dev.)
25	2.78 (± 1.03)
120	3.14 (± 0.91)
180	4.30 (± 2.70)
230	4.40 (± 1.40)
320	3.04 (± 0.83)
550	4.40 (± 1.40)
650	6.12 (± 5.93)

Thermal treatments between 25 °C and 650 °C yield slight variations in the Ce wt% of the CeNP@MOF808 composite, however the significant overlap of errors means that there is no statistically significant difference between samples in the Ce loading. The increase in variation of Ce wt% loading for CeNP@MOF808 thermally treated at 650 °C, with a standard deviation of 5.93 wt%, was significantly different to the variation seen for lower temperature thermal treatments. This higher variation for thermal treatments at 650 °C likely arises from the aggregation of Ce based species which are localised to certain portions of the sample giving a wide spread of wt%. This would be consistent with the loss of crystallinity of the MOF808 host, whereby CeNP could aggregate – although one would expect this aggregation to occur above 320 °C when crystallinity is lost, not 650 °C.

The formate:BTC ratio was determined by digestion ^{1}H NMR to be 1.01 ± 0.3 for CeNP@MOF808, in Chapter 2. The effect of thermal treatment temperature on the formate:BTC ratio for CeNP@MOF808 was investigated using digestion ^{1}H NMR spectroscopy (see Table 3.4).

Table 3.4: formate:BTC ratio of CeNP@MOF808, determined *via* digestion ^{1}H NMR spectroscopy, as a function of thermal treatment temperature.

Temperature (°C)	Formate:BTC
25	1.01 ± 0.3
120	1.19
180	0.91
230	0.70
320	Insoluble
550	Insoluble
650	Insoluble

There is a general trend in that increasing the thermal treatment temperature from 25 °C to 230 °C results in a decrease in the formate:BTC ratio of CeNP@MOF808, from 1.01 (± 0.3) to 0.70, respectively. However, due to the limited number of digestion ^{1}H NMR measurements performed on the thermally treated samples, no error values could be determined. The error value of CeNP@MOF808 not thermally treated (*i.e.* at 25 °C) overlaps with the ratios determined for the thermally treated samples (at 120, 180 and 230 °C) such that no statistically significant change in the formate:BTC ratio can be concluded from thermal treatments up to 230 °C. The mere presence of formate in the CeNP@MOF808 digestion ^{1}H NMR after thermal treatment at 230 °C could be significant however. The presence of formate contrasts with observations made in a separate study, where digestion ^{1}H NMR spectra of MOF808 before and after thermally treatment at 250 °C resulted in the complete loss of the formate resonance. Although it should be noted that the separate study performed the thermal treatment on MOF808 for a longer period of time (16 hours) and alkaline digestion was used, rather than the acidic digestion adopted in this study, to record the digestion ^{1}H NMR.[14] Thermal treatments of CeNP@MOF808 at temperatures above 230 °C, namely 320,

550 and 650 °C, yielded a material that was insoluble in acidified DMSO, coinciding with the point at which the CeNP@MOF808 composite undergoes a transition from crystalline to amorphous (see Figure 3.5) and cluster – linker cleavage occurs *ca.* 600 °C (see Figure 3.4).

In Chapter 2 elemental microanalysis of the CeNP@MOF808 composite showed C%, H% and N% of 25.78%, 3.60%, 1.01%, respectively. The C%, H% and N% for CeNP@MOF808 at 25 °C are arbitrary as the samples are 'wet' with toluene fowling the reactive infiltration protocol. Elemental microanalysis was performed on samples of control MOF808 and CeNP@MOF808 thermally treated at 120, 180, 230 and 320 °C (see Table 3.5).

Table 3.5: C%, H% and N% of CeNP@MOF808, determined *via* elemental microanalysis, as a function of thermal treatment temperature.

Temperature (°C)	CHN %
25	25.78, 3.60, 1.01[d]
120	17.14, 2.02, 0.70
180	18.04, 1.42, 1.16
230	17.37, 1.27, 1.36
320	13.60, 1.26, 0.18
550	Not Acquired
650	Not Acquired

Between 120 °C and 230 °C, the values of C%, H% and N% for CeNP@MOF808 vary, but not in a statically significant manner. Therefore the CeNP@MOF808 composite is considered chemically unchanged between 25 °C and 230 °C, consistent with FT-IR absorption spectra which show retention of the MOF808 structural connectivity (see Figure 3.9 (b)). Between 230 °C and 320 °C there is a significant change in the C% and N% from 17.37% and 1.36% to 13.60% and 0.18%, respectively, for thermally treated CeNP@MOF808. This coincides with the loss of MOF808 crystallinity in the CeN@MOF808 composite (see Figure 3.5) and indicates a different material is formed relative to the CeNP@MOF808 composite.

3.2.7 Post-synthetic Modification of CeNP@MOF808: Thermal Treatment: Conclusions

In conclusion, thermal post-synthetic modification was successfully performed. TGA studies of control MOF808 showed that the thermal stability of MOF808 is unaffected by the control reactive infiltration protocol, with no changes in the TGA profiles of MOF808 relative to pristine and activated MOF808 under aerobic or anaerobic conditions. TGA studies of the composite CeNP@MOF808 indicated that the thermal stability of CeNP@MOF808 is unchanged relative to control MOF808 under anaerobic conditions, but altered under aerobic conditions – with a *ca.* 150 °C decrease in temperature for the cluster – linker cleavage. X-ray powder diffractograms of thermally treated CeNP@MOF808 highlighted that the crystalline stability, with regard to temperature rises, is unaffected by the incorporation of CeNP into the MOF808 host. Crystallinity of CeNP@MOF808 was lost within the temperature range of 230 °C and 320 °C, in agreement with literature. No evidence of crystalline CeO_2 was present in any X-ray powder diffractograms of thermally treated sample of CeNP@MOF808. TGA studies of thermally treated CeNP@MOF808 revealed that between 230 °C and 320 °C the region II decomposition is lost (*i.e.* collapse of cluster nodes). This coincides with the temperature window over which CeNP@MOF808 loses its crystalline structure, suggesting that the loss of crystallinity is associated with the collapse of the cluster nodes. FT-IR spectra acquired of the thermally treated CeNP@MOF808 composite showed that the structural connectivity of MOF808 was lost between 230 °C and 550 °C. EDX spectra of the thermally treated CeNP@MOF808 composite showed that the Ce wt% loading remained unchanged with thermal treatment, however variation increases substantially at 650 °C, suggesting aggregation. Digestion ^{1}H NMR spectra of thermally treated CeNP@MOF808 revealed that formate:BTC ratios do vary with thermal treatment temperature, but not to any degree that is statistically significant. Elemental microanalysis of the thermally treated CeNP@MOF808 showed that there is no change in the C%, H% and N%, between 120 °C and 230 °C. This suggests no change in the chemical composition of the composite with thermal treatment up to 230 °C, consistent with powder X-ray diffraction and FT-IR spectra results. The significant change in the C%, H% and N% between 230 °C and 320 °C suggests formation of a material different to that of the composite, again consistent with powder X-ray diffraction data. This is summarised in Table 3.6.

Table 3.6: Summarised TGA, PXRD, FT-IR, EDX, Digestion NMR and Elemental microanalysis data for thermally treated CeNP@MOF808.

Temperature (°C)[a]	% weight (TGA)	Crystallinity (PXRD)	BTC Linker and Zr_6 Cluster (FT-IR)[b]	Ce wt% (EDX)[c]	Formate: BTC (^{1}H NMR)	CHN % (microanalysis)	Speciation
25	100	Crystalline (MOF808)	Intact	2.78 (± 1.03)	1.01 (± 0.3)	25.78, 3.60, 1.01[d]	CeNP@MOF808
120	98	Crystalline (MOF808)	Intact	3.14 (± 0.91)	1.19	18.62, 1.94, 0.96	CeNP@MOF808
180	93	Crystalline (MOF808)	Intact	4.30 (± 2.70)	0.91	18.04, 1.42, 1.16	CeNP@MOF808
230	87	Crystalline (MOF808)	Intact	4.40 (± 1.40)	0.70	17.37, 1.27, 1.36	CeNP@MOF808
320	73	Amorphous	Not Acquired	3.04 (± 0.83)	Insoluble	13.60, 1.26, 0.18	CeNP/$Zr_6O_4(BTC)_2$
550	58	Crystalline (ZrO_2 or $Ce_xZr_{1-x}O_2$)	Lost	4.40 (± 1.40)	Insoluble	Not Acquired	ZrO_2 or $Ce_xZr_{1-x}O_2$
650	56	Crystalline (ZrO_2 or $Ce_xZr_{1-x}O_2$)	Lost	6.12 (± 5.93)	Insoluble	Not Acquired	ZrO_2 or $Ce_xZr_{1-x}O_2$

[a] Thermal treatment for 1 hour, under air.

[b] Stretching frequencies at ν = 1600, 1445 and 1380 cm^{-1} (BTC linker) and ν = 650 cm^{-1} (Zr_6 cluster nodes).

[c] Several scans taken over randomised particle surface areas, average value reported ± std. dev.

[d] These values are arbitrary in that the composite was 'wet' with toluene.

3.3 Post-synthetic Modification of CeNP@MOF808: Oxidative Treatment

Characterisation of cerium oxidation states in CeNP@MOF808, see Section 3.4, showed that the Ce^{3+} oxidation state dominated, making up *ca.* 75% of cerium ions. Therefore, a post-synthetic modification strategy was developed with the aim of oxidising the composite towards Ce^{4+} using H_2O_2, inducing a chemical change in the process to CeO_2.

Hydrogen peroxide, H_2O_2, is an incredibly powerful oxidising agent capable of oxidising a variety of organic and inorganic materials. Electrochemical studies of CeO_2 have established that within a neutral pH environment and zero applied potential, Ce favours aqueous Ce^{3+} ions, $[Ce(OH_2)_6]^{3+}$, rendering synthesis of Ceria nanoparticles under aqueous conditions difficult. Under the same acidic and electrochemical conditions (*i.e.* applied potential), the presence of highly oxidising H_2O_2 thermodynamically favours Ce forming CeO_2 with the cathodic reaction H_2O_2/H_2O always lying above the possible anodic reactions, $Ce(OH)_3/CeO_2$ and Ce^{3+}/CeO_2.[28] This is summarised in the Pourbaix diagram of cerium below (see Figure 3.10).

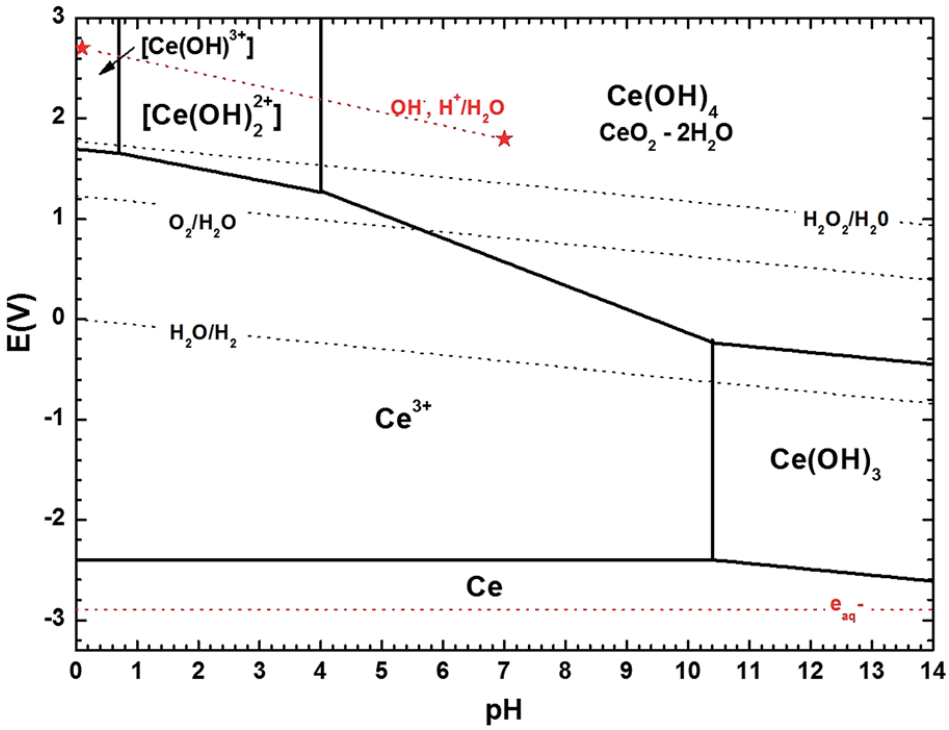

Figure 3.10: Pourbaix digram for cerium as a function of applied potential and pH, taken from RSC Adv., 2017, 7, 3831–3837.[28]

It was therefore postulated that exposure of CeNP@MOF808 to H_2O_2 would result in the formation of CeO_2. This has been shown to occur with $Ce(OH)_3$ nanoparticles encapsulated within liquid crystal matrices.[29] Identification of CeO_2 after treatment of CeNP@MOF808 with H_2O_2 would not only show the success of the post-synthetic oxidation methodology, but also provide further evidence that the initial speciation of the CeNPs in the CeNP@MOF808 composite was a cerium oxy-hydroxide species of the form: $CeO_x(OH)_y$.

In order to investigate the oxidative treatment of CeNP@MOF808, a sample, approximately 400 mg, was measured out in a centrifuge tube and subsequently suspended in 20 mL of 6% H_2O_2 solution. Upon addition of the 6% H_2O_2 solution an immediate colour from off-white to orange was observed, along with vigorous effervescence – both, indicative of a chemical reaction occurring. The effervescence was caused by the production of oxygen gas following the reduction of H_2O_2. The CeNP@MOF808 dispersion was sonicated for 20 minutes to form a fine suspension before stirring over night at room temperature. The CeNP@MOF808 solids were subsequently isolated *via* centrifugation and washed twice more with deionised water. The CeNP@MOF808 solids were dried *in vacuo* at 100 – 120 °C for 24 hours, revealing a dry, feel flowing orange powder, $CeNP^{[oxd]}$@MOF808 (see Scheme 3.1). This process was repeated using a weaker concentration of 0.6% H_2O_2 solution, where effervescence and a colour change from off-white to orange was still observed.

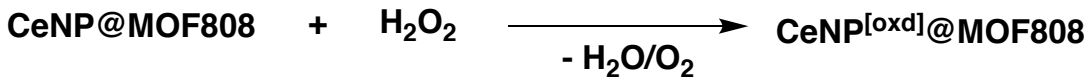

Scheme 3.1: Oxidative post-synthetic modification of CeNP@MOF808 to $CeNP^{[oxd]}$@MOF808.

Following successful synthesis of the $CeNP^{[oxd]}$@MOF808 composite it was studied using PXRD, Raman spectroscopy and EDX spectroscopy to establish what effect the oxidative treatment had on the structure of the composite material.

3.3.1 Powder X-ray Diffraction Studies of Oxidised CeNP@MOF808

The oxidised composite, CeNP[oxd]@MOF808, showed a PXRD diffractogram (see Figure 3.11) that was deficient of peaks that are characteristic of the MOF808, for both 0.6% and 6% H_2O_2 treatments.[30,31]

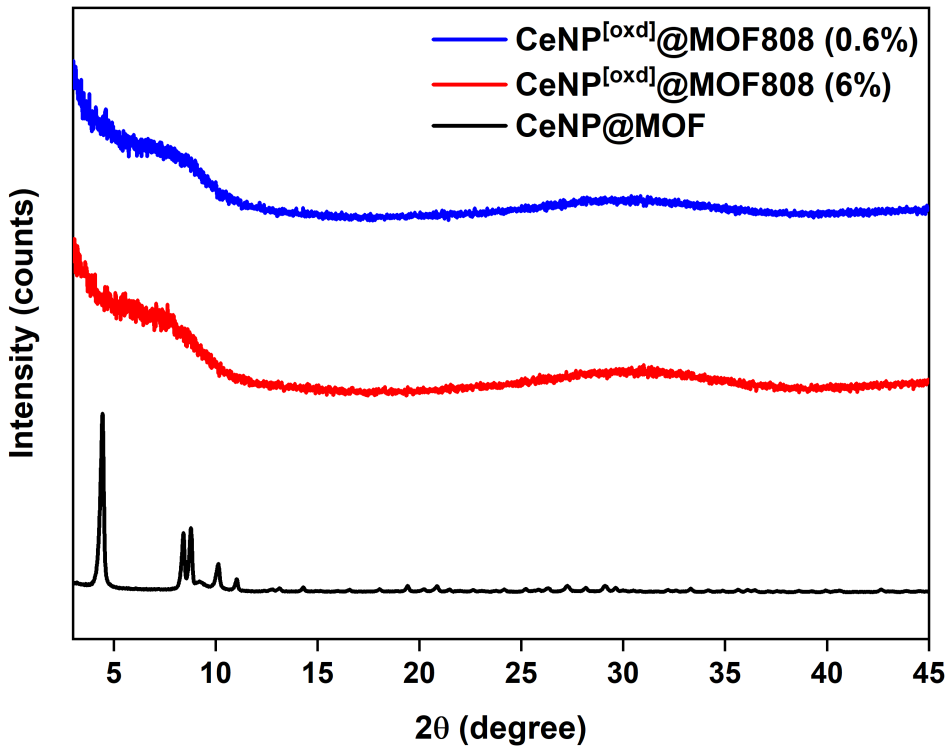

Figure 3.11: PXRD diffractograms of CeNP@MOF808, CeNP[oxd]@MOF808 (6% H_2O_2 treatment) and CeNP[oxd]@MOF808 (0.6% H_2O_2 treatment

These data are consistent with loss of crystallinity, the oxidation reaction had caused the host MOF structure to become amorphous and is not unexpected given the destructive nature of H_2O_2 towards small organic molecules, such as BTC linker which is integral to the structural rigidity of the MOF host. Several examples exists in the literature of MOFs being exposed to H_2O_2 and retaining their crystalline structure. MOF808 was adopted in one study as a catalyst for the oxidative desulfurisation of polycyclic thiophene based molecules, where oxidative was achieved using H_2O_2.[32] In this example, the MOF808 catalyst retained its crystalline

structure, although reflections were broadened, after several catalytic cycles with exposure to H_2O_2. This may be a result of the low H_2O_2 quantities adopted, with only 21 µL used in each catalytic cycle – significantly lower than the 20 mL of 0.6% and 6% H_2O_2 adopted in this study. A second study involved the use of MOF808 as a colorimetric detector for H_2O_2 concentration.[33] The MOF808 structure was exposed to varying concentrations of H_2O_2, from 10 µM to 15 mM, with the MOF808 crystallinity retained after the reaction. In a separate study, functionalised Zr based UiO-66 was adopted as biochemical H_2O_2 sensor. Here again the UiO-66 MOF retains its crystallinity after exposure to H_2O_2, with characteristic reflections visible in the PXRD diffractogram after sensing experiments.[34] This chemical stability when exposed to H_2O_2 most likely once again derives from the low quantities of H_2O_2 adopted in the study – 240 µL. It is possible therefore that exposure of the CeNP@MOF808 composite to lower volumes and concentrations of H_2O_2 could result in the retention of the MOF808 host crystalline structure, however given that the aim was to induce electronic changes in the composite lower quantity H_2O_2 exposures were not investigated.

No reflections were visible that could be associated with crystalline CeO_2, however once again this may be due to the small nature of the particles causing peaks to be sufficiently broadened into the baseline.[21] The presence of a broad baseline increase between 25-35° (see Figure 3.11) could be due to the presence of small CeO_2 nanoparticles, however this could not be independently confirmed through alternative spectroscopies.

3.3.2 Raman Spectroscopy Studies of Oxidised CeNP@MOF808

Raman spectroscopy involves the inelastic scattering of light whereby a source of incident light of a certain frequency is scattered by a material with the outgoing light having a different energy to that which was incident. When a bond is exposed to a beam of photons the electric field of the electromagnetic radiation causes the nuclei and electron clouds associated with that bond to oscillate in opposite directions, relative to one another. This results in the bond contracting and elongating – it vibrates – if this vibration results in the polarizability of the molecule changing then the vibration will be Raman active (*i.e.* it will appear in a Raman spectrum).[35] After a certain period of time the nuclei and electron clouds will return to different vibrational frequency, emitting a photon of light either with more or less energy relative to the incident photon that was absorbed.

The majority of photons are scattered from the material with an energy equal to that of the incident photon (elastic scattering), this is called Rayleigh scattering. Outgoing scattered photons with more energy relative to the incident photon is termed anti-Stokes scattering, while scattered photons with less energy relative to the incident photon is referred to as Stokes scattering. This is summarised schematically in Figure 3.12.

The difference between Raman spectroscopy and IR spectroscopy is that during an IR absorption, the molecule transitions between two real vibrational energy states, while with Raman scattering the molecule is excited to a virtual energy level.[35] This virtual energy level has an energy equal to that of the incident photon beam (EL) and is termed 'virtual' as it is an energy state not usually accessible to the molecules and it is only attained due to the distortion of the molecule during the vibration. The distorted state is short lived, with scattering occurring rapidly.

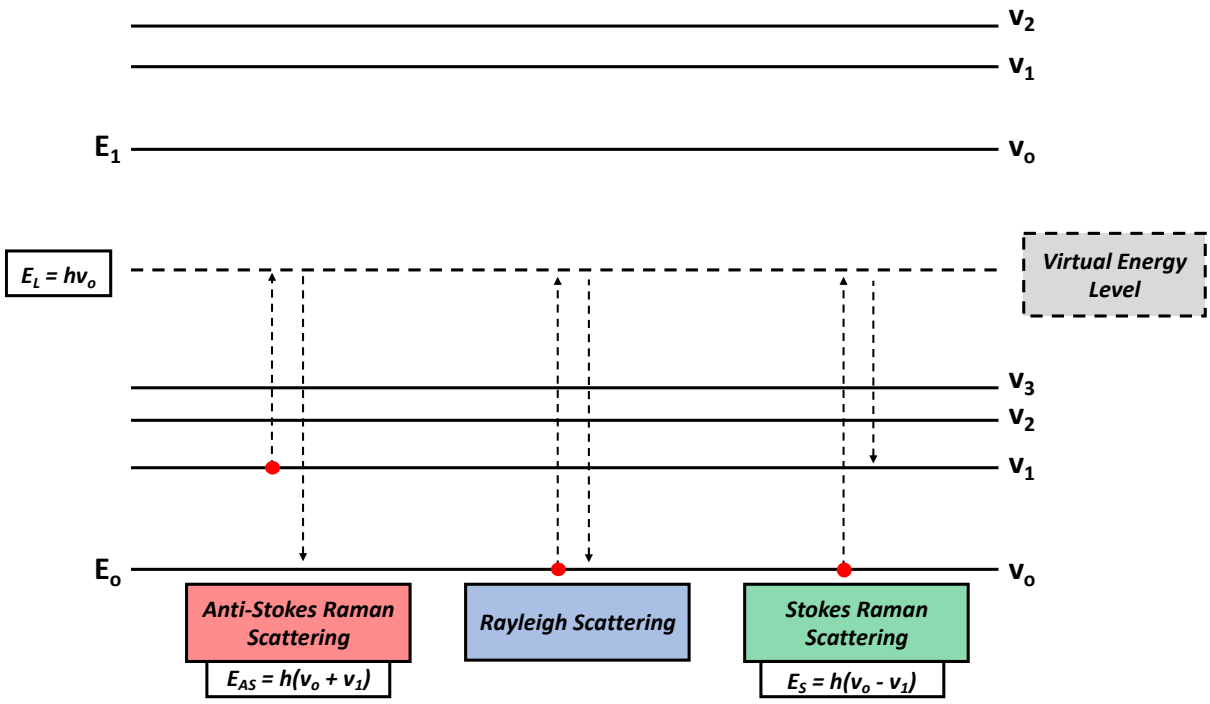

Figure 3.12: Schematic representation of energy level transitions associated with Rayleigh and Raman Scattering.

The Raman spectrum is recorded as the shift in energy relative to the incident photon energy, with Stokes scattered photons occurring at positive values and anti-Stokes scattered photons occurring at negative values. The peaks corresponding to Stokes scattering are often significantly more intense than their anti-Stokes counterparts due to the statistical distribution of energies at room temperature largely favouring the ground vibrational energy state (v_o). It is generally the case that symmetric vibrations yield the largest change in polarizability of the molecule and therefore the strongest Raman scattering. It is also possible to significantly increase the intensity of Raman peaks by applying incident light with an energy close to that of an absorption maxima associated with the compound analyte. This is known as the Resonance Raman effect.

There exists a wide body of data in the literature relating to the Raman scattering behaviour of CeO_2. Most notably, CeO_2 can be easily identified by the existence of a strong Raman peak at around 460 cm^{-1},[36-38] caused by the symmetric F_{2g} vibration of the Ce–O bond within the cubic lattice structure. A study published found that the position of the F_{2g} band is dependent

heavily upon the CeO_2 particle size and composition.[39] Decreasing the size of CeO_2 particles from 150 nm to 4 nm has been shown to result in a red-shift and broadening of the F_{2g} peak,[39] with the red shift arising from the greater lattice strain associated with the smaller particles and the broadening being due to an increased number of defects within the smaller particles. The reduction in CeO_2 particle size also results in the F_{2g} peak losing its Gaussian symmetry. In the same study, a variety of $Ce_{1-x}Zr_xO_2$ mixtures *via* Raman spectroscopy,[39] the F_{2g} peak at 460 cm^{-1} was found to be broadened and blue shifted with increasing Zr content in the solid solution. The $Ce_{1-x}Zr_xO_2$ mixture was initially found to be composed of two separate CeO_2 and ZrO_2 phases as-prepared, however following calcination at 1173 K the two phases merged to form a solid solution.

Raman spectra have been described in the literature for MOF-NP composites, including the CeNP@Ce-BDC composite synthesised by Hassan *et al*,[38] whereby the CeNP exhibit a strong, yet broad, F_{2g} peak at 426 cm^{-1}, significantly red-shifted from that of the CeNPs. This red shift is indicative of lattice expansion and increased strain from the reduction of Ce^{4+} to larger Ce^{3+}. Therefore, the F_{2g} stretch of the Ce–O bond is not only symptomatic of the mere presence of CeO_2, but also of the dominating oxidation state (Ce^{3+} *vs.* Ce^{4+}). A collection of weak and broad peaks are observed at 250, 540, 608 and 1171 cm^{-1} corresponding to lattice oxygen vacancies being present in the CeNP@Ce-MOF composite. These were absent from the CeNP controls.[38]

Figure 3.13 shows the Raman spectra for control MOF808 and CeNP@MOF808 (before oxidative post-synthetic modification) using a visible laser excitation source, λ_{ex} = 532 nm. Vibrations at Raman shifts of 800, 1000 and 1500 cm^{-1} are present in both the Raman spectrum of control MOF808 and the spectrum of CeNP@MOF808. These Raman shifts are characteristic of MOF808.[40] This is consistent with the MOF808 structure remaining intact following the reactive infiltration process. A Raman shift corresponding to the Ce–O F_{2g} stretch of CeO_2, typically found around 460 cm^{-1},[36] was not observed in the spectra of CeNP@MOF808, most probably due to either the small size of the CeNP or low loading weights of cerium. This consistent with the PXRD diffractogram of CeNP@MOF808 which showed a lack of reflections in the region expected for nanoceria.

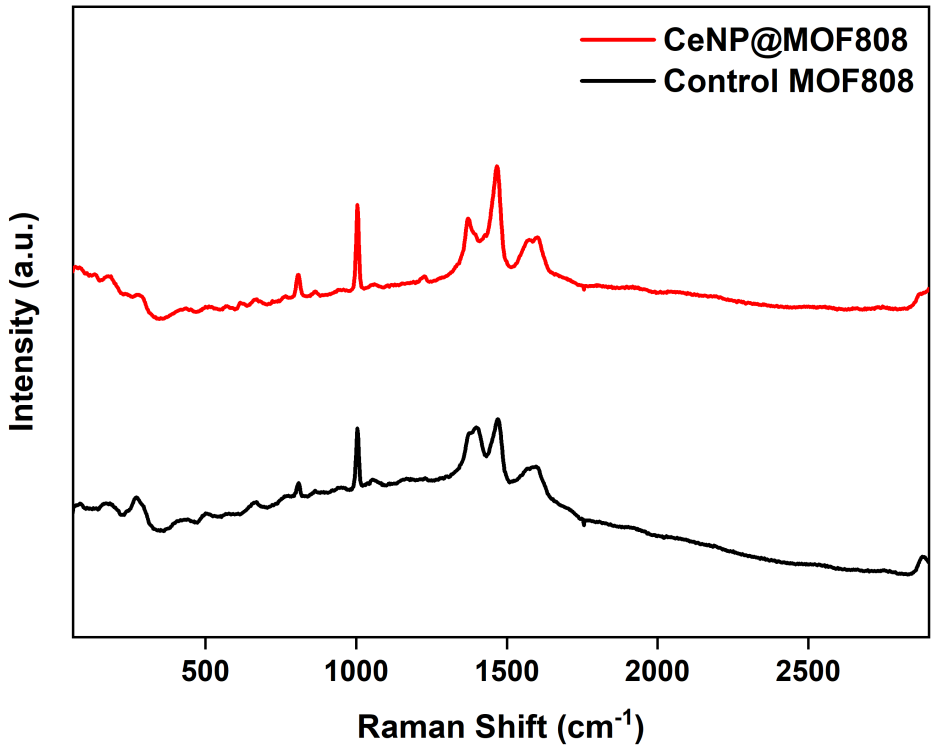

Figure 3.13: Raman Spectra of Control MOF808 and CeNP@MOF808 (λ_{ex} = 532 nm; visible).

The lack of a Raman active vibration at 460 cm^{-1} corresponding to the Ce-O F_{2g} stretch of CeO_2 was initially thought to originate from the low excitation energy associated with , λ_{ex} = 532 nm. Therefore Raman spectra were acquired using a higher energy excitation source, λ_{ex} = 325 nm, closer to the absorption maximum of CeO_2 (λ_{max} = 364 nm).

Using an excitation source closer to the absorption maximum of CeO_2 would enhance vibrational peak intensities through the resonance Raman effect.[41,42] Somewhat surprisingly the use of higher energy excitation actually reduced the signal-noise-ratio, with a linear slopping background, making the spectrum intractable (see Supplementary Figure 3.15).

Figure 3.14 shows the Raman spectra for the oxidised composite, $CeNP^{[oxd]}$@MOF808, for 6% H_2O_2 treatments. Interestingly, the Raman spectra shows, albeit significantly at reduced intensity, vibrations at Raman shifts characteristic of MOF808.[40] Taken together with the loss of crystalline reflections in the PXRD pattern (see Figure 3.11) this suggests that although the

MOF host loses its crystalline structure during the oxidative post-synthetic modification process, the moieties characteristic of MOF808 (*e.g.* organic linker and cluster nodes) remain.

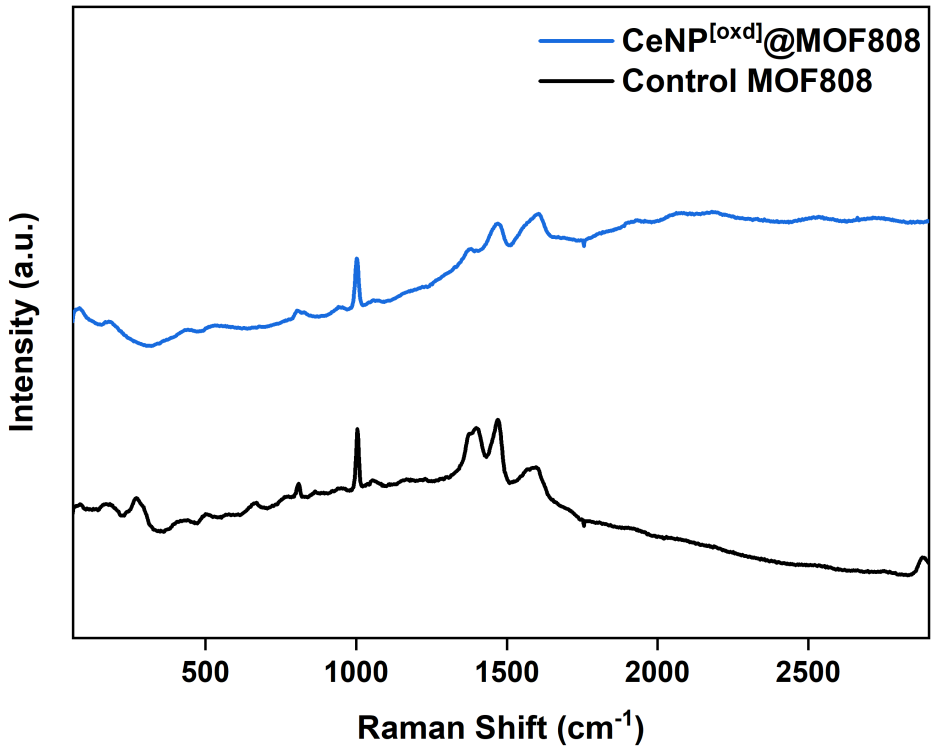

Figure 3.14: Raman Spectra of Control MOF808 and CeNP$^{[oxd]}$@MOF808 (λ_{ex} = 532 nm; visible).

A Raman spectrum of CeNP$^{[oxd]}$@MOF808 was acquired using a higher energy excitation source (λ_{ex} = 325 nm, UV). However, as seen with CeNP@MOF808, the higher energy laser simply causes a reduction in the signal-noise-ratio, with a linear slopping background (see Supplementary Figure 3.15).

3.3.3 Energy Dispersive X-ray Spectroscopy Studies of Oxidised CeNP@MOF808

The EDX spectra taken of the oxidised composite, CeNP$^{[oxd]}$@MOF808, showed a similar Ce loading wt% to that of CeNP@MOF808 (2.78 ± 1.03 wt%) at 3.41 ± 0.90 wt% and 4.06 ± 1.34 wt% for 6% and 0.6% H_2O_2 oxidative treatments, respectively. This suggests that the CeNP

remain bound within the composite and not removed following the oxidative post-synthetic modification.

3.3.4 Post-synthetic Modification of CeNP@MOF808: Oxidative Treatment: Conclusions

In conclusion, oxidative post-synthetic modification of the CeNP@MOF808 composite was investigated. X-ray powder diffractograms CeNP$^{[oxd]}$@MOF808 showed the loss of the MOF808 host crystallinity, with both low (0.6%) and high (6%) H_2O_2 concentration oxidative treatments. There was no observable reflections corresponding to nanoceria in the diffractograms of CeNP$^{[oxd]}$@MOF808. Lower energy (visible excitation, λ_{ex} = 532 nm) Raman spectra of CeNP@MOF808 showed peaks characteristic of MOF808, in agreement with previous PXRD and FT-IR analyses of CeNP@MOF808 in Chapter 2 showing the MOF808 host retains its structure following reactive infiltration. Lower energy Raman spectra (visible excitation, λ_{ex} = 532 nm) of CeNP$^{[oxd]}$@MOF808 showed peaks again characteristic of MOF808, although at reduced intensities, indicating that the oxidative post-synthetic treatment of CeNP@MOF808 may remove the crystallinity of the host, as indicated by powder X-ray diffractograms, but it does not degrade the structure (i.e. destruction of the organic linker and metal cluster nodes).Ce wt% determined by energy dispersive X-ray spectroscopy of CeNP$^{[oxd]}$@MOF808 showed that Ce loading wt% remain unchanged from CeNP@MOF808 following the oxidative post-synthetic treatment.

3.4 Cerium Oxidation State Determination

Through studies detailed in Sections 3.2 and 3.3 it was shown that both thermal and oxidative post-synthetic treatments of the composite CeNP@MOF808 resulted in structural changes, relative to the MOF808 host structure. The question then arose as to what effect the thermal and oxidative treatments had on the electronic structure of CeNP@MOF808 (*i.e.* what Ce oxidation states are present and what are their relative proportions). In order to answer this question it was first required that the electronic structure of CeNP@MOF808 be determined as a reference. In determining the metal oxidation states in a solid state composite multiple spectroscopic techniques are available, however each technique often has biases that derive from the experimental set up (*e.g.* high energy excitation source, vacuums, surface sensitivity, limited sensitivity). In order to account for these internal biases or errors, it is good scientific practice to characterise the electronic structure using independent spectroscopic techniques. This process is known as 'orthogonal analysis' and improves the reliability of the electronic characterisation.[43-45]

The ability to reliably quantify Ce oxidation is useful in many areas of material design, particularly catalysis. Multiple studies have shown that the catalytic activity of Ce based catalysts is primarily a function of the Ce^{3+} proportion. For example, in the catalysis of methane combustion, CeO_2 catalysts of two different morphologies, layered and 'sheaf-like', were characterised *via* XPS as having Ce^{3+} proportions of 14% and 16%, respectively. In turn, the sheaf-like structured CeO_2 demonstrated higher catalysis rates of methane combustion compared to the layered CeO_2, with conversions of 17.13×10 mol m^{-2} s^{-1} and 11.69×10 mol m^{-2} s^{-1}.[46] In a separate study a series of $CoAlO_x/CeO_2$ composites were synthesised through various techniques, including impregnation (-IWI) and plasma treatment (-P). The two composites were characterised using XPS and revealed Ce^{3+} proportions of 24% and 26%, for $CoAlO_x/CeO_2$–IWI and $CoAlO_x/CeO_2$–P, respectively. The $CoAlO_x/CeO_2$–P composite in turn exhibited a greater catalytic activity compared to $CoAlO_x/CeO_2$–IWI in the combustion of methane, with T_{50} (temperature at 50% conversion of methane) temperatures of 415 °C and 511 °C, respectively.[47] Though these are only two examples

taken from the literature, it is clear that the performance of CeO_2 based catalysts is highly dependent upon the Ce^{3+} proportions, and therefore it is essential that reliable methodologies exist to determine correctly Ce oxidation sates. Here we look to expand the traditional methodology of cerium oxidation characterisation in a through a combined analysis of three separate techniques: X-ray Photoelectron Spectroscopy (XPS), X-ray Absorption Spectroscopy (XAS) and Electron Energy Loss Spectroscopy (EELS), in order to identify, quantify and locate different cerium oxidation states.

3.4.1 X-ray Absorption Spectroscopy (XAS)

X-ray Absorption Spectroscopy (XAS) is a collective term for a number of spectroscopic techniques that involve the interaction of condensed matter with X-rays. When exposed to high energy X-rays, core electrons within atoms of the sample absorb the photons of radiation and move to higher energy levels (see Figure 3.15). This is subsequently recorded by a detector as an 'edge jump'. Edge jumps are specific to the elemental identity of an atom as energy levels are quantised and specific to a particular element, *e.g.* the K edge is at 22.1 keV for ruthenium and 40.4 keV for cerium.[48,49]

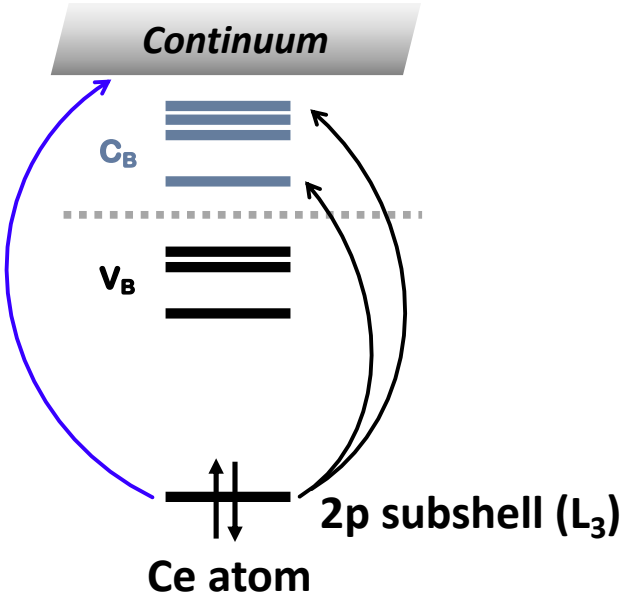

Figure 3.15: Schematic representation of core electron transitions during X-ray Absorption Spectroscopy.

An XAS spectrum results from the measurement of absorption coefficient (μ) as a function of the incident X-ray energy.[50] This is achieved directly in transmission mode, where the number of X-ray photons transmitted (I_T) through the sample is measured relative to the incident beam. Alternatively, the spectrum can be recorded indirectly, in fluorescence mode, where the number of fluorescent X-ray photons emitted (I_F) from the sample is measured relative to the incident beam. Photons are typically counted using ionisation chambers, see Figure 3.16 below.

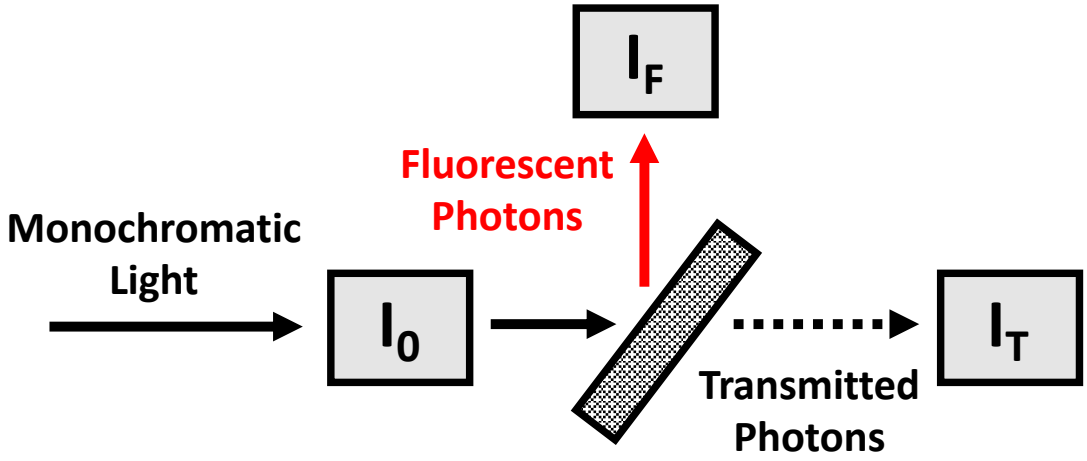

Figure 3.16: Schematic representation of the experimental set-ups used to record X-ray absorption spectra in transmission and fluorescence mode.

Either experimental set up yields a typical X-ray absorption spectrum with a classic step feature representing the edge jump and a continued absorption plateau. Further away from the edge, at higher X-ray energies, the core electrons absorb photons with such significant quantities of energy that they are expelled from the atom entirely, into the continuum. This gives two distinct areas within the X-ray absorption spectrum; the region close to the edge jump, so called 'near edge structure' and the region far extended from the edge jump, referred to as 'extended fine structure'. These two different regions of the spectrum correspond to distinctly different atomic transitions and as such are treated as separate, yet related, spectroscopic techniques. The latter is referred to as 'extended X-ray absorption fine structure' (EXAFS), while the former is termed 'X-ray absorption near edge structure' (XANES). Both techniques were

employed when studying the CeNP@MOF808 composite, however our initial attention focused on XANES, as it allows for characterisation of Ce^{3+} and Ce^{4+} oxidation state proportions.

XANES spectroscopy is a useful technique in identifying particular oxidation states of elements in a sample, and quantifying their relative proportions. The edge jump position is both a function of the atomic number (*i.e.* the chemical element: Ce), but also the atomic oxidation state (*i.e.* the charge: Ce^{3+} and Ce^{4+}). Higher oxidation states, tend to show higher energy edge jumps.[51] This is a result of the core electrons acquiring higher binding energies as a result of successive formal oxidations, yielding metal ions of increasingly positive charge. Edge structures are denoted based on the electron shell the core electron originates from, in Figure 3.15 the edge is referred to as an L_{III} edge as the excited core electron comes from the L (n = 2) electron shell. As well as identifying specific oxidation states present, XANES can also be used to determine relative proportions of different oxidation states present through variable methodologies (*e.g.* linear regression, empirical fitting, *etc.*). In the particular case of cerium this is made simple by the fact that cerium has two common oxidation states accessible to it: Ce^{3+} and Ce^{4+}. The next section of the thesis will look at the XANES spectra acquired for the CeNP@MOF808 composite and various methods of processing the data, identifying Ce^{3+} and Ce^{4+} oxidation states and determining their relative proportions.

3.4.2 XANES Studies of CeNP@MOF808

The Ce L_{III} – XANES spectrum of CeNP@MOF808 was measured and shown below in Figure 3.17, with commercial CeO_2 and $Ce(NO_3)_3$ as references in order to distinguish between Ce^{3+} and Ce^{4+} oxidation states in the composite samples. All spectra were calibrated relative to Cr foil edge at 5989 eV, see Supplementary Figure 3.16. Ce L_{III} – XANES allows for the distinction of separate oxidation states due to the shapes, sizes and positions of absorption peaks. The Ce^{3+} valence state alone is distinctive in that it appears as a single absorption peak at 5726 eV associated with the $2p^5 4f^1 5d^1$ excited state.[52] The Ce^{4+} valence state manifests itself as two crystal field split absorption peaks, at 5730 eV and 5737 eV associated with the $2p^5 4f^0 5d^1$

excited state.[52] Crystal field splitting is facilitated by the fluorite structure of Ce^{4+} in CeO_2.[53,54] As evident from Figure 3.17, the CeNP@MOF808 composite displays spectroscopic signatures that would be indicative of both Ce^{3+} and Ce^{4+} oxidation states being present, with absorption peaks at 5727 eV and 5737 eV.

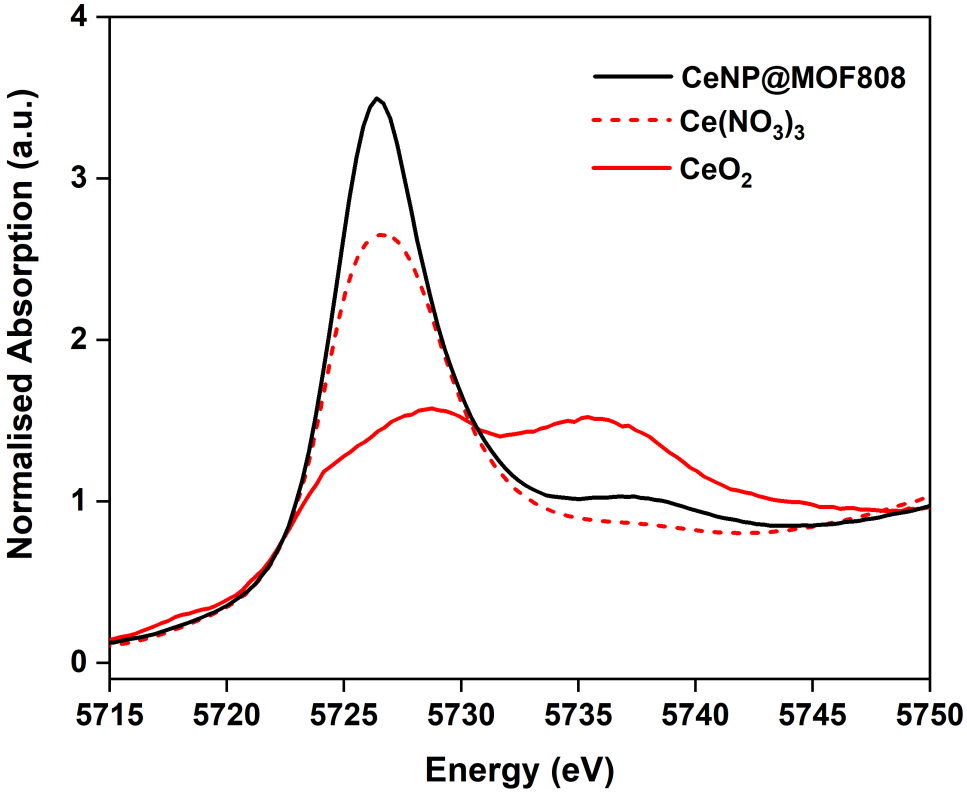

Figure 3.17 Ce L_{III} – XANES Spectrum of CeNP@MOF808.

Using the empirical based methods established in literature it was possible to deconvolute the XANES spectra and fit the constituent peaks, associated with the Ce^{3+} and Ce^{4+} oxidation states, with model Gaussian functions, this is shown below in Figure 3.18.[53-55] The step-like structure of the absorption edge occurs due to transitions to continuum states and eventual expulsion of a photoelectron, this is accounted for using an arctangent function in the deconvolution of the XANES spectra. Other functions have been used in the literature to fit Ce oxidation states in XANES spectra, such as Lorentzian functions which are, like Gaussian functions, symmetrical about their centre points. It is however the case the function of best fit is dependent on the sample and spectrometer used, that is there is no one size fits all

approach.[29,56] Our data were modelled with both Gaussian and Lorentzian functions and found that the Gaussian functions gave a significantly better fit.

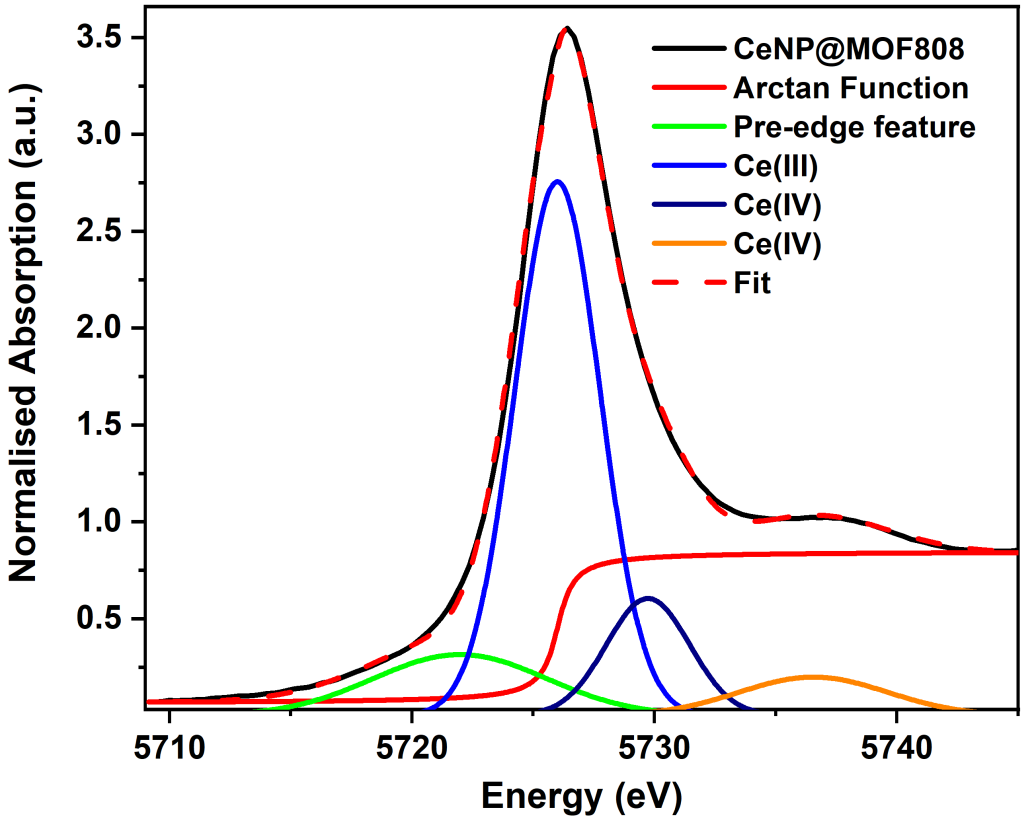

Figure 3.18 Ce L_{III} – XANES Spectrum of CeNP@MOF808, with deconvoluted Gaussian peaks and sum fitted function (dashed trace) shown. Note that the 'pre-edge' feature seen in figure is associated with the partially occupied f-electron of the ceria fluorite structure.

By integrating the area under each Gaussian fitted peak, then subsequently taking the ratio of the area of the Ce^{3+} fitted peak to the total area of all the fitted peaks it was possible to approximate the percentage of Ce^{3+} present in the CeNP@MOF808 samples using eqn. 2:

$$Ce^{3+}\% = \frac{A_{Ce^{3+}}}{\sum(A_{Ce^{3+}} + A_{Ce^{4+}})} \qquad (eqn. 2)$$

It was calculated, in duplicate repeated measurements, that the Ce^{3+} proportions in the CeNP@MOF808 samples were 75%. Typical error values quoted in literature for Ce oxidation state proportions determined *via* XANES are ± 10%.[43,57] This is interesting in that the initial

precursor that undergoes reactive infiltration, CeN''_3, is composed completely of Ce^{3+} and therefore at some point during the reactive infiltration process a small portion of the Ce^{3+} was oxidised to Ce^{4+}. Multiple sources of oxidation are hypothesised, including the reaction with oxygen species that make up the MOF808 structure, such as the formate modulator of the cluster nodes: $Zr_6O_4(OH)_4(\mathbf{OOCH})_6$. However, the formate:BTC ratios, presented in Chapter 2, are essentially unchanged between control MOF808, 1.17 ± 0.03, and CeNP@MOF808, 1.01 ± 0.30. Therefore, formate is unlikely to be a source of oxidation in the reactive infiltration process. An alternative sources of oxidation of CeN''_3 includes the reaction of the precursor with residual DMF within the MOF808 pores, however DMF remains present in the digested NMR samples of CeNP@MOF808 (δ_{DMF} = 7.8 ppm) – although the exact amount present is unknown (*i.e.* some DMF could be consumed during the reactive infiltration process). Oxidation of the CeN''_3 may occur through the reaction with atmospheric oxygen/moisture once immediately removed from the anaerobic nitrogen atmosphere. It appeared unlikely that the oxidation of CeN''_3 originated from the reaction with cluster oxide and hydroxide species, $Zr_6\mathbf{O}_4(\mathbf{OH})_4(HCOO)_6$, in that pK_a values measured by potentiometric titration in Chapter 2 remain unchanged following reactive infiltration, suggesting these protic sites were not involved in the oxidation reaction.

The CeNP@MOF808 stands out as a rare example of a material with a significantly high proportion of Ce^{3+} which results from the 'gentle' and low energy nature of the reactive infiltration process, in stark comparison to literature precedent where energy intensive techniques yield materials with mostly Ce^{4+} – regardless of the oxidation of the starting precursor. Previous attempts by J. T. Hupp *et al* to synthesise ceria type clusters within Zr based MOF NU-1000 using Ce based complexes $Ce(Cp^{iPr})_3$ and $Ce[OC(^tBu)CHC(^tBu)O]_4$ resulted in the formation of composites with Ce^{3+} proportions (determined *via* XPS) of 15% and 0%, respectively.[58] There are, however, examples further afield where $Ce(OH)_3$ NPs have been incorporated into liquid crystal matrices, *via* the alkaline hydrolysis of $Ce(NO_3)_3$ at 70 °C, to form composites where the Ce ions are largely in the Ce^{3+} oxidation state, 78 – 93% (percentages vary depending upon the initial amount of $Ce(NO_3)_3$ starting material used).[29] Comparison of Ce^{3+} in CeNP@MOF808 with literature examples are shown below in Table 3.7.

Table 3.7: Comparison of Ce^{3+} proportions of CeNP@MOF808 with literature examples.

Composite Sample	Ce^{3+} %	Methodology	Ref.
$CeO_x(OH)_y$@NU-1000	0 – 15[a]	XPS	58
$Ce(OH)_3$@LC	78 – 93[b]	XAS	29
CeNP@MOF808	75	XAS	This Work.
[b] 0% for $Ce[OC(^tBu)CHC(^tBu)O]_4$ and 15% for $Ce(Cp^{iPr})_3$.			
[b] percentage varies based on the initial amount of $Ce(NO_3)_3$ precursor used.			

Alternative methods were investigated for quantifying Ce^{3+} proportions from the XANES spectra – including linear combination analysis,[59] however these failed to yield coherent results. The failure of linear regression methods is postulated to arise from the significant differences in local atomic environments of the Ce in the CeNP@MOF808 samples in comparison to the reference materials (CeO_2 and $Ce(NO_3)_3$). Empirical fitting neglects the possible dependence of the position of the spectral features on the fine details of the local atomic environment of the Ce.[53] Neglecting the influence of such small structural changes on the energy of the spectral features may be a good approximation since the aim is to determine the fraction of Ce^{3+} and Ce^{4+}. It should be noted that previous comparisons of Ce^{3+} proportions in materials by XANES using both linear combination analysis and empirical methods have shown good agreement, although the good agreement may be a reflection of the references (micron-sized CeO_2 and Ce_2S_3) being similar chemically to the sample material (nanoceria).[45]

The stability of the Ce^{3+} proportion was investigated *via* Ce L_{III} – XANES (see Figure 3.19), where stability in this context refers to the ability of the Ce^{3+} ions to resist oxidation to Ce^{4+} with prolonged exposure to atmospheric oxygen. CeNP@MOF808 showed good stability towards long-term exposure to atmospheric oxygen, with Ce^{3+} remaining essentially unchanged after several months of exposure, this is evident by the presence of absorption peaks, with unchanged absorption intensities, at 5727 eV and 5737 eV. Thus, it was concluded that the Ce^{3+} ions in CeNP@MOF808 are relatively resistant to oxidation with prolonged exposures to oxygen. This contrasts with free CeNPs which have shown a tendency to shift Ce^{3+} proportions when aged in different media.[60,61]

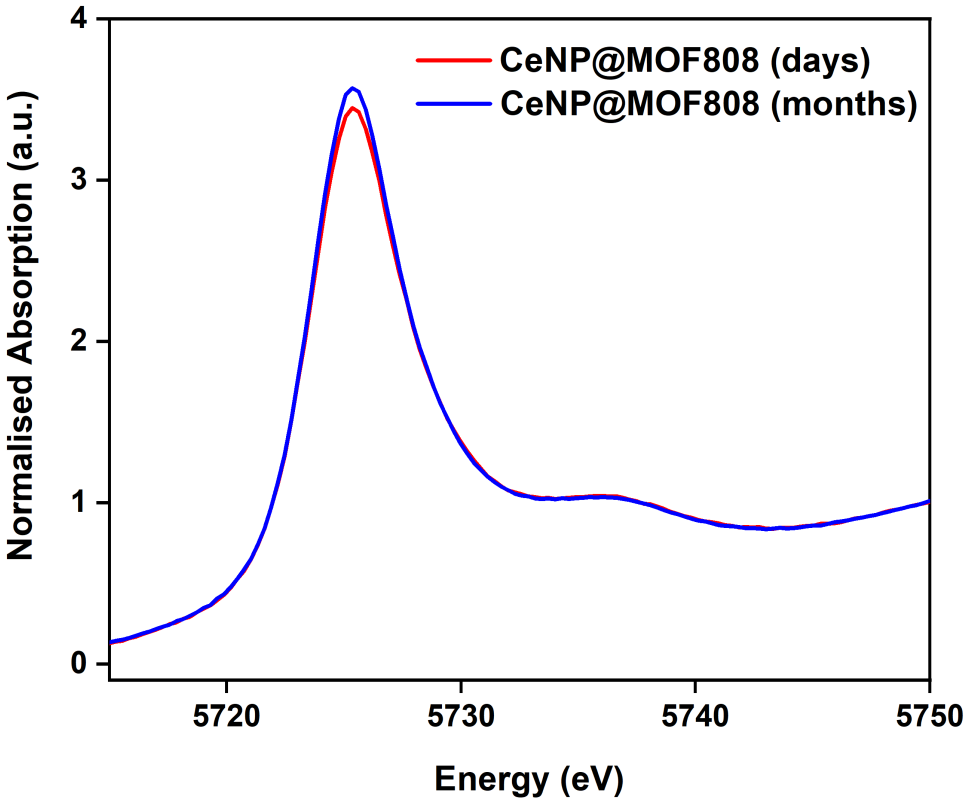

Figure 3.19: Ce L_{III} – XANES Spectrum of CeNP@MOF808 aged in atmospheric oxygen for several days vs. several months.

3.4.3 XANES Studies of Thermal Treatment of CeNP@MOF808

As noted previously in Section 3.2.2, the thermal decomposition of CeNP@MOF808 yields several decomposition events which correspond to particular structural changes within the MOF808 matrix. In order to ascertain what effect, if any, such thermal treatments had on the stability of the dominant Ce^{3+} proportions, samples of CeNP@MOF808 were thermally treated for 1 hour, in air, at 180, 230, 320, 550 and 650 °C. Subsequent XANES profiles were recorded and showed that Ce^{3+} proportions were dependent upon the crystallinity of MOF808 in the composite. As seen in Figure 3.20, thermal treatments up to 230 °C showed no significant change in Ce^{3+} proportions, at 82% (*c.f.* 75% Ce^{3+} for untreated CeNP@MOF808 samples). However, following thermal treatment at 320 °C, where the crystallinity of MOF808 is lost (see Figure 3.5), the Ce^{3+} proportions are significantly reduced to 40%. Further thermal

treatments at 550 °C and 650 °C showed a continued decreases in Ce^{3+} proportions towards 16%. A plausible explanation could be that significant stability is offered to the CeNPs by the MOF808 framework and heating beyond 230 °C results in the loss of crystallinity and in turn removes the stabilising effect of the MOF structure, allowing significant swings in the Ce^{3+} proportions to occur.[62,63] This reduction in Ce^{3+} oxidation states, particularly at 550 °C and 650 °C, coincides with a significant increase in the variation of Ce wt% measured *via* EDX spectroscopy (see Table 3.3), indicative of CeNP aggregation.

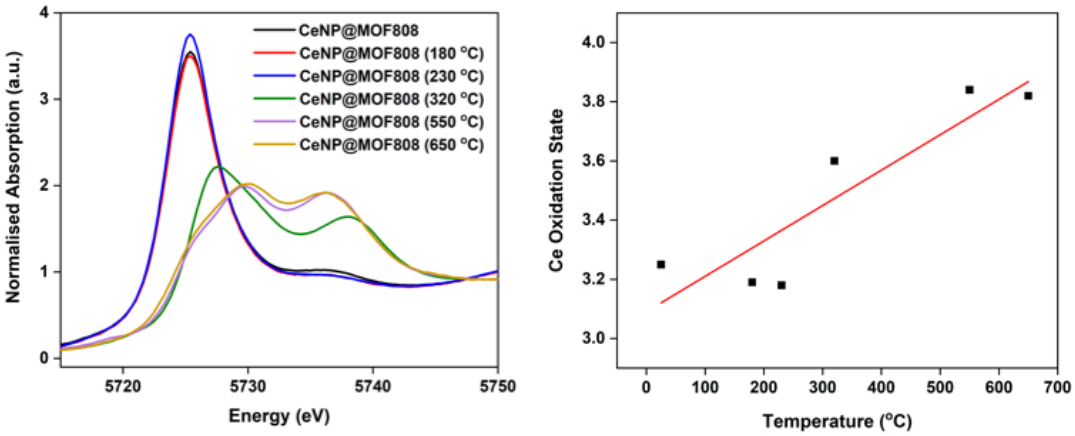

Figure 3.20: Ce L_{III} – XANES Spectrum of CeNP@MOF808 thermally treated at 180, 230, 320, 550 and 650 °C, with a linear correlation of 0.9.

The general trend of shifting towards higher Ce^{4+} proportions when ceria is calcined at higher temperatures in air is consistent with multiple examples reported in the literature (summarised in Table 3.8). M. Stastny *et al* reported a *ca.* 15% increase in Ce^{4+} content, relative to Ce^{3+}, when calcination temperatures increase from 200 °C to 500 °C.[64] It is however worth noting that the calcination was performed on bulk ceria and not nanoparticle species, that calcination was during synthesis and not post-synthesis and that the Ce oxidation states were determined using XPS, which is biased towards surface oxidation state changes. D. K. Shuh *et al* reported qualitatively *via* XANES analysis, that when cerium based sol-gel glasses (initially the Ce^{3+} prevails) are calcined in air at 110 °C there is partial oxidation of the Ce^{3+} state to Ce^{4+}, above 400 °C there is complete oxidation to the Ce^{4+} state.[65] This trend was observed in sol-gel glasses synthesised using both $Ce(NO_3)_3$ and $CeCl_3$. R. I. Walton *et al*

established a similar trend where XANES studies of nanocrystalline cerium titanate pyrochlores calcined to 150 °C showed complete oxidation to the Ce^{4+} state.[66] These literature examples set a clear trend that cerium based materials when calcined in air tend towards the Ce^{4+} state, with the temperature range over which 100% conversion is achieved dependent upon the exact speciation of the Ce environment.

Table 3.8: Comparison of Ce^{3+} proportions and temperature of CeNP@MOF808 with literature examples.

Samples	Initial Temperature (°C)	Initial Ce^{3+} (%)	Final Temperature (°C)	Final Ce^{3+} (%)	Method
CeO_2[64]	200	25	600	15	XPS
Ce sol-gel glass[65]	25	90	400	0	XAS
$(Na_{0.33}Ce_{0.66})_2Ti_2O_7$[66]	50	0	150	0	XAS
CeNP@MOF808[a]	25	75	650	18	XAS
[a] This work					

3.4.4 XANES Studies of Oxidative Treatment of CeNP@MOF808

Oxidative treatment of the CeNP@MOF808 composite with H_2O_2 showed a significant decrease in the Ce^{3+} proportions, with the XANES spectra of the oxidised samples showing the characteristic fingerprint of the Ce^{4+} oxidation state, see Figure 3.21. Interestingly, treatment with 6% and 0.6% H_2O_2 solutions yielded similar final Ce^{3+} proportions in $CeNP^{[oxd]}$@MOF808 at 9% and 12%, respectively, despite the order of magnitude difference in concentration. The significant shift in Ce^{3+} proportions, from 75% in CeNP@MOF808 to *ca.* 10% in $CeNP^{[oxd]}$@MOF808 coincides with the loss of the MOF808 crystalline structure following oxidative treatment (see Figure 3.11). This significant decrease in Ce^{3+} proportions with loss of the MOF808 host crystallinity was similar to the decrease in Ce^{3+} proportions observed when thermal treatments above 320 °C caused MOF808 to lose its crystallinity (see Figure 3.20). Therefore, there is a growing body of evidence that the disproportionate quantity of Ce^{3+} states found in CeNP@MOF808 is accommodated/stabilised by the MOF808

hosts ordered, crystalline arrangement, offering stability to the CeNP. This can be termed 'nanoconfinement' where the small dimensions of the material yield properties that are distinct from that of the bulk material, in this case the favouring of the Ce^{3+} states.

The degree of oxidation was similar to that seen with the $Ce(OH)_3$@LC composite which showed a reduction of Ce^{3+} proportions from *ca.* 85% to *ca.* 10%, with variation based on the initial amount of precursor used, following oxidation with H_2O_2.[29]

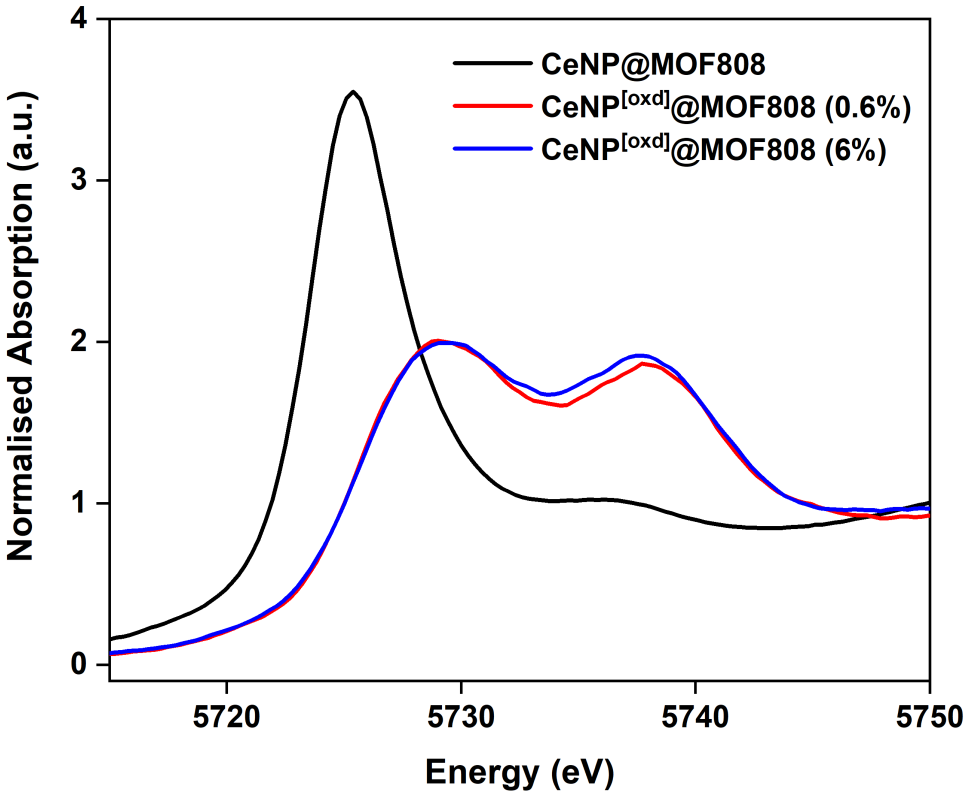

Figure 3.21: Ce L_{III} – XANES Spectrum of CeNP@MOF808 and $CeNP^{[oxd]}$@MOF808 using 0.6 and 6% H_2O_2.

We have designed a material, CeNP@MOF808, that possesses both Ce^{3+} and Ce^{4+} valence states, with the Ce^{3+} state being the dominant state at 75% proportions. Further, the Ce^{3+} ions present in CeNP@MOF808 are resistant to oxidation upon calcination to moderately high temperatures and prolonged exposure to atmospheric oxygen. This places CeNP@MOF808

well as a potential catalyst in industrial processes with retained crystallinity and Ce^{3+} proportions up to 230 °C and a long shelf life.

3.4.5 XANES Studies: Conclusions

In conclusion, XANES studies of CeNP@MOF808 were successfully achieved, showing a 3:1 mixture of Ce^{3+}:Ce^{4+} oxidation states in the composite. Thermal treatments of CeNP@MOF808 up to 230 °C showed no statistically significant changes in the Ce^{3+} proportions. However, thermal post-synthetic modification treatments at 320 °C, and above, showed a significant reductions in the Ce^{3+} proportions. This coincides with the point at which the composite loses crystallinity. Oxidative post-synthetic modification treatments of CeNP@MOF808 with H_2O_2, yielding $CeNP^{[oxd]}$@MOF808, showed a stark reductions in Ce^{3+} proportions, again coinciding with a loss of crystallinity.

3.4.6 Extended X-ray Absorption Fine Structure (EXAFS) Studies of CeNP@MOF808

In contrast to the XANES region of the XAS spectrum, the EXAFS region corresponds to core electron transitions where the electron is ejected from the atom entirely into the continuum.[50] This results in the ionisation of the metal atom and formation of an outgoing photo-electron wave. In a condensed matter environment, such as solid state CeNP@MOF808, the propagating photo-electron wave interacts with atoms in close proximity to the absorbing atom (local structure), scattering back towards the absorbing atom a second photo-electron wave. Photo-electron scattering can take place through multiple mechanisms (see Figure 3.22), however, the most dominant is single scattering where the photo-electron wave is scattered by one single scattering atom, before the scattered photo-electron wave returns to the absorbing atom. The absorbing and scattering photo-electron waves interact with another (constructively and destructively) to yield the maxima and minima of the EXAFS region.

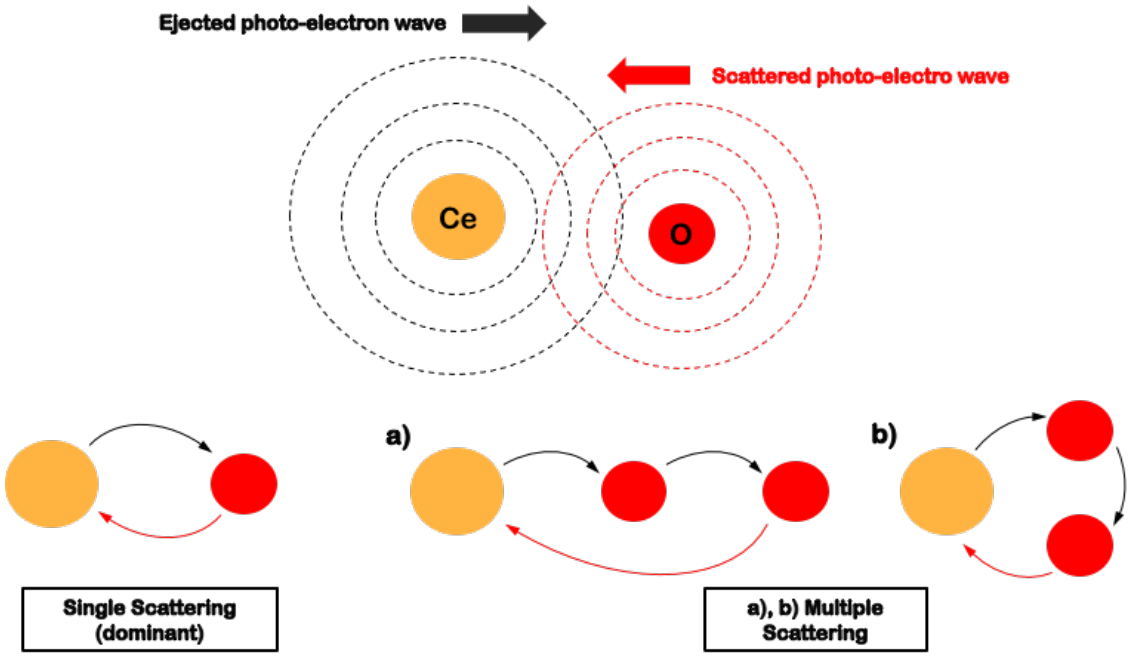

Figure 3.22: Schematic representation of the possible photo-electron scattering mechanisms.[67]

The EXAFS region of the XAS spectrum can be modelled using eqn. 3 shown below:

$$\chi(k) = \sum \frac{Nf(k)e^{-2k^2\sigma^2}}{kR^2} sin[2kR + \delta(k)]{S_o}^2 \ (eqn.3)$$

Where N, R and $\boldsymbol{\sigma}^2$ are the number of scattering atoms, distance from the absorber to the scatterer and the mean-square disorder of neighbour distance respectively. The $\boldsymbol{\sigma}^2$ is related to the disorder of the structural and thermal disorder. F(k), $\boldsymbol{\delta}$(k) and S_o^2 are the scattering amplitude, scattering phase shift and the Amplitude reduction term, respectively. F(k) and $\boldsymbol{\delta}$(k) are dependent upon the atomic number of the scatterer helping define the species of the scatterer, while S_o^2 is an empirical based factor, related to the relaxation of the other electrons in the absorbing atom.[68] By using atomic coordinates obtained from X-ray diffraction data,[21,69,70] theoretical scattering paths can be computed for known absorber and scatter atoms (*e.g.* Ce and O). In this process the amplitude and phase associated with the scattering atom is fixed, then N, R and $\boldsymbol{\sigma}^2$ are varied iteratively until the theoretical fit converges with the experimental scatter paths in the XAS spectrum. Based on the chemistry of MOF808, CeN''_3 and NMR experiments (where HN'' was observed to form) it was

postulated that possible speciations of the Ce in CeNP@MOF808 included CeO_2, Ce_2O_3 and $Ce(OH)_3$. Shown below in Figure 3.23, Figure 3.24 and Figure 3.25 are the imaginary and corresponding Fourier Transform EXAFS spectra of CeNP@MOF808 and model spectra based on scatter pathways of the previously hypothesised possible speciations. Note that the first shell (Ce – O) crystal structures are included as inserts for reference.

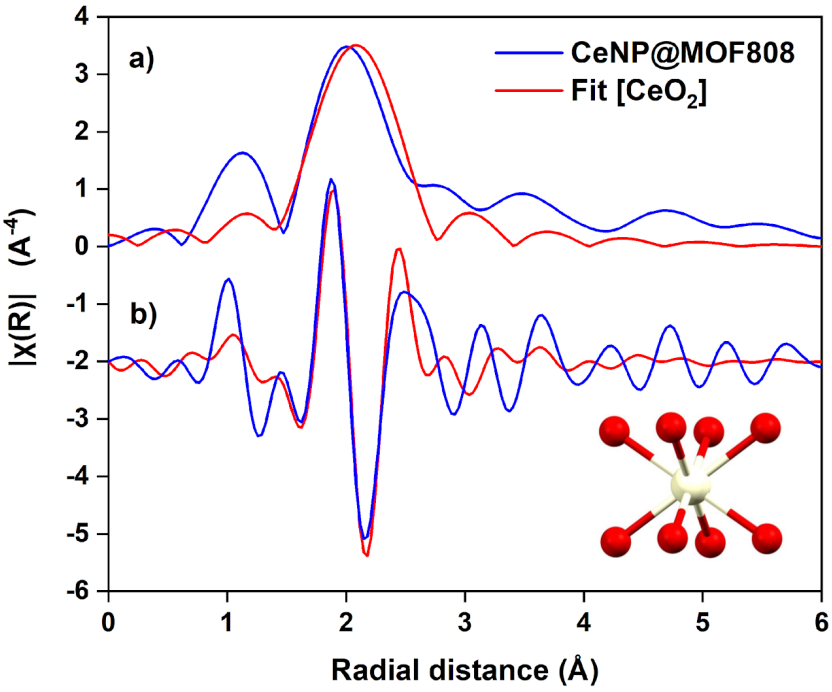

Figure 3.23: First shell fit k^2 weighted $\chi(k)$ EXAFS spectra and corresponding Fourier transform EXAFS spectra (CeO_2 scattering pathway).

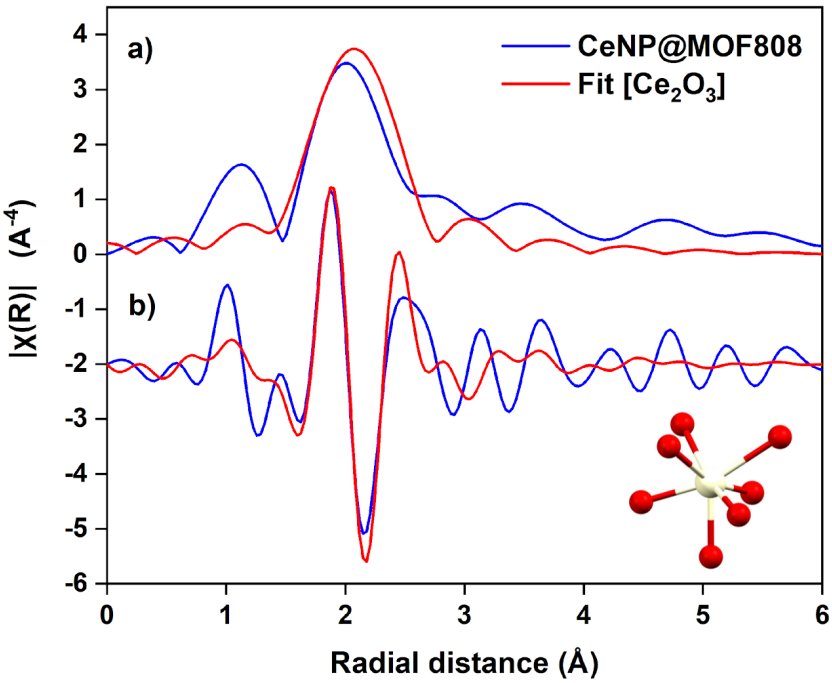

Figure 3.24: First shell fit k^2 weighted χ(k) EXAFS spectra and corresponding Fourier transform EXAFS spectra (Ce_2O_3 scattering pathway).

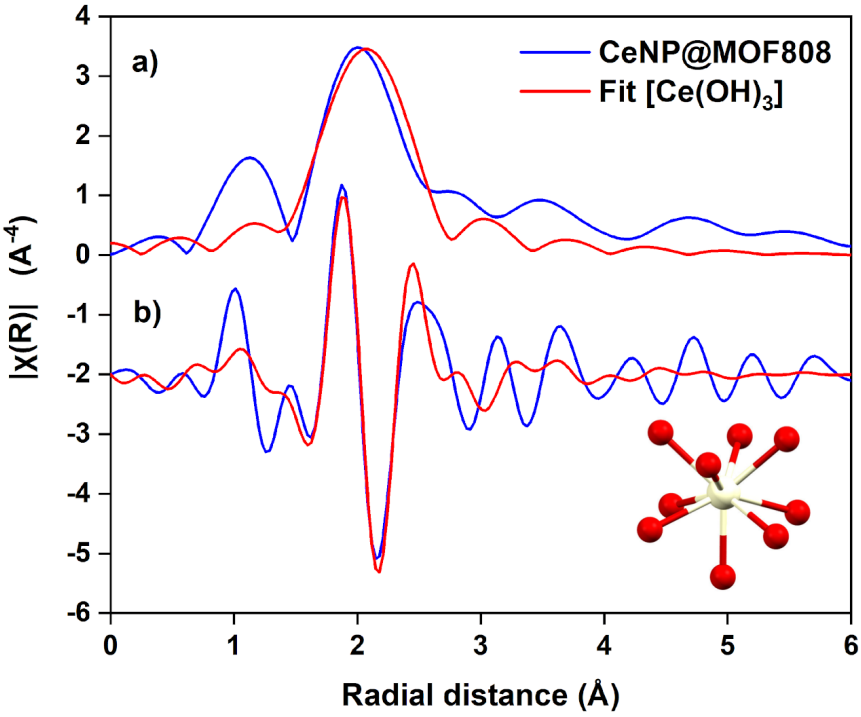

Figure 3.25: First shell fit k^2 weighted χ(k) EXAFS spectra and corresponding Fourier transform EXAFS spectra ($Ce(OH)_3$ scattering pathway).

These EXAFS spectra correspond to first shell fits, therefore only scattering atoms in the first shell vicinity of the absorbing Ce atom (*i.e*., 1 Å < R < 3 Å) are accounted for. As a result of the limited shell fitting, the fitted spectra poorly merge with the raw composite spectra. Summarised below in Table 3.9 are the EXAFS equation variables which reflects the 'goodness of fit' of the fitted spectra with the raw EXAFS spectra of CeNP@MOF8008.

Table 3.9: Summarised EXAFS equation variables based on pre-assumed structures $Ce(OH)_3$, CeO_2 and Ce_2O_3.

Structure	**Scatter Path**	**N**	**R (Å)**	**delR**	**σ^2 (Å^2)**	**E_0 (eV)**	**R_{fac}**
$Ce(OH)_3$	Ce-O	5.5	2.54	0.01	0.00838	5.35 ± 3.52	0.070
CeO_2	Ce-O	5.4	2.55	0.21	0.00685	7.701 ± 4.1	0.088
Ce_2O_3	Ce-O	5.3	2.54	0.23	0.00696	7.325 ± 4.06	0.094
Using $S_0^2 = 0.85$,[71] 3 < k < 7.9, 1 < R < 3, No. independent points = 8.							

Using both CeO_2, Ce_2O_3 and $Ce(OH)_3$ starting points resulted in the first shell Ce-O scattering path data being fit with R = *ca.* 2.5 Å, more consistent with $Ce(OH)_3$ (Ce – O: 2.529 Å; $Ce(OH)_3$ *vs.* 2.342 Å; CeO_2) and the XANES data showing an absorption profile similar to that of $Ce(OH)_3$. The coordination numbers in both cases were 5-6, however there is a large error (± 25%) when determining coordination numbers *via* EXAFS hence why they are off from the expected coordination number of 9 for $Ce(OH)_3$. This arises from the fact that N and S_o^2 are correlated and modulated by $\boldsymbol{\sigma}^2$ giving the coordination number estimates a large uncertainty. The speciation being closer to that of $Ce(OH)_3$ than CeO_2, also fits with the observed XANES data where the dominant oxidation state is +3. However, it has been reported in several studies that sub-stoichiometric CeO_{2-x} can achieved significant proportions of Ce^{3+}, with x = 1.5. The speciation of $Ce(OH)_3$ would agree with the lack of observed reflections in the PXRD diffractograms of CeNP@MOF808 at 28°, 32° and 47° characteristic of CeO_2, although no reflections were observed at 16°, 17°, 28°, 32°, 35°, 40° and 43°, corresponding to $Ce(OH)_3$.

EXAFS is an average measurement, looking at the entire amount of material, and therefore there may be small local differences in speciation that allow for some Ce^{4+}. Only the first shell scattering paths could be characterised by EXAFS analysis.

3.4.7 X-ray Photoelectron Spectroscopy (XPS)

X-ray photoelectron spectroscopy (XPS) was developed by Swedish physicist Kai Siegbahn (originally termed Electron Spectroscopy for Chemical Analysis, ESCA) for which he was awarded the Nobel prize in Physics in 1981. XPS is fundamentally based upon the photoelectric effect which was described in Albert Einstein's Annus Mirabilis papers in 1905,[72] and taken together with Max Planck's theory of quantisation of light formed the fundamental basis for quantum theory. The photoelectric effect involves exposing a metal surface to light of varying energy (*i.e.* wavelength), above a certain energy of light electrons are ejected from the metal surface (so called 'photoelectrons'). The ejection of photoelectrons was found to be wholly dependent upon the wavelength of light, not the intensity – hence supporting the quantised particle model of light proposed by Max Planck.[72] This minimum energy of light required to eject photoelectrons is termed the work function or binding energy. The process of generating the photoelectron involves the X-ray photon being absorbed by a core shell electron and excited to such an extent that the electron is ejected from the atom. The ejected photoelectron leaves the atom with a kinetic energy value (E_K) equal to the photon energy ($h\nu$) minus the binding energy (E_B) of the electron shell ($E_K = h\nu - E_B$).[73] XPS involves placing a sample surface under vacuum and exposing it to high energy, monochromatic X-rays, often Al Kα characteristic X-rays at 1486.6 eV. The bombarding X-rays cause the ejection of photoelectrons that are collected and passed through a hemispherical deflection analyser (HDA) that disperses and segregates the photoelectrons based on their kinetic energy values. These streams of deflected electrons move in a circular path and collide with the electron multiplier detector surface, registering as a signal for a particular kinetic energy value of a certain intensity. X-ray photoelectron spectroscopy is, unlike complementary X-ray absorption spectroscopy, a highly surface sensitive technique. This surface sensitivity arises from the mean free path associated with photoelectrons ejected from the atoms of the sample.[74] When electrons with a particular kinetic energy value move through a solid material it can collide with other electrons and lose part or all of its energy through inelastic collisions.

The average distance a photoelectron, of a particular kinetic energy, can travel before such a collision is known at the inelastic mean free path (MFP).[74] The MFP is a function of the kinetic energy values of the ejected photoelectrons (see Figure 3.26), and for standard XPS characterisations with Al Kα excitation sources the MFP is less 10 nm.[74,75] Therefore, any photoelectrons formed deep within the solid structure cannot escape and be detected, leaving only photoelectrons origination from the surface of the sample to be detected.

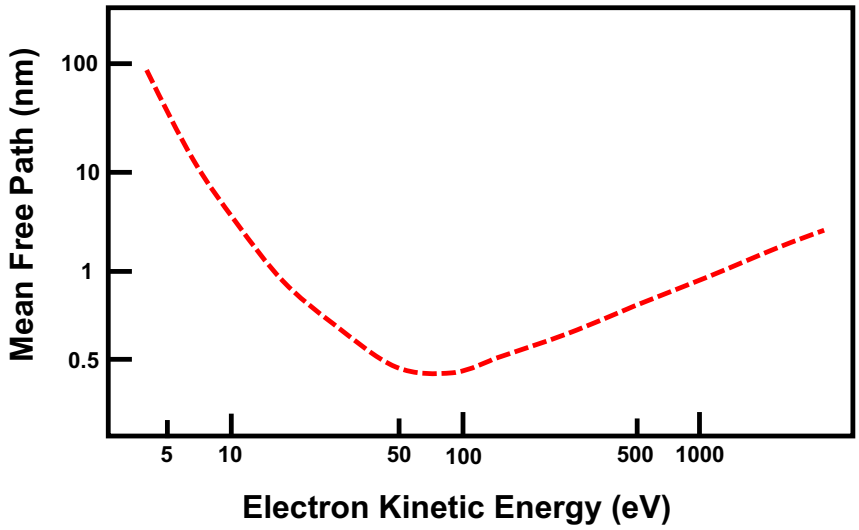

Figure 3.26: Inelastic mean free path (MFP) as a function of an electron's kinetic energy.

The binding energy measured during XPS is, like the edge jump in XAS, *chemically sensitive*, that is the value is dependent upon both the chemical identity of the atom to which the photoelectron originates and its formal charge (*i.e.* oxidation state). The kinetic energy of the photoelectrons is inversely proportional to the binding energy of the electron. All atoms exhibit at least one transition for a particular electronic state, this is manifests as the 'main peak' in the X-ray photoelectron spectrum and corresponds to the excitement of a core electron beyond the conduction band into the continuum (*i.e.* ionisation).

Satellite peaks can be observed surrounding the main peak, shown schematically in Figure 3.27, these correspond to transitions that yield an excited final state and occur when the ejected photoelectron interacts and excites an electron or hole in the valence band to the conduction band.[76,77] Two types of satellite peaks arise therefore: excitations of valence electrons abstracting energy from the photoelectron, yielding higher binding energy peaks termed 'shake-up' satellites; excitations of valence holes imparting energy on the

photoelectron, yielding lower binding energy peaks termed 'shake-down' peaks. Shake-down satellites tend to be rarer as they arise from particular electronic states whereby holes are present in the valence band. Shakedown peaks are however noted to occur within the X-ray photoelectron spectra of the cerium 3d subshell.[77]

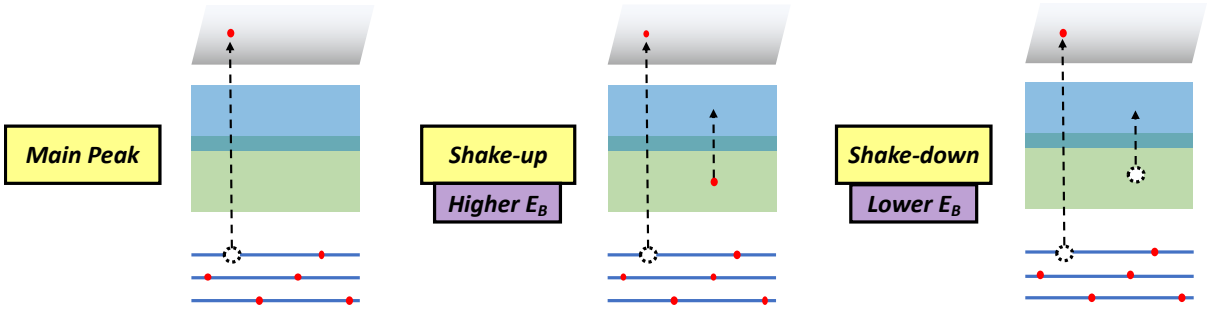

Figure 3.27: Schematic representation of possible core electron transitions during XPS.

3.4.8 XPS of Cerium

The Ce 3d X-ray photoelectron spectrum is well studied and assigned in the literature. Ejected photoelectrons originating from subshells with non-zero angular momentum (*e.g.* 3d) exhibit spin-orbit splitting whereby the electron spin (+1/2 or -1/2) couples with the orbital angular momentum (3d; $l = 2$), giving rise to 5/2 and 3/2 spin-orbit peaks. Therefore, each transition from the Ce 3d subshell manifest itself as two peaks in the X-ray photoelectron spectrum, with $3d_{3/2}$ peaks denoted '*u*', while $3d_{5/2}$ peaks denoted '*v*'. The relative intensities of the spin-orbit split $3d_{3/2}$ and $3d_{5/2}$ peaks is based on the associated degeneracies (2j + 1), with 4 and 6 for '*u*' and '*v*', respectively. This results in the ratio of the u and v peak intensities being 2:3 and helps in the deconvolution process in assigning specific peaks. The main peak and associated satellites are assigned in Table 3.10 below according to literature precedent.[78,79]

Table 3.10: Summary of peaks associated with the Ce 3d XPS spectrum.

Subshell	Notation	Electronic Final State	Oxidation State	Energy (eV)
$3d_{3/2}$	*u'''*	$3d^9 4f^0 2p^6$	Ce^{4+}	916

	u''	$3d^9 4f^1 2p^5$	Ce^{4+}	906 - 907
	u'	$3d^9 4f^1 2p^6$	Ce^{3+}	903 - 904
	u	$3d^9 4f^2 2p^4$	Ce^{4+}	900 - 901
	u_o	$3d^9 4f^2 2p^5$	Ce^{3+}	899
$3d_{5/2}$	*v*'''	$3d^9 4f^0 2p^6$	Ce^{4+}	898
	v''	$3d^9 4f^1 2p^5$	Ce^{4+}	888
	v'	$3d^9 4f^1 2p^6$	Ce^{3+}	885
	v	$3d^9 4f^2 2p^4$	Ce^{4+}	882
	v_o	$3d^9 4f^2 2p^5$	Ce^{3+}	880

The proportions of Ce^{3+} and Ce^{4+} can be quantified by deconvolution of the Ce 3d x-ray photoelectron spectrum and subsequent integration of areas of the deconvoluted peaks.[45,80] Whereby the Ce^{3+}% is given by:

$$Ce^{3+}\% = \frac{v_o + v' + u_o + u'}{\sum(v+u)} \ (eqn. 4)$$

It has been postulated in the literature that the well-defined and separated *u*''' peak could be employed to directly monitor the reduction of Ce^{4+} to Ce^{3+} as the formation of Ce^{3+} would result in a concurrent decrease in the intensity of the *u*''' peak.[79] However, quantitative examination has shown there is no direct linear correlation between the decrease in the intensity of u''' and the intensity of Ce^{3+} peaks such as u' or v'. In fact, u' and v' increase in intensity significantly before u''' decreases in intensity.[79] This results from hybridisation effects.

As stated previously, XPS is a surface based technique with Ce^{3+} proportions not necessarily representative of the bulk composition, with discrepancies noted in the literature between XPS and XAS determined Ce^{3+} proportions. Literature studies have shown that XPS tends to yield higher proportions of Ce^{3+} relative to XAS, for the same materials. Even when accounting

for the surface enrichment using a core-shell model, the Ce^{3+} proportions remain higher for XPS.[45] A number of factors can account for this difference in Ce^{3+} proportions: surface reduction of Ce^{4+} by the high energy X-rays, fast reduction dynamics associated with the CeNPs and diffuse depth profiles of the Ce^{3+} proportions inside the CeNPs. This demonstrates the importance of using complementary techniques in determining Ce^{3+} proportions.[45] A separate study quoted in literature, details the exposure of CeNPs to X-ray under ultrahigh vacuum, whereby an increased power of X-rays and longer length of exposure both were found to significantly increase the proportion of Ce^{3+} determined *via* XPS, with the former yielding significant differences in proportions. Therefore, all Ce^{3+} determined by XPS should be referenced with power and length of exposure to X-rays.[81] Redox active materials such as CeO_2 often exist in dynamic equilibrium with atmospheric oxygen, hence placing the material under ultra-high vacuum tends to favour the position of the equilibrium shifting to replenish lost atmospheric oxygen in the closed vacuum system, yielding a higher proportion of Ce^{3+} states.

3.4.9 XPS of MOF808

Similarly with cerium, the Zr 3d X-ray photoelectron spectrum exhibits two spin-orbit split peaks corresponding to $3d_{3/2}$ and $3d_{5/2}$. Studies into the oxidation of the surface of Zr metal at various temperatures showed the initial presence of two spin-orbit split peaks at 178.7 eV and 181.1 eV due to elemental Zr (*i.e.* zero oxidation state).[82] With elevated temperatures, in the presence of O_2, the surface of the Zr metal becomes oxidized with multiple peaks appearing due to Zr^{1+}. Zr^{2+}, Zr^{3+} and Zr^{4+}. The presence of Zr^{1+}. Zr^{2+}, Zr^{3+} was indicative of the formation of a suboxide (ZrO_{2-x}) layer between the metal surface and the fully oxidised (Zr^{4+}, ZrO_2) outer surface. The peaks at 182.7 eV and 185.0 eV are characteristic of Zr^{4+} in ZrO_2.[82,83] Due to the similarities in coordination sphere of Zr^{4+} in ZrO_2 and $Zr_6O_4(OH)_4(OOCH)_6(BTC)_2$ (MOF808), the XPS peaks for MOF808 Zr^{4+} are similar to those of ZrO_2, at 182.5 eV and 184.9 eV.[84] Interestingly, XPS studies into the interaction of MOF808 with organoarsenic acid p-arsanilic acid (ASA) showed that Zr^{4+} peaks were shifted to lower binding energies, 181.5 eV and 183.9 eV. This is due to the greater electronegativity of the O-As group compared to displaced aqua and hydroxyl ligands, leading to a change in electron binding energies. This

highlights the chemical sensitivity of XPS and would highlight any chemical bonding to the Zr_6 clusters.[84]

3.4.10 XPS Studies of CeNP@MOF808

X-ray photoelectron spectra of CeNP@MOF808 were recorded under vacuum. The photoelectron spectra, shown below in Figure 3.28, revealed two main peaks and associated shoulder events. Fitting and application of a Shirley type background allowed for the deconvolution of the spectra and showed four constituent peaks, two main peaks and two shake down satellite structures at 905 (u'), 886 (v'), 901 (u_o), 882 (v_o) eV. These peaks correspond to ordinary excitations of 3d core electrons (u'/v') and excited final states (u_o/v_o) of the Ce^{3+} oxidation state. No peaks corresponding to Ce^{4+} are evident in the photoelectron spectra of CeNP@MOF808. The appearance of signals are 905 eV and 901 eV is consistent with the surface of CeNP@MOF808 being purely Ce^{3+}. This contrasts with the XANES measurements that show a 3:1 mixture of Ce^{3+}:Ce^{4+} states (see Figure 3.18), respectively, and indicates surface enrichment of Ce^{3+}, consistent with literature observations. This would indicate that the Ce^{4+} ions reside within the CeNP@MOF808 particles and are only accessible internally *via* MOF pore channels. As noted previously, exposure of Ce based samples to X-ray sources can cause reductions of the Ce^{4+} to Ce^{3+}, therefore biasing the measurement towards higher Ce^{3+} proportions and therefore could also explain the surface Ce^{3+} enrichment.

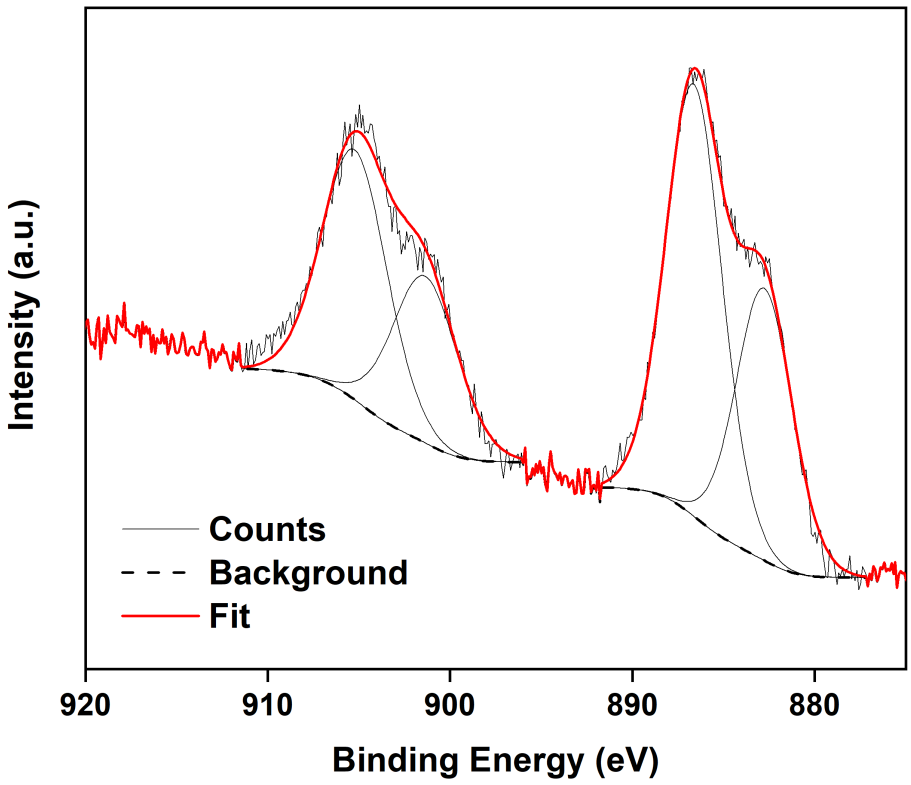

Figure 3.28 Ce 3d X-ray Photoelectron Spectrum of CeNP@MOF808 composite.

CeNP@MOF808 samples were exposed to a stream of ionized Ar^+ for 600 seconds to etch samples several layers before recording a separate Ce 3d photoelectron spectrum. The etched CeNP@MOF808 samples revealed a photoelectron spectrum, see Figure 3.29, identical to that of CeNP@MOF808 (see Figure 3.28), with peaks observed at 905, 901, 886 and 881 eV. This indicates that the surface of the etched sample is identical to that of the unetched sample, composed entirely of Ce^{3+} surface states. This is somewhat surprising given that bulk XANES measurements suggested the existence of Ce^{4+} states within the CeNP@MOF808 sample. There is sparse disclosure in the literature relating to the etching of MOF materials using ionized Ar^+. However, looking further afield several studies have been published which show that solid state materials remain largely unchanged chemically following etching with Ar^+.[85,86] That is the Ar^+ beam simply erodes the top level surface, exposing inner layers of material, rather than reacting with the material itself. It is unlikely therefore that the Ar^+ beam changes the MOF structural integrity.

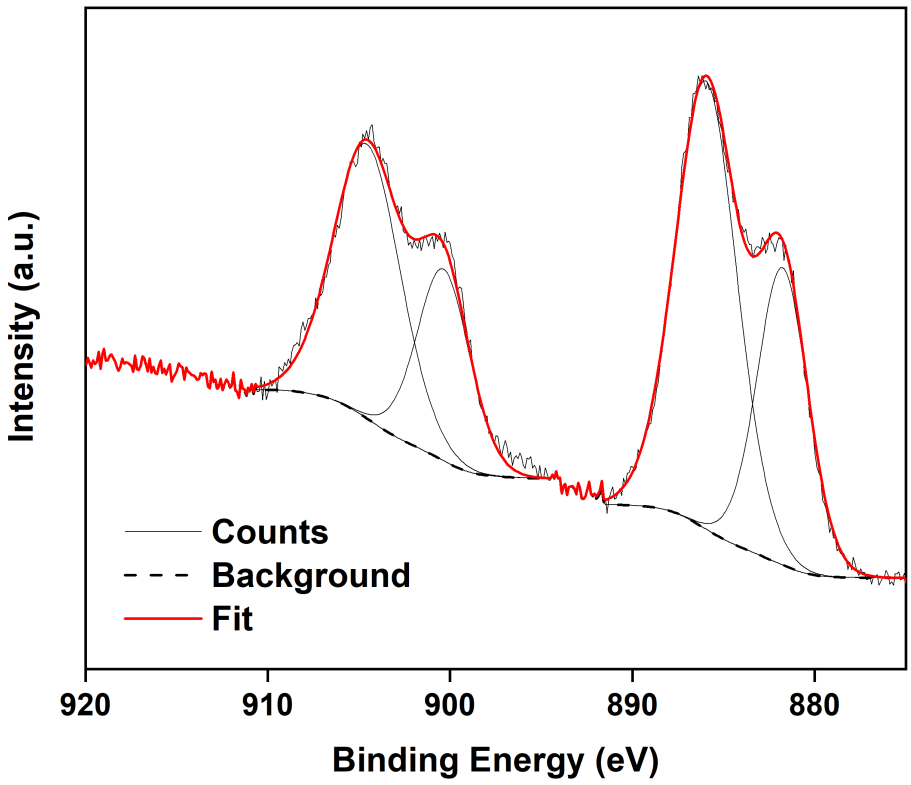

Figure 3.29 Ce 3d X-ray Photoelectron Spectrum of etched (600 second, Ar^+ etching) CeNP@MOF808.

It is important to highlight that the powder morphology of the CeNP@MOF808 sample limits the ability of the etching process to access bulk material in the sample. This is due to surface contamination that can arise from various particle domains within the powder sample. This is shown schematically below in Figure 3.30.

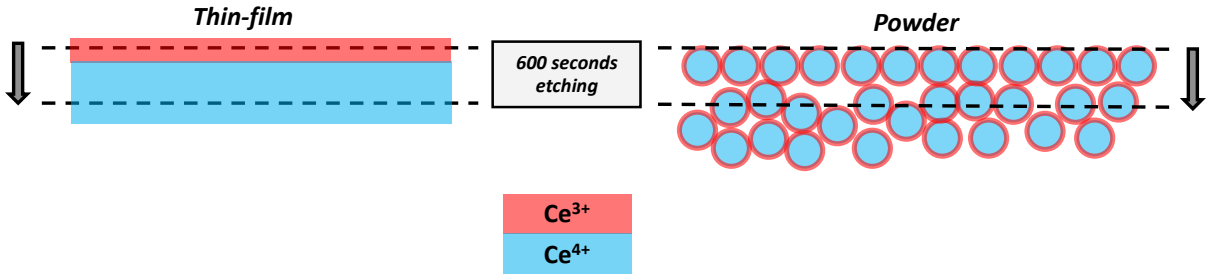

Figure 3.30: Schematic representation of the surface contamination of oxidation state analysis in powder samples.

This surface contamination, in combination with *in-situ* reduction of Ce^{4+} to Ce^{3+} *via* exposure to X-rays and ion beams could result in an artificially high Ce^{3+} content in the etched sample, deviating somewhat from the XANES determined values of 75% Ce^{3+} and 25% Ce^{4+}.

O 1s photoelectron spectra were recorded for both CeNP@MOF808 and the etched surface (see Figure 3.31). Due to 1s photoelectron ejections originating from an $l = 0$ orbital, there is no spin-orbit splitting component to the peaks, therefore the number of peaks is equal to the number of oxygen environments.

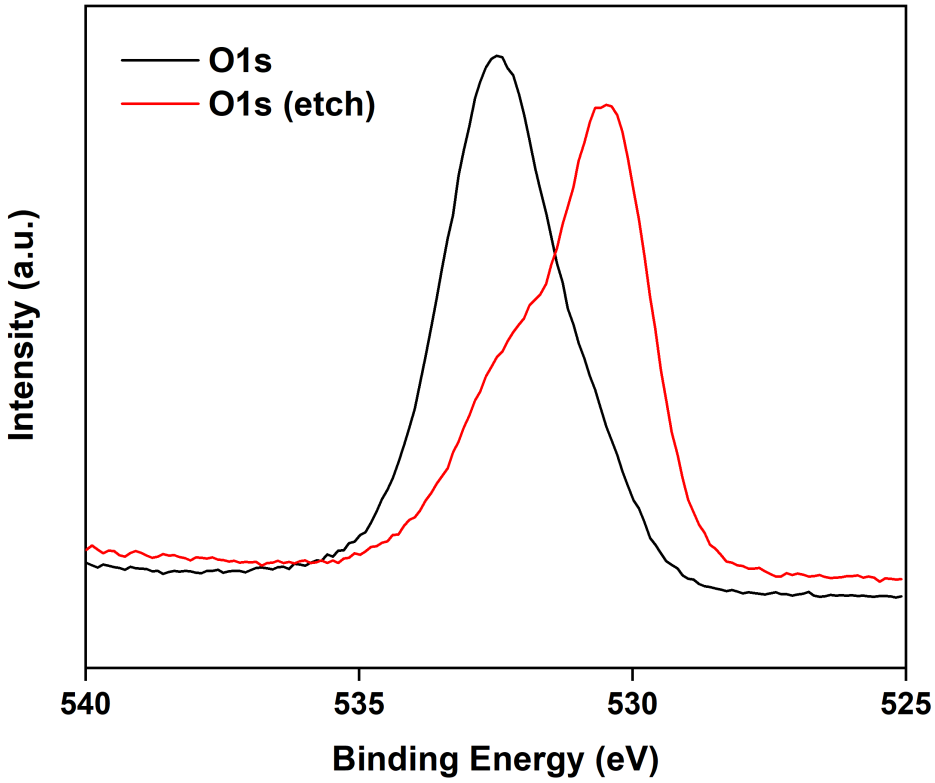

Figure 3.31: O 1s X-ray Photoelectron Spectrums of CeNP@MOF808 (black) and etched CeNP@MOF808 (red; 600 second, Ar^+ etching).

The photoelectron spectrum of the CeNP@MOF808 sample surface exhibits a symmetric peak at 532.5 eV, similar to that observed in literature for MOF808 at 532 eV.[1] Deconvolution of the O 1s peak, for CeNP@MOF808, reveals two oxygen environments (see Supplementary

Figure 3.11), however given the limitations of the fit one should be cautious in making any chemical assignments.

The photoelectron spectrum of the etched CeNP@MOF808 reveals a distinctively different peak structure, with a shift to 530 eV and a loss of peak symmetry. Deconvolution of the O1s peak for the etched CeNP@MOF808 sample revealed two oxygen environments (see Supplementary Figure 3.12), however conclusions from this are limited once again by the limitations of the poor fit. The distinct shift in the O1s peak is indicative of a change in the oxygen environments of CeNP@MOF808 from surface to bulk. Given that the Ce oxidation states remain constant from surface to bulk this change in oxygen could be due to changes in MOF oxygen environments. It could also be a result of the reactive infiltration process that results in formation of different oxide-hydroxide species on the surface *vs.* inside the interior structure.

3.4.11 XPS Studies of Oxidative Treatment of CeNP@MOF808

Exposure of the CeNP@MOF808 to hydrogen peroxide solution (6%) resulted in an instant effervescence of gas and colour change from white to orange, $CeNP^{[oxd]}$@MOF808. X-ray photoelectron spectra of $CeNP^{[oxd]}$@MOF808 were recorded under identical conditions to those used for CeNP@MOF808. The photoelectron spectra revealed a more complicated line structure, with several overlapping peaks present, see Figure 3.32. Application of a Shirley background and subsequent deconvolution revealed 10 peaks in total, 6 associated with the Ce^{4+} state at 917 (u’’’), 906 (u’’), 902 (u), 899 (v’’’), 886 (v’’), 883 (v) eV and a further 4 due to the Ce^{3+} state at 905 (u’), 900 (u_o), 886 (v’) and 881 (v_o). The 6 peaks associated from the Ce^{4+} arise due to Ce 3d excitations as noted in literature, with those at u’’’/v’’’ arising from the $3d^9 4f^0 2p^6$ final state (normal photoelectron ejection), u’’/v’’ caused by the $3d^9 4f^1 2p^5$ final state and u/v due to the $3d^9 4f^2 2p^4$ final state.

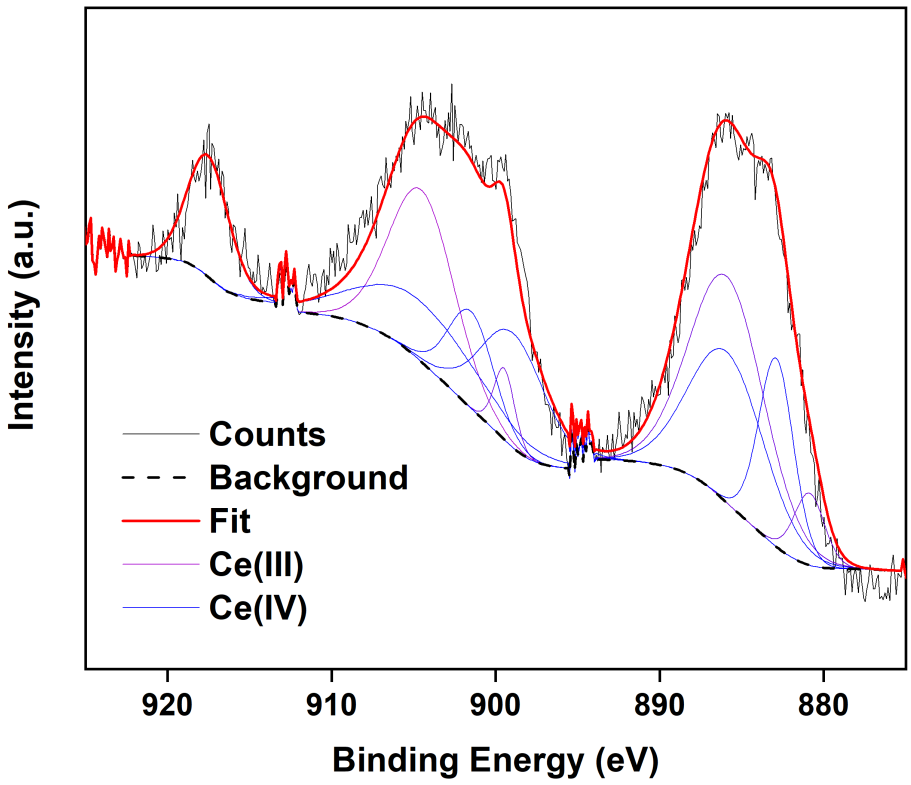

Figure 3.32 Ce 3d X-ray Photoelectron Spectrum of CeNP[oxd]@MOF808.

As established previously in literature, it is possible to determine the proportions of Ce^{3+} and Ce^{4+} states using relative sum areas of the integrated peak structures (see equation 4).[45,80] By taking the ratio of the area of peaks associated with the Ce^{3+} state to the total sum peak area, the Ce^{3+}% was determined to be 43%. The significant decrease in Ce^{3+} concentration on the surface of CeNP@MOF808 can be attributed to the strongly oxidising nature of H_2O_2 (6%). In contrast to previous attempts made to oxidise CeNP held within a liquid crystal framework (LCF), it was noteworthy that the decrease in Ce^{3+} content was somewhat greater, going from *ca.* 80% to <10% Ce^{3+}. This demonstrates an important principle in that the exact nature of the matrix (*e.g.* MOF *vs.* LCF) can have a distinct influence over the stability and redox activity of the encapsulated nanoparticles. One would extrapolate from this that alternative frameworks would offer platforms on which different degrees of redox activity could be accessed. Therefore, we offer the foundations for a modular platform from which the redox activity of CeNP can be possibly modulated for specific applications (*e.g*. catalysis).

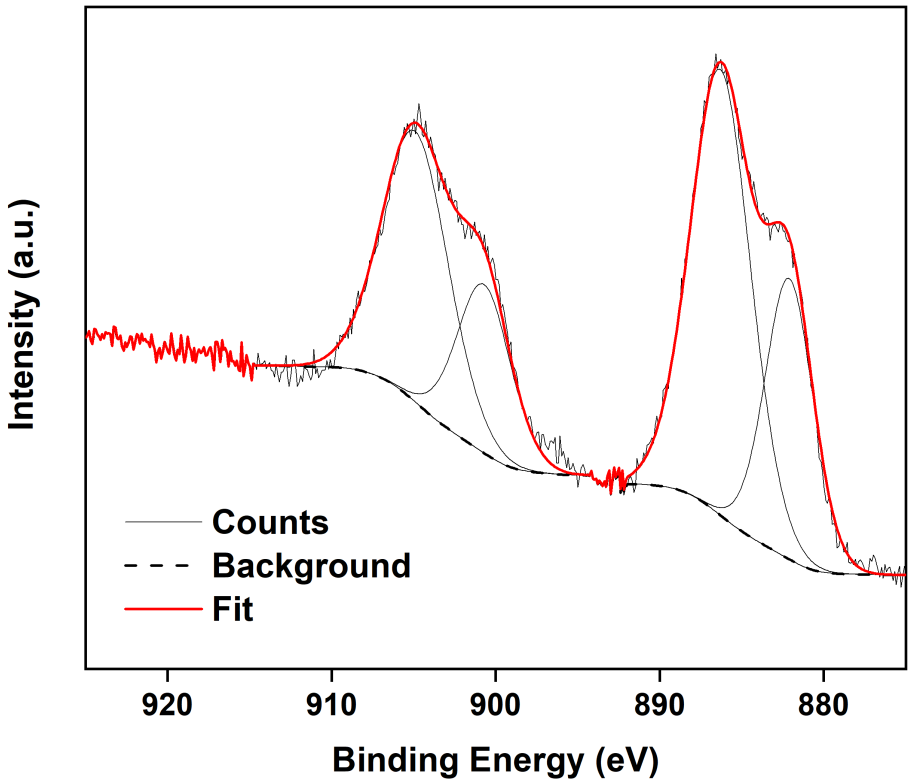

Figure 3.33 Ce 3d X-ray Photoelectron Spectrum of etched (600 second, Ar^+ etching) $CeNP^{[oxd]}$@MOF808.

Samples were etched using a stream of ionized Ar^+ for 600 seconds. Interestingly, the etched Ce 3d photoelectron spectra lacked any peak structures associated with the Ce^{4+} state. As shown above in Figure 3.33, the etched sample exhibits only Ce^{3+} states. This suggests that during the oxidation process with H_2O_2 the Ce^{3+} states more deeply imbedded within the MOF matrix are not significantly oxidised. A possible explanation for this lack of Ce^{3+} oxidation is that with the collapse of the MOF808 framework, H_2O_2 may be largely impermeable to the structure, limiting its oxidising ability. The previously mentioned sources of surface contamination are not considered in the case of $CeNP^{[oxd]}$@MOF808 given that any surface contamination would show Ce^{4+} states being present. Therefore it is concluded that the localisation of the Ce^{4+} states to the surface is an authentic attribute of $CeNP^{[oxd]}$@MOF808, although it should be noted that the exposure to X-rays and ionised Ar^+ can cause artificial *in-situ* changes in oxidation state.

Interestingly, the O 1s photoelectron spectrum for CeNP[oxd]@MOF808 shows an asymmetric peak at 531 eV (see Figure 3.34). This contrasts with the O 1s photoelectron spectrum of CeNP@MOF808 which showed a symmetric peak around 532.5 eV (see Figure 3.34), suggesting changes in the oxygen environments of CeNP@MOF808 after oxidative post-synthetic modification.

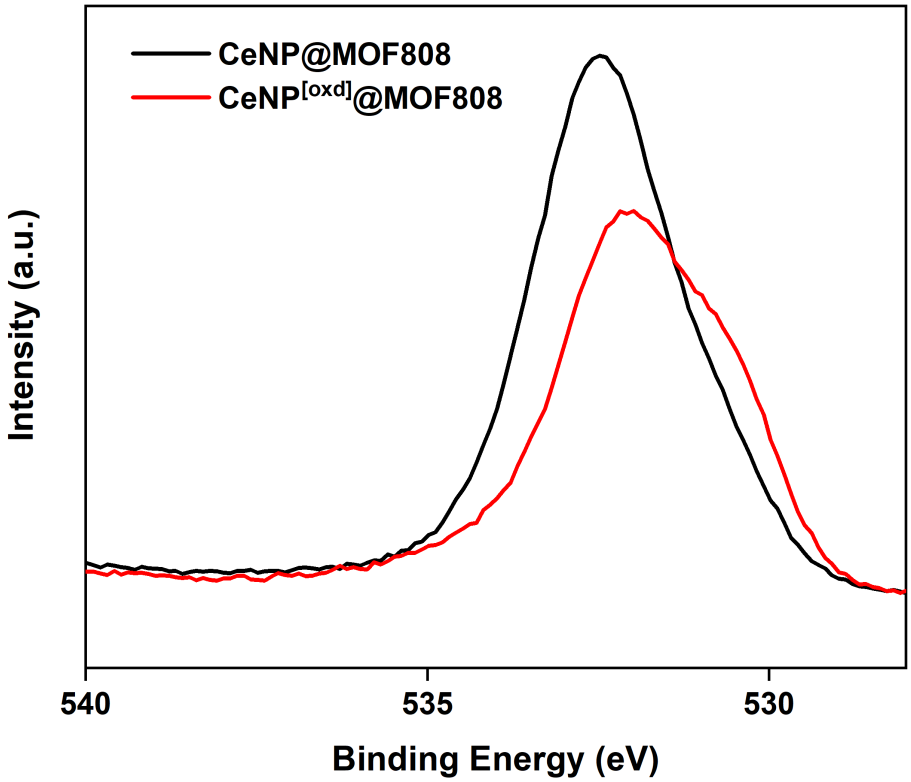

Figure 3.34: O 1s X-ray Photoelectron Spectra of CeNP@MOF808 and CeNP[oxd]@MOF808.

Etching of the CeNP[oxd]@MOF808 samples reveals a O 1s spectrum whereby the peak has lost its symmetry and been shifted to 530 eV – similar again to observations seen with CeNP@MOF808 when etched (see Figure 3.31). This is indicative that changes in oxygen environment between surface and bulk are independent of the cerium oxidation states, and therefore more likely related to MOF oxygen environments.

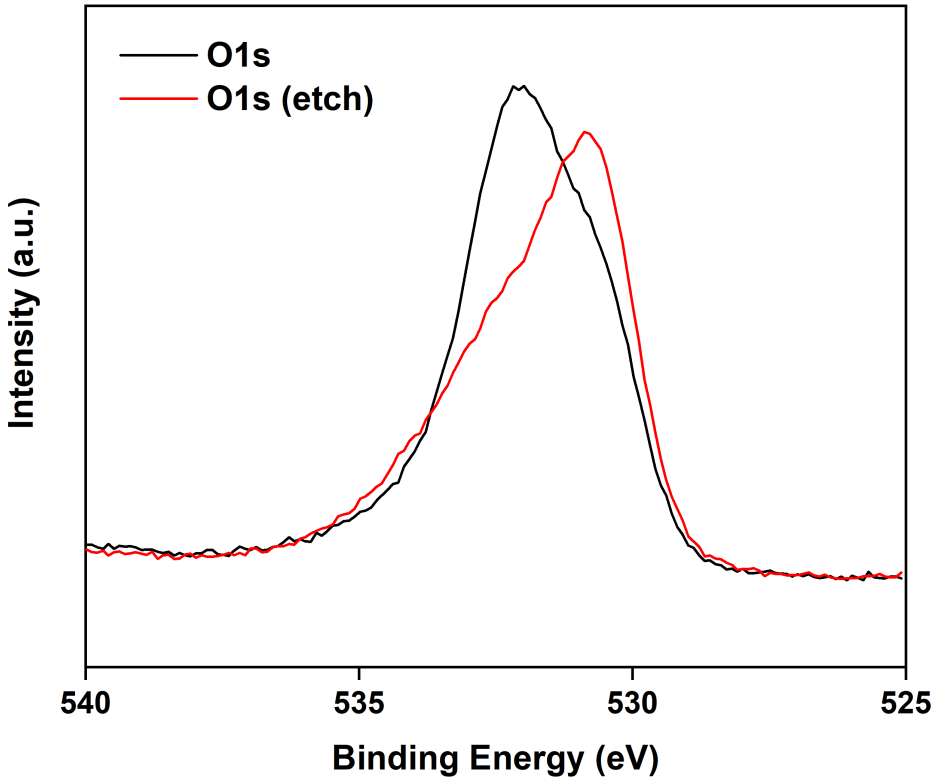

Figure 3.35: :O 1s X-ray Photoelectron Spectrum of CeNP$^{[oxd]}$@MOF808 and etched CeNP$^{[oxd]}$@MOF808 (600 second, Ar^{+} etching).

3.4.12 XPS Studies: Conclusions

In conclusion, Ce 3d XPS studies of CeNP@MOF808 were performed successfully and indicated only Ce^{3+} states present in the composite – before and after sample etching. Ce 3d XPS studies of CeNP$^{[oxd]}$@MOF808 showed a mixture of Ce^{3+} and Ce^{4+} oxidation states, in agreement with XANES studies, although biased towards the Ce^{3+} state by the surface sensitive nature of the technique. O 1s XPS studies of CeNP@MOF808 and CeNP$^{[oxd]}$@MOF808 were also successfully achieved, showing a distinct change in the oxygen chemical environment.

3.4.13 Scanning Transmission Electron Microscopy (STEM)

Electron microscopy operates on a similar basis to that of optical microscopy, only that the image contrast in electron microscopy arises from scattering of the electron beam, as

opposed to optical microscopy which relies on the absorption of light energy. Electron microscopy employs a series of magnetic lenses to focus an electron beam onto a small sample that must be below ~100nm thickness in order to be electron-transparent. There are two types of electron microscopy adopted in this sample: transmission electron microscopy (TEM) and scanning transmission electron microscopy (STEM). Both types of electron microscopy operate on the same fundamental principle of electron interaction (*i.e.* scattering) with the sample deriving the image contrast of that sample, however they have reversed optics. STEM mode operates with the objective lens above the sample, with an array of detectors below the sample (see Figure 3.36).[87]

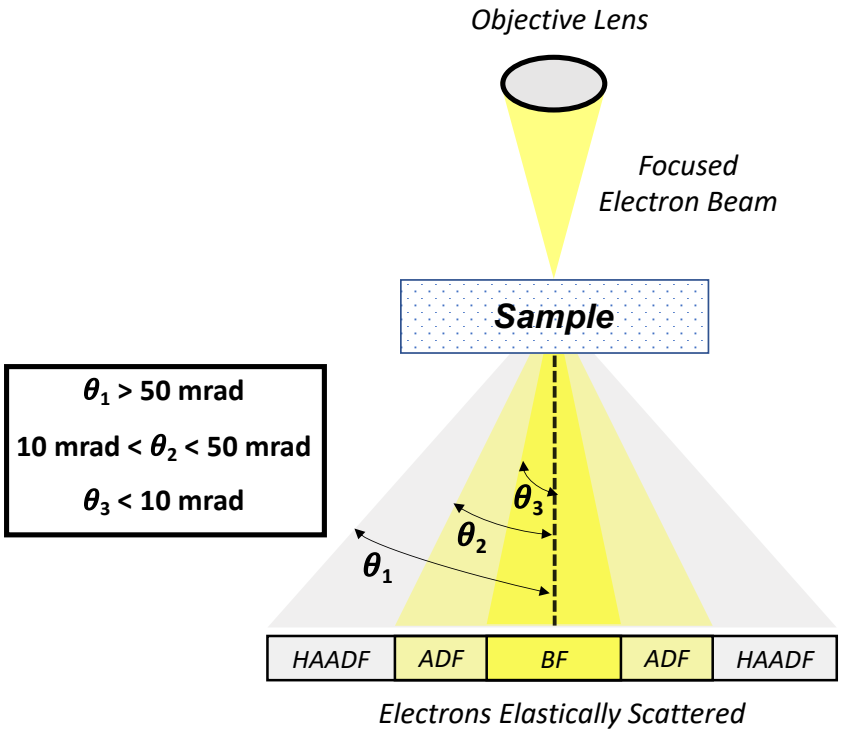

Figure 3.36: Schematic representation of the various degrees of electron scattering, and corresponding fields of contrast, in STEM. Note that TEM features the objective lens beneath the sample

Un-scattered electrons, or those scattering only through small angles (less than 10 mrad) relative to the normal axis, are detected in the bright field (BF) mode. Bright field images will typically show a bright background, upon which particles of the sample appear darker.[87]

Electrons scattered at higher angles (greater than 10 mrad) can be used to form dark field (DF) images; for the technique of STEM, these are collected with annular detectors that subtend a finite range of angles at the sample.[87] Extreme scattering of the electrons are detected using so-called high angle annular dark field (HAADF) detectors. An advantage of the latter imaging mode is that the scattering angles used are larger than those relating to Bragg angle and other diffractive scattering events, so that the HAADF image intensity reflects variations in the sample thickness and atomic number alone. DF and HAADF images are complementary in the sense that the background is usually dark and material appears bright, with thicker, heavier material appearing brightest.

The electrons scatter from the atoms present within the sample with differential scattering cross-sections that depend on the atomic number and nature of the scattering interaction. The elastically scattered electrons collected in the dark field signal arise specifically due to Rutherford scattering from partially screened nuclei. This scattering increases with atomic number (Z) of the atom with an exponential relationship of $Z^{1.7}$.[88,89] Therefore the contrast of dark field STEM images will appear brighter for heavier atoms. A simple method for generating imaging contrast is to use detectors that subtend different angles at the sample.

3.4.14 STEM Studies of CeNP@MOF808 and $CeNP^{[oxd]}$@MOF808

Characterisation of MOF materials within STEM imaging is often complicated by the interaction of the organic linker with the high energy electron beam, making MOF materials highly sensitive and prone to beam damage. MOF particles are often susceptible to surface charging on exposure to high energy electron beams, causing crystallites to clump together. Several types of damage can occur within a sample, however most reports have identified radiolysis is the primary mechanism behind beam damage of MOF samples.[90] Radiolysis involves the scission of covalent bonds of the organic linker, leading to the collapse of the framework structure. Therefore, care had to be taken to assess the level of damage produced for a given set of imaging conditions with the CeNP@MOF808 samples, with low beam energies and short acquisition times being preferable for these specimens.

Low and high magnification TEM images of CeNP@MOF808 and CeNP$^{[oxd]}$@MOF808 shown in Figure 3.37 revealed no large-scale differences in particle morphology or size. Both materials had particles that ranged from 50 – 100 nm in diameter, with no obvious structures (*i.e.* NPs) within the composite particles.

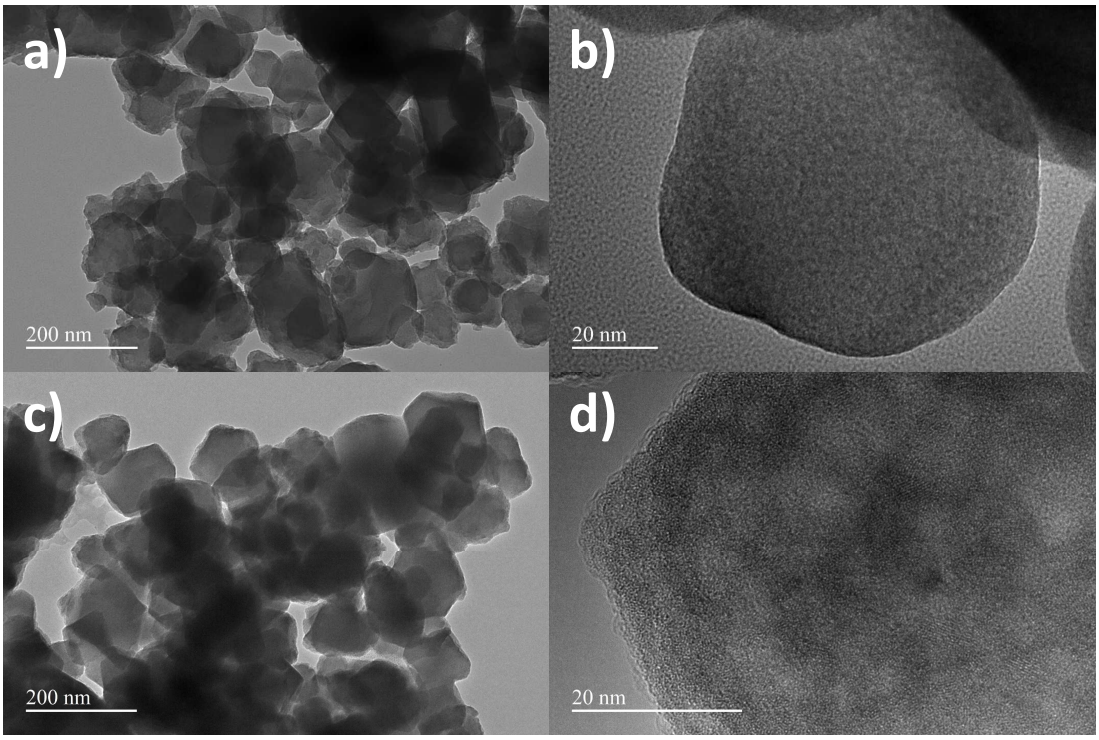

Figure 3.37: Low/high magnification TEM images, BF. (a) and (b) CeNP@MOF808, (c) and (d) CeNP$^{[oxd]}$@MOF808.

HAADF images of CeNP@MOF808 and CeNP$^{[oxd]}$MOF808 are shown in Figure 3.38. Given that the composite CeNP@MOF808 consists of elements Ce, Zr, O and C, in order of decreasing Z, we would expect to regions with higher Ce loading to appear brightest in the dark field images. The presence of lattice fringes within the internal structure of CeNP@MOF808, see Figure 3.38 (a), suggests a crystalline material and is consistent with previous bulk X-ray powder diffractograms, detailed in Chapter 2, showing a MOF crystalline structure for CeNP@MOF808. In contrast, electron diffraction patterns of CeNP@MOF808 suggest an amorphous material (see Supplementary Figure 3.17). It could be that the apparent lack of reflections in the electron diffraction is due to previously discussed beam damage (*via* a radiolysis mechanism) of the MOF structure. Particles of CeNP@MOF808 exhibit brighter

halos around their surfaces (see red arrow annotation), suggesting accumulation of Ce within a *ca.* 10 nm shell of the outer surface of the MOF particle. This is in agreement with the diffusion resistant mechanism whereby the CeN''_3 precursor largely reacts with the surface of the MOF particles, rather than completely percolating into the material.

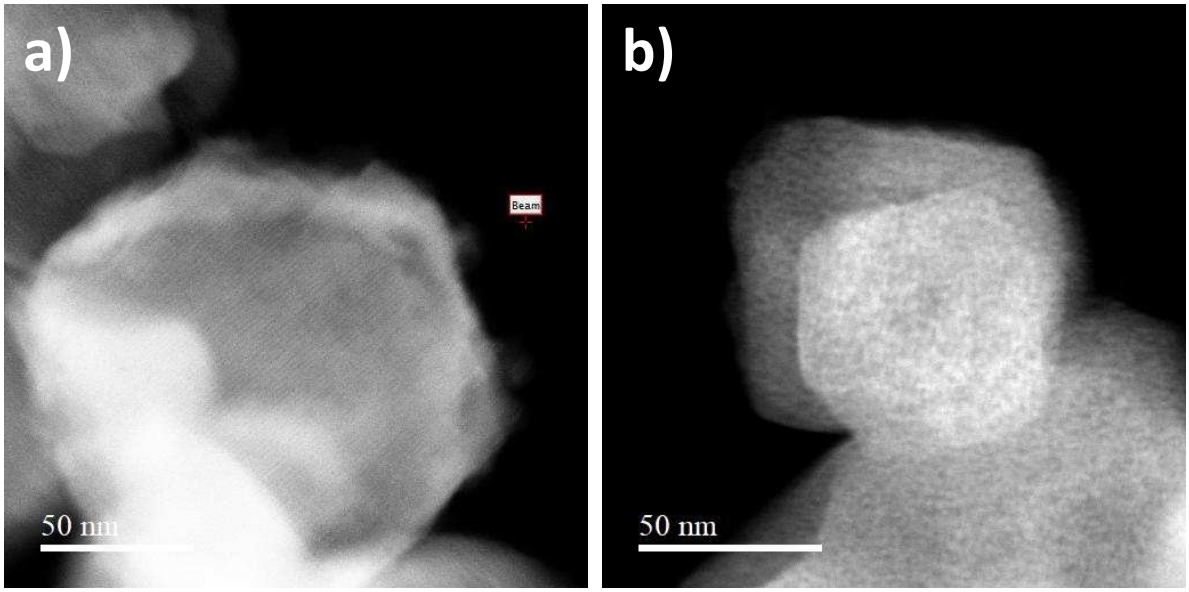

Figure 3.38 HAADF images of (a) CeNP@MOF808 and (b) $CeNP^{[oxd]}$@MOF808.

The absence of electron diffraction reflections in TEM (see Supplementary Figure 3.17) and lattice fringes in the HAADF STEM images of $CeNP^{[oxd]}$@MOF808, shown in Figure 3.38 (b), is consistent with the bulk X-ray powder diffractograms showing an amorphous material (see Figure 3.11). Both data sets imply that the exposure of the composite material to the highly oxidising H_2O_2 solution results in the loss of sample crystallinity.

Neither CeNP@MOF808 nor $CeNP^{[oxd]}$@MOF808 seemed to have discrete Ce-rich nanoparticles (CeNP), which would manifest as distinct bright dots in STEM imaging, reflecting the higher atomic number and density within the nanoparticles. Instead, the more uniform contrast (except at MOF particle edges) is consistent with a more uniform distribution of Ce throughout the MOF. To illustrate this concept, a typical HAADF image for a metal NP-MOF composite is shown below in Figure 3.39, where discrete Pt nanoparticles are formed within a MIL-101-Cr host framework and are clearly visible as bright spots in HAADF STEM imaging.[91] These have been observed in several published guest@MOF systems and are considered the

benchmark for establishing NP@MOF composite materials, where NPs are of both metallic and ceramic structure.[91-94]

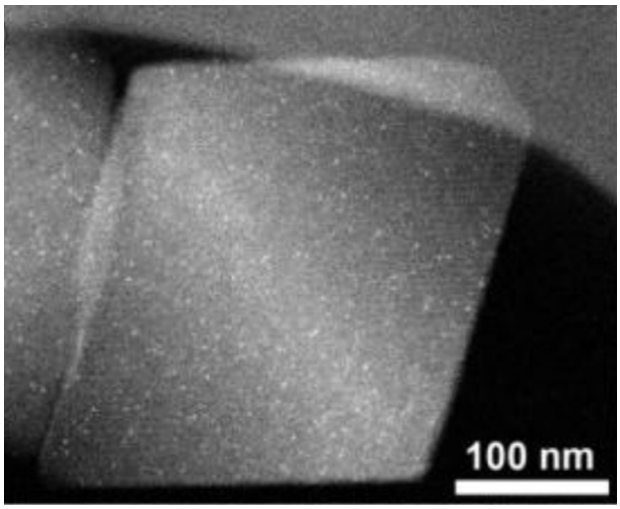

Figure 3.39: HAADF images of composite Pt@MIL-101-Cr taken from *Nanomaterials*, 2016, **6**, 45, with 'dot' pattern showing the formation of discrete, well defined metallic Pt nanoparticles.[91]

The presence of light halos around the surface of CeNP@MOF808 particles is suggestive of the accumulation of a nanoscale coating of Ce based material within the outermost shell of the MOF particle. This has been observed in attempts to substitute Zr^{4+} ions with Ti^{4+} and Hf^{4+} in the SBU of UiO-66 through a post-synthetic exchange (PSE) mechanism,[95] whereby instead of achieving ion substitution, the Ti/Hf ions form a oxide coating (TiO_2/HfO_2) on the particle surface. These oxide coatings appear as 'fluffy' halos around the MOF particle surface in BF TEM images.

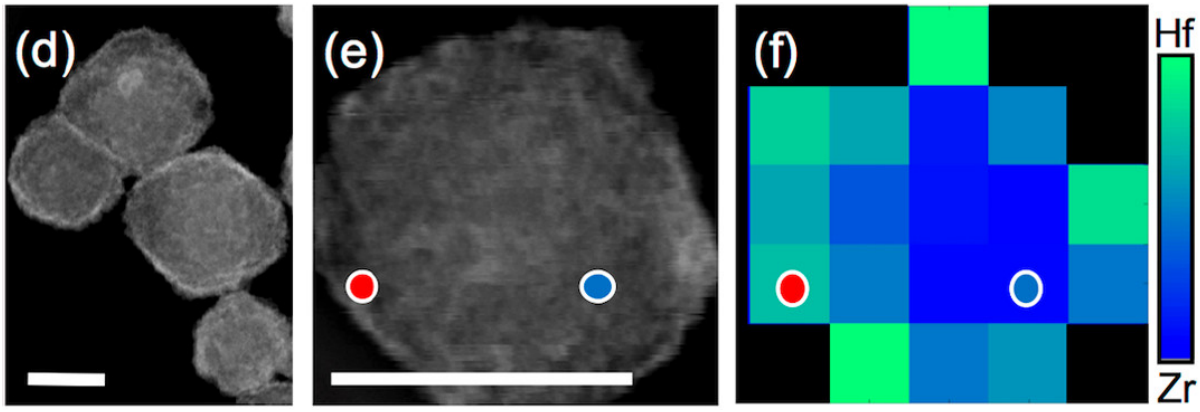

Figure 3.40: a-b)HAADF images and EDX scans, c) of UiO-66@HfO_2 (same particle in images b and c), with formation of light 'halos' around particle edges showing the accumulation of a HfO_2 nanolayer. Note red and blue dots correspond to points where EDX spectra were taken, not shown here.[95]

While the 'halo' structures observed for the UiO-66@HfO_2 systems are similar to those observed in the HAADF images of CeNP@MOF808 (Figure 3.38), similar halo structures are not observed in the BF TEM image of CeNP@MOF808 (Figure 3.37). Furthermore these halo structures were only observed on certain particles and may result as an artefact of the MOF synthesis, rather than the reactive infiltration process. It is possible that beam damage, which would initially be largely limited to the MOF particle surface, may also be a cause for the observation of halo structures in the HAADF images of CeNP@MOF808, where the collapse of the MOF808 structure has an localised increase in density.

3.4.15 STEM Studies: Conclusions

In conclusion, the particle morphology of CeNP@MOF808 and $CeNP^{[oxd]}$@MOF808 was successfully characterised through STEM studies - despite the noted sensitivity of the host framework towards high energy electron beams. STEM images of the CeNP@MOF808 and $CeNP^{[oxd]}$@MOF808 composites both showed particles *ca.* 50 – 100 nm in diameter, consistent with SEM studies detailed in Chapter 2. HAADF images of the CeNP@MOF808 composite revealed a *ca.* 10 nm shell on the outer surface of the MOF particles, indicative of the formation of a coating with a heavier metal (*e.g.* Ce). These coatings were absent in the

HAADF images of CeNP[oxd]@MOF808.Particles of CeNP@MOF808 composite showed lattice fringes, consistent with powder X-ray diffractograms noted in Chapter 2 which indicated retention of the MOF808 host crystallinity following reactive infiltration. Neither CeNP@MOF808 or CeNP[oxd]@MOF808 showed a distinctive 'dot pattern' which would be indicative of discrete CeNP within the MOF particles.

3.4.16 Electron Energy Loss Spectroscopy (EELS)

Electron energy loss spectroscopy (EELS) relies on high energy electron beams interacting with condensed matter through inelastic collisions.[96] The incident electrons have an energy of E_0, while scattered electrons have an energy loss associated with quantised transitions within the metal ion. In the case of cerium the 3d to 4f transition, with the final excited state of $3d^9 4f^{n+1}$ where n = 0 for Ce^{4+} and n = 1 for Ce^{3+}, was chosen as it yields sharp line features that are easily resolved. The energy loss peak associated with this transition is spin-orbit split, $3d_{3/2}$ and $3d_{5/2}$, yielding two peaks at 883 eV and 901 eV, referred to as the M_5 and M_4 edges, respectively.[97-99] Multiple studies have shown that the position of the edges and relative intensity depend on the oxidation state proportions cerium within the material. Higher M_5/M_4 intensity ratios are indicative of a greater proportion of Ce^{3+}.[98,99]

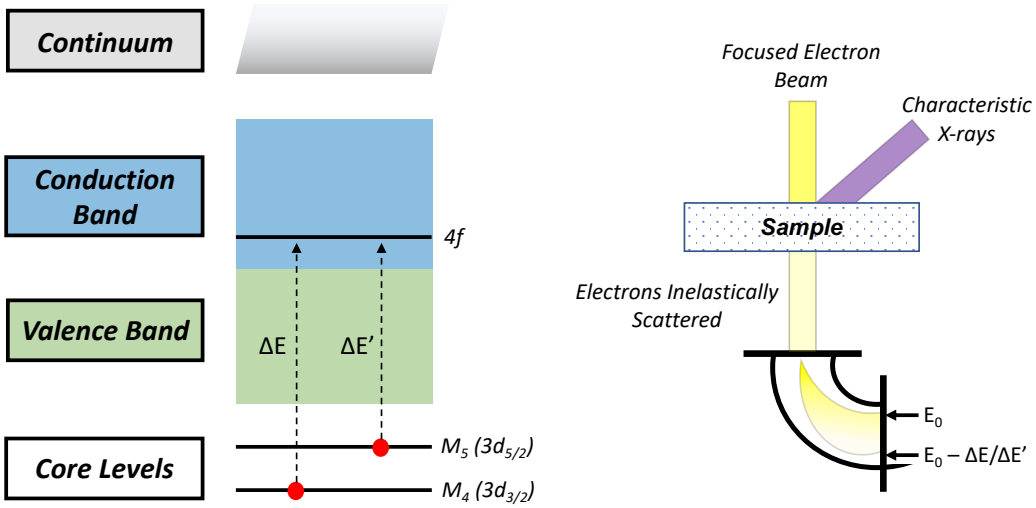

Figure 3.41: Schematic representation of electronic interactions in condensed matter leading to the formation of M_5 and M_4 peaks in EELS spectra.

3.4.17 EELS Studies of CeNP@MOF808 and CeNP[oxd]@MOF808

EELS spectra were acquired for the CeNP@MOF808 sample and have been processed to show a comparison of the M_5/M_4 peak intensities for the edge and core of particle shown in Figure 3.42.

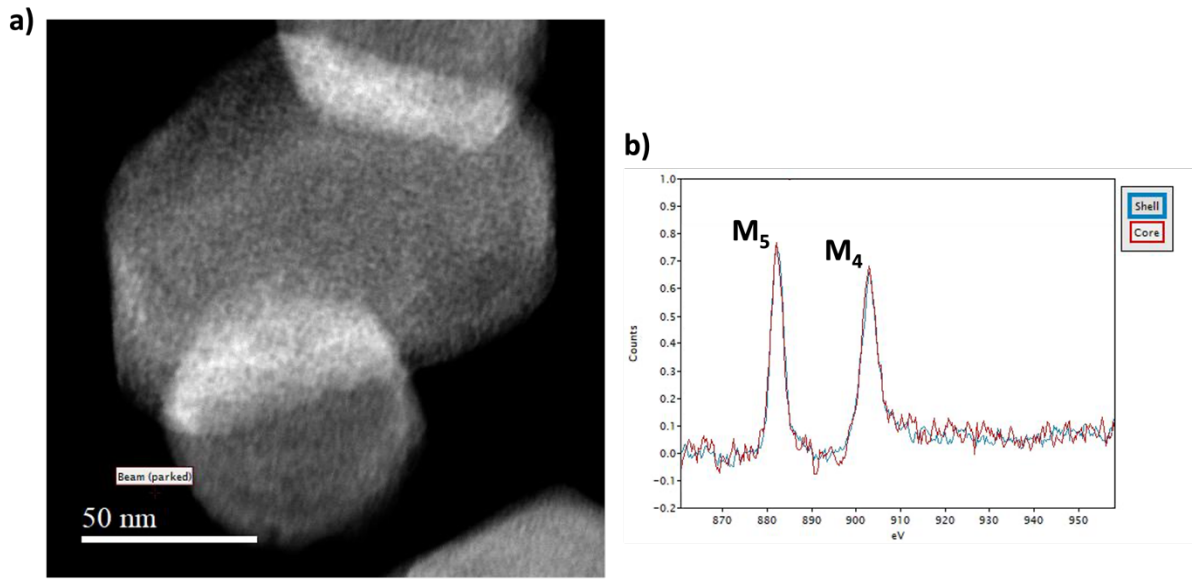

Figure 3.42: a) HAADF image of CeNP@MOF808, b) EELS spectra of shell (outside) and core (inside) of CeNP@MOF808 particle.

The M_5 edge is higher in intensity relative to the M_4 edge, which is indicative of the Ce^{3+} oxidation state dominating. A uniform ratio across the particle suggests that the Ce^{3+} oxidation state is broadly uniform too, and lacks, for example, a core-shell distribution that has been previously seen with cerium materials.[98] This is not unsurprising given than inhomogeneous distribution of Ce^{3+} states would only be expected with discrete, well defined CeNP, which are not observed in either the TEM images (see Figure 3.37) or HAADF images (see Figure 3.38) of CeNP@MOF808. This is consistent with XANES (see Figure 3.17) and XPS (see Figure 3.28) analysis which suggest a majority presence of the Ce^{3+} state.

EELS spectra were subsequently acquired for the CeNP[oxd]@MOF808 sample and have been processed to show a comparison of the M_5/M_4 peak intensities for the edge and core of particle shown in Figure 3.43.

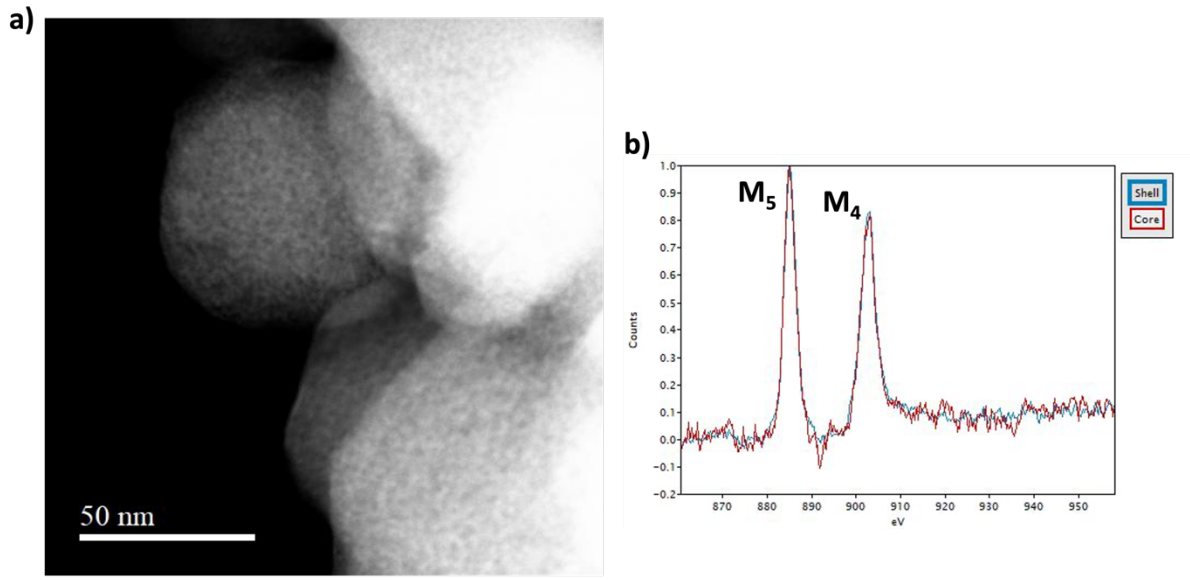

Figure 3.43: a) HAADF image of CeNP[oxd]@MOF808, b) EELS spectra of shell (outside) and core (inside) of CeNP[oxd]@MOF808 particle.

The M_5 edge is higher in intensity relative to the M_4 edge, as seen with the CeNP@MOF808 composite, which is indicative of the Ce^{3+} oxidation state dominating. This contradicts previous observations with XANES (see Figure 3.21) and XPS (Figure 3.32) analysis which suggest significant proportions of Ce^{4+}, 91% and 57%, respectively The large discrepancy in Ce^{3+} proportions determined using EELS compared to other oxidation state characterisation techniques was expected, given that EELS relies on a high energy beam of electrons as the excitation source which have been shown to reduce Ce^{4+} to Ce^{3+} *in-situ*.[100]

3.4.18 EELS Studies: Conclusions

In conclusion, EELS spectra of CeNP@MOF808 and CeNP[oxd]@MOF808 showed M_5/M_4 ratios that were suggestive of only the Ce^{3+} oxidation state being present in both samples. This contrasts with both XANES and XPS studies which showed, to different degrees based on bulk vs. surface specificity, that both samples contained a mixture of Ce^{3+} and Ce^{4+} states. The reason for this divergence in oxidation state determination most likely originates in the reduction of Ce^{4+} to Ce^{3+} states induced by the high energy electron beam.

3.4.19 Summary of Ce Oxidation States of CeNP@MOF808 and CeNP[oxd]@MOF808

Sample	Ce^{3+} (%)		Error
	CeNP@MOF808	CeNP[oxd]@MOF808	
XPS	100	43[a]	± 0.1 ▪ Vacuum applied ▪ High energy X-rays
XAS	75	9-12[c]	± 10
EELS	100	100[a]	▪ *In-situ* electron reduction
Raman	No F_{2g}	No F_{2g}	▪ Low loading weights of Ce
EDX (Ce wt%)[d]	2.78 (± 1.03)	4.06 (± 1.33)[b] 3.41 (± 0.90)[a]	▪ N/A

[a] Oxidation with 6% H_2O_2

[b] Oxidation with 0.6% H_2O_2

[c] Higher Ce^{3+} % for 0.6 % H_2O_2

[d] Errors reported as ± std. dev.

3.5 Conclusions

Following on from the successful development and application of the novel methodology of reactive infiltration, allowing for the synthesis of composite CeNP@MOF808, post-synthetic modifications were investigated. Two post-synthetic modifications were investigated: thermal treatments and oxidative treatments. The thermal post-synthetic modifications revealed a structural and crystalline stability of the composite up to 230 °C. Oxidative post-synthetic modifications showed loss of the composites crystallinity. Both post-synthetic modifications failed to yield successful formation of CeO_2 NP.

The relative proportions of Ce^{3+} and Ce^{4+} oxidation states are incredibly important to the chemical properties of cerium based materials, particularly in the field of catalytic applications. Therefore the ability to reliably identify and quantify Ce^{3+} and Ce^{4+} oxidation states is of significant importance. The work presented in Chapter 3 has demonstrated the importance of independent 'orthogonal' spectroscopic techniques in achieving the characterisation of Ce oxidation states. Through a combination of XANES, XPS and EELS studies it was possible to characterise the CeNP@MOF808 composite as having 3:1 Ce^{3+}:Ce^{4+} oxidation state proportions, with total dominance (*i.e.* 100%) of the Ce^{3+} state at the composite particle surface. The combination of independent spectroscopic techniques allowed for reliable characterisation of Ce oxidation states in post-synthetically modified CeNP@MOF808 samples.

3.6 Experimental Details for Chapter 3

3.6.1 Thermal Post-synthetic Modification Protocol

50 mg of each sample (control MOF808 or CeNP@MOF808) was weighed out accurately using an analytical grade balance into: a) a glass vial and placed subsequently into an oven for the low temperature treatments (120, 180 and 230 °C) or b) a ceramic heating dish and subsequently placed into a furnace for the high temperature treatments (550 °C and 650 °C). Each sample was thermally treated for one hour at the given temperature and then removed carefully using heat-proof gloves and tongs. The thermally treated samples were left to cool and if required were transferred back into a glass vial with a lid.

3.6.2 Oxidative Post-synthetic Modification Protocol

4 mL of a 30% w/v H_2O_2 aqueous solution was dissolved in deionised water, up to 20 mL, yielding a 6% w/v solution.

0.4 mL of a a 30% w/v H_2O_2 aqueous solution was dissolved in deionised water, up to 20 mL, yielding a 0.6% w/v solution.

Two separate centrifuge tubes were charged, separately, with 200 mg of CeNP@MOF808 and a small stirrer bar. 20 mL of 6% w/v H2O2 solution was added subsequently to the both centrifuge tubes. Effervescence and an immediate colour change, from off-white to orange, was observed upon addition of the H_2O_2 solution. The reaction mixtures were left for 10 minutes before being sonicated for 20 minutes, with the centrifuge tubes shaken and vented half-way to allow for release of any gases. The sonicated mixtures appeared as a cloudy, homogeneous suspensions and were left to stir at room temperature overnight. The mixtures were then centrifuged for 20 minutes at 4000 rpm, with solids subsequently isolated from the supernatant. Solids in both centrifuge tubes were then redispersed in 20 mL of deionised water, separately, and sonicated for 20 minutes – with shaking and venting half-way. Sonicated samples were stirred vigorously for 2 hours, after which solids were isolated *via*

centrifugation. The washing step outlined previously was repeated for a second time. The two washed samples were then stirred overnight in 40 mL of deionised water, separately. The samples were then centrifuged for 20 minutes at 4000 rpm, with the solids isolated from the supernatant and then combined using ca. 20 mL of deionised water. Single, combined sample slurry was centrifuged for 20 minutes at 4000 rpm. Solids isolated from the supernatant and transferred so a Schlenk flask where the sample was dried in vacuo (using external trap), at 60 °C in an oil bath, until the solids appeared visibly dry. The dried solids appeared orange and were then dried *in vacuo* (directly attached to Schlenk line), at 100 °C in an oil bath, for 18 hours and for a further 9 hours at 120 °C in an oil bath. Orange solids isolated after heating: $CeNP^{[oxd]}$@MOF808.

Process was repeated using 0.6% w/v H_2O_2 solution.

3.6.3 Thermogravimetric Analysis Measurements

Measurements for thermogravimetric analysis (TGA) were carried out using a TA Instruments Q-500 thermogravimetric analyser, with the sample (1–3 mg) held on a platinum pan under a continuous flow of either air or nitrogen gas. Measurements were collected from room temperature to 800 °C with a heating rate of 10 °C min^{-1}.

3.6.4 Powder X-ray Diffraction Measurements

Powder X-Ray Diffraction (PXRD) measurements were carried out at 298 K, in the Bragg-Brentano geometry, using a Rigaku Miniflex600 benchtop diffractometer CuK_α (λ = 1.4505 Å). Powdered samples were centred on a bracket and diffraction patterns were measured from 3 to 45° with a step size of 0.01° and speed of 10.0° min^{-1}. For all samples, the spinning speed of 10 rpm was used.

3.6.5 Infrared Spectroscopy Measurements

ATR – IR spectra were collected using a Shimadzu FTIR 8400S spectrometer. Abbreviations indicating strength of bands were used as follows: s = strong, m = medium, w = weak, sh = shoulder.

3.6.6 Energy Dispersive X-ray Spectroscopy Measurements

EDX measurements were obtained by James Gallagher, University of Glasgow, by taking three surface profiles on 3 separate particles to ensure representative elemental weight percentage, elemental weight percentages are determined as average values ± the standard deviation. Samples were scattered on pure carbon tabs and mounted on aluminium stubs. Samples were coated using a Polaron SC7640 sputter coater with Au/Pd target to make them electrically conductive. The EDX detector used was an Oxford Instruments X-act system with INCA 500 software and calibrated relative to a Cu reference. All EDX scans were taken at 5000 magnification.

3.6.7 Nuclear Magnetic Resonance Measurements

^{1}H NMR data was recorded on either a Bruker AVIII 400 MHz instrument or Bruker AVI 500 MHz instrument, referenced internally to the appropriate residual protio-solvent and reported relative to tetramethylsilane (δ = 0 ppm). All spectra were recorded at a constant temperature of 300 K. Coupling constants (J) are reported in hertz (Hz). Standard abbreviations indicating multiplicity were used as follows: m = multiplet, d = doublet, t = triplet, s = singlet. Digestion NMR data were obtained by suspending *ca.* 0.5 mg of sample in d_6-DMSO (2-3 mL) and mixing with 2-3 drops of D_2SO_4. Samples were sonicated for *ca.* 15 minutes to form a cloudy colloidal mixture that was transferred to a NMR tube and heated gently with agitation, up to 189 °C, until a clear solution formed.

3.6.8 Elemental Microanalysis Measurements

Elemental microanalysis acquired using an Exeter CE-440 elemental analyser. Samples measured in duplicate.

3.6.9 X-ray Absorption Spectroscopy Measurements

Samples prepared based on heavy elements weight percentages; with masses determined to ensure sufficient transmission of the X-ray beamline. Samples mixed with α – Cellulose into a fine homogenous powder and pressed into 1.3 cm^2 pellets using Specac Atlas GS15011 Manual Hydraulic Press at 1 – 3 tons of pressure. Measurements taken at the Ce L_3 edge (5723 eV). Si(111) double crystal monochromator was used to select the energies. Pt coated mirror used to reject higher harmonics from the beam. The photon flux of the incoming and transmitted X-ray beam was detected with two ionization chambers I_0 and I_t, respectively, filled with appropriate mixtures of N_2/Ar. A third ionization chamber (I_{ref}) was used in series to simultaneously measure a reference metal foil (Cr metal foil). Fluorescence data were collected using a 36 element solid state Ge detector. XANES absorption spectra were deconvoluted using empirical based peak fitting methods described in literature. The transition to continuum states, with the concurrent expulsion of a photoelectron, in the XANES spectra is accounted for using an arctangent function. The corrected XANES spectra are then fitted for using symmetric Gaussian functions.

3.6.10 X-ray Photoelectron Spectroscopy Measurements

XPS profiling was performed using a Thermo Scientific K-Alpha XPS system using monochromatic Al K_α radiation at 1486.6 eV X-ray source. CasaXPS software was used to analyse the binding energy of the data, referenced to adventitious C 1s peak at 284.8 eV. Ce 3d and O 1s regions were scanned at the surface and after a 300 seconds etch, with each scan lasting 20 seconds. Etching was achieved using an Ar ion beam with a voltage of 1 keV and current of 1.55 µA. Quantification of Ce^{3+} proportions was based on literature precedent, with peaks assigned based on positions, spin-orbit splitting (*ca.* 18.6 eV) and relative areas (spin-orbit split peak areas should have a ratio of ca. 0.67 based on degeneracy). Spin-orbit split peaks were each individually integrated based on the fitted Shirley background, with the ratio of sum areas taken to be proportional to the ratio of Ce^{3+}/Ce^{4+} proportions.

3.6.11 STEM and Electron Energy Loss Spectroscopy Measurements

High-angle annular dark-field scanning transmission electron microscopy (HAADF-STEM) and transmission electron microscopy (TEM) data were recorded on a probe-corrected JEOL ARM200cF instrument with a cold field emission source operating at an acceleration voltage of 200 kV. Elemental mapping was performed by electron energy-loss spectroscopy (EELS) using a Gatan 965 Quantum ER post-column spectrometer.

3.7 Supplementary Information for Chapter 3

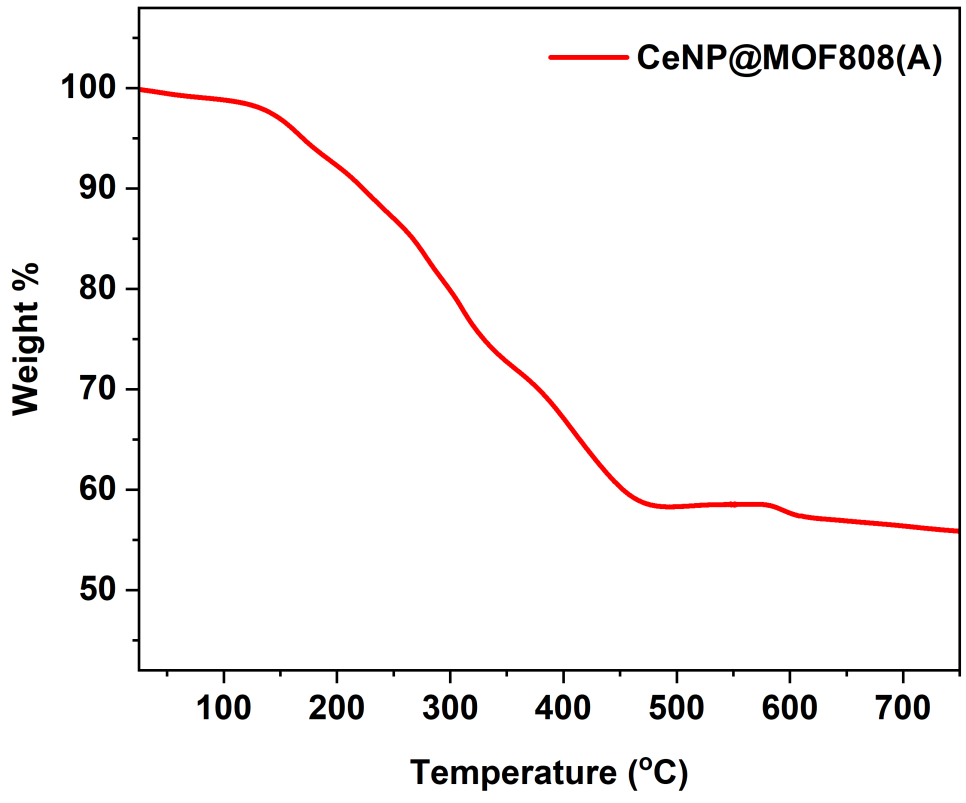

Supplementary Figure 3.1: TGA plot for CeNP@MOF808, under air.

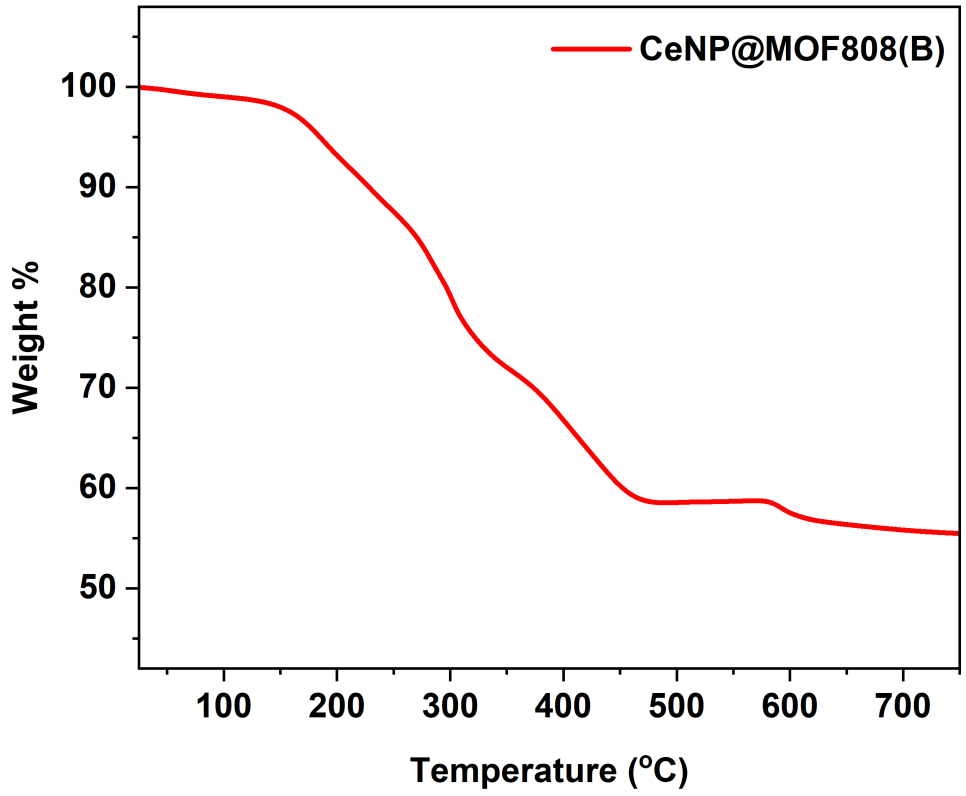

Supplementary Figure 3.2: TGA plot for CeNP@MOF808, replicated B, under air.

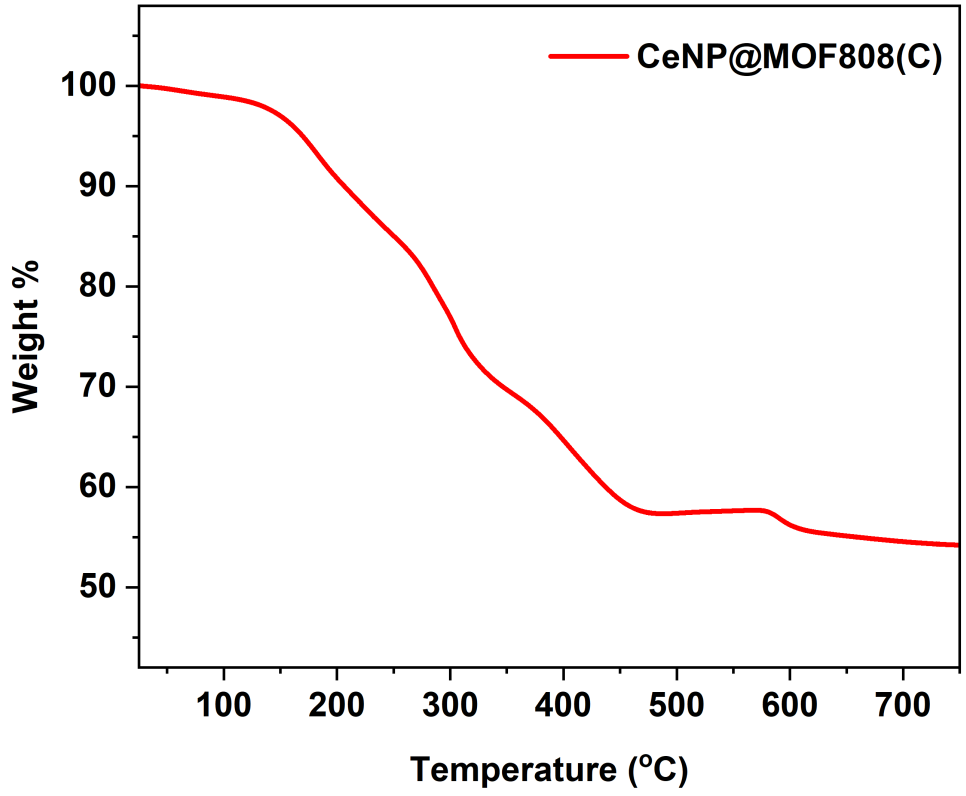

Supplementary Figure 3.3: TGA plot for CeNP@MOF808, replicated C, under air.

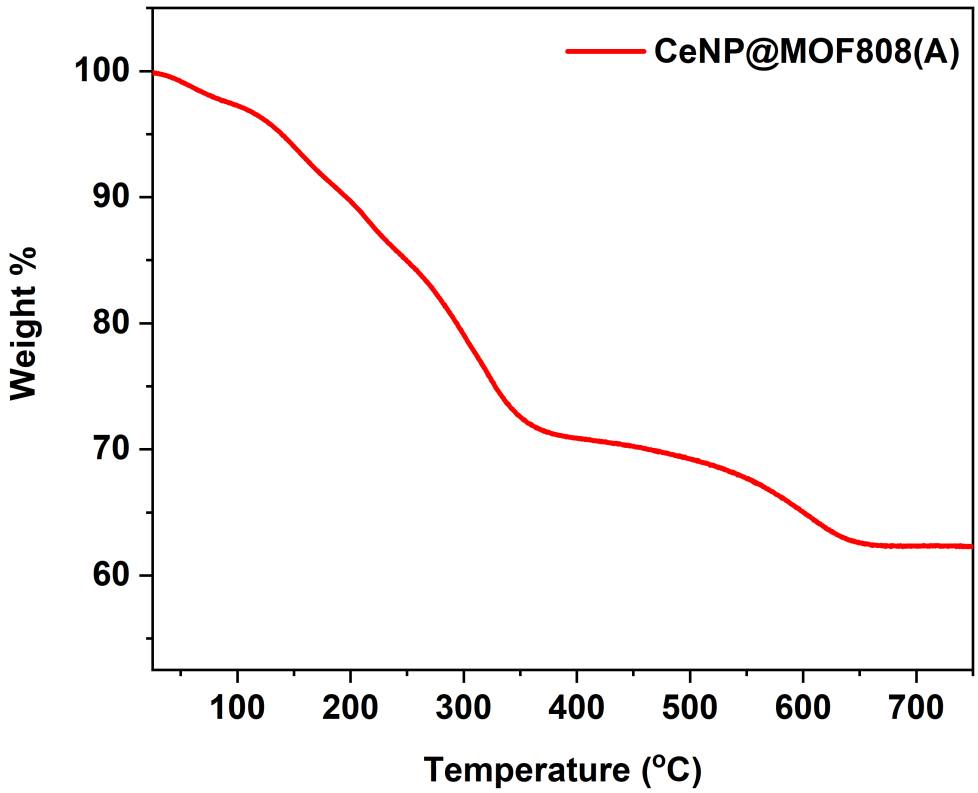

Supplementary Figure 3.4: TGA plot for CeNP@MOF808, under nitrogen.

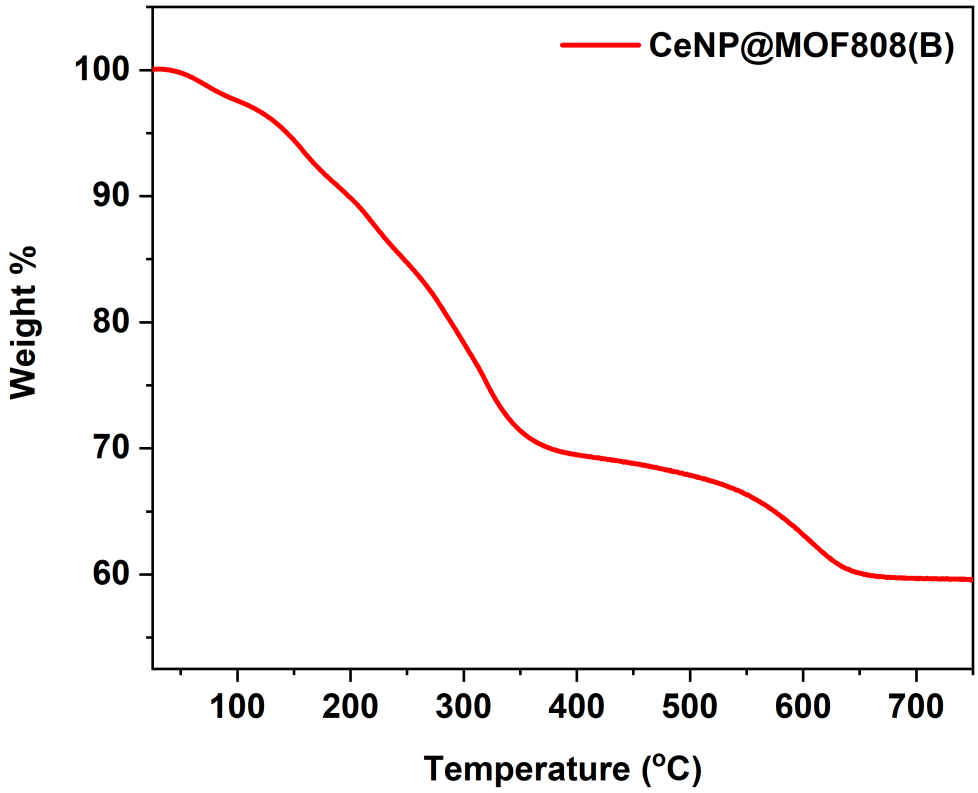

Supplementary Figure 3.5: TGA plot for CeNP@MOF808, replicated B, under nitrogen.

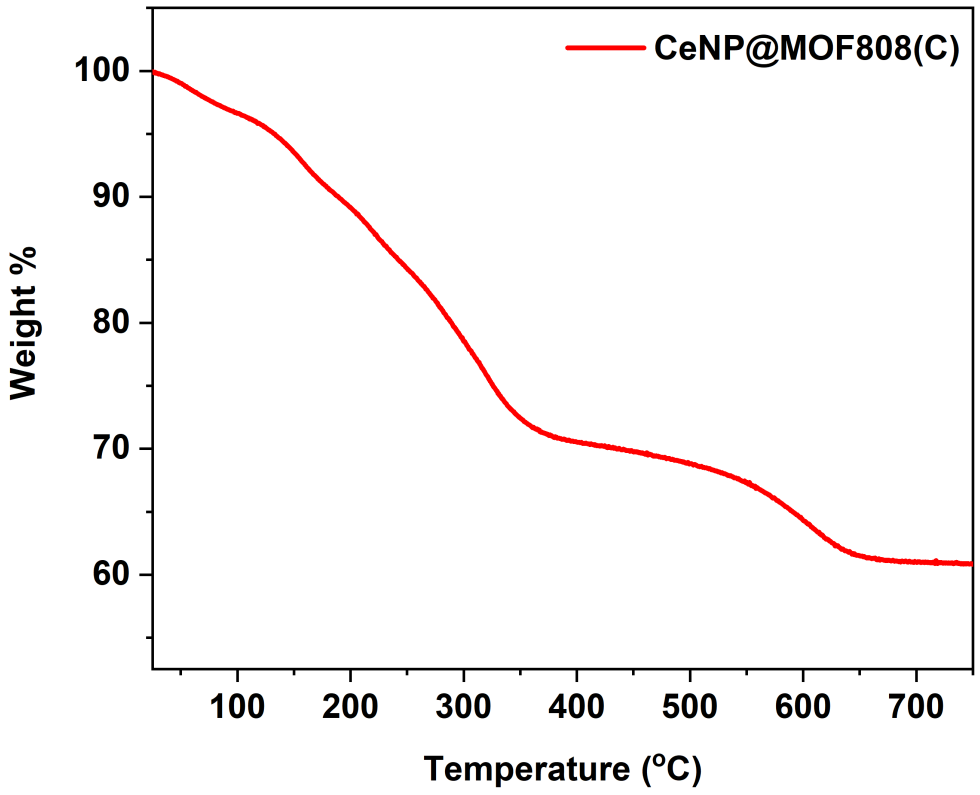

Supplementary Figure 3.6: TGA plot for CeNP@MOF808, replicated C, under nitrogen.

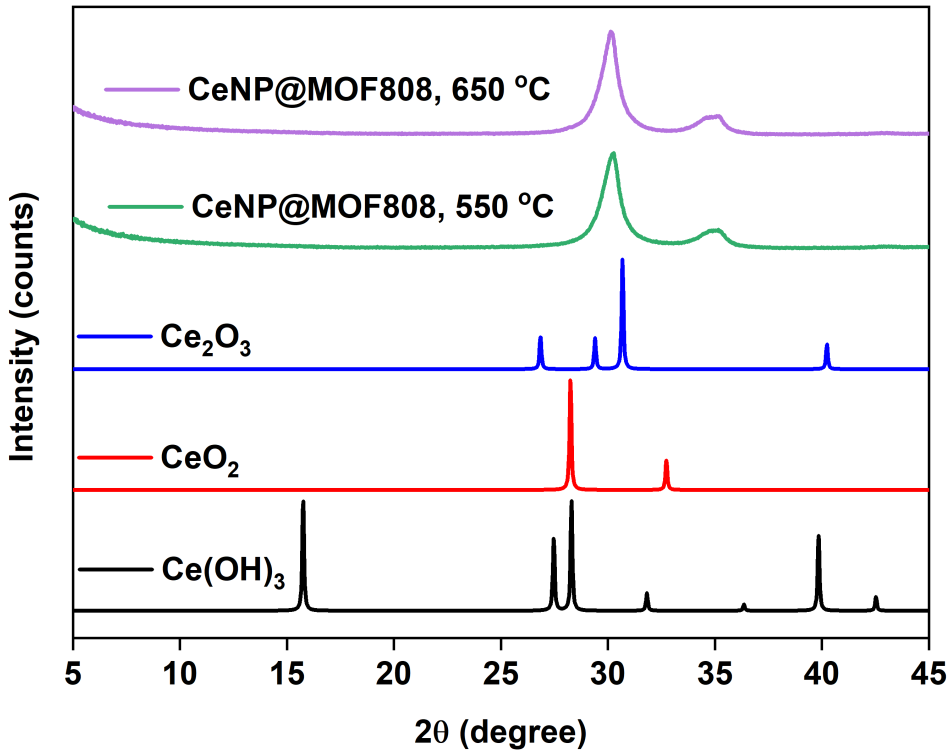

Supplementary Figure 3.7: Powder X-ray diffractograms of thermally treated CeNP@MOF808, at 550 °C and 650 °C, with reference Ce_2O_3, CeO_2 and $Ce(OH)_3$ diffractograms.

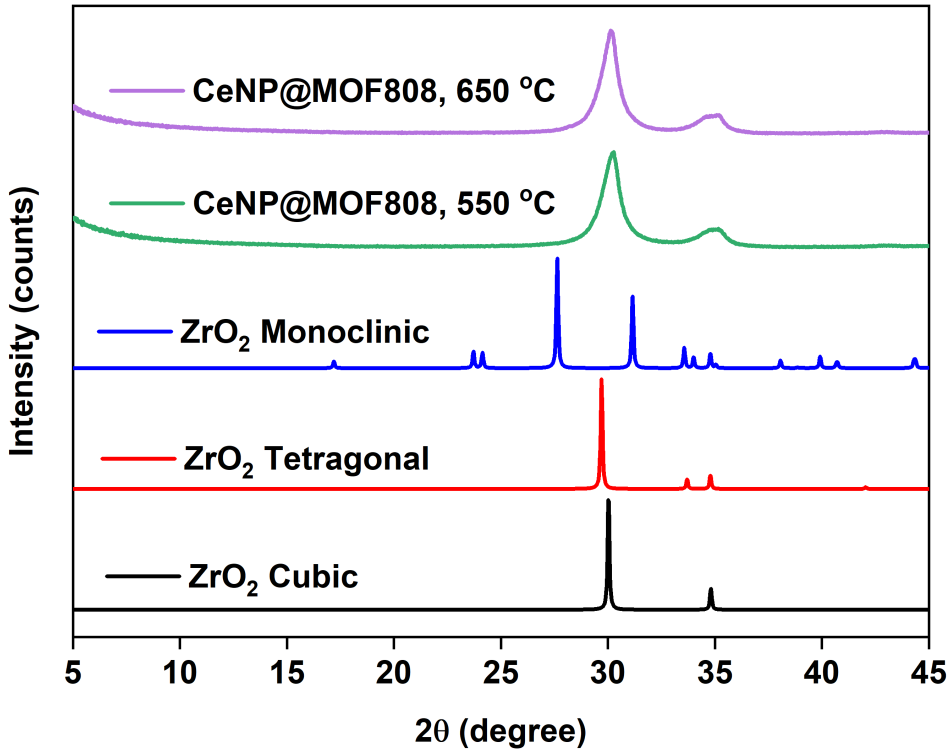

Supplementary Figure 3.8: Powder X-ray diffractograms of thermally treated CeNP@MOF808, at 550 °C and 650 °C, with reference ZrO_2 diffractograms.

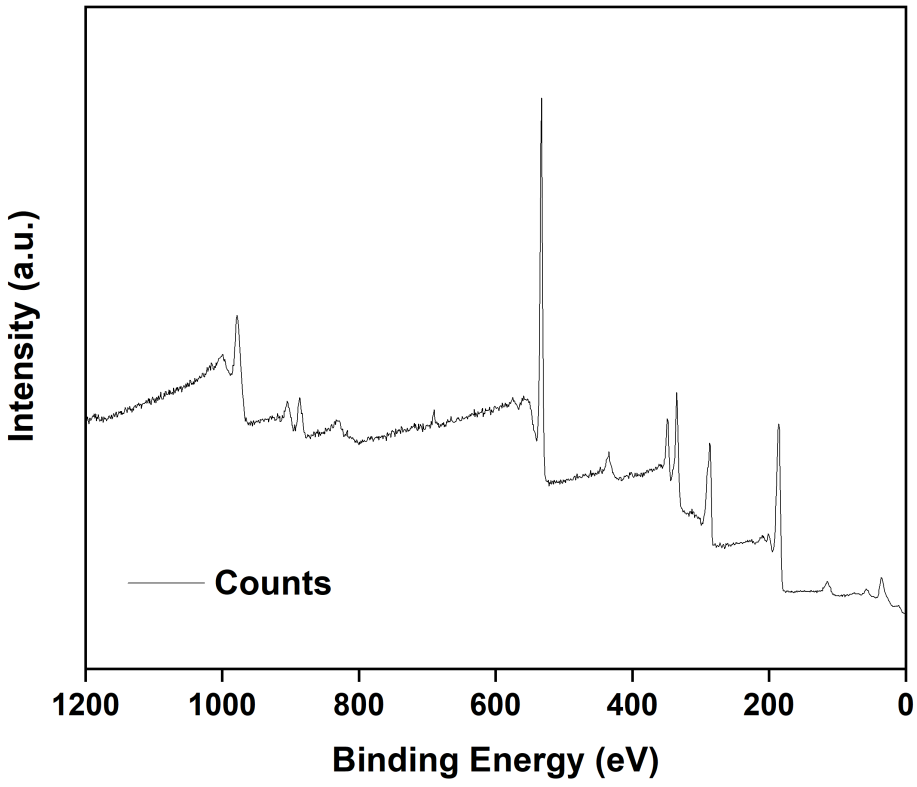

Supplementary Figure 3.9: XPS survey scan of CeNP@MOF808.

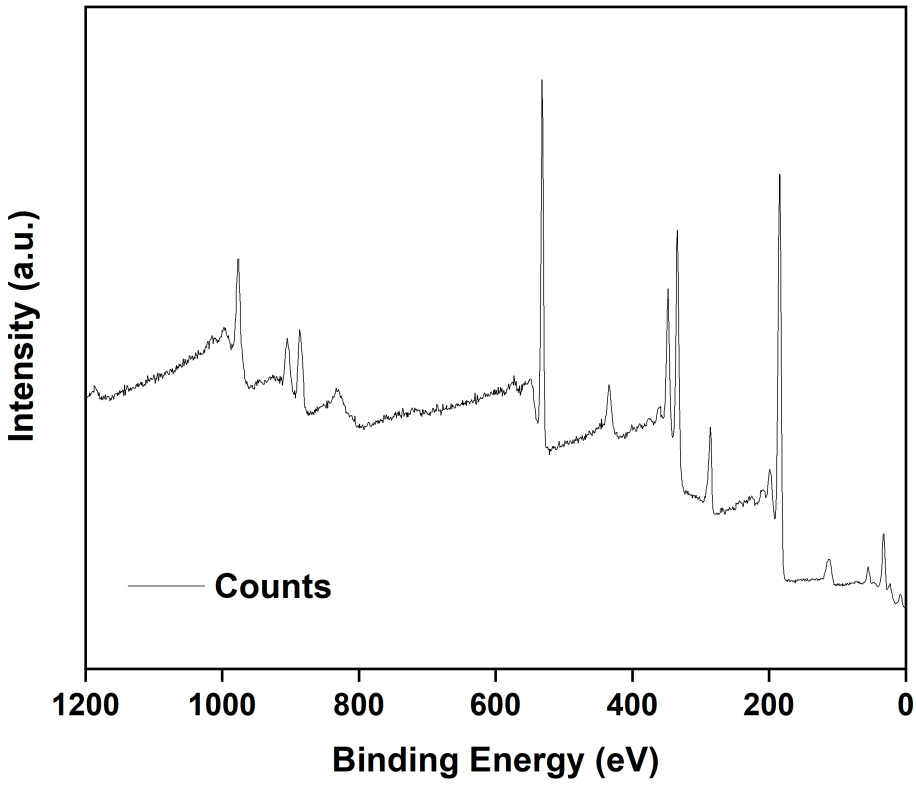

Supplementary Figure 3.10: XPS survey scan of CeNP@MOF808 (etched).

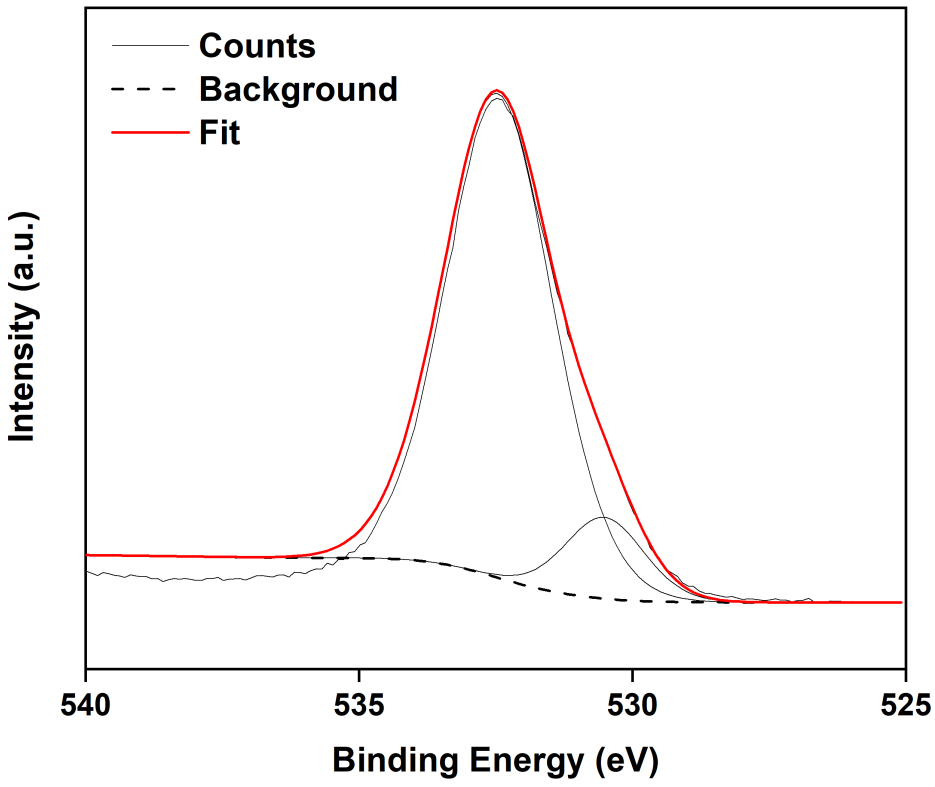

Supplementary Figure 3.11: O 1s XPS spectrum of CeNP@MOF808 (deconvoluted).

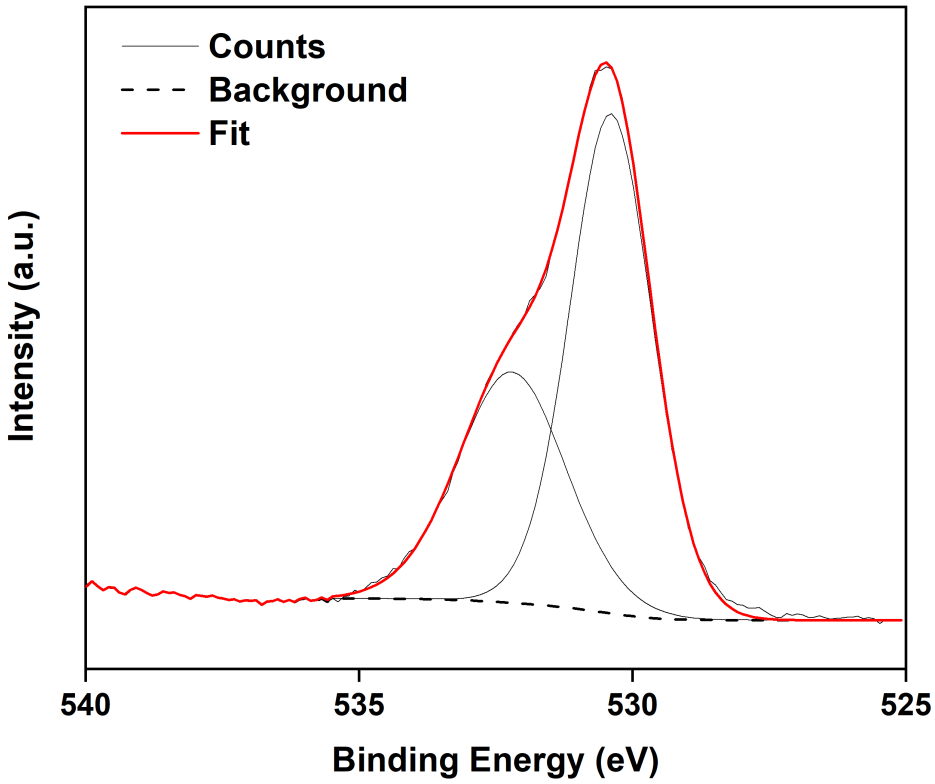

Supplementary Figure 3.12: O 1s XPS spectrum of CeNP@MOF808 (etched, deconvoluted).

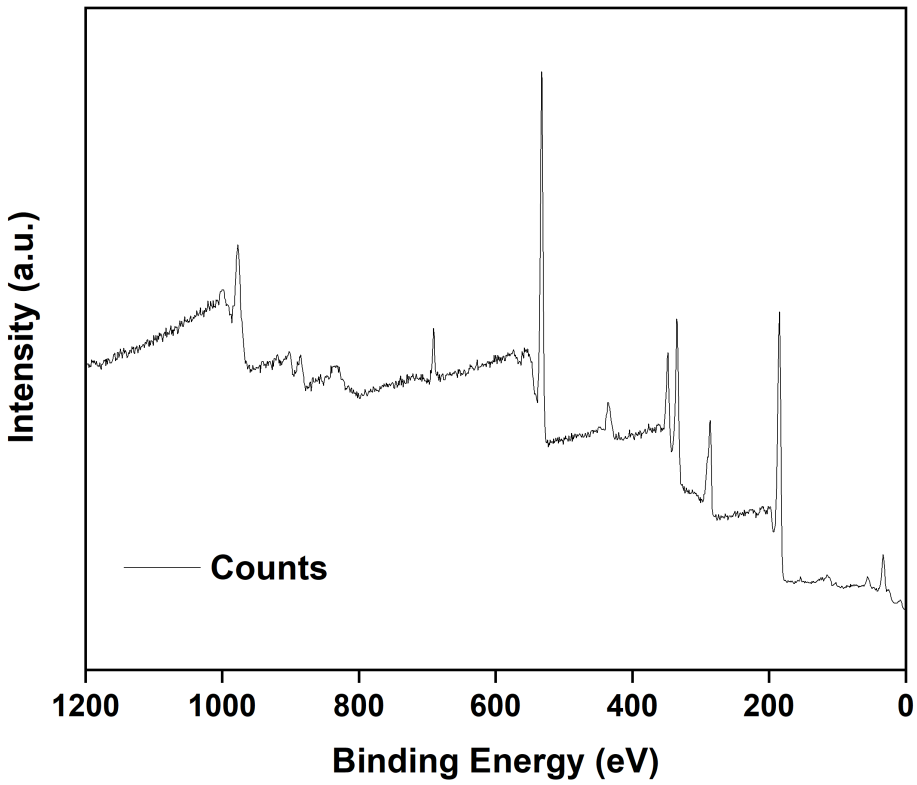

Supplementary Figure 3.13: XPS survey scan of CeNP$^{[oxd]}$@MOF808.

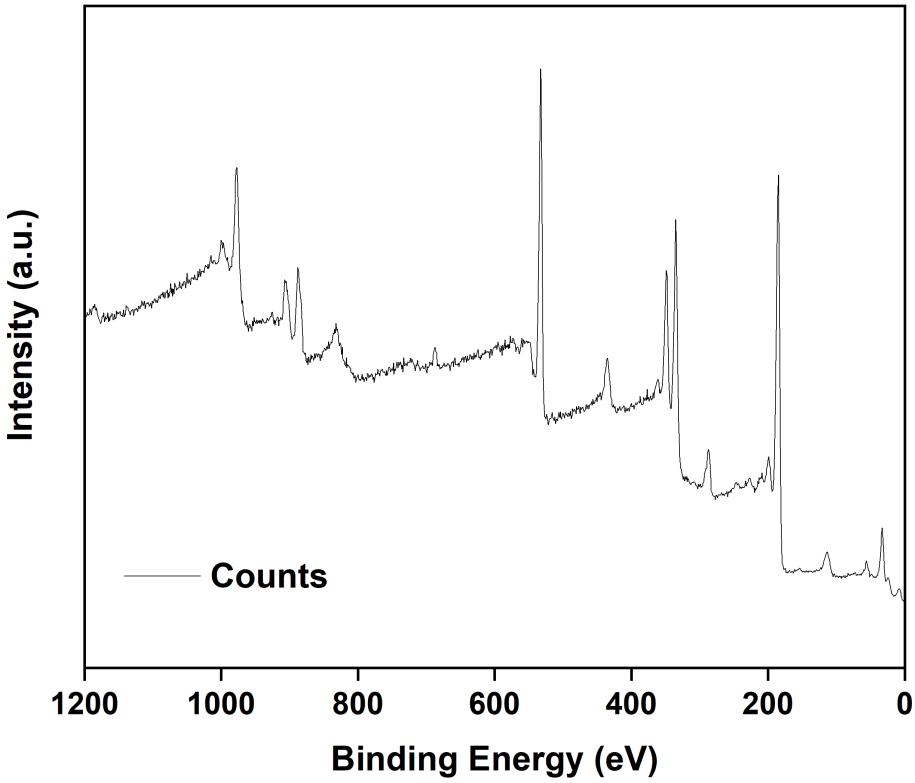

Supplementary Figure 3.14: XPS survey scan of CeNP$^{[oxd]}$@MOF808 (etched).

Supplementary Table 3.1: Selected peaks from the deconvolution of the XPS spectrum of CeNP$^{[oxd]}$@MOF808.

Peak	Centre (eV)	Area (a.u.)	FWHM	Height
1	917.58 (u''')	1611.0405	2.97026	501.75
2	904.48 (u')	3632.587	4.694	714.38
3	898.98 (v''')	2300.63	4.6945	476.16
4	906.48 (u'')	2308.228	9.02649	247.16
5	899.48 (u_o)	471.31	1.47032	296.34
6	901.78924 (u)	1413.3165	3.23432	403.34
7	886.21973 (v')	5447.2305	5.34435	941.14
8	886.28251 (v'')	3630.3835	5.34397	627.52
9	880.88 (v_o)	707.1285	2.17831	299.79
10	882.88 (v)	2119.743	2.49736	783.71

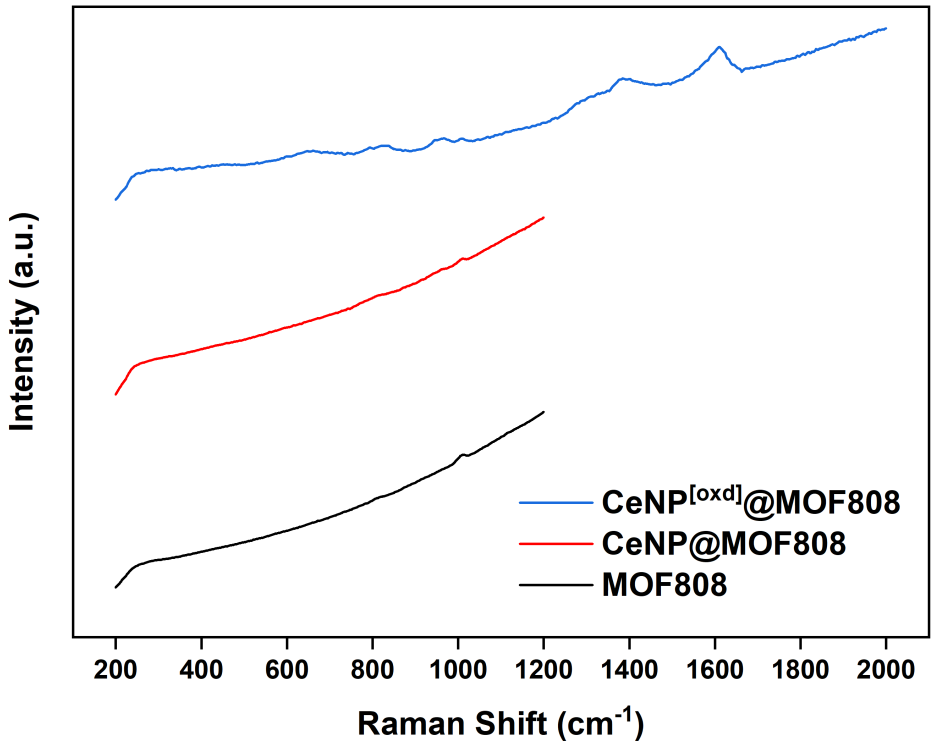

Supplementary Figure 3.15: Raman Spectra of Control MOF808, CeNP@MOF808 and CeNP$^{[oxd]}$@MOF808 (λ_{ex} = 325 nm; UV).

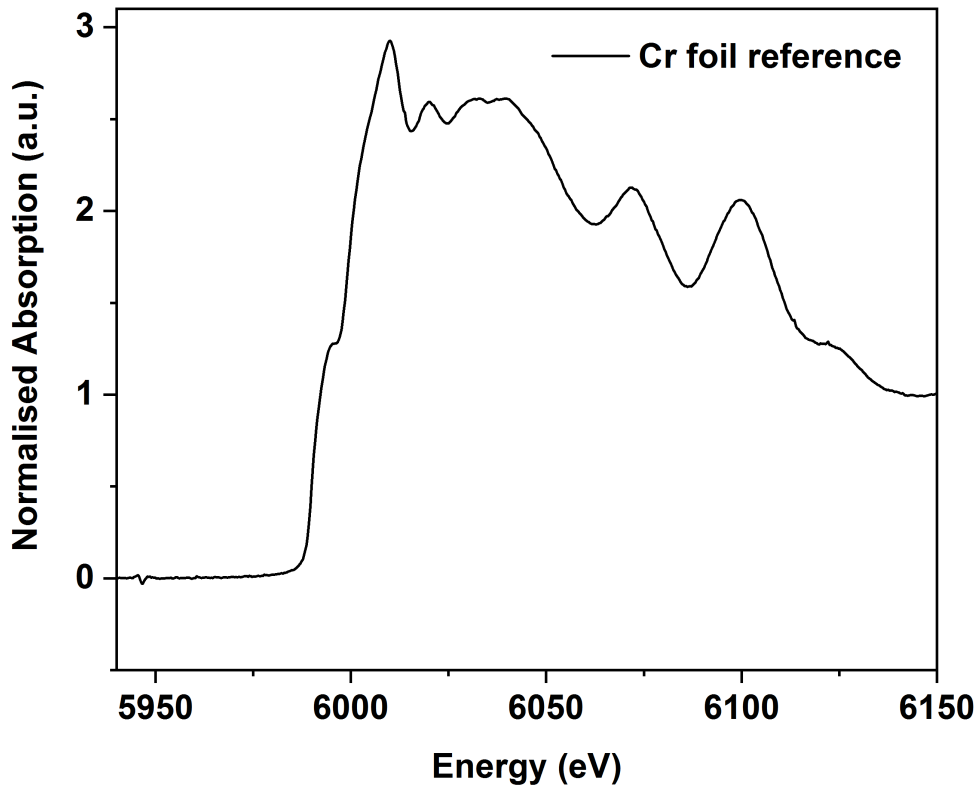

Supplementary Figure 3.16: XANES spectra of Cr foil; edge reference at 5989 eV.

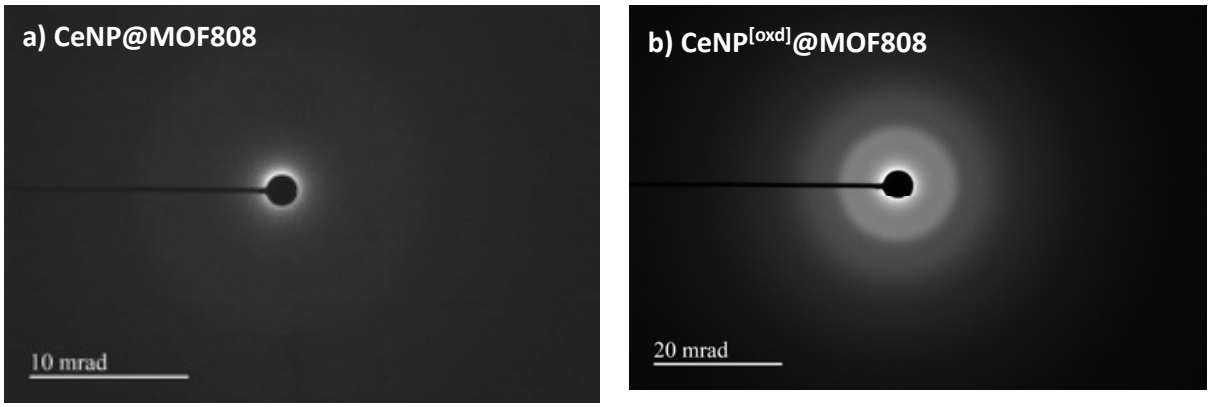

Supplementary Figure 3.17: TEM electron diffractograms of a) CeNP@MOF808 and b) CeNP$^{[oxd]}$@MOF808.

3.8 References for Chapter 3

1. C. Ardila-Suárez, A. M. Díaz-Lasprilla, L. A. Díaz-Vaca, P. B. Balbuena, V. G. Baldovino-Medrano and G. E. Ramírez-Caballero, *CrystEngComm*, 2019, **21**, 3014-3030.
2. E. Plessers, G. Fu, C. Y. X. Tan, D. E. De Vos and M. B. Roeffaers, *Catalysts*, 2016, **6**, 104.
3. A. Lin, A. A. Ibrahim, P. Arab, H. M. El-Kaderi and M. S. El-Shall, *ACS Applied Materials & Interfaces*, 2017, **9**, 17961-17968.
4. R. Sule and A. K. Mishra, *Applied Sciences*, 2019, **9**, 4407.
5. H. Lu, L. Zhang, B. Wang, Y. Long, M. Zhang, J. Ma, A. Khan, S. P. Chowdhury, X. Zhou and Y. Ni, *Cellulose*, 2019, **26**, 4909-4920.
6. M. Wilklow-Marnell and W. D. Jones, *Molecular Catalysis*, 2017, **439**, 9-14.
7. P. M. Shah, A. N. Day, T. E. Davies, D. J. Morgan and S. H. Taylor, *Applied Catalysis B: Environmental*, 2019, **253**, 331-340.
8. Q. Wang, K. L. Yeung and M. A. Bañares, *Catalysis Today*, 2020, **356**, 141-154.
9. A. Hayat, D. Andreescu, G. Bulbul and S. Andreescu, *Journal of colloid and interface science*, 2014, **418**, 240-245.
10. G. A. Bodkhe, B. S. Hedau, M. A. Deshmukh, H. K. Patil, S. M. Shirsat, D. M. Phase, K. K. Pandey and M. D. Shirsat, *Journal of Materials Science*, 2021, **56**, 474-487.
11. G. A. Bodkhe, B. S. Hedau, M. A. Deshmukh, H. K. Patil, S. M. Shirsat, D. M. Phase, K. K. Pandey and M. D. Shirsat, *Frontiers in Chemistry*, 2020, **8**, 803.
12. P. Hester, S. Xu, W. Liang, N. Al-Janabi, R. Vakili, P. Hill, C. A. Muryn, X. Chen, P. A. Martin and X. Fan, *Journal of Catalysis*, 2016, **340**, 85-94.
13. W. Liang, H. Chevreau, F. Ragon, P. D. Southon, V. K. Peterson and D. M. D'Alessandro, *CrystEngComm*, 2014, **16**, 6530-6533.
14. E. Aunan, C. W. Affolter, U. Olsbye and K. P. Lillerud, *Chemistry of Materials*, 2021, **33**, 1471-1476.

15. P. Khajuria, R. Mahajan and R. Prakash, *Journal of Materials Science: Materials in Electronics*, 2021, **32**, 27441-27448.
16. F. Shi, Y. Li, H. Wang and Q. Zhang, *Progress in Natural Science: Materials International*, 2012, **22**, 15-20.
17. D. Manoharan, A. Loganathan, V. Kurapati and V. J. Nesamony, *Ultrasonics Sonochemistry*, 2015, **23**, 174-184.
18. K. Healey, W. Liang, P. D. Southon, T. L. Church and D. M. D'Alessandro, *Journal of Materials Chemistry A*, 2016, **4**, 10816-10819.
19. M. Kohantorabi and M. R. Gholami, *Applied Physics A*, 2018, **124**, 1-17.
20. P. Periyat, F. Laffir, S. Tofail and E. Magner, *RSC advances*, 2011, **1**, 1794-1798.
21. C. Artini, G. A. Costa, M. Pani, A. Lausi and J. Plaisier, *Journal of Solid State Chemistry*, 2012, **190**, 24-28.
22. S. Sahoo*, M. Mohapatra, A. Singh and S. Anand, *Materials and Manufacturing Processes*, 2010, **25**, 982-989.
23. A. B. Sifontes, M. Rosales, F. J. Méndez, O. Oviedo and T. Zoltan, *Journal of Nanomaterials*, 2013, **2013**.
24. J. Feng, Y. Zhong, M. Xie, M. Li and S. Jiang, *Catalysis Letters*, 2021, **151**, 86-94.
25. J. Xu, J. Liu, Z. Li, X. Wang, Y. Xu, S. Chen and Z. Wang, *New Journal of Chemistry*, 2019, **43**, 4092-4099.
26. N. Horti, M. Kamatagi, S. Nataraj, M. Wari and S. Inamdar, *Nano Express*, 2020, **1**, 010022.
27. S. Kouva, K. Honkala, L. Lefferts and J. Kanervo, *Catalysis science & technology*, 2015, **5**, 3473-3490.
28. P. Abellan, T. Moser, I. T. Lucas, J. Grate, J. Evans and N. Browning, *RSC advances*, 2017, **7**, 3831-3837.
29. D. R. Bohn, F. O. Lobato, A. S. Thill, L. Steffens, M. Raabe, B. Donida, C. R. Vargas, D. J. Moura, F. Bernardi and F. Poletto, *Journal of Materials Chemistry B*, 2018, **6**, 4920-4928.

30. C. Ardila-Suárez, J. Rodríguez-Pereira, V. G. Baldovino-Medrano and G. E. Ramírez-Caballero, *CrystEngComm*, 2019, **21**, 1407-1415.
31. J. E. Efome, D. Rana, T. Matsuura and C. Q. Lan, *ACS applied materials & interfaces*, 2018, **10**, 18619-18629.
32. H.-Q. Zheng, Y.-N. Zeng, J. Chen, R.-G. Lin, W.-E. Zhuang, R. Cao and Z.-J. Lin, *Inorganic Chemistry*, 2019, **58**, 6983-6992.
33. H.-Q. Zheng, C.-Y. Liu, X.-Y. Zeng, J. Chen, J. Lü, R.-G. Lin, R. Cao, Z.-J. Lin and J.-W. Su, *Inorganic chemistry*, 2018, **57**, 9096-9104.
34. S. Banesh, V. Trivedi and S. Biswas, *Inorganic chemistry*, 2018, **57**, 14574-14581.
35. E. Smith and G. Dent, *Modern Raman spectroscopy: a practical approach*, John Wiley & Sons, 2019.
36. W. Weber, K. Hass and J. McBride, *Physical Review B*, 1993, **48**, 178.
37. R. Schmitt, A. Nenning, O. Kraynis, R. Korobko, A. I. Frenkel, I. Lubomirsky, S. M. Haile and J. L. Rupp, *Chemical Society Reviews*, 2020, **49**, 554-592.
38. M. H. Hassan, D. Andreescu and S. Andreescu, *ACS Applied Nano Materials*, 2020, **3**, 3288-3294.
39. S. Loridant, *Catalysis Today*, 2021, **373**, 98-111.
40. J. Cure, E. Mattson, K. Cocq, H. Assi, S. Jensen, K. Tan, M. Catalano, S. Yuan, H. Wang and L. Feng, *Journal of Materials Chemistry A*, 2019, **7**, 17536-17546.
41. O. Kraynis, I. Lubomirsky and T. Livneh, *The Journal of Physical Chemistry C*, 2019, **123**, 24111-24117.
42. D. P. Strommen and K. Nakamoto, *Journal of Chemical Education*, 1977, **54**, 474.
43. G. B. Della Mea, L. P. Matte, A. S. Thill, F. O. Lobato, E. V. Benvenutti, L. T. Arenas, A. Jürgensen, R. Hergenröder, F. Poletto and F. Bernardi, *Applied Surface Science*, 2017, **422**, 1102-1112.
44. C. M. Sims, R. A. Maier, A. C. Johnston-Peck, J. M. Gorham, V. A. Hackley and B. C. Nelson, *Nanotechnology*, 2018, **30**, 085703.
45. F. Zhang, P. Wang, J. Koberstein, S. Khalid and S.-W. Chan, *Surface Science*, 2004, **563**, 74-82.

46. S. Li, Y. Zhang, Z. Wang, W. Du and G. Zhu, *Chemistry Letters*, 2020, **49**, 461-464.
47. X. Fan, L. Li, F. Jing, J. Li and W. Chu, *Fuel*, 2018, **225**, 588-595.
48. K. Getty, M. U. Delgado-Jaime and P. Kennepohl, *Inorganica chimica acta*, 2008, **361**, 1059-1065.
49. A. Funatsuki, M. Takaoka, K. Shiota, D. Kokubu and Y. Suzuki, *Analytical Sciences*, 2016, **32**, 207-213.
50. J. K. Kowalska, F. A. Lima, C. J. Pollock, J. A. Rees and S. DeBeer, *Israel Journal of Chemistry*, 2016, **56**, 803-815.
51. S. D. Conradson, I. Al Mahamid, D. L. Clark, N. J. Hess, E. A. Hudson, M. P. Neu, P. D. Palmer, W. H. Runde and C. D. Tait, *Polyhedron*, 1998, **17**, 599-602.
52. F. Le Normand, L. Hilaire, K. Kili, G. Krill and G. Maire, *The Journal of Physical Chemistry*, 1988, **92**, 2561-2568.
53. F. Benedetti, L. Amidani, J. S. P. Cresi, F. Boscherini, S. Valeri, S. D'Addato, V. Nicolini, G. Malavasi and P. Luches, *Physical Chemistry Chemical Physics*, 2018, **20**, 23507-23514.
54. A. H. Clark, N. Acerbi, P. A. Chater, S. Hayama, P. Collier, T. I. Hyde and G. Sankar, *Physical Chemistry Chemical Physics*, 2020, **22**, 18882-18890.
55. H. R. Marchbank, A. H. Clark, T. I. Hyde, H. Y. Playford, M. G. Tucker, D. Thompsett, J. M. Fisher, K. W. Chapman, K. A. Beyer and M. Monte, *ChemPhysChem*, 2016, **17**, 3494-3503.
56. V. Jain, M. C. Biesinger and M. R. Linford, *Applied Surface Science*, 2018, **447**, 548-553.
57. Y. Takahashi, H. Sakami and M. Nomura, *Analytica Chimica Acta*, 2002, **468**, 345-354.
58. J. Liu, L. R. Redfern, Y. Liao, T. Islamoglu, A. Atilgan, O. K. Farha and J. T. Hupp, *ACS applied materials & interfaces*, 2019, **11**, 47822-47829.
59. D. Ferraro, I. G. Tredici, P. Ghigna, H. Castillio-Michel, A. Falqui, C. Di Benedetto, G. Alberti, V. Ricci, U. Anselmi-Tamburini and P. Sommi, *Nanoscale*, 2017, **9**, 1527-1538.

60. W. Zhang, Y. Dan, H. Shi and X. Ma, *ACS Sustainable Chemistry & Engineering*, 2016, **4**, 5424-5431.
61. S. V. Kuchibhatla, A. S. Karakoti, D. R. Baer, S. Samudrala, M. H. Engelhard, J. E. Amonette, S. Thevuthasan and S. Seal, *The Journal of Physical Chemistry C*, 2012, **116**, 14108-14114.
62. L. Chen, R. Luque and Y. Li, *Chemical Society Reviews*, 2017, **46**, 4614-4630.
63. Q. Yang, Q. Xu and H.-L. Jiang, *Chemical Society Reviews*, 2017, **46**, 4774-4808.
64. I. Sharma and S. K. Pattanayek.
65. Z. Assefa, R. Haire, D. Caulder and D. Shuh, *Spectrochimica Acta Part A: Molecular and Biomolecular Spectroscopy*, 2004, **60**, 1873-1881.
66. D. R. Modeshia, C. S. Wright, J. L. Payne, G. Sankar, S. G. Fiddy and R. I. Walton, *The Journal of Physical Chemistry C*, 2007, **111**, 14035-14039.
67. J. E. Penner-Hahn, *Comprehensive Coordination Chemistry II*, 2003, **2**, 159-186.
68. M. Newville, 2014.
69. D. F. Mullica, J. D. Oliver and W. Milllgan, *Acta Crystallographica Section B: Structural Crystallography and Crystal Chemistry*, 1979, **35**, 2668-2670.
70. W. Zachariasen, *Zeitschrift für Physikalische Chemie*, 1926, **123**, 134-150.
71. E. K. Dann, E. K. Gibson, R. A. Catlow, P. Collier, T. Eralp Erden, D. Gianolio, C. Hardacre, A. Kroner, A. Raj and A. Goguet, *Chemistry of Materials*, 2017, **29**, 7515-7523.
72. P. C. Deshmukh and S. Venkataraman, *Bulletin of Indian Physics Teachers Association, published in two parts: September & October Issues of*, 2006.
73. C. S. Fadley, *Journal of Electron Spectroscopy and Related Phenomena*, 2010, **178**, 2-32.
74. B. Ziaja, D. van der Spoel, A. Szöke and J. Hajdu, *Physical Review B*, 2001, **64**, 214104.
75. C. J. Powell, *Journal of Vacuum Science & Technology A: Vacuum, Surfaces, and Films*, 2020, **38**, 023209.
76. M.-N. Shariati, Acta Universitatis Upsaliensis, 2012.

77. N. Radutoiu and C. Teodorescu, *Digest Journal of Nanomaterials & Biostructures (DJNB)*, 2013, **8**.
78. S. Deshpande, S. Patil, S. V. Kuchibhatla and S. Seal, *Applied Physics Letters*, 2005, **87**, 133113.
79. M. Romeo, K. Bak, J. El Fallah, F. Le Normand and L. Hilaire, *Surface and Interface Analysis*, 1993, **20**, 508-512.
80. A. Laachir, V. Perrichon, A. Badri, J. Lamotte, E. Catherine, J. C. Lavalley, J. El Fallah, L. Hilaire, F. Le Normand and E. Quéméré, *Journal of the Chemical Society, Faraday Transactions*, 1991, **87**, 1601-1609.
81. M. C. Spadaro, S. D'Addato, G. Gasperi, F. Benedetti, P. Luches, V. Grillo, G. Bertoni and S. Valeri, *Beilstein Journal of Nanotechnology*, 2015, **6**, 60-67.
82. I. Bespalov, M. Datler, S. Buhr, W. Drachsel, G. Rupprechter and Y. Suchorski, *Ultramicroscopy*, 2015, **159**, 147-151.
83. J. Liu, M. Liao, M. Imura, A. Tanaka, H. Iwai and Y. Koide, *Scientific Reports*, 2014, **4**, 1-5.
84. Z.-J. Lin, H.-Q. Zheng, Y.-N. Zeng, Y.-L. Wang, J. Chen, G.-J. Cao, J.-F. Gu and B. Chen, *Chemical Engineering Journal*, 2019, **378**, 122196.
85. G. Chen, E. J. H. Cheung, Y. Cao, J. Pan and A. J. Danner, *Nanoscale Research Letters*, 2021, **16**, 1-9.
86. H. S. Fogler and S. H. Fogler, *Elements of chemical reaction engineering*, Pearson Educacion, 1999.
87. S. G. Wolf, E. Shimoni, M. Elbaum and L. Houben, in *Cellular Imaging*, Springer, 2018, pp. 33-60.
88. S. Hillyard and J. Silcox, *Ultramicroscopy*, 1995, **58**, 6-17.
89. O. L. Krivanek, M. F. Chisholm, V. Nicolosi, T. J. Pennycook, G. J. Corbin, N. Dellby, M. F. Murfitt, C. S. Own, Z. S. Szilagyi, M. P. Oxley, S. T. Pantelides and S. J. Pennycook, *Nature*, 2010, **464**, 571-574.
90. J. Zhang, N. Cheng and B. Ge, *Advances in Physics: X*, 2022, **7**, 2046157.

91. K. Leus, J. Dendooven, N. Tahir, R. K. Ramachandran, M. Meledina, S. Turner, G. Van Tendeloo, J. L. Goeman, J. Van der Eycken, C. Detavernier and P. Van Der Voort, *Nanomaterials*, 2016, **6**, 45.
92. G. Li, S. Zhao, Y. Zhang and Z. Tang, *Advanced Materials*, 2018, **30**, 1800702.
93. D. Esken, S. Turner, C. Wiktor, S. B. Kalidindi, G. Van Tendeloo and R. A. Fischer, *Journal of the American Chemical Society*, 2011, **133**, 16370-16373.
94. Y. Shen, T. Pan, P. Wu, J. Huang, H. Li, I. E. Khalil, S. Li, B. Zheng, J. Wu, Q. Wang, W. Zhang, W. D. Wei and F. Huo, *CCS Chemistry*, 2021, **3**, 1607-1614.
95. M. S. Denny, L. R. Parent, J. P. Patterson, S. K. Meena, H. Pham, P. Abellan, Q. M. Ramasse, F. Paesani, N. C. Gianneschi and S. M. Cohen, *Journal of the American Chemical Society*, 2018, **140**, 1348-1357.
96. Q. J. Wang and Y.-W. Chung, *Encyclopedia of tribology*, Springer, 2013.
97. J. Fortner and E. Buck, *Applied physics letters*, 1996, **68**, 3817-3819.
98. L. Wu, H. Wiesmann, A. Moodenbaugh, R. Klie, Y. Zhu, D. Welch and M. Suenaga, *Physical Review B*, 2004, **69**, 125415.
99. X. Hao, A. Yoko, C. Chen, K. Inoue, M. Saito, G. Seong, S. Takami, T. Adschiri and Y. Ikuhara, *Small*, 2018, **14**, 1802915.
100. A. C. Johnston-Peck, J. S. DuChene, A. D. Roberts, W. D. Wei and A. A. Herzing, *Ultramicroscopy*, 2016, **170**, 1-9.

4 Catalytic Applications of CeNP@MOF808: Hydrolysis of DMNP

4.1 Abstract

Zirconium based metal organic frameworks. such as MOF808, have been shown previously to catalyse the hydrolysis of nerve agent simulants such as dimethyl *p*-nitrophenylphosphate (DMNP). Computational studies have shown that the hydrolysis of DMNP occurs at the Zr cluster nodes of the framework. However, studies looking into the enhancement of catalytic rates by introduction of a secondary, cooperative metal sites are limited. The design and optimisation of experimental procedures using ^{31}P NMR spectroscopy for measuring the rate of DMNP hydrolysis using heterogeneous catalyst CeNP@MOF808 is herein reported. Optimisation of the experimental procedures involved identifying and controlling for a number of experimental variables including quantity of catalyst, sonication time of catalyst suspension and time delay between sonication of catalyst suspension ceasing and subsequent mixing with DMNP. Sonication of the catalyst suspension was found to be essential for successful catalysis, as well as the minimisation of the time delay between sonication and addition of DMNP. In order to build statistically reliable data sets, multiple repeat measurements were made using both CeNP@MOF808 and control MOF808 as catalytic materials. Control reactions were also run without catalytic material and without *N*-ethylmorpholine. DMNP hydrolysis conversion plots were fitted using negative exponential decay functions ($f(x) = y_0 + A_1e^{-x/t1}$) with average $t_{1/2}$ values for CeNP@MOF808 and control MOF808 composites being 2.4 minutes and 3.7 minutes, respectively. After removal of an experimental outlier, the average $t_{1/2}$ value for CeNP@MOF808 was reduced to 1.9 minutes. This was statistically faster than that of control MOF808. These results demonstrate that the addition of redox active CeNPs into the MOF framework enhances the catalytic activity of the MOF towards the hydrolysis of nerve agent simulant DMNP, which we postulate to be due to cooperative effects between CeNP and Zr_6 cluster nodes. These results demonstrate the applicability of the CeNP@MOF808 composite as a catalyst in the hydrolysis of an organophosphate chemical weapon simulant, DMNP, and we anticipate this will allow for further investigation into alternative, industrially relevant catalytic reactions involving phosphate based reagents (*e.g.* nerve agents, pesticides and pollutants).

4.2 General Introduction to Chemical Weapons and Nerve Agents

Following on from the successful optimisation of reactive infiltration with CeN''_3 and MOF808 and characterisation, both structural and electronic, of the resulting composite CeNP@MOF808, it was postulated that the high proportion of Ce^{3+} (75 – 100%) coupled with the presence of Zr^{4+} centres may offer a potent catalytic system. Several nerve agent hydrolysis reaction systems have been observed in the literature to be catalysed by inorganic substances featuring Ce and/or Zr centres. The most notable, and widely applied example, is the adoption of CeO_2/ZrO_2 three-way catalytic convertors in the conversion of harmful NO_x, CO and unburned hydrocarbons into N_2 and CO_2. However, given the specialised reaction set-up required to monitor these reactions and the thermal stability of the composite (crystallinity lost between 230 – 320 °C and decomposition onset beyond 320 °C, see Chapter 3), it was concluded that catalytic conversion of combustion product gases was not an appropriate reaction to probe the catalytic abilities of the composite, with the MOF808 host being unsuited for the reaction conditions. Indeed what was required was a simple reaction which has shown to be catalysed by Ce/Zr materials (homogeneous or heterogeneous), which could be monitored using standard laboratory analytical apparatus (*e.g.* NMR, UV-vis, chromatography *etc*.) and had industrial/society utility (*i.e.* served a wider purpose with an application). To this end, it was concluded that the degradation of organophosphate nerve agents was an appropriate reaction to screen the catalytic potential of the composite. The catalytic degradation of nerve agents has been demonstrated in various studies using Ce/Zr materials, and specifically Zr-MOF based materials. Furthermore the degradation reaction can be easily monitored using standard analytical techniques. It is important at this point to highlight the immense utility of a composite material that is able to decompose nerve agents, given their lethal potency at small doses (*e.g.* milligram quantities of nerve agents can kill an adult human) the ability to quickly destroy these chemicals is of significant importance to society.

It is essential to understand the general properties of chemical weapons, nerve agents in particular, and the research so far in developing catalytic materials to quickly and safely degrade them. In the following sections I will set out a concise overview of nerve agents, the attempts made to develop materials to catalytically degrade nerve agents (both

homogeneously and heterogeneously) and present a summary of catalytic abilities of these materials expressed as $t_{1/2}$ values (*i.e.* the time taken for half the nerve agent to degrade).

4.3 General Introduction to Chemical Weapons and Nerve Agents

The Chemical Weapons Conventions (CWC) invited national signatories in 1993 and was brought into international law in 1997 with the establishment of the Organisation for the Prohibition of Chemical Weapons (OPCW), which still operates internationally to this day. The CWC divides chemical weapons, also termed chemical warfare agents (CWA), into three schedules, each of which have legally binding obligations from signatory nations. Chemical warfare agents are chemical substances that possess toxic properties and are used to kill, injure or incapacitate human beings. Chemical warfare agents can be simple substances such as chlorine gas, which was used during WW1 by both allied and central powers, or more advanced reagents that are coupled with vectorisation agents to help them disperse (*e.g.* nerve agent aerosols). Chemical warfare agents can be classified based on their mechanisms of action and their resulting physiological effects on human beings (see Figure 4.1).[1] Over the last decade (2011 – 2021), due to several international incidents involving the use of nerve agents, materials that can efficiently breakdown nerve agents have become a prime topic of interest among the scientific community.

Nerve agents are composed of phosphorus based compounds, organophosphates, and are highly toxic even in small quantities: a single drop of the VX agent can cause rapid death to a human being. The general structure of organophosphates was first described in 1937 by Schrader with the important distinction being made that not all organophosphates are highly toxic to human beings, with many organophosphates finding use as pest-control agents in the agricultural industry, particularly in the developing world.[2,3] Organophosphates can be manufactured on a large scale, are liquid at room temperature and atmospheric pressure and can be dispersed as fine aerosol sprays, making them ideal candidates as chemical weapons, yielding significant harm. Nerve agents can be divided into two sub-groups based on historical developments and differences in volatility: G-series (volatile) and V-series (non-volatile), see Figure 4.1. This is an important consideration as the volatility of a nerve agent determines its best suited mode of delivery and hence dictates the required methodology of destruction

and/or treatment. For example, volatile G-type nerve agents are expected to be absorbed very quickly through the mucous membranes leading to rapid poisoning and requiring immediate treatment. In contrast, percutaneous exposure of non-volatile V-type nerve agents would result in a slow build-up of toxic blood levels. As a consequence, the recognisable symptoms of nerve agent poisoning are not immediate, and will only develop after a time delay, possibly up to several hours. The differences in volatility also result in very different natural persistence times, G-series agents such as Sarin (GB) will only persist in soil in convenient climates (sunshine, slight wind, 15 °C) for several hours, while V-series agent can persist for much longer periods of time (*e.g.* at – 10 °C and dry climates, they can last for up to 4 months).[2]

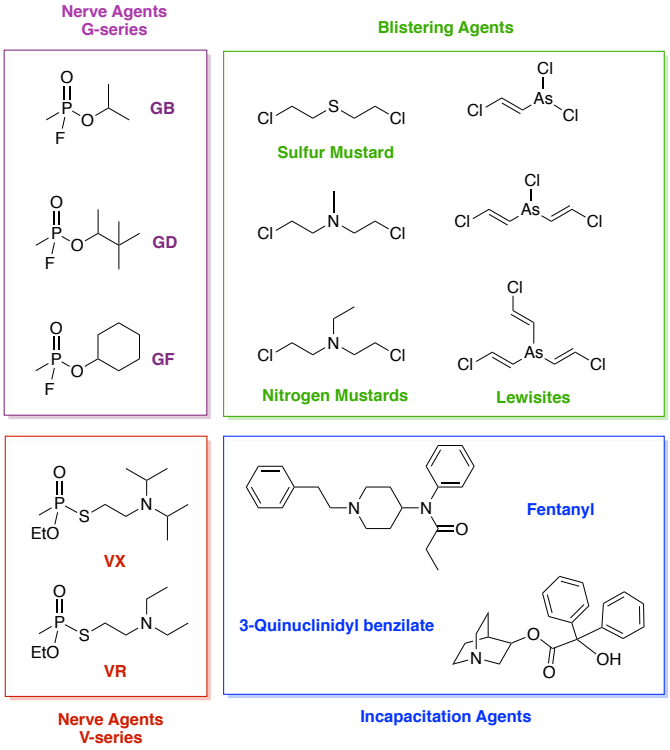

Figure 4.1: Selected Chemical Warfare Agents based on their resulting physiological effects.

Nerve agents, and organophosphates in general, have the same general mechanism of action within the human body: the inhibition of serine esterases such as acetylcholinesterase (AChE), carboxylesterases and neuropath target esterase.[2] Acetylcholine (Ach) is neurotransmitter, found at the synapses of neurons within neural networks in close proximity to receptor cells, acting as a chemical carrier for electrical nerve impulses between neurons by binding to

receptor cells. AChE is a highly efficient enzyme that catalyses the hydrolysis of Ach (10,000 Ach molecules broken down per second), freeing the receptor cells of ACh and allowing the nervous and muscular systems to come to rest.[2] Once in the blood stream, the nerve agent molecule binds covalently and irreversibly to the serine residue of the AChE active site, rendering the enzyme inactive (see Scheme 4.1). This results in a build-up of Ach on receptor cells, yielding muscular spasms, respiratory failure and fatal cardiac arrest.[1] Even in the unlikely event of survival, the nerve agents can cross the blood-brain barrier and cause severe brain damage.

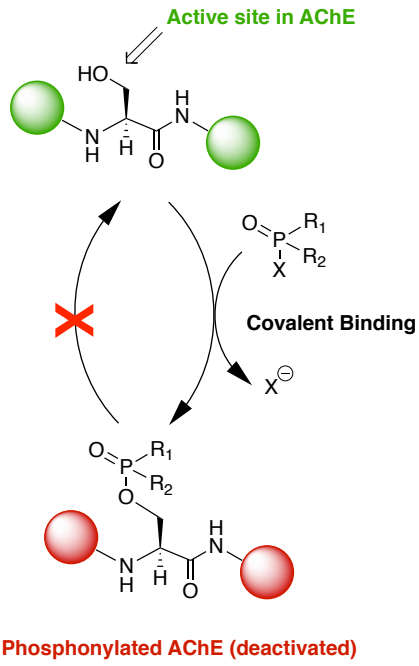

Scheme 4.1: Irreversible covalent binding of general organophosphate structure to serine residue of AChE active site.

Multiple mechanisms exist for dealing with nerve agent exposure, including therapeutic treatments for those suffering from nerve agent poisoning and defensive actions in anticipation of exposure, such as coatings, filters and decontamination of contaminated areas and objects. Decontamination of contaminated areas falls into one of two categories: one-step, destruction based on pyrolysis or neutralisation based on chemical treatments.[4] Pyrolysis based destructions allows for the full and irreversible destruction of nerve agents and contaminated objects using extreme conditions of heat and pressure, requiring specific

heavy duty equipment on a dedicated site. Neutralisation by contrast occurs under less drastic conditions and is highly versatile with numerous methodologies available, the most common and efficient being hydrolysis of the nerve agent under basic conditions.[4]

4.4 Ce and Zr Catalysis for Nerve Agent Hydrolysis

4.4.1 Homogeneous Ce and Zr Catalysts for Nerve Agent Hydrolysis

While the CeNP@MOF808 composite is in the solid state compared to the reactants in an aqueous state (therefore heterogeneous based catalysis), it is important to highlight that several examples have been noted in the literature of successful organophosphate and nerve agent hydrolysis using Ce and Zr homogeneous catalysts. Often in the literature mechanisms are presented to explain the catalytic hydrolysis of the nerve agent, while these would most likely be different to that of the CeNP@MOF808 composite, there may be similarities which are important to understand. There are a number of terms that are employed to describe the destruction of nerve agent materials, including neutralisation, hydrolysis and decomposition. These are often used interchangeably in the literature despite their chemical differences. In this chapter, the destruction of nerve agents will be referred to as hydrolysis unless water is not a participating reactant (*e.g*. methanolysis with methanol).

Aqueous solutions of Zr^{4+} and Ce^{4+} salts have been shown to exhibit catalytic activity towards the hydrolysis of organophosphates. The hydrolysis of dimethyl phosphonoformate (DMPF) was shown to be significantly enhanced by the presence of Zr^{4+} and Ce^{4+} cations, under acidic conditions (pH 1.7-3.1).[5] The reaction kinetics were monitored *via* ^{1}H NMR by following the formation of MeOD, with pseudo-first-order rate constants (k_{obs}) of 4.4×10^{-4} s^{-1} and 5.2×10^{-4} s^{-1} for Zr^{4+} and Ce^{4+}, respectively at a concentration of 25 mM. Despite similar rates of catalysis, distinctly different chemoselectivities were observed, with Zr^{4+} showing preferential hydrolysis of the P–OR bond, while Ce^{4+} overwhelmingly hydrolysed the C–OR bond of the diester (see Scheme 4.2).

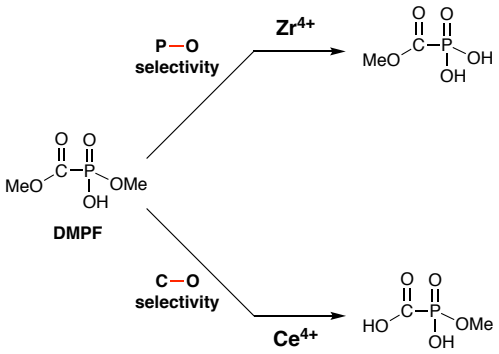

Scheme 4.2 Chemoselectivity exhibited by homogeneous catalyst Zr^{4+} and Ce^{4+} salts towards the hydrolysis of dimethyl phosphonoformate (DMPF).

These differences in selectivity were initially proposed to arise from the different solution structures postulated to exist for the metal ions in solution.[5] A well-known phenomenon of metal-aqua complexes is that water molecules are activated (*i.e.* their pK_a values are reduced relative to water) when coordinated to Lewis acidic metal centres, yielding acidic protons that deprotonate to form polynuclear hydroxo-metal species. Aqueous Zr^{4+} ions tend to predominately form tetramers ($Zr_4(OH)_8^{8+}$) and octamers ($Zr_8(OH)_{20}^{12+}$) in solution, while Ce^{4+} ions form predominately smaller, discrete dimers ($Ce_2(OH)_x^{8-x+}$) and hexamers ($Ce_6(OH)_{12}^{12+}$). This highlights the importance of having metal centres in close proximity in the form of multimetallic species in order achieve hydrolysis of organophosphate esters. However, further examination of the dependence of $\log(k_{obs})$ on $\log[M^{4+}]$ (M = Zr, Ce) yielded gradients less than 1, indicating that higher order complexes (dimers, tetramers, *etc.*) are not the major catalytic species involved in the reactions – had this been the case, k_{obs} vs. $[M^{4+}]$ slope would show an upward curvature with the gradient >1. This highlights the complex nature of the catalysis and the difficulty in determining mechanistic information. Indeed, it may be possible that the chemoslectively arises from the differences in Lewis acidity of the metal ions and the ionic radius. Zr^{4+} ions, at a mildly acidic pH (4.7), have also shown the ability of catalyse the hydrolysis of phosphatidylcholine, a biological based organophosphate ester.[6] However, the overall reaction yields were low after 20 hours (less than 10%), compared to Ce^{4+} which demonstrated substantial conversion of the phosphatidylcholine after 20 hours, approaching 80-90% conversion.[6] The unprecedented activity displayed by the homogeneous Ce^{4+} ions towards the hydrolysis of organophosphates is hypothesised to originate from the mixing of Ce^{4+} 4f orbitals and P=O bond orbitals.[7] XAS investigations into the interaction of

diphenylphosphate (DPP) with aqueous solutions of $Ce(NH_4)_2(NO_3)_6$ as the homogeneous source of Ce^{4+} ions showed the formation of cluster species in the Ce^{4+} solution, with the EXAFS regions showing Ce–O and Ce–Ce distances of 1.8 Å and 3.6 Å, respectively. This is indicative of the formation of Ce cluster molecules in solution. Upon addition of DPP to the Ce^{4+} salt solutions the intensity of EXAFS signal corresponding to the Ce–Ce bond is reduced to almost zero at a 1:1 molar ratio (Ce:DPP). This is indicative of strong interactions occurring between the DPP molecule and the Ce^{4+} centres (see Figure 4.2).

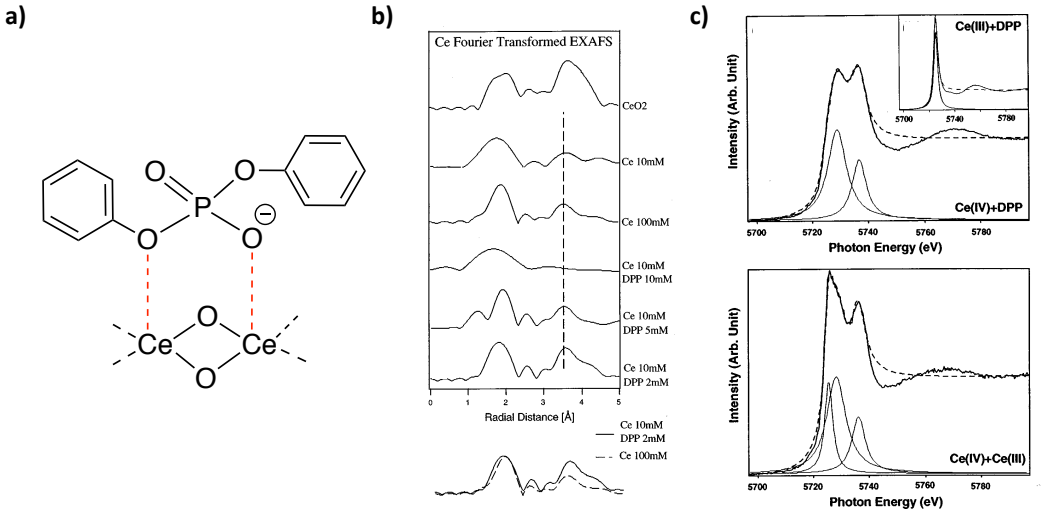

Figure 4.2 a) DPP-Ce complex, b) EXAFS spectra of CeO_2 (based on crystal structure), $(NH_4)_2Ce(NO_3)_6$ at 10 mM, 100 mM, $(NH_4)_2Ce(NO_3)_6$ and DPP at 10 and 10 mM, 10 and 5 mM, 10 and 3 mM – Ce---Ce distance marked at 3.6 Å by broken line, c) XANES spectra of Ce^{4+} standard and DPP (insert of Ce^{3+} standard and DPP), below XANES spectra of Ce^{4+} and Ce^{3+} mixed.[7]

Further evidence supporting this conclusion came from the XANES analysis, showing mixed $4f^1$ and $4f^0$ states, with the number of 4f electrons on the Ce ion of the Ce–DPP complex calculated to be 0.67, suggesting significant orbital mixing and charge transfer towards the Ce ions from DPP molecule (see Figure 4.2). Orbital mixing of this kind has been observed with other Ce^{4+} species, including in the solid state structure of CeO_2 where the 2p orbitals of O mix with the 4f orbitals of Ce^{4+} yielding a partial charge transfer between the two ions. This observation was consistent with XPS spectra taken of the Ce–DPP complex that showed a similar reduction of the Ce^{4+} state to Ce^{3+}, with the number of 4f electrons calculated to be

0.69.[7] The strong interaction between the Ce^{4+} centre and the organophosphate yields an intermediate with the phosphorus centre susceptible to nucleophilic attack. This mixing of orbitals was not observed with Ce^{3+} ions however, with XANES studies showing no significant charge transfer from the organophosphate reagent to the Ce^{3+} centre in solution.[7] should be noted however that Ce^{4+} aqueous salts are limited in that above a pH of 4 they spontaneous precipitate out of solution as $Ce(OH)_4$, rendering them catalytically inactive.[8]

4.4.2 Heterogeneous Ce and Zr Catalysts for Nerve Agent Hydrolysis

As with homogeneous based catalysis, there exists a wide range of examples of heterogeneous based catalysts in the solid state that catalyse the hydrolysis of nerve agents at a solid-aqueous phase barrier on the surface of the catalyst.

Metal oxides (MO) generally show reactivity towards nerve agents, such as VX and GD *via* surface hydroxyl groups and/or physisorbed water, resulting in hydrolysis of the exposed nerve agent.[9,10] When taken from the bulk to the nanoscale dimension, nanometal oxides (nMO) show enhanced hydrolysis kinetics towards many nerve agents due to the increased surface area and number of defect sites.[9] The hydrolysis of nerve agents VX and GD are shown in Scheme 4.3, where the hydrolysis of VX yields ethyl methyl phosphonic acid (EMPA) which acts as an auto-catalyst for the hydrolysis reaction.

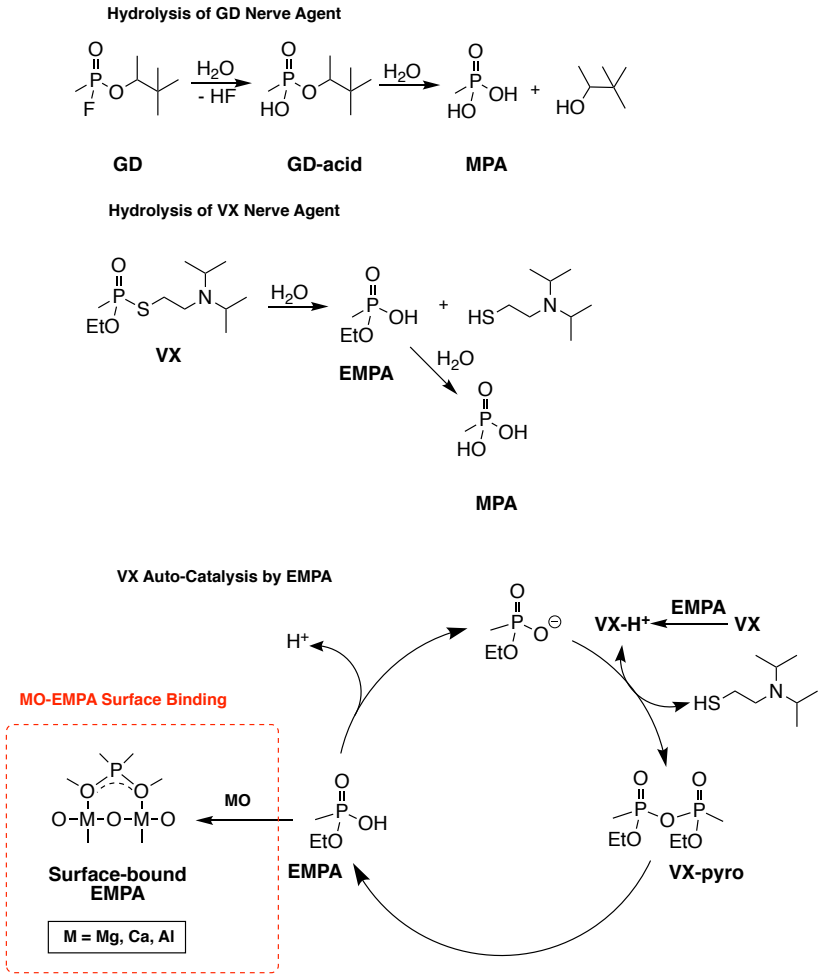

Scheme 4.3 Two-stage hydrolysis of nerve agents GD and VX. Catalytic cycle for VX hydrolysis where EMPA acts as an auto-catalyst.

Highly basic oxides such as MgO and CaO have the disadvantage that the basic surface irreversibly binds to the autocatalytic by-product of the VX hydrolysis (with solid-state ^{31}P NMR resonance corresponding to EMPA showing a broad resonance at 25.2 ppm, consistent with surface bound magnesium phosphates),[9] rendering the surface effectively self-poisoned and inactive towards VX hydrolysis (see Scheme 4.3). As a result, nanostructured MgO has a lengthy steady-state, first-order $t_{1/2}$ value of 68 hours for VX.[9] In order to overcome the limitations of basic MO catalysts, hydrolysis catalysed by less basic oxide surfaces has been investigated, namely TiO_2 in the polymorphic form of anatase.[11,12] The lack of EMPA adsorption to the surface results in enhanced $t_{1/2}$ conversion times, with anatase TiO_2 exhibiting $t_{1/2}$ = 4.3 hours.[11] Developments of nanostructured titania-based materials have shown enhanced catalytic activities towards the hydrolysis of the VX nerve agent. Titania in

the form of nanotubular titania (NTT) exhibits open-ended cylindrical structures with coaxial pairs of titania sheets. The NNT tubes have diameters *ca.* 5 nm and d-spacing between the sheets of 8.7 Å. This results in NNT possessing a high surface area of 250 m^2/g (c.f. 'normal' nanocrystalline titania 50 m^2/g), with surface hydroxyl concentrations of 33 $\mu eq/m^2$ and tightly encapsulated water molecules – yielding an ideal material for nerve agent hydrolysis. The solid-state ^{31}P NMR resonance of the decomposition product EMPA was visible as a sharp singlet at 20.2 ppm, indicative of a lack of strong binding between the EMPA and titania surface.[11] This resulted in nanotubular titania exhibiting a $t_{1/2}$ value of 58 minutes, reduced further to 25 minutes with the introduction of 20 wt% water.[11] The mechanism by which titania acts is proposed to be similar to that for the auto-catalytic reaction with EMPA (see Scheme 4.3), where the acidity of bridging hydroxyl groups (pKa = 2.9) is similar to that of EMPA (pKa = 2.16) and therefore it is assumed that the surface hydroxyl groups substitute in for EMPA forming the key rate-determining intermediate shown in Figure 4.3.

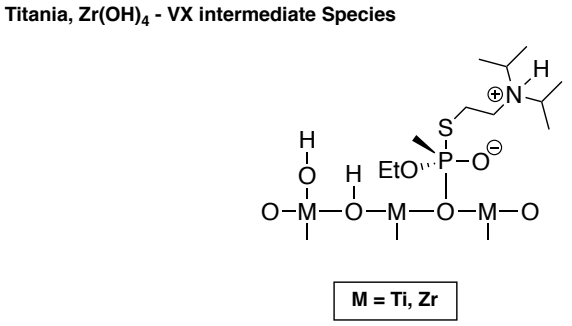

Figure 4.3 VX-Titania/$Zr(OH)_4$ Intermediate.

Constructing nanocrystalline titania with smaller particles and significantly higher surface areas (*ca.* 490 m^2/g) results in enhanced VX nerve agent hydrolysis, with $t_{1/2}$ being reduced to less than 2 minutes – significant improvements relative to nanotubular titania.[13] Nanocrystalline titania has also shown remarkable catalytic activities towards the hydrolysis of the nerve agent VX when deposited on water-based acrylic paint surfaces, with $t_{1/2}$ = 8.2 hours – interestingly, this catalytic activity is significantly hindered when the nanocrystalline titania is imbedded within the acrylic paint, rather than concentrated on the surface.[12] This is attributed to the slow diffusion of VX through the acrylic structure with a slow initial rate ($t_{1/2}$

= 17 hours), followed by a faster sustained reaction rate of ($t_{1/2}$ = 7.7 hours) as the reaction progresses due to the build-up of auto-catalytic EMPA.[12]

With zirconium directly below titanium in the periodic table, it was hypothesised that zirconium based hydroxide species would also exhibit catalysis towards nerve agent hydrolysis. Zirconium hydroxide is amorphous in the bulk scale, with localised crystallinity which leads to high surface areas in excess of 400 m^2/g, yielding a highly porous material. Zirconium hydroxide was shown to exhibit near-instantaneous catalytic breakdown of the nerve agent VX, with $t_{1/2}$ less than 1 minute.[14] This is again postulated to arise from surface hydroxyl groups that protonate the VX and catalyse the reaction in a manner similar to that of titania materials and EMPA. Thermal calcination of zirconium hydroxide results in a significant decrease in nerve agent hydrolysis rates with temperature. Zirconium hydroxide thermally calcined at 150, 300, 500 and 900 °C exhibited catalytic activities of $t_{1/2}$ = 3 minutes, 9 minutes, 19 hours and 42 hours, respectively.[14] TEM images taken of the calcined samples showed a significant decrease in surface area with temperature, which would impede the catalysis due to restricted access to surface active sites. However, more importantly, solid-state ^{1}H NMR spectroscopy showed that with thermal calcination there is a concurrent dehydroxylation of the zirconium hydroxide surface. This was further verified through potentiometric titration analysis, showing a commensurate decrease in the number of acidic hydroxyl groups upon calcination.[14] This loss of acidic hydroxyl groups is equivalent to the loss of catalytically active sites, and therefore reduces the rate of nerve agent hydrolysis.

Recent studies have shown that nanoceria engineered to include oxygen vacancies within the lattice structure (formed *via* alkaline hydrolysis of $CeCl_3$ in the presence of H_2O_2) functionally mimics the phosphotriesterase enzyme, catalysing the hydrolysis of paraoxon (DENP) to diethylphosphate (DEP), with $t_{1/2}$ = 10 minutes, at 45 °C.[15] The presence of surface oxygen vacancies was confirmed *via* Raman spectroscopy, with the appearance of a broad peak at *ca.* 600 cm^{-1}. Deconvolution of the Ce 3d XPS spectra revealed mixed Ce^{3+} and Ce^{4+} states, with the Ce^{3+} state accounting for 14% of Ce ions at the surface.[15] The oxygen vacancies resulted in the formation of active site-like hotspots on the CeO_{2-y} surface where Ce^{3+} and Ce^{4+} ions in close proximity exhibit synergistic interactions that allows for favourable binding of paraoxon and water to the surface to allow for efficient hydrolysis of the paraoxon reagent (see Figure

4.4). The catalyst was also noted to avoid previous examples of catalyst poisoning occurring through the irreversible binding of product phosphates to the surface and resultant blocking of catalyst active sites (*e.g.* CaO, MgO and Al_2O_3).

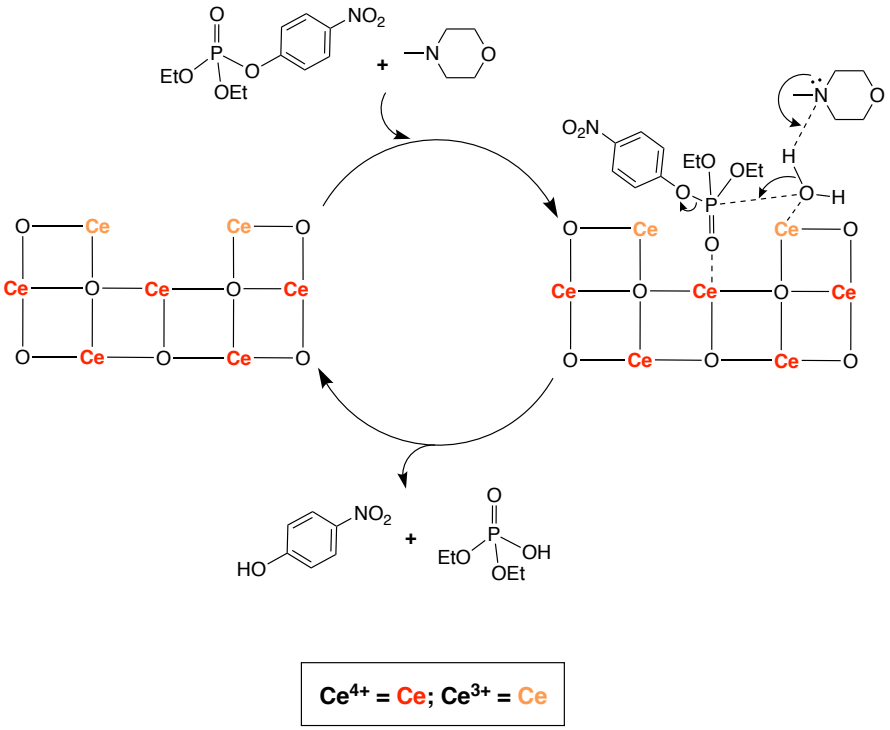

Figure 4.4 Catalytic cycle for the decomposition of paraoxon with vacancy engineered ceria (CeO_{2-x}).

Further modification of vacancy-engineered nanoceria by incorporation of Zr^{4+} ions into the lattice structure yields a more catalytically active material that also exhibits an unusual two-stage hydrolysis process whereby the DMNP reagents are hydrolysed to yield the less toxic diester dimethyl phosphate (DMP) which is subsequently hydrolysed again to yield the still less toxic monomethyl phosphate (MMP).[16] The mechanism of DMNP degradation involves the formation of an unusual intermediate with a covalent interaction between the diester and the surface Ce^{3+} centres, allowing for the cleavage of the diester bond (see Figure 4.5). Zr ions were incorporated into the CeO_{2-y} structure *via* co-precipitation methods, changing the molar Zr:Ce ratio to 1%, 5% and 10%. These values were confirmed *via* XPS and ICP analysis, with the Zr ions being found to largely accumulate at the surface of the $Zr_xCe_{1-x}O_{2-y}$. Deconvolution of the Ce 3d XPS spectra also revealed Ce^{3+} and Ce^{4+} states, indicating the

partial reduction of Ce^{4+} to Ce^{3+} and the presence of oxygen vacancies on the catalyst surface. As expected, with increasing Zr content, the Ce^{3+} % proportionally increases from 20% Ce^{3+} for 1% Zr to 32% Ce^{3+} for 10% Zr. The catalytic activity of $Zr_xCe_{1-x}O_{2-x}$ was found to be significantly dependent upon the Zr content with activity following the order: 1% Zr> 5% Zr> 10% Zr, with $t_{1/2}$ values of 1.2, 10.2 and 14.5 minutes respectively.[16] This relationship with Zr content is most likely due to the substitution of Ce^{4+} by Z^{4+} on the surface, which will in turn reduce the number of catalytically active Ce^{4+} sites on the surface and yield a less catalytic material. In both vacancy engineered nanoceria (CeO_{2-y}) and $Zr_xCe_{1-x}O_{2-y}$ it is the surface Ce^{4+} state that is proposed as the primary binding site for the P=O bonds of the organophosphate reagents while the Ce^{3+} site possess the coordinated H_2O and/or OH^- required for nucleophilic attack. This is consistent with the previously discussed EXAFS studies into the interaction of organophosphate DPP with Ce^{3+} and Ce^{4+} ions, where significant charge transfer was observed only between DPP and Ce^{4+}, indicating significant orbital overlap.[7]

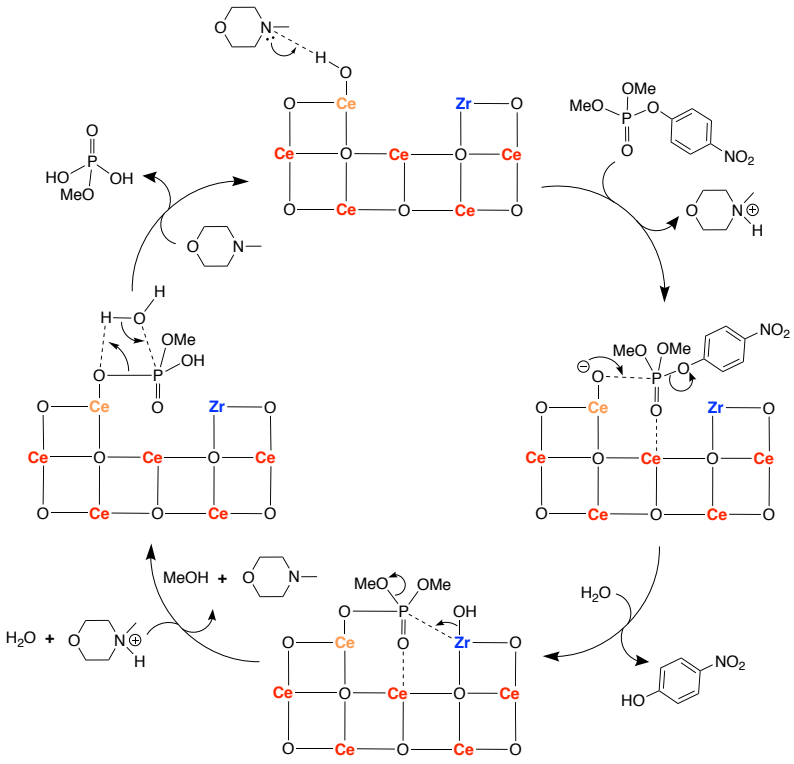

Figure 4.5 Catalytic cycle for the hydrolysis of DMNP with $Zr_xCe_{1-x}O_{2-y}$ catalysts.

4.4.3 Zr_6 Based Metal Organic Framework Catalysts for Nerve Agent Hydrolysis

Given the exceptional catalytic rates exhibited by $Zr(OH)_4$, it can be extrapolated theoretically that materials containing Zr–OH moieties and high surface areas and porosities would be ideal catalysts for nerve agent hydrolysis – this is readily available with Zr_6 based metal organic framework structures (MOFs).

A number of Zr_6 based MOFs have been shown to exhibit catalytic activity towards the hydrolysis of organophosphate reagents. *In-situ* ^{31}P NMR studies were performed using UiO-66 ($Zr_6(\mu_3\text{-}O)_4(\mu_3\text{-}OH)_4(BDC)_6$; BDC = benzenedicarboxylate) to investigate the catalytic activity towards the hydrolysis of DMNP.[17] Due to the small apertures of UiO-66 (*ca.* 6 Å), the accessible catalytically active sites are restricted to the surface of the MOF network.[17] This results in UiO-66 exhibiting slow hydrolysis rates, with $t_{1/2}$ = 35 minutes (at 1.5 µmol/ 2.5 mg catalyst loading). UV-vis studies of the hydrolysis of DMNP were performed with Zr_6 based MOF NU-1000 ($Zr_6(\mu_3\text{-}O)_4(\mu_3\text{-}OH)_4(OH_2)_4(TBAPy)_2$; TBAPy = tetratopic 1,3,6,8-(*p*-benzoate)pyrene), conversely, which has significantly larger pores (*ca.* 31 Å) meaning that DMNP reagent molecules can easily percolate the porous MOF network and access multiple catalytic sites (both surface and interior). NU-1000 exhibits faster hydrolysis of DMNP, relative to UiO-66, with $t_{1/2}$ = 15 minutes (at 1.5 µmol/ 3 mg catalyst loading). This is postulated not only to arise due to the larger, more accessible 'open' pores of NU-1000, but also the presence of labile H_2O ligands coordinated to the Zr_6 clusters – these are not present in the UiO-66 Zr_6 clusters, reducing their accessibility and increasing the activation energy associated with DMNP binding to the metal nodes. To investigate the possible mechanisms for the NU-1000 catalysis of DMNP hydrolysis, DFT studies were performed.[18] DMNP was found to form hydrogen bonds with the coordinated water and hydroxide ligands of the Zr_6 cluster nodes of NU-1000. The DMNP molecule also forms π- π interactions with the TBAPy organic linker of NU-1000, with optimal distances for association being 3.1 Å. The coordinated water molecule is removed from the Zr_6 cluster to simulate water ligand dissociation, followed by DMNP binding to the Lewis acidic Zr^{4+} centre *via* the P=O group. This electrostatic interaction takes precedence over the π- π interactions, additional interactions form between the –OMe groups of DMNP and the bridging oxide ligands. The thermodynamic driving force for the

reaction is the stability of the hydrolysed product which is 48 kJ mol^{-1} downhill in free energy relative to the separated reactants (see Figure 4.6).[18] Overall, the mechanism suggests that the rate of catalysis is related to the ease of displacement of the coordinated water ligand.

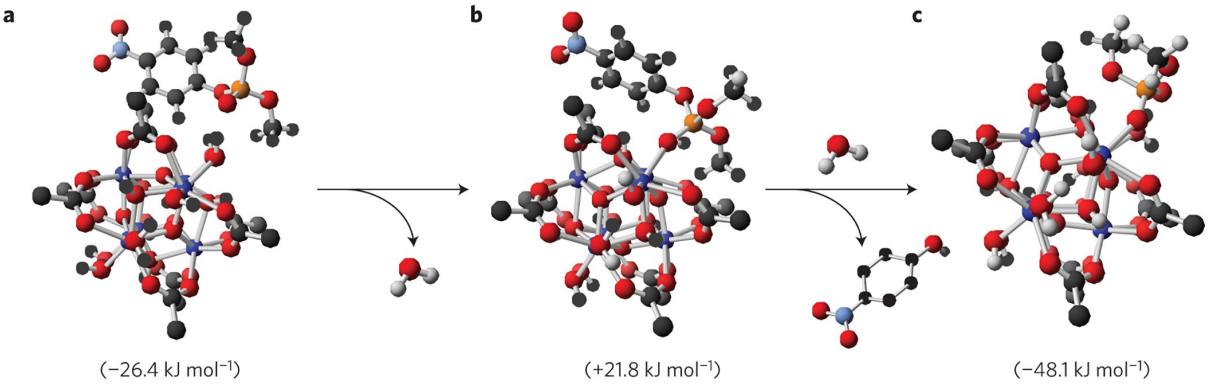

Figure 4.6 Association and reaction energies predicted by DFT. Step a) DMNP binding (ΔG_{assoc}), b) DMNP replacing H_2O molecule (ΔG_{rxn}) and c) Hydrolysis of DMNP (ΔG_{rxn}).[18]

Dehydration of the NU-1000 network *in vacuo* at 300 °C removes coordinated water and terminal hydroxide ligands and converts bridging hydroxides to bridging oxides, NU-1000-dehyd: $Zr_6(\mu\text{-}O)_8(TBAPy)_2$. This resulted in 4 out of the 6 Zr^{4+} ions in the Zr_6 cluster becoming coordinatively unsaturated and open to direct coordination with DMNP. This results in dehydrated NU-1000 being significantly more catalytic towards DMNP hydrolysis than the parent NU-1000, with $t_{1/2}$ = 1.5 minutes. The opening of Zr_6 clusters enhances the catalytic rate of hydrolysis of DMNP and is consistent with a mechanism involving P=O binding to these Zr^{4+} sites and being dependent upon water displacement for access. Dehydration of the UiO-66 network at 250 °C resulted in dehydroxylation of the cluster with the nodes reacting to from Zr_6O_6 clusters (see Scheme 4.4).[19] The dehydroxylated cluster was investigated *via* UV-vis spectroscopy towards the hydrolysis of DMNP and found to catalyse the reaction *ca.* 10 times faster than hydroxylated UiO-66.[20] This is consistent with observations made with NU-1000 where dehydration/dehydroxylation results in the Zr_6 cluster nodes opening up and becoming more accessible to nerve agent binding.[18]

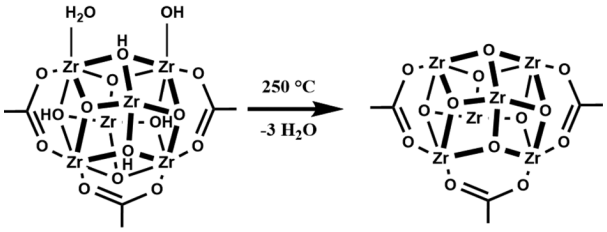

Scheme 4.4 Dehydration of the Zr_6 cluster nodes of UiO-66 resulting in the removal of coordinated hydroxide and water ligands.[20]

The catalytic activity of zirconium based MOF808, $Zr_6(\mu\text{-}O)_4(\mu\text{-}OH)_4(OOCH)_6(BTC)_2$ (BTC = benzenetricarboxylate), towards DMNP hydrolysis was investigated *via in-situ* ^{31}P NMR. Thermal activation of MOF808 in fresh DMF results in loss of formate modulator ligands within the Zr_6 cluster nodes: $Zr_6(\mu_3\text{-}O)_4(\mu_3\text{-}OH)_4(OH_2)_6(OH)_6(BTC)_2$.[21] The thermally activated MOF808 structure has an increased number of labile H_2O ligands coordinated to the Zr^{4+} metal centres, yielding a superior catalytic material. For of 1.5 and 0.7 μmols of activated MOF808 catalyst loadings, $t_{1/2}$ less than 30 seconds, while for 0.3 μmols (0.5 mg of catalyst) $t_{1/2}$ = 30 seconds.[21] Therefore the number of water molecules coordinated to the Zr_6 cluster nodes, the accessibility of the nodes to DMNP molecules and the ease at which coordinated water molecules are displaced are key factors to consider in modulating the catalytic rate. This point was further reinforced by a separate UV-vis study into the catalytic hydrolysis of DMNP by UiO-66 as a function of pH.[20] Despite previous investigations of DMNP hydrolysis all taking place under alkaline conditions (pH = 10.2 , 0.4 M *N*-ethylmorpholine, standard procedure), and the typical phosphate ester hydrolysis mechanism entailing a nucleophilic attack of DMNP by aqueous hydroxide, the rate of the hydrolysis accelerates as the solution pH is lowered (see Figure 4.7). This is attributed to pH dependent composition changes at the Zr_6 cluster nodes. The unexpected behaviour can be understood in terms of the RDS being the displacement of the of the coordinated water molecule by the DMNP reagent at a defect site (UiO-66 does not normally contain coordinated water, it is only when BDC linkers are missing that water can coordinate). Once the DMNP is bound to the Zr^{4+} metal centre the phosphorus-oxygen bond is weakened and more prone to nucleophilic attack by hydroxide in a fast step. At high pH values the majority of the MOF coordinated water molecules are deprotonated and converted into substitution resistant hydroxide ligands. Lowering the pH of the solution progressively returns these coordinated hydroxide ligands to their aqua form

and therefore increases the rate of the RDS, and consequently the overall rate of the catalytic hydrolysis (see Figure 4.7). When the pH is low enough (*ca.* pH = 8.8) nearly all the OH ligands have been converted to coordinated water and the rate of DMNP hydrolysis becomes pH independent.[20]

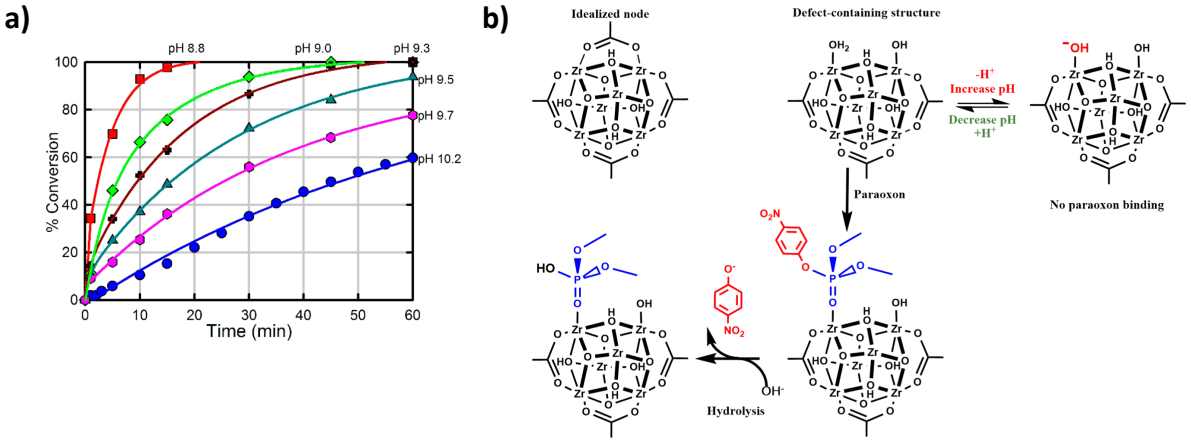

Figure 4.7 a) Conversion (%) vs. time (minutes) plots for various solution pH values (8.8 – 10.2), b) Compositional changes to Zr_6 cluster nodes of defected UiO-66.[20]

Chemical functionalisation of the organic linker that connects the Zr_6 cluster nodes has been shown to offer enhanced catalytic activities towards DMNP hydrolysis.[22] UV-vis studies of DMNP exposure to UiO-66-X (X = NO_2, OH and NH_2), where X is a substituent added to the organic benzenedicarboxylate linker, have shown that despite all three substituents being capable of participating in hydrogen bonding, only X = NH_2 enhanced the rate of DMNP hydrolysis relative to UiO-66, $t_{1/2}$ = 1 minutes vs. 35 minutes, respectively. Both NO_2 and OH linker substituents showed catalytic conversions slower than that of UiO-66, $t_{1/2}$ = 45 minutes and 60 minutes, respectively (see Figure 4.8).[22] The incorporation of the Bronsted basic –NH_2 group in UiO-66-NH_2 is postulated to mimic the biochemistry in the phosphotriesterase enzyme where the hydrolysis is enhanced by the presence of a proximal anchored base that aids proton transfer.[23] Based on the observations made above, the conclusion was drawn that the amino moiety enhances the catalytic activity as a Bronsted base, rather than a hydrogen bonding moiety. Furthermore, considering there is no difference between UiO-66, UiO-66-NO_2 (EWG) and UiO-66-$(OH)_2$ (EDG) then the electronic and steric influences of the substituents on the RDS kinetics of the hydrolysis reaction is minimal. Functionalisation of a

similar nature was made with UiO-67 ($Zr_6(\mu\text{-}O)_4(\mu\text{-}OH)_4(bpdc)_6$; bpdc = biphenyldicarboxylate) whereby the biphenyldicarboxylate linker was functionalised with two basic moieties: NH_2 and NMe_2, of differing basicity (see Figure 4.8).[22] The UiO-67-NMe_2 catalyst was found to be less efficient towards DMNP hydrolysis relative to UiO-67-NH_2, with $t_{1/2}$ values of 7 minutes and 3.5 minutes, respectively. This observation was consistent with the functionalised amino group acting as a Bronsted base whereby a proton is transferred to and from the base during the catalytic cycle, whereby the ease at which the conjugate acid form of the amino group can be deprotonated is proportional to the rate of catalysis. Therefore, the NH_2 substituent (which is less basic compared to the NMe_2 substituent) is regenerated with greater ease at the final point of the catalytic cycle and more effective as a Bronsted base during the catalysis.

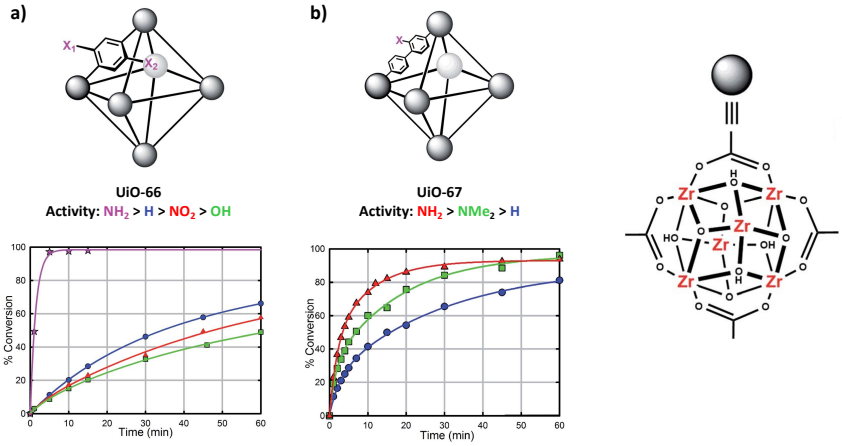

Figure 4.8 a) Cluster of UiO-66 showing functionalisation of the BDC linker above and the conversion (%) vs. time (minutes) plot below, b) Cluster of UiO-67 showing functionalisation of the bpdc linker above and the conversion (%) vs. time (minutes) plot below.[22]

The effectiveness of Zr_6 based MOFs towards nerve agent hydrolysis has been shown to depend upon physical properties of the MOF material, such as crystallite size. The catalytic hydrolysis of DMNP was investigated as a function of NU-1000 crystallite size, with particles ranging from 15,000 nm to 75 nm.[24] To control for the dimensions of the nanosized crystals of NU-1000, a low concentration of benzoic acid modulator was used in combination with another modulator, trifluoroacetic acid, during the synthesis of NU-1000. Solutions were heated at differing temperatures and for differing times in order to obtain NU-1000 crystals of differing sizes. PXRD and nitrogen sorption experiments on the various NU-1000 crystallite

sizes indicated that the crystallinity and mesoporosity of NU-1000 was maintained in the nanosized particles. A significant enhancement of the rate of hydrolysis was observed for the nanosized crystals compared to microcrystals (see Figure 4.9).[24] This observed rate enhancement was attributed to the larger relative external surface area and/or the faster diffusion of the DMNP through the nanosized crystals compared to the microcrystals.

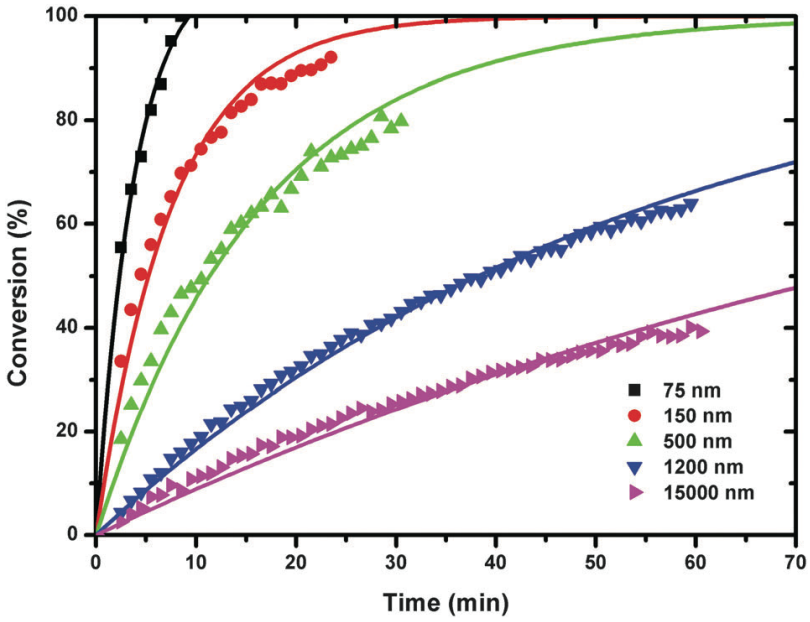

Figure 4.9 Conversion (%) vs. time (minutes) for the hydrolysis of DMNP with NU-1000 crystallites ranging from 75 nm to 15,000 nm in dimension.[24]

4.4.4 Ce–Zr Based Metal Organic Framework Catalysts for Nerve Agent Hydrolysis

As noted previously, in both homogeneous and heterogeneous systems, Ce can show enhanced catalytic activity towards the hydrolysis of organophosphates when either used separately or in combination with Zr – acting cooperatively. To this end a number of studies have shown that when Ce metal centres are introduced to a Zr_6 MOF structure, enhanced organophosphate hydrolysis rates are observed.

An investigation into the catalytic hydrolysis of DMNP with UiO-66 and a Ce analogue of UiO-66, Ce-BDC ($Ce_6(\mu\text{-}O)_4(\mu\text{-}OH)_4(BDC)_6$; BDC = benzenedicarboxylate) was performed using *in-*

situ ^{31}P NMR spectroscopy. Ce-BDC was synthesised hydrothermally, exhibiting high specific surface areas of 1250 m^2 g^{-1}, which was comparable to that of UiO-66. Ce-BDC exhibited an enhanced catalytic half-life of 8 minutes, compared to that of UiO-66, with a half-life of 19 minutes for the hydrolysis of DMNP (see Figure 4.10).[25] This is impressive given the fact that the Ce-BDC was composed of larger crystallites, in comparison to UiO-66, and therefore would be even more catalytic had the particles been of the same size.[24]

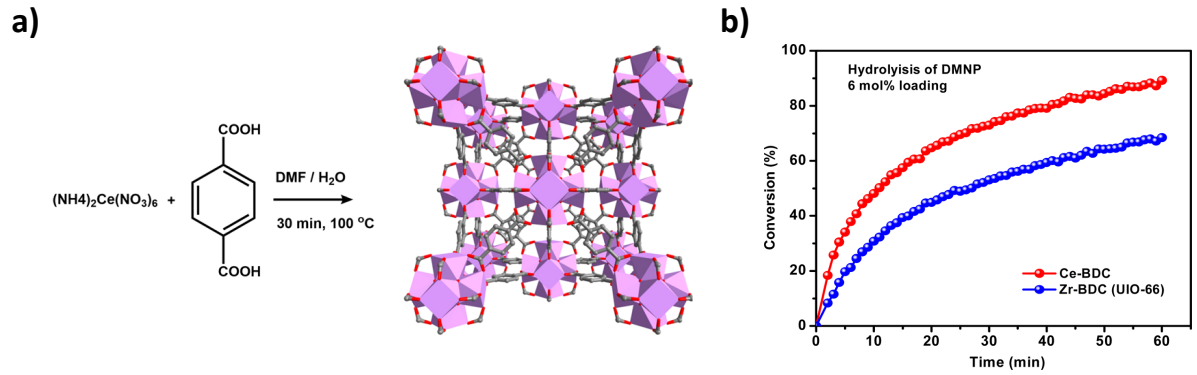

Figure 4.10 a) hydrothermal synthesis of Ce-BDC MOF, b) Conversion (%) vs. time (minutes) for the hydrolysis of DMNP with Ce-BDC and UiO-66.[25]

Diffuse reflectance infrared Fourier transform (DRIFT) spectra recorded for UiO-66 and Ce-BDC showed a significant redshift in the OH stretch for Ce-BDC, indicative of a weaker OH bond to the Ce_6 node. Given that previous studies postulated mechanisms whereby the displacement of coordinated H_2O or OH^- ligands was the RDS, it is possible that the more labile OH ligand in Ce-BDC manifests as enhanced catalytic activities.[17,18,20,21] Analogous experiments performed using GD (Soman) instead of DMNP showed a similar trend in catalytic conversion rates, although somewhat reduced differences in the overall $t_{1/2}$ values at 3 minutes and 4 minutes for Ce-BDC and UiO-66, respectively. The reduction in the $t_{1/2}$ differences for Ce-BDC and UiO-66 most likely arises from the differences in hydrolysis mechanisms for DMNP and GD, in the hydrolysis of DMNP a P–O bond is being broken, while for GD a P–F bond is being broken. Since, P–F bonds area weaker ($\mathbf{\Delta}H_f$ = 439 kj mol-1) compared to P–O bonds ($\mathbf{\Delta}H_f$ = 597 kJ mol^{-1}) it follows logically that any catalyst would be able to hydrolyse GD at a faster rate compared to DMNP.[26] Further developments were made to the Ce-BDC catalytic system by replacing the aqueous based *N*-ethylmorpholine buffer

system with solid-state polyethyleneimine (PEI) which acts as a heterogeneous buffer system.[25] The Ce-BDC:PEI composite showed a half-life for DMNP hydrolysis of 4.5 minutes, significantly shorter than the 8 minutes for the aqueous buffer system. This modification is particularly important for potential applications in solid suits, masks, decontamination wipes *etc*., where aqueous solutions of *N*-ethylmorpholine are impractical.

As described previously in the introduction, studies have shown that through a combined process of etching and stabilisation, Ce nanoparticles (CeNP) can be incorporated into the Ce-BDC MOF framework.[27] In the process pre-made CeNPs are dispersed in a solution of the BDC linker, to which $(NH_4)_2Ce(NO_3)_6$ salt was added and heated to 100 °C, yielding a precipitate of CeNP@Ce-BDC (see Figure 4.11).

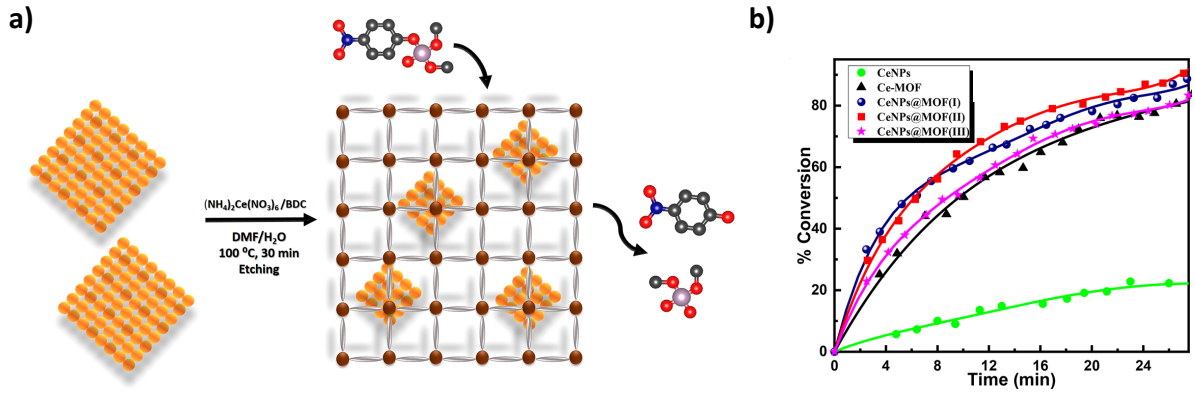

Figure 4.11 a) Formation of CeNP@Ce-BDC composite via etching and stabilisation of pre-made CeNPs within a Ce-BDC framework, b) Conversion (%) vs. time (minutes) for the hydrolysis of DMNP with CeNP@Ce-BDC (I, II and II = 22.5, 45 and 90 mg of CeNP respectively), CeNPs and Ce-MOF (*i.e.* Ce-BDC).[27]

TEM images of the CeNP@Ce-BDC composite revealed a homogeneous distribution of the CeNPs throughout the MOF matrix, with the incorporated CeNPs having an average size smaller compared to free CeNPs due to the chemical etching process. The stabilisation of the CeNPs enhances the nanoparticle activity, prevents aggregation and provides ease of accessibility to active sites. The resulting CeNP@Ce-BDC composites showed enhanced degradation kinetics towards the hydrolysis of DMNP relative to both parent materials, CeNP and Ce-BDC.[27] XPS characterisation of the 3d spectral region for CeNP@Ce-BDC revealed a

Ce^{3+} content of 30.7%, while Ce-BDC had a content of 26.1% and CeNP a content of 3.4%. Consequently, CeNP@Ce-BDC showed the strongest catalytic performance (measured *via* ^{31}P NMR spectroscopy) with a $t_{1/2}$ value of 6.2 minutes compared to 9 minutes for Ce-BDC.[25,27] The presence of a higher Ce^{3+} fraction and additional oxygen vacancies in the CeNP@Ce-BDC composite was hypothesised to allow for preferential binding of the H_2O/OH^- molecules to the Ce^{3+} sites, while the DMNP binds to the adjacent Ce^{4+} site through the P=O bond, facilitating nucleophilic attack at the phosphorus centre *via* an S_N2 reaction.[27] This hypothesised mechanism is similar to that proposed for the vacancy engineered ceria, whereby Ce^{3+} and Ce^{4+} ions in close proximity exhibit synergistic interactions that allows for favourable binding of water and DMNP to the surface to allow for efficient hydrolysis of the DMNP reagent (see Figure 4.4).[15] Solvothermal insertion of $Ce(Cp^{iPr})_3$ ($Cp^{i}Pr = C_5[CH\{CH_3\}_2]_5$) or $Ce(tmhd)_4$ (tmhd = 2,2,6,6-tetramethyl-3,5-heptanedionate) into NU-1000 *via* and subsequent high temperature treatment at 120 °C resulted in the formation of Ce cluster NU-1000 composites $CeNP^n$@NU-1000 (see Figure 4.12).[28]

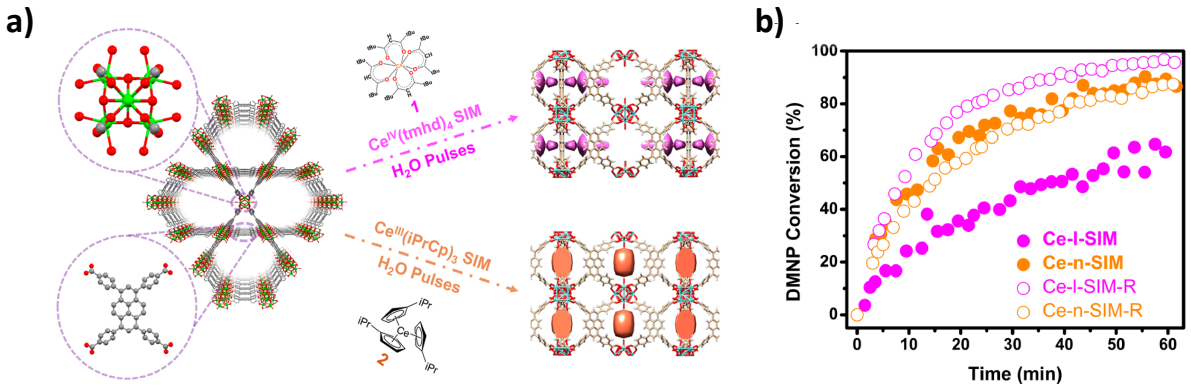

Figure 4.12 a) Solvothermal insertion of precursors $Ce(Cp^{iPr})_3$ and $Ce(tmhd)_4$ into NU-1000, followed by pulsed steam treatment, b) Conversion (%) vs. time (minutes) plot for the hydrolysis of DMNP with Ce-l-SIM (*i.e.* $CeNP^l$@Ce-BDC) and Ce-n-SIM (*i.e.* $CeNP^n$@Ce-BDC), Ce-l-SIM-R and Ce-n-SIM-R the reduced equivalents, respectively.[28]

Solvothermal insertion of $Ce(Cp^{iPr})_3$ resulted in the formation of the $CeNP^n$@NU-1000 composite and showed a reduction in BET surface area from 2160 m^2/g to 1240 m^2/g, with difference envelope density analysis and pair function distribution analysis of X-ray scattering indicating small clusters of a few Ce ions (*e.g.* $Ce_3O_xH_y$) located between the Zr_6 nodes.

CeNP^n@NU-1000 exhibited catalytic activity towards the hydrolysis of DMNP, with a half-life of 11 minutes (see Figure 4.12), shorter than that measured for NU-1000 at 15 minutes.[28] This enhanced catalytic activity is postulated to arise from the significant Ce^{3+} proportion present in CeNP^n@NU-1000. XPS analysis of CeNP^n@NU-1000 revealed a Ce 3d region with peaks characteristic of Ce^{3+} and Ce^{4+}, deconvolution of this region and subsequent fitting revealed Ce^{3+} proportions of 15%. Treatment of CeNP^n@NU-1000 with the reducing agent sodium borohydride caused an increase in the Ce^{3+} content to 21%. DMNP hydrolysis studies with the reduced CeNP^n@NU-1000 revealed a half-life that had surprisingly increased, despite the increased proportion of Ce^{3+}, to 14 minutes (see Figure 4.12).[28] This may be due to both Ce^{3+} and Ce^{4+} being required for catalytic activity though synergistic cooperative interactions, whereby the DMNP reagents binds selectively to the highly Lewis acidic Ce^{4+}, weakening the P=O bond. Water and/or hydroxide ligands coordinate subsequently to the Ce^{3+} and are more labile relative to those bound to Ce^{4+} and Zr^{4+}, easily attacking the P centre of the DMNP and yielding an efficient catalytic cycle. Contrastingly, the solvothermal insertion of $Ce(tmhd)_4$ resulted in the formation of the CeNP^l@NU-1000 composite and showed a similar reduction in BET surface area from 2160 m^2/g to 1450 m^2/g, with X-ray scattering indicating that larger clusters (*e.g.* $Ce_{90}O_wH_z$) form in close proximity to the linker, interacting with the tetraphenylpyrene moieties and not grafting to the Zr_6 clusters. Deconvolution of the XPS Ce 3d spectral region for CeNP^l@NU-1000 showed only Ce^{4+} states present, with DMNP hydrolysis rates substantially reduced with $t_{1/2}$ = 31 minutes (see Figure 4.12). Interestingly, in contrast to the reduction of CeNP^n@NU-1000 which showed no real change in catalytic hydrolysis rates when the Ce^{3+} proportion increases from 15% to 21%, the reduction of CeNP^l@NU-1000 increases the Ce^{3+} proportion from 0% to 6% and yields a concurrent increase in the rate of DMNP hydrolysis with $t_{1/2}$ = 7 minutes (see Figure 4.12).[28] This indicates that the catalytic system goes well beyond a simple proportional relationship between the Ce^{3+} content and the rate of hydrolysis, rather there is a compositional 'sweet point' where the Ce^{3+} and Ce^{4+} proportions work synergistically to yield enhanced catalytic rates. This has been mirrored in previous observations with solid-state, heterogeneous $Ce_{1-x}Zr_xO_{2-y}$ catalytic systems for nerve agent hydrolysis.[16]

The heterogeneous catalytic hydrolysis of DMNP using Zr_6 and Ce–Zr based MOFs is summarised below in Table 4.1, with overall catalytic abilities characterised using the $t_{1/2}$

values. Given the sensitivity of the $t_{1/2}$ to the experimental protocol adopted, experimental parameters are also noted, including: the spectroscopic technique used to follow the decomposition reaction, loading weight of catalyst, method of suspending MOF particles and MOF particle size.

Table 4.1: Summarised catalysis data, $t_{1/2}$ values and experimental parameters, for Zr6 and Ce–Zr based MOFs in the catalytic hydrolysis of DMNP.

MOF	Half-life ($t_{1/2}$)	Spectroscopy	Loading Weight	MOF Suspension treatment	MOF Particle Size	Reference
MOF808	< 30 seconds	$^{31}P\{^{1}H\}$ NMR (inc. filtration @ 30 seconds)	0.8 mg	Stirred in 1.05 mL of 0.4 M buffer solution for 15 minutes. DMNP (4 μL; 25 μmol) added and swirled for 10 seconds.	*ca.* 250 nm (DLS)	[21]
NU-1000	15 minutes	UV-vis (@ 407 nm)	3.0 mg	Stirred in 1 mL of 0.45 M buffer solution for 15 minutes. DMNP (4 μL; 25 μmol) added to the suspension.	n/a	[18]
NU-1000	2 minutes	$^{31}P\{^{1}H\}$ NMR (inc. filtration @ 30 seconds)	0.8 mg	Stirred in 1 mL of 0.4 M buffer solution for 15 minutes. DMNP (4 μL; 25 μmol) added and swirled for 10 seconds.	75 nm	[24]

NU-1000-dehydrated	1.5 minutes	UV-vis (@ 407 nm)	3.0 mg	Stirred in 1 mL of 0.45 M buffer solution for 15 minutes. DMNP (4 μL; 25 μmol) added to the suspension.	n/a	[18]
UiO-66	35 minutes	UV-vis (@ 407 nm)	2.5 mg	Stirred in *ca.* 1 mL of 0.45 M buffer solution for 30 minutes. DMNP (4 μL; 25 μmol) added to the suspension.	400 nm	[22]
UiO-66-NH_2	1 minute					
UiO-67	4.5 minutes					
UiO-67-NH_2	2 minutes					
Ce-BDC	8 minutes	$^{31}P\{^1H\}$ NMR	3.0 mg	Sonicated in 1 mL 0.45 M buffer solution for 15 seconds. DMNP (4 μL; 25 μmol) added to the suspension and vigorously shaken for 15 seconds.	630-700 nm	[25]
CeNP@Ce-BDC	6.2 minutes	$^{31}P\{^1H\}$ NMR	3.0 mg	Sonicated in 1 mL of 10% D_2O, pH adjusted to pH 10 using 0.45 M buffer solution,	*ca.* 300 nm	[27]

				for 1 minute. DMNP (4 μL; 25 μmol) added and vortexed for 15 seconds.		
CeNP^{n}@NU-1000	11 minutes	^{31}P{^{1}H} NMR	1.95 mg	Sonicated in 1.05 mL of 0.4 M buffer solution for 1 minute. DMNP (4 μL; 25 μmol) added and swirled for 15 seconds.	*ca.* 500 nm	[28]
CeNP^{n}@NU-1000 (reduced)	14 minutes				*ca.* 900 nm	
CeNP^{l}@NU-1000	31 minutes				*ca.* 600 nm	
CeNP^{l}@NU-1000 (reduced)	7 minutes				*ca.* 1000 nm	
CeNP@MOF808	1.9 minutes	^{31}P{^{1}H} NMR	0.5 mg	Sonicated in 1.05 mL of 0.4 M buffer solution for 2 minutes. DMNP (4 μL; 25 μmol) added after 30 seconds and swirled for 15 seconds.	*ca.* 100 – 200 nm	*This Work*
MOF808	3.7 minutes	^{31}P{^{1}H} NMR	0.5 mg	Sonicated in 1.05 mL of 0.4 M buffer solution for 2 minutes. DMNP (4 μL; 25 μmol) added after 30 seconds and swirled for 15 seconds.	*ca.* 100 – 200 nm	*This Work*

4.5 Results and Discussion: Catalytic Applications of CeNP@MOF808: Hydrolysis of DMNP

4.5.1 Aims: Optimisation of Experimental Protocol for the Catalytic Hydrolysis of DMNP using CeNP@MOF808

As established in Section 4.4.3 MOF808 has previously demonstrated catalytic activity towards the hydrolysis of DMNP. However, it should be noted that repeated/recycled catalytic measurements were not performed and therefore by the exact definition of a catalyst (*i.e.*, a substance which increases the rate of catalytic hydrolysis and is not consumed by the hydrolysis reaction) the composite, CeNP@MOF808, could not be confirmed to be a catalyst in the pure sense. That being said, throughout this chapter the composite shall be referred to as a catalyst given that the material shows enhanced rates of reaction and that the host matrix, MOF808, has previously demonstrated catalytic potential by its own standing.

From the outset, the question arose as to what was the optimal set up to study the catalytic activity of the composite CeNP@MOF808 towards nerve agent hydrolysis. Based on literature precedent, several protocols were available. The experimental studies were based on previously established literature procedures for following the catalytic hydrolysis of DMNP *via* $^{31}P\{^{1}H\}$ NMR using different Zr based MOF structures.[18,21,24,25,27-29] As reported in previous chapters, the introduction of CeNP to MOF808 resulted in a retention of the MOF microscopic and macroscopic structure. Cerium is a catalytically active metal centre towards multiple types of reactions, and has been shown to work cooperatively with other Lewis acidic metal centres such as Zr. The aim was determine what effect, if any, the introduction of cerium metal ions to MOF808 had on the catalytic hydrolysis of DMNP – a reaction which MOF808 has previously demonstrated catalytic activity towards. Given that the aim was to establish an enhancement of catalytic activity, rather than establish catalytic activity itself, statistically reliable data sets of hydrolysis conversion times were required for both CeNP@MOF808 and MOF808. Therefore, an optimised experimental procedure was required. The process of optimising the experimental set up was achieved through a combination of adaptation from literature precedent (see Table 4.1), integration of chemical sensibility (*i.e.* knowing how best to handle and work with the chemicals chosen) and logistical management.

4.5.2 General Experimental Protocol for the Catalytic Hydrolysis of DMNP using CeNP@MOF808

Given below in Figure 4.13 is a flow diagram schematic of the individual steps in the *general* experimental set up for monitoring the progress of the catalytic hydrolysis of DMNP. Step **1** involved weighing out the sample (CeNP@MOF808 or MOF808) by difference using an analytical grade balance and subsequently (step **2**) dispersing the catalyst powder in 1.05 mL of 0.4 M *N*-ethylmorpholine buffer solution, using a micropipette. The dispersion was sonicated (step **3**) for several minutes at room temperature to form a homogeneous suspension, to which 4 μL of DMNP was added (step **4**). The solution was swirled for several seconds and then transferred to an NMR tube, step **5**, using a Pasteur pipette, where $^{31}P\{^{1}H\}$ NMR spectra were recorded periodically to monitor the hydrolysis of DMNP, step **6**. Once a general experimental set up was established, several stages of the procedure required optimisation in order to minimise (a) sources of error and (b) the time taken from mixing the catalyst suspension.

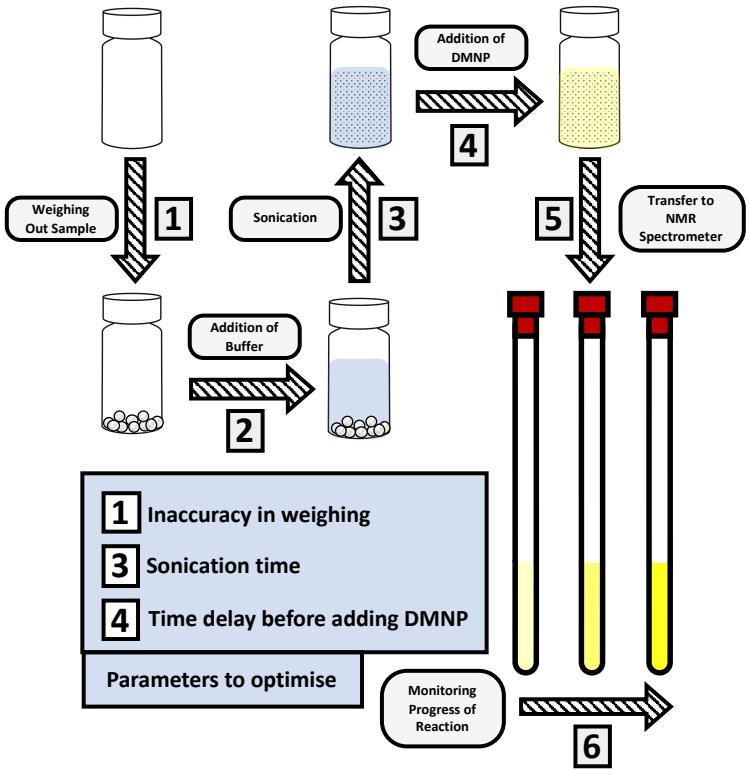

Figure 4.13: Schematic overview of experimental protocol for monitoring the catalytic hydrolysis of DMNP with CeNP@MOF808.

Several factors in the general experimental set up shown previously were determined without significant experimentation. For example, it was concluded that in concern for safety, DMNP would be employed as a nerve agent simulant, substituting for an actual nerve agent which would be several times more toxic and extremely difficult to handle under normal laboratory conditions. This was consistent with literature studies which often used DMNP as a nerve agent substitute and would allow for appropriate comparisons in hydrolysis times. [18,21,24,25,27-29] Several studies of the catalytic hydrolysis of DMNP using MOF based catalysts have opted for UV-vis spectroscopy in order to monitor the progress of the hydrolysis reaction.[18,22] Monitoring the reaction *via* UV-vis spectroscopy has the advantage over NMR in that spectra can be recorded almost immediately upon mixing the samples (unlike NMR where locking and shimming sets the lower end limit of acquisition at t = 4 minutes). However, there are several disadvantages associated with UV-vis spectroscopy including primarily that the suspension of catalyst particles, either composite or control MOF808, would scatter a significant portion of the incident light and prevent spectrum acquisition. Therefore, it was concluded that NMR

spectroscopy, focusing on changes in the phosphorus chemical environment, was the optimal spectroscopic technique for monitoring the progress of the DMNP hydrolysis reaction.

As seen in Table 4.1 Zr_6 based MOFs such as NU-1000, UiO-66, UiO-67 and MOF808 have been shown in previous studies to catalyse the hydrolysis of DMNP.[21] The hydrolysis reaction is postulated to occur at the Zr_6 cluster nodes, whereby the DMNP displaces either H_2O or OH^- ligands coordinated to the Zr_6 nodes by binding through the P=O bond. This polarises the P=O bond further to favour nucleophilic attack from H_2O or OH^- (coordinated or free in solution), yielding nitrophenoxide and dimethyl phosphonic acid (DMP). At a catalyst loading weight between 1.1 and 0.8 mg of MOF808, the half-life of DMNP was determined to be less than 30 seconds, as of writing this is the most efficient catalyst reported towards DMNP hydrolysis (see Table 4.1).[21] However, two significant caveats should be noted when comparing catalytic conversion times to the previously quoted value of less than 30 seconds. The first is that the reaction set up was adapted to allow for a measurement to be recorded at 30 seconds, with the reaction mixture filtered using a syringe to remove MOF particles, terminating the catalytic reaction. Secondly, MOF materials are not well defined in their stoichiometry, which each MOF structure being highly sensitive to changes in precursors, reaction temperatures and post-synthetic treatments (*e.g.* solvent washing stages and activation). For this reason, control MOF808 was adopted as a more appropriate reference material, rather than literature values, to control for differences in MOF chemistry associated with synthesis. All reported examples of Zr_6 based MOF catalysis of DMNP hydrolysis have resulted in a single, one step hydrolysis reaction, with no further hydrolysis of the DMP to MMP or phosphate observed. Both the starting material, DMNP, and the hydrolysis product, DMP, have one phosphorus environment which changes chemically as the reaction proceeds (see Scheme 4.5 – phosphorus labelled red).

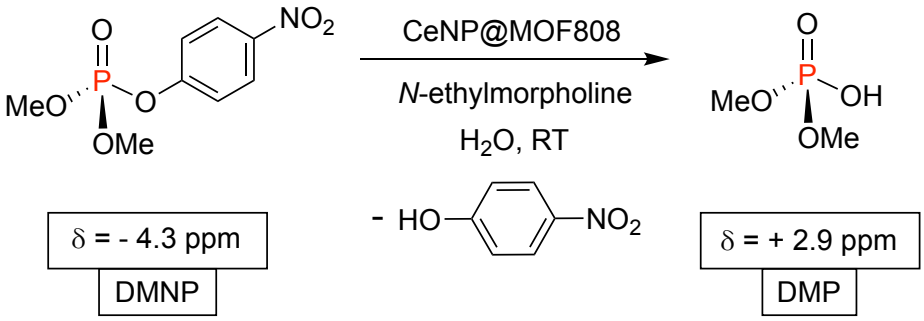

Scheme 4.5: Catalytic hydrolysis of nerve agent simulant DMNP by CeNP@MOF808

This change in chemical environment around the phosphorus atom can act as a spectroscopic handle for following the course of the hydrolysis reaction and quantifying the conversion per unit time *via* $^{31}P\{^{1}H\}$ NMR. Using the relative integrals of the two phosphorus environments it is possible to determine the percentage conversion for the reaction at a given time, see Eqn.5, where I_R and I_P are the relative integrals of ^{31}P resonances of DMNP and DMP, respectively, in the $^{31}P\{^{1}H\}$ NMR spectrum. $^{31}P\{^{1}H\}$ NMR has the added advantage that any further hydrolysis products would be observable, that is if the remaining two methoxy groups of DMP were hydrolysed. In contrast, using UV-vis spectroscopy would be again be limited in this regard in that the reaction progress is monitored *via* the formation of hydrolysis product nitrophenoxide (λ_{max} = 407 nm), whereby further hydrolysis products MMP and phosphate would remain undetected.[17,18,20,22]

$$Hydrolysis\ Conversion\ (\%) = \frac{I_P}{I_R + I_P} \times 100\% \qquad (Eqn.5)$$

The buffer solution is essential for the reaction proceed by acting in a manner similar to that of the proximal base in the enzyme PTE as a proton shuttle, therefore, without the buffer the hydrolysis reaction does not take place.[23] The influence of the presence of the buffer, *N*-ethylmorpholine, was investigated through a series of $^{31}P\{^{1}H\}$ NMR experiments. 0.5 mg of catalytic material (CeNP@MOF808 and MOF808) was sonicated for two minutes in 1.05 mL of deionised water (buffer absent), followed by a time delay of 30 seconds before mixing with 4 μL of DMNP. The rection mixtures were subsequently transferred to NMR tubes with $^{31}P\{1H\}$ NMR spectra recorded several minutes and several hours after the initial mixing of the

suspension with DMNP. These experiments were repeated in duplicate. CeNP@MOF808 exhibited a slow conversion of DMNP in the absence of buffer, with 9% conversion after 3 minutes and 30% conversion after 6.5 hours (see Supplementary Figure 4.1 and Figure 4.14 for respective $^{31}P\{^{1}H\}$ NMR spectra). Control MOF808 also exhibited slow conversion of DMNP in the absence of buffer solution, and a lower conversion relative to that exhibited by CeNP@MOF808, with 3% conversion after 8 minutes, and 21% conversion after 6.5 hours (see Supplementary Figure 4.2 and Supplementary Figure 4.3 for respective $^{31}P\{^{1}H\}$ NMR spectra).

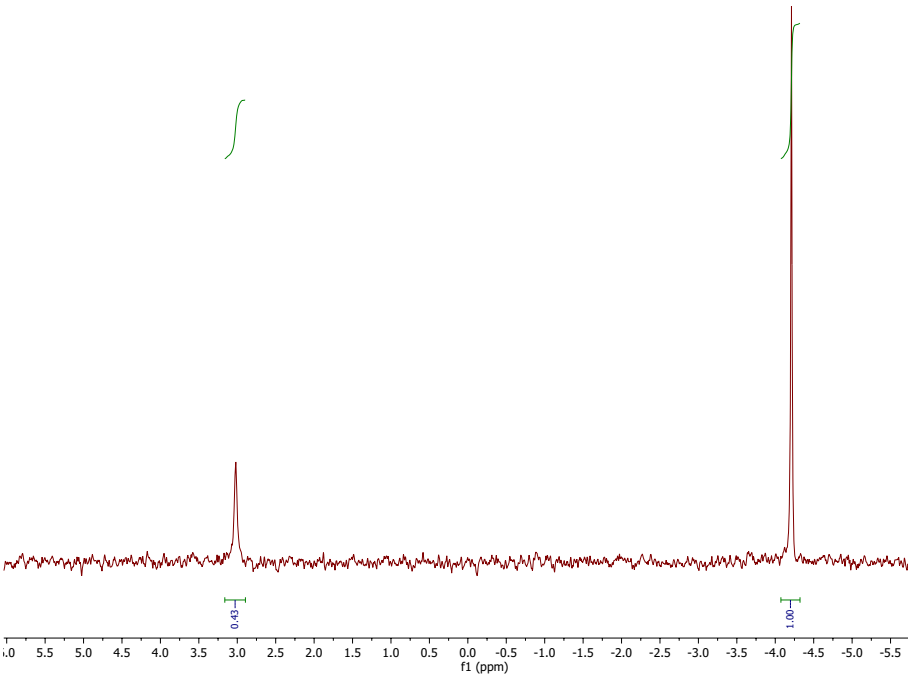

Figure 4.14: $^{31}P\{^{1}H\}$ NMR spectrum for catalytic hydrolysis of DMNP using 0.5 mg of CeNP@MOF808 in the absence of buffer after 6.5 hours, showing 30% conversion of DMNP. No resonance observed at δ = 5.1 ppm.

This demonstrated that the presence of basic *N*-ethylmorpholine is essential for fast conversion of DMNP – consistent with all reported literature involving Zr_6 based MOF catalysts for DMNP hydrolysis. While CeNP@MOF808 exhibited significantly better conversion of DMNP relative to control MOF808 in the absence of buffer, there was insufficient numbers of data sets to indicate a catalytic enhancement of the MOF808 material by the incorporation of CeNPs.

Another possible source of error was the decomposition of neat DMNP once the bottle had been opened and exposed to air. However, upon investigation this was found to be insignificant as the DMNP is resistant to hydrolysis in air over several days. As can be seen in Figure 4.15 a single resonance is present at δ = -4.3 ppm corresponding to unreacted DMNP after 9 days following exposure to air.

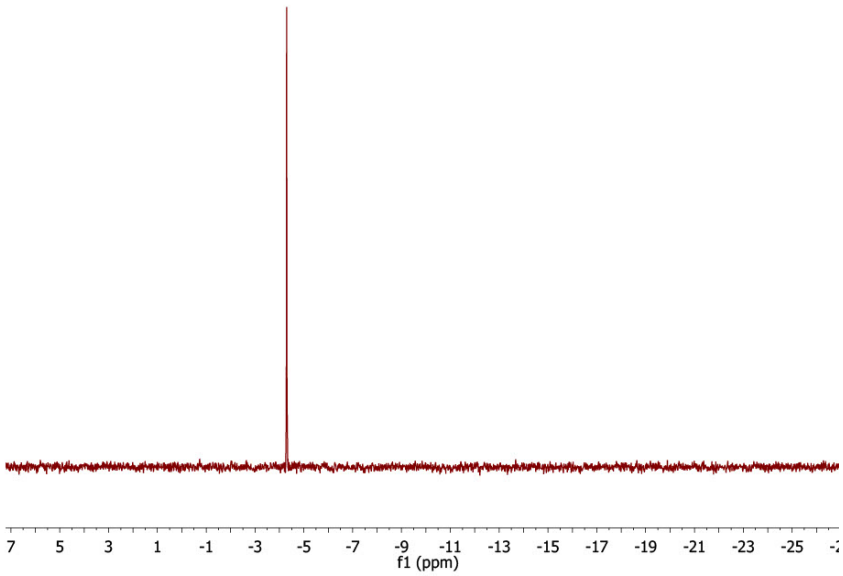

Figure 4.15 $^{31}P\{^{1}H\}$ NMR Spectrum of neat DMNP reagent after 9 days of exposure to air.

Note: DMNP δ = -4.3 ppm.

4.5.3 Optimisation of Experimental Protocol for the Catalytic Hydrolysis of DMNP using CeNP@MOF808

By minimising the time elapsed between mixing the suspension with DMNP (t = 0 minutes) and the first $^{31}P\{^{1}H\}$ NMR spectrum being recorded for the reaction mixture (t minutes), it would be easier to determine any statistical differences in reaction times between the composite CeNP@MOF808 and the reference host structure MOF808. Various sources of error were identified within the experimental protocol that had to be optimised: inaccuracies in weighing catalytic samples using the analytical grade balance (step **1**, Figure 4.13), time window over which the catalyst sample was sonicated to form a suspension (step 3, Figure 4.13) and the subsequent time lag between sonication ceasing and DMNP being added to the suspension (step **4**, Figure 4.13). These sources of error were all derived from the fact that the catalytic activity of heterogeneous materials such as CeNP@MOF808 and MOF808 are a function of the distance DMNP molecules have to travel before reaching the catalytic surface of the composite particles (*i.e.*, mass transport limited); any action which decreases this distance will in turn increase the activity displayed by the catalyst. The error associated with step **1** arises simply in that if there is more catalytic material weighed out, the more catalytic material there will be per unit volume and therefore DMNP molecules must travel a shorter distance before reaching the composite surface, yielding a higher catalytic activity. Therefore, an appropriate mass of catalytic material had to be identified and remain as consistent as possible across multiple repeated measurements. The error introduced in steps **3** arises due to differences in sonication times yielding different particulate sizes of the catalyst powder, with varied particulate dispersion concentrations and related catalytic activities. Thus, again an appropriate sonication time had to be identified and kept fixed across repeated measurements. Similarly, step **4** has a source of error related to the time delay, with longer time delays between sonication ceasing and subsequent addition of DMNP allowing for catalyst particles to aggregate and increasing the distance DMNP molecules must travel before reaching the composite surface, reducing the catalyst activity. Therefore, the optimisation process aimed to minimises these errors through a standardised, streamlined process which could then be replicated several times for both CeNP@MOF808 and control MOF808 in order to build up to statistically comparable data sets that would allow for

confident conclusions to be made from comparisons of catalyst reaction times. It should be noted that several inherent, instrumental sources of error were identified but could not be optimised, these included: calibration shifts in the analytical balance; dispensing errors when using the micropipette, dispensing both buffer solution and DMNP, which is calibrated to deionised water with a density of 1 g/cm^3 and time lags associated with the locking and shimming of the probe in the NMR spectrometer. The source of error associated with the locking and shimming of the probe meant that it would be practically impossible to achieve a NMR measurements before t = 4 minutes (i.e. 4 minutes between the initial mixing of the catalyst suspension with DMNP and the first $^{31}P\{^1H\}$ NMR spectrum being recorded). However, it was judged that by minimising all other sources of error and ensuring that enough replicated results were collected that strong statistical comparisons could be drawn from the conversion times for CeNP@MOF808 and control MOF808.

4.5.3.1 Optimisation of Catalyst Loading Weight: Catalytic Hydrolysis of DMNP with CeNP@MOF808

The first stage to be optimised in the experimental set up for investigating the hydrolysis of DMNP with CeNP@MOF808 was step **1** (see Figure 4.13). What was required was an appropriate amount of material that would: (a) exhibit sufficient activity to allow complete conversion over a time period of 30 minutes; (b) was not an excessive amount that would achieve 100% conversion with the t = 4 minutes inherent time delay; (c) was not sufficient to create a dense suspension in the NMR tube, rendering acquisition of a spectrum impossible and (d) an appropriate amount to allow for several repeated measurements to be performed. Based on literature precedent of using from 0.8 – 2 mg of MOF catalyst loading when investigating the hydrolysis of DMNP (see Table 4.1), initial investigations opted for a 2 mg loading of catalyst weight. 2 mg of control MOF808, CeNP@MOF808 and pristine MOF808 (pristine MOF808 refers to MOF808 which has not been activated under vacuum at 120 °C) were weighed out separately using an analytical grade balance and then each suspended in 1.05 mL of 0.4 M *N*-ethylmorpholine buffer solution (pH = 10.2). 4 µL of DMNP was then added to the suspensions *via* micropipette and swirled for *ca.* 15 seconds, the suspension was then pipetted into an NMR tube and placed into the NMR spectrometer. For all three samples

(control MOF808, CeNP@MOF808 and pristine MOF808), at 2 mg loading weight, samples showed complete conversion of the DMNP reagent after 5 minutes with no differences in conversion rate observed. As can be seen in Figure 4.16 for CeNP@MOF808, after 5 minutes only one resonance can be observed in the $^{31}P\{^{1}H\}$ NMR spectrum, at δ = 2.9 ppm corresponding to the decomposition product, MMP, this indicates that complete conversion was achieved after 5 minutes of the DMNP being mixed with the catalyst suspension. The same observations were made in Figure 4.17 and Figure 4.18,corresponding to control MOF808 and pristine MOF808 respectively. With resonances on visible at δ = 2.9 ppm, indicating complete conversion to the decomposition product MMP after 5 minutes.

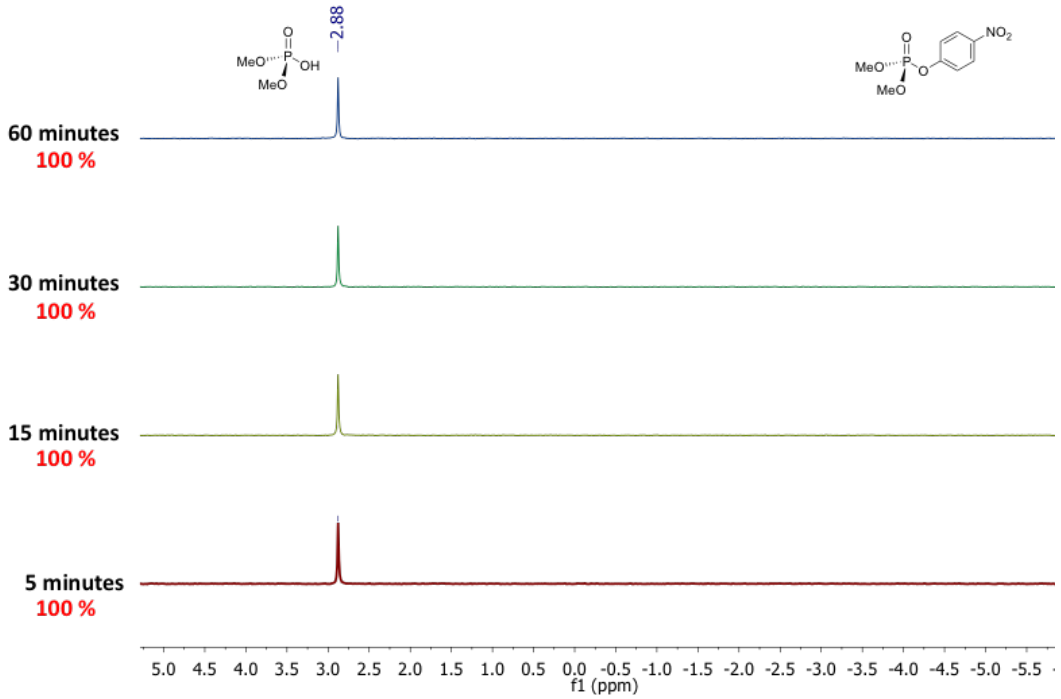

Figure 4.16: Stacked $^{31}P\{^{1}H\}$ NMR spectra for catalytic hydrolysis of DMNP using 2 mg of CeNP@MOF808 (5.6 μmol [Zr], 0.4 μmol [Ce]). Time stamps (black) and % conversions (red) shown on left-hand side.

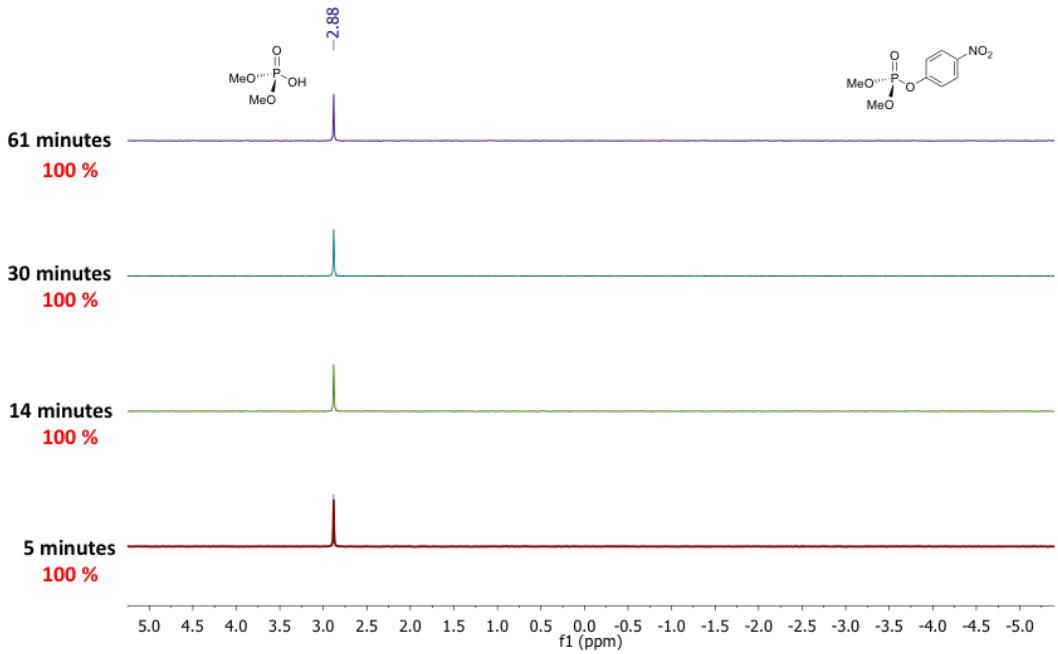

Figure 4.17: Stacked $^{31}P\{^{1}H\}$ NMR spectra for catalytic hydrolysis of DMNP using 2 mg of control MOF808 (7 μmol [Zr], 0 μmol [Ce]). Time stamps (black) and % conversions (red) shown on left-hand side.

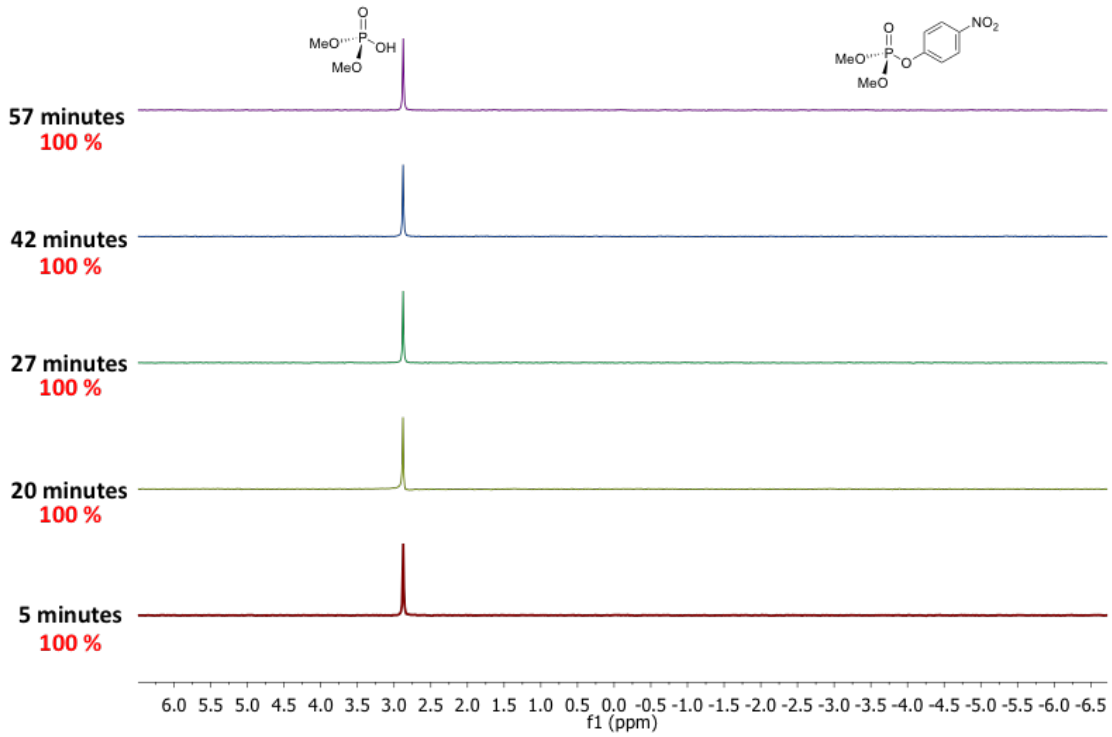

Figure 4.18: Stacked $^{31}P\{^{1}H\}$ NMR spectra for catalytic hydrolysis of DMNP using 2 mg of pristine (as synthesised) MOF808 (8.1 μmol [Zr], 0 μmol [Ce]). Time stamps (black) and % conversions (red) shown on left-hand side.

The procedure for recording the $^{31}P\{^{1}H\}$ NMR spectrum involves several steps including tunning of the probe, locking of the probe onto the residual solvent signal and shimming of the magnetic field around the sample. All of these steps results in an in-built time delay of *ca.* 5 minutes before spectra can be acquired, from which conversions can be calculated, during which time the hydrolysis reaction is taking place within the NMR tube. Given that the experimental set up is limited *i.e.* 5 minutes is the lowest t (time) value that can be measured, a catalyst loading weight of 2 mg was deemed impractical given the fast catalysis rates associated with this loading weight. In order to compare the composite, CeNP@MOF808, to the reference structure MOF808, it was required that conversion be observed within the NMR timescale. This would allow for statistical comparison of the conversions to determine what influence the introduction of cerium ions to the MOF808 structure had on its catalytic abilities. Thus, a lower loading weight of catalyst was required, which would have a lower catalytic activity, allowing the conversion to be observed within a practical timescale. A second series

of experiments were therefore conducted using a smaller catalytic loading weight of 0.5 mg of catalyst or control materials (CeNP@MOF808, control MOF808 and pristine MOF808).

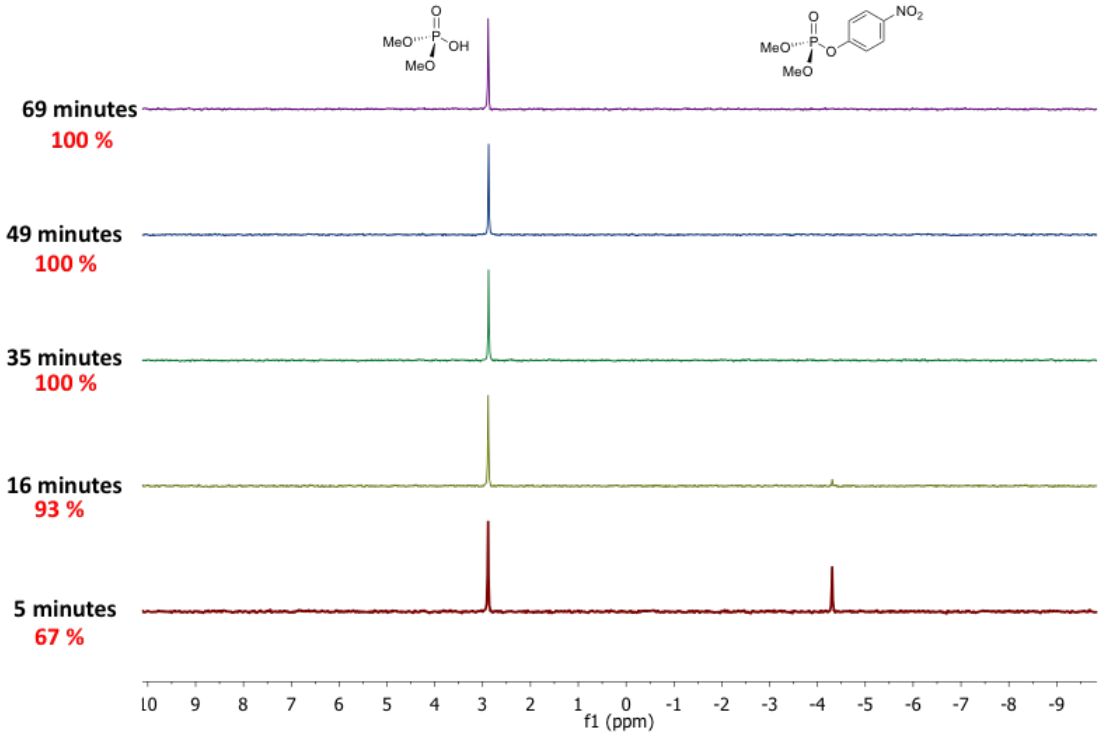

Figure 4.19: Stacked $^{31}P\{^{1}H\}$ NMR spectra for catalytic hydrolysis of DMNP using 0.5 mg of of CeNP@MOF808 (1.4 μmol [Zr], 0.1 μmol [Ce]). Time stamps (black) and % conversions (red) shown on left-hand side.

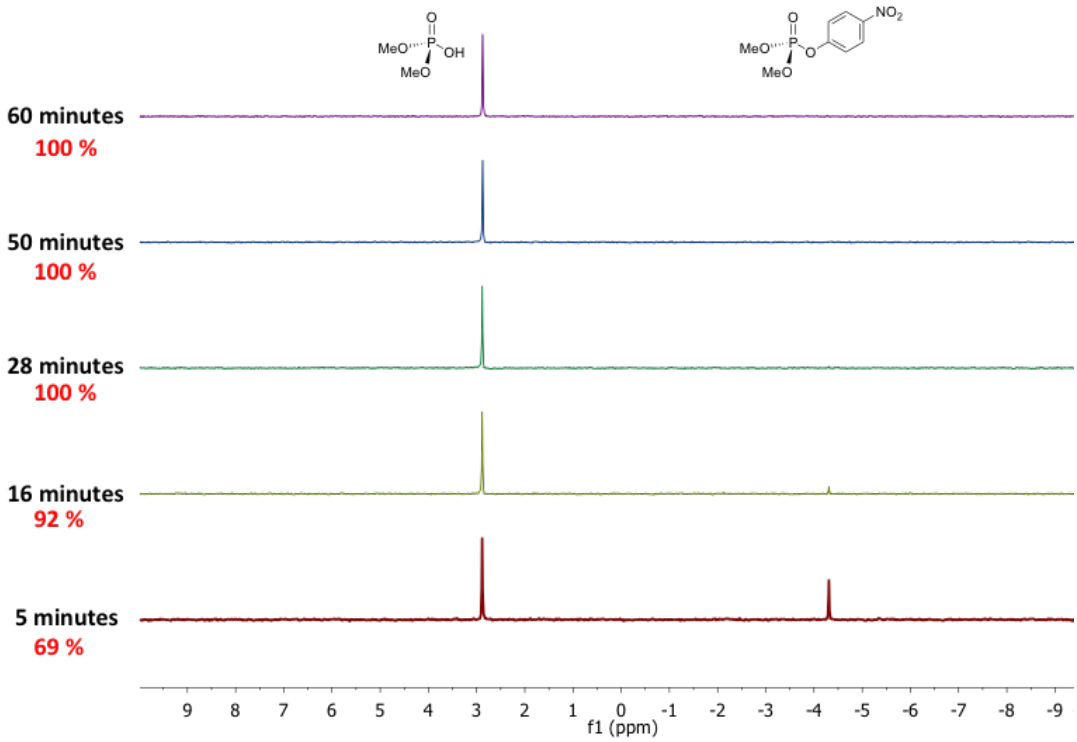

Figure 4.20: Stacked $^{31}P\{^{1}H\}$ NMR spectra for catalytic hydrolysis of DMNP using 0.5 mg of control MOF808 (1.8 μmol [Zr], 0 μmol [Ce]). Time stamps (black) and % conversions (red) shown on left-hand side.

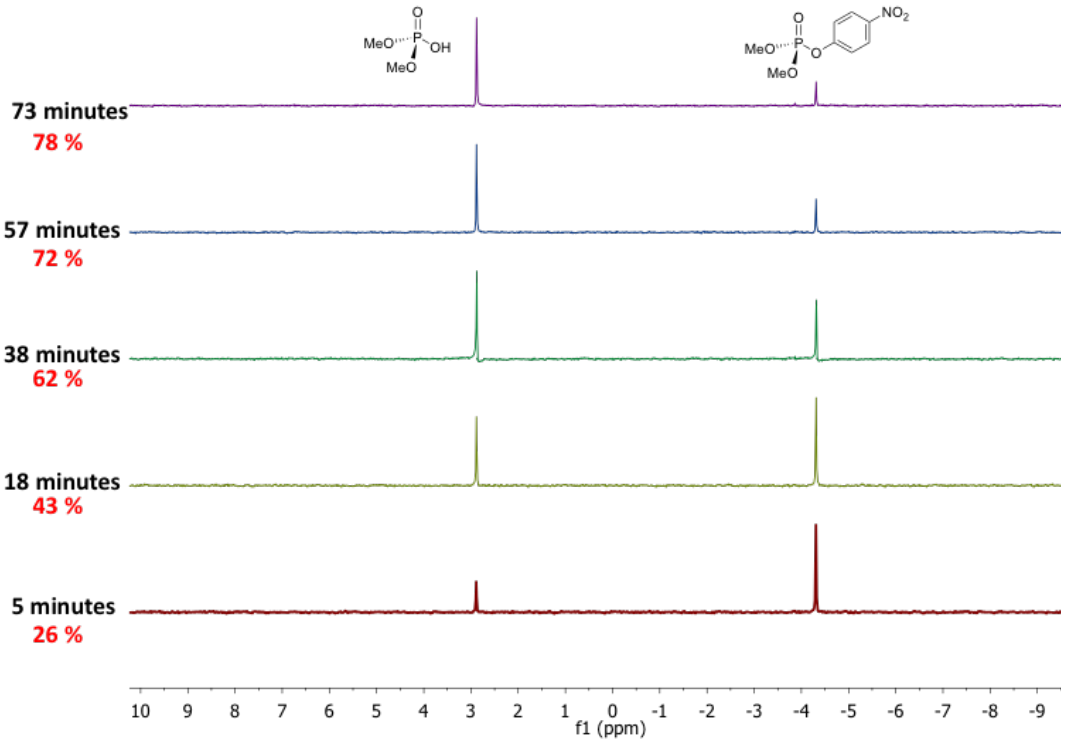

Figure 4.21: Stacked $^{31}P\{^{1}H\}$ NMR spectra for catalytic hydrolysis of DMNP using 0.5 mg of pristine (as synthesised) MOF808 (2.0 μmol [Zr], 0 μmol [Ce]). Time stamps (black) and % conversions (red) shown on left-hand side.

The aim was to reduce the rate of the catalytic hydrolysis of DMNP and allow for conversion to be observed within a practical time window, and this was achieved with a catalyst loading of 0.5 mg. As can be seen in Figure 4.19 and Figure 4.20 both CeNP@MOF808 and control MOF808 showed complete conversion after *ca.* 30 minutes, with only one resonance at δ = 2.9 ppm, indicating full conversion to DMP. It could be concluded that the lower catalytic loading of 0.5 mg of material allowed for conversion of the DMNP to be observed *via* $^{31}P\{^{1}H\}$ NMR spectroscopy and within a practical time window – as expected for a heterogeneous based catalyst.[21] Pristine MOF808 failed to show complete conversion, within the observed time frame, achieving 78% after *ca.* 70 minutes, see Figure 4.21. This suggests that the activation process of thermally pre-treating the MOF (as is the case with both control MOF808 and CeNP@MOF808) yields a more catalytically active material towards DMNP hydrolysis. One possible mechanism may be the introduction of a greater number of free metal sites at the Zr_6 cluster which act as catalytic sites. This has been observed in other Zr_6 MOF based catalysts including MOF808, NU-1000 and UiO-66, where dehydration/dehydroxylation yields

free metal sites at the Zr_6 cluster nodes which are more readily accessible and produce rate-determining steps that are faster and therefore have faster rates of reaction overall.[18,20,21] However, it should be noted that computational studies on the hydrolysis of GB (Sarin) have shown that for MOF808 the rate-determining step (RDS) is the nucleophilic attack of the coordinated P=O bond, not the displacement of coordinated H_2O/OH^-, this was in contrast to UiO-66 and NU-1000 where the binding of Sarin to the Zr_6 clusters was the RDS.[30] DMNP was not featured in these computational studies however, and given the different structures and hydrolysis kinetics exhibited by DMNP and Sarin it is reasonable to assume different rate-determining steps. A comparison of catalytic hydrolyses of DMNP with CeNP@MOF808, MOF808 control and pristine MOF808 is show in Figure 4.22. Conversion is clearly observed within an appropriate timescale when a catalyst loading of 0.5 mg of CeNP@MOF808 or MOF808 is used. However, it is not possible to distinguish any differences in catalysis rates due to the insufficient number of data points before 100% conversion. In both cases where CeNP@MOF808 and MOF808 were adopted as catalysts, only two $^{31}P\{^1H\}$ NMR spectra were recorded that showed conversions below 100%. Therefore, it was appropriate to further investigate lower catalyst loadings, with the aim again to reduce the catalytic activity, and while this would result in longer experimental times, it would allow for the acquisition of more data points before 100% conversion of DMNP.

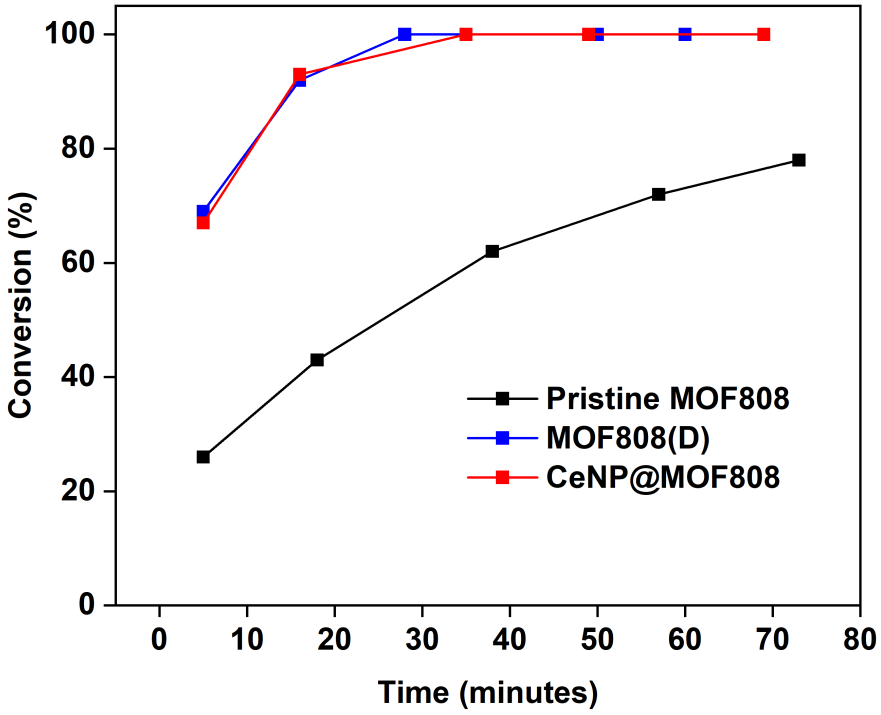

Figure 4.22 Conversion vs. time plot for the catalytic hydrolysis of DMNP to dimethoxyphosphoric acid using 0.5 mg loadings of pristine MOF808, MOF808(D) and CeNP@MOF808, monitored via $^{31}P\{^{1}H\}$ NMR

$^{31}P\{^{1}H\}$ NMR spectra for the catalytic hydrolyses of DMNP using 0.2 mg loading weights of CeNP@MOF808 and MOF808 are show in Figure 4.23 and Figure 4.24, respectively. Measurements were performed in duplicate with reaction conversion % shown as ranges where appropriate in Figure 4.23 and Figure 4.24. Pristine MOF808 was not measured at these lower loading weights as it had already proven to be inefficient towards catalytic hydrolysis compared to CeNP@MOF808 and control MOF808 at 0.5 mg loadings (see Figure 4.22). The data for CeNP@MOF808 suggested significantly higher catalytic activity relative to control MOF808. After 36 minutes, 95% conversion of the DMNP reagent had been observed, for both duplicate measurements, when using CeNP@MOF808, while only 60-77% conversion had been observed when using control MOF808. However, this is inconsistent with catalytic hydrolysis data for a catalyst loading of 0.5 mg – with both CeNP@MOF808 and control MOF808 displaying indistinguishable conversion profiles and suggests that the apparent greater catalytic activity of CeNP@MOF808 relative to MOF808 is not a real effect. This discrepancy between the catalytic conversions with CeNP@MOF808 and control MOF808 at 0.5 and 0.2 mg loading weights most likely arises from the significant source of error

introduced when weighing such small quantities of sample at 0.2 mg. In general, the small the sample weighed out, the more of an influence error in measurements will have relative to the absolute quantity of material. For example, a 0.1 mg error acquired when weighing out 0.5 mg of catalyst would result in a 20 % error in the measurement, while the same weighing error would result in a 50 % error in the measurement of 0.2 mg of catalyst. Therefore, given that the aim was to identify a loading weight of the catalytic sample that would allow for the hydrolytic conversion of DMNP to DMP to be observed within a reasonable time window, while also allowing for a sufficient number of $^{31}P\{^{1}H\}$ NMR spectra to be acquired before 100% is achieved, it was concluded that 0.5 mg would be the optimum loading weight with $^{31}P\{^{1}H\}$ NMR spectra recorded at more regular intervals allowing for a greater number of data points to be acquired.

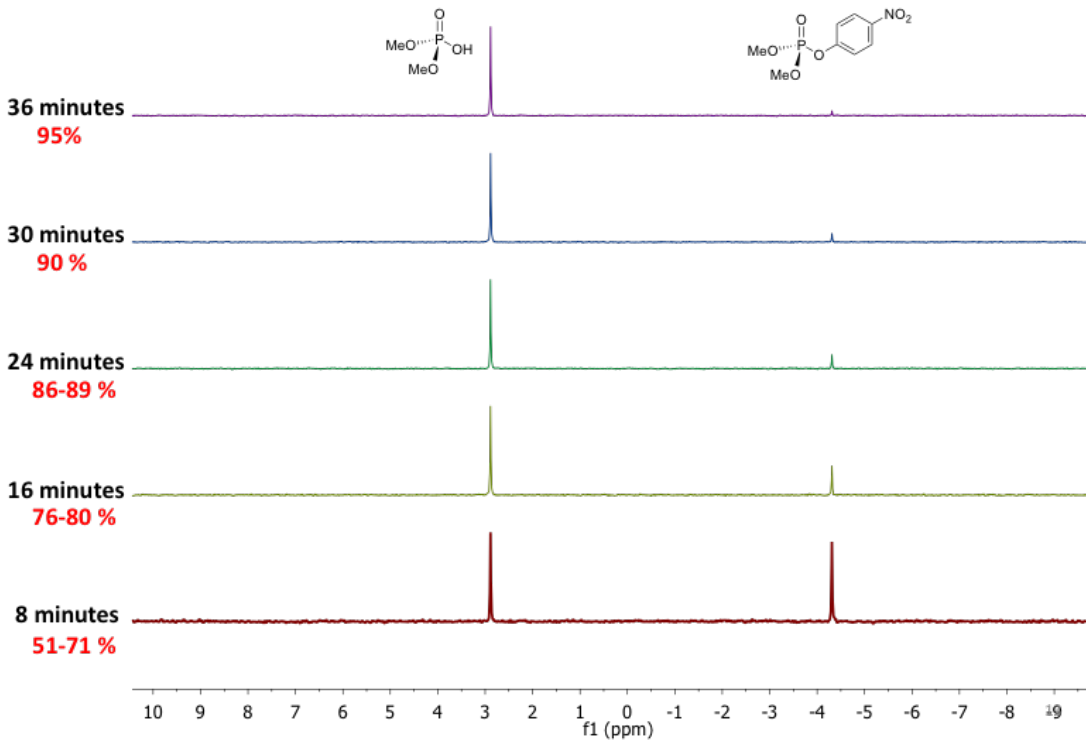

Figure 4.23: Stacked $^{31}P\{^{1}H\}$ NMR spectra for catalytic hydrolysis of DMNP using 0.2 mg of of CeNP@MOF808 (0.6 μmol [Zr], 0.04 μmol [Ce]). Time stamps (black) and % conversions (red) shown on left-hand side.

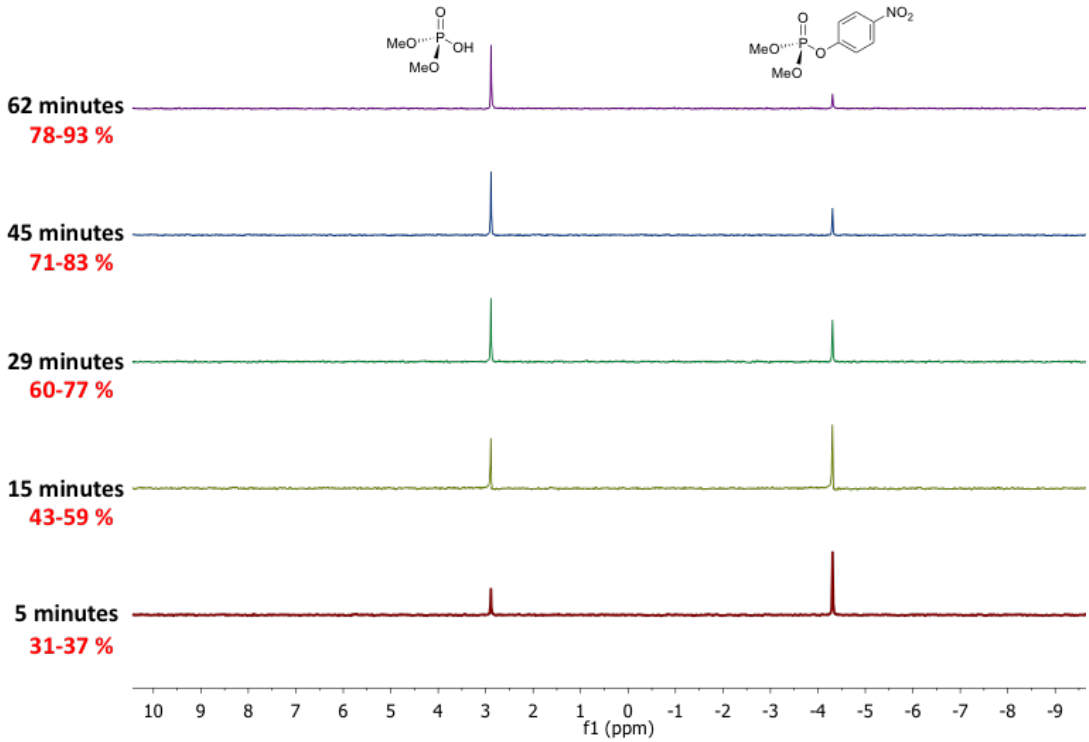

Figure 4.24: Stacked $^{31}P\{^{1}H\}$ NMR spectra for catalytic hydrolysis of DMNP using 0.2 mg of control MOF808 (0.7 μmol [Zr], 0 μmol [Ce]). Time stamps (black) and % conversions (red) shown on left-hand side.

4.5.3.2 Optimisation of Catalyst Suspension Sonication Time: Catalytic Hydrolysis of DMNP with CeNP@MOF808

Both catalytic materials, CeNP@MOF808 and MOF808 are highly charged, static solids – where the particles easily agglomerate into larger aggregates. This is a source of error in that between measurements, depending upon the handling of the solid sample (*e.g.,* if it is placed onto a metal surface, in contact with charged surfaces, *etc*.) the solid powder would have different degrees of dispersion in suspension, yielding different distances of travel DMNP molecules would have to travel in order to reach the composite surface (mass transport). Therefore, to account for mass transport limitations, various sonication times were investigated with the aim of identifying the shortest sonication time that yielded a homogeneous suspension (see step **3** in Figure 4.13). Note here that the term 'homogeneous suspension' refers to a somewhat fleeting homogeneity, whereby once sonicated the suspension will remain largely homogeneous for several minutes, during which time the DMNP can be added and the reaction initiated. Based on the optimisation of the catalytic loading weight, 0.5 mg of catalyst (MOF808) was weighed out using an analytical grade balance into a 1 dram (3.7 mL) vial and subsequently suspended in 1.05 mL of 0.4 M *N*-ethylmorpholine buffer solution. Vials were then placed into a large beaker containing deionised water which was itself placed into an ultrasonic bath. The catalyst suspension samples were then sonicated for a specified time, noting the homogeneity of the catalyst suspension immediately upon sonication ceasing. Determination of homogeneity of the suspension was achieved through visual examination, where a homogeneous suspension was defined as having no large particles visible which could be seen freely floating upon up turning the sample several times after sonication.

Table 4.2: Summary of MOF808 catalyst suspension appearance after various sonication times.

Sonication Time	**Catalyst Suspension Appearance**
10 seconds	Large particulates / inhomogeneous
30 seconds	Large particulates / inhomogeneous
1 minute	Small particulates / inhomogeneous

2 minutes	No visible particulates / homogeneous
3 minutes	No visible particulates / homogeneous
4 minutes	No visible particulates / homogeneous
5 minutes	No visible particulates / homogeneous

Summarised in Table 4.2 are the various sonication times investigated and the appearance of the MOF808 suspension after the sonication time ceasing. Note here that it was assumed that MOF808 and CeNP@MOF808 would exhibit similar dispersion abilities and therefore only MOF808 was investigated. Sonication times from 10 seconds to 1 minute failed to yield a homogeneous MOF808 suspension, with large and small particulates easily visible upon upturning the vial several times. A sonication time of 2 minutes was the shortest time that resulted in the formation of a homogeneous MOF808 suspension. All sonication times beyond 2 minutes also resulted in homogeneous MOF808 suspensions, however the tendency of the sonic bath to heat up after 3 minutes meant that 2 minutes was the optimum sonication time for catalyst suspension sample.

4.5.3.3 Optimisation of Time Delay Between Sonication Ceasing and DMNP Being Added: Catalytic Hydrolysis of DMNP with CeNP@MOF808

While 2 minutes of sonication was sufficient to yield a homogeneous suspension of MOF808 in the buffer solution, the homogeneity is fleeting – after several minutes the particles would begin to agglomerate and settle as a powder at the bottom of the vial if left undisturbed. This is a source of error to the experimental technique in that the larger the time period elapsed between sonication ceasing and DMNP being added to the catalyst suspension, the more likely particles will agglomerate and settle – increasing mass transport limitations and reducing the associated catalytic activity. Therefore, a consistent time delay, which allowed for the suspension to remain homogeneous while also being experimentally practicable, had to be identified and remain consistent between repeated measurements. 0.5 mg of the catalyst MOF808, was dispersed in 1.05 mL of *N*-ethylmorpholine buffer solution and sonicated for 2 minutes to achieve a fleeting homogeneous suspension.

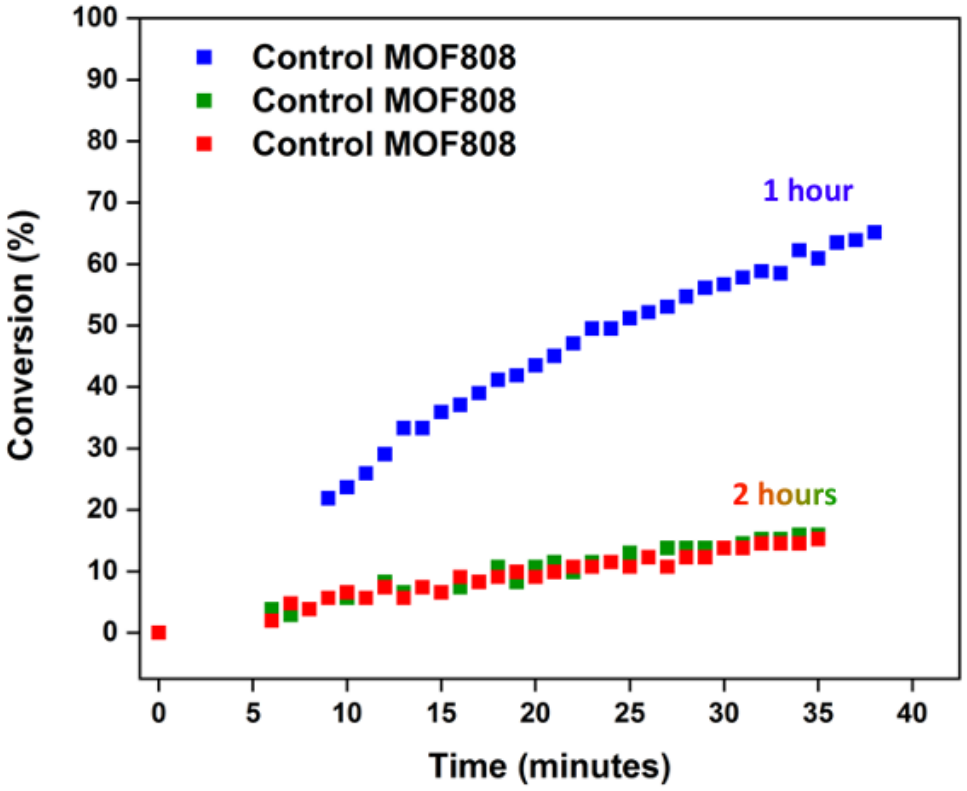

Figure 4.25: Conversion vs. time plot for the catalytic hydrolysis of DMNP to dimethoxyphosphoric acid using 0.5 mg loadings of control MOF808 with time delays

between sonication ceasing and mixing with DMNP of 1 (blue) and 2 hours (red and green), monitored via $^{31}P\{^{1}H\}$ NMR.

The DMNP conversion plots are shown previously in Figure 4.25 for MOF808 suspensions left for 1 and 2 hours before mixing with DMNP. A delay of 1 hour resulted in conversions reaching *ca.* 65% after 35 minutes, delays of 2 hours resulted in conversions reaching *ca.* 15% after 35 minutes. This demonstrates the strong influence that the time gap between sonication ceasing and mixing the suspension with DMNP has on the overall catalytic activity of the catalyst suspension, with longer time gaps yielding lower conversion rates. This is in line with the general model of heterogeneous catalysis, whereby longer time gaps will allow for greater solid particle aggregation and resulting in lower surface areas and reduced catalytic activities. This set of experiments was then repeated, only the change being that both CeNP@MOF808 and control MOF808 were used as catalytic materials, and the time delay was significantly reduced 4 minutes and 1.5 minutes. Conversion plots for the catalytic hydrolysis of DMNP using both CeNP@MOF808 and control MOF808 are shown below in Figure 4.26. Note that the catalytic conversion with control MOF808 with a 4 minute delay was repeated.

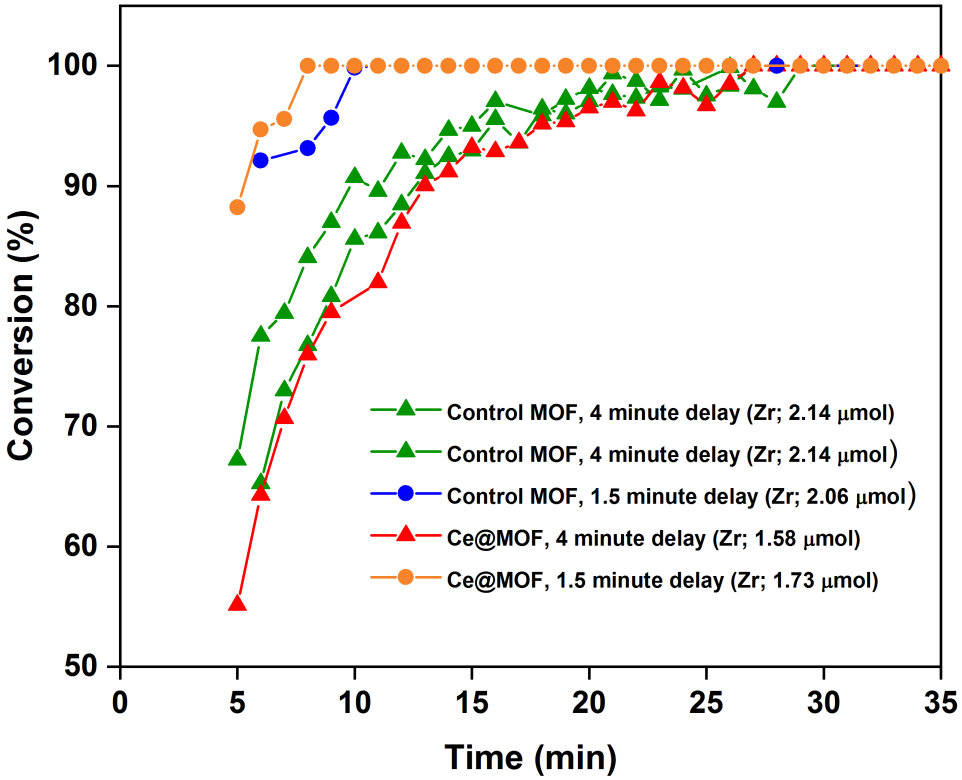

Figure 4.26 Conversion vs. time plot for the catalytic hydrolysis of DMNP to dimethoxyphosphoric acid using 0.5 mg loadings of control MOF808 and CeNP@MOF808 with time delays between sonication ceasing and mixing with DMNP of 1.5 (circle points) and 4 (triangle points) minutes, monitored via $^{31}P\{^{1}H\}$ NMR.

As expected, and consistent with the conversion observed when the time delay was 1 – 2 hours long (see Figure 4.25), catalytic conversions are faster when the time delay between sonication ceasing and mixing with DMNP is reduced from 4 minutes to 1.5 minutes. The 1.5 minute time delay resulted in the catalyst suspension achieving 100% conversion after 10 minutes, while the 4 minute delay resulted in the catalyst suspension achieving 100% conversion after 25 minutes, a significantly longer reaction time. Both catalyst samples, CeNP@MOF808 and control MOF808, exhibited this enhanced catalytic activity with reduced time delays between sonication ceasing and mixing with DMNP.

Further reductions in the time delay failed to materialise in any significantly observable increases in conversion rate with both CeNP@MOF808 and control MOF808, with 1.5 minutes

and 30 seconds delay times showing indistinguishable and overlapping conversion plot data (see Figure 4.27).

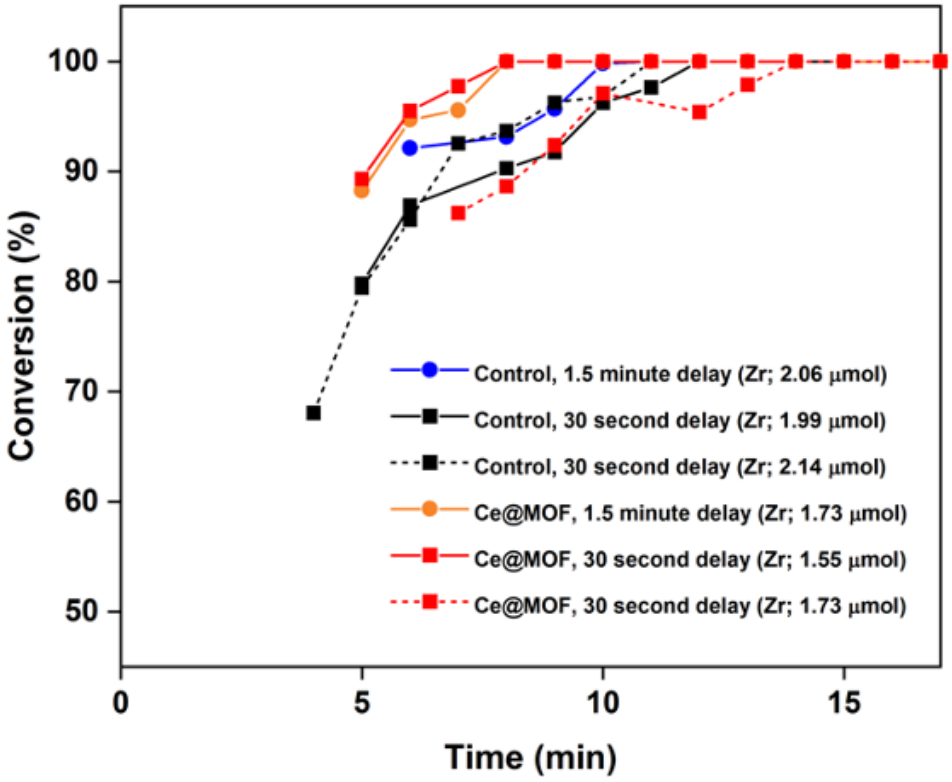

Figure 4.27 Catalytic conversions for 0.5 mg of control MOF808 and CeNP@MOF808 with 30 seconds – 1.5 minutes elapsed between sonication and mixing.

A separate factor that had to be considered was that weight for weight, control MOF808 would have a higher number of Zr_6 nodes compared with CeNP@MOF808, and that this could influence the catalytic activity, with control MOF808 having a greater number of active sites and therefore a greater catalytic activity. Based on EDX and ICP-OES determined wt% of Zr it was possible to calculate the respective quantities of Zr in µmols for both control MOF808 and CeNP@MOF808, these have been included in Figure 4.26 and Figure 4.27. There was no observable relationship between the Zr µmol amounts and the rate of conversions. As seen in Figure 4.26, for a time delay of 1.5 minutes CeNP@MOF808, with a lower Zr content (1.73 µmols), exhibits a higher conversion rate compared to control MOF808, with a higher Zr content (2.06 µmols). Whereas, for a time delay of 4 minutes, CeNP@MOF808 with a lower Zr content (1.58 µmols) shows a lower conversation rate compared to control MOF808 with

a higher Zr content (2.14 μmols). Furthermore, in Figure 4.27 it can be observed that CeNP@MOF808 with a higher Zr content (1.73 μmols), displays a lower conversation rate to CeNP@MOF808 with a lower Zr content (1.55 μmols), despite the fact that both have the same time delay between sonication and mixing with DMNP.

Despite there being no observable differences in catalytic hydrolysis rates of DMNP when the time delay between sonication ceasing and mixing the suspension with DMNP is reduced from 1.5 minutes to 30 seconds, it was concluded that 30 seconds would be the standard time delay applied to all repeated measurements as it would allow for earlier t (time) data points to be collected. Overall, three experimental parameters were optimised in the general experimental protocol (see Figure 4.13) for monitoring the catalytic hydrolysis of DMNP, these are summarised in Table 4.3 below.

Table 4.3: Optimised parameters for stages 1, 3 and 4 for the general experimental procedure in monitoring the catalytic hydrolysis of DMNP.

Step	Parameter	Optimised Condition
1	Catalyst Loading	0.5 mg
3	Catalyst Suspension Sonication Time	2 minutes
4	Time Delay	30 seconds

4.5.4 Catalytic Studies of CeNP@MOF808 Towards DMNP Hydrolysis

Following on from the optimisation studies an optimised procedure was established that involved sonicating 0.5 mg of MOF sample in 1.05 mL of aqueous 0.4 M *N*-ethylmorpholine solution for 2 minutes and subsequently adding DMNP within 30 seconds of the sonication ceasing. Eight separate repeat measurements were taken for both CeNP@MOF808 and control MOF808 (see Figure 4.28) and each monitored *via* $^{31}P\{^{1}H\}$ NMR over *ca.* 30 minutes. Conversion plots for both CeNP@MOF808 and control MOF808 show the same general structure of an inverse exponential decay function that plateaus between 7 and 30 minutes. That the conversion plots appear similar after each repeated measurement for both

CeNP@MOF808 and control MOF808 is an indication of the reproducibility of the measurement. However, it is a limitation of optimised experimental protocol (see Figure 4.13 and Table 4.3) that the earliest $^{31}P\{^{1}H\}$ NMR that can be acquired is 4 minutes after mixing DMNP with the catalytic suspension. This is specific to this optimised experimental protocol.

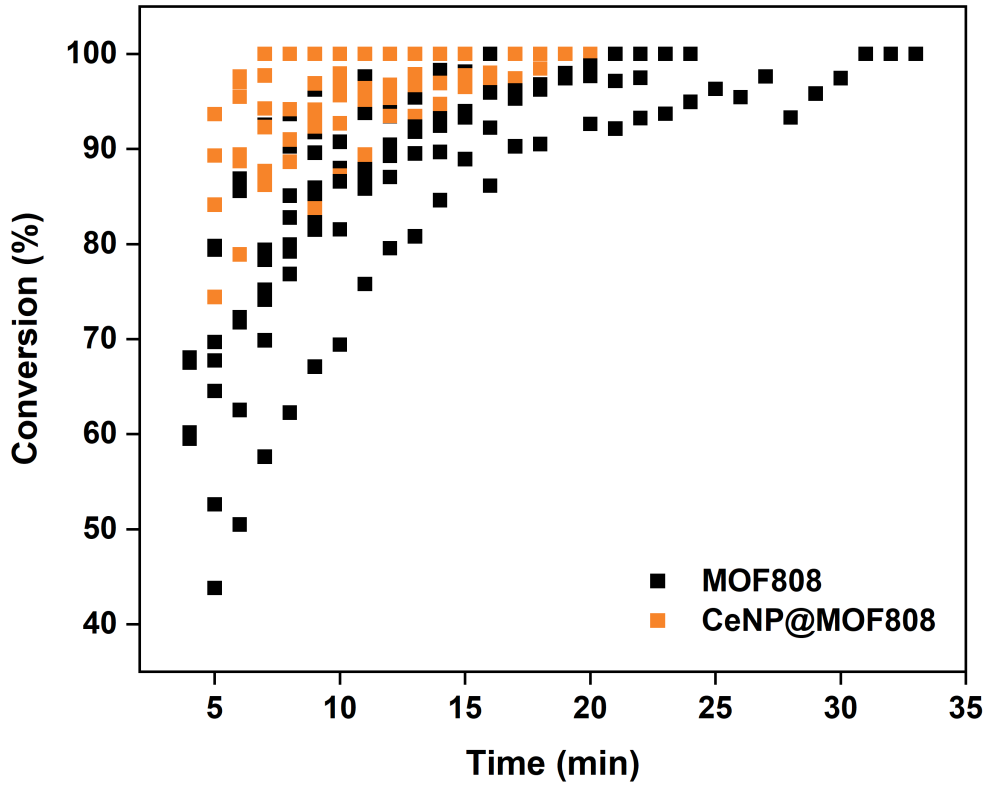

Figure 4.28: Conversion plots for the catalytic hydrolysis of DMNP with 0.5 mg of MOF808 and CeNP@MOF808, time delay of 30 seconds.

While there appears to be a clear clustering of conversion plots towards faster conversions for CeNP@MOF808, in comparison to those of the control MOF808, the two data sets have significant variability and overlap (Figure 4.28). Thus, conclusive statements relating to differences in catalytic conversion rates for CeNP@MOF808 and control MOF808(D) must be made with statistical justification.

By fitting each conversion plot, as seen in Figure 4.28 above, with an exponential decay function of the type $f(x) = y_0 + A_1e^{-x/t1}$, $t_{1/2}$ values can be subsequently determined for each conversion plot. Considering these $t_{1/2}$ values in aggregate, average $t_{1/2}$ conversion times for

catalytic hydrolysis of DMNP with CeNP@MOF808 and control MOF808 were calculated to be: 2.4 minutes (144 seconds) and 3.7 minutes (222 seconds) respectively (see Figure 4.29).

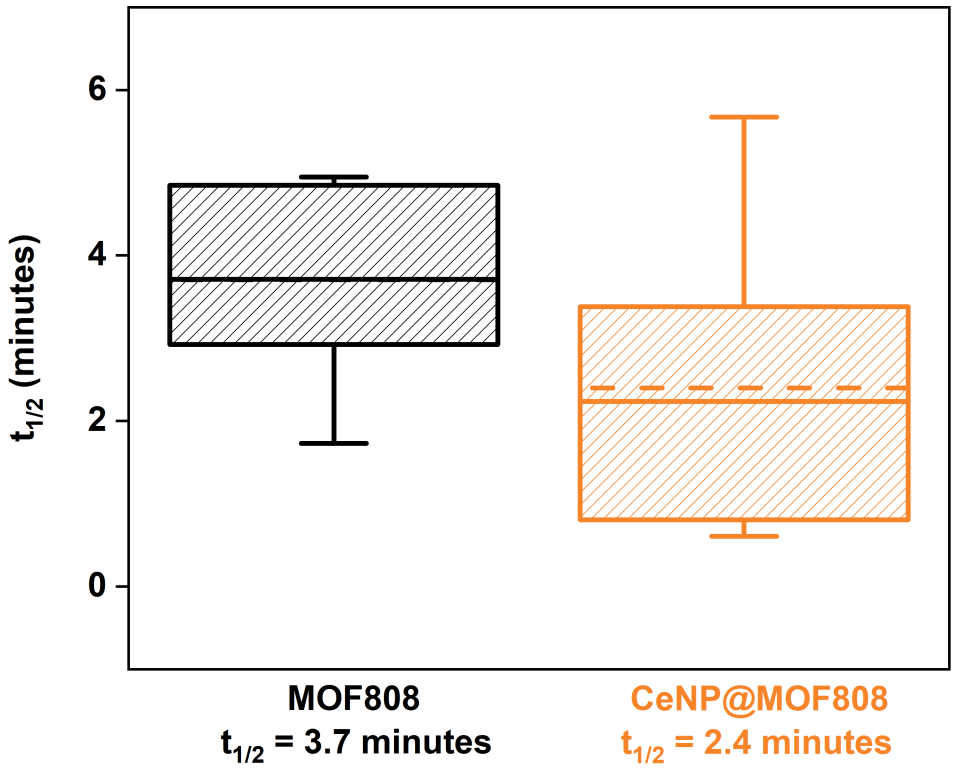

Figure 4.29: Box and whisker plot showing $t_{1/2}$ ranges for the catalytic hydrolysis of DMNP with 0.5 mg of MOF808 (8 data points) and CeNP@MOF808 (7 data points). Top and bottom whiskers represent "maximum" and "minimum" values in the data range, solid dividing line represents median values, broken dividing line represents mean values and the top and bottom of the box plots representing the 75th and 25th percentile respectively.

Without excluding any outliers, T-test calculations were then used to determine the statistical significance of differences in average $t_{1/2}$ values for the two samples with their specific variances. T-test calculations work by determining a t-value that represents the mean-to-variance ratio of the compounded data sets (CeNP@MOF808 and control MOF808). If the calculated t-value is greater than a critical value (determined based on the degrees of freedom and p = 0.05 confidence interval) then the difference in mean values of the two data

sets is *statistically significant*, the opposite is true if the t-value is lower than the critical value. T-test calculations revealed that the difference in average $t_{1/2}$ values were not significantly different from 0 and therefore the Null Hypothesis was accepted.

From Figure 4.29 above it can be seen that there is a high variability in the CeNP@MOF808 $t_{1/2}$ values. However, previous T-test analysis fails to take into consideration any outliers that exist within the data sets. One significant outlier was identified within the CeNP@MOF808 data set, more specifically data set 4 (see Figure 4.31) and removed. It is important when removing one or more data points that reasoning is provided for why it should be removed. Failure to do so often leads to the process of 'p-hacking' whereby data sets are selectively constructed whereby data points that would suggest no statistical significance in a finding are discriminately removed. As can be seen from the exponential decay fitting for data set 4 in Figure 4.31, while the fit did converge – when compared to the other data sets it is limited and a poor fit. This resulted in data set 4 producing a $t_{1/2}$ value significantly larger than the other data sets, thus skewing the mean $t_{1/2}$ value for CeNP@MOF808 towards longer conversion times and reducing the statistical significance of the difference with the $t_{1/2}$ value for the MOF808 data sets. Therefore data point 4 could be removed from the aggregated CeNP@MOF808 data set with justification. It is also worth to note that the number of repeated measurements collected in this study was somewhat out-with regular procedures adopted when measuring the $t_{1/2}$ values of MOF based catalysts towards DMNP hydrolysis. Of the studies noted in Table 4.1, which include monitoring the hydrolysis of DMNP using Zr based MOFs including MOF808, NU-1000, UiO-66, UiO-67, Ce-BDC, CeNP@Ce-BDC and CeNP@NU-1000 – none repeated the measurements and derived an average $t_{1/2}$. This is particularly surprising given the conclusions that were drawn, for example in the case of comparing Ce-BDC and CeNP@Ce-BDC where there was a reduction $t_{1/2}$ value from 9 minutes from 6.2 minutes. The authors then conclude that the incorporation of the cerium based nanoparticles into the framework show a clear enhancement of the MOF catalytic properties, without showing more than one data set for both Ce-BDC and CeNP@Ce-BDC. Thus, relative to literature the comparisons made in this study (with several measurements made for both CeNP@MOF808 and MOF808) are well supported by statistical comparisons.

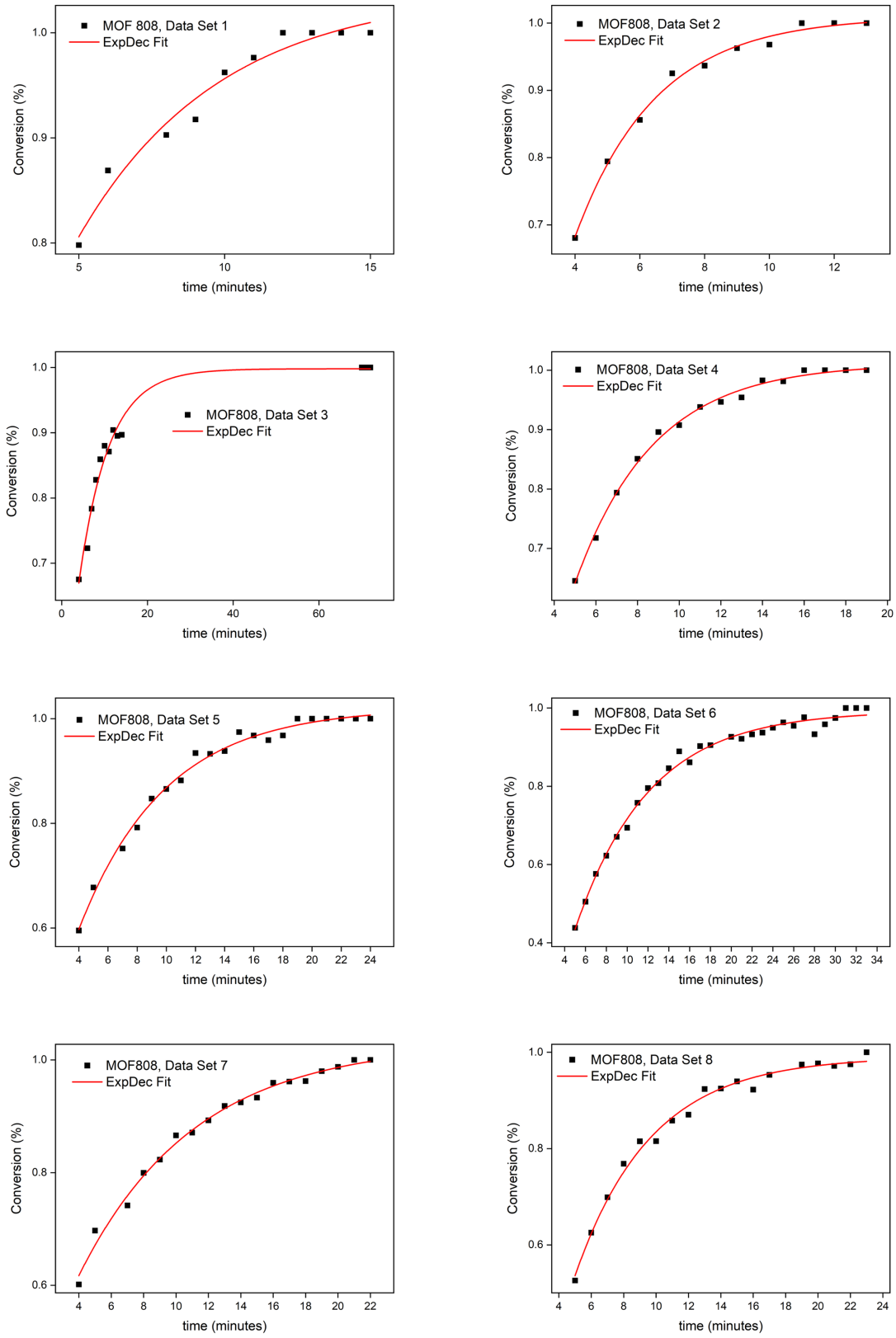

Figure 4.30: Exponential decay fitting of the control MOF808 DMNP hydrolysis data set, 8 separate functions all converged successfully with adj. R^2 in the range of 0.96 – 0.99.

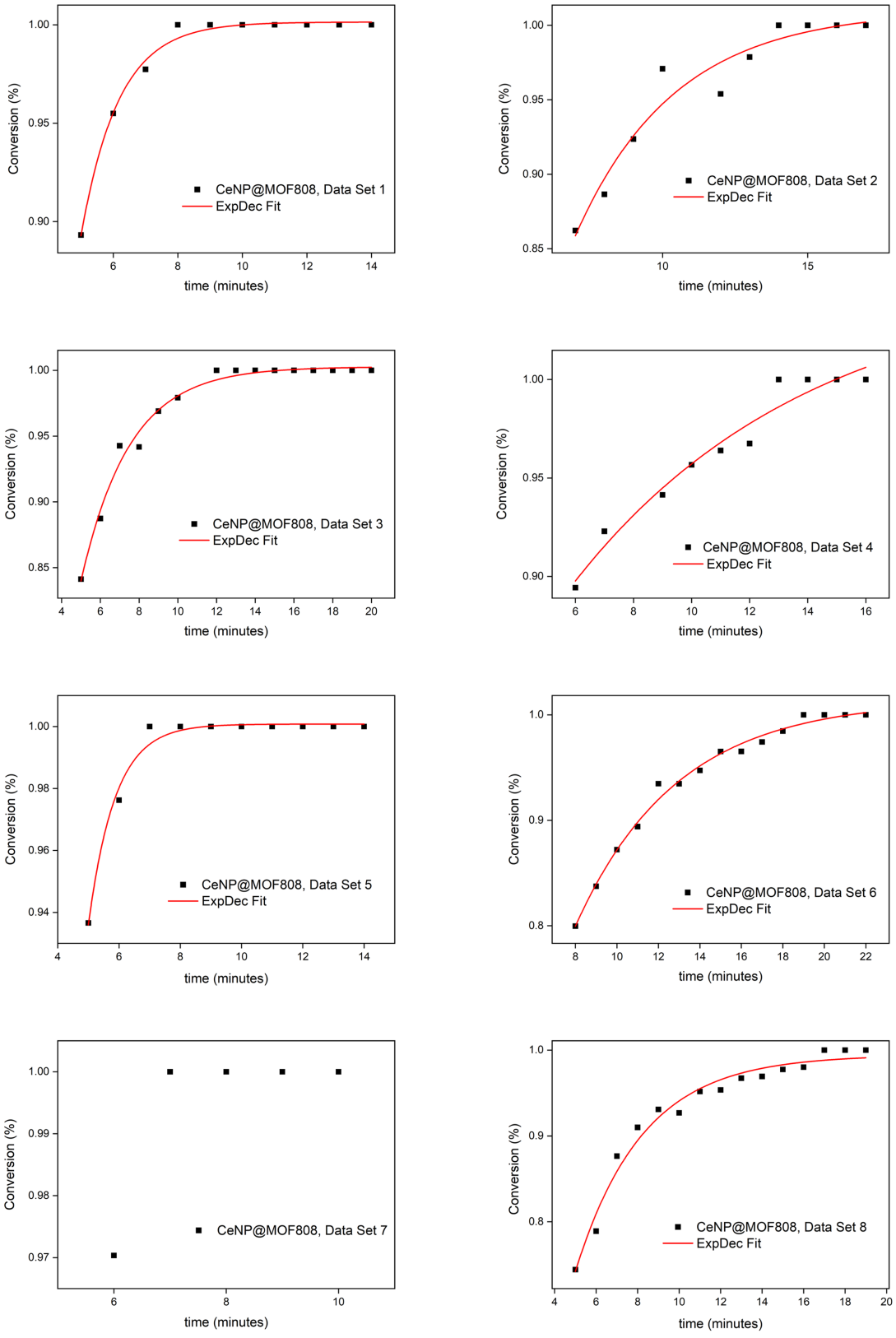

Figure 4.31 Exponential decay fitting of the CeNP@MOF808 DMNP hydrolysis data set, 7 separate functions converged successfully with adj. R^2 in the range of 0.93 – 0.99.

As seen below in Figure 4.32 removing this single outlier (CeNP@MOF808 data set 4) yields a smaller average and significantly reduced variability in the CeNP@MOF808 $t_{1/2}$ values.

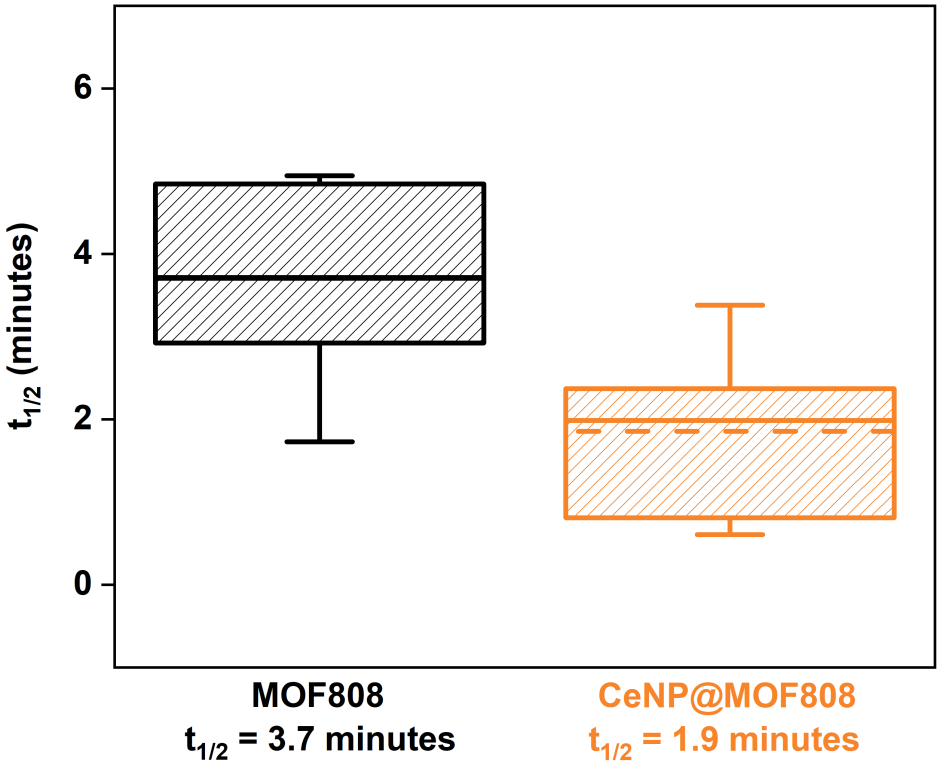

Figure 4.32 Box and whisker plot showing $t_{1/2}$ ranges for the catalytic hydrolysis of DMNP with 0.5 mg of MOF808 and CeNP@MOF808. Top and bottom whiskers represent "maximum" and "minimum" values in the data range, solid dividing line represents median values, broken dividing line represents mean values and the top and bottom of the box plots representing the 75th and 25th percentile respectively.

Applying a T-test once again revealed that the difference between average $t_{1/2}$ values for the MOF808 (222 seconds) and CeNP@MOF808 (114 seconds) data sets were now significantly different and out-with the chance occurred by common error. Therefore, the incorporation of cerium based nanoparticles into MOF808 have been shown to enhance the catalytic activity of MOF808 towards the hydrolysis of DMNP. It should also be noted that the incorporation of the CeNPs into the MOF808 structure did not inhibit the catalytic abilities of the MOF structure. This is consistent with literature observations made for $Zr_xCe_{1-x}O_2$ catalysts which exhibited faster DMNP conversions with increasing Ce%, with $t_{1/2}$ values of 1.2 (99% Ce), 10.2 (95% Ce) and 14.5 (90% Ce) minutes.[16] Similarly, Zr_6 based MOF catalyst

NU-1000, with a DMNP hydrolysis $t_{1/2}$ value of 15 minutes, showed a significant improvement in catalytic activity by the introduction of $Ce_3O_xH_y$ clusters into the NU-1000 framework, with a reduced DMNP hydrolysis $t_{1/2}$ value of 11 minutes.

It is the case that both of the catalytic materials, control MOF808and CeNP@MOF808, exhibit catalytic conversions that are significantly longer compared to that reported in literature for MOF808, with a catalyst loading of 0.5 mg of MOF808 yielding a $t_{1/2}$ value of 30 seconds.[21] There are several explanations for this divergence in catalytic activity between MOF808 in this study and those reported in literature. MOF808 used in this study was synthesised using $ZrCl_4$ salt, while the activated MOF808 used in the literature studies, with an exceptionally low $t_{1/2}$ value of less than 30 seconds, was synthesised using $ZrOCl_2$ salt. It has been shown in separate studies that the morphology and surface area of MOF808 materials depends somewhat on the precursor choice, with MOF808 synthesised from $ZrCl_4$ having a surface area of 1349 $m^2\ g^{-1}$ while MOF808 synthesised from $ZrOCl_2$ yields a lower total surface areas of 1096 $m^2\ g^{-1}$.[31] It is reasonable then to postulate that the high catalytic hydrolysis rates of DMNP by MOF808 in the literature ($t_{1/2} \leq 30$ seconds) could arise from a larger surface area compared with the composite CeNP@MOF808 ($t_{1/2}$ = 1.9 minutes). This point is rendered moot however, in that the CeNP@MOF808 composite had a larger surface area of 1248 $m^2\ g^{-1}$ compared with that reported for MOF808 synthesised from $ZrOCl_2$. The role for including control MOF808, surface area of 1349 $m^2\ g^{-1}$, was to account for this and therefore it can be concluded that by incorporating CeNP in the MOF808 framework, there is an enhancement in the catalytic activity towards the hydrolysis of the nerve agent simulant DMNP.

However, several other factors result in the divergent catalytic activities observed between control MOF808 and literature MOF808. Firstly, in the literature study performed into the hydrolysis of DMNP using activated MOF808, the data point at t = 30 seconds was obtained by filtering the reaction mixture with a 200 nm filter syringe and subsequently recording the $^{31}P\{^1H\}$ NMR, this assumes however that all particles are removed from the reaction mixture 'killing' the reaction. SEM and LDS measurements give an average MOF particle size of 250 nm, however as with any measurement normal distribution can be assumed and so a significant number of particles will fall below 250 nm and possibly 200 nm – passing through the filter into the reaction mixture, artificially increasing the conversion at t = 30 seconds. This

would work to skew the $t_{1/2}$ value of activated MOF808 in the literature to faster conversion times. However, authors of the study did account for this possibility and included multiple measurements of the ^{31}P NMR spectrum of the filtered solution for several minutes, showing no significant growth of the MMP resonance and therefore proving successful stalling of the reaction conversion.[21] The experimental procedure adopted in this study lacked any filtration step, therefore measurements of the $^{31}P\{^{1}H\}$ NMR spectra could only be started on the reaction mixture once the in-built time delay of *ca.* 5 minutes (owing to tunning and locking of the probe and shimming of the magnetic field) was elapsed. Secondly, activated MOF808 referenced in literature was activated thermally by heating in fresh DMF solvent to remove modulator ligands from the Zr_6 clusters to yield $Zr_6(\mu_3\text{-}O)_4(\mu_3\text{-}OH)_4(OH_2)_6(OH)_6(BTC)_2$ whereby the Zr_6 nodes are not only more accessible but also in close proximity to coordinated nucleophiles H_2O and OH^-.

In truth, it may be a combination of factors which lead to the enhanced catalytic rates of CeNP@MOF808 relative to control MOF808 in the hydrolysis of nerve agent simulant DMNP. Whereby the presence of Ce^{3+}/Ce^{4+} ions, additional hydroxide nucleophile ligands (*e.g.* speciation of CeNP in the form of) and the greater number of open metal cluster nodes all work in tandem to create a more catalytic system.

4.6 Conclusions

Through the process of optimisation it was possible to devise a standardised experimental methodology which allowed for multiple $^{31}P\{^{1}H\}$ NMR spectra to be acquired while monitoring the catalytic hydrolysis of DMNP using novel CeNP@MOF808 and control MOF808. By optimising the process two key aims were achieved: firstly, as many data points as practically possible were acquired within a sensible time period and secondly, measurements were repeated in a standardised and consistent manner with each step in the experimental protocol specified and remaining consistent between measurements. The multiple $^{31}P\{^{1}H\}$ NMR spectra acquired were processed to yield conversion vs. time plots which were successfully fitted with inverse exponential decay functions to derive $t_{1/2}$ values.

Several $t_{1/2}$ values were tabulated for both CeNP@MOF808 and control MOF808, these values were aggregated to give average values of 1.9 minutes and 3.7 minutes respectively. When the average $t_{1/2}$ values were compared for both materials, with variances considered, T-test results showed that the difference in the average $t_{1/2}$ values were statistically significant. This increase in catalytic ability is consistent with literature, suggesting that incorporating Ce ions into the MOF structure improves the catalytic potential of the material.

This work represents an advancement in the understanding of composite MOF materials, in particular how porous materials can be made more catalytically active by introducing cerium based nanostructures within the framework with mixed Ce^{3+}/Ce^{4+} oxidation states. Through the process of optimisation, this work sets model upon which future studies should be performed when measuring catalytic activities of MOF materials towards organophosphates; namely that the experimental procedure should be standardised between measurements to improve the reproducibility of the results and that several repeated measurements should be made in order to establish the statistical significance of any apparent catalytic enhancement

4.7 Experimental Details for Chapter 4

All reagents were purchased from commercial sources and used without further purification. MOF808 was synthesized as reported previously.

4.7.1 Optimisation (Quantity of Catalytic Material)

Hydrolysis profiles were recorded by *in-situ* $^{31}P\{^{1}H\}$ NMR measurements in air at room temperature. Various quantities of catalytic material (MOF808 and CeNP@MOF808) were screened (2 mg, 0.5 mg, 0.2 mg). A specified quantity of catalytic material (2 mg, 0.5 mg, 0.2 mg) was weighed out, by difference, using an analytical grade balance. The catalytic material was loaded into a 1 dram vial and subsequently mixed with 0.4 M *N*-ethylmorpholine solution (1.05 mL; 0.05 mL *N*-ethylmorpholine, 0.9mL DI water, 0.1 mL D_2O). The vial was sonicated for 30 seconds, forming a fleeting homogeneous suspension, after which DMNP (4 µL; 25 mmol) was added to the mixture solution and swirled for 15 seconds. The reaction mixture was then transferred to an NMR tube and the spectrum was measured within several minutes of the reaction starting.

4.7.2 Optimisation (Sonication Time)

Sonication time was screened (30 seconds, 1 minute, 2 minutes) for 0.5 mg of catalytic material. Samples were inspected visually for signs of homogeneity (i.e. no observable free-flowing pieces of MOF material) by shaking the vial in various directions.

4.7.3 Optimisation (Time Delay)

Hydrolysis profiles were recorded by *in-situ* $^{31}P\{^{1}H\}$ NMR measurements at room temperature. Various time delays were screened (2 hours, 1 hour, 4 minutes, 1.5 minutes and 30 seconds). The catalytic material (0.5 mg) was loaded into a 1 dram vial and 0.4 M *N*-ethylmorpholine solution (1.05 mL; 0.05 mL N-ethylmorpholine, 0.9mL DI water, 0.1 mL D_2O) was subsequently added. The mixture was sonicated for 2 minutes, forming a fleeting homogeneous suspension.

After a specified time delay (2 hours, 1 hour, 4 minutes, 1.5 minutes and 30 seconds) DMNP (4 µL; 25 mmol) was added to the suspension and swirled for 15 seconds. The reaction mixture was then transferred to an NMR tube and the spectrum was measured within several minutes of the reaction starting.

4.7.4 Optimised Procedure

Hydrolysis profiles were recorded by *in-situ* $^{31}P\{^{1}H\}$ NMR measurements at room temperature based on an optimised procedure that minimised experimental errors (weighing of material, inhomogeneity in suspensions and time delay between sonication and mixing) and allowed for conversions to be observed over a reasonable time period (*i.e. ca.* 30 minutes). A MOF808 catalyst (*ca.* 0.5 mg) or CeNP@MOF808 catalyst (*ca.* 0.5 mg) was loaded into a 1 dram vial, separately, by weighing by difference using an analytical grade scale. 0.4 M *N*-ethylmorpholine solution (1.05 mL; 0.05 mL N-ethylmorpholine, 0.9mL DI water, 0.1 mL D_2O) was added to the vial. The vial was then placed into a beaker containing a small reservoir of deionised water. The beaker was placed into a sonic bath, and clamped into place. The samples were sonicated for 2 minutes to disperse the MOF sample homogeneously. After 30 seconds of sonication ceasing, DMNP (4 μL; 25 mmol) was added to the mixture solution and swirled for 15 seconds. The reaction mixture was then transferred to an NMR tube, using a Pasteur pipette, and the $^{31}P\{^{1}H\}$ NMR spectrum was immediately measured; the first data point was collected *ca.* 5 minutes after the start of the reaction. The progress of the reaction was monitored with 1 min increments for 30 minutes. Reactions were repeated a total of 6 times for each material (MOF808 and CeNP@MOF808) to build up comparable data sets.

4.7.5 Data Fitting

All conversion-time plots for the hydrolysis of DMNP were fitted using an exponential decay function of the type $f(x) = y_0 + A_1e^{-x/t1}$. For all conversion plots relating to MOF808 fitting successfully converged, giving fits with adj. R^2 values in the range of 0.96 – 0.99 (see Table 4.4 and Figure 4.30), while for CeNP@MOF808 7 out of the 8 conversion plots were successfully fitted, giving adj. R^2 values in the range of 0.93 – 0.99 (see Table 4.4 and Figure 4.31). Failure to fit data set 7 for CeNP@MOF808 resulted from only one data point existing below 100% conversion, leading to an insufficient number of data points to appropriately fit the data.

Table 4.4: Exponential decay fit parameters for MOF808 and CeNP@MOF808 data sets.

Data Set	Exponential Decay Fitting ($f(x) = y_0 + A_1e^{-x/t1}$)					
	y_0	A_1	t_1	k	$t_{1/2}$	R^2
MOF808						
1	1.03912	-0.65695	4.82949	0.20706	3.34755	0.95898
2	1.00971	-1.63015	2.49288	0.40114	1.72793	0.99257
3	0.99802	-0.58614	6.90754	0.14477	4.78794	0.97242
4	1.01132	-1.3971	3.76199	0.26582	2.60762	0.99515
5	1.021	-0.83634	5.88475	0.16993	4.079	0.98994
6	0.99254	-1.13135	7.08031	0.14124	4.9077	0.99077
7	1.03057	-0.7244	7.13782	0.1401	4.94756	0.99063
8	0.99071	-1.32411	4.67801	0.21377	3.24255	0.98952
CeNP@MOF808						
1	1.0014	-7.95007	1.16468	0.8586	0.80729	0.99085
2	1.01026	-1.17508	3.41827	0.29255	2.36936	0.92905
3	1.00266	-1.20089	2.50215	0.39966	1.73436	0.98442
4	1.05145	-0.3202	8.1814	0.12223	5.67091	0.95074
5	1.00078	-20.14352	0.87127	1.14776	0.60392	0.982
6	1.01433	-1.10793	4.87695	0.20505	3.38044	0.99043
7	/	/	/	/	/	/

8	0.99431	-1.18813	3.22628	0.30995	2.23628	0.97241

4.7.6 T-test Procedure

Independent two-sample T-tests were performed using the Origin software statistics package to determine if the differences in average $t_{1/2}$ conversion times were statistically significant – that is the difference is a result of something other than chance/error. T-test results from considering all $t_{1/2}$ values (i.e. not including outliers) and selected $t_{1/2}$ values (i.*e.* excluding outliers) are shown below in and respectively:

Table 4.5: T-test results for comparing $t_{1/2}$ values for MOF808 and CeNP@MOF808 (w/out excluding outliers).

Sample	n	mean	σ	σ^2 (variance)
MOF808 $t_{1/2}$	8	3.70598	1.18066	1.39396
CeNP@MOF808 $t_{1/2}$	7	2.40037	1.72692	2.98225
t-value	1.72972			
Critical value (p = 0.05)	2.160			
T-test	Accept the Null Hypothesis			

Table 4.6: T-test results for comparing $t_{1/2}$ values for MOF808 and CeNP@MOF808 (excluding outliers).

Sample	n	mean	σ	σ^2 (variance)
MOF808 $t_{1/2}$	8	3.70598	1.18066	1.39396
CeNP@MOF808 $t_{1/2}$	6	1.85528	1.04061	1.08287
t-value	3.04762			
Critical value (p = 0.05)	2.180			
T-test	Reject the Null Hypothesis			

4.8 Supplementary Information for Chapter 4

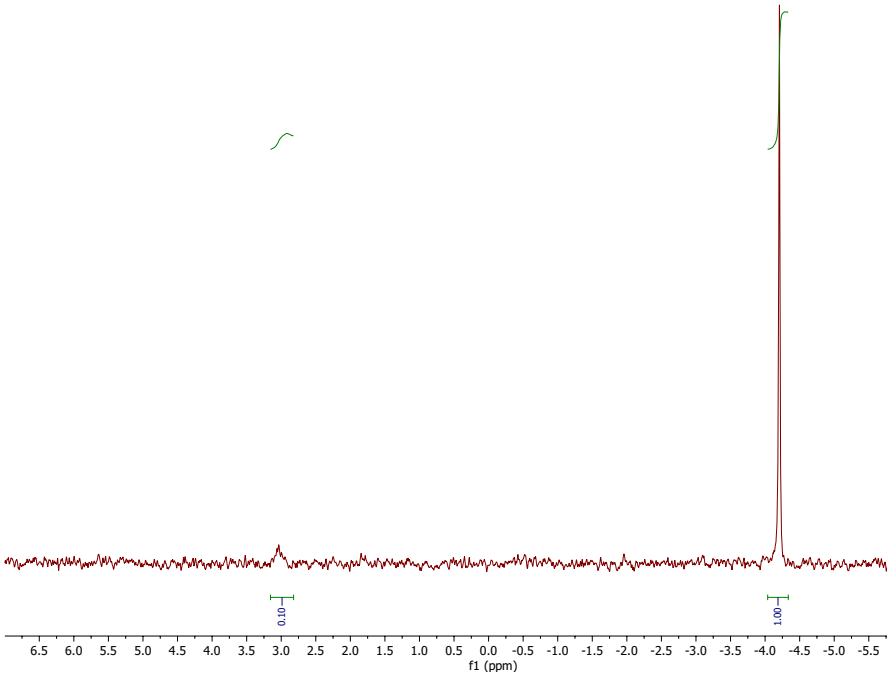

Supplementary Figure 4.1: $^{31}P\{^{1}H\}$ NMR spectrum for catalytic hydrolysis of DMNP using 0.5 mg of CeNP@MOF808 in the absence of buffer after 3 minutes, showing 9% conversion of DMNP. No resonance observed at δ = 5.1 ppm.

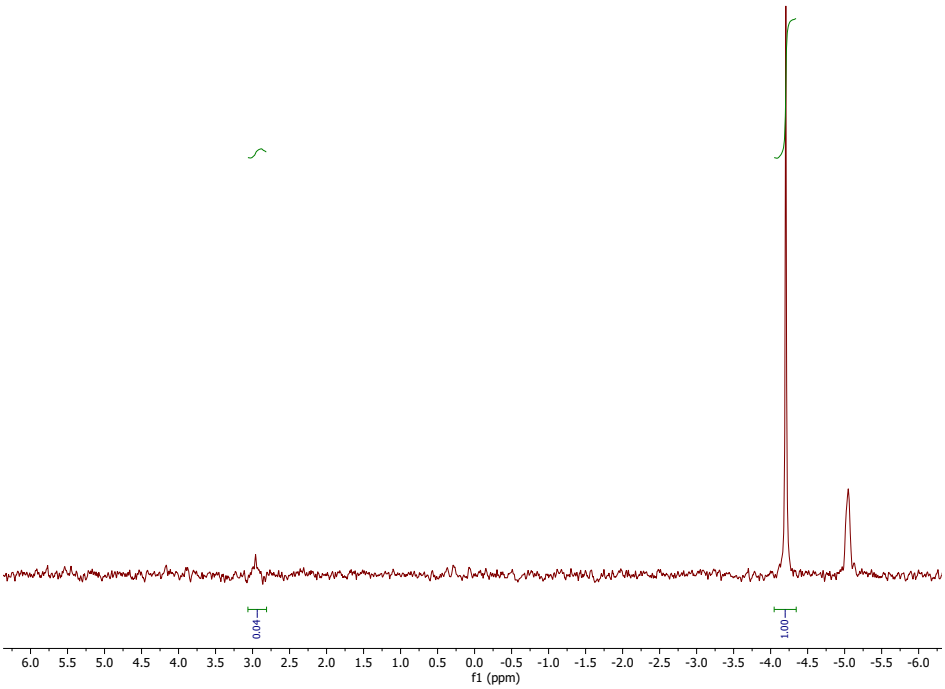

Supplementary Figure 4.2: $^{31}P\{^{1}H\}$ NMR spectrum for catalytic hydrolysis of DMNP using 0.5 mg of control MOF808 in the absence of buffer after 8 minutes, showing 3.8% conversion of DMNP. Resonance at δ = 5.1 ppm is an unknown species/intermediate.

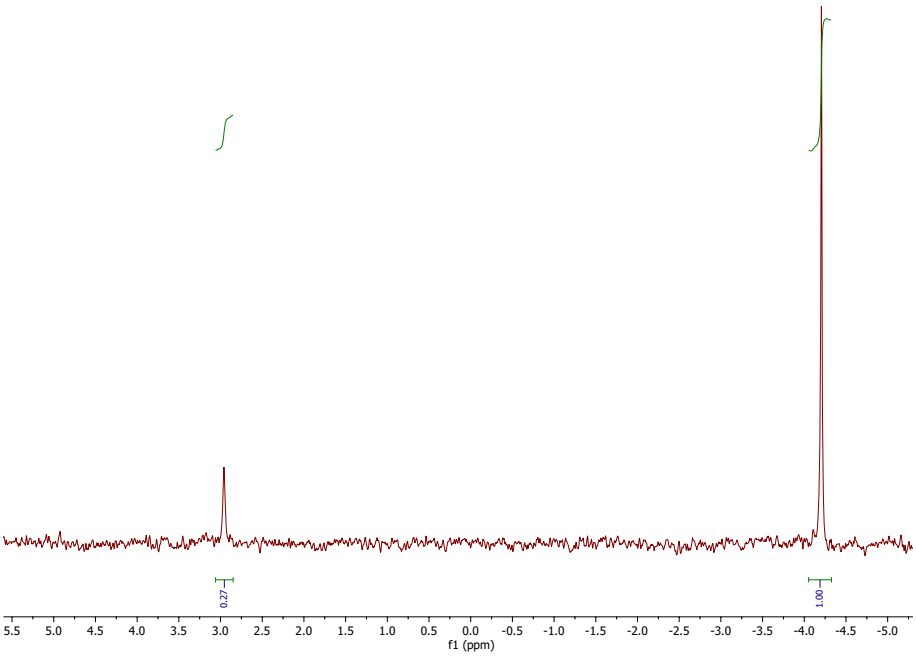

Supplementary Figure 4.3: $^{31}P\{^{1}H\}$ NMR spectrum for catalytic hydrolysis of DMNP using 0.5 mg of control MOF808 in the absence of buffer after 6.5 hours, showing 21% conversion of DMNP. No resonance observed at δ = 5.1 ppm.

4.9 References for Chapter 4

1. C. A. Valdez, R. N. Leif, S. Hok and B. R. Hart, 2018, **37**.
2. F. Worek, J. Jenner and H. Thiermann, *Chemical warfare toxicology: volume 2: management of poisoning*, Royal Society of Chemistry, 2016.
3. D. Schrader, *Angewandte Chemie*, 1950, **62**, 471-473.
4. B. Picard, I. Chataigner, J. Maddaluno and J. Legros, *Organic & Biomolecular Chemistry*, 2019, **17**, 6528-6537.
5. R. A. Moss, H. Morales-Rojas, S. Vijayaraghavan and J. Tian, *Journal of the American Chemical Society*, 2004, **126**, 10923-10936.
6. M. Kassai, R. Teopipithaporn and K. B. Grant, *Journal of Inorganic Biochemistry*, 2011, **105**, 215-223.
7. H. Shigekawa, M. Ishida, K. Miyake, R. Shioda, Y. Iijima, T. Imai, H. Takahashi, J. Sumaoka and M. Komiyama, *Applied physics letters*, 1999, **74**, 460-462.
8. P. Abellan, T. Moser, I. T. Lucas, J. Grate, J. Evans and N. Browning, *RSC advances*, 2017, **7**, 3831-3837.
9. G. W. Wagner, P. W. Bartram, O. Koper and K. J. Klabunde, *The Journal of Physical Chemistry B*, 1999, **103**, 3225-3228.
10. G. W. Wagner, L. R. Procell, R. J. O'Connor, S. Munavalli, C. L. Carnes, P. N. Kapoor and K. J. Klabunde, *Journal of the American Chemical Society*, 2001, **123**, 1636-1644.
11. G. W. Wagner, Q. Chen and Y. Wu, *The Journal of Physical Chemistry C*, 2008, **112**, 11901-11906.
12. G. W. Wagner, G. W. Peterson and J. J. Mahle, *Industrial & engineering chemistry research*, 2012, **51**, 3598-3603.
13. G. W. Wagner, *Decontamination Efficacy of Candidate Nanocrystalline Sorbents with Comparison to SDS A-200 Sorbent: Reactivity and Chemical Agent Resistant Coating Panel Testing*, EDGEWOOD CHEMICAL BIOLOGICAL CENTER ABERDEEN PROVING GROUND MD, 2010.
14. T. J. Bandosz, M. Laskoski, J. Mahle, G. Mogilevsky, G. W. Peterson, J. A. Rossin and G. W. Wagner, *The Journal of Physical Chemistry C*, 2012, **116**, 11606-11614.
15. A. A. Vernekar, T. Das and G. Mugesh, *Angewandte Chemie International Edition*, 2016, **55**, 1412-1416.

16. K. Khulbe, P. Roy, A. Radhakrishnan and G. Mugesh, *ChemCatChem*, 2018, **10**, 4826-4831.
17. M. J. Katz, J. E. Mondloch, R. K. Totten, J. K. Park, S. T. Nguyen, O. K. Farha and J. T. Hupp, *Angewandte Chemie*, 2014, **126**, 507-511.
18. J. E. Mondloch, M. J. Katz, W. C. Isley Iii, P. Ghosh, P. Liao, W. Bury, G. W. Wagner, M. G. Hall, J. B. DeCoste and G. W. Peterson, *Nature materials*, 2015, **14**, 512-516.
19. L. Valenzano, B. Civalleri, S. Chavan, S. Bordiga, M. H. Nilsen, S. Jakobsen, K. P. Lillerud and C. Lamberti, *Chemistry of Materials*, 2011, **23**, 1700-1718.
20. M. J. Katz, R. C. Klet, S.-Y. Moon, J. E. Mondloch, J. T. Hupp and O. K. Farha, *ACS Catalysis*, 2015, **5**, 4637-4642.
21. S. Y. Moon, Y. Liu, J. T. Hupp and O. K. Farha, *Angewandte Chemie*, 2015, **127**, 6899-6903.
22. M. J. Katz, S.-Y. Moon, J. E. Mondloch, M. H. Beyzavi, C. J. Stephenson, J. T. Hupp and O. K. Farha, *Chemical Science*, 2015, **6**, 2286-2291.
23. S. D. Aubert, Y. Li and F. M. Raushel, *Biochemistry*, 2004, **43**, 5707-5715.
24. P. Li, R. C. Klet, S.-Y. Moon, T. C. Wang, P. Deria, A. W. Peters, B. M. Klahr, H.-J. Park, S. S. Al-Juaid and J. T. Hupp, *Chemical communications*, 2015, **51**, 10925-10928.
25. T. Islamoglu, A. Atilgan, S.-Y. Moon, G. W. Peterson, J. B. DeCoste, M. Hall, J. T. Hupp and O. K. Farha, *Chemistry of Materials*, 2017, **29**, 2672-2675.
26. T. L. Cottrell, *The strengths of chemical bonds*, Butterworths Scientific Publications, 1958.
27. M. H. Hassan, D. Andreescu and S. Andreescu, *ACS Applied Nano Materials*, 2020, **3**, 3288-3294.
28. J. Liu, L. R. Redfern, Y. Liao, T. Islamoglu, A. Atilgan, O. K. Farha and J. T. Hupp, *ACS applied materials & interfaces*, 2019, **11**, 47822-47829.
29. S. Y. Moon, E. Proussaloglou, G. W. Peterson, J. B. DeCoste, M. G. Hall, A. J. Howarth, J. T. Hupp and O. K. Farha, *Chemistry–A European Journal*, 2016, **22**, 14864-14868.
30. M. R. Momeni and C. J. Cramer, *ACS applied materials & interfaces*, 2018, **10**, 18435-18439.
31. C. Ardila-Suárez, J. Rodríguez-Pereira, V. G. Baldovino-Medrano and G. E. Ramírez-Caballero, *CrystEngComm*, 2019, **21**, 1407-1415.

5 Synthesis, Characterisation and Materials Applications of Cerium β-ketoiminate Precursors

5.1 Abstract

Main group β-ketoiminate complexes have been previously used in the synthesis of oxide materials through bottom-up methodologies. The research presented in Chapter 5 extends this chemistry to the f-elements. Metal precursor choice is particularly important in f-element chemistry. Therefore, the use of a highly basic lanthanide precursor, LnN''_3 (Ln = Y, Ce; N'' = $N(SiMe_3)_2$) and control of the β-ketoimine sterics, $OC(Me)CHC(Me)NH^iPr$ (HL^1), resulted in the synthesis of lanthanide β-ketoiminate complexes, $Ln_nL^1_{3n}$ (**1,** Ln = Y, n = 1; **2**, Ce, n = 2), in good yields and high purity *via* a simple protonolysis reaction. Compounds **1** and **2** were fully characterised using a number of techniques including ^1H NMR, Evan's measurements and IR spectroscopy, UV-vis spectroscopy and single-crystal X-ray diffraction. Attempts to synthesise the **2** *via* the salt metathesis reaction of $Ce(OTf)_3$ (OTf = O_3SCF_3) and KL^1 were explored but failed to reach conclusion due to the incomplete deprotonation of HL^1. The use of **2** as a molecular precursor for forming nanostructured composite CeNP'@MOF808, *via* the reactive infiltration within MOF808, was investigated. CeNP'@MOF808 was fully characterised using a number of techniques including TGA, PXRD, EDX, XAS and digestion NMR. This second, novel composite nanomaterial, CeNP'@MOF808, was shown to have near-identical characteristics electronically and structurally to the composite synthesised in previous studies (see Chapter 2) using metal precursor CeN''_3 (CeNP@MOF808). β-ketoiminate complexes have been shown previously to form oxide materials through thermal decomposition at relatively low temperatures. Therefore, studies were performed to investigate whether **2** displayed low temperature decomposition behaviour under nitrogen and air atmospheres. These results serve to highlight the versatile nature of **2** as a molecular precursor to a variety of cerium nanomaterials. Thus, laying the foundations for further modifications and materials development.

5.2 What Is a Precursor?

Depending upon the field of research, what constitutes a precursor can be largely subjective. In the particular field of materials deposition a molecular precursor can be defined as a molecular compound containing one or more atoms that are key constituent of the target material and are deposited upon decomposition (*i.e*. elimination of the coordinated ligands for coordination complexes) of the precursor molecule. An example would be in the materials synthesis of Al_2O_3 thin-films, the precursor would in theory contain Al and O atoms in the correct proportions to yield Al_2O_3 when decomposed. Here, coordination complexes offer a useful pathway as precursor materials.

Metal-organic coordination complexes are those featuring metal and carbon atoms and tend to, but not always, be incredibly air and moisture sensitive molecules. This is often harnessed within materials synthesis to aid the formation of target materials, for example in the synthesis of thin-film materials through metal-organic chemical vapour deposition (MOCVD). Metal-organic coordination complexes also have the added advantage of being versatile in their coordination structures, by simply changing the coordinating ligand architecture it is possible to change the reactivity, volatility and thermal stability of the precursor. To this end the thesis will present an investigation into the synthesis and characterisation of precursor molecules featuring lanthanide metal centres (Y, La and Ce) and further applied one of these novel precursors to materials synthesis of CeO_2 nanostructures using two different deposition techniques: thermal decomposition and reactive infiltration within a complementary host framework (as seen in Chapter 2).

Note that the exact nature of the nanostructures is dependent upon the deposition technique and so what was most desired was a precursor molecule that could be applied to several different deposition techniques, what can be referred to as a 'broad spectrum' precursor. This is sought after as it allows us to maximise the potential materials outputs from one single precursor molecule. The precursor design was influenced by several factors, both relating to general precursor properties, but also specific to lanthanide chemistry. Firstly, the precursor had to be single source, meaning that the molecule featured both Ce and O atoms in the correct proportions to allow for the assembly of CeO_2.[1] Therefore, ligands where chosen

which contained oxygen donor atoms. Second, the ligands has to be easily modifiable, allowing for changes in the physical and chemical properties of the precursor, this would ease the fine tuning of the precursor stability and ease of handling. Finally, sources of contamination were kept to a minimum and thus ligands containing halogens were not considered as halogen contamination is common in materials deposition, negatively effecting the properties of the deposited material.[2] Considering these points, along with the fact that ligands of this type have shown to form precursor complexes with a range of main group and transition metal centres,[3-8] β–ketoiminate ligands were chosen as the target ligand system.

5.3 Aims: Synthesis of Molecular Ln Precursor Complexes

The aim was to synthesise a precursor molecule in a low cost, simplified synthetic route with high yields and minimal steps. Several lanthanide centres were investigated, including: Y, La and Ce – but of key interest was those featuring Ce metal centres with the aim of assembling CeO_2 nanostructures. β–ketoiminate ligands are well established in the literature and relatively easy to synthesise in high yields through a Dean-Stark condensation reaction.

5.4 Synthesis of β–ketoimine Ligand **HL^1**

Synthesis of the β–ketoimines was adapted from literature procedure.[3] The ligand (OC(Me)CHC(Me)NH^{i}Pr), **HL^1**, was synthesised *via* a reversible condensation reaction between 1 equivalent of 2,4-pentanedione and 2 equivalents of 2-isopropylamine in toluene, at 130 °C, for 16 hours under reflux (see Scheme 5.1). A Dean-Stark reflux condenser was used during the reaction to continuously remove water from the reaction system, preventing equilibrium being attained and thus driving the reaction to completion. A colour change from bright yellow to dark brown was observed. The solution was dried over anhydrous $MgSO_4$ and filtered through fluted filter paper yielding a light orange solution, with was isolated from the toluene solvent *in vacuo* and degassed, forming a dark brown-amber liquid: **HL^1**, in high yields of 80%.

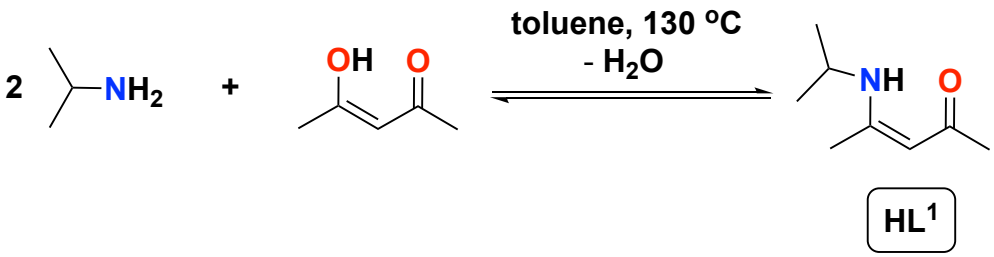

Scheme 5.1: Condensation reaction between 2,4-pentanedione and 2-isopropylamine to form HL^1.

A similar synthetic route was adopted for the synthesis of (OC(Me)CHC(Me)NHPh), **HL^2**, although it was obtained in significantly poorer yields (4%). Therefore further synthesis of coordination complexes with **HL^2** were limited.

5.5 ^{1}H NMR Studies of **HL^1**

The room temperature ^{1}H NMR spectrum of **HL^1** (OC(Me)CHC(Me) NH^{i}Pr), in d_6-benzene (see Figure 5.1), shows 6 resonances, corresponding to 6 proton environments.

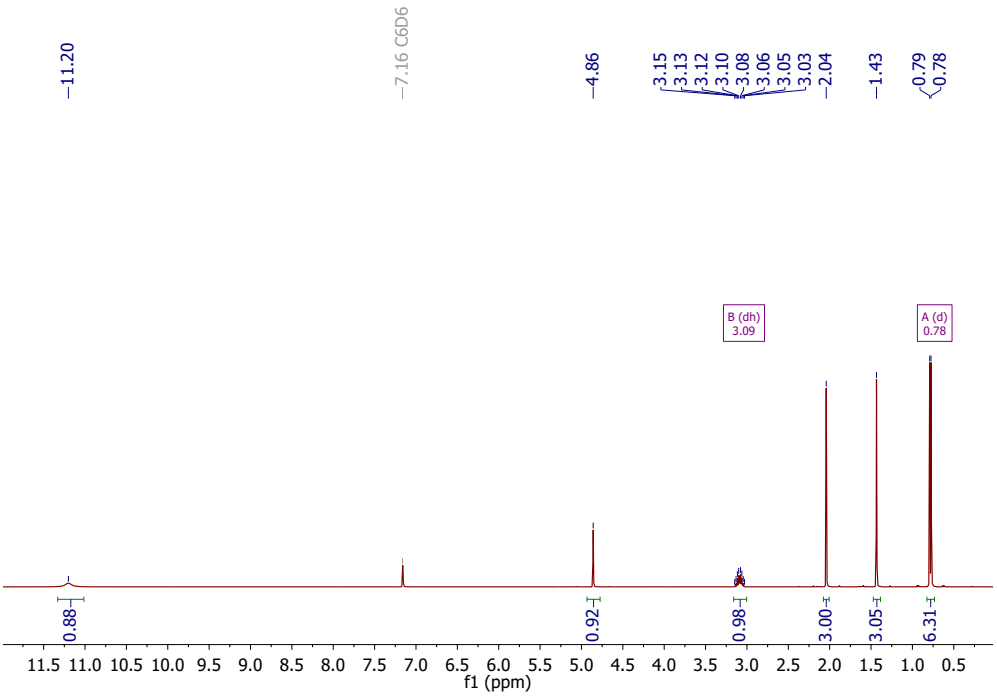

Figure 5.1 ^{1}H-NMR (d_6-benzene) of **HL^1**.

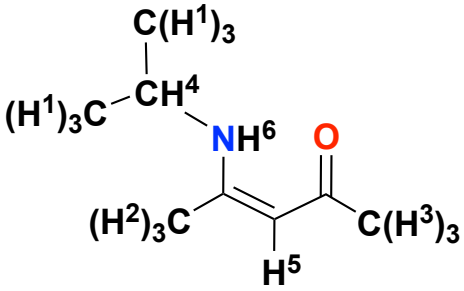

Figure 5.2: Ligand HL^1 with proton environments labelled.

Individual proton environments in ligand HL^1 are labelled in Figure 5.2. Aliphatic proton environments appear at chemical shift values of δ = 0.78 (H^1), 1.43 (H^2) and 2.04 (H^3) ppm. These values agree well literature values for **HL^1**, in $CDCl_3$, of δ = 1.19 (H^1), 1.91 (H^2) and 1.94 (H^3) ppm.[9] The methyl groups of the isopropyl pendant (H^1) group are observed as expected as a doublet at δ = 0.78 ppm, with $^3J_{HH}$ coupling of 6.4 Hz, consistent with the $^3J_{HH}$ coupling observed for **HL^1** in $CDCl_3$.[9] The methine proton of the isopropyl group (H^4) appears as a multiplet, $^3J_{HH}$ = 6.4 Hz, at δ = 3.09 ppm, consistent with literature observations of HL^1 in $CDCl_3$ at δ = 3.62 ppm.[9] The resonance is shifted downfield due to the neighbouring nitrogen atom, with a strong negative inductive effect that deshields the methine proton environment. The presence of π–bonds within the molecule, coupled with highly electronegative oxygen and nitrogen atoms of the keto and imine groups helps to deshield the backbone methine proton environment (H^5), consequently shifting it downfield to δ = 4.86 ppm, consistent with literature observations of HL^1 in $CDCl_3$ at δ = 4.86 ppm.[9] The imine hydrogen (H^6) appears as a broad singlet at δ = 11.20 ppm due to the protons corresponding labile nature. This is in good agreement with the value observed for HL^1 in $CDCl_3$ at δ = 10.85 ppm.[9]

5.6 Synthesis of Lanthanide β–ketoiminate Complexes **1** and **2**

Two synthetic pathways were applicable to the synthesis of lanthanide β–ketoiminate complexes: protonolysis and metathesis. Each methodology has its own advantages and disadvantages, however only protonolysis proved successful. The metathesis synthesis, which involved first deprotonating the β–ketoimine ligand, **HL^1** (OC(Me)CHC(Me)NH^{i}Pr), with strongly basic KN'', forming potassium salt, **KL^1**. Following on from this the aim was to react

KL^{1} with $Ce(OTf)_3$ to form the β–ketoiminate complex with Ce. However, ^{1}H-NMR analysis of **KL**^{1} revealed incomplete deprotonation with a residual minor product, see Figure 5.3. Several attempts made to remove the residual product through recrystallisation were unsuccessful, with a major ketoiminate product (high intensity resonances) and a minor ketoiminate product (low intensity resonances) remaining.

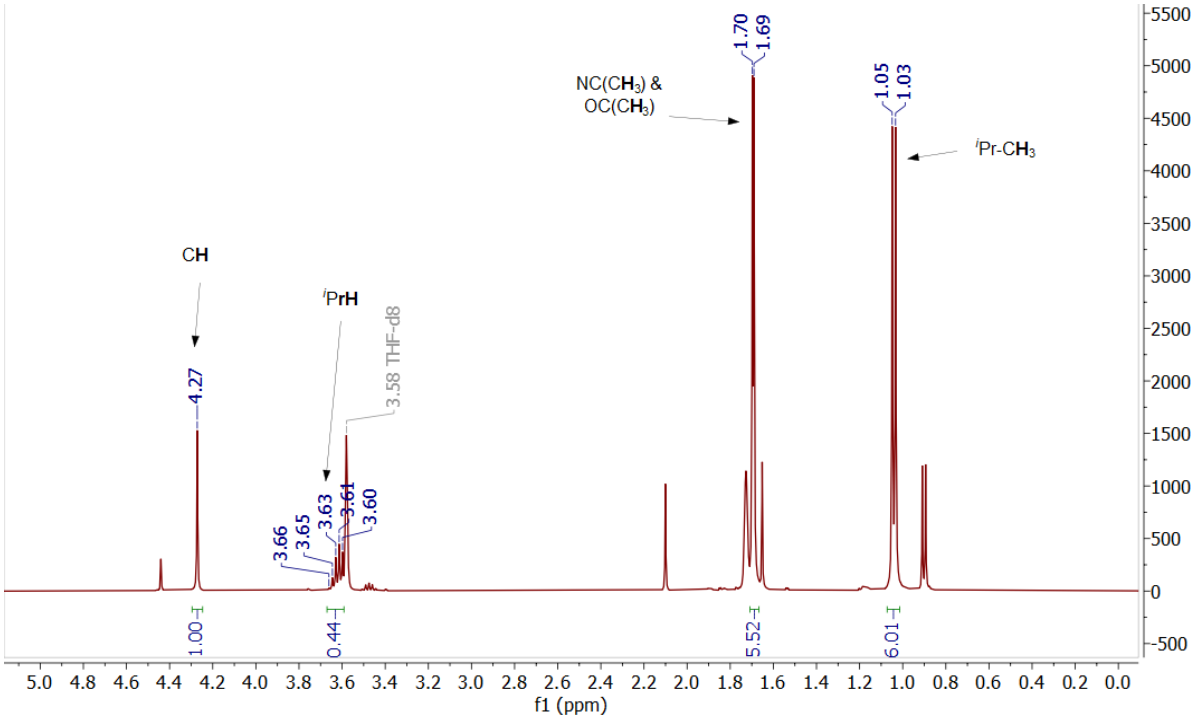

Figure 5.3: ^{1}H NMR (d_8-THF) of KN''.HL^{1} with major product resonances labelled. Minor product appears as lower intensity resonances shifted relative to HL^{1}.

Therefore, the decision was made to investigate the synthesis of lanthanide β–ketoiminate complexes through the alternative synthetic methodology of protonolysis.

LnN''_3 (Ln = Y, Ce, N'' = $N(SiMe_3)_2$) was chosen as the basic metal source in the protonolysis methodology. This was due to the ease of preparation from inexpensive Ln_2O_3 starting materials, see section, and their highly basic nature allowing for ease of protonolysis.

The first lanthanide metal centre to be investigated in forming lanthanide β–ketoiminate complexes was yttrium, due to its diamagnetic nature, allowing for simple characterisation *via* ^{1}H NMR. Compound **1** was synthesised *via* the protonolysis of YN''_3 with **HL**^{1}

(OC(Me)CHC(Me)NH^{i}Pr), driven thermodynamically by the elimination of HN'', at room temperature and pressure (see Scheme 5.2). Note that the LnN''$_3$ were all synthesised in a manner similar to that of CeN''$_3$, detailed in Chapter 2, with specific experimental parameters found in Section 5.10. The dropwise addition of **HL^1** to a toluene solution of YN''$_3$, yielded a distinct colour change from colourless to pale yellow. The reaction mixture was stirred for 1 hour before removing the toluene under vacuum to give cream solids. The solids were recrystallised in minimal hexanes and subsequently washed with hexanes. The cream coloured solids Y{OC(Me)CHC(Me)N^{i}Pr}$_3$ (**1**) were isolated in a yield of 63%. Compound **2** is synthesised in a manner similar to compound **1**, however the reaction time is significantly shorter, with yellow solids forming after 10 minutes (see Scheme 5.2). Bright yellow solids were isolated under vacuum washed with hexanes. Solids were then recrystallised from minimal THF and washed with hexanes. This afforded a bright yellow powder Ce$_2${OC(Me)CHC(Me)N^{i}Pr}$_6$ (**2**) in a moderate yield of 51%.

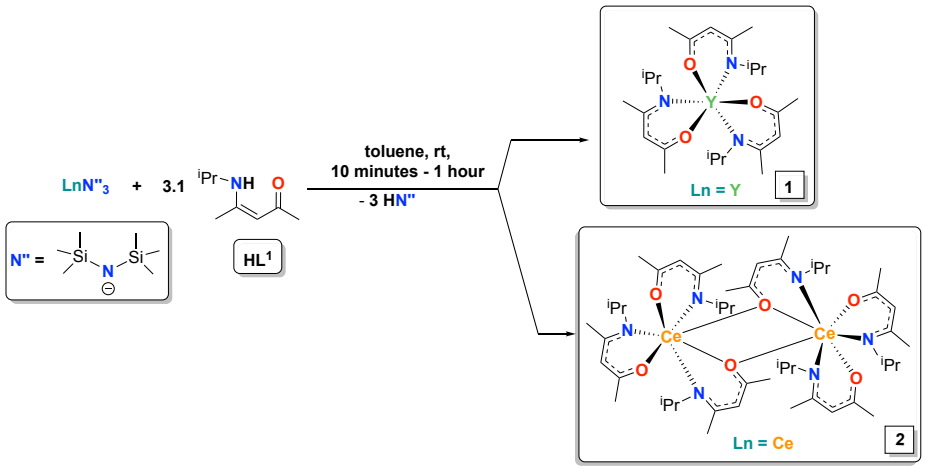

Scheme 5.2 Protonolysis of LnN''$_3$ with **HL^1** to yield compounds **1** (Ln = Y) and **2** (Ln = Ce).

The room temperature ^{1}H–NMR spectrum of **1** (Figure 5.4) in d_6-benzene, at room temperature, shows 5 resonances, accounting for the 5 different proton environments, as expected in **1**. No broad singlet resonance was observed downfield in the region of 11 ppm, indicating the lack of an imine proton environment (H^6, see Figure 5.2). This was expected and consistent with deprotonation of ligand **HL^1** by basic YN''$_3$. Aliphatic proton environments were observed at chemical shift values of δ = 1.39 (H^1), 1.73 (H^2) and 1.90 (H^3) ppm, with only H^3 shifting upfield relative to **HL^1**, while the remaining two aliphatic environments (H^1 and H^2)

are shifted downfield. This shift in resonance positions relative to the free ligand is indicative of coordination to the Y^{3+} metal centre. The coupling measured for methyl protons on the ^{i}Pr moiety (H^1) is $^3J_{HH}$ = 6.7 Hz, consistent with the value of $^3J_{HH}$ = 6.7 Hz observed in free ligand **HL^1**. The protons on the ^{i}Pr moieties of coordinated β–ketoiminate remain magnetically equivalent, this is in contrast to , Zn[OC(OEt)CHC(Me)N^{i}Pr]$_2$ which results in the ^{i}Pr methyls being magnetically inequivalent, observed at 1.09 and 1.10 ppm in the ratio of 6:6.[10] The backbone methine proton environment (H^5) of **1** is shifted downfield relative to that of the free ligand **HL^1**, consistent with coordination to the Y^{3+} metal centre. No additional resonances were visible, indicating the purity of **1**.

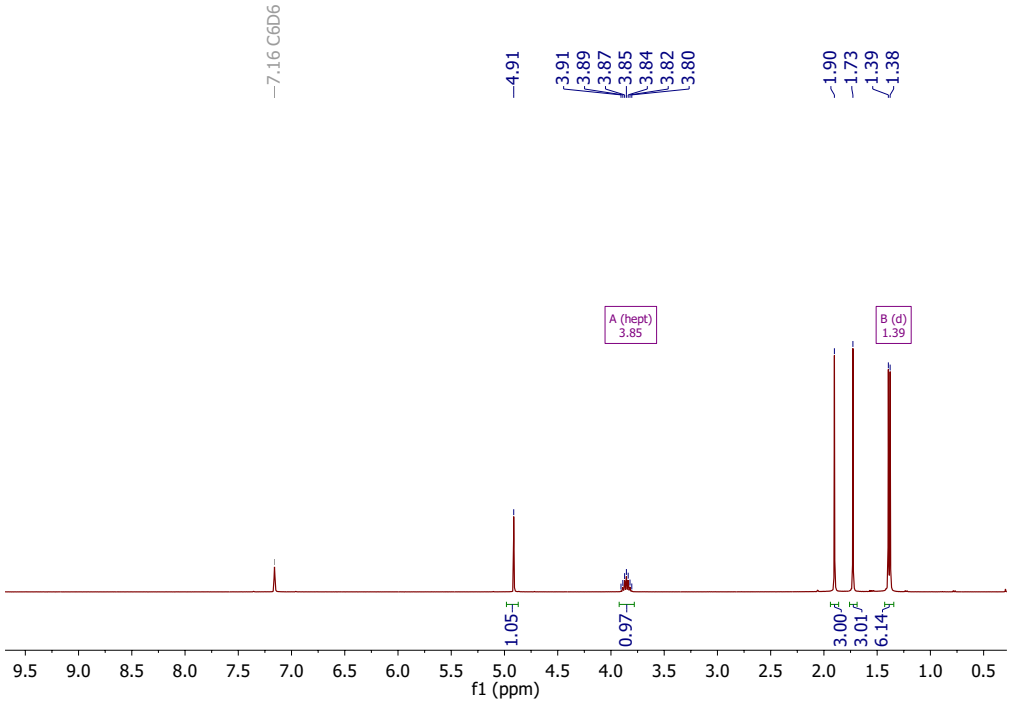

Figure 5.4 ^{1}H-NMR (d_6-benzene) of **1**.

Following on from the successful synthesis and characterisation of 1 *via* ^{1}H NMR attention turned to characterisation of the β–ketoiminate complex with the larger and paramagnetic Ce^{3+}, compound **2**.The ^{1}H–NMR spectrum of **2**, see Figure 5.5, in d_6-benzene, at room temperature, shows resonances 5 resonances; similar to the ^{1}H–NMR of **1** (see Figure 5.4).

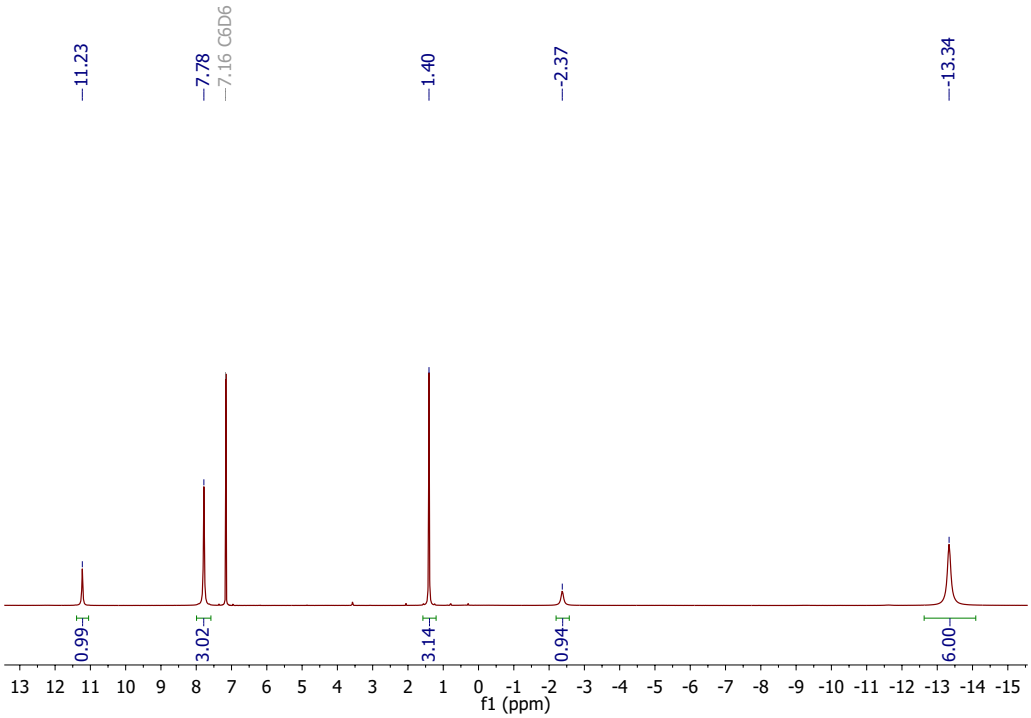

Figure 5.5: 1H-NMR (d_6-benzene) of **2**.

The resonances corresponding to proton environments on **2** are significantly shifted relative to those of both **HL[1]** and **1**, as well as significantly broadened. This is indicative of a paramagnetic species in solution: Ce^{3+} $4f^1$ $^2F_{5/2}$ ground state.[11,12] Due to the paramagnetic nature of the molecule, two Ce^{3+} centres each featuring one unpaired f^1 electron, Evans' method measurements were performed on compound **2** in in d_6-benzene. Evan's method measurements involved dissolving the paramagnetic material in an appropriate deuterated solvent and adding a sealed capillary tube containing the same deuterated solvent. A typical ^{1}H NMR spectra is then acquired which will contain two residual resonance associated with protonated solvent. The difference in chemical shift value between these two residual solvent resonances can determine the magnetic moment of the paramagnetic material using the Lande Formula (eqn. 6). A variety of possible magnetic moments were dependent upon the interaction of the two Ce^{3+} paramagnetic centres.

$$\mu_L = g_j\sqrt{J(J+1)}\,\mu_B \quad \text{(eqn. 6)}$$

In a system where the two Ce^{3+} centres are completely antiferromagnetically coupled: $\mu_L = 0$ μ_B, in a system where the two Ce^{3+} centres are non-interacting: $\mu_L = 3.59$ μ_B and in a system where the two Ce^{3+} centres are ferromagnetically coupled: $\mu_L = 4.56$ μ_B. A series of three Evans' measurements yielded an average μ_{eff} value of 3.05 ± 0.10 μ_B.

Table 5.1: Evans' Method Measurements of compound **2** in d_6-benzene (triplicate repeat).

Concentration of **2** (M)	Shift of benzene resonance (Hz)	μ_{eff} (μ_B)
0.0144	93.0	3.15
0.0205	116.3	2.96
0.0161	95.9	3.04

This value is in agreement with a mostly non-interacting system with slight antiferromagnetic coupling between the two Ce^{3+} metal centres, consistent with crystallographic data (Figure 5.11) showing a dimeric structure. Often in multimetallic systems the terminal and bridging ligands show magnetic non-equivalence.[13-15] The absence of additional resonances for **2** shows that terminal and bridging β–ketoiminate ligands are magnetically equivalent in **2** and confirms the purity of 2. The ^{1}H–NMR spectrum of compound **2** was recorded in d_8–THF (see Figure 5.6) and showed no additional resonances and minimal shifting, as expected with changing solvent, in resonance positions when compared with the ^{1}H – NMR spectrum of **2** in in d_6-benzene (see Figure 5.5).

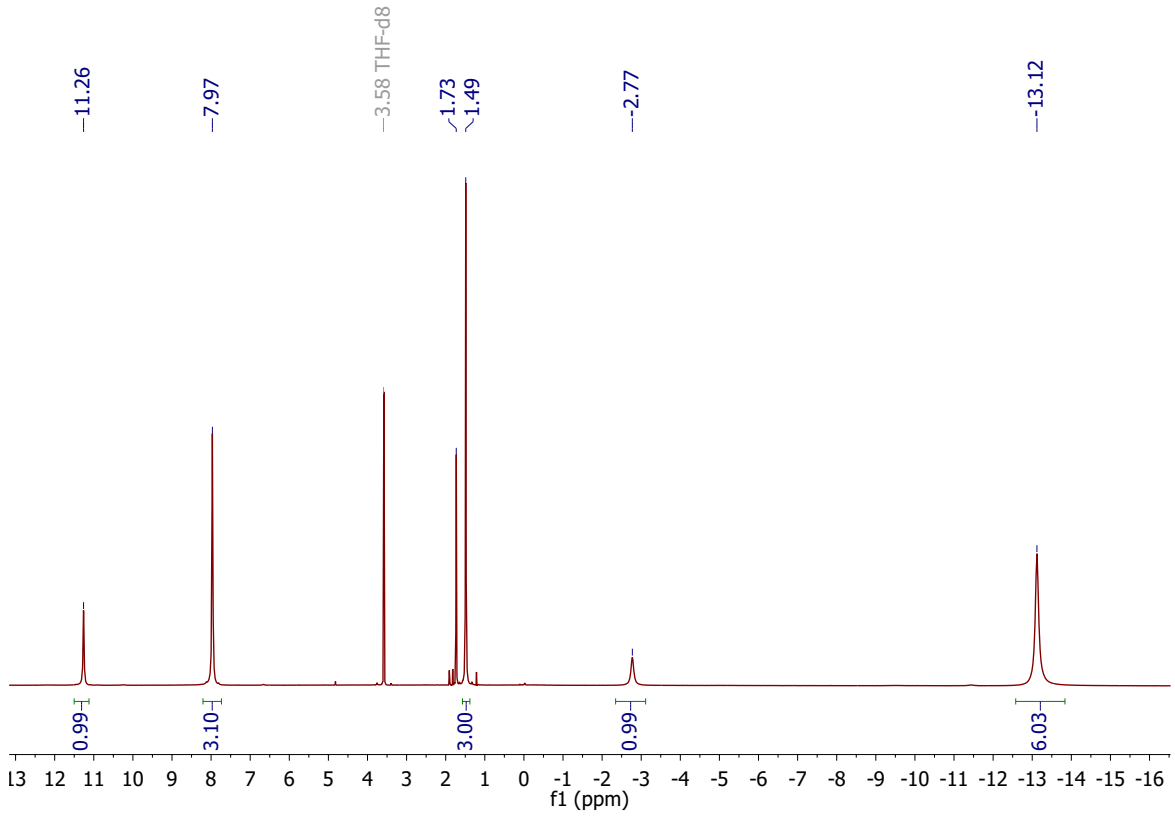

Figure 5.6: 1H-NMR (d_8-THF) of **2**.

5.6.1 Electronic Absorption and Vibrational Spectroscopy Studies of 1 and 2

The electronic absorption spectra of compounds **HL^1**, **1**, and **2** are shown overlaid below in Figure 5.7.

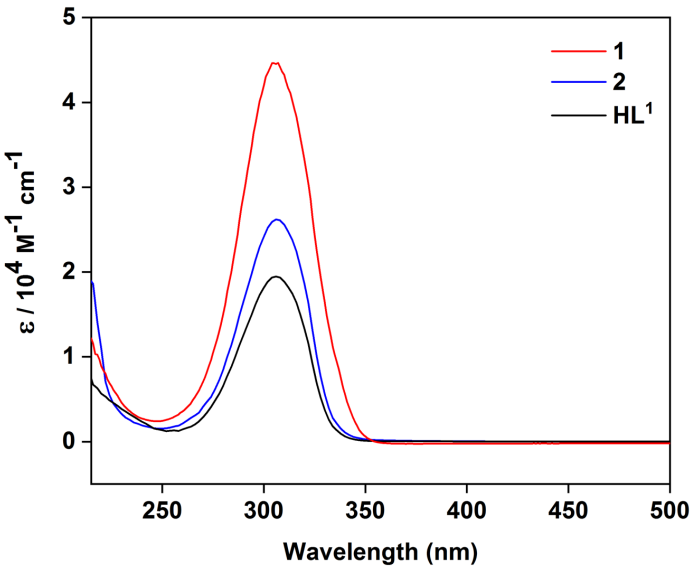

Figure 5.7 UV – vis Electronic Absorption Spectrum of compounds **1**, **2** and **HL^1** in THF.

HL[1] shows a broad absorption envelope, with at λ_{max} = 303 nm (19000 M^{-1} cm^{-1}). This is consistent with β–ketoimine (λ_{max} = 322 nm) and β–diketimine (λ_{max} = 268 nm) ligands, where the transition is assigned as a π–π* transition.[16,17]

Compounds **1** and **2** show absorption envelopes at λ_{max} = 303 nm also, with ε = 45,000 M^{-1} cm^{-1} and 26,000 M^{-1} cm^{-1}, respectively. This was contrary to the macro-appearance of the solids, with **1** being a beige cream colour and **2** being a bright yellow. The lack of red- or blue-shifts in the λ_{max} was initially surprising given the general tendency of various ligand based transitions to shift in energy upon metal coordination. Examples of electronic spectra for these types of lanthanide β–ketoiminates was sparse in the literature, however multiple examples could be found for similar ligand systems with lanthanides and transition metals. For example, the coordination of $Ln(acac)_3$ (Ln = Eu, Tb) to 4,4'-dimethoxy 2,2'-bipyridine ligands resulted in a red shift of λ_{max} from 258 nm to 275 nm (Eu) and 280 nm (Tb) due to the perturbation of π molecular orbitals on the aromatic ligand upon coordination by the metal.[18] While the coordination of $[YTp_2]^+$ synthons to dithioxalate (dto^{2-}) resulted in a red shift of λ_{max} from 505 nm to 540 nm.[19] The coordination of the aforementioned ligand, $EtO_2CC_6H_4N(Me)CH_2C(Me)NC_6H_4CO_2Et$, to Ni(II) results in a red shift of λ_{max} from 268 nm to 276 nm in $NiCl(OHEt)\{EtO_2CC_6H_4N(Me)CHC(Me)NC_6H_4CO_2Et\}$.[17] The high energy nature of the absorption and $\log_{10}(\varepsilon) \approx 4$ is consistent with a π–π* ligand based transition for compounds **1** and **2**. d-block metal coordination compounds with β – diketonate ligand acac, $Ti(acac)_3$, $Sc(acac)_3$ and $Cr(acac)_3$, all show λ_{max} values in the region of 300 nm and are assigned to π – π* transitions.[20] Coordination compounds of d-block metals Co(II), Cu(II) and Ni(II) with β – diketiminate ligand 2-$NH_2C_5H_4N$-p-bromophenolate displays π–π* transitions at approximately 300 nm.[21] Ln coordination compounds with fluorinated β – diketonate ligand hfac (hfac = $CF_3COCHCOCF_3$), $Ln(hfac)_3(OPArF)(OH_2)$ (Ln = Sm, Eu, Tb, Er, Yb; ArF = C_6F_5), exhibit λ_{max} values in the region of 300 nm and are attributed to π – π* transitions.[22]

The ATR-IR spectrum of **HL[1]** is shown below in Figure 5.8. Weak stretching frequencies at 2971, 2929, 2870 cm^{-1} correspond to aliphatic sp^3 C–H vibrations. The strong stretching frequency at 1605 cm^{-1} was assigned to the C=O vibration, while those at 1570 cm^{-1} and 1515 cm^{-1} were assigned to C=N and C=C vibrations, respectively. The 1305 cm^{-1} stretch was assigned to the C–N vibration.

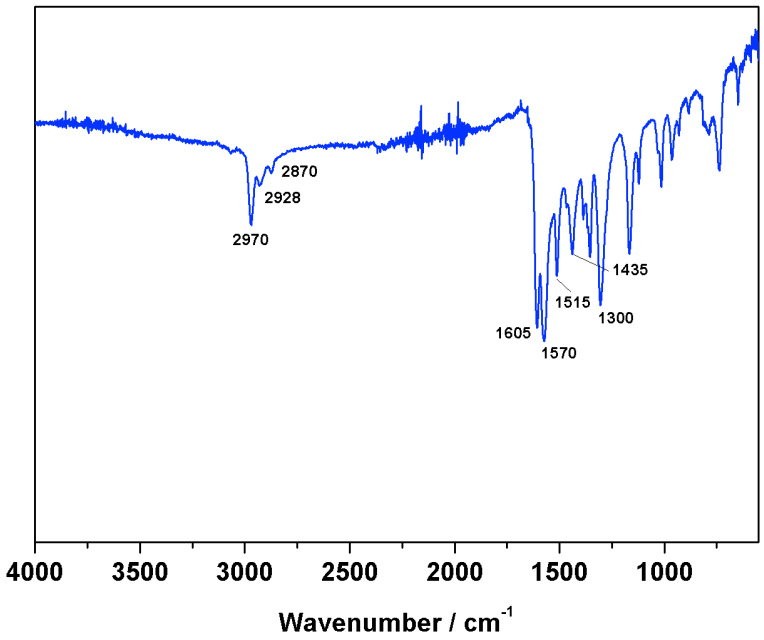

Figure 5.8: ATR-IR Spectrum of **HL**[1].

The ATR-IR spectra of **HL**[1] noticeably lacks any $\tilde{\nu}_{NH}$ stretching frequencies in the expected region of 3450 – 3350 cm^{-1}, possibly due to extensive tautomerisation, lessening the N – H bond character.[23,24]

The ART-IR spectra of compounds **1** and **2** is shown below in Figure 5.9. Comparing compounds **1**, **2** with **HL**[1] there is a small reduction in the stretching frequencies corresponding to the C=O, C=N and C–C bonds of the β – ketoiminate ligand, consistent with metal coordination to the O, N-donor atoms.[21]

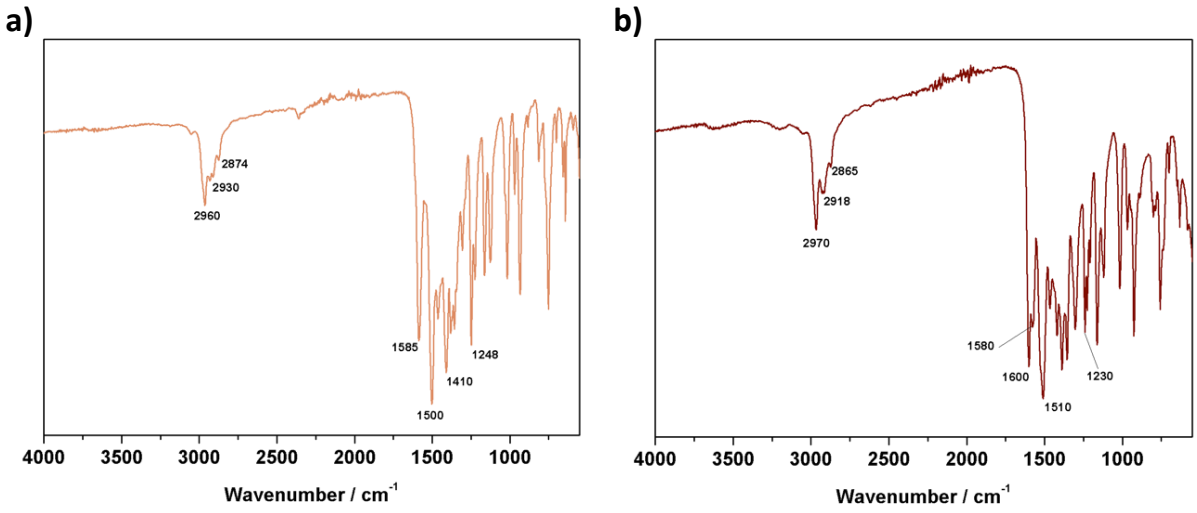

Figure 5.9: ATR-IR Spectrum of (a) **1** and (b) **2**.

5.6.2 Single Crystallography Studies of **1** and **2**

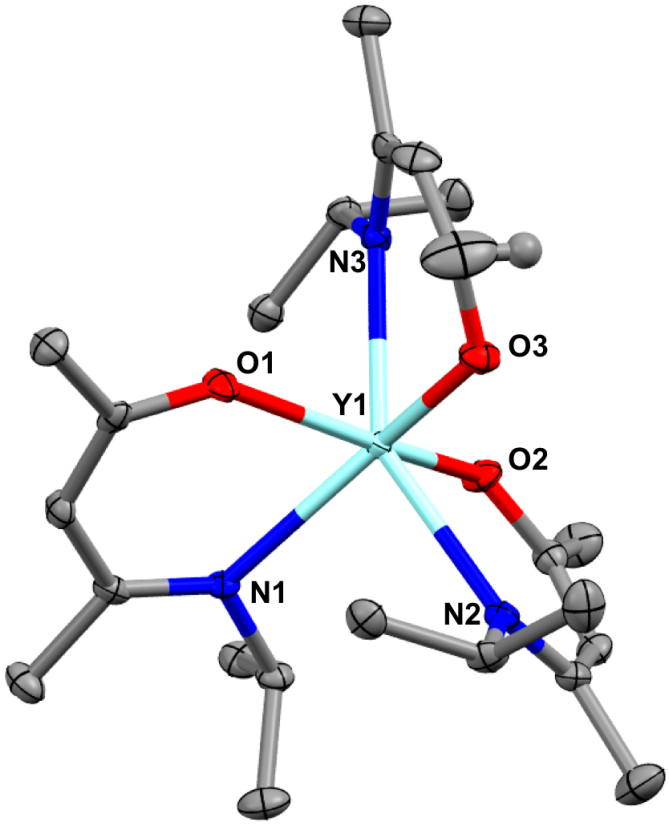

Figure 5.10 Crystal structure of **1**; thermal ellipsoids drawn at 50% probability and hydrogen atoms omitted for clarity. Selected distances (Å): Y1–O1 2.1943(16), Y1–O2 2.2046(16), Y1–O3 2.1644(16), Y1–N1 2.4634(19), Y1–N2 2.4751(19), Y1–N3 2.4585(19).

Single crystals suitable for X-ray diffraction of **1** were grown by cooling a saturated toluene solution to –35 °C over 18 hours, the molecular structure is shown in Figure 5.10. The yttrium metal centre is 6–coordinate, and the three β–ketoiminate ligands are in a distorted trigonal prismatic geometry. The Y–O distances are in the range of 2.1644(16)–2.2046(16) Å and Y–N distances in the range of 2.4585(19)–2.4751(19) Å. These are consistent with those of other yttrium β–ketoiminate compounds, for example $Y\{OC(Ph)CHC(Me)N(p\text{-chlorophenyl})\}_3$ with Y–O distances and Y–N distances in the range of 2.161(4)–2.174(3) Å and 2.422(5)–2.445(4) Å, respectively.[25]

Single crystals suitable for X-ray diffraction of **2** were grown by cooling from either a saturated toluene solution (**2.toluene**) or a saturated THF solution (**2.THF**) , to – 35 °C over 18 hours, the molecular structures are shown in Figure 5.11 and Figure 5.12, respectively.

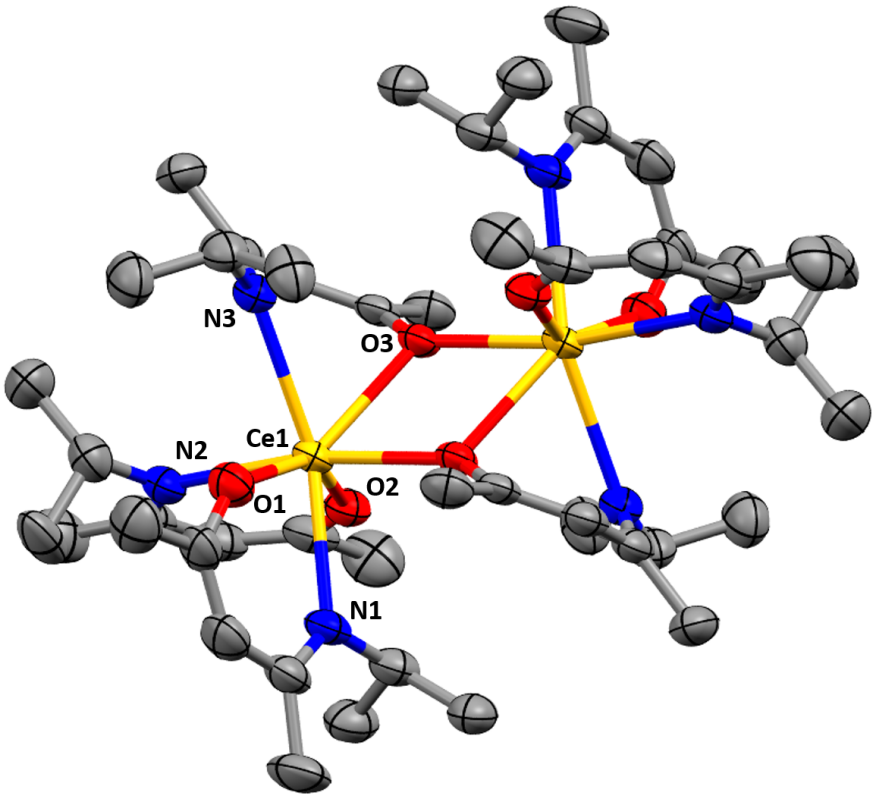

Figure 5.11 Crystal structure of **2.toluene**; thermal ellipsoids drawn at 50% probability, hydrogen atoms and toluene solvent of crystallisation omitted for clarity. Selected distances (Å) and angles (°): Ce1–O1 2.323(5), Ce1–O2 2.323(4), Ce1–O3 2.347(4), Ce1–^{inversion}O3 2.482(4), Ce1–N1 2.645(5), Ce1–N2 2.627(6), Ce1–N3 2.645(5), O3–Ce1–^{inversion}O3 65.9(2).

The crystal structure of **2.toluene** shows a dimeric cerium β–ketoiminate complex. This contrasts with compound **1** which is monomeric. The dimer vs. monomer difference most likely arises from difference in the ionic radii of the lanthanides: with Ce (1.03 Å) larger than Y(0.89 Å).[26] The cerium metal centre adopts a 7 coordinate, distorted capped octahedral geometry with two terminally coordinated β–ketoiminate ligands and one bridging β–ketoiminate ligand, coordinating simultaneously to both Ce centres through μ–O3. The terminal Ce–O bond distances of 2.323(5) Å are in agreement with those of related cerium β–ketoiminate compounds: Ce{OC(^{t}Bu)CHC(Me)N(CH_2CH_2OMe)}$_3$ with Ce–O distances of

2.349(3)–2.385(3) Å and Ce_2{2-(2-benzoxyazol-2-yl)phenolate}$_6$ with Ce–O distances at 2.285(2)–2.300(2) Å.[27,28] The bridging Ce–O bonds are longer than the terminal Ce–O bonds at 2.437(4)–2.482(4) Å and in agreement with reported values for bridging Ce – O bonds in Ce_2{2-(2-benzoxyazol-2-yl)phenolate}$_6$, in the range of 2.436(2) – 2.437(2) Å.[28] The Ce–N bonds of **2.toluene** at 2.627(6)–2.645(5) Å are consistent with those reported for Ce_2{2-(2-benzoxyazol-2-yl)phenolate}$_6$ in the range of 2.595(2)–2.672(2) Å and Ce{OC(^{t}Bu)CHC(Me)N(CH_2CH_2OMe)}$_3$ in the range of 2.616(4) – 2.684(4) Å.[27,28] The {Ce_2O_2} moiety features an inversion centre that generates a parallelogram with opposing bonds being of equal lengths, with a longer Ce–O bond at 2.482(4) Å and a shorter Ce–O bond at 2.347(4) Å. This moiety has been observed in a variety of reported cerium compounds including those with β – ketoiminate ligands and those without.[29-31] Naturally the dimensions of the {Ce_2O_2} parallelogram moiety varies depending on the oxygen bridging ligand and other coordinated ligand. Compound **2.toluene** exhibits O3–Ce1–O3 bond angles of 65.9(2)°, in agreement with Ce_2{2-(2-benzoxyazol-2-yl)phenolate}$_6$ O–Ce–O bond angles of 67.56(6)°.[28] $Ce_2[(TMP)_2(\mu\text{-OEt})]_2$ (TMP = 2,2,6,6-tetramethylpiperidinate) exhibits larger O–Ce–O bond angles of 72.11(5)°, while Ce_2{(salen)(μ-O^{t}Bu)}$_2$ (salen = 1,2-bis(2,4-di-*t*-butyl phenolate)ethylenediamine)) displays O–Ce–O bond angles of 71.30° and torsion angles of -30.48(5)°.[29,30] Compound 2 exhibits a planar parallelogram with torsion angles of 0°.

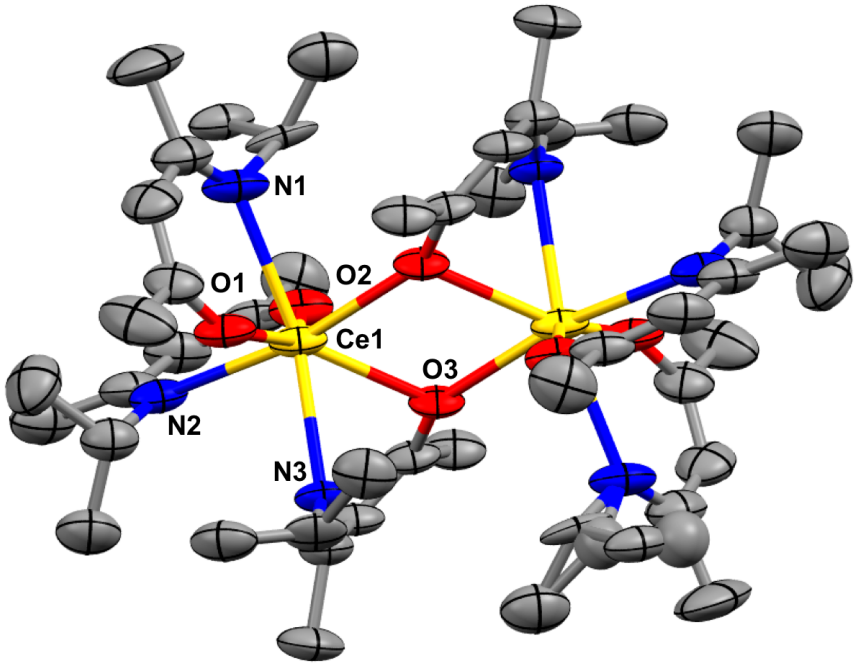

Figure 5.12: Crystal structure of **2.THF**; thermal ellipsoids drawn at 50% probability, hydrogen atoms omitted for clarity. Disordered THF accounted for using SQUEEZE function.

Compound **2.THF** shows statistically similar bond lengths and angles to those of **2.tolune**, see Table 5.2 below. The crystal structure of compound **2.THF** also demonstrates that the β–ketoiminate ligand is a superior μ–O donor compared to THF, with THF failing to coordinate to the metal centre or break up the $\{Ce_2O_2\}$ parallelogram structure.

Table 5.2 Dimensions of selected bonds for **1**, **2.toluene** and **2.THF**

	1	**2a**	**2b**
Ln – O^{term} (Å)	2.1644(16) – 2.2046(16)	2.326(4) – 2.333(3)	2.323(5)
Ln – O^{brdg} (Å)	N/A	2.451(4) – 2.489(5)	2.437(4) – 2.482(4)
Ln – N (Å)	2.4585(19) – 2.4751(19)	2.624(6) – 2.661(6)	2.627(6) – 2.645(5)
O – Ln – O (°)	N/A	65.99(15)	65.9(2)

Ln --- Ln (Å)	N/A	4.1437(9)	4.1270(7)

^{term} – terminal coordinated oxygen, ^{brdg} – bridging coordinated oxygen.

5.6.3 Conclusions: Synthesis of β–ketoiminate Complexes **1** and **2**

By considering both the typical structures used for precursors and the chemistry of lanthanides it was possible to synthesise and characterise two lanthanide β–ketoiminate complexes; $Y\{OC(Me)CHC(Me)N^{i}Pr\}_3$ (**1**) and $Ce_2\{OC(Me)CHC(Me)N^{i}Pr\}_6$ (**2**). Both complexes **1** and **2** were synthesised successfully *via* a simple protonolysis route. Alternative synthetic routes were considered, mainly metathesis, however these yielded intractable results and were not explored further. Purity of **1** and **2** was confirmed *via* 1H NMR, with contact shifts indicative also of successful coordination to the lanthanide centre. Single crystal X-ray diffraction studies of **1** and **2** revealed a contrasting monomeric and dimeric structures, owing most likely to the difference in ionic radii of Y(0.89 Å) and Ce (1.03 Å). Given the versatile nature and multiple applications associated with CeO_2, it was decided to proceed with molecule **2** as a precursor in materials synthesis investigations. The pre-formed Ce – O bonds in the range of 2.3 – 2.5 Å, coupled with the air/moisture sensitivity and ease of synthesis made molecule **2** the obvious choice for forming CeO_2 based materials. Two routes of materials synthesis from precursor were investigated: thermal decomposition and reactive infiltration (introduced in chapters and previously). In the next section we will look exclusively at the synthesis of materials *via* the thermal decomposition of precursor compound **2** under different atmospheric conditions, and compare directly with the previously adopted precursor molecule: CeN''_3.

5.7 Thermal Decomposition Studies of **2**

Thermal decomposition of metal based precursors is a simple, yet effective, mechanism of forming nanostructures of binary metal compounds (*e.g.* oxides, sulfides, selenides, nitrides, *etc*.).[32-35] Nanostructures often include nanoparticles and thin-films, depending on the exact nature of the deposition method, temperature range and ligand scaffolding surrounding the

metal centre of the precursor. Several examples have been reported in the literature of thermogravimetric behaviour of cerium based complexes.[36-39] The decomposition temperature is largely a function of the coordinating ligand environment, with no published examples of decomposition from cerium based β – ketoiminate precursor molecules. However, examples further afield of β – ketoiminate precursor molecules incorporating Zn metal have been noted.[3,4] Here we investigate the thermal decomposition properties of the novel precursor: $Ce_2\{OC(Me)CHC(Me)N(^iPr)\}_6$ (**2**). The aim of these studies was to establish whether the precursor decomposes, if so how easily does it decompose (*i.e.* low temperature, single step decomposition) and what are the possible decomposition products. Several possible decomposition products are accessible to the **2** complex based on abundance of oxygen atoms present in the molecule and the Ce–O bond length range of 2.3 – 2.5 Å (see Table 5.2), including CeO_2, Ce_2O_3 and $Ce(OH)_3$ which would have % mass losses of 69, 71 and 66% respectively, under both aerobic and anaerobic atmospheres (see Figure 5.13).

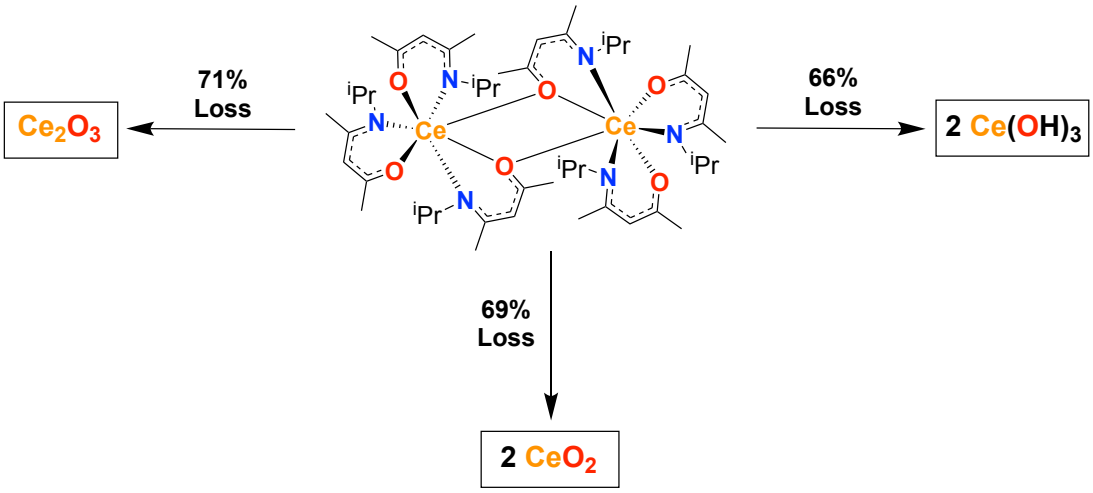

Figure 5.13: Schematic representation of decomposition pathways accessible to **2** with percentage mass losses noted for each pathway.

The TGA thermograms of **2**, under both aerobic (air) and anaerobic (N_2) atmospheres, are shown in Figure 5.14.

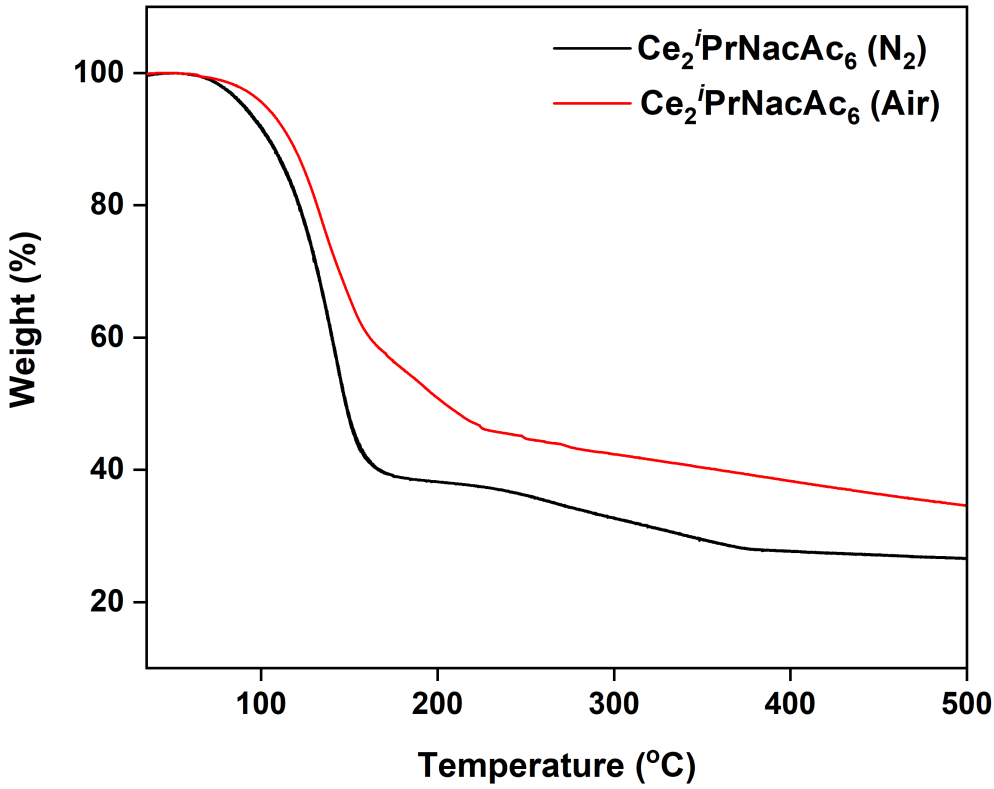

Figure 5.14: TGA thermograms of **2** under aerobic (air, red) and anaerobic (N_2, black) conditions.

The TGA thermogram under aerobic conditions exhibits a low temperature decomposition event, in the range of 110–230 °C. There is a moderate downward slope beyond 230 °C, with the trace levelling off beyond 500 °C indicating complete decomposition, with a mass loss of 65%. A mass loss of 65% slightly less than the predicted value of 69% assuming formation of CeO_2 as the final decomposition product and is closer to that of $Ce(OH)_3$ as the final decomposition product (predicted mass loss of 66%). Powder X-ray diffraction of the decomposed residue remaining after heating to 500 °C was recorded and revealed a completely amorphous solid, with no reflections corresponding to any of the theorised decomposition products (CeO_2, Ce_2O_3, $Ce(OH)_3$), see Figure 5.15.

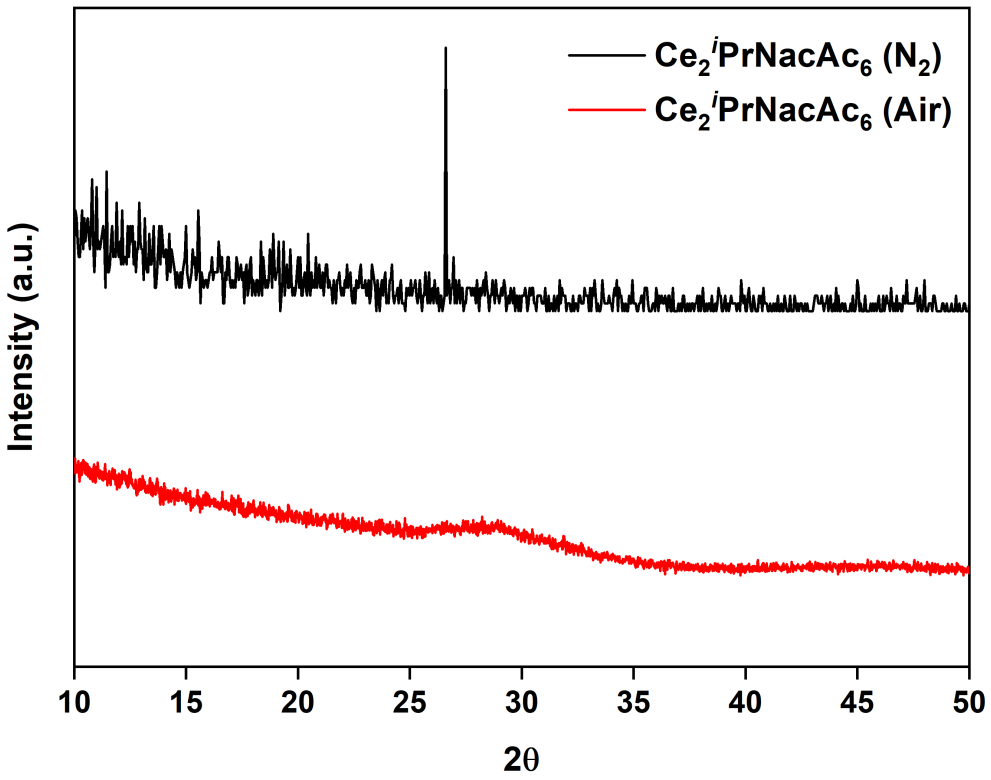

Figure 5.15: Diffractograms of residue formed after thermal decomposition of **2** under aerobic and anaerobic atmospheres.

The TGA thermogram of **2** under anaerobic conditions, see Figure 5.14, exhibits a lower temperature decomposition event relative to that under aerobic conditions, in the range of 100–180 °C. There is a distinct, yet small and gradual, second decomposition event over the temperature range of 230–380 °C. The TGA trace levels off beyond 400 °C with a mass loss of 74%, larger than that observed under aerobic conditions (where oxidation toward CeO_2 would be expected and in keeping with the lower % mass loss). The larger mass loss of 74% under anaerobic conditions is in keeping with the formation of sub-stoichiometric CeO_{2-x} given that the lack of excess oxygen would favour lower oxygen content in the final decomposition product. Although it should be noted that there is excess oxygen internally within the precursor structure to facilitate the formation of stoichiometric CeO_2, however oxygen may be used up during decomposition to form gaseous carbon based by-products (*e.g.* CO_2), leading to a deficiency of oxygen under anaerobic conditions and the formation of a sub-stoichiometric cerium oxide product.

Powder diffraction analysis of the anaerobic decomposition residue of **2**, see Figure 5.15, revealed an amorphous solid, similar to that for the decomposition under aerobic conditions. A reflection at 2θ = 26° was present in the diffractogram of the residue of **2** formed under anaerobic atmospheres, which was not present in the diffractogram of the residue formed under aerobic conditions. Initially it was believed this could be the (111) reflection of CeO_2, favoured by preferred orientation, at 2θ = 28°. However, on closer inspection, with direct comparison with the diffractogram of CeO2 it is several degrees away from the (111) reflection of CeO_2, see Figure 5.16.

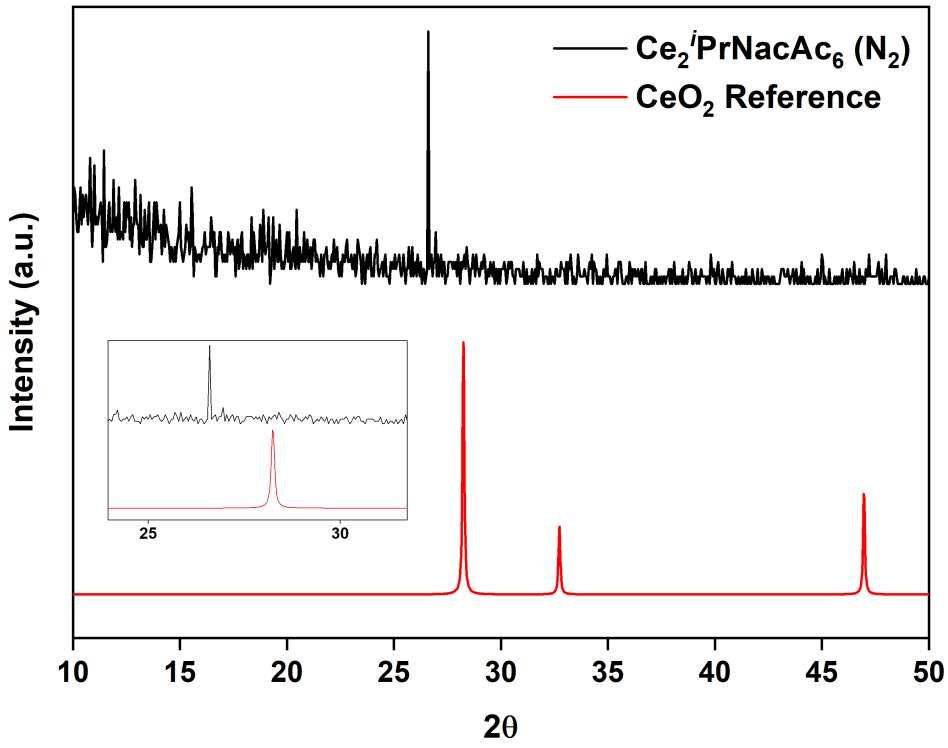

Figure 5.16: Diffractograms of residue formed after thermal decomposition of **2** under atmospheres and reference CeO_2.

These results are interesting when compared with various literature examples which often show Ce based complexes undergoing complete sublimation at low temperatures. Precursors of this nature are often applied to materials synthesis whereby the precursor is vapourised and subsequently deposited and/or reacted on a certain substrate surface. K. D. Pollard *et al* published a series of Ce based heteroleptic complexes featuring fluorinated acac ligands

(hfac: $OC(CF_3)CHC(CF_3)O$) and multidentate glyme ethers, $MeO(CH_2CH_2O)_nMe$ (n = 1, 2, 3), which all completely evaporated when heated up to 300 °C, leaving behind no decomposition residue.[36]

H. C. Aspinall *et al* studied the thermal properties of a number of Ce based ether alkanoate and amino alkanoate complexes, the ether alkanoate complexes showed complete vaporisation, while the amino alkanoate complexes exhibited decomposition, leaving behind a residue of CeO_2.[37] The authors did not provide any data beyond the % mass loss as evidence of the final speciation of the decomposition product, include powder X-ray diffractograms, therefore the crystallinity of the final product was unknown. The thermal properties of Ce(thd) (thd: 2,2,6,6-tetramethylheptane-3,5-dionate; $OCMe_3CHCMe_3O$) were also studied and showed complete vaporisation past 300 °C.[37] In comparison, our complex, **2**, showed decomposition well before 300 °C, highlighting the importance of the coordinated ligands to the thermal stability of the decomposing precursor.

Several further examples have been noted from the literature and serve to further enforce this point, see Table 5.3.

There exists several examples in the literature of Zn based β–ketoiminate precursor molecules that show ideal decomposition behaviour. $Zn\{OC(Me)CHC(Me)N(^iPr)\}_2$ and a mixture of $\{ZnEtOC(Me)CHC(Me)N(^iPr)\}_2$ and $Zn\{OC(Me)CHC(Me)N(^iPr)\}_2$ have both shown to exhibit clean, single step low temperature decomposition events in the ranges of 200 – 288 °C and 150 – 350 °C.[3,4] Following decomposition both precursors were shown to form a residue that consisted of crystalline ZnO. It is interesting that precursors of an analogous nature, Ce and Zn β–ketoiminates, exhibit similar decomposition temperatures and yet by changing the metal centre from Zn to Ce, the resultant product is not crystalline. This contrast highlights the importance of both ligand architecture and the choice of metal centre on modulating the decomposition properties of a precursor. This point was further illustrated upon investigating the thermal decomposition of the precursor CeN''_3.

The thermal decomposition of CeN''_3 was investigated to understand what changes, if any, changing the surrounding ligands on the Ce centre has on the thermal properties of the

precursor molecule. It also served to investigate whether CeN''$_3$ could act as a broad spectrum precursor, being applied to materials synthesis *via* multiple different routes (*e.g.* thermal decomposition, reactive infiltration. *etc.*). CeN''$_3$ is smaller and monomeric, compared to the larger dimeric **2**, it features a Ce centre with three coordinated monodentate bissilylamide ligands. The TGA thermogram of CeN''$_3$ under aerobic (air) and anaerobic (N_2) conditions is shown in Figure 5.17.

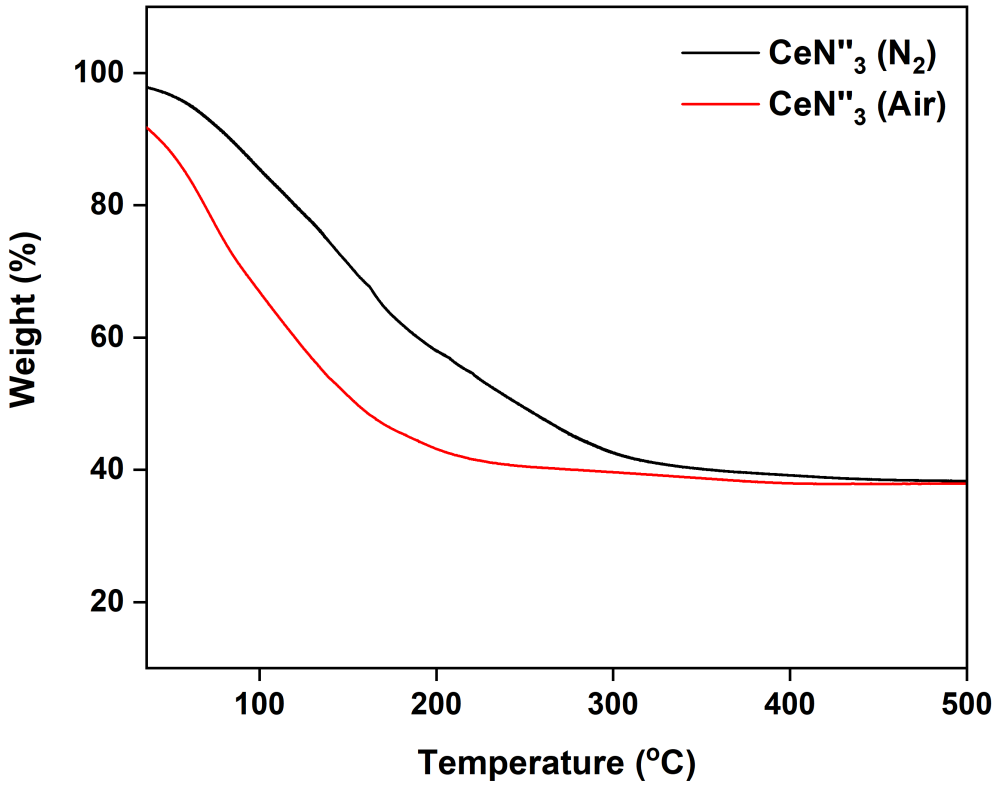

Figure 5.17: TGA thermograms of CeN''$_3$ under aerobic (air, red) and anaerobic (N2, black) conditions.

Interestingly, CeN''$_3$ exhibits immediate decomposition at 25 °C while loading into the TGA balance, under both aerobic and anaerobic atmospheres, with a final mass loss of 62% after 500 °C. The early onset decomposition of CeN''$_3$ highlights the highly reactive nature of the CeN''$_3$ molecule when compared to **2**. This reactivity most likely emanates from the small monomeric structure and low tridentate coordination sphere surrounding the Ce centre in

CeN''_3, while **2** has a stabilising dimeric structure, steric shielding of the Ce centre, heptadentate coordination sphere and chelate effect stabilisation. Therefore, β – ketoiminate ligands should be considered when trying to improve the 'handling ability' of precursor molecules in open air settings. The β–ketoiminate complex **2** demonstrated a more well defined, smaller temperature range, decomposition compared to CeN''_3. Similar to the decomposition of **2**, the final decomposition products was amorphous with no reflection characteristic of (CeO_2, Ce_2O_3, $Ce(OH)_3$), under both aerobic and anaerobic conditions (see Figure 5.18).

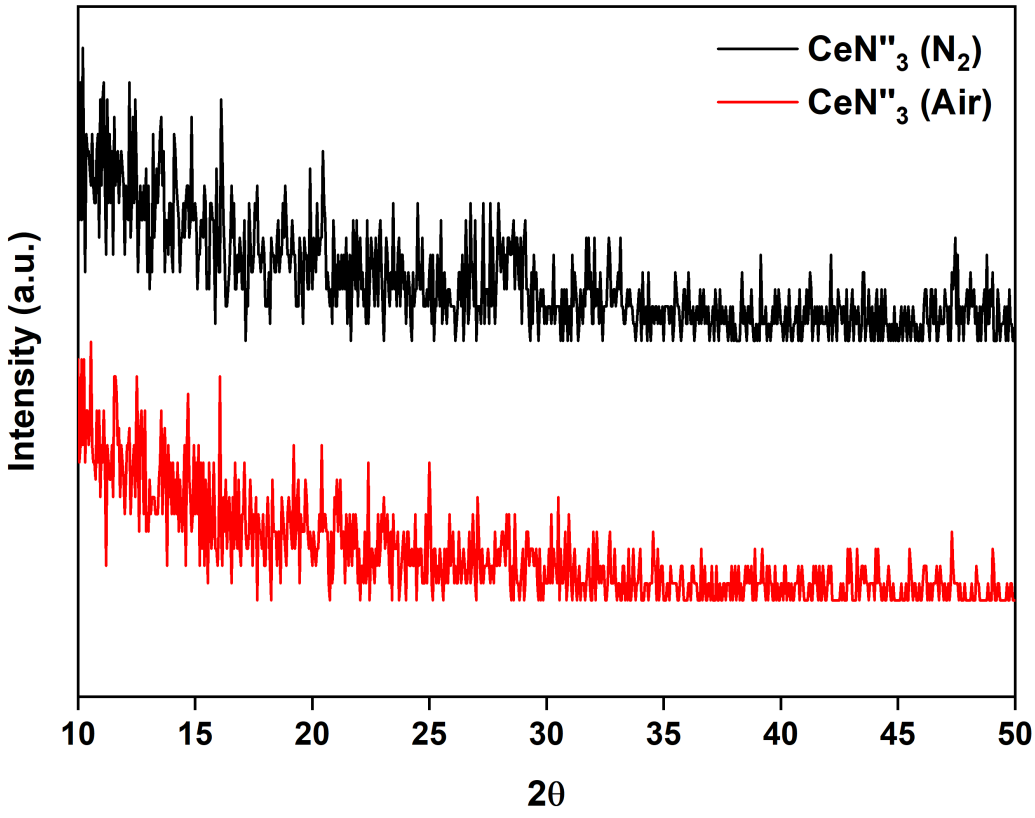

Figure 5.18: Diffractograms of residue formed after thermal decomposition of CeN''_3 under aerobic and anaerobic atmospheres.

The final mass loss of 62% is somewhat divergent from the theoretical value of 72% under aerobic conditions, assuming the formation of CeO_2, and 75% under anaerobic conditions, assuming the formation of CeN.

5.7.1 Conclusions: thermal decomposition of cerium β – ketoiminate precursor

Thermal decomposition studies of **2** revealed relatively low decomposition temperature ranges under both aerobic and anaerobic conditions, 110–230 °C and 100–380 °C, respectively. This is in keeping with the decomposition ranges observed for a number of Ce based precursors (see Table 5.3 below). Compound 2 does not undergo complete vaporisation, a prerequisite for any precursor molecule undergoing thermal decomposition, leaving behind a residue. The percentage mass losses under both aerobic and anaerobic conditions, 65% and 74% respectively, are consistent with the formation of CeO_2 and sub-stoichiometric CeO_{2-x} respectively, upon thermally decomposing **2**. However, the lack of crystalline reflections to corroborate this final decomposition composition limits the weight that can be placed on this conclusion, although the percentage mass loss has been used as a standalone speciation identifier in previous thermal decomposition studies of Ce precursors. Thermal decomposition studies of the alternative precursor, CeN''_3, highlight the importance of ligand design for tunning precursor properties, with the CeN''_3 exhibiting immediate decomposition and a wide temperature range over which decomposition occurs. Therefore, compound **2** proved to be a better precursor candidate in the synthesis of CeO_2 materials in comparison to CeN''_3, with an ease of handling, lower temperature decomposition range and shaper loss of mass.

Following on from the thermal decomposition method of materials synthesis, a second synthetic route to forming CeO_2 materials was investigated based on the optimised methodology introduced in Chapter 2: reactive infiltration.

Table 5.3: Summarised TGA data (inc. atmosphere, decomposition temperature range, mass lost and decomposition product) of selected Zn and Ce based precursors.

Precursor	Ligand type	Atmosphere	Decomposition Temperature, T_D (°C)	Mass Loss (%)	Decomposition Product and Ref.
$Zn\{OC(Me)CHC(Me)N(^{i}Pr)\}_2$[a]	β – ketoiminate	Not Noted	200 – 288	94	ZnO (crystalline)[3]
$Zn\{OC(Me)CHC(Me)N(^{n}Bu)\}_2$	β – ketoiminate	N_2	150 – 400	98	Minimal vaporisation residue[5]
$Zn\{OC(OEt)CHC(Me)N(^{i}Pr)\}_2$	β – ketoiminoester	N_2	250 – 400	100	Complete Sublimation[5]
$Zn\{OC(OEt)CHC(Me)N(Dipp)\}_2$[b]	β – ketoiminoester	N_2	100 – 420	75	Carbon contaminated ZnO (amorphous)[40]
$\{Zn(Et)OC(Me)CHC(Me)N(^{i}Pr)\}_2$: $Zn\{OC(Me)CHC(Me)N(^{i}Pr)\}_2$[c]	Alkyl / β – ketoiminate	N_2	150 – 350	67	ZnO (crystalline)[4]

$Ce(hfac)_3(\kappa^2\text{-}MeOC_2H_4OMe)$ [d]	Glyme / fluorinated acetate	Not Noted	40 – 180	100	Complete Sublimation[36]
$Ce(hfac)_3(\kappa^3\text{-}MeOC_2H_4OC_2H_4OMe)$[d]	Glyme / fluorinated acetate	Not Noted	130 – 230	100	Complete Sublimation[36]
$Ce(hfac)_3(\kappa^3\text{-}MeOC_2H_4OC_2H_4OC_2H_4OMe)$[d]	Glyme / fluorinated acetate	Not Noted	70 – 210	100	Complete Sublimation[36]
$\{Ce(hfac)_3\}_2(\mu\text{-}MeOC_2H_4OC_2H_4OC_2H_4OC_2H_4OMe)$[d]	Glyme / fluorinated acetate	Not Noted	60 – 280	>95	Minimal vaporisation residue[36]
$Ce(dmap)_4$[e]	Amino alkanoate	N_2	75 – 200, 210 – 310	70	CeO_2 [37]
$Ce(dmop)_4$[f]	Oxazolyl alkanoate	N_2	200 – 300	74	CeO_2 [37]
$Ce(mmp)_4$[g]	Alkoxy alkanoate	N_2	170 – 250	>98.5	Minimal vaporisation residue[37]
$Ce(thd)_4$[h]	Diketonate	N_2	200 – 300	100	Complete Sublimation[37]
$Ce(2\text{-ethylhexanoate})_3$	Carboxylate	H_2/Ar	300 – 700	67	CeO_2 [38]
$Ce(^{i\text{Pr}}Cp)_2(^{i\text{Pr}}amd)$[i]	Cyclopentadienyl / amidinate	N_2	200 – 320	100	Complete Sublimation[39]

CeL_2[j]	Fluorinated enaminolate	Not Noted	200 – 350	64	Impure Decomposition Product[41]
CeL'_2[k]	Fluorinated enaminolate	Not Noted	200 – 300	88	CeO_2 [41]
2 *(this work)*	β – ketoiminate	N_2	100 – 180, 230 – 380	74	Amorphous CeO_{2-x}
		Air	110 – 230	65	
CeN''_3 *(this work)*	Bis-silylamide	N_2	Immediate Decomposition	60	Amorphous Residue
		Air			

[a] – No single crystal X-ray structure indicating monomeric or polymeric structure.

[b] – Dipp = 1,3-diisopropyl phenyl

[c] – Inseparable mixture formed with homoleptic by-product.

[d] – hfac: $OC(CF_3)CHC(CF_3)O$

[e] – dmap: 1-(dimethylamino)propan-2-olate; $OCH(Me)CH_2NMe_2$, decomposition product CeO_2 speciation consistent with 70% mass loss (theoretical: 69%).

[f] – 2-(4,4-dimethyl-4,5-dihydrooxazol-2-yl)propan-2-ol, decomposition product CeO_2 speciation consistent with 74% mass loss (theoretical: 78%).

[g] – mmp: 1-methoxy-2-methylpropan-2-olate; $OCMe_2CH_2OMe$.

[h] – thd: 2,2,6,6-tetramethylheptane-3,5-dionate; $OCMe_3CHCMe_3O$.

[i] – $^{i\text{Pr}}$amd = $N(^{i}Pr)C(Me)N(^{i}Pr)$

[j] – L = *N,N*'-bis(4,4,4-trifluorobut-1-en-3-one)- ethylenediamine

[k] – L' = N,N'-bis(4,4,5,5,5-pentafluoropent-1-en-3-one)- ethylenediamine

5.8 Reactive Infiltration Studies of **2**

In Chapter 2 it was established that it was possible to assemble a CeNP@MOF808 composite using the optimised methodology of reactive infiltration. Reactive infiltration works on the premise that when a complementary system of host-guest is adopted, the guest can react within the host structure to assemble into nanoparticles. In the case of MOF808 and CeN''_3 the complementary nature is derived from the highly protic nature of MOF808 and the strong basicity of CeN''_3. Within this system the protonated forms of the ligand (HN'') are eliminated and act as a thermodynamic driving force for the reaction. At this point the question arises if alternative precursors can function in a similar way to CeN''_3, and what effect, if any, will changing the coordinating ligand environment have on the reactive infiltration process and the resulting composite properties. Compound **2** is like CeN''_3 a basic and highly air/moisture sensitive precursor. However, as observed during the thermal decomposition studies of both precursors, **2** exhibits greater air/moisture stability and is more easily handled compared to CeN''_3. Therefore, reactive infiltration using **2** and MOF808 was adopted as a comparative system.

In a methodology similar to that adopted with CeN''_3 and MOF808, a series of NMR scale reactions were recorded on a small sub-10 mg scale at 20 wt% loading of **2** relative to the MOF808 host. Here it was expected that successful reactive infiltration would be observed *via* the loss of a noticeable resonance (paramagnetically shifted) at δ = -13.34 ppm corresponding to the isopropyl methyl protons (H^1, see Figure 5.2). Interestingly, in contrast to the NMR scale reactive infiltration of CeN''_3 with MOF808, there is no significant loss of resonances corresponding to the precursor complex, see Figure 5.19. This demonstrates that reactive infiltration was slower in comparison to CeN''_3. However, the decision was made to continue with the scaled up reactive infiltration given the longer reaction times, coupled with dynamic stirring, would tend towards faster reaction kinetics and therefore compensate for the slower reactivity of **2** during reactive infiltration.

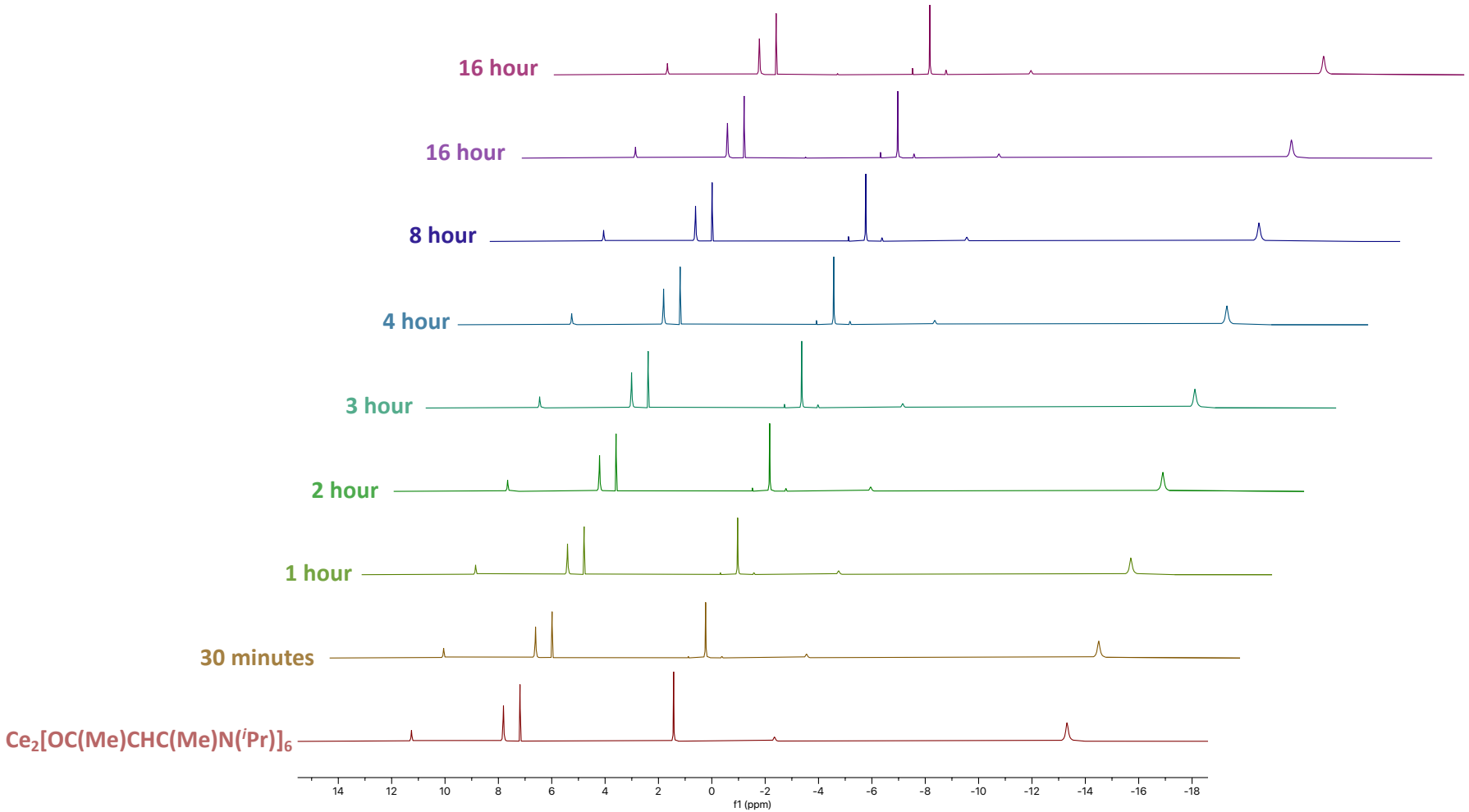

Figure 5.19: Stacked ^{1}H NMR spectra for the reactive infiltration of with MOF808. From bottom to top: increasing time of reaction.

In a scaled up methodology similar to that adopted for the reactive infiltration of CeN''_3 with MOF808, 70 mg of **2** was dissolved completely into 10 mL of dry toluene to form a bright yellow solution. 350 mg of MOF808 was suspended into the solution of **2** and stirred continuously for 17 hours. After 17 hours the suspension had turned from bright yellow to a pale cream colour, similar to the colour change observed for the reaction between CeN''_3 and MOF808, suggesting significant loss of **2** from the solution phase and successful reactive infiltration. The suspension was removed from the inert N_2 atmosphere, centrifuged and washed several times with toluene. The composite, CeNP'@MOF808, was subsequently analysed using a variety of techniques to establish what effect, if any, the infiltration of the precursor had on the MOF structure and how the composite compared in properties to CeNP@MOF808. The physical and electronic characterisation of both composites, formed by reactive infiltration of CeN''_3 and $Ce_2[OC(Me)CHC(Me)N(^iPr)]_6$ are summarised below in Table 5.4.

Table 5.4: Summary of characterisation data (EDX loading weights of Ce, XANES determined Ce^{3+} %, PXRD crystallinity, pK_a and formate:BTC) for CeNP@MOF808 and CeNP'@MOF808.

	CeNP@MOF808	CeNP'@MOF808
Ce wt % (*via* EDX)	2.8 (± 1.0)	3.3 (± 0.8)
Ce^{3+} % (XANES)	75	75
Crystallinity (PXRD)	MOF crystallinity retained, no additional reflections	MOF crystallinity retained, no additional reflections
pK_a (Titration)	3.8, 5.8, 8.7	3.8, 6.1, 9.5
Formate:BTC (Digestion ^1H NMR)	1.01 (± 0.30)	0.77

EDX measurements taken over several sample surface areas of CeNP'@MOF808 revealed a Ce wt% loading of 3.3 ± 0.8, statistically indistinguishable from the Ce wt% loading of

CeNP@MOF808. Therefore, the presence of Ce after several stages of washing the composite (which would remove any Ce not composited within the structure) is evidence of successful reactive infiltration and consistent with the objective colour change from bright yellow to pale cream.

Both composites are showed a retention of MOF crystallinity (see Figure 5.20), with no additional reflections corresponding to Ce based nanomaterials (*e.g.* CeO_2, Ce_2O_3, $Ce(OH)_3$). As previously stated, the lack of additional reflections following reactive infiltration of the precursor molecule, either CeN''_3 or $Ce_2[OC(Me)CHC(Me)N(^iPr)]_6$, could arise due to a number of factors, including: relatively small loading weights, small nanoparticle sizes, complex speciation or amorphous structure of the composited particles.

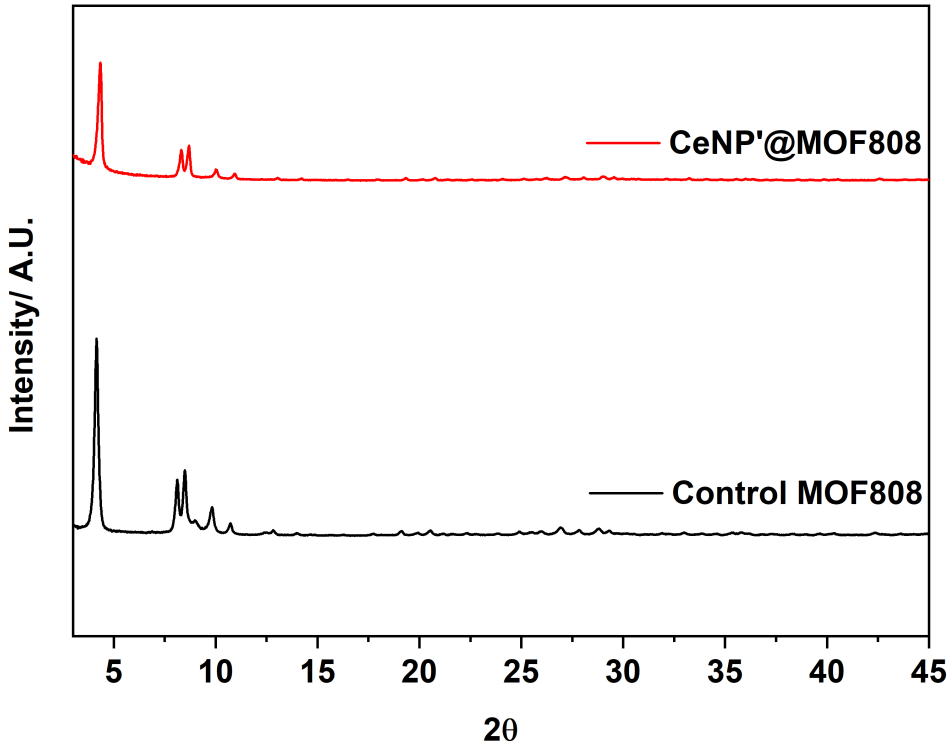

Figure 5.20: Diffractograms of Control MOF808 and CeNP'@MOF808.

Potentiometric titrations performed on both composites revealed largely similar pK_a values of 3.8, 5.8, 8.7 and 3.8, 6.1 and 9.5 for CeNP@MOF808 and CeNP'@MOF808 (see Figure 5.21), respectively, although there is a noticeable decrease in the acidity of the third pK_a value

associated with terminally coordinate hydroxide ions. This indicates that in both reactive infiltration systems the cluster nodes are largely unaffected by the loading process, with the coordinated bridging hydroxide and water molecules not significantly involved in the reactive infiltration process (*e.g.* as a source of oxygen). The third pK_a value, $pK_a(3)$ = 9.5, of CeNP'@MOF808 deviates from both the value for CeNP@MOF808 ($pK_a(3)$ = 8.7) and control MOF808 ($pK_a(3)$ = 8.7) This would suggest some reaction occurring between **2** and terminally coordinated hydroxide ligands of the cluster, causing an increase in the third pKa value. However, if the **2** precursor had reacted completely with the terminal hydroxide ligands we would expect this pK_a value to no longer be detected as the hydroxide moiety would presumably form a ceria oxy cluster and lose associated acidity. This leaves the interpretation open as to whether the precursor reacts directly with the terminal hydroxide ligand or merely shifts it's acidity through acid-base interactions or through loading.

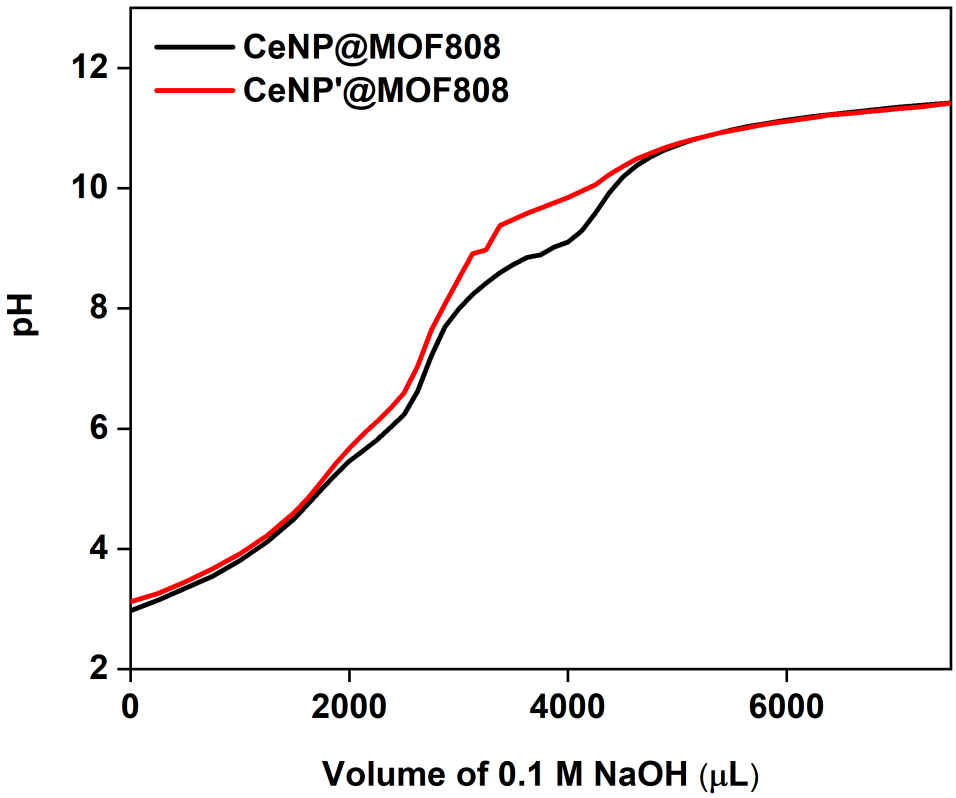

Figure 5.21: Potentiometric titration curve of Control MOF808 and CeNP'@MOF808.

Digestion ^{1}H NMR of CeNP'@MOF808 revealed a formate:BTC of 0.77 (average value, see Figure 5.22 and Figure 5.23), this was statistically indistinguishable from the CeNP@MOF808 composite which showed a formate:BTC of 1.01 ± 0.30. Therefore, there is no significant differences in formate modulator and BTC linker quantities between the two composites.

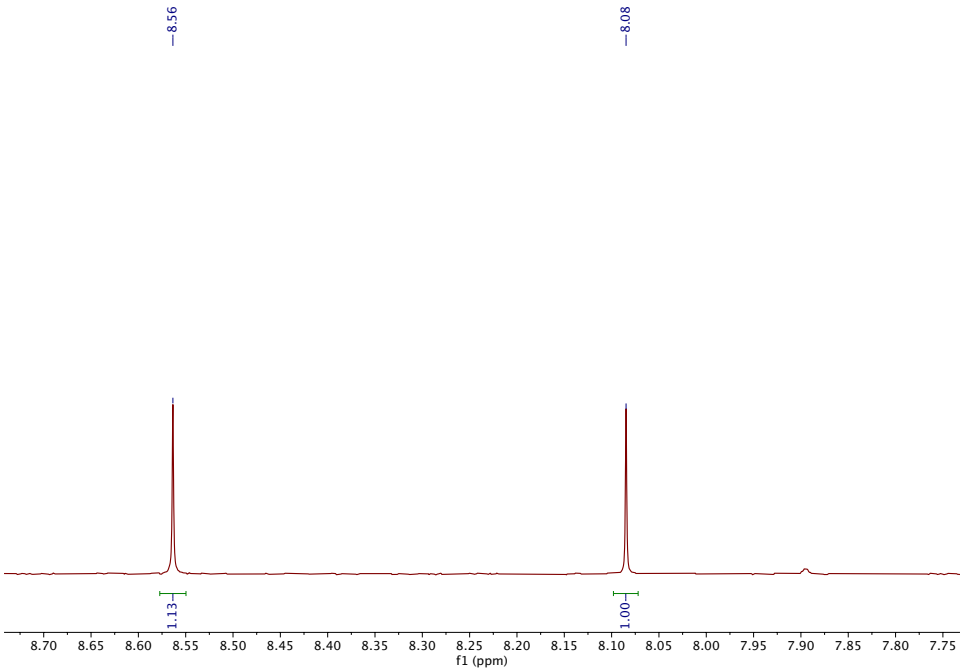

Figure 5.22: Digestion ^{1}H NMR of CeNP'@MOF808.

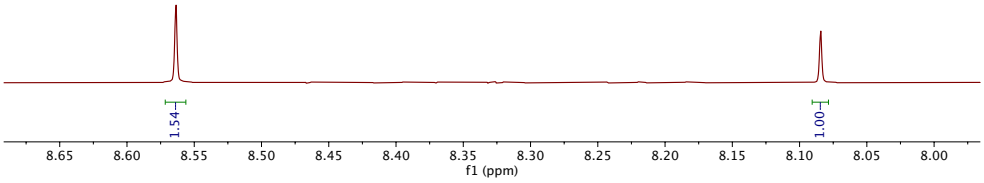

Figure 5.23: Digestion ^{1}H NMR of CeNP'@MOF808 (repeated).

Both composites showed identical Ce^{3+} proportions, at 75% (see Figure 5.24). This highlights that the soft-low energy nature of the reactive infiltration methodology offers an encouraging pathway for the formation of Ce^{3+} dominated composite materials, when using Ce^{3+} based precursors (*i.e.* reactive infiltration largely conserves the oxidation state of the precursor).

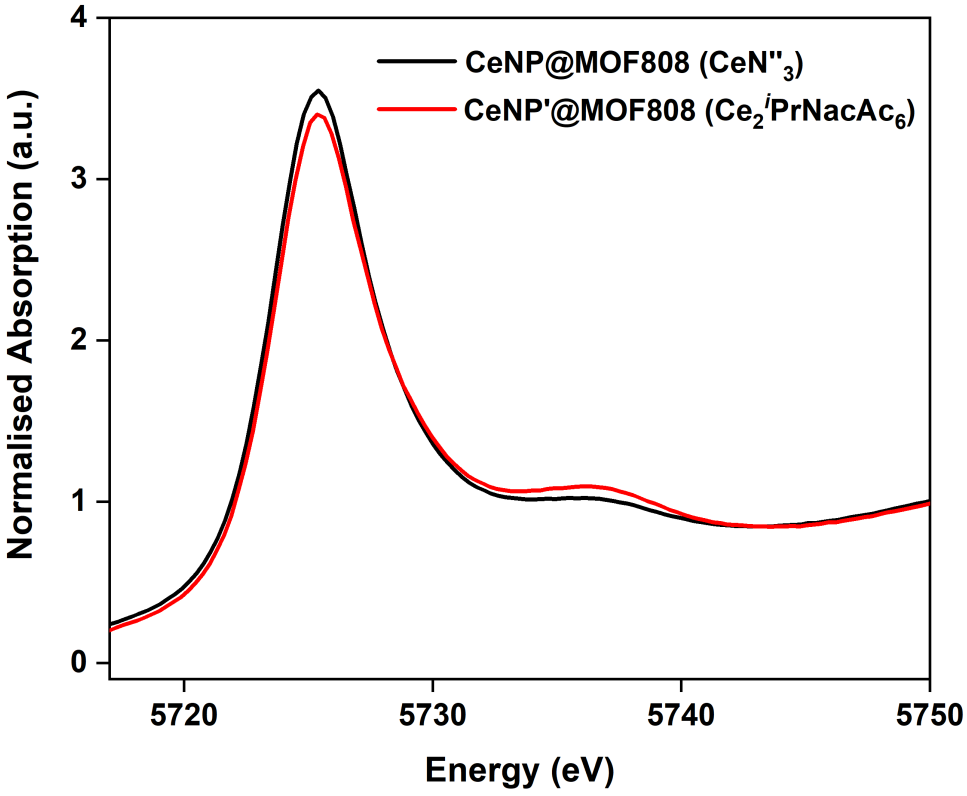

Figure 5.24: Ce L_{III} – XANES Spectrum of CeNP@MOF808 and CeNP'@MOF808.

5.8.1 Conclusions: Reactive Infiltration of **2**

Reactive infiltration was first introduced as a synthetic methodology for compositing Ce based nanomaterials within MOF host structures in Chapter 2 using the precursor CeN''_3. Following on from the successful optimisation of this synthetic methodology it was possible to replicate the synthesis using the novel precursor **2**. As summarised in Table 5.4, the composite formed *via* the reactive infiltration of novel precursor molecule **2** with MOF808: CeNP'@MOF808, is similar to that formed by the reactive infiltration of CeN''_3 with MOF808 in terms of Ce loading

wt%, MOF crystallinity, formate:BTC ratios and Ce^{3+} proportions. The only deviation between the two composites is in the third pK_a value determined *via* potentiometric titration, but even these values are similar as to suggest to significant variation in cluster node acidity. The successful reactive infiltration of **2** with MOF808 demonstrates the versatility of the reactive infiltration process, with the reactive infiltration methodology able to operate with precursors of significantly different architecture and with varying reactivity.

5.9 Conclusions

Harnessing lanthanide synthetic techniques, and guided by an array of typical molecular precursor examples, it was possible to synthesise and fully characterise two novel lanthanide β – ketoiminate complexes: $Y\{OC(Me)CHC(Me)N^{i}Pr\}_3$ (**1**) and $Ce_2\{OC(Me)CHC(Me)N^{i}Pr\}_6$ (**2**). Compounds **2** was subsequently employed as a molecular precursor, due to its Ce–O bond dimensions, in the range of 2.3–2.5 Å and Ce–O coordination sphere, both of which favour the formation of Ceria type nanomaterials. Thermal decomposition studies of **2** showed precursor with a low temperature decomposition range under both aerobic and anaerobic conditions, 110–230 °C and 100–380 °C, respectively. Percentage mass losses under bother aerobic and anaerobic conditions were indicative of 2 forming CeO_{2-x} or $Ce(OH)_3$ type materials upon thermal decomposition, although powder X-ray diffraction failed to elucidate this characterisation further. Compound **2** demonstrated improved thermal stability relative to CeN''_3, highlighting the importance of ligand choice when designing molecular precursors for materials synthesis.

An ideal precursor is one that can be applied to multiple different synthetic methodologies for forming solid state materials. In order to investigate the versatile materials applications of Compound **2**, reactive infiltration was performed with **2** and MOF808 as the complementary guest-host pairing. Reaction infiltration between **2** and MOF808 was successful forming a composite, CeNP'@MOF808, with similar properties to that formed by the reactive infiltration of CeN''_3 with MOF808, CeNP@MOF808 (see Table 5.4).

While compound **2** shows promise as a materials precursor, it is notable that through the synthetic methodologies of thermal decomposition and reactive infiltration, neither resulted in the successful formation of *crystalline* CeO_2 nanostructures. Following on from this work, the main aim should be to apply compound 2 to a variety of alternative synthetic methodologies in the hope of achieving the formation of crystalline CeO_2 nanostructures.

5.10 Experimental Details for Chapter 5: Synthesis

5.10.1 Synthesis of $Y(OTf)_3$

A Teflon-sealed ampoule was charged with Y_2O_3 (3.95 g, 17.5 mmol, 1 eqv) and suspended in 20 mL of deionised water. HOTf (17.30 g, 115.3 mmol, 6.6 eqv) was added to the suspension, with stirring, resulting in an immediate vigorous fuming of the solution. The reaction mixture was sealed under partial vacuum and refluxed at 101 °C for 18 hours. After 18 hours all solids had dissolved, leaving a colourless solution. Water was removed *via* rotary evaporation in a pear-shaped evaporation flask. White solids were isolated on a Gooch crucible and washed with Et_2O (4 × 10 mL) and hexanes (2 × 10 mL), and dried at 220 °C for 36 hours; yielding a white free flowing powder $Y(OTf)_3$ (6.90 g, 12.9 mmol, 37%). $^{19}F\{^1H\}$ NMR (d_3-MeCN): δ –79.23 (s, C***F***$_3SO_4$) ppm.

5.10.2 Synthesis of $Ce(OTf)_3$

$Ce(OTf)_3$ was synthesised in a manner analogous to $Y(OTf)_3$; using $Ce_2(CO_3)_3.xH_2O$ (4.64 g, 10.1 mmol, 1 eqv), HOTf (10.00 g, 66.7 mmol, 6.6 eqv); yielding a white free flowing powder $Ce(OTf)_3$ (5.76 g, 9.8 mmol, 49%). $^{19}F\{^1H\}$ NMR (d_3-MeCN): δ –76.40 (s, C***F***$_3SO_4$) ppm.

5.10.3 Synthesis of KN''

A Teflon-sealed ampoule was charged with KH (2.0 g, 50 mmol, 1 eqv) and suspended in 20 mL of toluene. The colourless liquid of HN'' (8.05 g, 50 mmol, 1 eqv) was degassed by three freeze–thaw cycles and added to the KH suspension *via* cannula at –78 °C, with stirring. The mixture equilibrated to room temperature for 20 minutes. The reaction mixture was refluxed at 120 °C for 12 hours under partial vacuum, giving a colour change from light grey to orange after 1 hour; and to dark brown after 12 hours. The reaction mixture is filtered on a frit through dry Celite®, leaving a dark brown residue. The residue was washed with hexanes (2 × 10 mL). The washings and filtrate were combined in a Schlenk flask and cooled at –15 °C for 12 hours after which white crystals crystallised out of solution. The mother liquor was

removed from the crystals *via* cannula. Crystals were washed with cold hexanes (2 × 20 mL) at –78 °C. The white crystals were dried under vacuum for 30 minutes yielding a white free flowing powder KN'' (4.90 g, 24.62 mmol, 49%). ^{1}H NMR (d_6-benzene): δ 0.13 (s, Si***Me***$_3$) ppm.

5.10.4 Synthesis of YN''$_3$

A Schlenk flask was charged with Y(OTf)$_3$ (2.36 g, 4.4 mmol, 1 eqv) and suspended in 30 mL of THF. A separate Schlenk flask was charged with KN'' (2.72 g, 13.64 mmol, 3.1 eqv) and dissolved in 20 mL of THF forming a pale-yellow solution. The KN'' solution was added to Y(OTf)$_3$ suspension *via* cannula, with stirring. The reaction mixture was stirred for 1 hour at room temperature, before the THF was removed *in vacuo* yielding white solids which were dried for 1 hour *in vacuo*. The white solids were crushed into a fine powder, inside the Schlenk flask in the glovebox, and extracted into hexanes (3 × 15 mL). The hexane washings were combined, reduced to saturation *in vacuo* and recrystallised over 18 hours by slow-cooling to –15 °C using an isopropyl alcohol jacket within a dewar vessel. Large pale-yellow crystals were isolated from the mother liquor *via* cannula and washed with dry hexanes (2 × 10 mL) at –78 °C. Colourless crystals dried *in vacuo* for 30 minutes yielding a white free-flowing powder YN''$_3$ (1.52 g, 2.67 mmol, 61%). ^{1}H NMR (d_6-benzene): δ 0.30 (s, Si***Me***$_3$) ppm.

5.10.5 Synthesis of CeN''$_3$

A Schlenk flask was charged with Ce(OTf)$_3$ (3.16 g, 5.38 mmol, 1 eqv) and suspended in 30 mL of THF. A separate Schlenk flask was charged with KN'' (3.32 g, 16.68 mmol, 3.1 eqv) and dissolved in 20 mL of THF forming a pale-yellow solution. The KN'' was added to the Ce(OTf)3 suspension *via* cannula, with stirring. The reaction mixture was stirred for 1 hour at room temperature, before the THF was removed *in vacuo* yielding cream-yellow solids which were dried for 1 hour *in vacuo*. The cream-yellow solids were extracted into dry toluene (3 × 10 mL). The toluene washings were combined, reduced to saturation *in vacuo* and recrystallised over 18 hours by slow-cooling to –15 °C using an isopropyl alcohol jacket within a dewar vessel. Yellow needle-like crystals were isolated from the mother liquor *via* cannula and washed with dry hexanes (2 × 10 mL) at –78 °C. Yellow solids dried *in vacuo* for 30 minutes

yielding a bright yellow free-flowing powder CeN''$_3$ (1.91 g, 3.08 mmol, 57%). ^{1}H NMR (d_6-benzene): δ –3.40 (s, Si***Me***$_3$) ppm.

5.10.6 Synthesis of OC(Me)CHC(Me)NH^{i}Pr (**HL^1**)

A round bottom flask was charged with 2,4-pentanedione (14.18 g, 141.6 mmol, 1 eqv) and dissolved in 50 mL of toluene giving a pale-yellow solution. 2-isopropylamine (16.72 g, 282.8 mmol, 2 eqv) was added dropwise to the 2,4-pentanedione solution, with stirring at room temperature, precipitating a yellow solid, vigorous fuming and an exothermic release of heat. The reaction mixture was refluxed at 130 °C for 16 hours in a Dean-Stark apparatus giving a colour change from bright yellow to dark brown. The solution was dried over anhydrous $MgSO_4$ and filtered through fluted filter paper yielding a light orange solution. The filtrate was transferred to a Schlenk flask and the toluene removed *in vacuo* to give a dark orange oil. The oil was degassed by three freeze–thaw cycles, in a Teflon-sealed ampoule, to remove dissolved oxygen gas. **HL^1** (16.00 g, 113.5 mmol, 80%). ^{1}H NMR (d_6-benzene): δ 0.78 (6H, d $^3J_{HH}$ = 6.4 Hz, ^{i}Pr-***Me***), 1.43 (3H, s, NC***Me***), 2.04 (3H, s, OC***Me***), 3.09 (1H, sept, $^3J_{HH}$ = 12.9 Hz, 6.4 Hz, ^{i}Pr-C***H***), 4.86 (1H, s, C***H***), 11.20 (1H, br s, N***H***) ppm. IR (ATR)/cm^{-1}: *v*C – H 2970 (w) *v*C – H 2928 (w) *v*C – H 2872 (w) *v*C = O 1605 (m) *v*C – N 1570 (m) *v*C – C 1515 (m) *v*C – N 1300 (m). MS (EI) : m/z = 142 (**L^{1}H$_2^+$**) amu. UV-vis (THF) λ_{max}/nm (ε/M^{-1} cm^{-1}): 306 (19000).

5.10.7 Synthesis of OC(Me)CHC(Me)NHPh (**HL^2**)

2,4-pentanedione (11.43 g, 114 mmol, 1 eqv) was dissolved in toluene (50 mL), inside a round bottom flask, to give a pale-yellow solution. Phenylamine (21.23 g, 228 mmol, 2 eqv) was added dropwise to the 2,4-pentanedione solution, with stirring at room temperature, precipitating a yellow solid, vigorous fuming and an exothermic release of heat. The reaction mixture was refluxed at 180 °C for 16 hours in a Dean-Stark apparatus resulting in a dark brown solution forming. The dark brown solution vacuum was distilled to giving a yellow-cream solid and dried *in vacuo* for 1 hour. **HL^2** (670 mg, 4 mmol, 4%). ^{1}H NMR (d_6-benzene): δ 1.58 (3H, s, CN***Me***), 2.05 (3H, s, CO***Me***), 4.98 (1H, s, sp^2-C***H***), 6.70 (2H, d, J = 7.8 Hz, ortho

sp^2-C***H***), 6.82 (1H, t, J = 7.3 Hz, para sp^2-C***H***), 6.92 (2H, t, J = 7.3 Hz, meta sp^2-C***H***), 13.07 (1H, s, N***H***) ppm.

5.10.8 Synthesis **1** and **2**

*5.10.8.1 Synthesis of Y(L^1)$_3$ (**1**)*

YN''$_3$ (530 mg, 0.93 mmol, 1 eqv) was dissolved in toluene (30 mL), inside a Schlenk flask, forming a colourless solution. **HL^1** (407 mg, 2.88 mmol, 3.1 eqv) was added dropwise to the YN''$_3$ solution, with stirring, resulting in a colour change from colourless to pale yellow. The solution was stirred for 1 hour at room temperature, with toluene subsequently removed under vacuum and the resulting pale cream powder dried *in vacuo* for 2 hours. Pale cream solids were dissolved in minimal hexanes (15 mL) and recrystallised over 18 hours at –15 °C in an isopropyl alcohol cooling jacket. Pale yellow crystals were isolated from the mother liquor *via* cannula transfer, washed twice with hexanes (2 × 10 mL) and dried *in vacuo* for 30 minutes to give a bright yellow powder, Y(L^1)$_3$ **1** (300 mg, 0.59 mmol, 63%). IR (ATR): 2960 (w, ν_{CH}) 2930 (w, ν_{CH}) 2874 (w, ν_{CH}) 1585 (s, ν_{CO}) 1500 (s, ν_{CN}) 1410 (w, ν_{CC}) 1248 (s, ν_{CN}). ^{1}H NMR (d_6-benzene): δ 1.39 (6H, d, J = 6.7 Hz, C***Me***$_2$) 1.73 (3H, s, CN***Me***) 1.90 (3H, s, CO***Me***) 3.85 (1H, m, J = 6.9 Hz, C***H***Me$_2$) 4.91 (1H, s, sp^2-C***H***) ppm. Absorption spectrum (THF) λ_{max} / nm (ε / 10^4 M^{-1} cm^{-1}): 306 (4.5).

*5.10.8.2 Synthesis of Ce_2(L^1)$_6$ (**2**)*

CeN''$_3$ (3 g, 4.84 mmol, 1 eqv) was dissolved in toluene (60 mL), inside a Schlenk flask, forming a bright yellow solution. **HL^1** (1.89 g, 15 mmol, 3.1 eqv) was added dropwise to the CeN''$_3$ solution, with stirring, resulting in a colour change from bright yellow to dark orange. The solution was stirred for 10 minutes at room temperature, with toluene subsequently removed under vacuum and the resulting dark orange solid dried *in vacuo* for 2 hours. The dark orange solids were crushed into a fine, granular powder, inside the Schlenk flask in the glovebox, and subsequently washed with dry hexanes (3 × 15 mL) at –78 °C. The orange solids were dissolved in excess THF (100 mL), reduced to saturation and recrystallised over 18 hours at –15 °C in an

isopropyl alcohol cooling jacket. Bright yellow crystals were isolated from the mother liquor *via* cannula transfer, washed with hexanes (3 × 15 mL) and dried *in vacuo* for 1 hour. Upon drying crystals form a bright yellow powder, $Ce_2(L^1)_6$ **2a** (1.37 g, 1.22 mmol, 51%). IR (ATR): 2970 (w, ν_{CH}) 2918 (w, ν_{CH}) 2865 (w, ν_{CH}) 1600 (m, ν_{CO}), 1580 (w, ν_{CN}) 1510 (m, ν_{CC}) 1230 (m, ν_{CN}). ^{1}H NMR (d_6-benzene): δ -13.34 (6H, s, C***Me***$_2$) -2.37 (1H, s, C***H***Me$_2$) 1.40 (3H, s, CN***Me***) 7.78 (3H, s, CO***Me***) 11.23 (1H, s, sp^2-C***H***) ppm. ^{1}H NMR (d_8-THF): δ -13.12 (6H, s, C***Me***$_2$) -2.77 (1H, s, C***H***Me$_2$) 1.49 (3H, s, CN***Me***) 7.97 (3H, s, CO***Me***) 11.26 (1H, s, sp^2-C***H***) ppm. Absorption spectrum (THF) λ_{max} / nm (ε / 10^4 M^{-1} cm^{-1}): 306 (2.6). Evans Method μ_{eff} (298 K, d_6-benzene) 3.05 ± 0.10 μ_B.

5.10.9 Compound **2** Reactive Infiltration with MOF808 – CeNP'@MOF808

Procedure analogous to that for CeN''_3 (see Chapter 2) using **2** (70 mg, 0.06 mmol, 20 wt%, 5.0 wt% Ce), MOF808 (350 mg) and toluene (10 mL). Note that no repeats of this reaction are performed. EDX: 3.3 ± 0.8 wt% Ce. PXRD (λ CuK: 1.54 Å): 2θ 4 (111) 8 (311) 9 (222) 10 (400) 11 (331)°. pK_a: 3.8, 6.1, 9.5. formate:BTC = 0.77.

5.11 Experimental Details for Chapter 5: Techniques and Characterisation

5.11.1 Nuclear Magnetic Resonance Measurements

^{1}H NMR data was recorded on either a Bruker AVIII 400 MHz instrument or Bruker AVI 500 MHz instrument, referenced internally to the appropriate residual protio-solvent and reported relative to tetramethylsilane (δ = 0 ppm). All spectra were recorded at a constant temperature of 300 K. Coupling constants (J) are reported in hertz (Hz). Standard abbreviations indicating multiplicity were used as follows: m = multiplet, d = doublet, t = triplet, s = singlet. Digestion NMR data were obtained by suspending ca. 0.5 mg of sample in d_6-DMSO (2-3 mL) and mixing with 2-3 drops of D_2SO_4. Samples were sonicated for *ca.* 15 minutes to form a cloudy colloidal mixture that was transferred to a NMR tube and heated gently with agitation, up to 189 °C, until a clear solution formed. The Evans method was performed by inserting a sealed capillary of NMR solvent into an NMR tube containing a

sample of known concentration, then measuring the difference (in Hz) between the chemical shift of the two solvent signals. This difference in chemical shift can then be used to determine the magnetic moment μ_{eff}.

5.11.2 UV-vis Measurements

UV – Vis electronic absorption spectra were collected using a Horiba Duetta combination absorbance and fluorescence spectrometer. Standard solutions prepared in dry volumetric flasks with anhydrous solvents

5.11.3 Infrared Spectroscopy Measurements

ATR–IR spectra were collected using a Shimadzu FTIR 8400S spectrometer. Abbreviations indicating strength of bands were used as follows: s = strong, m = medium, w = weak, sh = shoulder.

5.11.4 Energy Dispersive X-ray Spectroscopy Measurements

EDX measurements were obtained by taking three surface profiles on 3 separate particles to ensure representative elemental weight percentage, elemental weight percentages are determined as average values ± the standard deviation. Samples were scattered on pure carbon tabs and mounted on aluminium stubs. Samples were coated using a Polaron SC7640 sputter coater with Au/Pd target to make them electrically conductive. The EDX detector used was an Oxford Instruments X-act system with INCA 500 software and calibrated relative to a Cu reference. All EDX scans were taken at 5000 magnification.

5.11.5 X-ray Absorption Spectroscopy Measurements

Samples prepared based on heavy elements weight percentages; with masses determined to ensure sufficient transmission of the X-ray beamline. Samples mixed with α – Cellulose into a fine homogenous powder and pressed into 1.3 cm^2 pellets using Specac Atlas GS15011

Manual Hydraulic Press at 1 – 3 tons of pressure. Measurements taken at the Ce L_3 edge (5723 eV). Si(111) double crystal monochromator was used to select the energies. Pt coated mirror used to reject higher harmonics from the beam. The photon flux of the incoming and transmitted X-ray beam was detected with two ionization chambers I_0 and I_t, respectively, filled with appropriate mixtures of N_2/Ar. A third ionization chamber (I_{ref}) was used in series to simultaneously measure a reference metal foil (Cr metal foil). Fluorescence data were collected using a 36 element solid state Ge detector. XANES absorption spectra were deconvoluted using empirical based peak fitting methods described in literature. The transition to continuum states, with the concurrent expulsion of a photoelectron, in the XANES spectra is accounted for using an arctangent function. The corrected XANES spectra are then fitted for using symmetric Gaussian functions.

5.11.6 Single Crystal X-ray Diffraction Measurements

Single crystals suitable for X-ray diffraction were obtained by cooling concentrated solutions of either THF (**2a**) or toluene (**1**, **2b**) at –35 °C, over 18 hours. The crystals were coated with Fomblin ® and mounted on a Mitegen MicroMount. Data were collected for compounds **2a**, **2b** using a Bruker D8 VENTURE diffractometer equipped with a Photon II CPAD detector and an Oxford Cryosystems N-Helix device mounted on an IμS 3.0 (dual Cu and Mo) microfocus sealed tube generator. Data were collected for compound **1** by The National Crystallography Service (NCS): 2019NCSX0268. Structure solution and refinement for all structures were carried out with SHELXT[42] and SHELXL-2018[43] using the Olex2 software package.[44] Data collection and reduction were performed using the APEX3 or APEX2 programs. Corrections for incident and diffracted beam absorption effects were applied using empirical absorption corrections.[45] All non–hydrogen atoms were refined with anisotropic thermal parameters. Solvent molecule sites were found and included in the refinement of structure were generally refined with anisotropic thermal parameters. The positions of hydrogen atoms were calculated based on stereochemical considerations and included as part of a riding model with isotropic ADPs at 1.2 U_{eq} of the parent atom.

5.11.7 Powder X-ray Diffraction Measurements

Powder X-Ray Diffraction measurements were carried out at 25 °C, in the Bragg-Brentano geometry, using a Rigaku Miniflex600 benchtop diffractometer CuK_α (λ = 1.4505 Å). Powdered samples were centred on a bracket and diffraction patterns were measured from 3° to 45° with a step size of 0.01° and speed of 10.0° min^{-1}. For all samples, the spinning speed of 10 rpm was used.

5.11.8 Thermogravimetric Analysis Measurements

TGA is a technique that allows the continuous measurement of mass of a sample while subjecting the sample to a controlled thermal program, commonly through constant heating. For the complexes included in this study, decomposition occurs through the loss of organic ligand, resulting in a decrease in mass. By plotting the percentage mass as a function of increasing temperature, decomposition characteristics exhibited by the complex can be elucidated, such as decomposition temperature ranges, the number of decomposition stages (including initial decomposition temperatures), sublimation/volatilisation, total mass loss, and residual mass.

All analyses were carried out using measured using a PerkinElmer STA6000 TGA, sensitivity of 0.1 mg. The samples were heated from 30 °C (room temperature) up to a maximum of 500 °C, at a heating rate of 5−10 °C min^{-1}. Samples were sealed in aluminium crucibles that were pierced just before measurement to allow for mass loss, under aerobic (air) or anaerobic (N_2) atmospheres. This meant that there was an upper limit of 660 °C (melting point of the aluminium crucible), however it was decided to only test the thermal properties of the precursors up to a maximum of 500 °C, since decomposition at such a high temperature would render these precursors unfit for low temperature (<200 °C) depositions, regardless.

5.11.9 Potentiometric Titration Measurements

50.0 mg of CeNP'@MOF808 was suspended in a $NaNO_3$ solution (60 mL, 0.01 M). The suspension was sonicated for 20 minutes and subsequently allowed to equilibrate for 18

hours. The pH of the suspension was recorded using a Thermo scientific ORION STAR A214 pH/ISE meter equipped with an ORION Ross Ultra Combination pH probe. The pH probe was equilibrated at known pH values with buffers at pH values 4.01, 7.00 and 10.01. A solution of HCl (0.10 M) was added to the suspension dropwise, with stirring, in order to bring the pH to *ca.* 3.0. The suspension was then titrated first with 250 µL aliquots of NaOH (0.1 M) up to 1.5 mL, and then with aliquots of 125 µL up to 8.25 mL to improve the resolution of the data at the equivalence points. The titrations were performed at 25 °C. For determining the pK_a values, the equivalence points of the titration were calculated from the plots by taking the first derivative. The pK_a values were determined by calculating half the volume of base required to reach the equivalence point (either from the beginning of the titration or from the previous equivalence point), and reading off the pH after that quantity of base had been added.

5.12 References for Chapter 5

1. C. L. Daniels, D. L. Mendivelso-Perez, B. A. Rosales, D. You, S. Sahu, J. S. Jones, E. A. Smith, F. P. Gabbaï and J. Vela, *ACS omega*, 2019, **4**, 5197-5203.
2. J. An, Y. Beom Kim, J. Sun Park, J. Hyung Shim, T. M. Gür and F. B. Prinz, *Journal of Vacuum Science & Technology A: Vacuum, Surfaces, and Films*, 2012, **30**, 01A161.
3. C. E. Knapp, C. Dyer, N. P. Chadwick, R. Hazael and C. J. Carmalt, *Polyhedron*, 2018, **140**, 35-41.
4. M. A. Bhide, J. A. Manzi, C. E. Knapp and C. J. Carmalt, *Molecules*, 2021, **26**, 3165.
5. J. S. Matthews, O. O. Onakoya, T. S. Ouattara and R. J. Butcher, *Dalton Transactions*, 2006, 3806-3811.
6. X. Su, T. Kim, K. A. Abboud and L. McElwee-White, *Polyhedron*, 2019, **157**, 548-557.
7. Y.-H. Liu, Y.-C. Cheng, Y.-L. Tung, Y. Chi, Y.-L. Chen, C.-S. Liu, S.-M. Peng and G.-H. Lee, *Journal of Materials Chemistry*, 2003, **13**, 135-142.
8. E. Pousaneh, M. Korb, V. Dzhagan, M. Weber, J. Noll, M. Mehring, D. R. Zahn, S. E. Schulz and H. Lang, *Dalton Transactions*, 2018, **47**, 10002-10016.
9. S. Soltani-Ghoshkhaneh, M. Vakili, A. R. Berenji, V. Darugar and S. F. Tayyari, *Journal of molecular structure*, 2020, **1203**, 127440.
10. J. A. Manzi, C. E. Knapp, I. P. Parkin and C. J. Carmalt, *European Journal of Inorganic Chemistry*, 2015, **2015**, 3658-3665.
11. K. E. Schwarzhans, *Angewandte Chemie International Edition in English*, 1970, **9**, 946-953.
12. J. D. Satterlee, *Concepts in Magnetic Resonance*, 1990, **2**, 69-79.
13. M. Murakami, Y. Noda and K. Takegoshi, *Solid State Nuclear Magnetic Resonance*, 2019, **101**, 82-88.
14. S. L. Benjamin, Y.-P. Chang, M. Huggon, W. Levason and G. Reid, *Polyhedron*, 2015, **99**, 230-237.
15. G. S. Prakash, R. E. Williams, K. Wade, Á. Molnár and G. A. Olah, *Hypercarbon Chemistry*, John Wiley & Sons, 2011.
16. A. Amodio, G. Zanchin, F. De Stefano, A. Piovano, B. Palucci, V. Guiotto, R. Di Girolamo, G. Leone and E. Groppo, *Catalysts*, 2022, **12**, 119.

17. I. A. Saraireh, M. Altarawneh, J. Alhawarin, M. Salman, A. A. Abu-Yamin and R. Alasad, *Journal of Chemistry*, 2019, **2019**.
18. A. Bellusci, G. Barberio, A. Crispini, M. Ghedini, M. La Deda and D. Pucci, *Inorganic chemistry*, 2005, **44**, 1818-1825.
19. J. McGuire, B. Wilson, J. McAllister, H. N. Miras, C. Wilson, S. Sproules and J. H. Farnaby, *Dalton Transactions*, 2019, **48**, 5491-5495.
20. D. Barnum, *Journal of Inorganic and Nuclear Chemistry*, 1961, **21**, 221-237.
21. M. Jafari, M. Salehi, M. Kubicki, A. Arab and A. Khaleghian, *Inorganica Chimica Acta*, 2017, **462**, 329-335.
22. A. N. Swinburne, M. H. Langford Paden, T. L. Chan, S. Randall, F. Ortu, A. M. Kenwright and L. S. Natrajan, *Inorganics*, 2016, **4**, 27.
23. S. A. Patil, P. A. Medina, A. Antic, J. W. Ziller, J. K. Vohs and B. D. Fahlman, *Spectrochimica Acta Part A: Molecular and Biomolecular Spectroscopy*, 2015, **148**, 223-231.
24. T. Gietz and R. T. Boeré, *Inorganics*, 2017, **5**, 30.
25. Q. Xia, Y. Cui, D. Yuan, Y. Wang and Y. Yao, *Journal of Organometallic Chemistry*, 2017, **846**, 161-168.
26. R. T. Shannon and C. T. Prewitt, *Acta Crystallographica Section B: Structural Crystallography and Crystal Chemistry*, 1969, **25**, 925-946.
27. J. A. Belot, A. Wang, R. J. McNeely, L. Liable-Sands, A. L. Rheingold and T. J. Marks, *Chemical Vapor Deposition*, 1999, **5**, 65-69.
28. T. V. Balashova, A. P. Pushkarev, V. A. Ilichev, M. A. Lopatin, M. A. Katkova, E. V. Baranov, G. K. Fukin and M. N. Bochkarev, *Polyhedron*, 2013, **50**, 112-120.
29. P. B. Hitchcock, Q.-G. Huang, M. F. Lappert and X.-H. Wei, *Journal of Materials Chemistry*, 2004, **14**, 3266-3273.
30. E. M. Broderick, N. Guo, T. Wu, C. S. Vogel, C. Xu, J. Sutter, J. T. Miller, K. Meyer, T. Cantat and P. L. Diaconescu, *Chemical Communications*, 2011, **47**, 9897-9899.
31. S. Suh, J. Guan, L. A. Mîinea, J.-S. M. Lehn and D. M. Hoffman, *Chemistry of materials*, 2004, **16**, 1667-1673.
32. L. Guo, H. Arafune and N. Teramae, *Langmuir*, 2013, **29**, 4404-4412.
33. Y. K. Jung, J. I. Kim and J.-K. Lee, *Journal of the American Chemical Society*, 2010, **132**, 178-184.

34. M. D. Khan, M. A. Malik and N. Revaprasadu, *Coordination Chemistry Reviews*, 2019, **388**, 24-47.
35. M. J. Almond, C. E. Jenkins and D. A. Rice, *Journal of organometallic chemistry*, 1993, **443**, 137-143.
36. K. D. Pollard, H. A. Jenkins and R. J. Puddephatt, *Chemistry of materials*, 2000, **12**, 701-710.
37. H. C. Aspinall, J. Bacsa, A. C. Jones, J. S. Wrench, K. Black, P. R. Chalker, P. J. King, P. Marshall, M. Werner and H. O. Davies, *Inorganic Chemistry*, 2011, **50**, 11644-11652.
38. S. Morlens, L. Ortega, B. Rousseau, S. Phok, J. Deschanvre, P. Chaudouet and P. Odier, *Materials Science and Engineering: B*, 2003, **104**, 185-191.
39. M. Golalikhani, T. James, P. Van Buskirk, W. Noh, J. Lee, Z. Wang and J. F. Roeder, *Journal of Vacuum Science & Technology A: Vacuum, Surfaces, and Films*, 2018, **36**, 051502.
40. M. A. Bhide, C. J. Carmalt and C. E. Knapp, *ChemPlusChem*, 2022, **87**, e202100537.
41. J. Schlafer, D. Graf, G. Fornalczyk, A. Mettenborger and S. Mathur, *Inorganic Chemistry*, 2016, **55**, 5422-5429.
42. G. Sheldrick, *Acta Crystallogr., Sect. A: Found. Crystallogr*, 2008, **64**, 112-122.
43. G. Sheldrick, *Acta Crystallogr., Sect. A*, 2015, **71**, 3-8.
44. O. V. Dolomanov, L. J. Bourhis, R. J. Gildea, J. A. Howard and H. Puschmann, *Journal of applied crystallography*, 2009, **42**, 339-341.
45. R. Clark and J. Reid, *Acta Crystallographica Section A: Foundations of Crystallography*, 1995, **51**, 887-897.

6 Conclusions

6.1 Concluding Remarks

Chapter 2 introduced the novel, solution based methodology of reactive infiltration (RI) for synthesising cerium based nanocomposites. Reactive infiltration worked through the pairing of complementary precursor-host systems, specifically the highly basic CeN''_3 precursor and the protic MOF808 host structure. The precursor reacts spontaneously with the host structure, eliminating the protonated form of the ligand, yielding the composite structure: CeNP@MOF808. The complementary nature of the precursor-host system, coupled with the thermodynamic driving force of the protonated ligand elimination, allowed for RI to take place without any additional energetic interventions. Through a series of NMR scale reactions, the feasibility of RI was successfully confirmed and the methodology used to perform RI between CeN''_3 and MOF808 was optimised based on solvent polarity, activation temperature of MOF808 and reaction time. From this optimised methodology RI was scaled up and performed in triplicate to obtain significant quantities of the composite CeNP@MOF808. A control RI protocol was carried out in parallel to yield control MOF808 which would act as reference point in all subsequent characterisations. The CeNP@MOF808 composite was characterised using a number of spectroscopic and analytic techniques, including: SEM, EDX spectroscopy, ICP-OES, digestion NMR, elemental microanalysis, powder X-ray diffraction, potentiometric titrations, IR spectroscopy and N_2 adsorption isotherm studies. Through this combination of analyses it was found that the composite retained the macro- and microscopic structure of the MOF808 host following RI, with *ca.* 3 wt% loading of Ce within the CeNP@MOF808 composite. After successful characterisation of the CeNP@MOF808 composite the question arose as to whether post-synthetic modifications could be performed to alter the physio-electronic properties of the composite material.

Chapter 3 investigated the post-synthetic modification of CeNP@MOF808 *via* thermal and oxidative treatments. TGA profiles of CeNP@MOF808 were acquired under both aerobic (O_2) and anaerobic (N_2) atmospheres, revealing no shifts in decomposition events of the MOF808 host under anaerobic atmospheres. Under aerobic atmospheres there is a significant destabilising shift (*i.e.* towards lower temperatures), relative to MOF808, for the decomposition event corresponding to the combustion of BTC linkers. Guided by the TGA profiles of CeNP@MOF808 under both aerobic and anaerobic atmospheres, key post-

decomposition temperatures were identified as appropriate thermal treatment temperatures: 180, 230, 320, 550 and 650 °C. Characterisation of the thermally treated CeNP@MOF808 samples at these specified temperatures, though a combination of TGA, powder X-ray diffraction, IR spectroscopy, EDX spectroscopy, digestion NMR and elemental microanalysis, revealed three distinct materials over different temperature ranges. Between 180 °C and 230 °C, the CeNP@MOF808 composite retains all of the structural characteristics of the MOF808 host. Between 230 °C and 320 °C the CeNP@MOF808 composite loses the crystalline arrangement of the MOF808 host (*i.e.* becomes amorphous) and shows a significant shift, relative to CeNP@MOF808, in the elemental C%, H% and N%. Beyond 550 °C the CeNP@MOF808 composite forms a ZrO_2 crystalline structure, with IR absorption bands associated with ZrO_2. Oxidative post-synthetic modifications of the CeNP@MOF808 were successfully performed, whereby CeNP@MOF808 was exposed to H_2O_2 solution (6% and 0.6%) for several hours, forming $CeNP^{[oxd]}$@MOF808. The oxidised composite was characterised, through a combination of powder X-ray diffraction, Raman spectroscopy and EDX spectroscopy, revealing a loss of the crystallinity associated with the MOF808 host framework – although Raman shifts associated with vibrations MOF808 were still present in the Raman spectra of $CeNP^{[oxd]}$@MOF808, as were characteristic X-ray signals of Ce in the EDX spectra of $CeNP^{[oxd]}$@MOF808.

Being a redox active metal, it is important that any composite featuring Ce be characterised electronically as the Ce^{3+}:Ce^{4+} relative proportions can have a significant impact on any potential applications of the material – particularly catalysis. Through a combination of the XANES, XPS and EELS spectroscopies, the CeNP@MOF808 was characterised to have largely Ce^{3+} oxidation states present, *ca*. 75-100% Ce^{3+}. Differences in the exact proportion of Ce^{3+} determined via the different spectroscopic techniques was largely a reflection of the experimental conditions. XANES measurements reflected the oxidation states present in the bulk of the sample (75% Ce^{3+}), while XPS measurements reflected the oxidation states present at the surface of the sample particles (100% Ce^{3+}). EELS measurements indicated 100% Ce^{3+} states in the CeNP@MOF808 composite, however this was assumed to be a reflection of the high energy electron beam reducing and Ce^{4+} states to Ce^{3+} states. This highlighted the importance of adopting several, independent 'orthogonal' analyses when identifying and quantifying Ce oxidation states in a material. XANES studies of the CeNP@MOF808 composite

over time revealed that the Ce^{3+}:Ce^{4+} relative proportions were unchanged after several months of exposure to air. Electronic characterisation of the thermally treated CeNP@MOF808 samples, *via* XANES measurements, revealed Ce^{3+} proportions were statistically indistinguishable over the temperature range of 25 °C to 230 °C, however between 320 °C and 650 °C the Ce^{3+} proportions were reduced significantly, relative to CeNP@MOF808, to *ca.* 16%. This significant reduction in the Ce^{3+} proportions above 320 °C corresponds with the point at which the composite loses its crystalline arrangement. XANES and XPS measurements of $CeNP^{[oxd]}$@MOF808 revealed reductions in the Ce^{3+} proportions, relative to CeNP@MOF808, to *ca.* 10% (XANES) and *ca.* 40% (XPS) – with the higher proportion of Ce^{3+} states determined *via* XPS originating from the surface sensitivity of the technique. STEM images acquired for the CeNP@MOF808 composite failed to show any dot-like pattern in the MOF particles that would be indicative of the formation of discrete, well defined CeNP. HAADF images of CeNP@MOF808 showed the presence of light halos around the MOF particle surface, suggestive of a CeNP coating. EXAFS analysis of CeNP@MOF808, based on theoretical scatter pathways of possible CeNP speciations (CeO_2, Ce_2O_3, $Ce(OH)_3$) showed that the Ce–O bond distances in CeNP@MOF808 were 2.54 Å and fit best with $Ce(OH)_3$, with a residual bond error of 1% and R_{fac} value of 0.07. Therefore, in terms of speciation of the 'CeNP' component of the CeNP@MOF808 composite the data would suggest either a nanocoating of a cerium oxy-hydroxide species (*e.g.* $CeO_x(OH)_y$) on the MOF particle surface or a *ca.* 10 nm layer within the outer part of the MOF808 particle made up of small, ceria based clusters. Materials containing mixed Ce^{3+}/Ce^{4+} oxidation states often find use in the field of catalysis, specifically in the breakdown of small, organic molecules. It was of interest whether the CeNP@MOF808 composite would also exhibit catalytic activity towards these types of reaction.

Chapter 4 detailed the study of CeNP@MOF808 as a catalyst for the hydrolysis of nerve agent simulant DMNP. MOF808 has previously shown catalytic activity towards the hydrolysis of DMNP, however with the introduction of Ce^{3+}/Ce^{4+} oxidation states would the catalytic activity of the host be enhanced? A standard methodology for monitoring the hydrolysis of DMNP, *via* ^{31}P NMR, with samples CeNP@MOF808 and control MOF808 was successfully optimised. By having a standard methodology where various experimental parameters (*e.g.* catalyst loading weight, sonication time of catalyst suspension and time

delays before adding DMNP reagent) remained consistent between experiments, error could be minimised and statistical comparisons of catalysis rates for CeNP@MOF808 and control MOF808 made with greater confidence. Several catalytic hydrolysis reactions of DMNP were performed for both CeNP@MOF808 and control MOF808, monitored *via* ^{31}P NMR using the standard optimised methodology. Average $t_{1/2}$ values were computed for both CeNP@MOF808 ($t_{1/2}$ = 1.9 minutes) and control MOF808 ($t_{1/2}$ = 3.7 minutes). After removing outlier data points, T-tests were performed that indicated that the difference between the catalytic rates of CeNP@MOF808 and control MOF808 were statistically significant – indicating that the introduction of the mixed Ce^{3+}/Ce^{4+} states improved the catalytic activity of the MOF808 host towards the hydrolysis of DMNP.

Chapter 5, introduced the successful synthesis and characterisation of lanthanide β-ketoiminate complexes $Y\{OC(Me)CHC(Me)N^{i}Pr\}_3$ (**1**) and $Ce_2\{OC(Me)CHC(Me)N^{i}Pr\}_6$ (**2**). Compound **2** was subsequently investigated as a precursor for material synthesis *via* two different routes: thermal decomposition and RI. Thermal decomposition studies of **2**, through TGA, revealed relatively low, sharp decomposition temperature ranges under both aerobic and anaerobic conditions, 110–230 °C and 100–380 °C, respectively. Compound **2** does not undergo complete vaporisation, a prerequisite for any precursor molecule undergoing thermal decomposition, leaving behind a residue with mass loss consistent with CeO_2, under aerobic conditions. However, no reflections were observed in the powder X-ray diffractograms of the decomposition residue, after decomposition under both aerobic and anaerobic atmospheres, that were consistent with CeO_2, indicating an amorphous arrangement. Compound **2** proved to be a better precursor for the formation of CeO_2 *via* thermal decomposition when compared to CeN''_3, with **2** having a greater handling stability and a sharper, well defined decomposition temperature range. The composite formed *via* the RI of novel precursor molecule **2** with MOF808, CeNP'@MOF808, is similar in electro-physio properties to that formed by the RI of CeN''_3 with MOF808. The successful RI of **2** with MOF808 demonstrated the versatility of the RI process, with the RI methodology able to operate with precursors of significantly different architecture (*e.g.* CeN''_3 *vs.* **2**).

6.2 Future Work

This thesis has added to the scientific body of literature a novel methodology, known as reactive infiltration, for the synthesis of cerium based nanocomposites within a MOF host structure. Future investigations may aim to expand the materials investigated: either by adopting different lanthanide metals which may have desirable properties (e.g., Eu which exhibits luminescence or Dy which exhibits paramagnetism) or through the modification of the host framework (e.g., larger pore MOFs such as NU-1000). This would allow for a catalogue of composite materials to be established which would serve to better understand the link between the molecular precursor and the resultant physio-chemical properties of the parent composite material.

Studies of the catalytic behaviour of CeNP@MOF808 towards the hydrolysis of DMNP could be further expanded in a number of ways. One example could be including the use of cerium oxidic nanoparticles as a second control material, along with CeNP@MOF808 and control MOF808. This would establish if a cooperative effect occurs between the Ce-Zr metal centres of the CeNP@MOF808 composite. A second example could be the adoption of sophisticated spectroscopic techniques beyond ^{1}H NMR, this could include the use of X-ray absorption spectroscopy where the oxidation state/local structure of the Ce/Zr metals in the composite and/or oxidation state of the P centre of DMNP is followed in real-time.

Ce β-ketoiminate complexes were shown in this thesis to be promising examples of 'broad spectrum' precursor molecules whereby bulk materials could be assembled easily through various deposition techniques (e.g., thermal decomposition, reactive infiltration). This could be expanded again to include Ce β-ketoiminate complexes of different ligand architectures (i.e., various steric side groups), specifically the relationship between the Ce – O bond lengths in the precursor molecule vs. the Ce – O bond lengths in the deposited material would be of great interest given the relationship between bond dimensions of a material and its resultant properties.

7 Appendix

7.1 Crystallographic Data for **1**

Crystal data

$C_{24}H_{42}N_3O_3Y$	$Z = 4$
$M_r = 509.51$	$F(000) = 1080$
Triclinic, $P^{-}1$	$D_x = 1.286$ Mg m^{-3}
$a = 10.1741$ (3) Å	Mo Ka radiation, l = 0.71073 Å
$b = 10.8287$ (2) Å	Cell parameters from 28288 reflections
$c = 25.1190$ (4) Å	q = 1.6–31.2°
a = 79.405 (1)°	m = 2.24 mm^{-1}
b = 84.847 (2)°	$T = 100$ K
g = 75.485 (2)°	Plate, light yellow
$V = 2630.63$ (10) Å^3	0.38 × 0.13 × 0.08 mm

Data collection

XtaLAB AFC12 (RCD3): Kappa single diffractometer	12043 independent reflections
Radiation source: Rotating-anode X-ray tube, Rigaku (Mo) X-ray Source	9904 reflections with $I > 2s(I)$
Mirror monochromator	$R_{int} = 0.050$
Detector resolution: 10.0000 pixels mm^{-1}	$q_{max} = 27.5°$, $q_{min} = 1.7°$
w scans	h = -12®13
Absorption correction: multi-scan *CrysAlis PRO* 1.171.40.39a (Rigaku Oxford Diffraction, 2019) Empirical absorption correction using spherical harmonics, implemented in SCALE3 ABSPACK scaling algorithm.	k = -14®14
$T_{min} = 0.494$, $T_{max} = 1.000$	l = -32®32
60204 measured reflections	

Refinement

Refinement on F^2	Primary atom site location: dual
Least-squares matrix: full	Hydrogen site location: inferred from neighbouring sites
$R[F^2 > 2s(F^2)] = 0.044$	H-atom parameters constrained
$wR(F^2) = 0.076$	$w = 1/[s^2(F_o^2) + (0.0096P)^2 + 3.6366P]$ where $P = (F_o^2 + 2F_c^2)/3$

S = 1.13	$(D/s)_{max}$ = 0.001
12043 reflections	$D\rho_{max}$ = 0.49 e Å^{-3}
682 parameters	$D\rho_{min}$ = -1.03 e Å^{-3}
36 restraints	

Special details

Geometry. All esds (except the esd in the dihedral angle between two l.s. planes) are estimated using the full covariance matrix. The cell esds are taken into account individually in the estimation of esds in distances, angles and torsion angles; correlations between esds in cell parameters are only used when they are defined by crystal symmetry. An approximate (isotropic) treatment of cell esds is used for estimating esds involving l.s. planes.

*Fractional atomic coordinates and isotropic or equivalent isotropic displacement parameters (Å^2) for Compound **1***

	x	*y*	*z*	U_{iso}*/U_{eq}	Occ. (<1)
Y1	0.66389 (2)	0.36599 (2)	0.14305 (2)	0.01181 (6)	
O1	0.82931 (16)	0.46552 (15)	0.12186 (7)	0.0171 (4)	
O2	0.49472 (16)	0.29080 (15)	0.12368 (7)	0.0182 (4)	
O3	0.53454 (17)	0.42954 (16)	0.21090 (7)	0.0192 (4)	
N1	0.83122 (19)	0.25907 (18)	0.21231 (8)	0.0140 (4)	
N2	0.77101 (18)	0.19163 (18)	0.09044 (8)	0.0127 (4)	
N3	0.51727 (19)	0.57101 (18)	0.10064 (8)	0.0137 (4)	
C1	1.0331 (3)	0.5346 (3)	0.09805 (11)	0.0257 (6)	
H1A	1.034802	0.517958	0.060910	0.039*	
H1B	1.126318	0.514529	0.110002	0.039*	
H1C	0.989988	0.625876	0.099112	0.039*	
C2	0.9538 (2)	0.4510 (2)	0.13502 (10)	0.0166 (5)	
C3	1.0126 (2)	0.3659 (2)	0.17816 (10)	0.0171 (5)	
H3	1.103480	0.366000	0.184020	0.020*	
C4	0.9529 (2)	0.2756 (2)	0.21601 (10)	0.0167 (5)	
C5	1.0473 (3)	0.1980 (3)	0.26027 (12)	0.0295 (6)	
H5A	1.004097	0.212420	0.295801	0.044*	
H5B	1.132780	0.225663	0.255524	0.044*	
H5C	1.065773	0.105741	0.258031	0.044*	
C6	0.7845 (2)	0.1602 (2)	0.25388 (10)	0.0178 (5)	
H6	0.864335	0.086615	0.264263	0.021*	
C7	0.6802 (3)	0.1093 (2)	0.22977 (10)	0.0206 (5)	
H7A	0.596537	0.177647	0.223929	0.031*	

H7B	0.660287	0.034816	0.254815	0.031*	
H7C	0.716824	0.082860	0.195077	0.031*	
C8	0.7231 (3)	0.2161 (3)	0.30457 (10)	0.0266 (6)	
H8A	0.790639	0.249168	0.319535	0.040*	
H8B	0.696260	0.148213	0.331613	0.040*	
H8C	0.643158	0.286782	0.295104	0.040*	
C9	0.3303 (2)	0.1849 (2)	0.10651 (11)	0.0197 (5)	
H9A	0.302933	0.165226	0.144936	0.030*	
H9B	0.324578	0.114060	0.088178	0.030*	
H9C	0.269790	0.265440	0.089738	0.030*	
C10	0.4744 (2)	0.2000 (2)	0.10141 (9)	0.0148 (5)	
C11	0.5734 (2)	0.1197 (2)	0.07486 (10)	0.0162 (5)	
H11	0.544518	0.059830	0.058102	0.019*	
C12	0.7158 (2)	0.1156 (2)	0.06942 (9)	0.0144 (5)	
C13	0.7954 (3)	0.0107 (2)	0.03849 (11)	0.0219 (6)	
H13A	0.879124	0.033574	0.022188	0.033*	
H13B	0.740211	0.002528	0.009875	0.033*	
H13C	0.818326	-0.071801	0.063409	0.033*	
C14	0.9214 (2)	0.1768 (2)	0.08778 (10)	0.0166 (5)	
H14	0.935582	0.234262	0.112595	0.020*	
C15	0.9753 (2)	0.2329 (2)	0.03244 (10)	0.0211 (5)	
H15A	0.963325	0.182442	0.005385	0.032*	
H15B	1.072109	0.229285	0.034082	0.032*	
H15C	0.925209	0.323064	0.022272	0.032*	
C16	1.0044 (3)	0.0425 (2)	0.11126 (11)	0.0246 (6)	
H16A	0.952799	0.003985	0.141873	0.037*	
H16B	1.090236	0.049910	0.123724	0.037*	
H16C	1.023463	-0.012550	0.083230	0.037*	
C17	0.3211 (4)	0.4213 (5)	0.2577 (2)	0.0459 (12)	0.75
H17A	0.333720	0.329070	0.256563	0.069*	0.75
H17B	0.224694	0.464966	0.254218	0.069*	0.75
H17C	0.351042	0.431448	0.292350	0.069*	0.75
C17A	0.3494 (12)	0.4655 (11)	0.2710 (4)	0.018 (3)*	0.25
H17D	0.356824	0.373681	0.285366	0.027*	0.25
H17E	0.253870	0.512881	0.272926	0.027*	0.25
H17F	0.402645	0.500403	0.292606	0.027*	0.25
C18	0.4043 (3)	0.4808 (3)	0.21140 (11)	0.0274 (6)	
C19	0.3392 (3)	0.5702 (2)	0.17088 (11)	0.0237 (6)	

H19	0.244458	0.603199	0.177306	0.028*	
C20	0.3958 (2)	0.6207 (2)	0.11981 (10)	0.0169 (5)	
C21	0.3000 (3)	0.7364 (2)	0.08827 (11)	0.0244 (6)	
H21A	0.345591	0.807604	0.077823	0.037*	
H21B	0.218289	0.764152	0.111009	0.037*	
H21C	0.274412	0.712222	0.055633	0.037*	
C22	0.5619 (2)	0.6323 (2)	0.04669 (10)	0.0160 (5)	
H22	0.479906	0.674842	0.025082	0.019*	
C23	0.6533 (3)	0.5288 (2)	0.01718 (10)	0.0196 (5)	
H23A	0.742969	0.501122	0.032819	0.029*	
H23B	0.662967	0.564414	-0.021365	0.029*	
H23C	0.612632	0.454409	0.021140	0.029*	
C24	0.6361 (3)	0.7354 (2)	0.05253 (10)	0.0211 (5)	
H24A	0.575364	0.801247	0.071179	0.032*	
H24B	0.663656	0.775957	0.016510	0.032*	
H24C	0.716848	0.694893	0.073642	0.032*	
Y2	0.71450 (3)	0.75955 (2)	0.35445 (2)	0.02548 (7)	
O4	0.55595 (17)	0.93518 (19)	0.35888 (7)	0.0258 (4)	
O5	0.87925 (18)	0.8075 (2)	0.30015 (8)	0.0330 (5)	
O6	0.8927 (4)	0.5857 (4)	0.38060 (17)	0.0244 (8)	0.5
O6A	0.5291 (5)	0.6746 (4)	0.39085 (16)	0.0256 (9)	0.5
N4	0.5983 (2)	0.78987 (19)	0.26987 (8)	0.0181 (4)	
N5	0.8388 (2)	0.8528 (2)	0.41098 (9)	0.0225 (5)	
N6	0.6087 (4)	0.5908 (4)	0.39320 (16)	0.0174 (9)	0.5
N6A	0.8100 (4)	0.5434 (4)	0.39957 (17)	0.0186 (9)	0.5
C25	0.3495 (3)	1.0923 (3)	0.36366 (11)	0.0292 (6)	
H25A	0.329961	1.055745	0.401361	0.044*	
H25B	0.264382	1.125233	0.344716	0.044*	
H25C	0.393817	1.163191	0.362927	0.044*	
C26	0.4422 (3)	0.9887 (2)	0.33598 (10)	0.0204 (5)	
C27	0.4056 (3)	0.9600 (2)	0.28956 (10)	0.0218 (5)	
H27	0.317900	1.005637	0.277632	0.026*	
C28	0.4828 (3)	0.8698 (2)	0.25650 (10)	0.0200 (5)	
C29	0.4192 (3)	0.8761 (3)	0.20324 (11)	0.0279 (6)	
H29A	0.478859	0.903449	0.172929	0.042*	
H29B	0.330663	0.938506	0.201793	0.042*	
H29C	0.406953	0.790490	0.200695	0.042*	
C30	0.6685 (3)	0.7026 (2)	0.23122 (10)	0.0235 (6)	

H30	0.598491	0.679269	0.212050	0.028*	
C31	0.7533 (3)	0.5797 (3)	0.26316 (12)	0.0337 (7)	
H31A	0.829704	0.599718	0.278183	0.051*	
H31B	0.788139	0.515885	0.239107	0.051*	
H31C	0.696750	0.544309	0.292782	0.051*	
C32	0.7576 (3)	0.7689 (3)	0.18925 (11)	0.0262 (6)	
H32A	0.701001	0.846756	0.168637	0.039*	
H32B	0.802993	0.709510	0.164476	0.039*	
H32C	0.826063	0.792996	0.207649	0.039*	
C33	1.0955 (3)	0.8077 (3)	0.25770 (12)	0.0315 (7)	
H33A	1.103186	0.722312	0.248139	0.047*	
H33B	1.184855	0.814438	0.266754	0.047*	
H33C	1.062306	0.874953	0.226870	0.047*	
C34	0.9980 (3)	0.8250 (2)	0.30548 (11)	0.0239 (6)	
C35	1.0366 (3)	0.8584 (3)	0.35044 (12)	0.0290 (6)	
H35	1.126299	0.870534	0.348793	0.035*	
C36	0.9584 (3)	0.8772 (3)	0.39973 (12)	0.0310 (7)	
C37	1.0296 (4)	0.9271 (4)	0.43921 (15)	0.0582 (11)	
H37A	0.968698	1.004346	0.450546	0.087*	
H37B	1.112379	0.949140	0.421396	0.087*	
H37C	1.053447	0.859970	0.471061	0.087*	
C38	0.7700 (3)	0.8759 (3)	0.46440 (11)	0.0263 (6)	
H38	0.840833	0.859252	0.491677	0.032*	
C39	0.6878 (3)	1.0157 (3)	0.46085 (11)	0.0321 (7)	
H39A	0.748671	1.074245	0.450255	0.048*	
H39B	0.643104	1.029051	0.496260	0.048*	
H39C	0.618952	1.033732	0.433765	0.048*	
C40	0.6789 (3)	0.7835 (3)	0.48247 (12)	0.0377 (7)	
H40A	0.603146	0.805004	0.458247	0.057*	
H40B	0.643256	0.790861	0.519615	0.057*	
H40C	0.731246	0.694672	0.481263	0.057*	
C41	1.0493 (7)	0.3848 (6)	0.4028 (3)	0.0359 (15)	0.5
H41A	1.087693	0.382825	0.365633	0.054*	0.5
H41B	1.049525	0.296507	0.420923	0.054*	0.5
H41C	1.104068	0.422016	0.422652	0.054*	0.5
C41A	0.3640 (6)	0.5517 (6)	0.4142 (3)	0.0369 (15)	0.5
H41D	0.322423	0.589310	0.446100	0.055*	0.5
H41E	0.360200	0.460688	0.419517	0.055*	0.5

H41F	0.314258	0.599183	0.382076	0.055*	0.5
C42	0.9056 (6)	0.4662 (5)	0.4013 (2)	0.0229 (11)	0.5
C42A	0.5103 (6)	0.5609 (6)	0.4062 (2)	0.0228 (11)	0.5
C43	0.8002 (11)	0.4123 (13)	0.4193 (7)	0.027 (2)	0.5
H43	0.823586	0.324579	0.436708	0.032*	0.5
C43A	0.6128 (10)	0.4520 (10)	0.4177 (4)	0.023 (2)	0.5
H43A	0.585486	0.372777	0.427262	0.028*	0.5
C44	0.6579 (10)	0.4702 (10)	0.4156 (4)	0.0216 (19)	0.5
C44A	0.7546 (11)	0.4422 (11)	0.4172 (5)	0.018 (2)	0.5
C45	0.5677 (7)	0.3782 (6)	0.4393 (3)	0.0441 (17)	0.5
H45A	0.477596	0.428344	0.449524	0.066*	0.5
H45B	0.608727	0.320626	0.471516	0.066*	0.5
H45C	0.558960	0.326496	0.412251	0.066*	0.5
C45A	0.8369 (6)	0.3085 (5)	0.4383 (3)	0.0343 (14)	0.5
H45D	0.850922	0.255073	0.409849	0.051*	0.5
H45E	0.788108	0.269440	0.469763	0.051*	0.5
H45F	0.925097	0.314130	0.449152	0.051*	0.5
C46	0.4616 (6)	0.6473 (6)	0.3844 (2)	0.0218 (12)	0.5
H46	0.457319	0.735321	0.362692	0.026*	0.5
C46A	0.9566 (6)	0.5325 (6)	0.4019 (2)	0.0250 (12)	0.5
H46A	0.969482	0.619154	0.383687	0.030*	0.5
C47	0.3750 (6)	0.6724 (6)	0.4368 (2)	0.0312 (13)	0.5
H47A	0.381729	0.590572	0.461954	0.047*	0.5
H47B	0.279851	0.710195	0.427949	0.047*	0.5
H47C	0.408409	0.732494	0.453844	0.047*	0.5
C47A	1.0051 (6)	0.5175 (6)	0.4591 (2)	0.0377 (15)	0.5
H47D	0.946428	0.584314	0.477863	0.057*	0.5
H47E	1.098917	0.526794	0.456924	0.057*	0.5
H47F	1.001166	0.431801	0.479170	0.057*	0.5
C48	0.3985 (6)	0.5790 (6)	0.3493 (2)	0.0339 (14)	0.5
H48A	0.459194	0.561618	0.317597	0.051*	0.5
H48B	0.310694	0.634308	0.337342	0.051*	0.5
H48C	0.384903	0.497210	0.370402	0.051*	0.5
C48A	1.0502 (6)	0.4365 (7)	0.3684 (3)	0.0392 (16)	0.5
H48D	1.057998	0.347945	0.387855	0.059*	0.5
H48E	1.140412	0.454910	0.363018	0.059*	0.5
H48F	1.011601	0.445600	0.333153	0.059*	0.5

*Atomic displacement parameters (Å^2) for Compound **1***

	U^{11}	U^{22}	U^{33}	U^{12}	U^{13}	U^{23}
Y1	0.01095 (11)	0.01066 (11)	0.01380 (11)	-0.00208 (8)	-0.00003 (9)	-0.00291 (9)
O1	0.0114 (8)	0.0178 (8)	0.0215 (9)	-0.0049 (7)	-0.0025 (7)	0.0010 (7)
O2	0.0113 (8)	0.0162 (8)	0.0282 (10)	-0.0022 (7)	0.0019 (7)	-0.0094 (7)
O3	0.0176 (9)	0.0201 (9)	0.0171 (9)	-0.0002 (7)	0.0022 (7)	-0.0037 (7)
N1	0.0134 (10)	0.0117 (9)	0.0163 (10)	-0.0028 (8)	0.0002 (8)	-0.0015 (8)
N2	0.0091 (9)	0.0139 (9)	0.0137 (10)	-0.0015 (8)	0.0021 (8)	-0.0020 (8)
N3	0.0140 (10)	0.0112 (9)	0.0161 (10)	-0.0030 (8)	-0.0010 (8)	-0.0026 (8)
C1	0.0183 (13)	0.0291 (14)	0.0287 (15)	-0.0105 (11)	0.0024 (11)	0.0029 (12)
C2	0.0140 (12)	0.0169 (12)	0.0204 (13)	-0.0056 (10)	0.0031 (10)	-0.0060 (10)
C3	0.0105 (11)	0.0194 (12)	0.0219 (13)	-0.0039 (10)	-0.0005 (10)	-0.0047 (10)
C4	0.0141 (12)	0.0143 (11)	0.0205 (13)	0.0004 (9)	-0.0030 (10)	-0.0042 (10)
C5	0.0218 (14)	0.0307 (15)	0.0342 (16)	-0.0068 (12)	-0.0114 (12)	0.0053 (12)
C6	0.0178 (13)	0.0144 (12)	0.0188 (12)	-0.0039 (10)	-0.0023 (10)	0.0036 (10)
C7	0.0236 (14)	0.0163 (12)	0.0223 (13)	-0.0083 (10)	0.0000 (11)	0.0003 (10)
C8	0.0371 (16)	0.0281 (14)	0.0168 (13)	-0.0148 (12)	0.0006 (12)	-0.0003 (11)
C9	0.0136 (12)	0.0222 (13)	0.0248 (14)	-0.0070 (10)	0.0012 (10)	-0.0046 (11)
C10	0.0156 (12)	0.0135 (11)	0.0147 (12)	-0.0050 (9)	-0.0049 (9)	0.0032 (9)
C11	0.0156 (12)	0.0160 (12)	0.0201 (13)	-0.0076 (10)	-0.0005 (10)	-0.0054 (10)
C12	0.0163 (12)	0.0114 (11)	0.0128 (11)	-0.0002 (9)	0.0024 (9)	-0.0011 (9)
C13	0.0192 (13)	0.0190 (13)	0.0289 (14)	-0.0047 (10)	0.0061 (11)	-0.0111 (11)
C14	0.0116 (12)	0.0177 (12)	0.0199 (13)	-0.0016 (9)	0.0018 (10)	-0.0052 (10)
C15	0.0150 (12)	0.0215 (13)	0.0264 (14)	-0.0048 (10)	0.0048 (11)	-0.0050 (11)
C16	0.0138 (13)	0.0259 (14)	0.0288 (15)	0.0002 (11)	-0.0002 (11)	0.0013 (11)
C17	0.024 (2)	0.059 (3)	0.042 (3)	-0.001 (2)	0.012 (2)	0.007 (2)
C18	0.0245 (15)	0.0251 (14)	0.0265 (15)	-0.0003 (11)	0.0111 (12)	-0.0028 (11)
C19	0.0133 (12)	0.0239 (13)	0.0301 (15)	0.0008 (10)	0.0052 (11)	-0.0053 (11)
C20	0.0156 (12)	0.0113 (11)	0.0250 (13)	-0.0020 (9)	-0.0031 (10)	-0.0066 (10)
C21	0.0196 (13)	0.0194 (13)	0.0299 (15)	0.0025 (11)	-0.0028 (11)	-0.0024 (11)
C22	0.0183 (12)	0.0134 (11)	0.0161 (12)	-0.0042 (10)	-0.0045 (10)	0.0004 (9)
C23	0.0213 (13)	0.0206 (13)	0.0161 (12)	-0.0033 (10)	-0.0028 (10)	-0.0027 (10)
C24	0.0282 (14)	0.0175 (12)	0.0197 (13)	-0.0101 (11)	-0.0034 (11)	-0.0005 (10)
Y2	0.04834 (18)	0.01259 (12)	0.01658 (13)	-0.00898 (12)	-0.00860 (12)	0.00058 (10)
O4	0.0159 (9)	0.0412 (11)	0.0208 (10)	-0.0028 (8)	-0.0026 (8)	-0.0112 (8)
O5	0.0178 (10)	0.0542 (13)	0.0306 (11)	-0.0019 (9)	-0.0037 (8)	-0.0240 (10)
O6	0.018 (2)	0.0178 (19)	0.034 (2)	0.0015 (17)	-0.0037 (19)	-0.0017 (17)

O6A	0.020 (2)	0.024 (2)	0.032 (2)	-0.007 (2)	0.0032 (18)	-0.0015 (17)
N4	0.0254 (12)	0.0163 (10)	0.0159 (10)	-0.0116 (9)	-0.0003 (9)	-0.0022 (8)
N5	0.0262 (12)	0.0204 (11)	0.0194 (11)	0.0027 (9)	-0.0064 (9)	-0.0082 (9)
N6	0.019 (2)	0.016 (2)	0.017 (2)	-0.004 (2)	0.0017 (18)	-0.0023 (17)
N6A	0.017 (2)	0.018 (2)	0.021 (2)	-0.005 (2)	-0.0039 (18)	0.0001 (17)
C25	0.0268 (15)	0.0302 (15)	0.0278 (15)	0.0005 (12)	-0.0048 (12)	-0.0059 (12)
C26	0.0183 (13)	0.0222 (13)	0.0207 (13)	-0.0088 (10)	0.0024 (10)	0.0004 (10)
C27	0.0196 (13)	0.0212 (13)	0.0246 (14)	-0.0063 (11)	-0.0049 (11)	0.0002 (11)
C28	0.0261 (14)	0.0215 (13)	0.0172 (13)	-0.0166 (11)	-0.0016 (11)	-0.0001 (10)
C29	0.0307 (15)	0.0355 (16)	0.0219 (14)	-0.0159 (13)	-0.0056 (12)	-0.0032 (12)
C30	0.0350 (15)	0.0197 (13)	0.0198 (13)	-0.0085 (11)	-0.0043 (11)	-0.0087 (10)
C31	0.057 (2)	0.0170 (13)	0.0287 (16)	-0.0075 (13)	-0.0080 (14)	-0.0074 (12)
C32	0.0321 (15)	0.0267 (14)	0.0207 (14)	-0.0050 (12)	-0.0017 (12)	-0.0090 (11)
C33	0.0269 (15)	0.0368 (16)	0.0283 (16)	-0.0033 (13)	0.0007 (12)	-0.0059 (13)
C34	0.0192 (14)	0.0223 (13)	0.0271 (14)	0.0046 (11)	-0.0038 (11)	-0.0083 (11)
C35	0.0195 (14)	0.0352 (16)	0.0344 (16)	-0.0039 (12)	-0.0055 (12)	-0.0132 (13)
C36	0.0255 (15)	0.0356 (16)	0.0331 (16)	0.0016 (13)	-0.0114 (13)	-0.0161 (13)
C37	0.040 (2)	0.101 (3)	0.050 (2)	-0.019 (2)	-0.0077 (17)	-0.047 (2)
C38	0.0321 (15)	0.0266 (14)	0.0187 (13)	0.0019 (12)	-0.0065 (12)	-0.0096 (11)
C39	0.0429 (18)	0.0283 (15)	0.0227 (15)	0.0001 (13)	0.0016 (13)	-0.0115 (12)
C40	0.063 (2)	0.0301 (16)	0.0201 (15)	-0.0110 (15)	-0.0035 (14)	-0.0033 (12)
C41	0.035 (4)	0.028 (3)	0.037 (4)	0.003 (3)	-0.003 (3)	-0.002 (3)
C41A	0.033 (3)	0.046 (4)	0.037 (4)	-0.025 (3)	0.000 (3)	0.001 (3)
C42	0.025 (3)	0.018 (3)	0.021 (3)	0.005 (3)	-0.005 (2)	-0.006 (2)
C42A	0.029 (3)	0.030 (3)	0.014 (3)	-0.017 (3)	-0.001 (2)	-0.001 (2)
C43	0.017 (6)	0.027 (6)	0.031 (4)	0.002 (4)	-0.003 (5)	0.001 (4)
C43A	0.020 (5)	0.024 (4)	0.029 (3)	-0.018 (3)	-0.001 (4)	0.006 (3)
C44	0.018 (6)	0.018 (4)	0.031 (3)	-0.013 (4)	0.006 (5)	-0.001 (3)
C44A	0.015 (6)	0.021 (5)	0.021 (3)	-0.009 (4)	-0.001 (5)	0.000 (4)
C45	0.043 (4)	0.020 (3)	0.063 (5)	-0.010 (3)	0.008 (3)	0.008 (3)
C45A	0.041 (4)	0.018 (3)	0.040 (4)	-0.007 (3)	-0.007 (3)	0.008 (3)
C46	0.022 (3)	0.023 (3)	0.021 (3)	-0.007 (3)	-0.003 (2)	-0.002 (2)
C46A	0.021 (3)	0.022 (3)	0.030 (3)	-0.003 (3)	0.001 (3)	-0.003 (3)
C47	0.023 (3)	0.036 (3)	0.033 (3)	-0.005 (2)	0.007 (2)	-0.009 (3)
C47A	0.029 (3)	0.043 (4)	0.039 (4)	-0.002 (3)	-0.008 (3)	-0.005 (3)
C48	0.031 (3)	0.040 (3)	0.036 (3)	-0.016 (3)	-0.003 (3)	-0.009 (3)
C48A	0.023 (3)	0.044 (4)	0.045 (4)	0.002 (3)	0.005 (3)	-0.012 (3)

*Geometric parameters (Å, º) for Compound **1***

Y1—O1	2.1943 (16)	Y2—N5	2.475 (2)
Y1—O2	2.2046 (16)	Y2—N6	2.364 (4)
Y1—O3	2.1644 (16)	Y2—N6A	2.406 (4)
Y1—N1	2.4634 (19)	O4—C26	1.291 (3)
Y1—N2	2.4751 (19)	O5—C34	1.292 (3)
Y1—N3	2.4585 (19)	O6—C42	1.281 (7)
O1—C2	1.301 (3)	O6A—C42A	1.277 (7)
O2—C10	1.284 (3)	N4—C28	1.303 (3)
O3—C18	1.302 (3)	N4—C30	1.490 (3)
N1—C4	1.308 (3)	N5—C36	1.305 (4)
N1—C6	1.489 (3)	N5—C38	1.490 (3)
N2—C12	1.311 (3)	N6—C44	1.313 (12)
N2—C14	1.494 (3)	N6—C46	1.489 (7)
N3—C20	1.305 (3)	N6A—C44A	1.342 (13)
N3—C22	1.481 (3)	N6A—C46A	1.472 (7)
C1—C2	1.502 (3)	C25—C26	1.506 (4)
C2—C3	1.362 (3)	C26—C27	1.365 (4)
C3—C4	1.443 (3)	C27—C28	1.435 (4)
C4—C5	1.519 (3)	C28—C29	1.521 (3)
C6—C7	1.525 (3)	C30—C31	1.522 (4)
C6—C8	1.526 (4)	C30—C32	1.525 (4)
C9—C10	1.507 (3)	C33—C34	1.495 (4)
C10—C11	1.367 (3)	C34—C35	1.364 (4)
C11—C12	1.433 (3)	C35—C36	1.429 (4)
C12—C13	1.517 (3)	C36—C37	1.524 (4)
C14—C15	1.524 (3)	C38—C39	1.526 (4)
C14—C16	1.529 (3)	C38—C40	1.513 (4)
C17—C18	1.519 (5)	C41—C42	1.506 (8)
C17A—C18	1.545 (12)	C41A—C42A	1.510 (8)
C18—C19	1.360 (4)	C42—C43	1.351 (17)
C19—C20	1.430 (4)	C42A—C43A	1.369 (13)
C20—C21	1.520 (3)	C43—C44	1.430 (10)
C22—C23	1.526 (3)	C43A—C44A	1.419 (11)
C22—C24	1.529 (3)	C44—C45	1.527 (9)
Y2—O4	2.1770 (18)	C44A—C45A	1.506 (10)
Y2—O5	2.169 (2)	C46—C47	1.545 (8)
Y2—O6	2.305 (4)	C46—C48	1.521 (8)

Y2—O6A	2.343 (4)	C46A—C47A	1.527 (8)
Y2—N4	2.453 (2)	C46A—C48A	1.542 (8)
O1—Y1—O2	153.56 (6)	O5—Y2—N6	144.18 (12)
O1—Y1—N1	76.06 (6)	O5—Y2—N6A	103.76 (12)
O1—Y1—N2	93.47 (6)	O6—Y2—N4	123.13 (11)
O1—Y1—N3	85.06 (6)	O6—Y2—N5	78.65 (11)
O2—Y1—N1	125.86 (6)	O6—Y2—N6	75.72 (14)
O2—Y1—N2	74.92 (6)	O6A—Y2—N4	82.21 (12)
O2—Y1—N3	81.35 (6)	O6A—Y2—N5	121.06 (12)
O3—Y1—O1	112.99 (6)	O6A—Y2—N6A	74.13 (15)
O3—Y1—O2	86.10 (6)	N4—Y2—N5	146.72 (7)
O3—Y1—N1	84.45 (6)	N6—Y2—N4	90.68 (11)
O3—Y1—N2	149.39 (6)	N6—Y2—N5	120.83 (11)
O3—Y1—N3	77.58 (6)	N6A—Y2—N4	119.15 (11)
N1—Y1—N2	87.49 (6)	N6A—Y2—N5	91.63 (11)
N3—Y1—N1	146.36 (6)	C26—O4—Y2	135.42 (17)
N3—Y1—N2	121.66 (6)	C34—O5—Y2	136.02 (18)
C2—O1—Y1	138.27 (15)	C42—O6—Y2	135.9 (4)
C10—O2—Y1	139.81 (15)	C42A—O6A—Y2	135.1 (4)
C18—O3—Y1	127.28 (17)	C28—N4—Y2	127.26 (17)
C4—N1—Y1	128.92 (16)	C28—N4—C30	118.1 (2)
C4—N1—C6	117.79 (19)	C30—N4—Y2	114.63 (15)
C6—N1—Y1	113.26 (14)	C36—N5—Y2	126.82 (18)
C12—N2—Y1	129.87 (15)	C36—N5—C38	118.2 (2)
C12—N2—C14	121.70 (19)	C38—N5—Y2	114.89 (16)
C14—N2—Y1	108.35 (13)	C44—N6—Y2	132.2 (5)
C20—N3—Y1	123.72 (16)	C44—N6—C46	123.3 (6)
C20—N3—C22	117.96 (19)	C46—N6—Y2	104.4 (3)
C22—N3—Y1	117.82 (14)	C44A—N6A—Y2	131.6 (5)
O1—C2—C1	115.1 (2)	C44A—N6A—C46A	121.9 (6)
O1—C2—C3	124.3 (2)	C46A—N6A—Y2	106.3 (4)
C3—C2—C1	120.6 (2)	O4—C26—C25	114.7 (2)
C2—C3—C4	127.6 (2)	O4—C26—C27	124.8 (2)
N1—C4—C3	124.0 (2)	C27—C26—C25	120.5 (2)
N1—C4—C5	122.9 (2)	C26—C27—C28	128.2 (2)
C3—C4—C5	113.2 (2)	N4—C28—C27	123.8 (2)
N1—C6—C7	109.33 (19)	N4—C28—C29	122.1 (2)

N1—C6—C8	111.32 (19)	C27—C28—C29	114.1 (2)
C7—C6—C8	110.1 (2)	N4—C30—C31	108.7 (2)
O2—C10—C9	115.3 (2)	N4—C30—C32	111.0 (2)
O2—C10—C11	124.3 (2)	C31—C30—C32	110.7 (2)
C11—C10—C9	120.4 (2)	O5—C34—C33	115.4 (2)
C10—C11—C12	127.4 (2)	O5—C34—C35	124.5 (3)
N2—C12—C11	123.4 (2)	C35—C34—C33	120.1 (3)
N2—C12—C13	124.0 (2)	C34—C35—C36	127.8 (3)
C11—C12—C13	112.5 (2)	N5—C36—C35	124.3 (2)
N2—C14—C15	112.89 (19)	N5—C36—C37	122.4 (3)
N2—C14—C16	115.15 (19)	C35—C36—C37	113.3 (3)
C15—C14—C16	114.1 (2)	N5—C38—C39	110.6 (2)
O3—C18—C17	115.6 (3)	N5—C38—C40	109.7 (2)
O3—C18—C17A	107.9 (5)	C40—C38—C39	110.5 (2)
O3—C18—C19	124.7 (2)	O6—C42—C41	115.3 (6)
C19—C18—C17	119.3 (3)	O6—C42—C43	124.1 (6)
C19—C18—C17A	123.6 (5)	C43—C42—C41	120.6 (6)
C18—C19—C20	127.9 (2)	O6A—C42A—C41A	115.9 (6)
N3—C20—C19	123.8 (2)	O6A—C42A—C43A	124.1 (6)
N3—C20—C21	122.2 (2)	C43A—C42A—C41A	119.9 (5)
C19—C20—C21	114.0 (2)	C42—C43—C44	128.4 (11)
N3—C22—C23	109.50 (18)	C42A—C43A—C44A	128.3 (8)
N3—C22—C24	110.47 (19)	N6—C44—C43	123.3 (9)
C23—C22—C24	110.8 (2)	N6—C44—C45	122.9 (8)
O4—Y2—O6	159.28 (11)	C43—C44—C45	113.8 (11)
O4—Y2—O6A	78.51 (11)	N6A—C44A—C43A	122.9 (8)
O4—Y2—N4	77.48 (7)	N6A—C44A—C45A	123.1 (8)
O4—Y2—N5	84.06 (7)	C43A—C44A—C45A	114.0 (10)
O4—Y2—N6	104.11 (12)	N6—C46—C47	114.0 (5)
O4—Y2—N6A	144.98 (12)	N6—C46—C48	114.6 (5)
O5—Y2—O4	108.92 (7)	C48—C46—C47	112.7 (5)
O5—Y2—O6	78.20 (11)	N6A—C46A—C47A	114.4 (5)
O5—Y2—O6A	161.91 (12)	N6A—C46A—C48A	115.4 (5)
O5—Y2—N4	83.40 (7)	C47A—C46A—C48A	112.5 (5)
O5—Y2—N5	76.68 (7)		

Document origin: *publCIF* [Westrip, S. P. (2010). *J. Apply. Cryst.*, **43**, 920-925].

7.2 Crystallographic Data for **2.toluene**

Crystal data

$C_{48}H_{84}Ce_2N_6O_6 \cdot 2(C_7H_8)$	$Z = 1$
$M_r = 1305.71$	$F(000) = 678$
Triclinic, $P\bar{1}$	$D_x = 1.330$ Mg m^{-3}
$a = 9.8443$ (9) Å	Mo $K\alpha$ radiation, l = 0.71073 Å
$b = 13.0661$ (11) Å	Cell parameters from 8356 reflections
$c = 14.2458$ (13) Å	q = 2.4–25.7°
a = 111.195 (3)°	m = 1.43 mm^{-1}
b = 97.658 (3)°	$T = 273$ K
g = 101.563 (3)°	Rod
$V = 1630.8$ (3) Å^3	0.15 × 0.05 × 0.01 mm

Data collection

Bruker APEX-II CCD diffractometer	4960 reflections with $I > 2s(I)$
f and w scans	$R_{int} = 0.065$
Absorption correction: multi-scan *SADABS2016*/2 (Bruker,2016/2) was used for absorption correction. wR2(int) was 0.0979 before and 0.0729 after correction. The Ratio of minimum to maximum transmission is 0.7147. The l/2 correction factor is Not present.	$q_{max} = 25.8°$, $q_{min} = 2.4°$
$T_{min} = 0.533$, $T_{max} = 0.745$	$h = -12$®11
17336 measured reflections	$k = -15$®14
6154 independent reflections	$l = -17$®17

Refinement

Refinement on F^2	Primary atom site location: dual
Least-squares matrix: full	Hydrogen site location: inferred from neighbouring sites
$R[F^2 > 2s(F^2)] = 0.065$	H-atom parameters constrained
$wR(F^2) = 0.180$	$w = 1/[s^2(F_o^2) + (0.1292P)^2]$ where $P = (F_o^2 + 2F_c^2)/3$
$S = 1.03$	$(D/s)_{max} = 0.002$
6154 reflections	$D\rho_{max} = 2.95$ e Å^{-3}
350 parameters	$D\rho_{min} = -2.25$ e Å^{-3}

27 restraints	

Special details

Geometry. All esds (except the esd in the dihedral angle between two l.s. planes) are estimated using the full covariance matrix. The cell esds are taken into account individually in the estimation of esds in distances, angles and torsion angles; correlations between esds in cell parameters are only used when they are defined by crystal symmetry. An approximate (isotropic) treatment of cell esds is used for estimating esds involving l.s. planes.

Fractional atomic coordinates and isotropic or equivalent isotropic displacement parameters (Å^2) for Compound ***2.toluene***

	x	*y*	*z*	U_{iso}*/U_{eq}	Occ. (<1)
Ce1	0.49437 (4)	0.58368 (3)	0.40195 (2)	0.03804 (17)	
O1	0.2967 (5)	0.5197 (4)	0.2662 (4)	0.0517 (12)	
O2	0.6667 (5)	0.7422 (4)	0.5242 (3)	0.0447 (10)	
O3	0.3666 (5)	0.5043 (4)	0.5060 (3)	0.0389 (10)	
N1	0.3191 (6)	0.7138 (5)	0.4510 (4)	0.0455 (13)	
N2	0.6216 (7)	0.7030 (5)	0.3090 (5)	0.0499 (14)	
N3	0.4454 (6)	0.5965 (5)	0.7271 (4)	0.0458 (13)	
C1	0.1073 (10)	0.4771 (9)	0.1255 (6)	0.073 (2)	
H1A	0.162551	0.489718	0.078089	0.109*	
H1B	0.019753	0.497144	0.113993	0.109*	
H1C	0.086768	0.398177	0.114745	0.109*	
C2	0.1890 (8)	0.5487 (7)	0.2333 (5)	0.0536 (18)	
C3	0.1440 (9)	0.6399 (8)	0.2918 (6)	0.060 (2)	
H3	0.063936	0.652023	0.259371	0.072*	
C4	0.2067 (8)	0.7187 (6)	0.3974 (6)	0.0526 (17)	
C5	0.1241 (11)	0.8046 (8)	0.4351 (7)	0.078 (3)	
H5A	0.041951	0.770856	0.453998	0.117*	
H5B	0.094230	0.828281	0.381094	0.117*	
H5C	0.183189	0.869471	0.494115	0.117*	
C6	0.3785 (8)	0.7937 (6)	0.5613 (6)	0.0513 (17)	
H6	0.452658	0.763314	0.585772	0.062*	
C7	0.4569 (10)	0.9121 (6)	0.5740 (7)	0.064 (2)	
H7A	0.526441	0.906337	0.532423	0.095*	
H7B	0.503503	0.956689	0.645217	0.095*	
H7C	0.390221	0.948039	0.552262	0.095*	
C8	0.2753 (9)	0.7931 (7)	0.6317 (6)	0.0583 (19)	

H8A	0.212780	0.838807	0.624327	0.087*	
H8B	0.327604	0.823793	0.702155	0.087*	
H8C	0.220229	0.716322	0.613125	0.087*	
C9	0.8465 (10)	0.9060 (7)	0.6401 (7)	0.075 (2)	
H9A	0.784342	0.926452	0.686134	0.112*	
H9B	0.905524	0.973729	0.639534	0.112*	
H9C	0.905377	0.865473	0.663160	0.112*	
C10	0.7600 (8)	0.8319 (6)	0.5337 (6)	0.0534 (17)	
C11	0.7836 (8)	0.8608 (6)	0.4529 (6)	0.0568 (18)	
H11	0.851859	0.929094	0.470256	0.068*	
C12	0.7185 (8)	0.8012 (6)	0.3466 (6)	0.0544 (18)	
C13	0.7745 (11)	0.8624 (8)	0.2824 (8)	0.078 (3)	
H13A	0.858510	0.841692	0.264077	0.117*	
H13B	0.797401	0.943225	0.321515	0.117*	
H13C	0.703373	0.841402	0.220795	0.117*	
C14	0.5631 (9)	0.6411 (7)	0.1985 (6)	0.0577 (18)	
H14	0.503416	0.567968	0.191643	0.069*	
C15	0.6751 (11)	0.6086 (9)	0.1340 (7)	0.072 (2)	
H15A	0.716759	0.671083	0.117426	0.108*	
H15B	0.629613	0.542702	0.071414	0.108*	
H15C	0.748098	0.592004	0.173430	0.108*	
C16	0.4608 (9)	0.6951 (9)	0.1575 (8)	0.074 (3)	
H16A	0.377238	0.686786	0.184912	0.111*	
H16B	0.434425	0.658219	0.083421	0.111*	
H16C	0.505613	0.774598	0.177958	0.111*	
C17	0.1217 (7)	0.4110 (6)	0.4285 (6)	0.0517 (17)	
H17A	0.147614	0.349591	0.379552	0.077*	
H17B	0.103828	0.463080	0.398125	0.077*	
H17C	0.037328	0.381127	0.447540	0.077*	
C18	0.2399 (7)	0.4721 (5)	0.5223 (5)	0.0408 (14)	
C19	0.2146 (8)	0.4915 (6)	0.6186 (5)	0.0459 (15)	
H19	0.129876	0.448310	0.622627	0.055*	
C20	0.3090 (8)	0.5737 (6)	0.7143 (6)	0.0458 (16)	
C21	0.2320 (9)	0.6340 (7)	0.7951 (6)	0.060 (2)	
H21A	0.292018	0.661393	0.862826	0.091*	
H21B	0.145390	0.581373	0.790526	0.091*	
H21C	0.210263	0.697004	0.782667	0.091*	
C22	0.5370 (9)	0.7005 (6)	0.8136 (5)	0.0544 (18)	

H22	0.483367	0.757871	0.830916	0.065*	
C23	0.6641 (9)	0.7451 (7)	0.7772 (6)	0.064 (2)	
H23A	0.715361	0.688346	0.756923	0.096*	
H23B	0.725266	0.812943	0.832321	0.096*	
H23C	0.632603	0.762293	0.719325	0.096*	
C24	0.5826 (10)	0.6793 (8)	0.9093 (6)	0.068 (2)	
H24A	0.499899	0.649057	0.929688	0.102*	
H24B	0.638002	0.749745	0.964269	0.102*	
H24C	0.638916	0.625745	0.894430	0.102*	
C1S	0.8570 (18)	1.0945 (16)	1.0327 (13)	0.072 (5)*	0.5
C2S	0.965 (2)	1.162 (3)	1.015 (3)	0.149 (14)*	0.5
H2S	1.053532	1.193873	1.060539	0.179*	0.5
C3S	0.939 (3)	1.182 (3)	0.926 (2)	0.125 (11)*	0.5
H3S	1.015479	1.216579	0.905438	0.150*	0.5
C4S	0.802 (3)	1.151 (3)	0.866 (2)	0.129 (10)*	0.5
H4S	0.782999	1.176370	0.813187	0.154*	0.5
C5S	0.698 (2)	1.083 (2)	0.8867 (18)	0.100 (7)*	0.5
H5S	0.607170	1.057549	0.844163	0.119*	0.5
C6S	0.719 (2)	1.050 (3)	0.968 (2)	0.147 (12)*	0.5
H6S	0.646884	1.001452	0.978974	0.176*	0.5
C7S	0.876 (3)	1.063 (4)	1.122 (3)	0.163 (15)*	0.5
H7SA	0.811441	1.089102	1.164627	0.245*	0.5
H7SB	0.972144	1.098526	1.162330	0.245*	0.5
H7SC	0.857209	0.982006	1.098757	0.245*	0.5
C8S	0.849 (2)	1.1341 (18)	0.9540 (15)	0.087 (6)*	0.5
C9S	0.941 (2)	1.138 (3)	1.035 (2)	0.113 (9)*	0.5
H9S	1.036487	1.176684	1.047923	0.136*	0.5
C10S	0.900 (3)	1.086 (4)	1.097 (3)	0.160 (15)*	0.5
H10S	0.966539	1.087587	1.150402	0.192*	0.5
C11S	0.760 (3)	1.033 (3)	1.081 (2)	0.121 (9)*	0.5
H11S	0.732628	0.996077	1.122951	0.145*	0.5
C12S	0.661 (2)	1.032 (3)	1.006 (2)	0.153 (13)*	0.5
H12S	0.564657	1.000509	0.999538	0.184*	0.5
C13S	0.705 (2)	1.080 (3)	0.938 (2)	0.138 (11)*	0.5
H13S	0.638937	1.076307	0.882746	0.166*	0.5
C14S	0.911 (3)	1.197 (3)	0.893 (3)	0.118 (10)*	0.5
H14A	0.971032	1.156958	0.854564	0.177*	0.5
H14B	0.966925	1.272425	0.939408	0.177*	0.5

H14C	0.835845	1.202154	0.846219	0.177*	0.5

*Atomic displacement parameters (Å^2) for Compound **2.toluene***

	U^{11}	U^{22}	U^{33}	U^{12}	U^{13}	U^{23}
Ce1	0.0452 (3)	0.0346 (2)	0.0435 (2)	0.02044 (17)	0.01080 (16)	0.02041 (16)
O1	0.050 (3)	0.057 (3)	0.056 (3)	0.020 (2)	0.011 (2)	0.028 (2)
O2	0.049 (3)	0.035 (2)	0.054 (3)	0.015 (2)	0.013 (2)	0.019 (2)
O3	0.040 (2)	0.038 (2)	0.048 (2)	0.0204 (19)	0.0114 (19)	0.0224 (19)
N1	0.050 (3)	0.038 (3)	0.060 (3)	0.022 (3)	0.014 (3)	0.025 (3)
N2	0.064 (4)	0.044 (3)	0.059 (3)	0.028 (3)	0.024 (3)	0.029 (3)
N3	0.058 (4)	0.040 (3)	0.047 (3)	0.020 (3)	0.014 (3)	0.020 (2)
C1	0.062 (5)	0.092 (7)	0.064 (5)	0.023 (5)	0.007 (4)	0.033 (5)
C2	0.052 (4)	0.074 (5)	0.052 (4)	0.030 (4)	0.013 (3)	0.037 (4)
C3	0.058 (5)	0.071 (5)	0.065 (5)	0.030 (4)	0.009 (4)	0.038 (4)
C4	0.058 (4)	0.051 (4)	0.069 (4)	0.028 (4)	0.020 (4)	0.037 (4)
C5	0.090 (7)	0.068 (5)	0.093 (6)	0.054 (5)	0.015 (5)	0.034 (5)
C6	0.052 (4)	0.040 (4)	0.069 (4)	0.020 (3)	0.016 (3)	0.026 (3)
C7	0.076 (5)	0.044 (4)	0.082 (5)	0.023 (4)	0.031 (4)	0.028 (4)
C8	0.073 (5)	0.046 (4)	0.065 (5)	0.028 (4)	0.026 (4)	0.024 (3)
C9	0.070 (6)	0.051 (5)	0.085 (6)	-0.002 (4)	0.002 (5)	0.021 (4)
C10	0.048 (4)	0.038 (4)	0.078 (5)	0.018 (3)	0.012 (3)	0.025 (3)
C11	0.059 (5)	0.039 (4)	0.080 (5)	0.018 (3)	0.022 (4)	0.028 (4)
C12	0.058 (5)	0.044 (4)	0.078 (5)	0.027 (4)	0.025 (4)	0.033 (4)
C13	0.079 (6)	0.065 (6)	0.108 (7)	0.018 (5)	0.034 (5)	0.050 (5)
C14	0.068 (5)	0.057 (4)	0.062 (4)	0.022 (4)	0.019 (4)	0.035 (4)
C15	0.087 (7)	0.082 (6)	0.072 (5)	0.042 (5)	0.038 (5)	0.040 (5)
C16	0.061 (5)	0.106 (7)	0.106 (7)	0.046 (5)	0.033 (5)	0.083 (6)
C17	0.042 (4)	0.052 (4)	0.064 (4)	0.020 (3)	0.008 (3)	0.023 (3)
C18	0.042 (4)	0.037 (3)	0.056 (4)	0.024 (3)	0.013 (3)	0.024 (3)
C19	0.047 (4)	0.040 (3)	0.065 (4)	0.023 (3)	0.021 (3)	0.029 (3)
C20	0.056 (4)	0.040 (3)	0.060 (4)	0.026 (3)	0.025 (3)	0.030 (3)
C21	0.074 (5)	0.056 (4)	0.068 (5)	0.036 (4)	0.036 (4)	0.027 (4)
C22	0.071 (5)	0.040 (4)	0.050 (4)	0.019 (4)	0.011 (3)	0.014 (3)
C23	0.071 (5)	0.051 (4)	0.058 (4)	-0.002 (4)	0.002 (4)	0.022 (3)
C24	0.085 (6)	0.067 (5)	0.051 (4)	0.019 (5)	0.009 (4)	0.024 (4)

*Geometric parameters (Å, º) for Compound **2.toluene***

Ce1—Ce1^{i}	4.1270 (7)	C16—H16A	0.9600
Ce1—O1	2.323 (5)	C16—H16B	0.9600
Ce1—O2	2.323 (4)	C16—H16C	0.9600
Ce1—O3	2.437 (4)	C17—H17A	0.9600
Ce1—O3^{i}	2.482 (4)	C17—H17B	0.9600
Ce1—N1	2.645 (5)	C17—H17C	0.9600
Ce1—N2	2.627 (6)	C17—C18	1.489 (9)
Ce1—N3^{i}	2.645 (5)	C18—C19	1.369 (9)
O1—C2	1.283 (8)	C19—H19	0.9300
O2—C10	1.287 (9)	C19—C20	1.442 (11)
O3—C18	1.313 (8)	C20—C21	1.529 (10)
N1—C4	1.285 (9)	C21—H21A	0.9600
N1—C6	1.491 (9)	C21—H21B	0.9600
N2—C12	1.312 (10)	C21—H21C	0.9600
N2—C14	1.454 (10)	C22—H22	0.9800
N3—C20	1.288 (9)	C22—C23	1.508 (11)
N3—C22	1.476 (9)	C22—C24	1.515 (11)
C1—H1A	0.9600	C23—H23A	0.9600
C1—H1B	0.9600	C23—H23B	0.9600
C1—H1C	0.9600	C23—H23C	0.9600
C1—C2	1.488 (11)	C24—H24A	0.9600
C2—C3	1.379 (12)	C24—H24B	0.9600
C3—H3	0.9300	C24—H24C	0.9600
C3—C4	1.443 (12)	C1S—C2S	1.355 (18)
C4—C5	1.502 (10)	C1S—C6S	1.412 (17)
C5—H5A	0.9600	C1S—C7S	1.476 (19)
C5—H5B	0.9600	C2S—H2S	0.9300
C5—H5C	0.9600	C2S—C3S	1.386 (18)
C6—H6	0.9800	C3S—H3S	0.9300
C6—C7	1.518 (10)	C3S—C4S	1.393 (19)
C6—C8	1.521 (10)	C4S—H4S	0.9300
C7—H7A	0.9600	C4S—C5S	1.359 (18)
C7—H7B	0.9600	C5S—H5S	0.9300
C7—H7C	0.9600	C5S—C6S	1.374 (19)
C8—H8A	0.9600	C6S—H6S	0.9300
C8—H8B	0.9600	C7S—H7SA	0.9600
C8—H8C	0.9600	C7S—H7SB	0.9600
C9—H9A	0.9600	C7S—H7SC	0.9600

C9—H9B	0.9600	C8S—C9S	1.346 (17)
C9—H9C	0.9600	C8S—C13S	1.403 (18)
C9—C10	1.492 (11)	C8S—C14S	1.504 (18)
C10—C11	1.370 (11)	C9S—H9S	0.9300
C11—H11	0.9300	C9S—C10S	1.347 (16)
C11—C12	1.413 (11)	C10S—H10S	0.9300
C12—C13	1.505 (11)	C10S—C11S	1.360 (16)
C13—H13A	0.9600	C11S—H11S	0.9300
C13—H13B	0.9600	C11S—C12S	1.344 (16)
C13—H13C	0.9600	C12S—H12S	0.9300
C14—H14	0.9800	C12S—C13S	1.402 (18)
C14—C15	1.554 (11)	C13S—H13S	0.9300
C14—C16	1.510 (10)	C14S—H14A	0.9600
C15—H15A	0.9600	C14S—H14B	0.9600
C15—H15B	0.9600	C14S—H14C	0.9600
C15—H15C	0.9600		
O1—Ce1—Ce1^{i}	118.34 (12)	C15—C14—H14	104.5
O1—Ce1—O3	93.87 (16)	C16—C14—H14	104.5
O1—Ce1—O3^{i}	136.32 (16)	C16—C14—C15	115.4 (7)
O1—Ce1—N1	70.09 (17)	C14—C15—H15A	109.5
O1—Ce1—N2	87.14 (18)	C14—C15—H15B	109.5
O1—Ce1—N3^{i}	80.38 (17)	C14—C15—H15C	109.5
O2—Ce1—Ce1^{i}	90.89 (11)	H15A—C15—H15B	109.5
O2—Ce1—O1	145.45 (16)	H15A—C15—H15C	109.5
O2—Ce1—O3^{i}	78.23 (15)	H15B—C15—H15C	109.5
O2—Ce1—O3	103.53 (15)	C14—C16—H16A	109.5
O2—Ce1—N1	84.41 (17)	C14—C16—H16B	109.5
O2—Ce1—N2	70.72 (18)	C14—C16—H16C	109.5
O2—Ce1—N3^{i}	123.39 (17)	H16A—C16—H16B	109.5
O3^{i}—Ce1—Ce1^{i}	32.62 (10)	H16A—C16—H16C	109.5
O3—Ce1—Ce1^{i}	33.30 (9)	H16B—C16—H16C	109.5
O3—Ce1—O3^{i}	65.91 (16)	H17A—C17—H17B	109.5
O3^{i}—Ce1—N1	134.54 (16)	H17A—C17—H17C	109.5
O3—Ce1—N1	78.16 (15)	H17B—C17—H17C	109.5
O3—Ce1—N2	169.80 (15)	C18—C17—H17A	109.5
O3^{i}—Ce1—N2	119.61 (17)	C18—C17—H17B	109.5
O3—Ce1—N3^{i}	102.11 (16)	C18—C17—H17C	109.5

O3^{i}—Ce1—N3^{i}	67.88 (15)	O3—C18—C17	116.0 (6)
N1—Ce1—Ce1^{i}	107.50 (12)	O3—C18—C19	123.4 (6)
N2—Ce1—Ce1^{i}	151.42 (13)	C19—C18—C17	120.6 (6)
N2—Ce1—N1	92.69 (17)	C18—C19—H19	117.4
N2—Ce1—N3^{i}	88.07 (17)	C18—C19—C20	125.1 (7)
N3^{i}—Ce1—Ce1^{i}	84.11 (12)	C20—C19—H19	117.4
N3^{i}—Ce1—N1	150.37 (18)	N3—C20—C19	122.1 (6)
C2—O1—Ce1	142.0 (5)	N3—C20—C21	124.1 (7)
C10—O2—Ce1	142.1 (5)	C19—C20—C21	113.7 (6)
C18—O3—Ce1^{i}	100.9 (3)	C20—C21—H21A	109.5
C4—N1—Ce1	131.8 (5)	C20—C21—H21B	109.5
C4—N1—C6	121.9 (6)	C20—C21—H21C	109.5
C6—N1—Ce1	106.2 (4)	H21A—C21—H21B	109.5
C12—N2—Ce1	131.0 (5)	H21A—C21—H21C	109.5
C12—N2—C14	121.5 (6)	H21B—C21—H21C	109.5
C14—N2—Ce1	107.5 (4)	N3—C22—H22	108.4
C20—N3—Ce1^{i}	107.5 (4)	N3—C22—C23	108.0 (6)
C20—N3—C22	120.2 (6)	N3—C22—C24	112.4 (6)
C22—N3—Ce1^{i}	131.6 (5)	C23—C22—H22	108.4
H1A—C1—H1B	109.5	C23—C22—C24	111.1 (7)
H1A—C1—H1C	109.5	C24—C22—H22	108.4
H1B—C1—H1C	109.5	C22—C23—H23A	109.5
C2—C1—H1A	109.5	C22—C23—H23B	109.5
C2—C1—H1B	109.5	C22—C23—H23C	109.5
C2—C1—H1C	109.5	H23A—C23—H23B	109.5
O1—C2—C1	116.9 (7)	H23A—C23—H23C	109.5
O1—C2—C3	124.3 (7)	H23B—C23—H23C	109.5
C3—C2—C1	118.8 (7)	C22—C24—H24A	109.5
C2—C3—H3	116.2	C22—C24—H24B	109.5
C2—C3—C4	127.5 (7)	C22—C24—H24C	109.5
C4—C3—H3	116.2	H24A—C24—H24B	109.5
N1—C4—C3	123.1 (7)	H24A—C24—H24C	109.5
N1—C4—C5	125.3 (7)	H24B—C24—H24C	109.5
C3—C4—C5	111.6 (7)	C2S—C1S—C6S	122 (2)
C4—C5—H5A	109.5	C2S—C1S—C7S	121.8 (15)
C4—C5—H5B	109.5	C6S—C1S—C7S	115.9 (14)
C4—C5—H5C	109.5	C1S—C2S—H2S	121.1
H5A—C5—H5B	109.5	C1S—C2S—C3S	118 (2)

H5A—C5—H5C	109.5	C3S—C2S—H2S	121.1
H5B—C5—H5C	109.5	C2S—C3S—H3S	119.2
N1—C6—H6	104.6	C2S—C3S—C4S	122 (2)
N1—C6—C7	113.0 (6)	C4S—C3S—H3S	119.2
N1—C6—C8	114.7 (6)	C3S—C4S—H4S	121.3
C7—C6—H6	104.6	C5S—C4S—C3S	117 (2)
C7—C6—C8	114.0 (6)	C5S—C4S—H4S	121.3
C8—C6—H6	104.6	C4S—C5S—H5S	118.3
C6—C7—H7A	109.5	C4S—C5S—C6S	123 (2)
C6—C7—H7B	109.5	C6S—C5S—H5S	118.3
C6—C7—H7C	109.5	C1S—C6S—H6S	121.7
H7A—C7—H7B	109.5	C5S—C6S—C1S	117 (2)
H7A—C7—H7C	109.5	C5S—C6S—H6S	121.7
H7B—C7—H7C	109.5	C1S—C7S—H7SA	109.5
C6—C8—H8A	109.5	C1S—C7S—H7SB	109.5
C6—C8—H8B	109.5	C1S—C7S—H7SC	109.5
C6—C8—H8C	109.5	H7SA—C7S—H7SB	109.5
H8A—C8—H8B	109.5	H7SA—C7S—H7SC	109.5
H8A—C8—H8C	109.5	H7SB—C7S—H7SC	109.5
H8B—C8—H8C	109.5	C9S—C8S—C13S	118.5 (8)
H9A—C9—H9B	109.5	C9S—C8S—C14S	116 (2)
H9A—C9—H9C	109.5	C13S—C8S—C14S	126 (2)
H9B—C9—H9C	109.5	C8S—C9S—H9S	119.0
C10—C9—H9A	109.5	C8S—C9S—C10S	122.1 (9)
C10—C9—H9B	109.5	C10S—C9S—H9S	119.0
C10—C9—H9C	109.5	C9S—C10S—H10S	120.2
O2—C10—C9	116.4 (7)	C9S—C10S—C11S	119.5 (9)
O2—C10—C11	123.9 (7)	C11S—C10S—H10S	120.2
C11—C10—C9	119.7 (7)	C10S—C11S—H11S	119.1
C10—C11—H11	115.5	C12S—C11S—C10S	121.8 (9)
C10—C11—C12	128.9 (7)	C12S—C11S—H11S	119.1
C12—C11—H11	115.5	C11S—C12S—H12S	120.8
N2—C12—C11	123.2 (7)	C11S—C12S—C13S	118.5 (9)
N2—C12—C13	124.4 (8)	C13S—C12S—H12S	120.8
C11—C12—C13	112.4 (7)	C8S—C13S—H13S	120.3
C12—C13—H13A	109.5	C12S—C13S—C8S	119.4 (8)
C12—C13—H13B	109.5	C12S—C13S—H13S	120.3
C12—C13—H13C	109.5	C8S—C14S—H14A	109.5

H13A—C13—H13B	109.5	C8S—C14S—H14B	109.5
H13A—C13—H13C	109.5	C8S—C14S—H14C	109.5
H13B—C13—H13C	109.5	H14A—C14S—H14B	109.5
N2—C14—H14	104.5	H14A—C14S—H14C	109.5
N2—C14—C15	114.5 (7)	H14B—C14S—H14C	109.5
N2—C14—C16	112.0 (7)		

Symmetry code: (i) -*x*+1, -*y*+1, -*z*+1.

Document origin: *publCIF* [Westrip, S. P. (2010). *J. Apply. Cryst.*, **43**, 920-925].

7.3 Crystallographic Data for **2.thf**

Crystal data

$C_{24}H_{42}CeN_3O_3$	$F(000)$ = 1156
M_r = 560.72	D_x = 1.197 Mg m^{-3}
Monoclinic, $P2_1/c$	Mo $K\alpha$ radiation, l = 0.71073 Å
a = 11.7780 (6) Å	Cell parameters from 9914 reflections
b = 29.0339 (17) Å	q = 2.4–28.3°
c = 9.9198 (5) Å	m = 1.49 mm^{-1}
b = 113.507 (2)°	T = 150 K
V = 3110.7 (3) Å^3	Plate, yellow
Z = 4	0.12 × 0.09 × 0.02 mm

Data collection

Bruker D8 VENTURE diffractometer	7719 independent reflections
Radiation source: microfocus sealed tube, INCOATEC Ims 3.0	4728 reflections with $I > 2s(I)$
Multilayer mirror optics monochromator	R_{int} = 0.099
Detector resolution: 7.4074 pixels mm^{-1}	q_{max} = 28.3°, q_{min} = 2.4°
f and w scans	h = -15®13
Absorption correction: multi-scan *SADABS2016*/2 (Bruker,2016/2) was used for absorption correction. wR2(int) was 0.1492 before and 0.0810 after correction. The Ratio of minimum to maximum transmission is 0.8289. The l/2 correction factor is Not present.	k = -38®38
T_{min} = 0.618, T_{max} = 0.746	l = -13®13
37554 measured reflections	

Refinement

Refinement on F^2	Hydrogen site location: inferred from neighbouring sites
Least-squares matrix: full	H-atom parameters constrained
$R[F^2 > 2s(F^2)]$ = 0.068	$w = 1/[s^2(F_o^2) + (0.0461P)^2 + 9.968P]$ where $P = (F_o^2 + 2F_c^2)/3$
$wR(F^2)$ = 0.163	$(D/s)_{max}$ = 0.001
S = 1.04	$D\tilde{n}_{max}$ = 1.59 e Å^{-3}

7719 reflections	$D\tilde{n}_{min}$ = -0.97 e Å^{-3}
302 parameters	Extinction correction: *SHELXL2018*/3 (Sheldrick 2018), $Fc^{*}=kFc[1+0.001xFc^{2}l^{3}/\sin(2q)]^{-1/4}$
12 restraints	Extinction coefficient: 0.0027 (3)

Special details

Geometry. All esds (except the esd in the dihedral angle between two l.s. planes) are estimated using the full covariance matrix. The cell esds are taken into account individually in the estimation of esds in distances, angles and torsion angles; correlations between esds in cell parameters are only used when they are defined by crystal symmetry. An approximate (isotropic) treatment of cell esds is used for estimating esds involving l.s. planes.
Refinement. One iPr group modelled over two partially occupied sites with occupancy 0.666/0.333. Minor component is modelled with isotropic adps. Distance restraints to C—C distances and adp similarity restraints applied. SQUEEZE used to account for a highly disordered THF molecule (two per dimer).

*Fractional atomic coordinates and isotropic or equivalent isotropic displacement parameters (Å^2) for Compound **2.thf***

	x	*y*	*z*	U_{iso}*/U_{eq}	Occ. (<1)
Ce1	0.49541 (3)	0.07128 (2)	0.98941 (3)	0.04917 (17)	
O1	0.6902 (4)	0.07459 (19)	1.1828 (4)	0.0593 (13)	
O2	0.4938 (4)	0.00102 (16)	1.1324 (4)	0.0488 (11)	
O3	0.3578 (4)	0.10488 (19)	0.7731 (4)	0.0574 (13)	
N1	0.5237 (5)	0.1524 (2)	1.1152 (6)	0.0555 (15)	
N2	0.2853 (5)	0.0627 (2)	1.0278 (6)	0.0498 (14)	
N3	0.6139 (5)	0.0976 (3)	0.8234 (7)	0.0655 (18)	
C1	0.8840 (7)	0.0829 (3)	1.3845 (9)	0.085 (3)	
H1A	0.871805	0.055933	1.436580	0.128*	
H1B	0.930624	0.106443	1.456074	0.128*	
H1C	0.930192	0.073921	1.325618	0.128*	
C2	0.7588 (6)	0.1023 (3)	1.2843 (7)	0.059 (2)	
C3	0.7298 (6)	0.1465 (3)	1.3040 (8)	0.068 (2)	
H3	0.791209	0.163158	1.381268	0.082*	
C4	0.6180 (7)	0.1706 (3)	1.2223 (8)	0.066 (2)	
C5	0.6204 (8)	0.2205 (3)	1.2743 (10)	0.087 (3)	
H5A	0.554481	0.238072	1.198817	0.131*	
H5B	0.700770	0.234360	1.291317	0.131*	
H5C	0.607342	0.220814	1.365845	0.131*	
C6	0.4069 (7)	0.1778 (3)	1.0393 (8)	0.064 (2)	

H6	0.348868	0.154824	0.971096	0.077*	
C7	0.4229 (10)	0.2152 (3)	0.9387 (10)	0.095 (3)	
H7A	0.453789	0.243526	0.995419	0.142*	
H7B	0.342941	0.221367	0.857753	0.142*	
H7C	0.482279	0.204678	0.898749	0.142*	
C8	0.3426 (7)	0.1941 (3)	1.1373 (9)	0.080 (3)	
H8A	0.343942	0.169322	1.205130	0.121*	
H8B	0.256640	0.202291	1.076151	0.121*	
H8C	0.385987	0.221079	1.193700	0.121*	
C9	0.6130 (7)	-0.0001 (3)	1.3904 (7)	0.064 (2)	
H9A	0.599249	-0.033098	1.398113	0.096*	
H9B	0.617198	0.015568	1.479796	0.096*	
H9C	0.691041	0.004465	1.378729	0.096*	
C10	0.5077 (6)	0.0196 (3)	1.2591 (6)	0.0530 (18)	
C11	0.4328 (6)	0.0524 (3)	1.2752 (7)	0.0557 (19)	
H11	0.462191	0.068549	1.366118	0.067*	
C12	0.3120 (6)	0.0654 (3)	1.1672 (7)	0.0524 (18)	
C13	0.2170 (8)	0.0777 (3)	1.2322 (9)	0.077 (3)	
H13A	0.160112	0.101259	1.170812	0.115*	
H13B	0.260349	0.089670	1.332147	0.115*	
H13C	0.170038	0.050139	1.234871	0.115*	
C14	0.1523 (6)	0.0642 (3)	0.9216 (8)	0.062 (2)	
H14	0.099920	0.052025	0.971787	0.075*	
C15	0.1099 (7)	0.1125 (3)	0.8682 (8)	0.074 (2)	
H15A	0.124482	0.132646	0.952769	0.110*	
H15B	0.021293	0.112133	0.804912	0.110*	
H15C	0.156341	0.124021	0.812338	0.110*	
C16	0.1391 (7)	0.0322 (3)	0.7939 (8)	0.072 (2)	
H16A	0.184480	0.045158	0.738660	0.108*	
H16B	0.051370	0.029180	0.728869	0.108*	
H16C	0.173000	0.001883	0.832354	0.108*	
C17	0.2261 (9)	0.1462 (4)	0.5643 (9)	0.102 (4)	
H17A	0.169452	0.120081	0.527101	0.153*	
H17B	0.231139	0.163192	0.481519	0.153*	
H17C	0.195356	0.166679	0.620792	0.153*	
C18	0.3526 (8)	0.1288 (3)	0.6619 (8)	0.066 (2)	
C19	0.4544 (9)	0.1379 (3)	0.6288 (9)	0.078 (3)	
H19	0.439391	0.156475	0.544482	0.094*	

C20	0.5780 (8)	0.1228 (3)	0.7061 (9)	0.072 (2)	
C21	0.6645 (11)	0.1389 (4)	0.6315 (12)	0.122 (4)	
H21A	0.750679	0.132438	0.696611	0.183*	
H21B	0.653996	0.172075	0.612268	0.183*	
H21C	0.643354	0.122359	0.538540	0.183*	
C22	0.7421 (8)	0.0735 (5)	0.9021 (10)	0.065 (5)	0.6667
H22	0.732838	0.051224	0.973889	0.078*	0.6667
C24	0.8399 (11)	0.1087 (5)	0.9918 (13)	0.067 (4)	0.6667
H24A	0.853389	0.130907	0.925217	0.100*	0.6667
H24B	0.917757	0.092755	1.048681	0.100*	0.6667
H24C	0.811283	0.124987	1.058979	0.100*	0.6667
C22A	0.7546 (12)	0.0861 (9)	0.887 (3)	0.076 (13)*	0.3333
H22A	0.760955	0.068950	0.976721	0.091*	0.3333
C23	0.7856 (8)	0.0467 (3)	0.8047 (10)	0.088 (3)	
H23A	0.722373	0.024080	0.749437	0.132*	0.6667
H23B	0.862583	0.030671	0.864310	0.132*	0.6667
H23C	0.800619	0.067588	0.735970	0.132*	0.6667
H23D	0.709530	0.030193	0.744832	0.132*	0.3333
H23E	0.843435	0.025419	0.875888	0.132*	0.3333
H23F	0.823698	0.059206	0.740902	0.132*	0.3333
C24A	0.813 (3)	0.1321 (9)	0.959 (4)	0.087 (13)*	0.3333
H24D	0.789848	0.156379	0.884160	0.131*	0.3333
H24E	0.903603	0.128944	1.003135	0.131*	0.3333
H24F	0.783606	0.140076	1.035162	0.131*	0.3333

*Atomic displacement parameters (Å^2) for Compound **2.thf***

	U^{11}	U^{22}	U^{33}	U^{12}	U^{13}	U^{23}
Ce1	0.0342 (2)	0.0876 (3)	0.02844 (19)	-0.0077 (2)	0.01537 (14)	-0.00779 (18)
O1	0.037 (2)	0.106 (4)	0.032 (2)	-0.010 (3)	0.0114 (19)	-0.011 (2)
O2	0.044 (2)	0.082 (3)	0.0248 (19)	-0.002 (2)	0.0177 (18)	-0.008 (2)
O3	0.041 (3)	0.102 (4)	0.034 (2)	0.001 (3)	0.020 (2)	0.002 (2)
N1	0.046 (3)	0.089 (5)	0.039 (3)	-0.014 (3)	0.025 (3)	-0.011 (3)
N2	0.031 (3)	0.077 (4)	0.048 (3)	-0.007 (3)	0.023 (2)	-0.005 (3)
N3	0.040 (3)	0.116 (6)	0.049 (3)	-0.019 (3)	0.028 (3)	-0.019 (4)
C1	0.057 (5)	0.116 (8)	0.065 (5)	-0.008 (5)	0.005 (4)	-0.023 (5)
C2	0.036 (4)	0.111 (7)	0.033 (3)	-0.013 (4)	0.015 (3)	-0.014 (4)
C3	0.037 (4)	0.114 (7)	0.052 (4)	-0.023 (4)	0.016 (3)	-0.031 (4)

C4	0.053 (5)	0.101 (7)	0.055 (4)	-0.018 (4)	0.035 (4)	-0.020 (4)
C5	0.073 (6)	0.110 (8)	0.090 (6)	-0.038 (5)	0.044 (5)	-0.043 (6)
C6	0.055 (5)	0.087 (6)	0.053 (4)	-0.005 (4)	0.024 (4)	-0.008 (4)
C7	0.132 (9)	0.086 (7)	0.072 (6)	-0.007 (6)	0.047 (6)	0.012 (5)
C8	0.057 (5)	0.109 (8)	0.082 (6)	0.000 (5)	0.035 (5)	-0.005 (5)
C9	0.057 (4)	0.106 (6)	0.031 (3)	-0.003 (5)	0.018 (3)	-0.012 (4)
C10	0.047 (4)	0.089 (5)	0.028 (3)	-0.010 (4)	0.021 (3)	-0.006 (3)
C11	0.046 (4)	0.094 (6)	0.035 (3)	-0.008 (4)	0.024 (3)	-0.012 (3)
C12	0.044 (4)	0.076 (5)	0.044 (3)	-0.005 (3)	0.025 (3)	-0.006 (3)
C13	0.066 (5)	0.114 (8)	0.070 (5)	-0.002 (5)	0.048 (4)	-0.024 (5)
C14	0.022 (3)	0.106 (7)	0.059 (4)	-0.008 (4)	0.017 (3)	-0.007 (4)
C15	0.044 (4)	0.120 (8)	0.061 (5)	0.013 (5)	0.025 (4)	0.009 (5)
C16	0.042 (4)	0.107 (7)	0.055 (4)	-0.001 (4)	0.006 (3)	-0.009 (4)
C17	0.098 (7)	0.161 (10)	0.048 (5)	0.050 (7)	0.031 (5)	0.016 (5)
C18	0.068 (5)	0.093 (6)	0.040 (4)	0.004 (5)	0.027 (4)	-0.006 (4)
C19	0.103 (7)	0.097 (7)	0.052 (4)	-0.007 (6)	0.049 (5)	-0.001 (4)
C20	0.072 (6)	0.098 (7)	0.063 (5)	-0.019 (5)	0.044 (5)	-0.017 (5)
C21	0.149 (10)	0.155 (11)	0.119 (8)	-0.053 (8)	0.112 (8)	-0.026 (7)
C22	0.036 (6)	0.137 (12)	0.027 (5)	-0.047 (7)	0.019 (4)	-0.018 (6)
C24	0.053 (7)	0.109 (12)	0.049 (6)	-0.032 (8)	0.031 (6)	-0.030 (8)
C23	0.063 (6)	0.126 (9)	0.079 (6)	-0.013 (6)	0.032 (5)	-0.011 (6)

*Geometric parameters (Å, º) for Compound **2.thf***

Ce1—Ce1^{i}	4.1437 (9)	C2—C3	1.361 (11)
Ce1—O1	2.333 (4)	C3—C4	1.425 (11)
Ce1—O2	2.489 (5)	C4—C5	1.533 (11)
Ce1—O2^{i}	2.451 (4)	C6—C7	1.538 (11)
Ce1—O3	2.326 (4)	C6—C8	1.526 (10)
Ce1—N1	2.624 (6)	C9—C10	1.508 (10)
Ce1—N2	2.661 (5)	C10—C11	1.351 (10)
Ce1—N3	2.661 (6)	C11—C12	1.448 (9)
Ce1—C10	3.020 (6)	C12—C13	1.540 (9)
O1—C2	1.291 (8)	C14—C15	1.511 (11)
O2—C10	1.315 (7)	C14—C16	1.527 (10)
O3—C18	1.284 (8)	C17—C18	1.504 (11)
N1—C4	1.304 (9)	C18—C19	1.389 (11)
N1—C6	1.475 (9)	C19—C20	1.417 (12)

N2—C12	1.293 (8)	C20—C21	1.550 (11)
N2—C14	1.500 (8)	C22—C24	1.532 (12)
N3—C20	1.294 (10)	C22—C23	1.482 (10)
N3—C22	1.562 (11)	C22A—C23	1.528 (17)
N3—C22A	1.557 (13)	C22A—C24A	1.542 (18)
C1—C2	1.519 (10)		
O1—Ce1—Ce1^{i}	90.13 (13)	C12—N2—Ce1	107.7 (4)
O1—Ce1—O2^{i}	102.31 (16)	C12—N2—C14	119.3 (5)
O1—Ce1—O2	78.10 (16)	C14—N2—Ce1	131.8 (4)
O1—Ce1—N1	71.05 (18)	C20—N3—Ce1	130.9 (5)
O1—Ce1—N2	123.51 (16)	C20—N3—C22	127.4 (7)
O1—Ce1—N3	84.85 (17)	C20—N3—C22A	113.4 (15)
O1—Ce1—C10	66.93 (17)	C22—N3—Ce1	101.7 (6)
O2^{i}—Ce1—Ce1^{i}	33.28 (10)	C22A—N3—Ce1	115.2 (14)
O2—Ce1—Ce1^{i}	32.70 (9)	O1—C2—C1	114.9 (7)
O2^{i}—Ce1—O2	65.99 (14)	O1—C2—C3	125.8 (7)
O2—Ce1—N1	119.53 (15)	C3—C2—C1	119.2 (7)
O2^{i}—Ce1—N1	169.03 (15)	C2—C3—C4	127.5 (7)
O2^{i}—Ce1—N2	102.97 (16)	N1—C4—C3	123.9 (8)
O2—Ce1—N2	67.82 (16)	N1—C4—C5	123.5 (8)
O2—Ce1—N3	135.55 (19)	C3—C4—C5	112.6 (7)
O2^{i}—Ce1—N3	78.34 (18)	N1—C6—C7	110.7 (7)
O2^{i}—Ce1—C10	91.01 (18)	N1—C6—C8	115.4 (6)
O2—Ce1—C10	25.36 (16)	C8—C6—C7	114.5 (8)
O3—Ce1—Ce1^{i}	117.41 (13)	O2—C10—Ce1	54.2 (3)
O3—Ce1—O1	146.75 (18)	O2—C10—C9	114.6 (6)
O3—Ce1—O2	135.12 (16)	O2—C10—C11	124.3 (6)
O3—Ce1—O2^{i}	93.35 (16)	C9—C10—Ce1	133.3 (5)
O3—Ce1—N1	88.38 (18)	C11—C10—Ce1	87.2 (4)
O3—Ce1—N2	79.95 (16)	C11—C10—C9	121.0 (6)
O3—Ce1—N3	69.69 (18)	C10—C11—C12	126.2 (6)
O3—Ce1—C10	142.68 (17)	N2—C12—C11	121.6 (6)
N1—Ce1—Ce1^{i}	151.26 (12)	N2—C12—C13	123.7 (6)
N1—Ce1—N2	88.01 (17)	C11—C12—C13	114.5 (6)
N1—Ce1—N3	92.16 (19)	N2—C14—C15	112.4 (6)
N1—Ce1—C10	94.17 (18)	N2—C14—C16	107.3 (6)
N2—Ce1—Ce1^{i}	84.60 (13)	C15—C14—C16	111.3 (7)

N2—Ce1—C10	62.98 (18)	O3—C18—C17	115.5 (7)
N3—Ce1—Ce1^{i}	108.02 (16)	O3—C18—C19	123.8 (8)
N3—Ce1—N2	149.62 (18)	C19—C18—C17	120.7 (8)
N3—Ce1—C10	147.1 (2)	C18—C19—C20	127.6 (8)
C10—Ce1—Ce1^{i}	57.83 (14)	N3—C20—C19	123.9 (7)
C2—O1—Ce1	140.5 (5)	N3—C20—C21	123.9 (9)
Ce1^{i}—O2—Ce1	114.01 (14)	C19—C20—C21	112.2 (8)
C10—O2—Ce1	100.5 (4)	C24—C22—N3	110.1 (11)
C10—O2—Ce1^{i}	144.2 (5)	C23—C22—N3	115.3 (7)
C18—O3—Ce1	142.8 (5)	C23—C22—C24	110.7 (9)
C4—N1—Ce1	131.0 (6)	C23—C22A—N3	112.9 (12)
C4—N1—C6	122.1 (7)	C23—C22A—C24A	137 (2)
C6—N1—Ce1	106.8 (4)	C24A—C22A—N3	102.0 (17)

Symmetry code: (i) -*x*+1, -*y*, -*z*+2.

Document origin: *publCIF* [Westrip, S. P. (2010). *J. Apply. Cryst.*, **43**, 920-925].